



Rochester Institute of Technology

Golisano Institute for Sustainability
190 Lomb Memorial Drive
Rochester, New York 14623-5608

September 28, 2017

Jeffrey A. Bradel
ONR Code 30
Office of Naval Research
875 North Randolph Street
Arlington, VA 22203-1995

RE: N00014-14-1-0789 Final Report

Dear Mr. Bradel:

The Golisano Institute for Sustainability at Rochester Institute of Technology is pleased to submit the Final Technical Report with SF298 for the "Technology Insertion for Recapitalization of Legacy Systems" project under award number N00014-14-1-0789.

If you have any technical questions regarding this report, the Principle Investigator, Dr. Nabil Nasr, can be reached at (585) 475-5106 or via email at nasr@rit.edu. For administrative or contracting inquiries, I can be reached at (585) 475-4325 or kxkasp@rit.edu.

Sincerely,

A handwritten signature in black ink, reading "Kathleen Kosciolk". The signature is written in a cursive, flowing style.

Kathleen Kosciolk
Assistant Director for Program Administration

cc: Administrative Office - ONR REG BOSTON N62879
Defense Technical Information Center
Naval Research Laboratory
File

Enclosures: RIT N00014-14-1-0789 Final Technical Report with SF298

REPORT DOCUMENTATION PAGE

Form Approved
OMB No. 0704-0188

The public reporting burden for this collection of information is estimated to average 1 hour per response, including the time for reviewing instructions, searching existing data sources, gathering and maintaining the data needed, and completing and reviewing the collection of information. Send comments regarding this burden estimate or any other aspect of this collection of information, including suggestions for reducing the burden, to Department of Defense, Washington Headquarters Services, Directorate for Information Operations and Reports (0704-0188), 1215 Jefferson Davis Highway, Suite 1204, Arlington, VA 22202-4302. Respondents should be aware that notwithstanding any other provision of law, no person shall be subject to any penalty for failing to comply with a collection of information if it does not display a currently valid OMB control number.

1. REPORT DATE (DD-MM-YYYY) 28-09-2017			2. REPORT TYPE Final		3. DATES COVERED (From - To) 01-07-2014 - 28-09-2017	
4. TITLE AND SUBTITLE Technology Insertion for Recapitalization of Legacy Systems Program Final Report					5a. CONTRACT NUMBER	
					5b. GRANT NUMBER N00014-14-1-0789	
					5c. PROGRAM ELEMENT NUMBER	
6. AUTHOR(S) Thurston, Michael, G; Haselkorn, Michael, H; McConky, Sean, P; Walluk, Mark, R; Nenadic, Nenad, G; Hurley, Gerald, M; Valant, Christopher; Nasr, Nabil, Z					5d. PROJECT NUMBER	
					5e. TASK NUMBER	
					5f. WORK UNIT NUMBER	
7. PERFORMING ORGANIZATION NAME(S) AND ADDRESS(ES) ROCHESTER INSTITUTE OF TECHNOLOGY 1 LOMB MEMORIAL DRIVE ROCHESTER, NY 14623-5603					8. PERFORMING ORGANIZATION REPORT NUMBER	
9. SPONSORING/MONITORING AGENCY NAME(S) AND ADDRESS(ES) Office of Naval Research 875 North Randolph Street Arlington, VA 22203-1995					10. SPONSOR/MONITOR'S ACRONYM(S) ONR	
					11. SPONSOR/MONITOR'S REPORT NUMBER(S)	
12. DISTRIBUTION/AVAILABILITY STATEMENT Approved for Public Release; distribution is Unlimited						
13. SUPPLEMENTARY NOTES						
14. ABSTRACT This final report for the Technology Insertion for Recapitalization of Legacy Systems program provides a summary of the research and results for each of the program's five sub-projects: A) Effect of Corrosion on Physical Properties of Highly Stressed Coated Components, B) Asset Life-cycle Management: Data Needs and Data Gaps Assessment, C) Subsystem and Component Reliability Synthesis Methodology, D) Evaluation of material properties and repair procedures in 5083 aluminum parts with thermal, impact and environmental stresses, and E) Evaluation of Additive Manufacturing for Dimensional Restoration of Cast Iron and Alloy Steel Components.						
15. SUBJECT TERMS Asset Life-cycle Management, Reliability, Corrosion, Additive Manufacturing, Aluminum Sensitization						
16. SECURITY CLASSIFICATION OF:			17. LIMITATION OF ABSTRACT	18. NUMBER OF PAGES	19a. NAME OF RESPONSIBLE PERSON	
a. REPORT	b. ABSTRACT	c. THIS PAGE			Nabil Nasr	
U	U	U	SAR	420	19b. TELEPHONE NUMBER (Include area code) 585-475-5106	



Technology Insertion for Recapitalization of Legacy Systems

Final Report

Prepared by:

Golisano Institute for Sustainability
Rochester Institute of Technology
190 Lomb Memorial Drive
Rochester, NY 14623
(585) 475-5101

Research Program 1:
Effect of Corrosion on Physical Properties
of Highly Stressed Coated Components

This research was conducted under Office of Naval Research Grant N00014-14-1-0789.

Report Generated by:

Golisano Institute for Sustainability
Rochester Institute of Technology
190 Lomb Memorial Drive
Rochester, NY 14623
(585) 475-5101

Table of Contents

1	Introduction	5
2	Program Objectives	6
3	Condition Assessment	6
3.1	Data Gathering	6
3.1.1	Initial Albany Depot Visit.....	6
3.1.2	Analysis of Torsion Bars Obtained during Second Albany Visit and Stored Outside.....	30
3.1.3	Investigation of Torsion Bars at Albany Depot	45
3.1.4	Examination of Torsion Bars off Vehicles from Albany June 16, 2015	46
3.1.5	Torsion Bars of Vehicles from Barstow.....	56
3.2	Non-Destructive Evaluation Method Research.....	65
3.2.1	Determining Polyethylene Coating Adherence.....	65
3.2.2	Non-Destructive Testing of Coating Adherence Techniques	66
3.2.3	Thermal Wave Inspection	70
3.2.4	Conclusions.....	71
4	Development of Acceptance Criteria	71
4.1	Data Gathering Process	71
4.1.1	Analysis for Refurbishment	71
4.2	Torsion Bar Overview and Operations	73
4.2.1	Component Characteristics and Properties	73
4.2.2	Use Profile	75
4.3	Failure modes.....	80
4.3.1	Overload.....	81
4.3.2	Background on fatigue	81
4.3.3	Background on Stress Corrosion Cracking	86
4.3.4	Background on Corrosion fatigue	89
4.3.5	Coating delamination	90
4.4	Replication of Properties and Test Specimen	91
4.4.1	Test Specimens	92
4.5	Specimen Tests	94
4.5.1	Ultimate strength test specimens.....	94
4.5.2	Fatigue Specimen Results	97
4.5.3	Corrosion Fatigue.....	102

4.6	Component Modeling	103
4.6.1	Pit size and modeling	104
4.6.2	Fatigue model calibration.....	106
4.6.3	Residual Stress	107
4.6.4	Superposition model	111
4.6.5	Results at spline, neck, and straight sections	113
4.7	Overall mechanical assessment for refurbishment.....	116
4.7.1	Inspection Acceptance Criteria	116
5	Remanufacturing Process Development	117
5.1	Cleaning	117
5.1.1	Removing Corrosion	117
5.1.2	Coating removal.....	134
5.2	Coating Selection	141
5.2.1	Coating Application Method Selection.....	143
5.2.2	Coating Composition Selection	145
5.3	Recoating Process Development.....	151
5.4	Recapitalization Cost Model.....	155
6	Conclusions	157

1 Introduction

Corrosion is a serious issue for vehicles, as well as construction and agriculture equipment utilized in a wide variety of environments. Road salt, salt water and other corrosive chemicals cause significant amounts of downtime for crucial equipment, while also significantly reducing the length of service of the vehicles. Highly stressed components, such as suspension systems, winches, and drivetrains, may see severe degradation of strength due to corrosion.

Table 1 Summary of 1997 shipment values of farm machinery and equipment, according to the 1997 Census

PRODUCT CLASS	1997 SHIPMENTS VALUE	ASSUMED CORROSION COST	
	(\$ x million)	5%	10%
Farm-type 2- and 4-wheel drive tractors	3,857	193	386
Diary equipment, sprayers, dusters, elevators, and blowers	745	37	75
Planting, seeding, and fertilizing machinery	1,080	54	108
Harvesting machinery	2,970	149	297
Haying machinery	664	33	66
Parts for farm machinery (sold separately)	1,425	71	143
Plows, harrows, rollers, pulverizers, cultivators, and weeders	609	30	61
Other farm machinery and equipment	1,837	92	184
Commercial turf and grounds care equipment	1,340	67	134
Farm machinery and equipment (not specified by kind)	439	22	44
TOTAL	\$14,966	748	1,498
AVERAGE: \$1.123 billion per year			

A significant amount of money is spent every year to combat corrosion in various industries. Table 1 shows the value of shipments of farm machinery and equipment and the assumed yearly costs of corrosion.¹ The transportation industry in the US is 2nd only to the utility industry in costs due to corrosion. Of the \$29.7 Billion dollars spent on corrosion in the transportation industry, \$23.4 Billion is spent on motor vehicles. \$14.46 Billion of the motor vehicle corrosion costs are due to depreciation of vehicles and another \$6.45 Billion is spent on maintenance made necessary by corrosion.²

One of the serious problems caused by corrosion is the reduction of metal thickness that can lead to the loss of mechanical strength and cause a structural failure or breakdown. Corrosion often occurs in very localized zones and can form crack-like defects or penetrate into the grain boundaries of the metal. Even small amounts of damage can cause considerable degradation in the strength of the material. In addition, corrosion can lead to accelerated failure of structural components under fatigue loading conditions.³ Fatigue cracks usually initiate from the corrosion pit sites. Under the interaction of cyclic load and the corrosive environment, cyclic loading facilitates the pitting process, and corrosion pits, acting as geometrical discontinuities, lead to crack initiation and propagation and then final failure.

¹ http://www.dnvusa.com/Binaries/agriculture_tcm153-379116.pdf

² <https://www.nace.org/uploadedFiles/Publications/ccsupp.pdf>

³ Pidaparti, R., Koombua, K., Delsayel, I. and Sharma, H., Degradation Experiments and Analysis of Corrosion Damage, International Journal of Damage Mechanics March 2010 vol. 19 no. 2 197-210

Coatings are often the first line of defense against corrosion. Coatings are effective in preventing corrosion because they isolate the metal from the environment. However, if the coating is damaged or dis-bonds from the surface, the metal is no longer isolated from the environment and corrosion can occur. Refurbishment of coated components requires replacement or repair of anti-corrosion coatings. One class of coatings that is particularly challenging to repair or replace is thermo-plastic coatings that are applied over large surfaces.

2 Program Objectives

Under the research effort, we will research the effects of corrosion on highly stressed coated components. The research will evaluate cost effective, non-destructive methods to estimate the corrosion damage to a hardened steel component, develop and evaluate approaches for corrosion removal and repair of corrosion damage, and develop methods for restoring organic corrosion control coatings. As a portion of this research, we will also apply analytical methods for quantifying the impact of the corrosion repairs on fatigue life of the component.

For this program, we will be evaluating Amphibious Assault Vehicle (AAV) torsion bar. The torsion bar is a component with an existing polyurea coating designed to protect the bar from corrosion. The torsion bar is made from 300M alloy steel which is also used in aerospace components, military vehicles, and motorsport applications. 300M has good fatigue strength, fracture resistance and impact strength.

3 Condition Assessment

3.1 Data Gathering

The goal of the data gathering task is to understand the extent of corrosion on the torsion bars. Initially, a sample of torsion bars were shipped to RIT for evaluation. A subsequent trip to the depot was utilized to collect a larger sample size of roughness and coating delamination data. After the second depot visit, another sample of bars was delivered to RIT from both the Albany and Barstow depots.

3.1.1 Initial Albany Depot Visit

The initial visit to observe the extent of corrosion on the stored torsion bars at the Albany Marine Maintenance Depot occurred on September 8-10, 2014. The purpose of the visit was to examine the torsion bars stored outside at the Albany depot and select and characterize the corrosion on the torsion bars that exhibited visually the most amount of corrosion. Eighteen torsion bars were selected for characterization.

The characterization consisted of examining the corrosion that developed on the surface using optical and scanning electron microscopy techniques.

Samples for corrosion evaluation were cut from torsion bars labeled 12 (three sections), 15C, 7, and 11. Also included in this study was a sample from torsion bar 15 that had that the oxide removed by hand scrubbing with a wire brush. Figure 1 shows the torsion bars samples used for the SEM analysis.

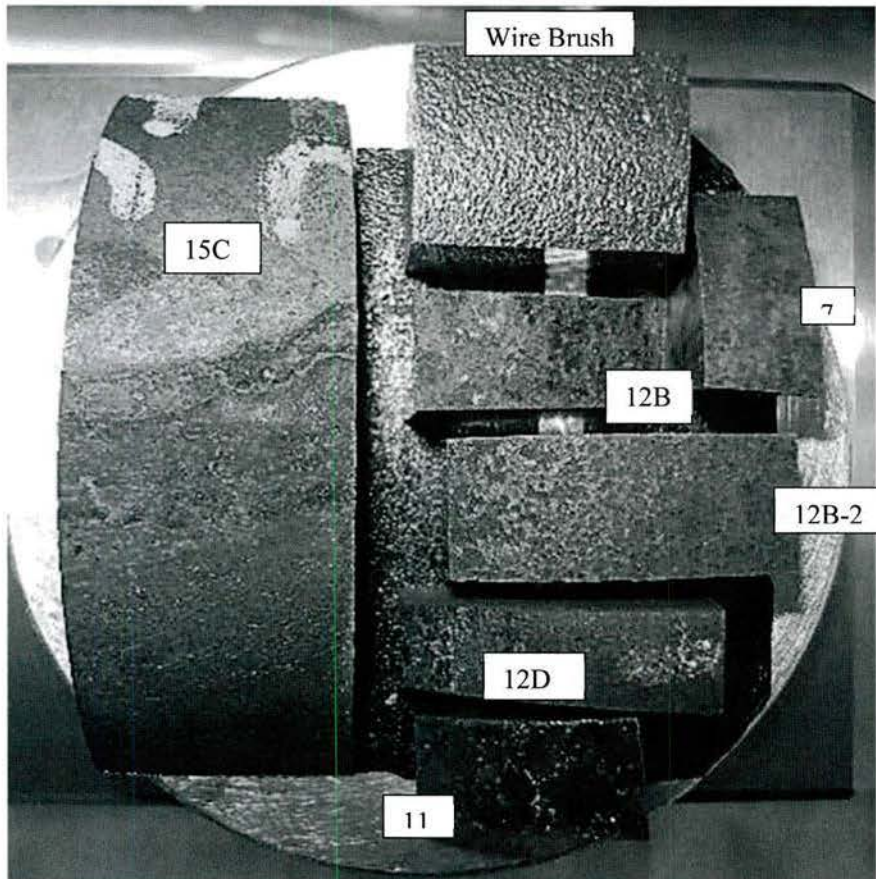


Figure 1 - Corroded Torsion Bar Specimens Examined in SEM

Figure 2 shows the locations on the torsion bars where the specimens were obtained. Specimen 11 was selected because the amount of corrosion on this torsion bar was similar to that observed on the majority of the rejected torsion bars observed at the Albany Maintenance Depot.

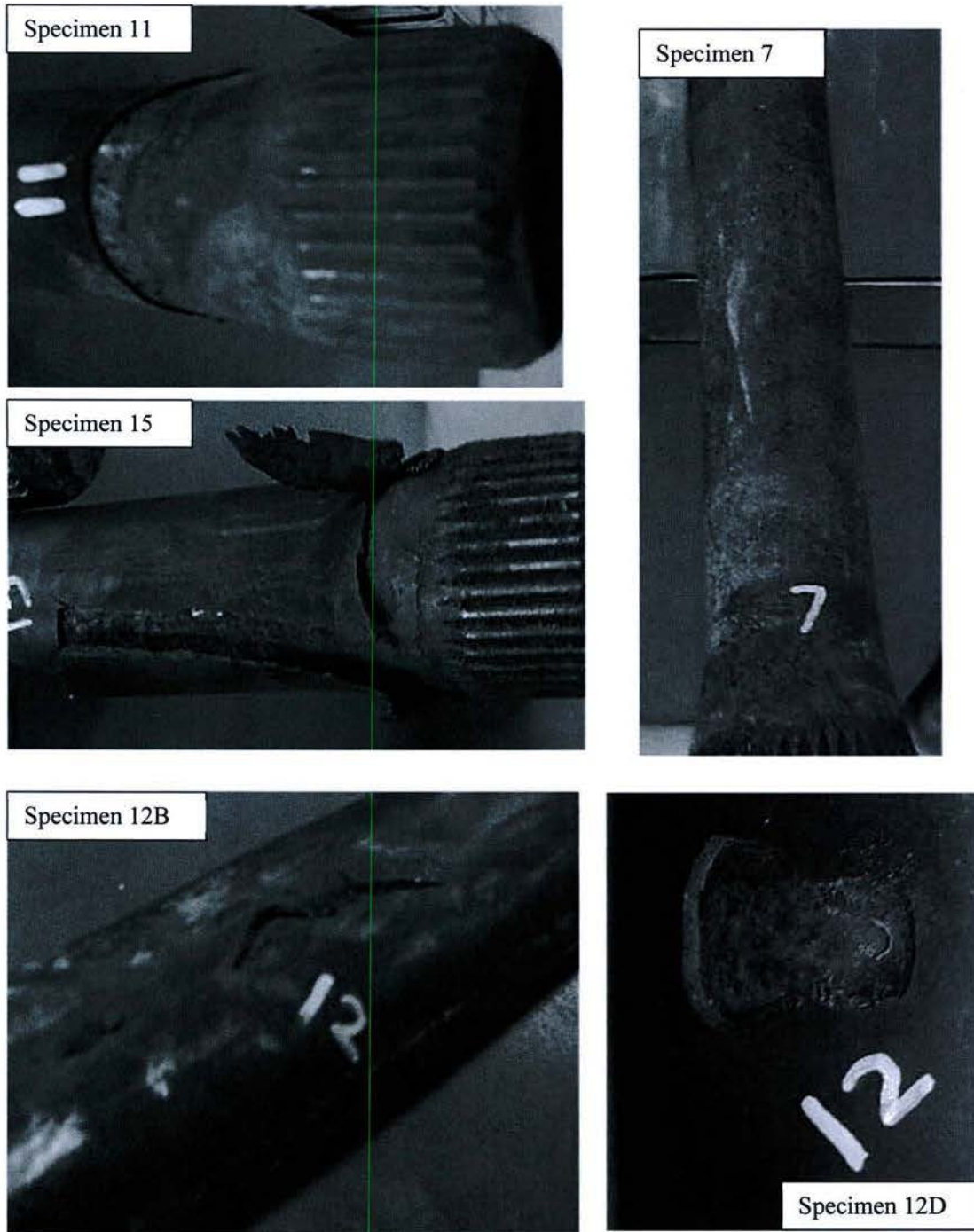


Figure 2 - Locations on Torsion Bars for Corrodes Torsion Bar Specimens Where Obtained

Typically, on these torsion bars the corrosion occurred at one end of the torsion bar, close to the spline, where the original coating had disbonded. Specimen 15 also exhibited corrosion close to the spline where the coating had disbonded but the coating disbond was greater on Specimen 15 than that observed on Specimen 11. In addition, there was a different corrosion pattern on the torsion bar in the region because the water penetrated beneath the disbonded coating. Specimen 7 was from a Gen 1 torsion bar and had the greatest amount corrosion observed on any torsion bar. Finally, the Specimens 12D, 12B and 12B-1 were taken from a torsion bar which experienced coating damage in a center region on the torsion bar where coating damage had occurred.

The optical and SEM photomicrographs of the corrosion layer that developed on the torsion bar specimens from the September 2014 Albany Depot visit are contained in Figure 4-Figure 30.

The severe corrosion on the Gen 1 torsion bar, Specimen 7 are illustrated in Figure 4-Figure 8. Both the optical and the SEM photomicrographs showed that the corrosion or oxide layer that developed on this specimen contained cracks (Figure 5) and pits (Figure 4 and Figure 8). The presence of both the pits and cracks are an indication that the oxide layer that developed was non-adherent. A non-adherent oxide layer will not act as a barrier and prevent or slow the formation of additional corrosion product on the surface of the torsion bar. As a result when a portion of the corrosion layer flakes from the surface the exposed metal will quickly oxidize.

The mechanism for the corrosion formation on the 300M alloy is the water and oxygen, iron and steel react, forming an oxide.⁴ The oxide that develops on the surface does not firmly adhere to the surface and will flake off, resulting in additional oxide formation and eventually pitting. Extensive pitting can result in weakness and disintegration of the metal, leading to failure. Obviously, because of the involvement with water, the corrosion occurs much more rapidly in moist conditions. However, there are a few other factors that determine the rate of corrosion. The presence of dissolved salt in the water increases the conductivity

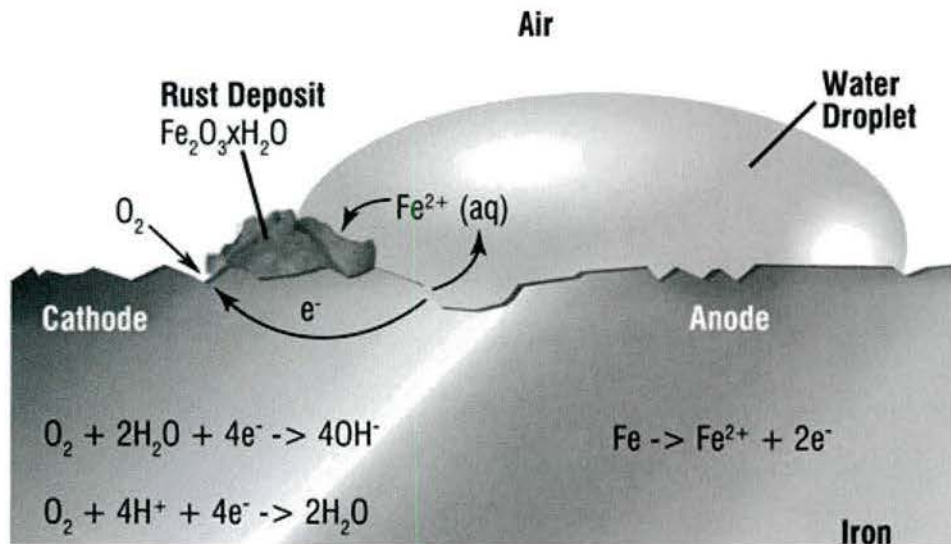
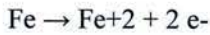


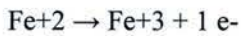
Figure 3 - Mechanism of Corrosion for 300M

of the aqueous solution formed at the surface of the metal and enhances the rate of electrochemical erosion. Another example is heat. The higher the temperature is, the higher the corrosion rate.

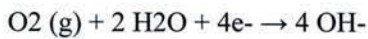
Figure 3 illustrates the corrosion process for 300M. This process begins with the oxidation of iron to ferrous (iron “+2”) ions by the water.



Next, in the presence of both iron and water the iron (+2) ions are further oxidized to form ferric (iron “+3”) ions.



The electrons provided from both oxidation steps are then used to reduce oxygen from the atmosphere surrounding the torsion bar and form hydroxide ions



The ferric ions then react with the hydroxide ions to form ferric oxide, which is then hydrated with varying amounts of water.

The non-dispersive X-ray analyses in Figure 7 showed that the corrosion layer that developed on torsion bar Specimen 7 consisted of iron (Fe) and oxygen (O). Also present in the corrosion layer was silica (Si) and chrome (Cr). Both the Si and Cr are alloys in the 300M that have higher oxidizing potentials than iron and as a result will also diffuse to the surface and form oxides.

The non-dispersive X-ray analysis also confirmed that there was oxide or corrosion products in the base of the pits. This confirmed that the mechanism of the pit formation was flaking of the non-adherent oxide. If a protective oxide layer had developed on the 330M, the pits would have been formed by galvanic corrosion and no oxide or corrosion layer would have been observed at the base of the pits.

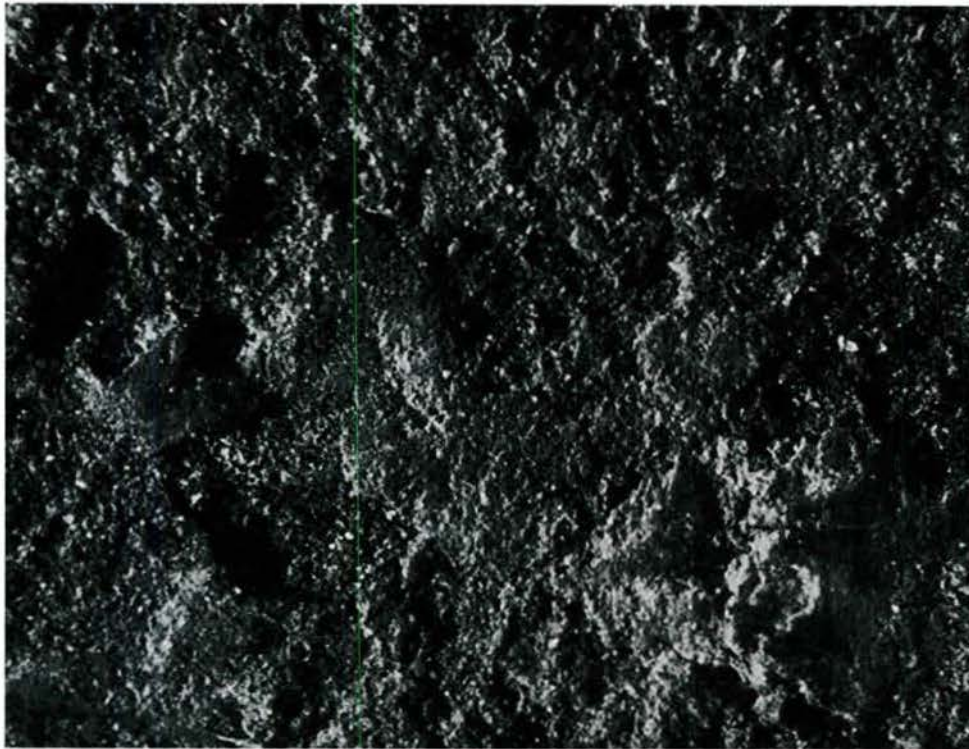


Figure 4 - Optical Photomicrograph of Surface of Specimen 7 (Mag 20x)



Figure 5 - SEM Photomicrograph of Corrosion on Surface of Specimen 7 (Mag 100x)

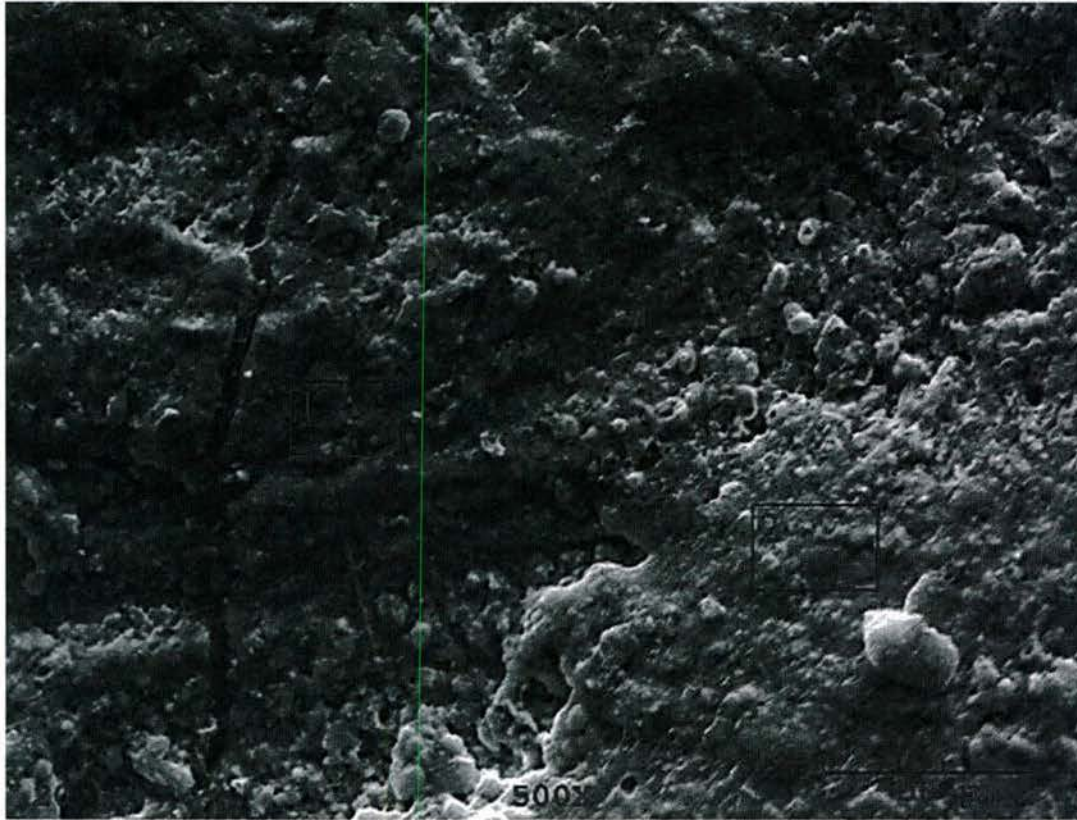


Figure 6 - Higher Magnification SEM Photomicrograph of Area within the Square in Figure 4 from Specimen 7 (Mag 500x)

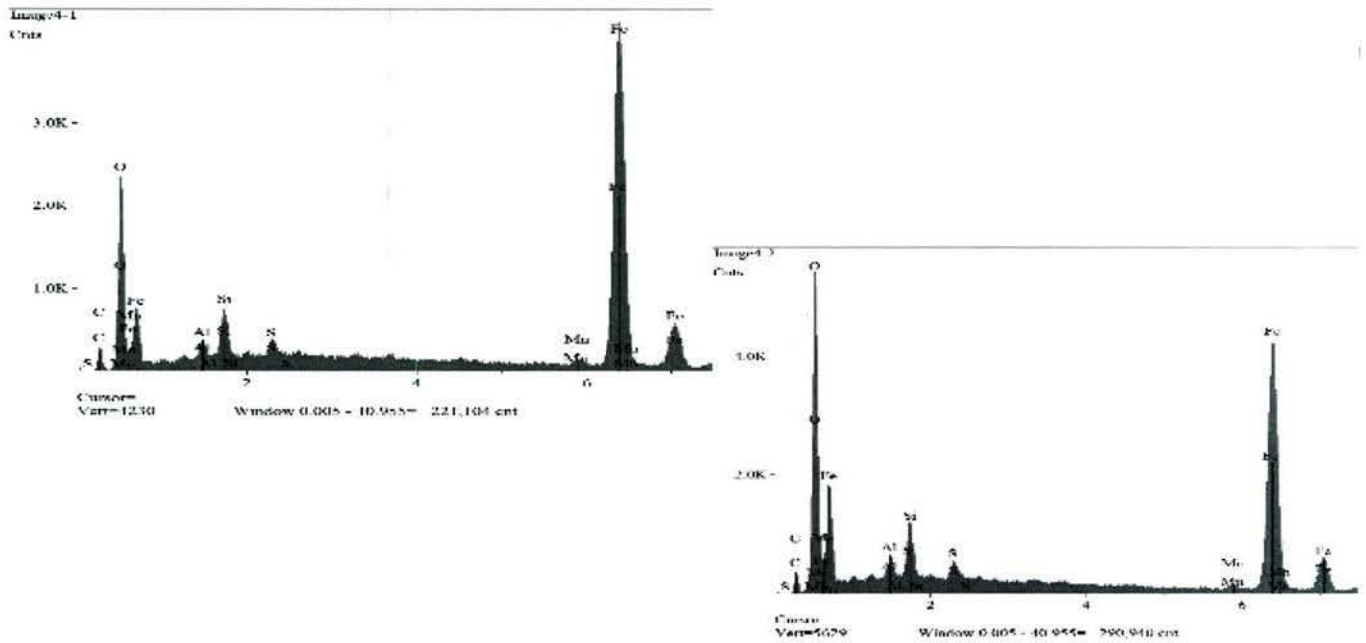


Figure 7 - Non-dispersive X-ray Analyses of Region 1 (Left) and Region 2 (Bottom) from Figure 5

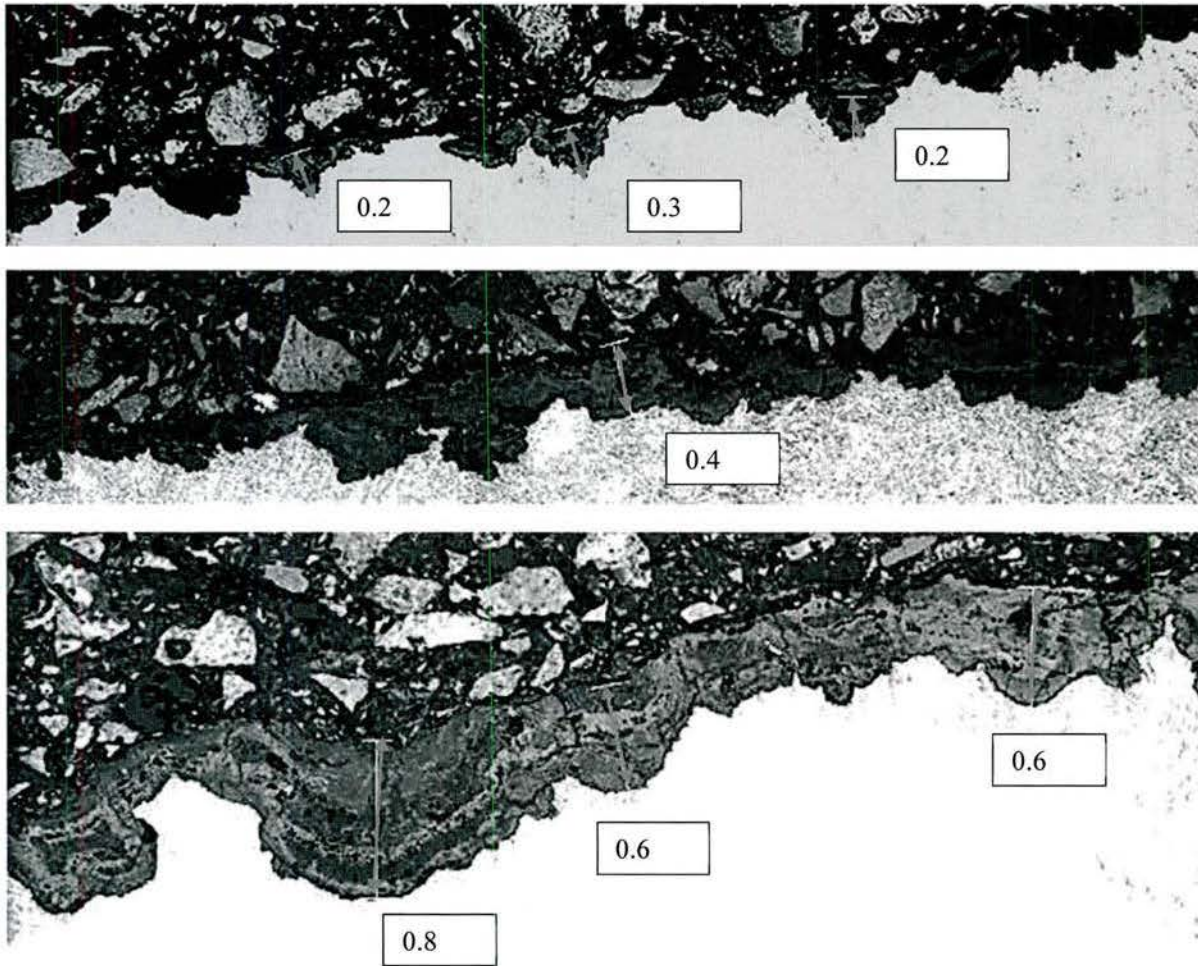


Figure 8 - Cross-Sectional Optical Photomicrographs of Oxide Layer That Developed on Three Regions on Specimen 7 (Mag 200x)

Figure 8 is a optical photomicrograph of a polished cross-sectional of Specimen 7 showing the thickness corrosion layer and pits that developed. These photomicrographs show that the corrosion layer that developed on this torsion bar was not uniform and ranged in thickness from 0.4 mm to 0.8 mm or (0.016-0.031 in). The pit depths ranged between 0.2-0.3 mm or 0.008 to 0.012 inch. Their circumference of the pits ranged between 0.4 -0.6 mm or 0.016 to 0.024 in.

Figure 9-Figure 18 show the corrosion layer that developed on Specimen 12D. This thick corrosion layer contained a significant amount of circular pits (Figure 10-Figure 16). Again, the non-dispersive X-ray analyses showed that there was oxide at the bottom surface of the pit confirming that the pits developed when the non-adherent oxide layer flaked from the surface of the torsion bar.

Figure 16 shows that the oxide layer that developed on this torsion bar specimen also contained a significant number of cracks. The cracks that formed in the oxide layer facilitate the flaking.



Figure 9 - Optical Photomicrograph of Surface of Specimen 12C (Mag 20x)



Figure 10 - SEM Photomicrograph of Surface of Specimen 12D (Mag 50X)

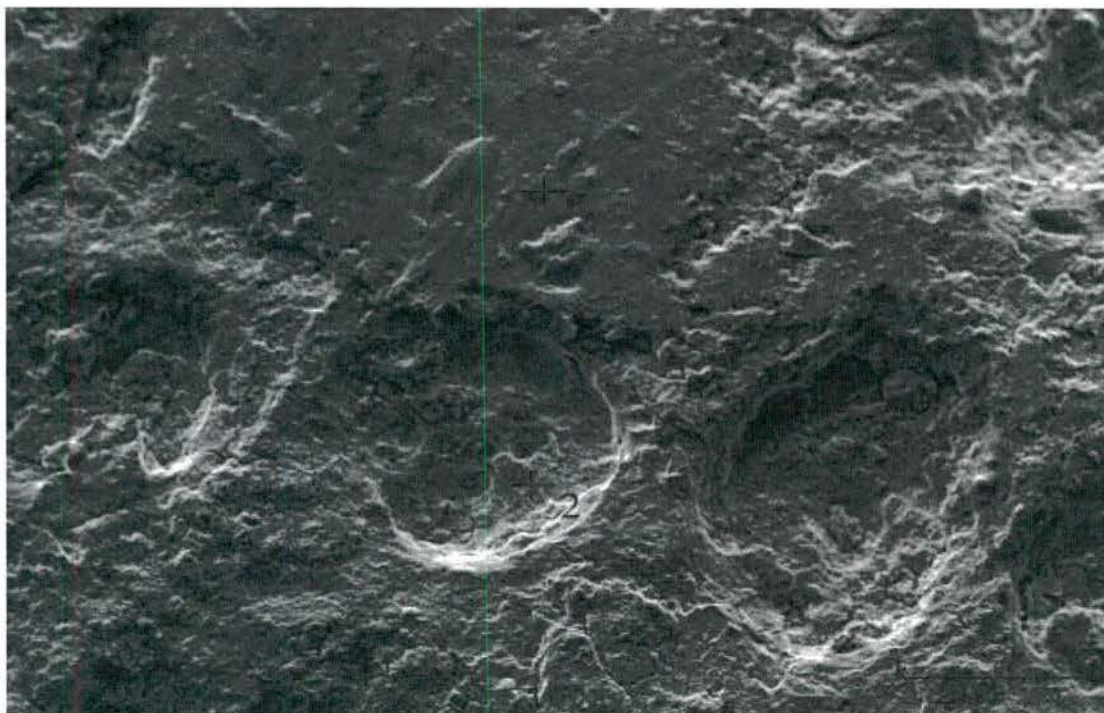


Figure 11 - SEM Photomicrograph of Highlighted Area of Specimen 12D in Figure 8 (Mag 100x)

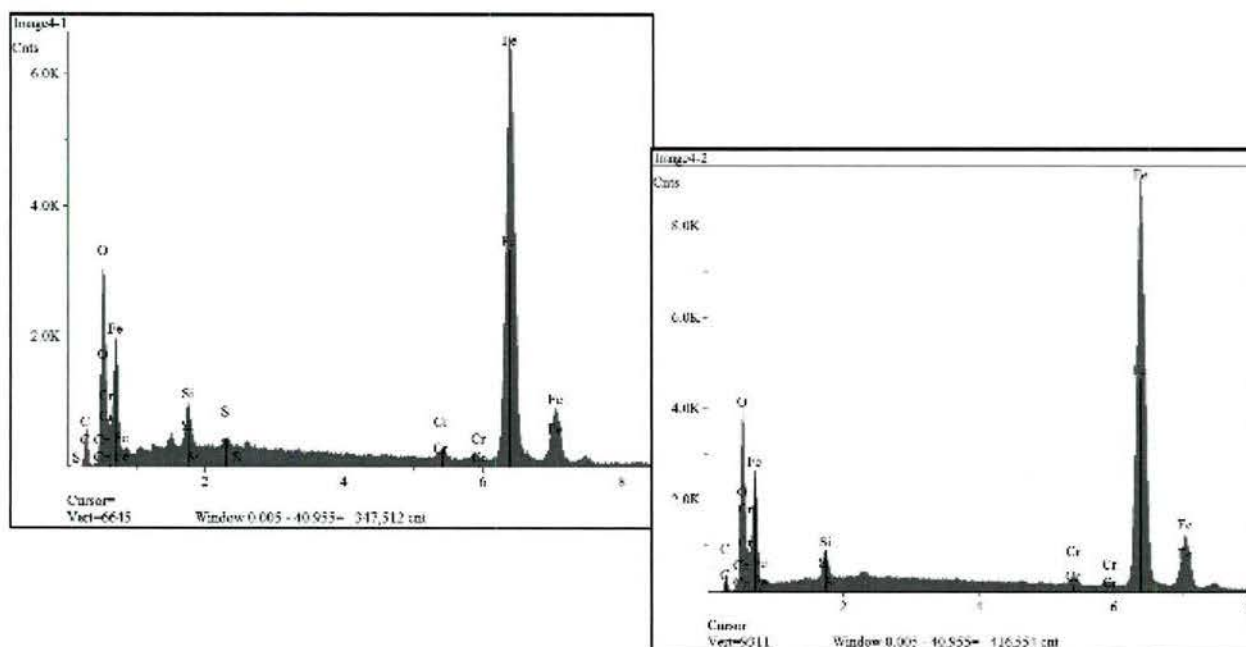


Figure 12 - Non-dispersive X-ray Analyses of Region 1 (Left) and Region 2 (Bottom)



Figure 13 - Optical Photomicrograph of Surface of Specimen 12D (Mag 20x)



Figure 14 - SEM Photomicrograph of Surface of Specimen 12D (Mag 50x)

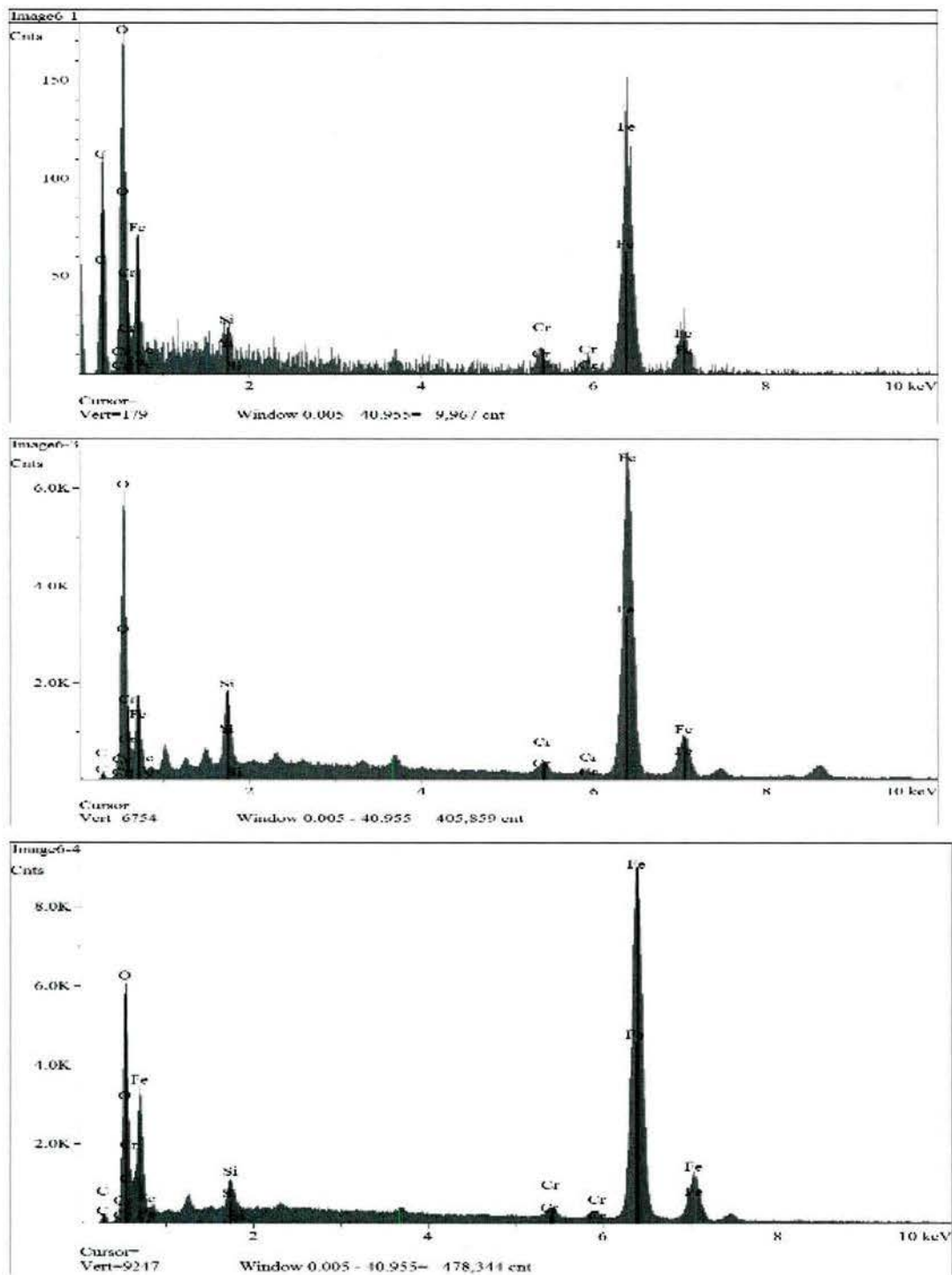


Figure 15 - Non-dispersive X-ray Analysis of Region 1 (top), Region 3 (middle), and Regions 2 and 4 (bottom) from Figure 10

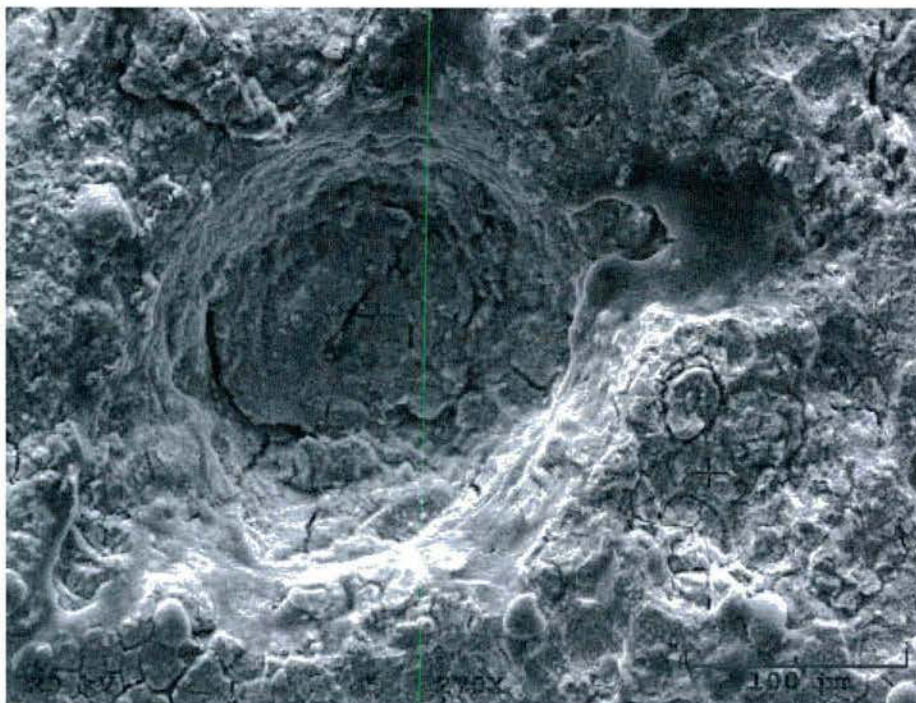


Figure 16 - SEM Photomicrograph of Surface of Specimen 12D (Mag 270x)

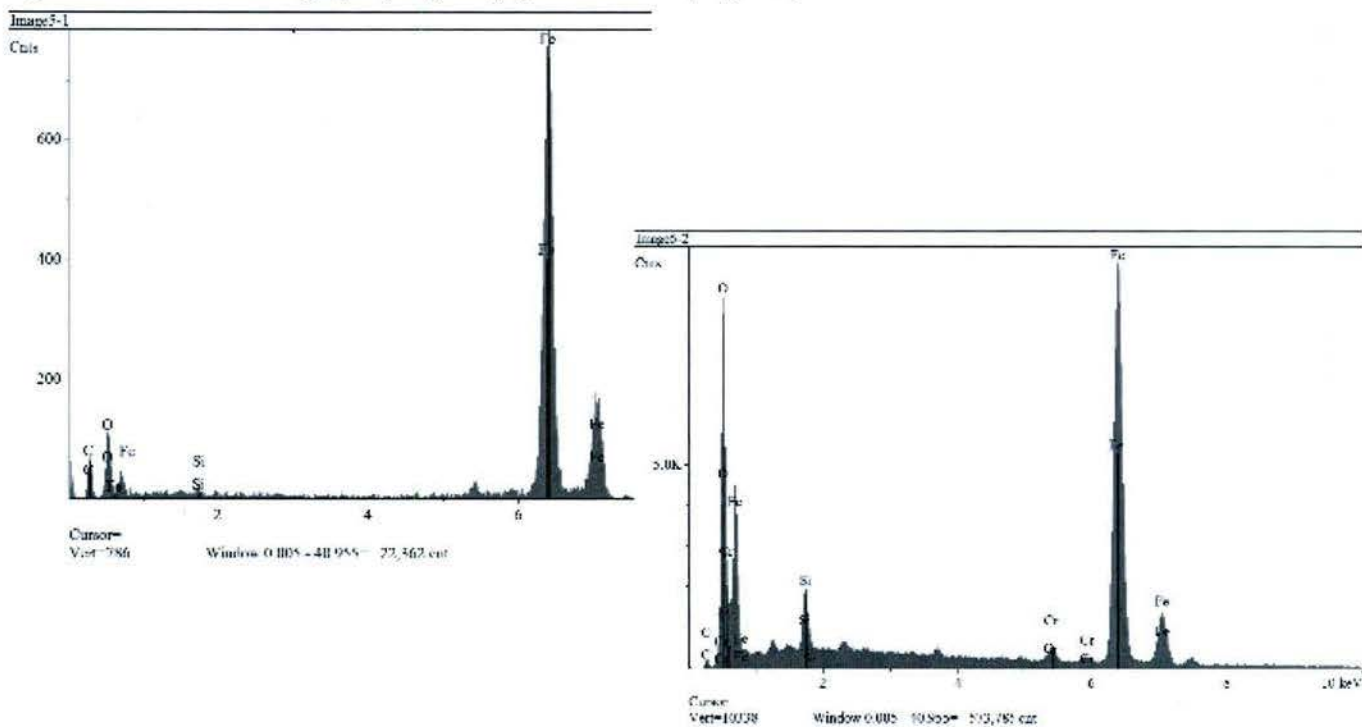


Figure 17 - Non-dispersive X-ray Analyses of Region 1 (Left) and Region 2

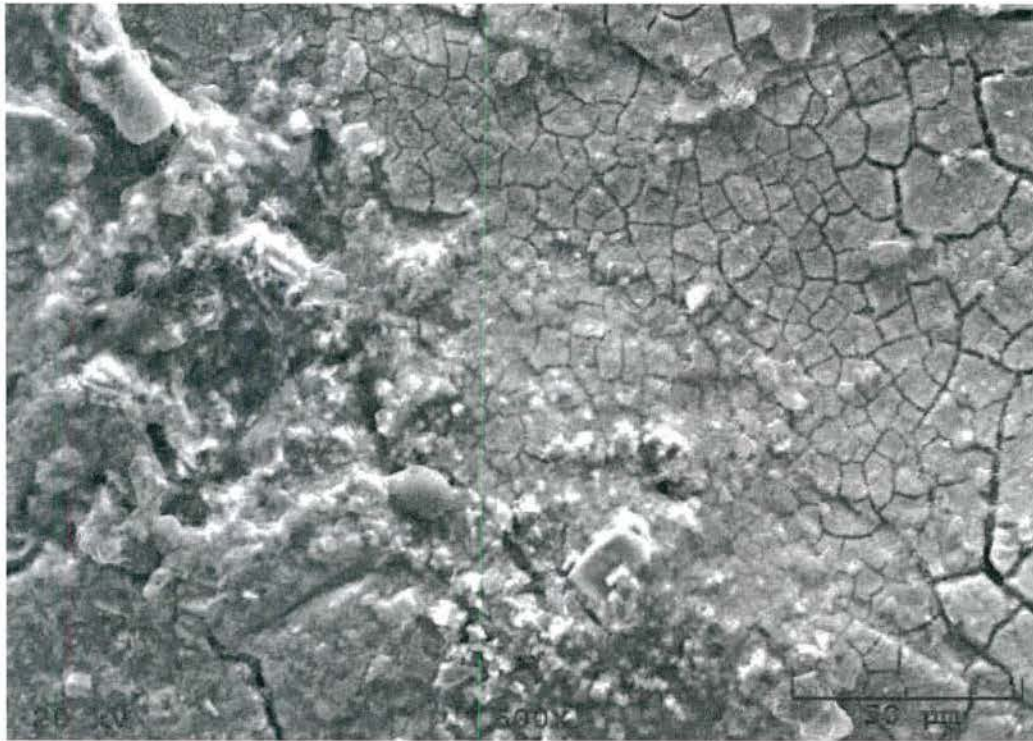


Figure 18 - SEM Photomicrograph of Surface of Specimen 12D (Mag 270x)

Optical photomicrographs of the polished cross-sections from Specimen 12D is contained in Figure 19. While the thickness of the corrosion layer that developed on this specimen was thinner than that observed on Specimen 7, ranging between 0.2 to 0.4 mm thick (0.008-0.016 in), the number and depth of the pit depths were significantly greater than those observed on Specimen 7. The pit depths on Specimen 12D ranged between 0.4 to 1.1 mm (0.016-0.043 inch) while the circumference of these pits ranged from 0.4 mm to 0.8 mm (0.016-0.031 inch). In addition, these cross-sectional photomicrographs from Specimen 12D show that the relatively large amount of pitting. The combination of the large number of pits observed along with the depth of these pits would significantly decrease in the mechanical and physical properties of the torsion bar if the pits are removed from the surface of the torsion bar by machining. For this reason, this torsion bar or any torsion bar with this type of corrosion layer is not a good candidate for remanufacturing.

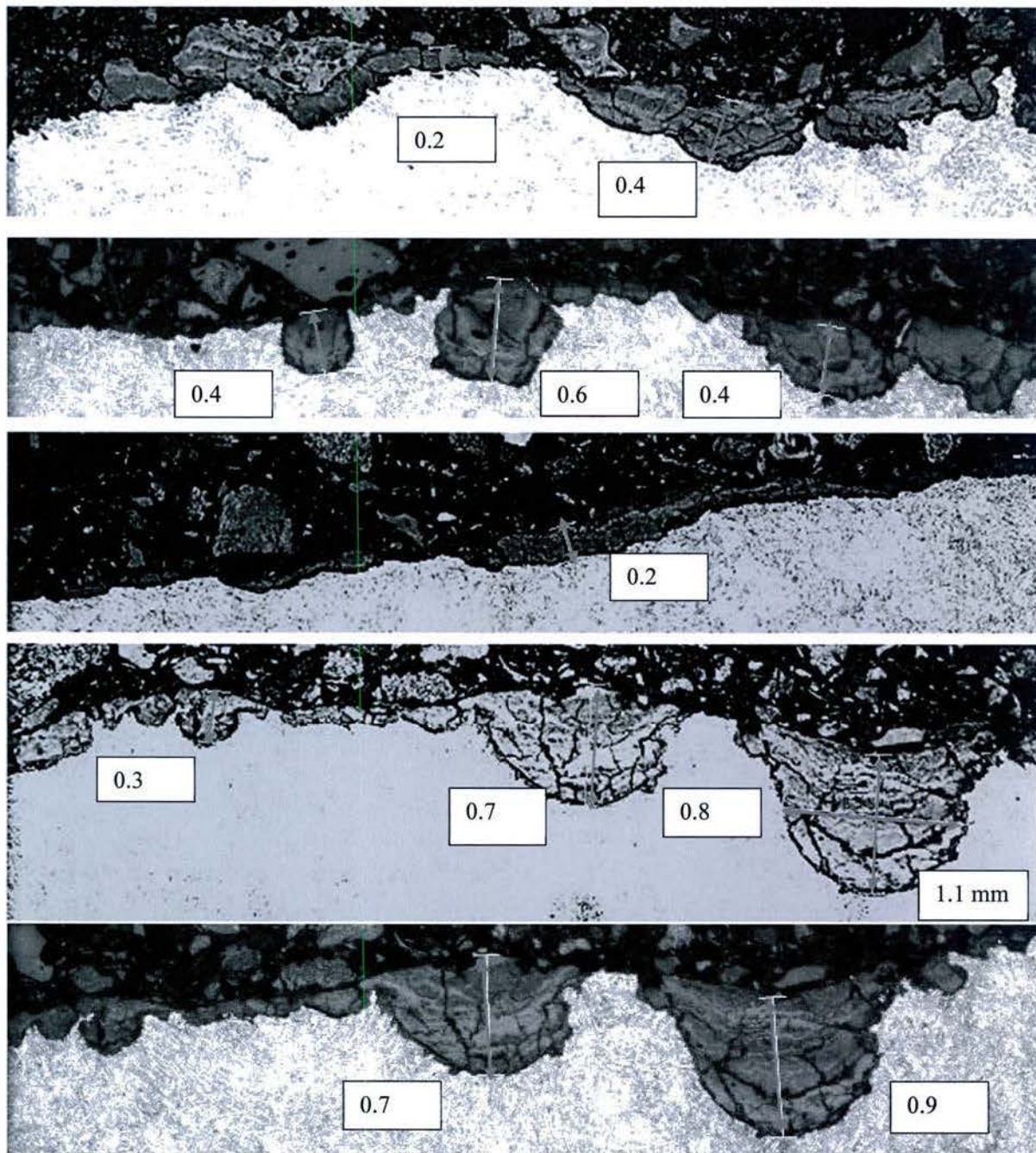


Figure 19 - Cross-Sectional Optical Photomicrographs of Oxide Layer That Developed on Five Regions on Specimen 12D (Mag 200x top, 500x bottom)

There was no visible evidence of pitting on Specimen 15. Again, the SEM analysis showed that the corrosion layer that developed on the 300M alloy was similar to that of the oxide layers that developed on the other torsion bars. In general, the oxide layer that developed was porous and contained a significant number of cracks (Figure 20 and Figure 23). The non-dispersive X-ray analysis of the corrosion layer that developed on this specimen (Figure 22 and Figure 24) also showed that the majority of the corrosion layer consisted of iron oxide with a small amount of silicon and chrome oxide.

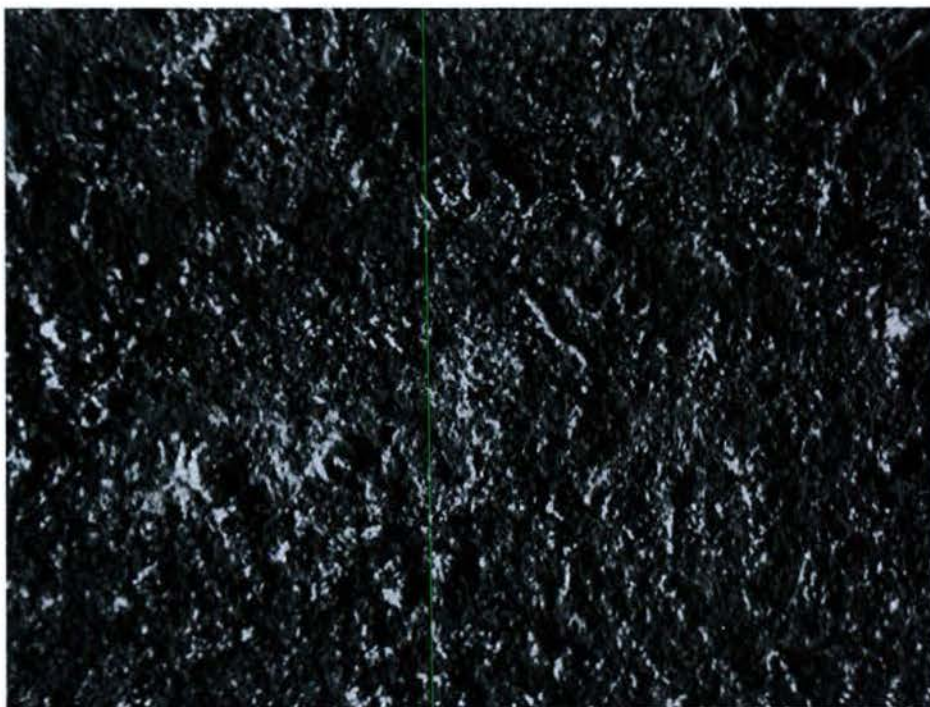


Figure 20 - Optical Photomicrograph of Surface of Specimen 15 (Mag 10x)

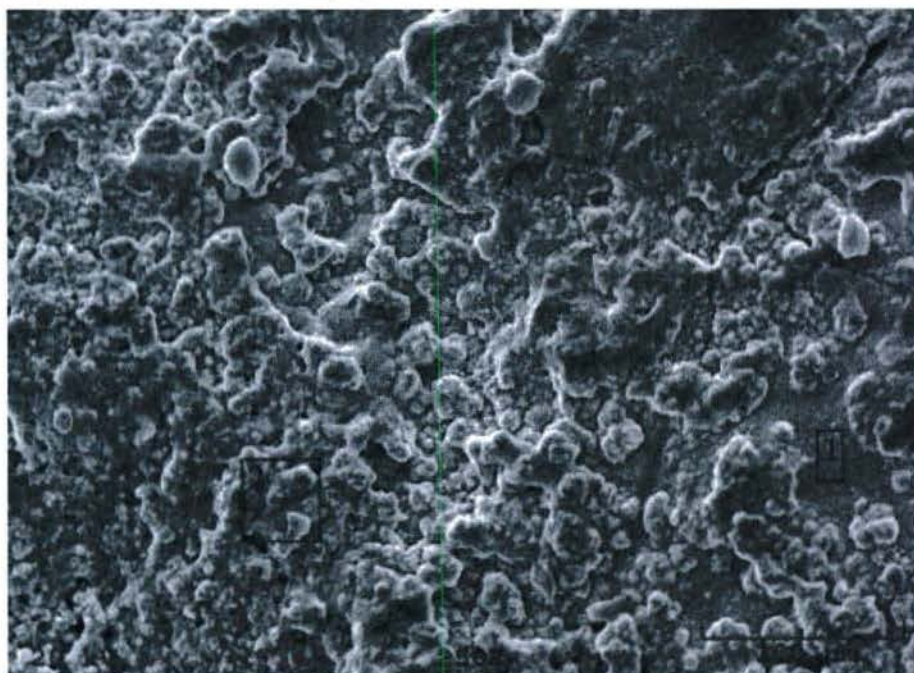


Figure 21 - SEM Photomicrograph of Surface of Specimen 15 (Mag 250x)

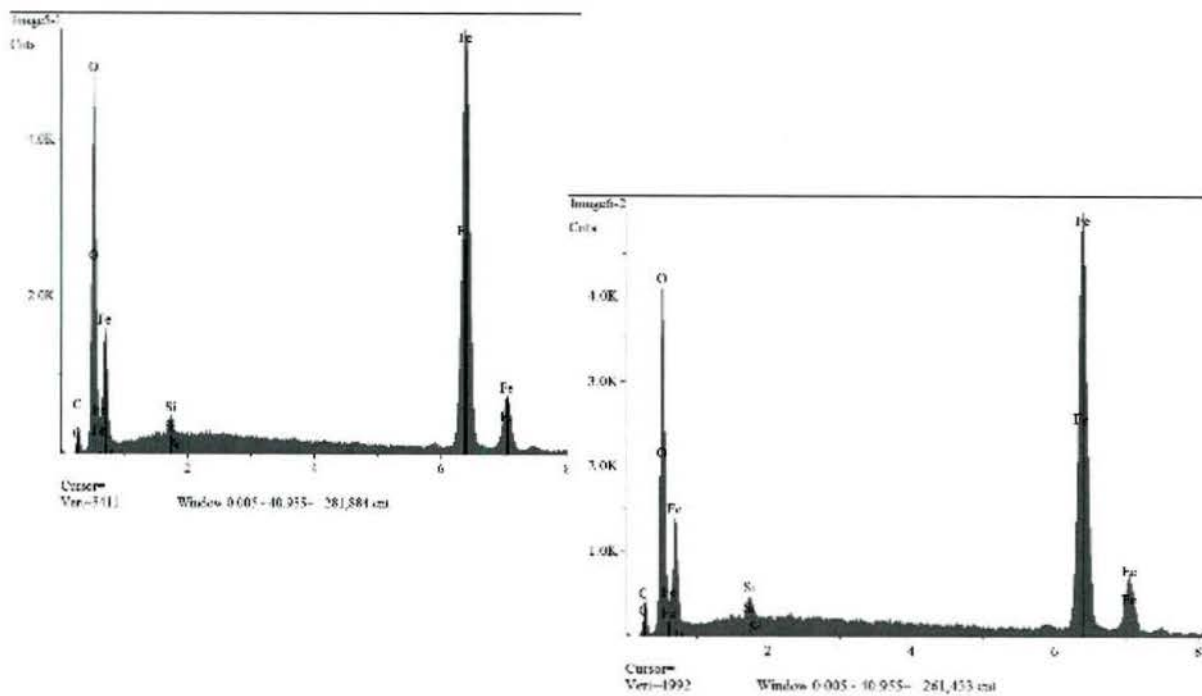


Figure 22 - Non-dispersive X-ray Analyses of Region 1 (Left) and Region 2



Figure 23 - SEM Photomicrograph of Heavy Corrosion Region in Specimen 15 (Mag 50x)

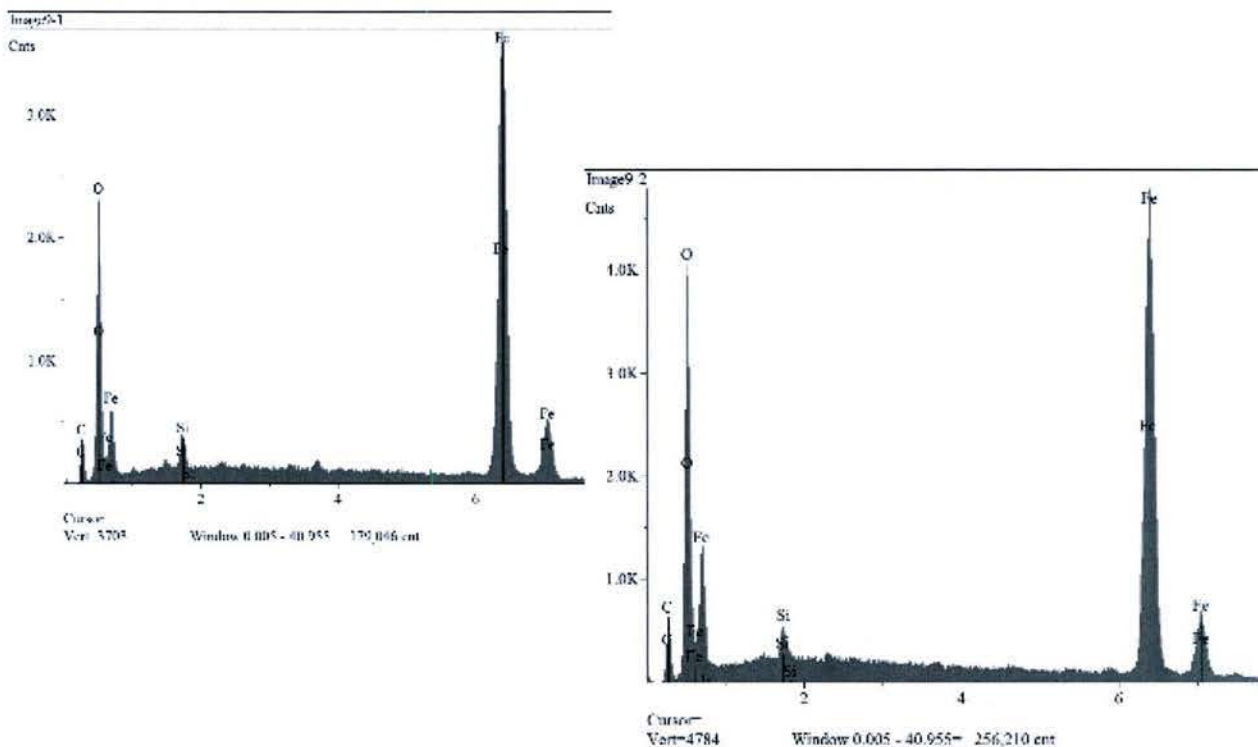


Figure 24 - Non-dispersive X-ray Analyses of Region 1 (Left) and Region 2

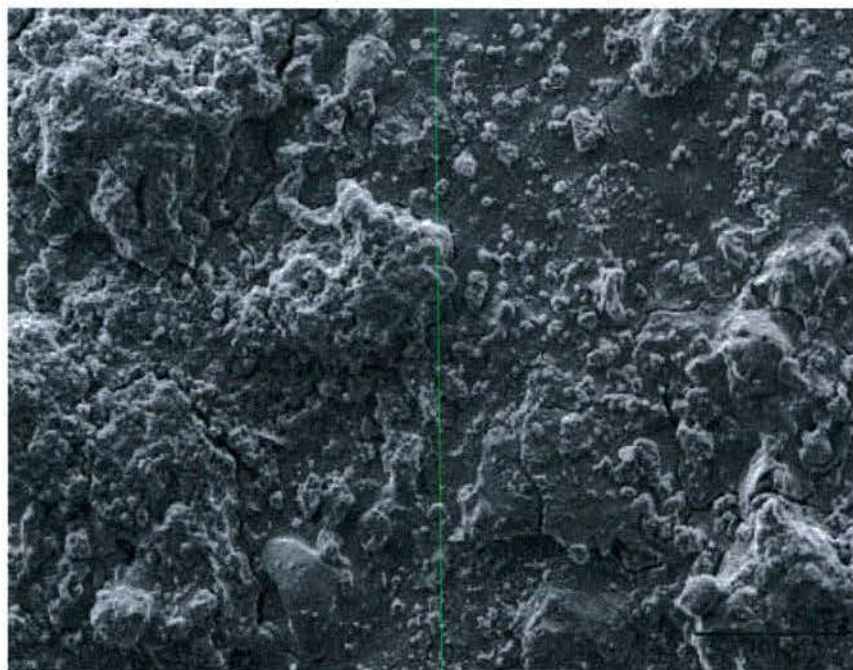


Figure 25 - SEM Photomicrograph of Surface of Specimen 11

The SEM photomicrographs show that the corrosion layer that developed in Specimen 11 was similar to corrosion layer that developed on Specimen 15. Again the corrosion layer was porous and non-adherent, as evident by the significant number of cracks present in the corrosion layer. The cross-sectional optical

photomicrograph of the oxide layer, Figure 27Figure 29, showed that while a thin, 1 mm thick, corrosion layer was observed on this specimen, there were numerous pits below the oxide layer ranging in depth from 0.3 mm to 0.5 mm (0.012 to 0.020 in). The circumference of this pits ranged between 3 to 10 mm (0.012 to 0.050 inches).



Figure 26 - SEM Photomicrograph of Surface of Specimen 11 (Mag 250x)

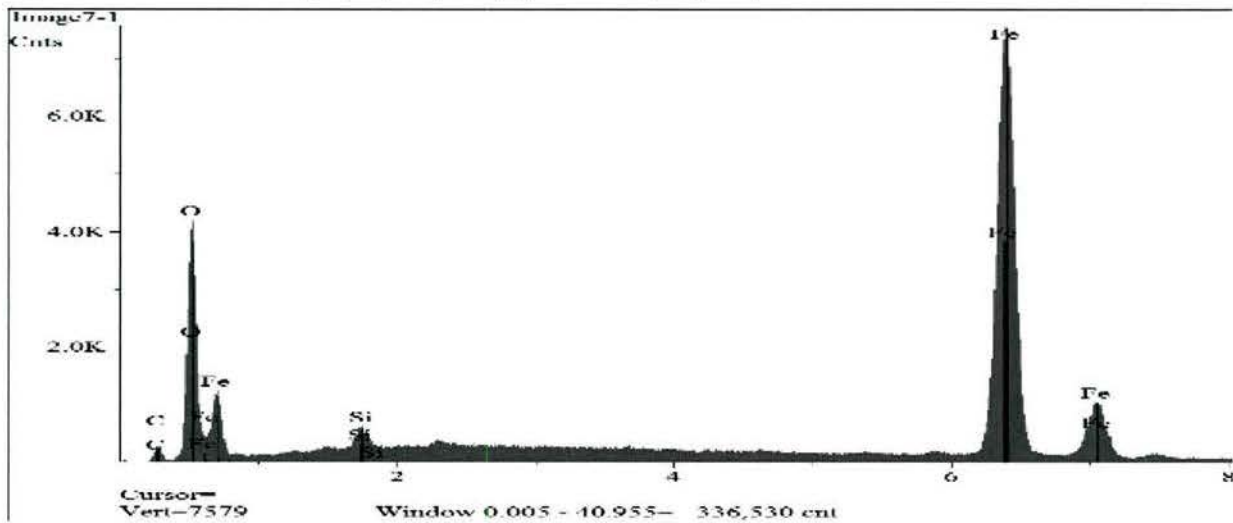


Figure 27 - Non-dispersive X-ray Analyses of Region 1 from Figure 26

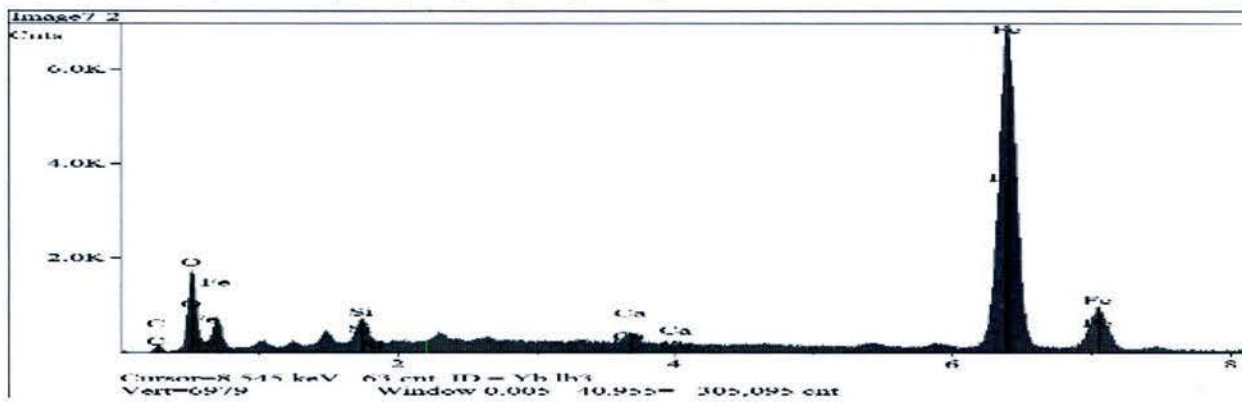


Figure 28 - Non-dispersive X-ray Analyses of Region 2 from Figure 26

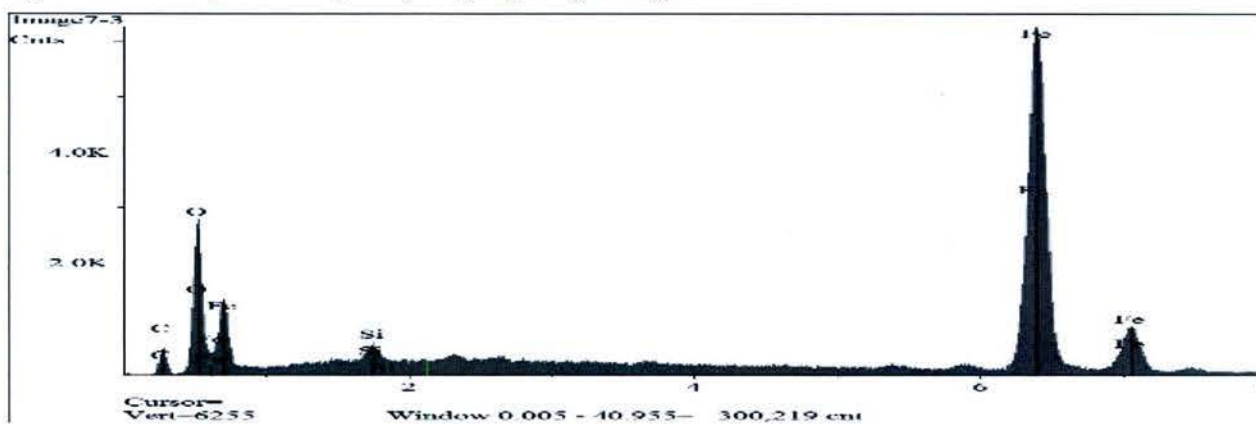


Figure 29 - Non-dispersive X-ray Analyses of Region 1 from Figure 26

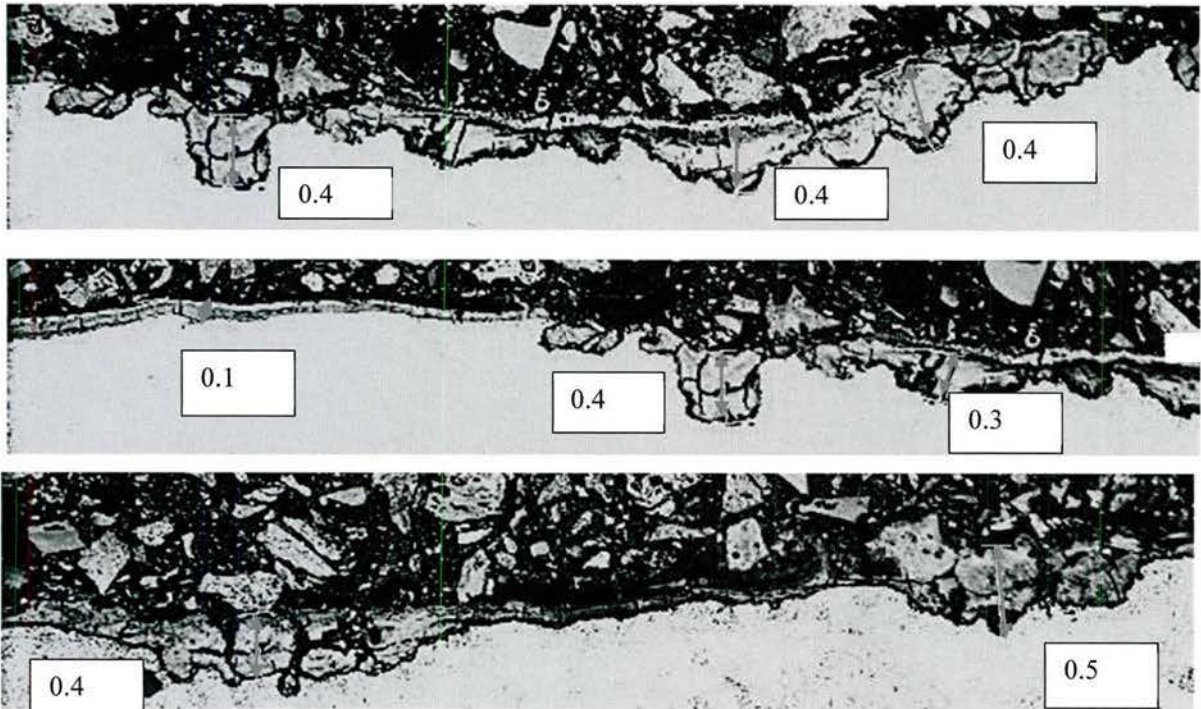


Figure 30 - Cross-Sectional Optical Photomicrographs of Oxide Layer That Developed on Three Regions on Specimen 11 (Mag 200x)

Figure 31 contains two cross-section optical photomicrographs of the corrosion layer that developed on Specimen 12D. Again, this specimen was from a region near the center of torsion bar 12 where the protective coating had been damaged exposing the 300M. These photomicrographs show that a 0.2 to 0.5 mm (0.008 to 0.020 inch) corrosion layer developed in this region. It is interesting to note that even though the corrosion layer had not flaked there was the beginning of a pit formation in the circled area in the lower photomicrograph.

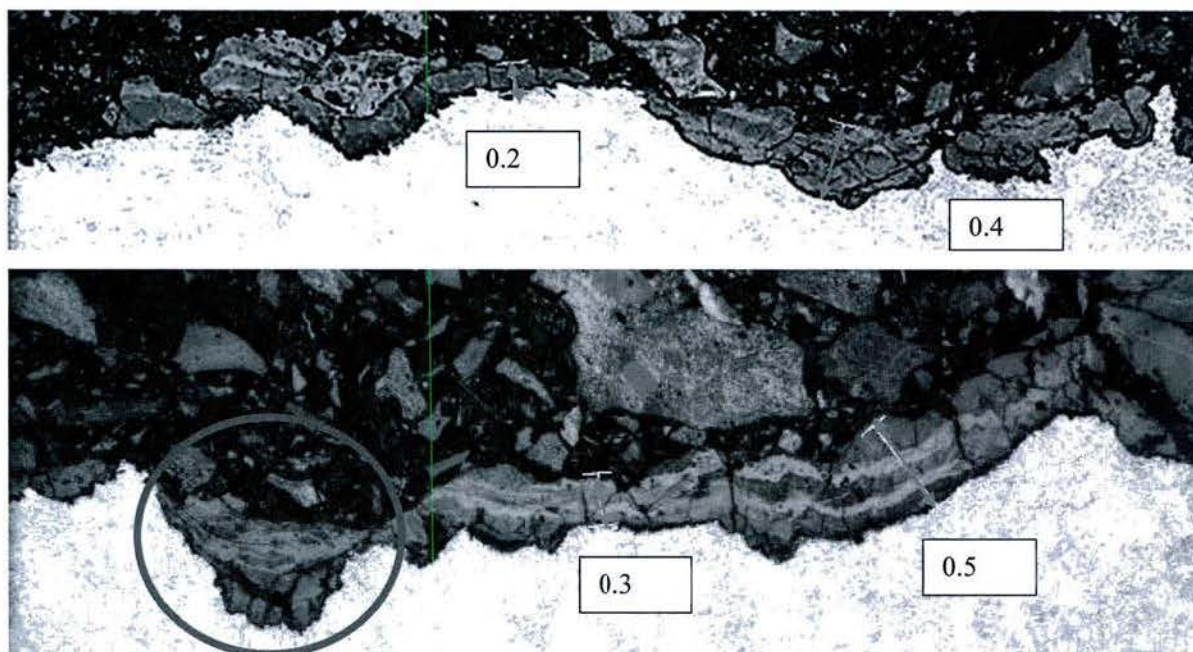


Figure 31 - Cross-Sectional Optical Photomicrographs of Oxide Layer That Developed on Two Regions on Specimen 12B (Mag 200x top, 500x bottom)

Summary of Optical and SEM Analysis of Corrosion Layer on the September 2014 Albany Depot Samples

The SEM analysis showed that thick porous oxide layers developed on all these torsion bar specimens. This analysis also showed that cracks developed within the porous oxide layer and that disbonding or flaking of the oxide layer occurred. Also observed within the oxide were “pits.” The physical appearance of these pits indicate that a round oxide particles had previously disbonded or flaked from this region. All the non-dispersive X-ray analyses showed that the oxide layer on all the samples consisted of iron oxide. The silicon and chrome peaks were caused by oxidation of the Si and Cr alloying agents in the 300M steel composition.

Measurements of the oxide layer thickness from the photomicrographs using image analysis software showed the oxide layers thicknesses ranged from:

- 0.2 to 0.8 mm for Specimen 7
- 0.1 to 0.5 mm for Specimen 11
- 0.2 to 0.5 mm for Specimen 12B, and
- 0.3 to 0.11 mm for Specimen 12D.

The cross-section photomicrographs also showed that the surface was very rough, which would be expected from a shot peened surface. The cross-sectional optical microscopy analysis of the oxide layers showed that the oxide layer that developed on the torsion bar specimens examined was non-uniform in thickness. Most of the regions of thick oxide formation occurred in the “valleys” of the shot peened surface. Spallation of the thick oxide layer from this region, which occurs because of residual stresses that develop within the oxide causes cracks to develop within the porous oxide layer (Figure 6, Figure 14, Figure 16, Figure 19,

and Figure 23). This cracks then caused the thick oxide layer that developed within the “valleys” of the shot peened surface to disbond or spall within the oxide layer close to the metal oxide interface, creating the “pits” within the oxide layer. The “pits” that develop within the oxide layer are illustrated in the SEM photomicrographs contained in Figure 9 to Figure 13.

Scanning Electron Microscope Analysis of Specimen 15 after Wire Brush Cleaning

Specimen 15 was “lightly” wire brushed cleaned to remove the corrosion that had developed on the surface. The wire brushing removed the heavy corrosion from the surface exposing the shot-peened surface. However, after wire brush cleaning the surface still had a reddish physical appearance and the non-dispersive X-ray analysis in Figure 33 showed that the “light” hand wire brushing did not remove all the corrosion from the surface of the sample because the non-dispersive X-ray analysis detected iron oxide on the surface.



Figure 32 - SEM Photomicrograph of Surface after Wire Brush Cleaning (Mag 20x)

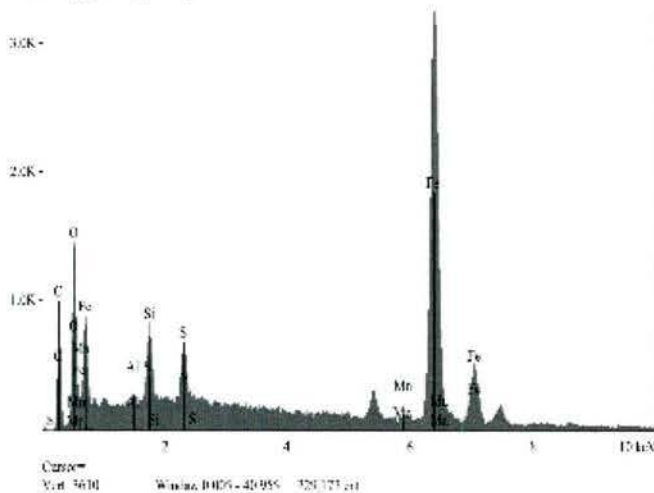


Figure 33 - Non-dispersive X-ray Analysis of Region 1 in Figure 32

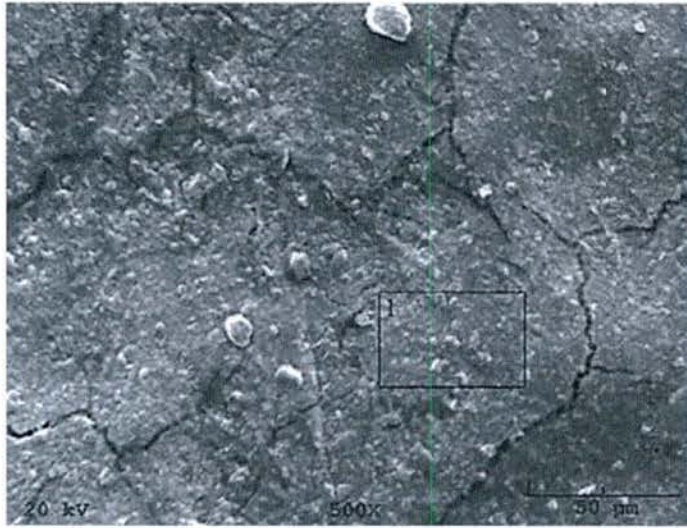


Figure 34 - SEM Photomicrograph of Surface after Wire Brush Cleaning (Mag 500x)

Figure 34, a higher magnification SEM photomicrograph of the surface of Specimen 15 after wire brush cleaning shows that after wire brush cleaning a dense corrosion layer still remained on the surface. In addition, there were numerous cracks observed in this corrosion layer.

This preliminary corrosion clean-up study showed that the corrosion layer cannot be completely removed by lightly rubbing the surface using a wire brush. While this method did not damage the surface it did not remove all the corrosion products from the surface of the 300M.

3.1.2 Analysis of Torsion Bars Obtained during Second Albany Visit and Stored Outside

The analysis of the torsion bars from the initial Albany visit concluded that these torsion bars were not good candidates for remanufacturing because of the pitting observed. However, those bars were selected because they had severe corrosion. Then again, there were a large number of torsion bars that had significantly less corrosion. Therefore, a second Albany depot visit was made to characterize the corrosion and determine the amount of coating damage on two sets of torsion bars:

1. Torsion bars that had been scrapped because of coating delamination and were stored outside, but exhibited less surface corrosion than those previously examined (84 torsion bars), and
2. Torsion bars that had been recently scrapped because of coating delamination and stored inside prior to the second visit (30 torsion bars).

The results of the examination were that out of 114 bars examined, 8 bars (7%) exhibited coating damage toward the middle of the bar' 54 bars (47%) had coating damage in more than 1 location, while the remaining 52 bars (46%) only had coating damage in one location. Finally, on 92 bars or 81% the coating damage was 2 inches or less.



Figure 35 - Coating Edge Damage on a Torsion Bar

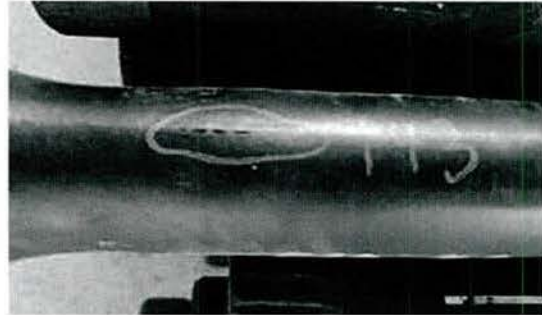


Figure 36 - Coating Center Damage on a Torsion Bar

During the second Albany visit to determine the extent of corrosion of the scrapped torsion bars the coating was removed back approximately six inches on several of the scrapped torsion bars. It was found that after the coating was slit on many of the scrapped torsion bars it could easily be removed (Figure 37), indicating that the adherence of the polyethylene coating was poor. In addition, as Figure 37 shows, the coating disbond occurred at the primer-metal interface. This conclusion is support by Figure 38 which shows the bottom surface of the coating that was removed from the torsion bar has the primer still attached (red color). Also note that when the coating was removed from the torsion bar in Figure 38 no primer was observed on the torsion bar (Primer would be red)

It was also observed that after the coating was slit and removed that there was a water oil mixture trapped under the coating (within the yellow square in Figure 39). While this water, oil mixture reduced the total amount of corrosion that developed on these torsion bars, because the mixture penetrated beneath the coating, because of the coatings poor adherence to the torsion bar, it also caused corrosion to occur beneath the coating away from the edges of the torsion bar.



Figure 37 - Coating Was Easily Removed After Slitting

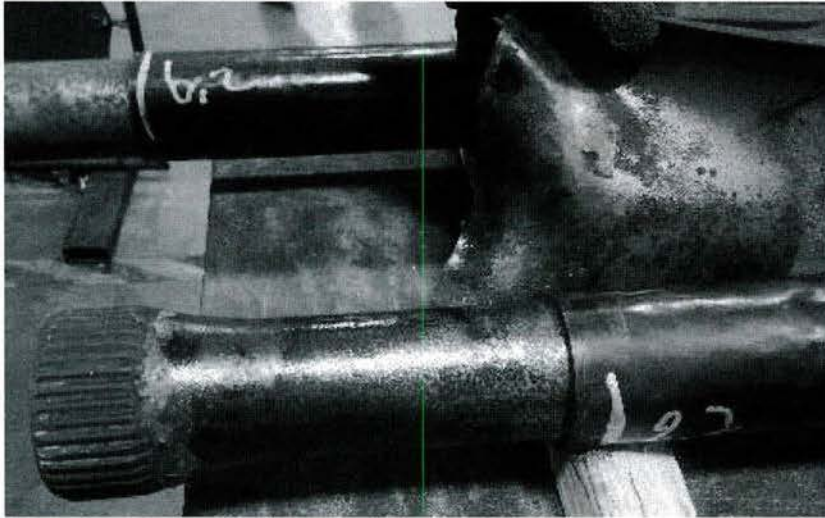


Figure 38 - Underside of Coating after Removal Showing Primer (red) Bonding to Coating

Torsion bar 55-2 was scrapped because of coating disbonding (Figure 39). Figure 39 shows that, in general, this torsion bar exhibited poor adherence. Also, when the coating was removed an oily film was observed on the surface of the torsion bar. This oily film reduced the amount of corrosion. The bottom photograph in Figure 1 shows the surface contained approximately 60% spot corrosion on the surface of the torsion bar according to ASTM D610-08 (2012).

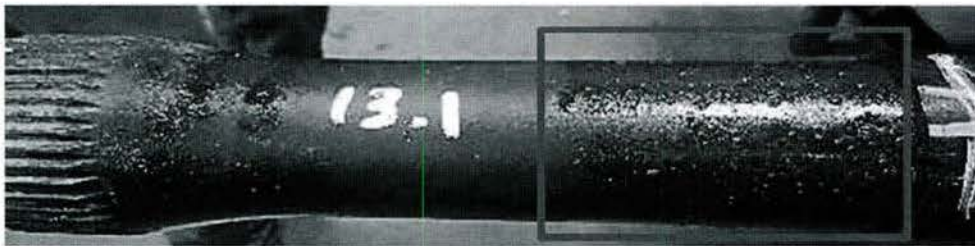


Figure 39 - Corrosion beneath Disbonded Coating

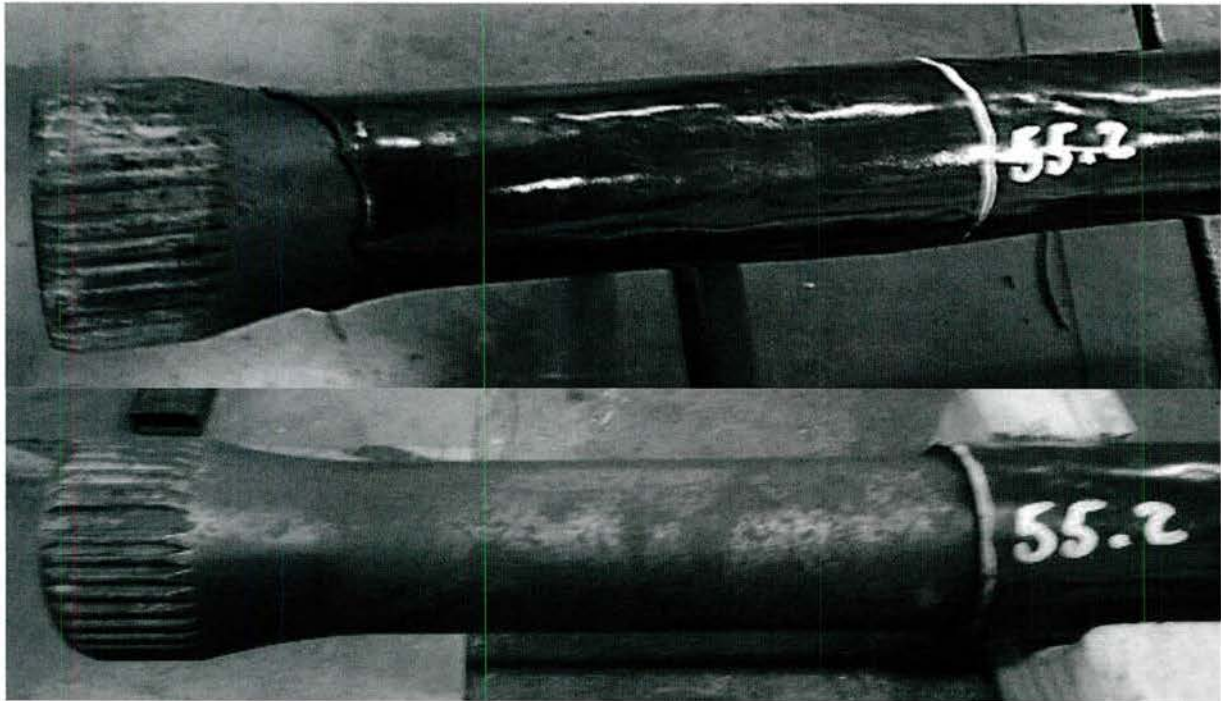


Figure 40 - Torsion Bar 55-2 Scrapped for Coating Disbonding. Top View Shows Coating Disbonding, Bottom View Shows Torsion Bar Surface after Coating Removal

Cross-Sectional optical photomicrographs of the oxide formation on Torsion Bar 55-2 are shown in Figure 41 and Figure 42. These photomicrographs show that a thin oxide layer, less than 0.001 inch thick, developed on the surface. They also show that surface pitting also occurred. The pits ranged in depth from 0.003 to 0.007 inch.

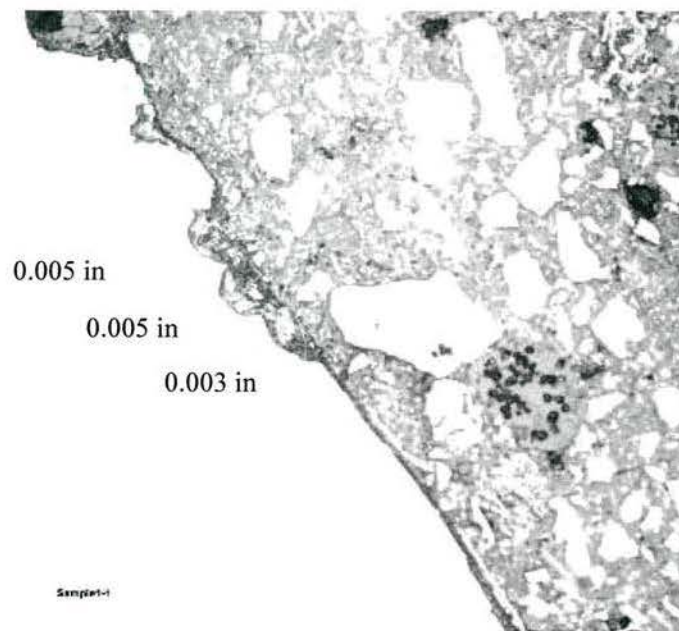


Figure 41 - Optical Photomicrograph of Oxide Layer on Region 1 of Torsion Bar 55-2 (Mag 200x)

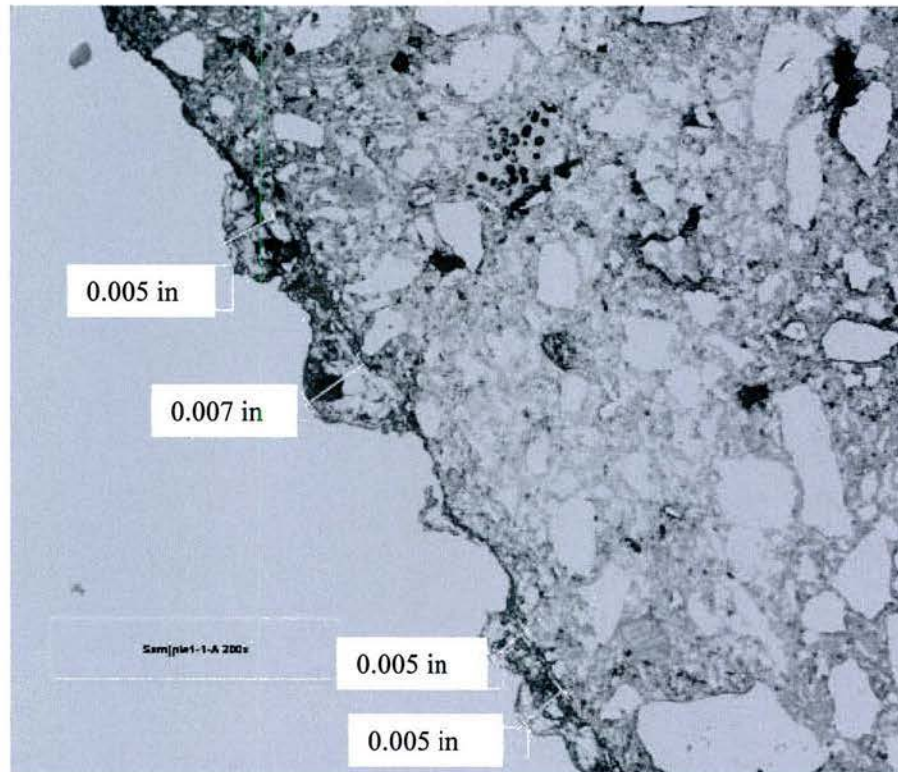


Figure 42 - Optical Photomicrograph of Oxide Layer on Region 2 of Torsion Bar 55-2 (Mag 200x)

Figure 43 is a Scanning Electron Microscopy (SEM) photomicrograph shows that the corrosion layer that developed on Torsion Bar 55-2 was non-uniform consisting of regions of thin oxide formation (Region A) along with regions of heavier oxide formation (Region B).



Figure 43 - SEM Photomicrograph of the Corrosion on Torsion Bar 55-2



Figure 45 - SEM Photomicrograph of the Thick (left) and Thin (Right) Corrosion Layers on Torsion Bar 55-2

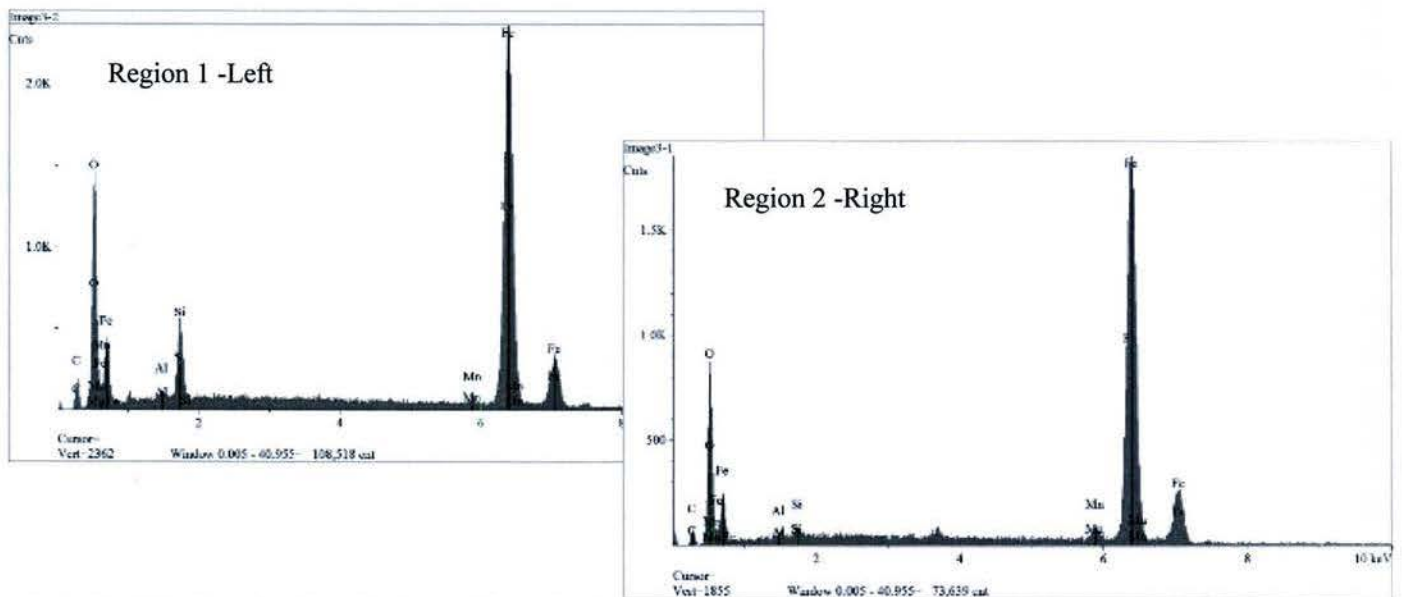


Figure 44 - Non-dispersive X-ray Analyses of Corrosion Layer on Torsion Bar 55-2

Figure 45 and the non-dispersive X-ray analyses in Figure 44 showed that the thick and thin corrosion layers consisted of iron oxide. The difference between the two layers was the thicker layer contained more

oxygen than the thinner layer. Thus, it contained more Fe_2O_3 and Fe_3O_4 than the thinner layer which consists mostly of FeO . It is interesting to note that there were cracks present in both the thick and thin oxide layers.



Figure 46 - Torsion Bar 53-2 Scrapped for Coating Disbonding. Top View Shows Coating Disbonding, Bottom View Shows Torsion Bar Surface after Coating Removal

Torsion bar 53-2 (Figure 46) was also scrapped because of coating disbonding close to the spline. Again the coating had poor adherence and could easily be removed revealing an oily residue on the surface of the torsion bar. Figure 47, a cross-sectional optical photomicrograph of the surface of torsion bar 53-2 shows again a very thin oxide layer developed on the surface. The cross-sectional optical photomicrographs also showed that a 0.001 inch thick oxide layer developed on the surface of this torsion bar there was surface pitting. The pits range in depth from 0.003 to 0.005 inch.

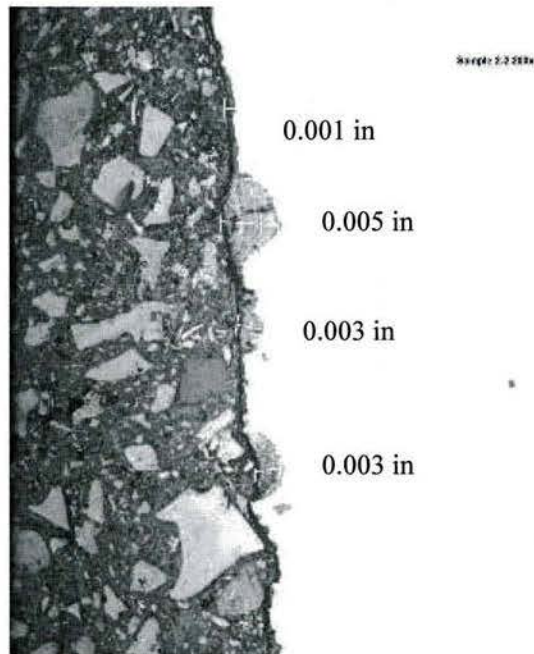


Figure 47 - Cross-Sectional Optical Photomicrograph of Corrosion Layer on Torsion Bar 53.2



Figure 48 - Higher Magnification SEM photomicrograph of Surface Oxide from Torsion Bar 53-2 (Mag 100x)

Scanning electron microscopy (SEM) photomicrographs of the oxide layer that developed on the surface of this torsion bar are shown in Figure 48. Figure 48 shows that a continuous oxide layer developed on the surface of torsion bar 53.2. Again the oxide that developed was non-protective showing areas of delamination (Region within square in Figure 48) and cracks (arrows in Figure 48).

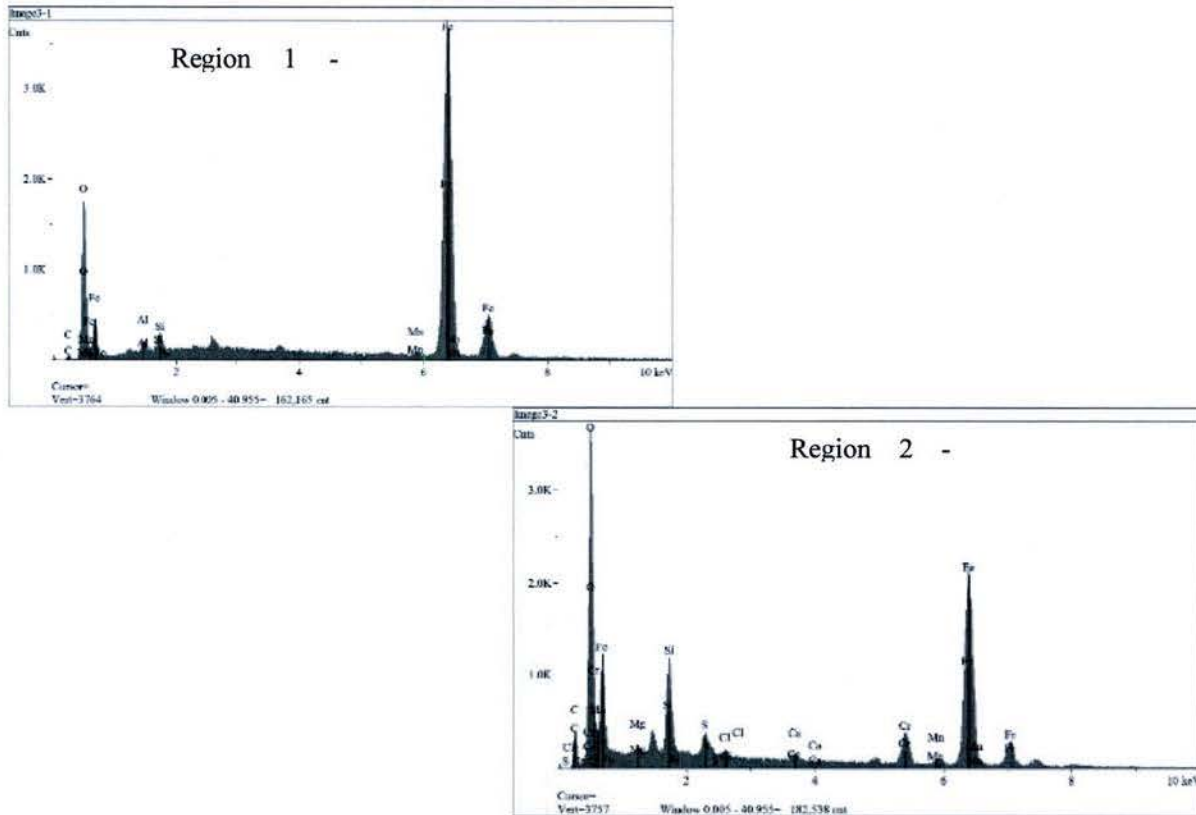


Figure 49 - Non-dispersive X-ray Analyses of Corrosion Layer on Torsion Bar 53-2

The non-dispersive X-ray analyses in Figure 49, again show that the oxide that developed is mainly iron oxide with some silicon oxide.

Torsion bar 55-2 was scrapped because of coating disbonding (Figure 51). Figure 51 Bottom shows that, in general, this torsion bar exhibited poor adherence. Also, when the coating was removed an oily film was observed on the surface of the torsion bar. This oily film reduced the amount of corrosion. The bottom photograph in Figure 1 shows the surface contained approximately 60% spot corrosion on the surface of the torsion bar according to ASTM D610-08 (2012)

Cross-Sectional optical photomicrographs of the oxide formation on Torsion Bar 55-2 are shown in Figure 50 and Figure 52. These photomicrographs show that a thin oxide layer, less than 0.001 inch thick developed on the surface. They also show that surface pitting also occurred. The pits ranged in depth from 0.003 to 0.007 inch

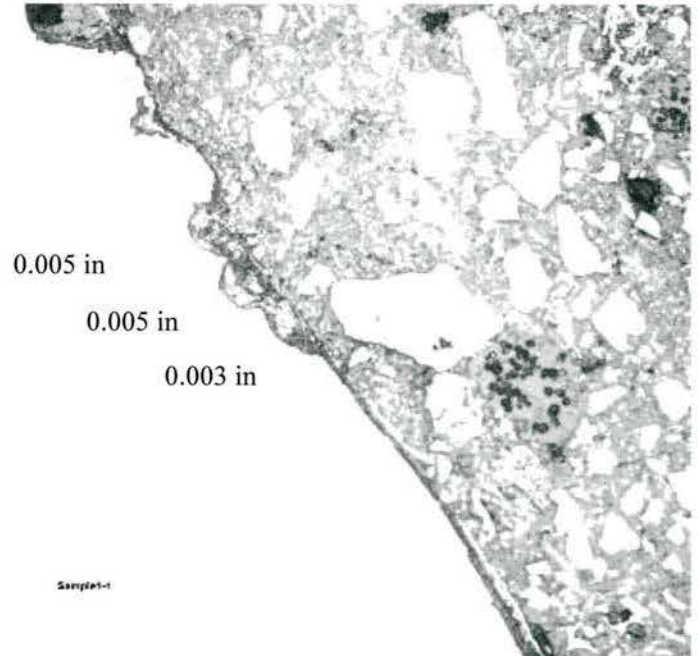


Figure 50 - Optical Photomicrograph of Oxide Layer on Region 1 of Torsion Bar 55-2 (Mag 200x)

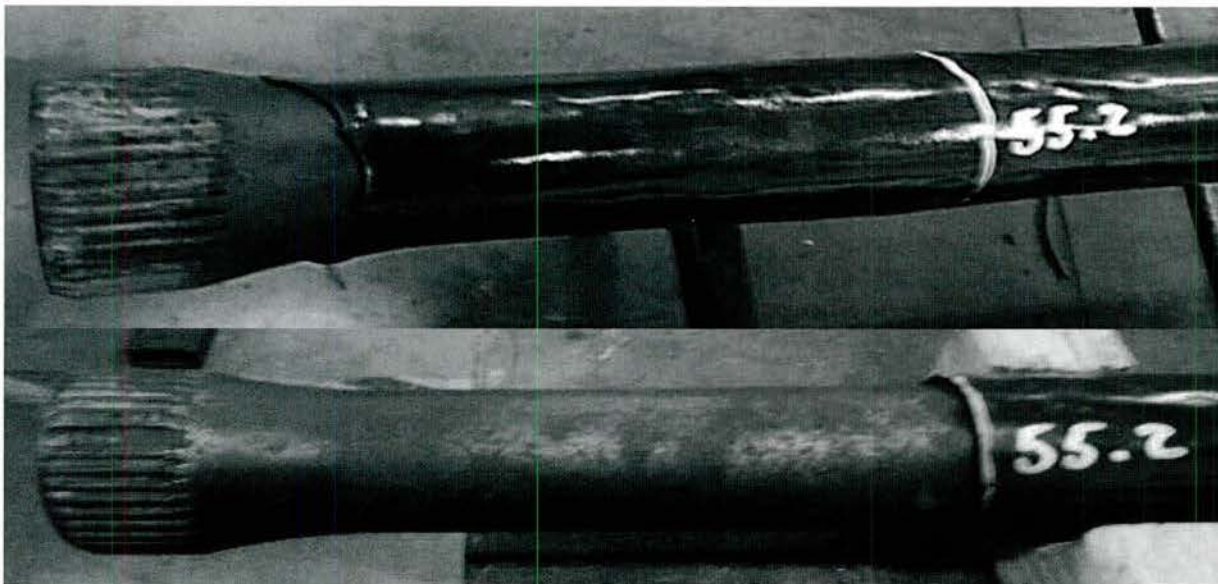


Figure 51 - Torsion Bar 55-2 Scrapped for Coating Disbonding. Top View Shows Coating Disbonding, Bottom View Shows Torsion Bar Surface after Coating Removal

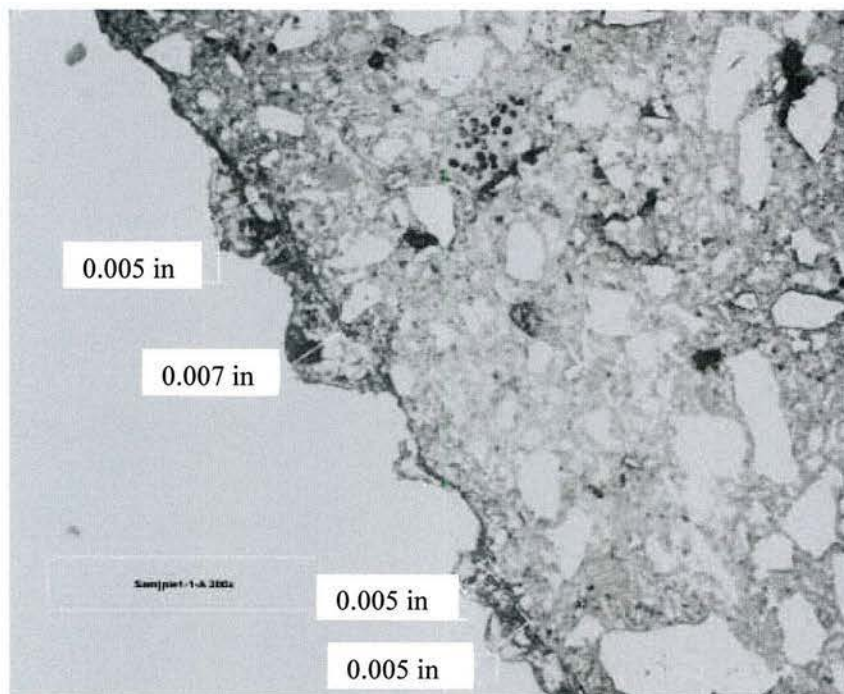


Figure 52 - Optical Photomicrograph of Oxide Layer on Region 2 of Torsion Bar 55-2 (Mag 200x)



Figure 53 - SEM Photomicrograph of the Corrosion on Torsion Bar 55-2

Figure 53 is a Scanning Electron Microscopy (SEM) photomicrograph shows that the corrosion layer that developed on Torsion Bar 55-2 was non-uniform consisting of regions of thin oxide formation (Region A) along with regions of heavier oxide formation (Region B).

Figure 55 and the non-dispersive X-ray analyses in Figure 54 showed that the thick and thin corrosion layers consisted of iron oxide. The difference between the two layers was the thicker layer contained more oxygen than the thinner layer. Thus, it contained more Fe_2O_3 and Fe_3O_4 than the thinner layer which is consists mostly of FeO . It is interesting to note that there were crack present in both the thick and thin oxide layers.



Figure 55 - SEM Photomicrograph of the Thick (left) and Thin (Right) Corrosion Layers on Torsion Bar 55-2

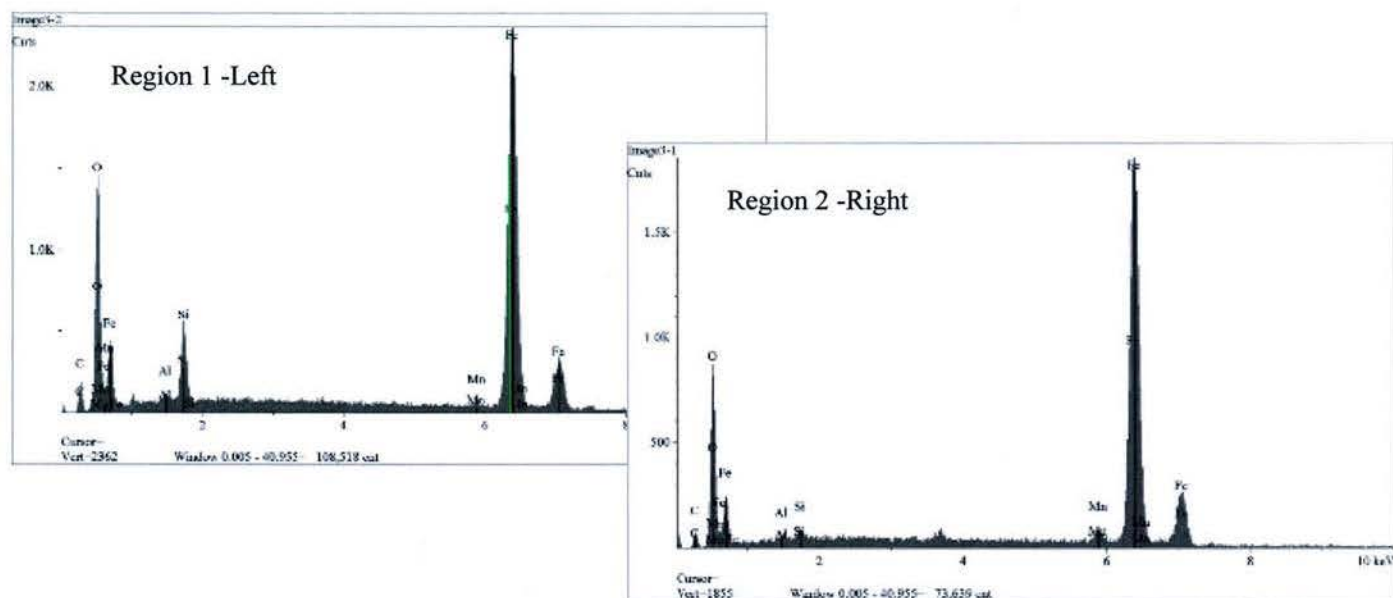


Figure 54 - Non-dispersive X-ray Analyses of Corrosion Layer on Torsion Bar 55-2

3.1.3 Investigation of Torsion Bars at Albany Depot

After the initial analysis of torsion bars, it was determined that a larger sampling of measurements was necessary. The goal of the second visit was to identify how far delamination of the coating extended up the bars from the bar ends. Additionally, surface roughness measurements of the bars after cleaning with a scotchbrite pad was performed in an attempt to identify typical roughness and pit depths.

Approximately 55 torsion bars were evaluated inside where the coating was actually removed and corrosion could be evaluated. In Figure 56, the blue line indicates the maximum distance from the splines that the damage occurs. The red line indicates the size of the damage area. For example, the peak around sample 18 indicates that the damage was approximately 9" from the spline end and was less than 1" in diameter. For the bars that were outside (samples 56+), the distance from the end was measured, but the extent of damage couldn't be measured without removing the coatings.

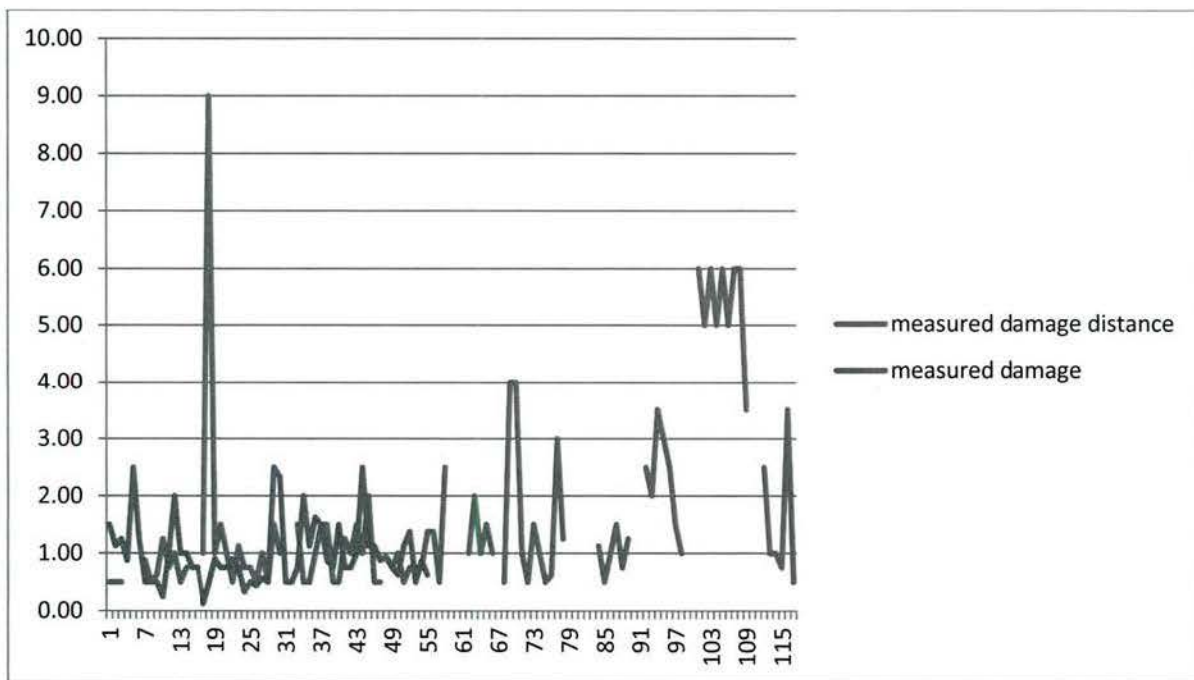


Figure 56 - Measured Damage on Torsion Bars

Additionally, for the torsion bars that were inside, every damage location was cleaned and the surface roughness measured. Those roughness measurements are plotted in Figure 57, along with lines of the minimum and maximum roughness for a new torsion bar.

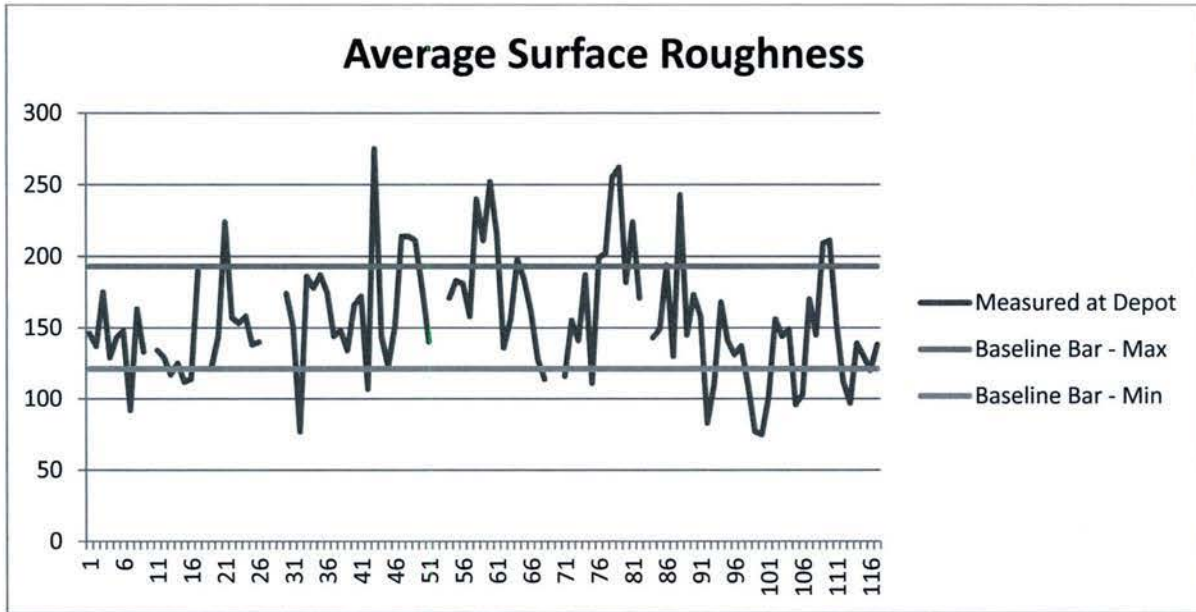


Figure 57 - Average Surface Roughness of Damage Areas

Based on the analysis at Albany, it was determined that further evaluation of bars was necessary. The average roughness indicates that a reasonable portion of the bars have pits that need to be repaired to pass the surface roughness requirements.

3.1.4 Examination of Torsion Bars off Vehicles from Albany June 16, 2015

Five scrapped torsion bars were shipped from Albany depot for analysis. Two of the bars had large holes in the coating. The remaining three bars had coating disbonding along one or both edges.



Figure 58 - Torsion Bar with Hole in Coating

Figure 58 and Figure 59 shows one of the torsion bars that exhibited a large hole. The physical appearance of the hole and surrounding area on these torsion bars indicate the coating failure was caused by heating the coating over its melting point. Figure 60 shows that there was light corrosion on the torsion bar where the coating was missing.

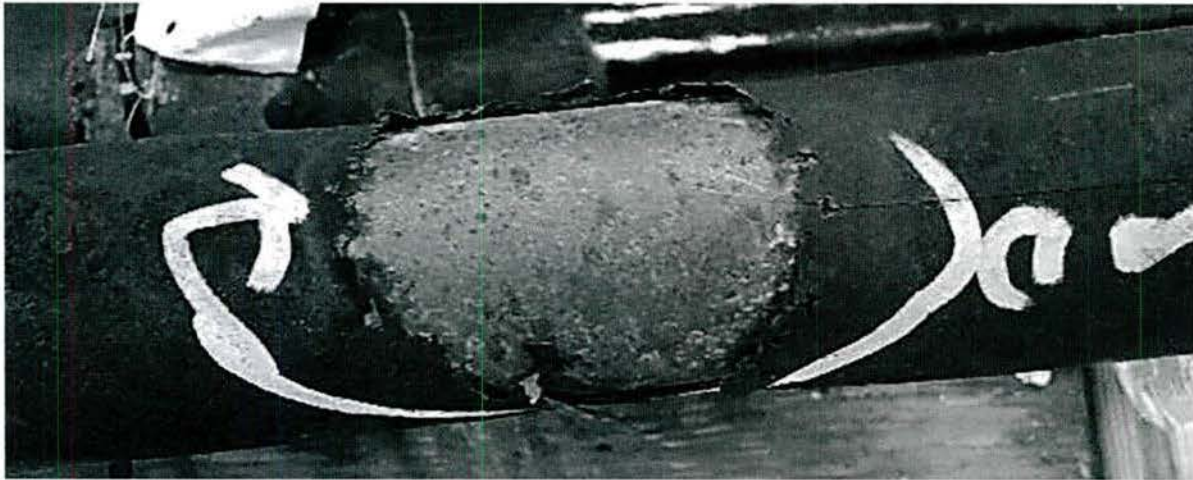


Figure 59 - Close-up of the Hole in Coating

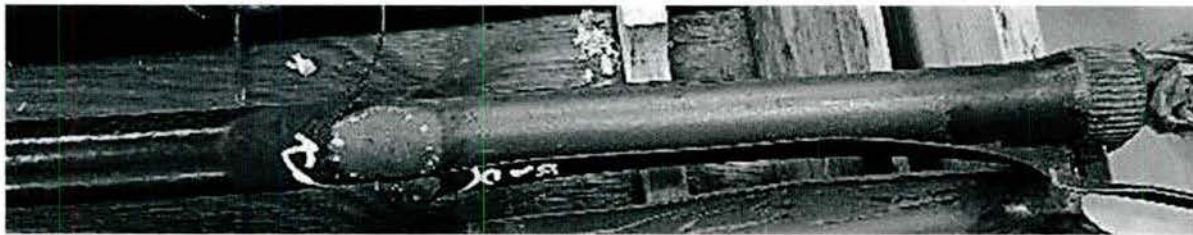


Figure 60 - Coating Stripped from Torsion Bar with Hole in Coating

In order to examine the surface the torsion bar around the hole the coating was removed from the torsion bar. The coating on this torsion bar was not bonded very well to the surface of the torsion bar. Once the coating was removed it was found that the entire surface of the torsion bar from the hole to the spline end exhibited corrosion. In addition, the corrosion beneath the poorly bonded coating was greater than the corrosion in the hole (Figure 61)

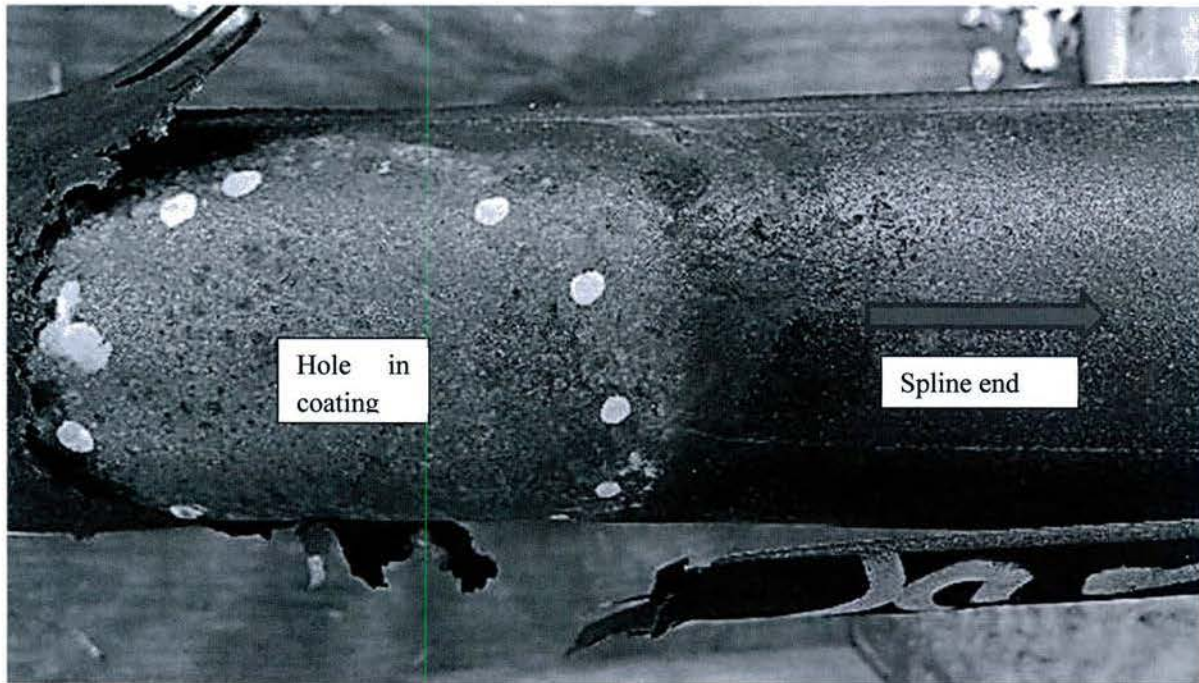


Figure 61 - Corrosion on Surface of Torsion Bar within Hole and Away from Hole

The remaining three torsion bars were scrapped because of coating disbonding from one or both of the edges away from the spline (Figure 62).



Figure 62 - Torsion Bar Send from Albany Depot Exhibiting Coating Disbonding



Figure 63 - Corrosion under Disbonded Coating on Torsion Bar

Figure 63 shows that the coating close to the spline had poor adherence and as result the surface beneath the coating exhibited 60 to 80 percent general rusting. However, as the adherence of the coating improved the amount of corrosion observed beneath the coating decreased (Region on bar in Figure 63 to the left of the line)

A second torsion bar which was scrapped for coating disbonding examined exhibited very light corrosion close to the spline when the coating was removed (Figure 64). In that region the coating has poor adherence. However, moving away from the end the coating adherence improved significantly and where there was good coating adherence there was very little, if any visual corrosion on the surface of the torsion bar (Figure 65).

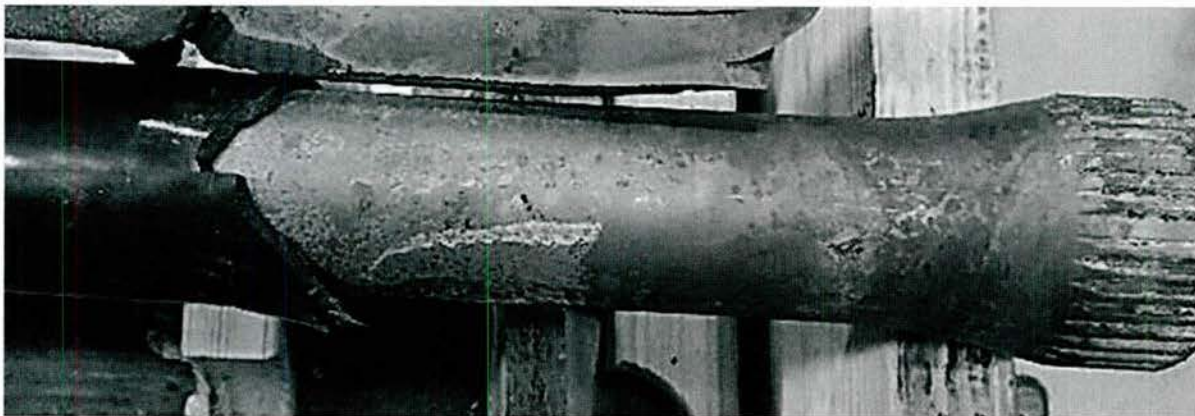


Figure 64 - Corrosion under Disbonded Coating on Second Torsion Bar



Figure 65 - Transition from Poor to Good Coating Adherence

Figure 66 shows a close-up of a region on the second torsion bar that exhibited good adherence. Again this figure showed that there was no corrosion under the polyethylene coating in this region.



Figure 66 - No Corrosion Observed Under Polyethylene Coating with Good Adherence

Figure 67 shows that corrosion developed under the poor adherent polyethylene coating. The small amount of corrosion observed was located in the depressions caused from the shot peening. The surface after coating removal in the good coating adherent region also showed some discoloration in the pits on the surface caused by the shot peening,

Scanning electron microscopy (SEM) photomicrograph analysis of the surfaces beneath poor and good adherence region in the torsion bar contain in Figure 65 are contained in Figures 48 - 50.

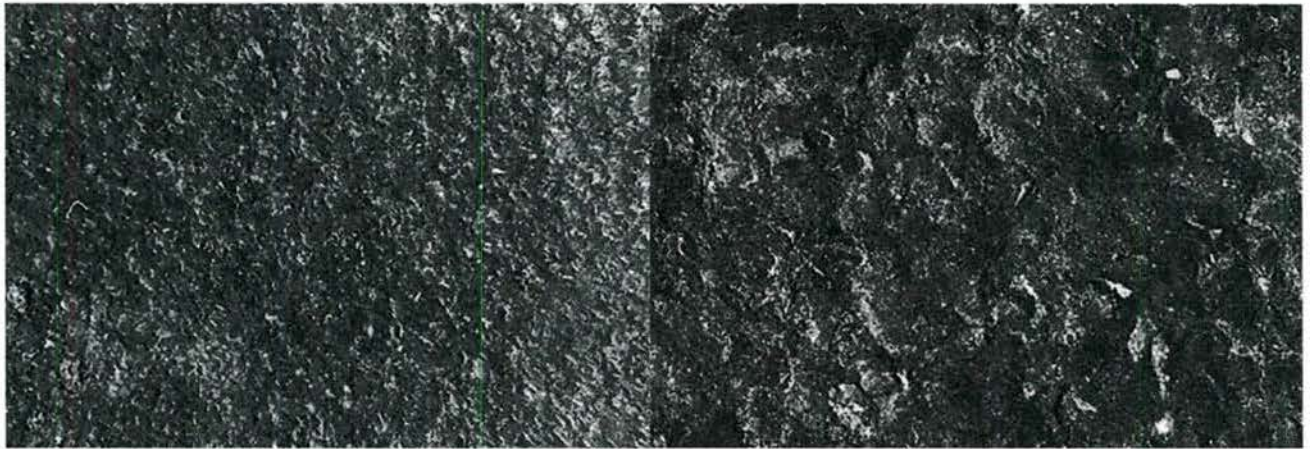


Figure 67 - Surface of Poor Adherence region from the Torsion Bar Shown in Figure 65 after Coating Removal (Mag 20x left, 100x Right)

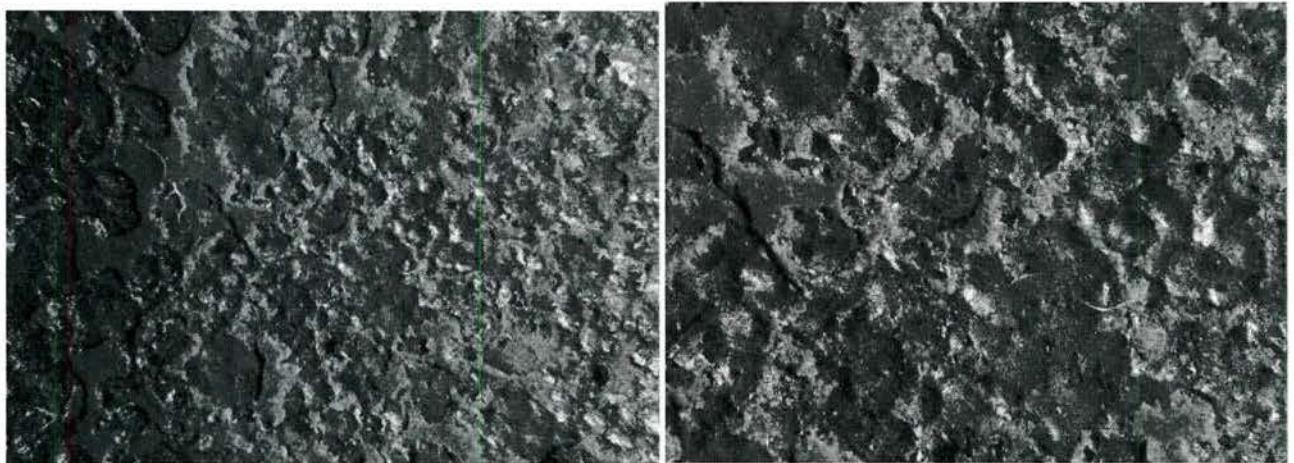


Figure 68 - Surface of Good Adherence Region from the Torsion Bar Shown in Figure 48 after Coating Removal (Mag 20x left, 100x Right)

Figure 52, a SEM photomicrograph of the surface beneath the region with poor coating adherence shows that a thin layer of primer still remained on the surface (Silicon peak in the non-dispersive X-ray pattern in Figure 52A) after the coating disbond. This figure also shows that small patches of oxide also was present on the surface (very large oxygen peak on the non-dispersive X-ray peak in Figure 52B)



Figure 69 - SEM Photomicrograph of Surface Beneath the Coating in a Poor Adherent Region from Figure 65 (Mag 33x)

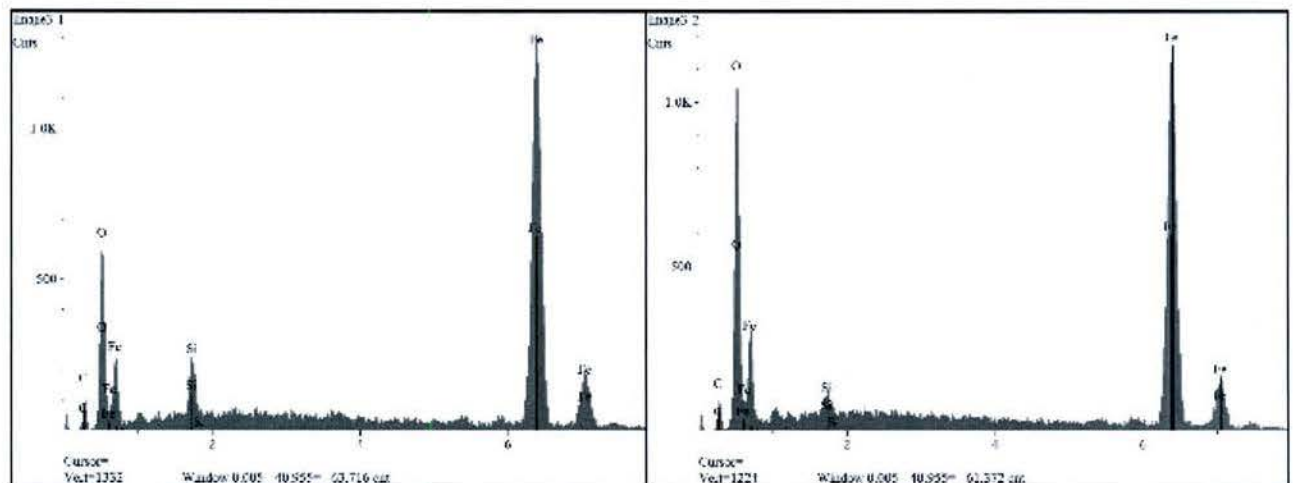


Figure 70 - Non-dispersive X-ray Analysis of Regions 1 (left) and 2 (right) in Figure 69

Figure 71 is a SEM photomicrograph of the surface beneath the region of good coating adherence from the sample in Figure 65. This analysis identified the red material on the surface as primer (Aluminum, silicon and oxygen peaks in Figure 72). The non-dispersive X-ray analysis in Figure 72 shows that after coating removal there was still a significant amount of primer remaining on the surface of the torsion bar. No oxide was observed on this surface after coating removal. Figure 73, a higher magnification SEM photomicrograph of the region between the thick regions of primer remaining on the surface after coating

removal and the non-dispersive X-ray analysis in Figure 74 also confirm there is a thin layer of primer remaining on the surface after coating removal. Again no oxide was observed on the surface.



Figure 71 - SEM Photomicrograph of Surface Beneath the Coating in a Good Adherent Region from Figure 65 (Mag 33x)

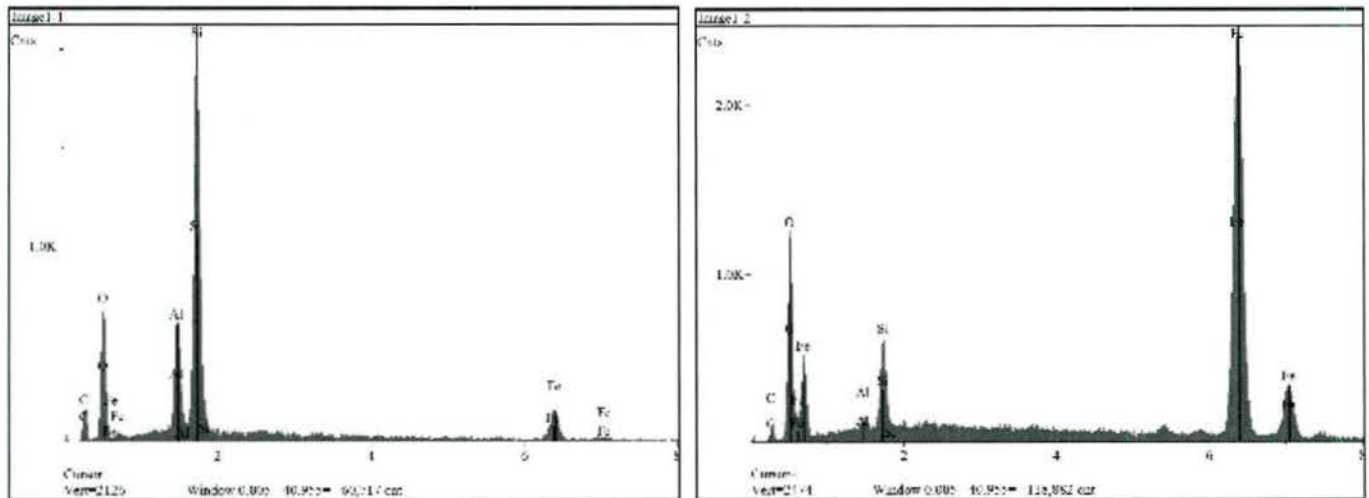


Figure 72 - Non-dispersive X-ray Analysis of Region 1 (left) and Region 2 (right) in Figure 71

Figures 55 and 56 contain cross-sectional optical photomicrographs of the oxide that developed under the poor adherent coating from the torsion bar in Figure 48. These photomicrographs illustrate that in this region that a non-continuous oxide layer developed and the depth of the pits that developed were 0.0008, 0.0009 and 0.0020 inch.

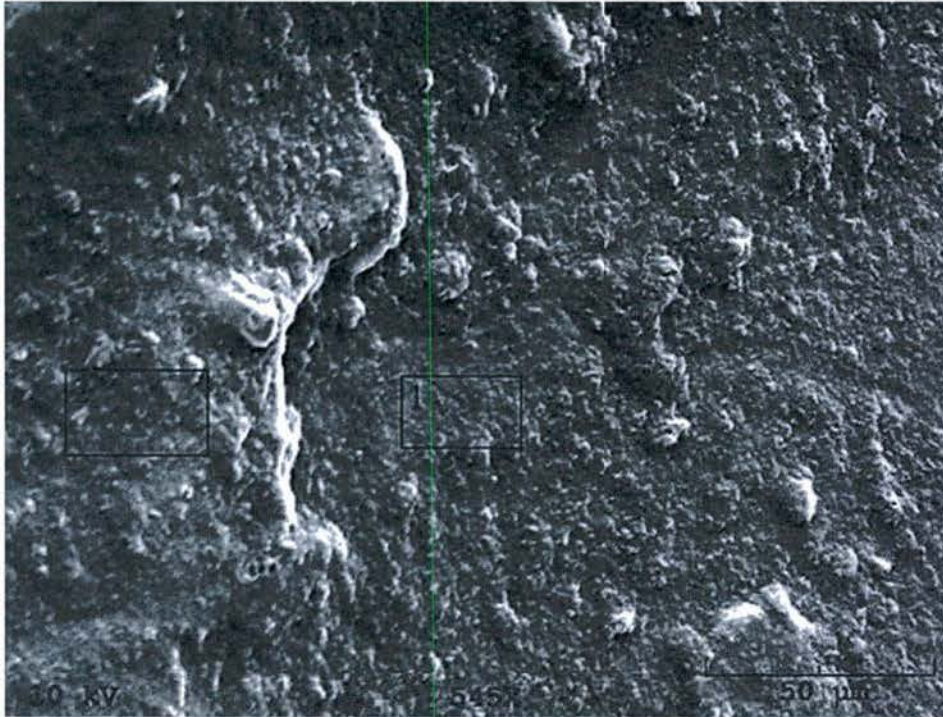


Figure 73 - SEM Photomicrograph of Surface Beneath the Coating in a Good Adherent Region from Figure 65 (Mag 33x)

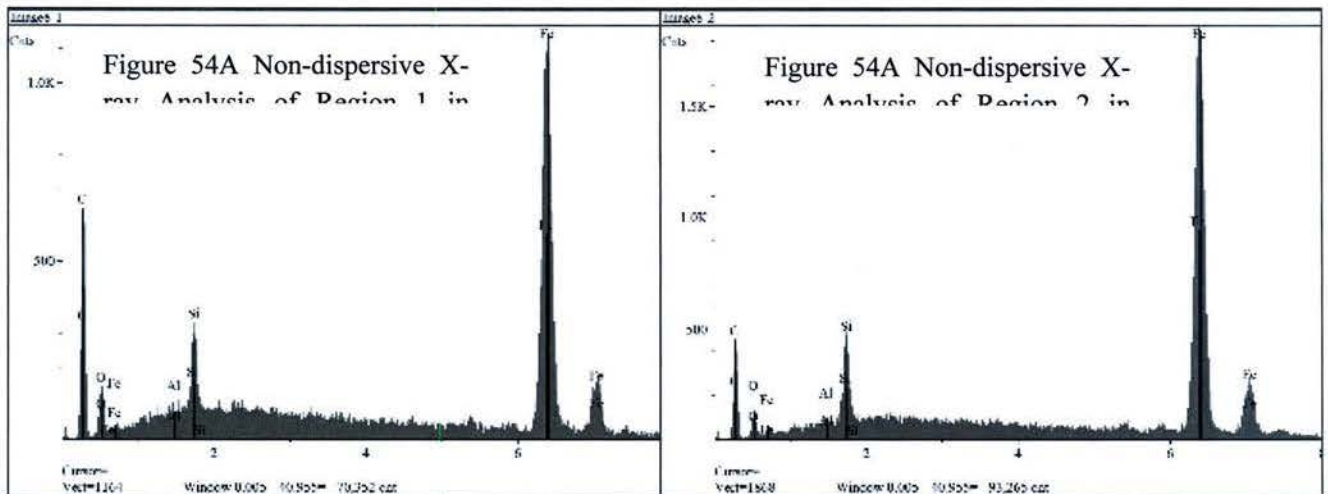


Figure 74 - Non-dispersive X-ray Analysis of Region 1 (left) and Region 2 (right) in Figure 73

Figures 55 and 56 contain cross-sectional optical photomicrographs of the oxide that developed under the poor adherent coating from the torsion bar in Figure 48. These photomicrographs illustrate that in this

region that a non-continuous oxide layer developed and the depth of the pits that developed were 0.0008, 0.0009 and 0.0020 inch.

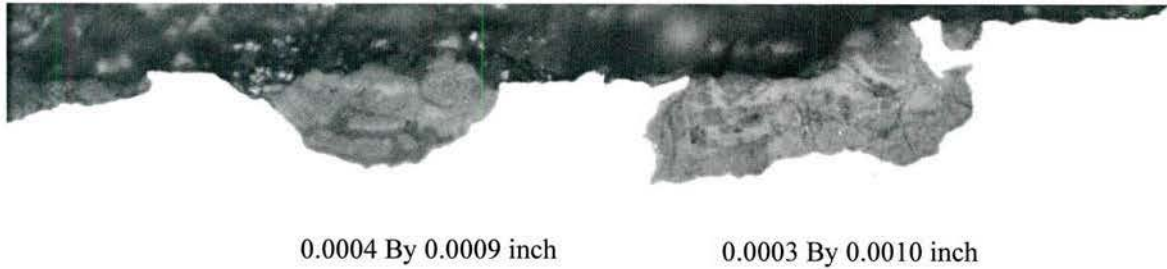


Figure 75 - Cross-sectional Optical Photomicrograph of Oxide Layer and Pitting on the Surface of the Torsion Bar in Figure 65 in the Poor Adherence region (Mag 1,000X)

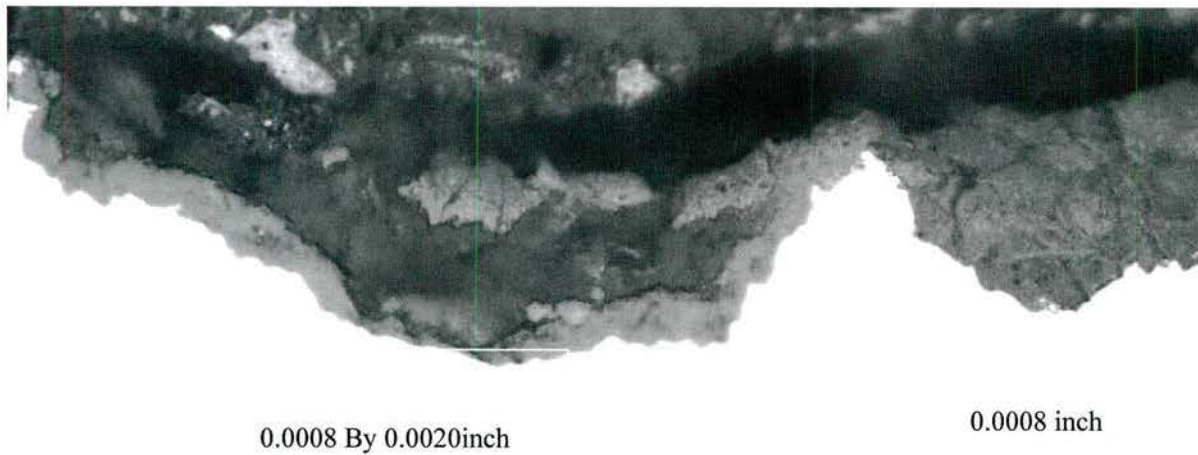


Figure 76 - Cross-sectional Optical Photomicrograph of Oxide Layer and Pitting on the Surface of the Torsion Bar in Figure 65 in the Poor Adherence region (Mag 1,000X)

3.1.5 Torsion Bars of Vehicles from Barstow

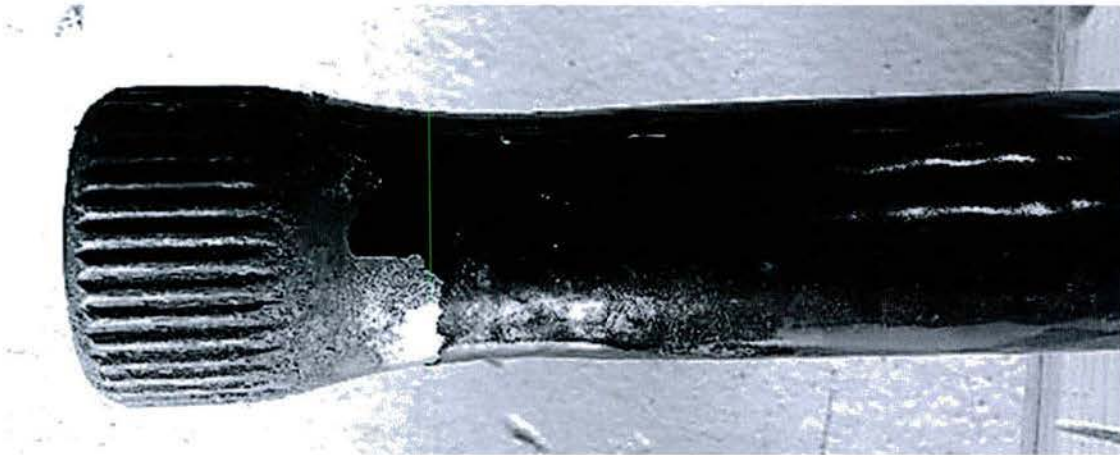


Figure 77 - Coating Delamination Close to Spline (Reason for Rejection)

Coating adherence from the torsion bars received from Barstow was variable. One torsion bar the bar that was scrapped because of coating delamination close to the spline (Figure 77) was found to have alternating regions of both good and poor coating adherence. Figure 78 shows that the coating adherence on that torsion bar ranged from poor close to the spline to very good (Blue region in Figure 78) and then back to poor (second orange box) followed by another region of good adherence (yellow circle). It is interesting to note that in all the regions of good adherence the remnants of the red primer was still attached to the surface of the torsion bar when the coating was removed, while in the regions which exhibited poor adherence (orange boxes) there was not primer remnants visible on the surface of the torsion bar. Thus, the adherence of the polyethylene coating is determined by how well the primer is bonded to the surface of the torsion bar.

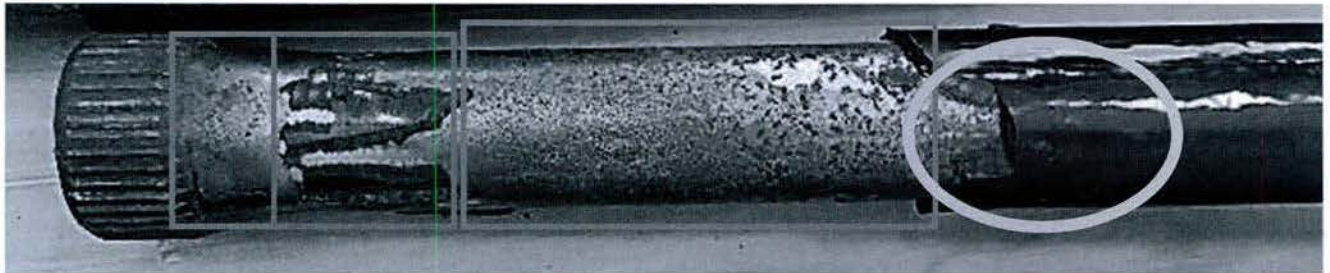


Figure 78 - Region of Good and Poor Adherence on Torsion bar From Barstow Depot (Red Regions poor Adherence, Blue Region Good Adherence)

In the regions where the polyethylene coating had poor adherence the torsion bar surface exhibited spot rusting. In accordance with ASTM D610-08 the rust grade was 1-S 50% rusted in both poor adherence regions (Figure 79). In the regions where the primer was well bonded to the torsion no significant rusting was observed under the coating (Blue box and yellow circle).

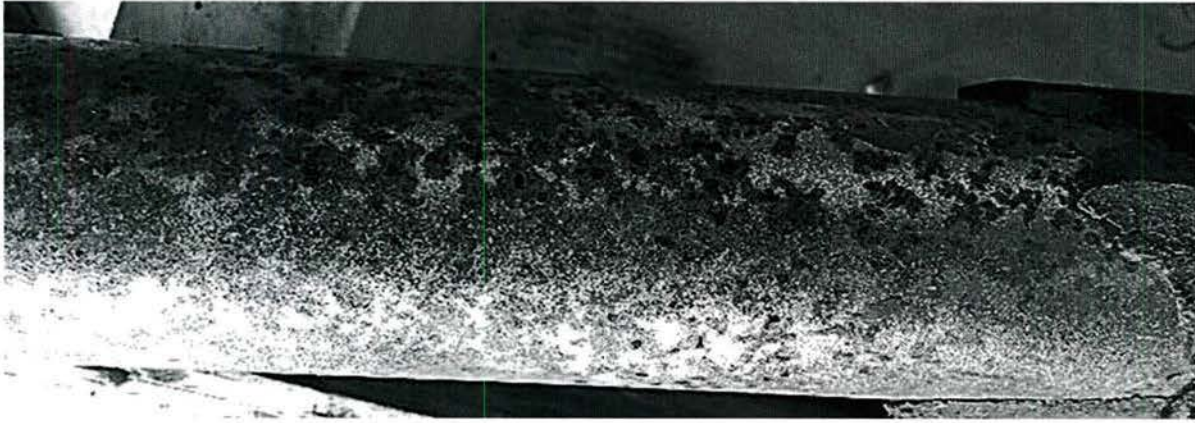


Figure 79 - Close-up View of the Corrosion That Developed Within the Region of Poor Primer Adherence

A second torsion bar removed from the Barstow vehicles which was also scrapped for coating disbonding close to the spline (Figure 80) showed that while the coating within 4 inches of the spline could easily be removed, (Red square in Figure 80) the remaining coating on this torsion bar had very good adherence and was very difficult to remove.

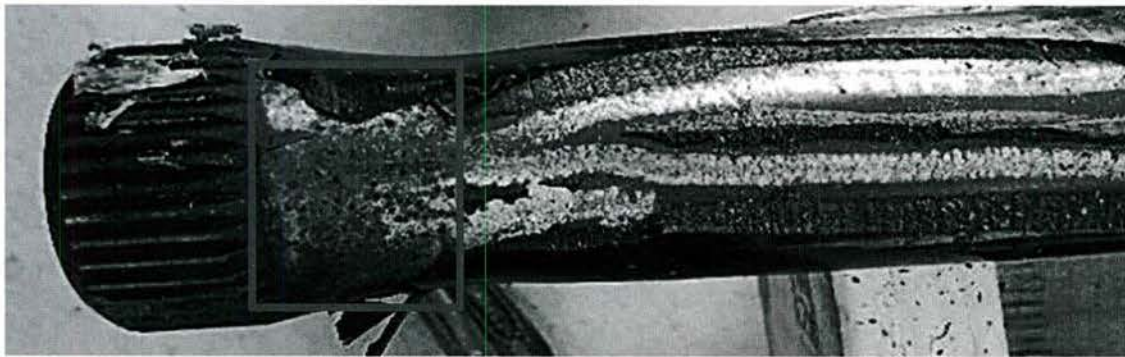


Figure 80 - Showing the Poor and Good Coating Adhesion Region on the Second Torsion Bar Examined (Red Box – poor Adhesion Region)

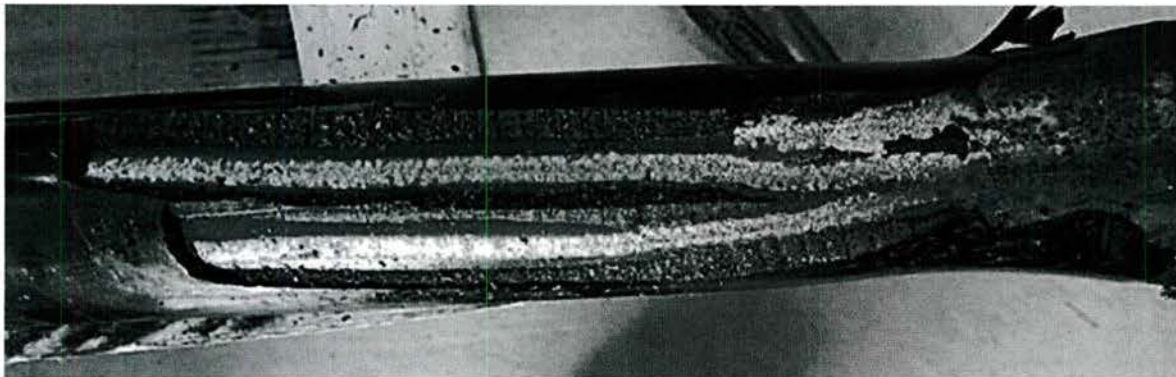


Figure 81 - Very Little Corrosion Observed Beneath the Polyethylene Coating in Region of Good Adherence.

Figure 81, a close-up picture of the second torsion bar, again shows that when there is good coating adhesion very little, if any corrosion was observed under the polyethylene coating.

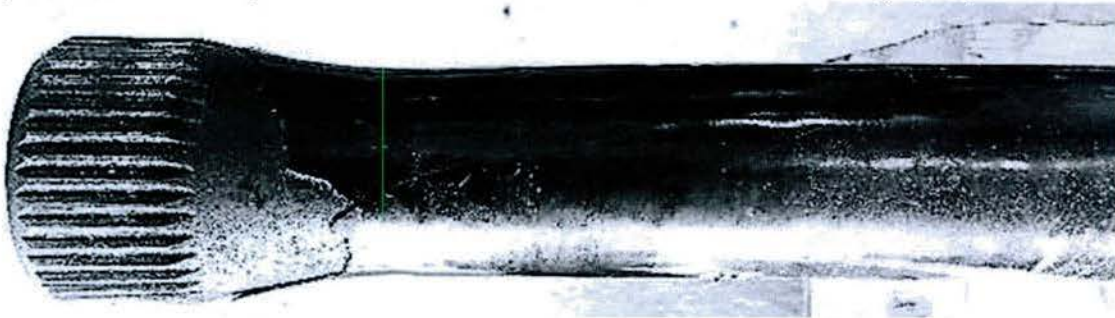


Figure 82 - Third Torsion Bar from Barstow Examined



Figure 83 - Coating Easily Removed Revealing an Oily Film

A third torsion bar received from Barstow, again scrapped because of coating disbonding, (Figure 82) exhibited very poor polyethylene coating adherence and when the coating was removed an oily film beneath the coating on the surface of the torsion bar was observed. The film (Figure 83) was similar to that observed on a number of torsion bars during the second Albany depot visit. However, Figure 84 shows that when the oily film was removed there was no corrosion was observed on the surface of the torsion bar.

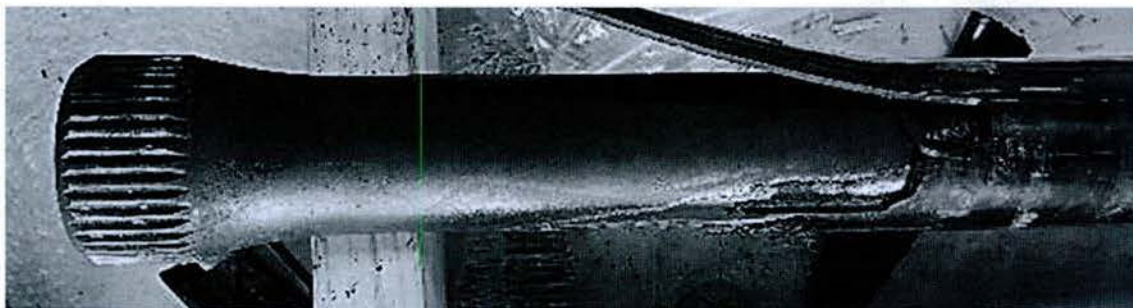


Figure 84 - Surface of Torsion Bar after Oily Film Removal

After the torsion bars were inspected, sections of two torsion bars examined were water-jet cut to obtain specimens for the optical and scanning electron microscopy examination of the corrosion that developed on the surface. Figure 85 shows the locations on the two bars from which this sample was cut.

Figure 65 is an optical photomicrograph of the surface from Barstow torsion bar B-1 after coating removal. This photomicrograph show that the primer was adhered to the surface of the torsion bar and when the coating was manually removed a portion of the primer remained on the surface. Away from the primer the surface had a copper color.



Figure 85 - Sections of Torsion Bars Cut for Examination of Corrosion on Surface

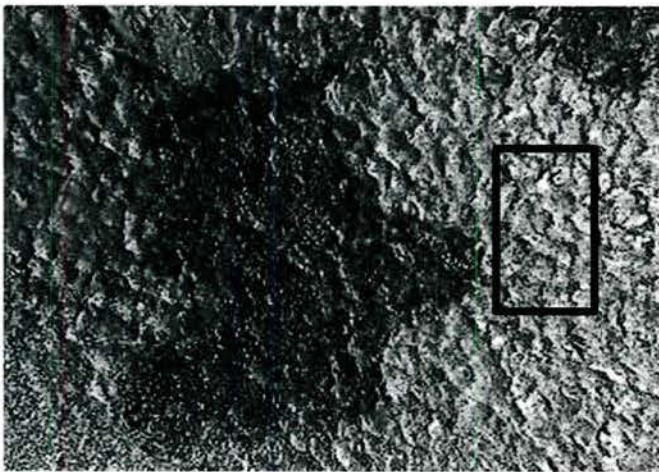


Figure 86 - Optical Photomicrograph of Surface of Torsion Bar B-1 after Coating Removal

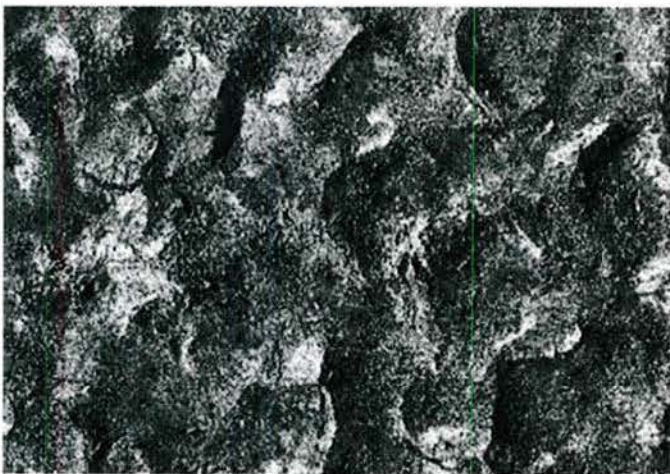


Figure 87 - Optical Photomicrograph of Surface of Torsion Bar B-1 Within the Black Rectangle in Figure 86

Figure 87, a higher magnification of the surface of B-1 shows discoloration on the surface of the torsion bar.

Figure 88 is a scanning electron microscope (SEM) photomicrograph of the surface of torsion bar B-1 after coating removal. The non-dispersive X-ray analyses in Figures 10A and 10B show that the “corrosion” or discoloration observed after coating removal was actually primer that was still remaining on the surface. The regions that look like mountains above the surface are regions where the primer disbonded from the polyethylene coating. The remaining regions, which show the shot peened surface, are regions where the primer disbonded from the torsion bar surface. However, the non-dispersive X-ray (Figure 68A and B) show that there was still a small amount of primer remaining on the surface after the coating disbonded. This small amount of primer prevented surface oxidation from occurring.

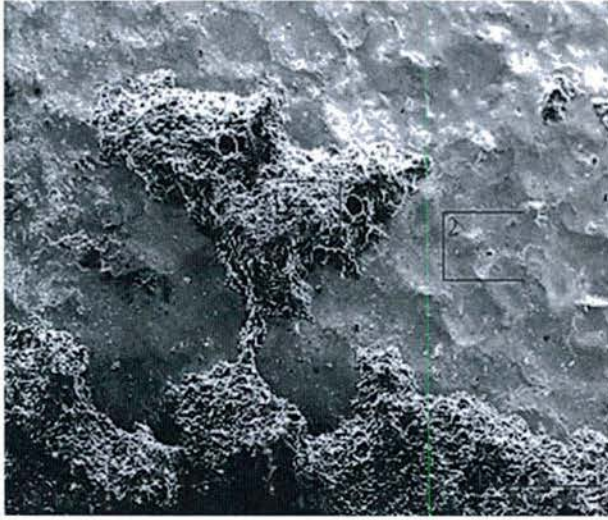


Figure 88 - SEM Photomicrograph of Surface of Torsion Bar B-1 after Coating Removal

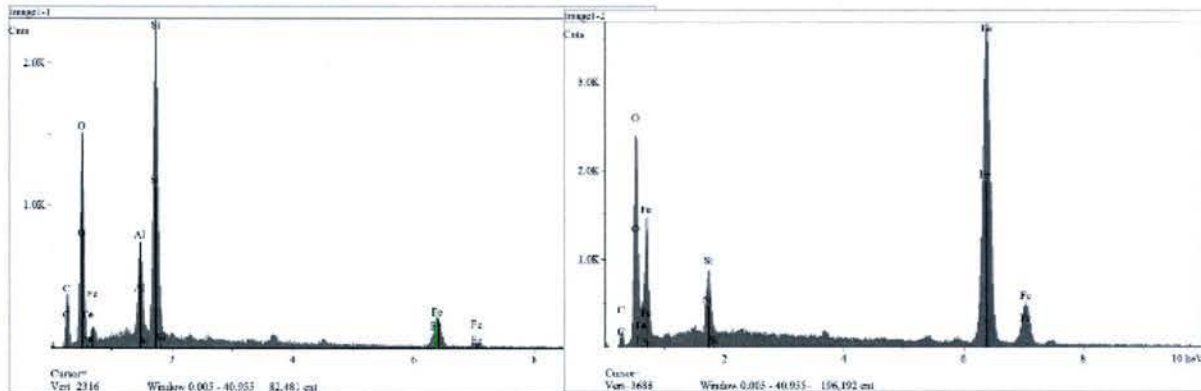


Figure 89 - Non-dispersive X-ray Analysis of Region 1 (left) and Region 2 (Right) in Figure 88

Figure 90 is a higher magnification SEM photomicrograph of the surface on Torsion bar B-1 in a region where the coating and primer had disbonded from the surface. (Rectangle in Figure 90). Again the non-dispersive X-ray analysis (Figure 91) showed that in this region a thin layer of primer remained on the surface and this small layer prevented any surface oxidation.

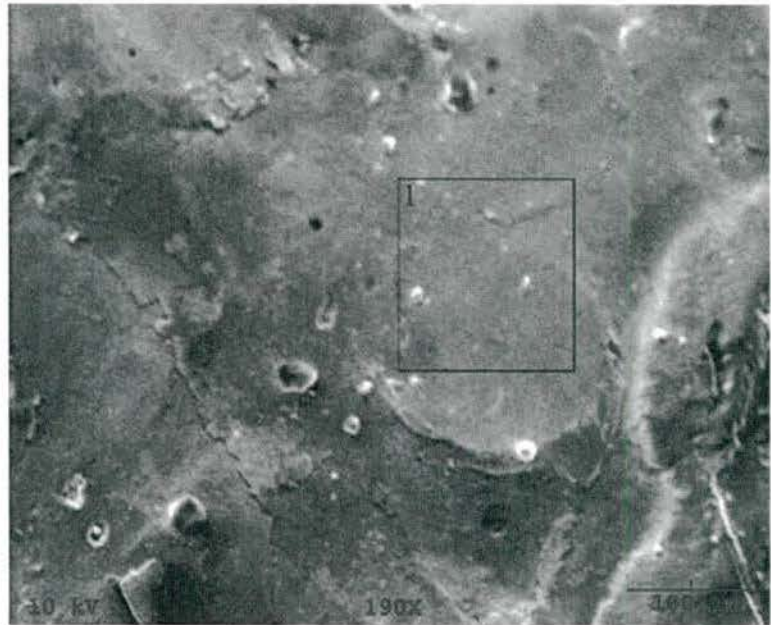


Figure 90 - High Magnification SEM Photomicrograph of Surface Where Coating and Primer Disbonded from the Surface of the Torsion Bar B-1 (Mag 190x)

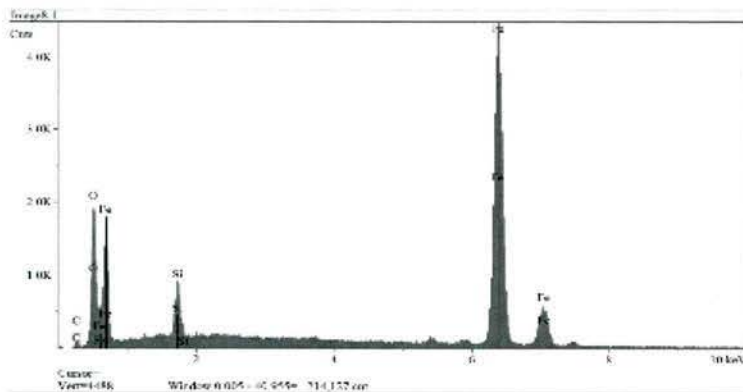


Figure 91 - Non-dispersive X-ray Analysis of Region 1 in Figure 90

Thus, for this specimen the discoloration was the result of the primer adhering to the surface and no significant amount of corrosion was observed.

Figure 92 and Figure 93 are optical photomicrographs of the surface of Torsion bar B-2 after coating removal. Again, since the coating on this torsion bar exhibited good adherence there was a significant amount of primer remaining on the surface.

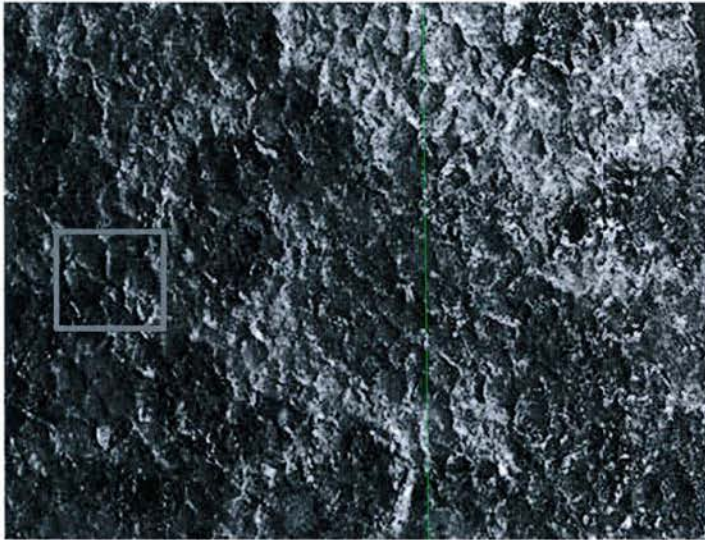


Figure 92 - Optical Photomicrograph of Surface of Torsion Bar B-2 after Coating Removal



Figure 93 - Optical Photomicrograph of Surface of Torsion Bar B-1 within the Highlighted Area in Figure 13 (Mag 100x)

Scanning electron photomicrographs of the surface of B-2 are shown in Figure 94. Again the SEM analysis shows that there is primer remaining on the surface after the coating removal. Also, very little surface oxidation was observed on this specimen.

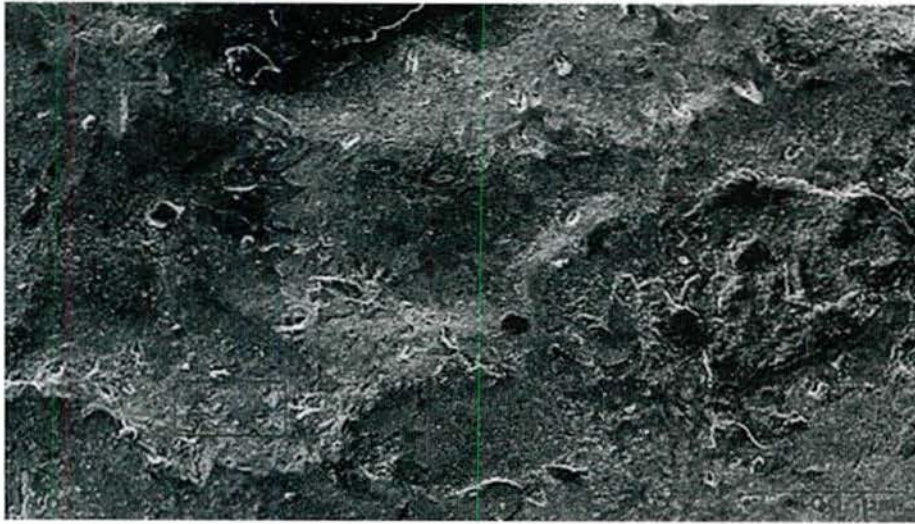


Figure 94 - SEM Photomicrograph of Surface Where Coating and Primer Disbonded from the Surface of the Torsion Bar B-2 (Mag 165x)

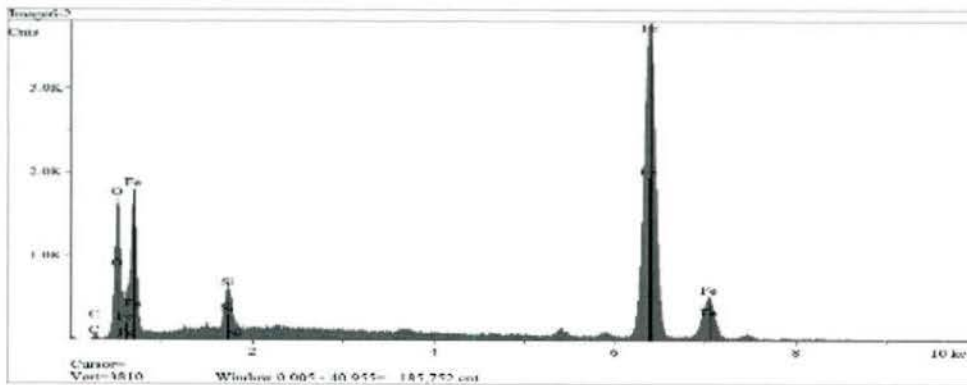


Figure 95 - Non-dispersive X-ray Analysis of Regions 1, 2 and 3 in Figure 94

Cross-sectional optical photomicrographs of the surfaces from the region that exhibited good coating adherence from the torsion bar in Figure 65 are contained in Figure 96 and Figure 97.



Figure 96 - Cross-sectional Optical Photomicrograph the Surface of the Torsion Bar in Figure 65 in the Good Adherence region – No oxide on surface (Mag 1,000X)

These photomicrographs show that the majority of the surface under the coating in the region where there was good coating adherence did not contain any oxide (Figure 95). However, there was some random oxide formation on this surface that results in pits that were 0.0003 wide by 0.0006 inch deep.



0.0003 By 0.0006 inch

Figure 97 - Cross-sectional Optical Photomicrograph of Oxide Layer and Pitting on the Surface of the Torsion Bar in Figure 65 in the Good Adherence region (Mag 1,000X)

3.2 Non-Destructive Evaluation Method Research

3.2.1 Determining Polyethylene Coating Adherence

How well a coating adheres to the surface of an article to which it is applied depends upon several factors, including: the coating composition, the surface composition, the condition of the surface prior to application of the coating, the presence of an undercoat or primer prior to application of the coating, the temperature and humidity during coating application, the method of curing or drying of the coating, and the time allowed for the coating to cure or dry⁵. However, even with rigidly controlled manufacturing processes, variations in coating adhesion will occur. These variations in coating adhesion have been occurring in AAV torsion bars.

One function of the AAV polyethylene coating is to act as a barrier to prevent corrosion on the surface of a torsion bar. However, when the coating disbonds from the torsion bar it exposes the metal substrate to the environment allowing corrosion to occur. If this corrosion becomes severe it could potentially cause a catastrophic failure of the torsion bar. Severe corrosion was believed to have been the cause of a number torsion bar failures prior to an engineering change that added the coating as a requirement during manufacture.



Figure 98 - Coating Disbond and Corrosion on Rejected AAV Torsion Bar

Since coating adherence is critical for a corrosion coating to function properly a method is needed to determine the extent of the coating disbonding on the torsion bars that have been rejected. Typically torsion bars that have been rejected for coating disbonding have exhibited varying amounts of corrosion.

Destructive Testing of Coating Adherence

Coating adherence can be determined two ways—destructively or non-destructively. Typically, to determine coating adhesion coatings are destructively tested using a material or device that is pressed against the coating surface for a certain duration and then removed. One example of a destructive test method (ASTM C633) utilizes a metal dolly with a flat circular surface that is secured to the coating using an adhesive. After the adhesive has cured, the dolly is pulled at various pressures until the dolly pulls the coating from the article or the adhesive detaches from the dolly or coating. While this test method determines the coating adherence it is a destructive test, and once the test is completed the test sample must be scrapped. In addition, in order to determine the adherence or disbonded regions on an AAV torsion bar coating a significant number of tests will be needed because of the size of the torsion bar. As this method

⁵ www.toscot.org/uploads/Adhesion_of_Coatings.pdf

destroys the sample being tested and requires a significant number of tests, it is impractical to use in a remanufacturing process for measuring the bond strength of the coating on the AAV torsion bar. For these reasons, RIT has chosen to forgo destructive adherence testing techniques and focus on non-destructive test methods for determining the coating adhesion on the AAV.

3.2.2 Non-Destructive Testing of Coating Adherence Techniques

There are several non-destructive inspection (NDI) techniques available that have the potential for identifying areas of disbonding in the coating. These techniques include x-ray, acoustic emission (AE), eddy current, ultrasonic and thermal wave imaging

The test method selection began by defining the selection criteria or specifications for the NDI technique. The criteria developed included:

1. Must be a quick and easy method and can be used while the torsion bar is on a lathe,
2. Must be reproducible,
3. Must be easily learned – do not have to be a NDI certified technician to perform testing
4. Must be capable of handling the AAV torsion bar geometry

Radiography (X-ray), a non-destructive testing (NDT) method that examines the volume of a specimen, uses X-rays and gamma-rays to produce a radiograph of a specimen, showing any changes in thickness, defects (internal and external), and assembly details to ensure optimum quality in your operation. . X-ray analysis can detect a coating disbond. However, because of the safety requirements and equipment costs, X-ray analysis would not be the best NDI technique for detecting coating disbands..

Acoustic emission (AE) is another NDI technique used for monitoring and evaluating structural integrity⁶. Acoustic Emission (AE) refers to the generation of transient elastic waves produced by a sudden redistribution of stress in a material. When a structure is subjected to an external stimulus (change in pressure, load, or temperature), localized sources trigger the release of energy, in the form of stress waves, which propagate to the surface and are recorded by sensor. Acoustic Emission is unlike most other nondestructive testing (NDT) techniques in two regards. The first difference pertains to the origin of the signal. Instead of supplying energy to the object under examination, AE simply listens for the energy released by the object. The second difference is that AE deals with dynamic processes, or changes, in a material. This is particularly meaningful because only active features (e.g. crack growth) are highlighted. The disadvantage of acoustic emission is that commercial AE systems can only estimate qualitatively how much damage is in the material. So, other NDE methods are still needed to do more thorough examinations and provide quantitative results. Moreover, service environments are generally very noisy, and the AE signals are usually very weak. Thus, signal discrimination and noise reduction are very difficult, yet extremely important for successful AE applications.

⁶ Alig, I. (Deutsches Kunststoff-Inst., Darmstadt, Germany); Bargmann, M.; Oehler, H.; Lellinger, D.; Wanner, M.; Koch, D., **Investigation of delamination mechanisms in polymer coatings by scanning acoustic microscopy**, *Journal of Physics D: Applied Physics*, v 44, n 3, p 034009 (10 pp.), 26 Jan. 2011

Eddy current testing induces and eddy current in the conducting surface of a metallic material because of electromagnetic induction⁷. Any defect in the material close to the surface disturbs the eddy current flow. Since the polyethylene coating is not magnetic this technique would not work for detecting coating disbonds.

Manual ultrasonic testing is one of the more common non-destructive testing methods performed on materials^{8,9,10}. This testing utilizes high frequency mechanical energy, i.e. sound waves, to conduct examinations and measurements on a test area. Typically, the UT inspection system consists of a transducer, pulser/receiver, and display unit. A pulser/receiver is an electronic device that can produce high voltage electrical pulses to the transducer. When driven by the pulser, the transducer generates high frequency ultrasonic sound energy into the material in the form of sound waves. When there are discontinuities such as inclusions, porosity, or a coating disbond in the sound path, part of the mechanical energy will be reflected from the discontinuities' (reflectors'). The reflected sound waves signal received by the transducer is then transformed back into an electrical signal and its intensity is shown on the display unit. Finally, the sound waves travel time can be directly related to the distance that the signal has travelled. From the signal, information about reflector location, size, orientation and other features can be determined.

Thermal imaging techniques simply involve pointing a camera at a component and looking at areas of uneven heating or localized hot spots¹¹. Infrared techniques can be used to detect flaws in materials or structures¹². The inspection technique monitors the flow of heat from the surface of a solid and this flow is

⁷ Uchanin, V.M., **Eddy-current flaw detection in structural elements**, *Materials Science*, v 42, n 4, p 494-501, July 2006

⁸ R. Raišutis, R. Kažys, L. Mažeika, E. Žukauskas, V. Samaitis L. Draudvilienė, A. Vladišauskas. **THE CONTACT TYPE NDT TECHNIQUE FOR DEFECT DETECTION IN MULTI-LAYERED COMPOSITE CONSTRUCTIONS USING ULTRASONIC GUIDED WAVES**, *The 12th International Conference of the Slovenian Society for Non-Destructive Testing, Application of Contemporary Non-Destructive Testing in Engineering, September 4-6, 2013, Portorož, Slovenia*

⁹ Parthasarathi, S., Aesoph, M.D.; Sampath, K.; Tittmann, B.R. **Thermal wave imaging and ultrasonic characterization of defects in plasma sprayed coatings** *Materials and Manufacturing Processes*, v 10, n 5, p 1077-86, 1995

¹⁰ Scherperell, D.E.; Fiore, N.F.; Kettler, R.A., **ULTRASONIC DETERMINATION OF THE ADHERENCE IN PORCELAIN ENAMEL**, *Materials Evaluation*, v 32, n 11, p 235-238, Nov 1974

¹¹ Viégas, Diego José Araújo, Póvoas, Yda Vieira; Santos, Frederico José Barros; de Carvalho, João Ribeiro **Utilization of the infrared thermography for the verification of the ceramic coating detachment**, *Electronic Journal of Geotechnical Engineering*, v 19, n 22, p 9915-9930, 2014

¹² Ptaszek, G.); Cawley, P.; Almond, D.; **Artificial disbonds for calibration of transient thermography inspection of thermal barrier coating systems**, Chimenti, D.E., *AIP Conference Proceedings*, v 1430, p 491-8, 2012

affected by internal flaws such as disbonds, voids or inclusions. Sound material, a good weld, or a solid bond will see heat dissipate rapidly through the material, whereas a defect will retain the heat for longer¹³.

After reviewing the advantages and disadvantages of each NDI test method it was to evaluate ultrasonic and thermal wave (thermography) technologies for detected polyethylene coating disbonds on the torsion bars. Table 2 is a comparison between ultrasonic and thermal imaging or thermography NDI techniques.

¹³ Parthasarathi,,; Aesoph, M.D.; Sampath, K.; Tittmann, B.R.. **Thermal wave imaging and ultrasonic characterization of defects in plasma sprayed coatings**, *Materials and Manufacturing Processes*, v 10, n 5, p 1077-86, 1995

Table 2 - Comparison of Properties between Ultrasonic and Thermal Imaging Techniques

NDT Method	Ultrasonic	Thermography
Description	Ultrasonic testing is based on the propagation of ultrasonic waves in the tested material. As the waves propagate they will be reflected off of defects, cracks, or gaps in the material. A disbond between the coating layer and the substrate will result in an unexpected wave propagation behavior.	Thermographic analysis uses a thermal imaging camera and an applied heat source to map where corrosion, defects or disbonds cause variation in heat dissipation. A disbond would show as cooler area if heat is applied internally or as a warmer area if applied externally.
	Minimal setup Mobile	Non-contact Easily distinguishable results Fast
	Not well established for this geometry and material Less intuitive	Involved setup Expensive equipment Requires test design

Results of Ultrasonic and Thermal Imaging Evaluation for detecting Coating Disbonds

Ultrasonic Inspection



Figure 99 - Olympus Ultrasonic Flaw Detector

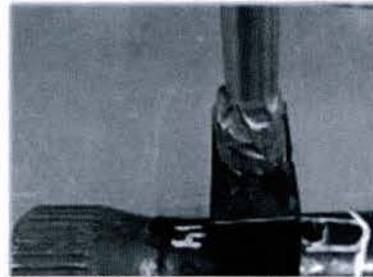


Figure 100 - Ultrasonic Testing for Coating Disbond

As

mentioned previously ultrasonic inspection can be used to detect coating disbonds. RIT's search of ultrasonic equipment identified Olympus and General Electric (GE) as major suppliers. Both companies came to RIT to provide a demonstration/evaluation of the technology on the AAV torsion bar. Several different probes were utilized and both the Olympus and GE probes were able to detect coating disbonds close to the edge, where the coating was relatively thin. However, the ability of this test method to detect coating disbonds decreased as the coating thickness increased. Increasing the frequency, in turn increased the penetration depth of the sound wave produced by the probe, did not improve the situation. Again both probes could not detect coating disbonds away from the splines in the regions where the coating increased in thickness at either the higher or lower ultrasonic frequencies.

The combination of the coating thickness and the large variation in coating thickness around the diameter and along the length of the coating applied to the torsion bar were major factors in preventing ultrasonic testing being able to detect coating disbonds.



Figure 101 - Ultrasonic Test Results

3.2.3 Thermal Wave Inspection

Two methods of thermal wave inspection were investigated. In one method, an electric current was run through the torsion bar to heat the metal. The second method used a heat gun to heat the coating. In both cases, the theory was the coating (Method 1) or base metal (Method 2) should be cooler in the areas where there was a coating disbond because in those regions the air gap, cause by the coating disbond, would act as an insulator reducing the amount of thermal wave transfer in that region.

Method 1 was unable to get enough electric current into the torsion bar to uniformly heat the bar along its entire length. Instead, the end got hotter than the center of the bar. Method 2 was able to heat the torsion bar more evenly. Figure 102 shows a thermal image of the heated bar and shows that at the end of the bar, where coating disbonding was observed, the temperature of the torsion bar was lower

than the regions away from this region. However, the uncoated spline region is also at a lower temperature. Therefore the difference in surface temperature may have been a result of the torsion bar diameter being greater in this region (more mass), and not necessarily because of a coating disbond. Again the variability in coating thickness prevented this method from being successful.

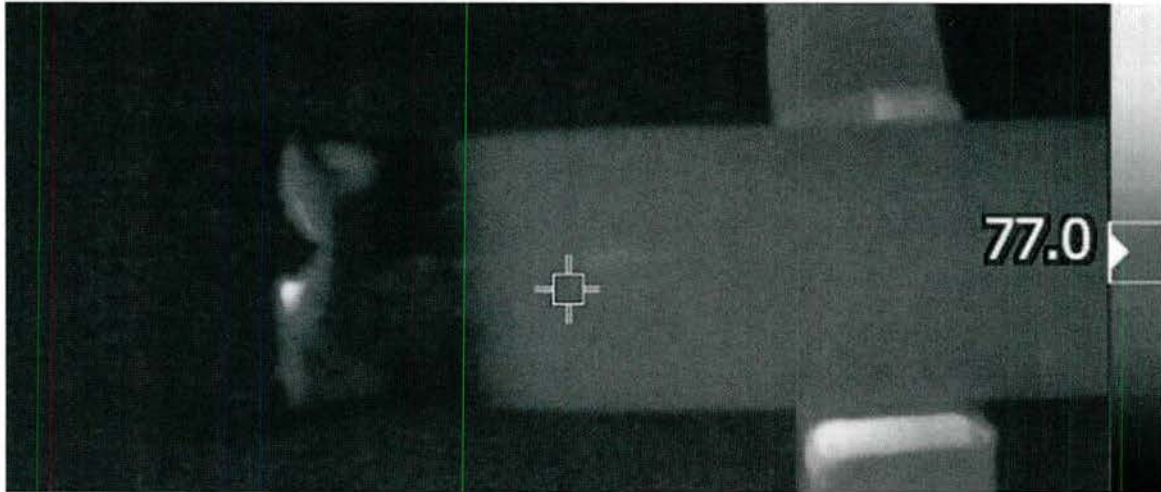


Figure 102 - Thermal Wave Image from Method 2

3.2.4 Conclusions

The literature review identified that ultrasonic and thermal wave imaging were the two best candidates to detect coating disbonds. Both techniques were evaluated. Neither of the techniques were able to conclusively detect coating disbonds. At this time, it is the recommendation of RIT that coating disbonding be visually identified when removing the coating.

4 Development of Acceptance Criteria

4.1 Data Gathering Process

4.1.1 Analysis for Refurbishment

The goal of analytical modeling for refurbishment is provide understanding of the useful remaining life of a component or subsystem, and to determine the acceptance criteria used in the screening process for components before they pass into the refurbishment stage. Modeling of a component provides decision makers with much of the information needed to evaluate the risks and rewards associated with a refurbishment program before processing of hardware begins. Although there are benefits to analytical modeling, such as providing a quicker understating of the potential problems, the use of modeling alone is not a substitute for testing of a component. Advantages from analytical modeling are more pronounced for components that require long time period test durations in order to observe failures or that require complex testing apparatus to accurately replicate operation. Setting up a framework at the initiation of a project for the analytical modeling process servers not only as a guide for engineers but can also highlight gaps in the information available that will be needed to successfully complete the project. An example of this analytical

modeling process will be demonstrated on the AAV torsion bar as a way to convey the steps required to complete a robust refurbishment project.

4.1.1.1 The Modeling Process

An overview of the modeling process used in this example is provided in the Figure 103; component material and geometric properties for the torsion bar were reviewed first. Once the loading and intrinsic properties of the component were understood then the potential failure modes associated with use of the torsion bar were examined through replication of these factors on sub-scale specimens. Material, environmental, and applied load testing was completed on the laboratory test specimens to evaluate their individual and combined effects the test specimen integrity. Models of the torsion bar were created that incorporated the data from the specimen test results in order to simulate the long term affects. Bounding the effects caused by loading of the component while in service allowed for the determination of the criteria used for screening the torsion bar for acceptance into the refurbishment process. The following report sections provide documentation of each step of this process as it was applied in the torsion bar example and, as a result, shows how it can be applied to other components in both commercial and armed services refurbishment programs.

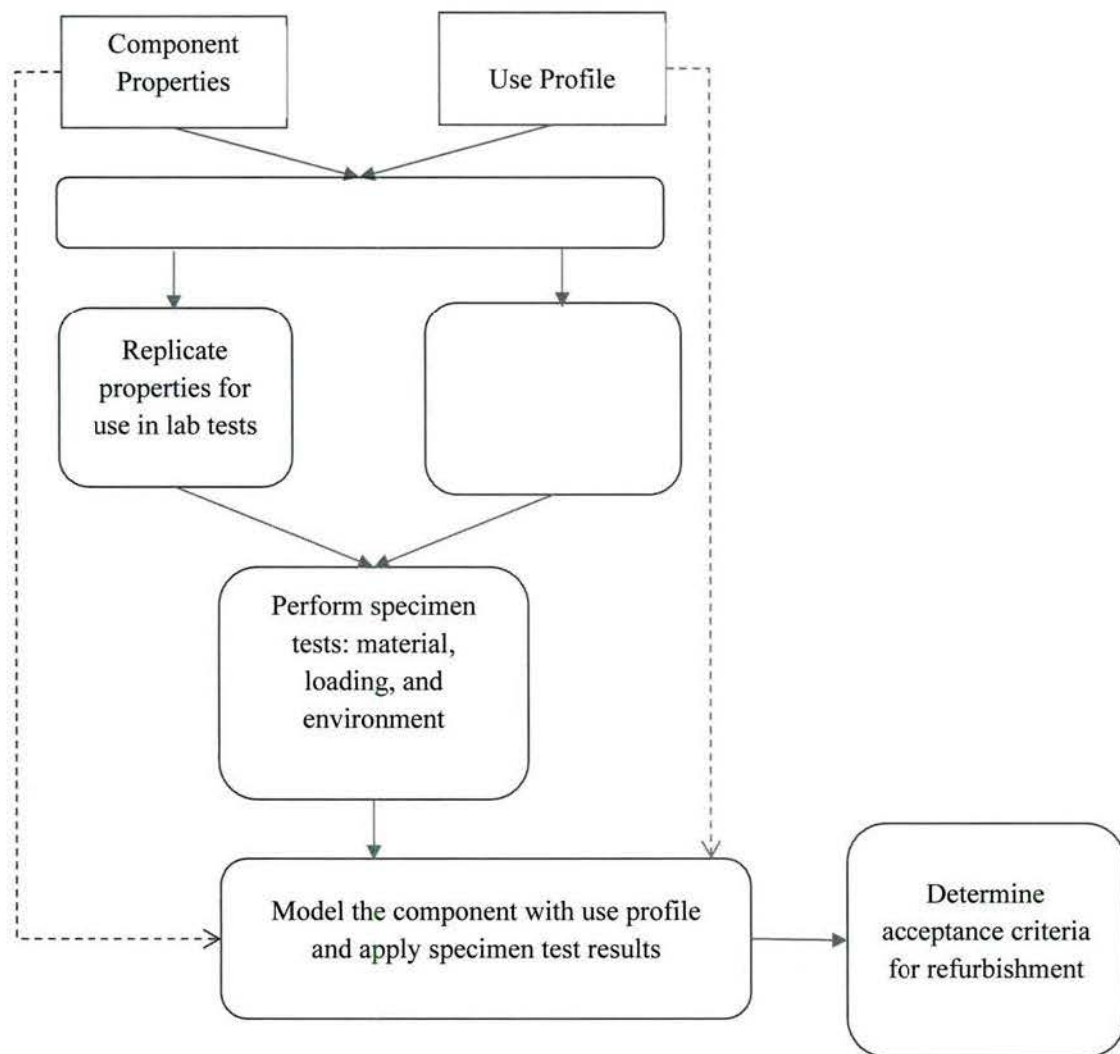


Figure 103- Mechanical Evaluation Process for Recapitalization

4.2 Torsion Bar Overview and Operations

4.2.1 Component Characteristics and Properties

Key to the refurbishment process was the availability of detailed data on the torsion bar and the ability to witness use of the component in actual operation. Without the data provided by the AAV Program Management Office the effort required to execute the project would have increased substantially and the level of confidence in the end result would have been as great. The documents provided include:

- Torsion Bar, Suspension dimensional drawing; Department of the Navy Drawing Number 7010599 Rev B including dimensions, notes, and initial processing information, refer to Figure 104 Torsion Bar Drawing Excerpt.

- Critical Item Product Function Specification for Torsion Bar, Suspension; Department of the Navy Drawing Number 7001119 Rev B including manufacturing requirements, processing, inspection, and first article testing of the metal bar.
- Protective Coating Specification for Torsion Bar, Suspension; Department of the Navy Drawing Number 7010600 Rev B including cleanliness, material, dimensions, testing, and first article requirements of the polyurethane coating.

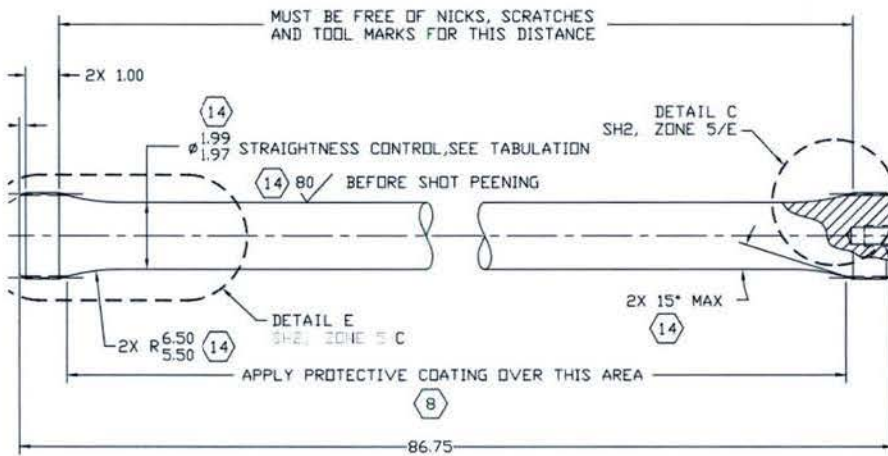


Figure 104- Torsion Bar Drawing Excerpt

Detail provided in the drawings allowed engineers to create three dimensional (3D) computer aided design (CAD) models of the torsion bar with enough resolution to accurately represent the critical features. Without this level of detail a reverse engineering project would have been implemented to identify the material via x-ray fluorescence, section the bar to evaluate the microstructure and hardness related to the heat treatment, and 3D laser scan the surface to capture the geometry. The torsion bar is an 86.75 inch long symmetric steel shaft with a 1.99 inch diameter straight section in the middle that tapers near the end to splines having a major diameter of 2.562 inch. A primer and polyurethane coating are applied from the middle up to the minor diameter on the splines.

Properties of the torsion bar that were identified from the drawings include a minimum through hardness of 51 Rockwell C, alloy 300M to AMS standard 6257, 200% shot peening coverage and intensity before and after a torsional preset of greater than 169.4°, and the final residual angle after the preset operation. These characteristics are valuable when performing mechanical stress analysis on the component under load conditions that it will experience in the field. Additionally, the properties of the material identified from these drawing specifications can shed light on potential failure modes associated with its use in typical Marine Corps environments, such as ocean water. Furthermore, the torsion bar drawing shows a revision in 2005 where the coated area of the bar was extended up the “neck” toward the splines. Based on conversations with AAV maintainers at the depot, the coating was extended to the splines for “Gen 2” bars to prevent potential failures. The primer applied beneath the coating is processed to MIL-P-53022 that specifies the pigment contain corrosion inhibitors and zinc phosphate that reduce the effects of

corrosion on the shaft. The total percentage of these compounds in the primer is approximately 12% by weight.

4.2.2 Use Profile

As shown in the process flow diagram, one of the first steps is to determine the Use Profile. Information for the Use Profile can be obtained from drawings, specifications, test data, analyses, and educated hypotheses, if needed. The loads employed for the stress and fatigue analysis for the torsion bar example were based on the values gathered from a) data recorded in a TARDEC 18 inch wall test performed in February 2005 b) endurance test section of Navy drawing 7001119, and c) visual estimates from brake and speed bump tests witnessed at the depot.

4.2.2.1 Torsional Loads

To begin determination of the Use Profile, ONR provided data on the displacement of the road wheels on the AAV as it ascended over an 18 inch wall. This data was obtained from a TARDEC test that provided sensor measurements for the port and starboard side road wheels. The data shows a maximum and minimum vertical displacement of 4.7 and -7.6 inches during the test that correspond to the Starboard wheel #3 and Port wheel #4 respectively. Displacement of three consecutive wheels on the port side is graphed in Figure 105 which shows that the positive direction is toward the chassis. The negative value corresponds with the calculated position for an unloaded bar.

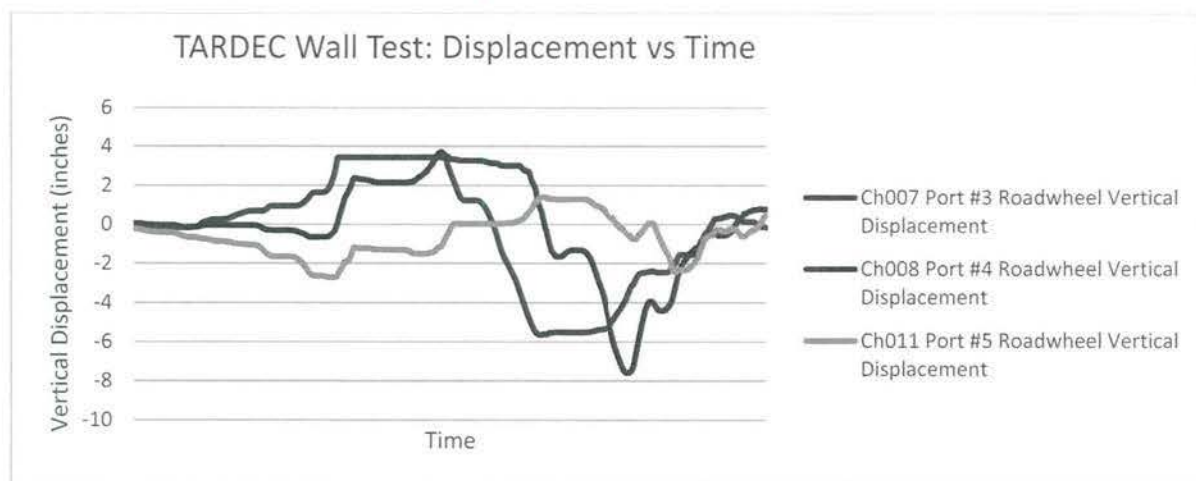


Figure 105- TARDEC Suspension Travel Data

To compare the loading between the TARDEC data and other load scenarios, the vertical displacements were converted into angular rotation about the center of the torsion bar. This conversion process to rotation required two main steps: 1) Determining the initial angle due to the vehicle weight 2) Calculating the final angle of rotation resulting from the vertical displacement measurement and initial angle. The initial angle of the support arm compared to level was found using a photograph of the AAV wheel assembly taken at the depot. The result of this study was an angle of approximately 37° from level, however, this method of calculation has uncertainty associated with it due to interpretation of the relative photograph dimensions, refer to Figure 106- Depiction of Transform from Cartesian to Polar Coordinates. The equation for a circle was used to calculate the final angle based on vertical displacement from TARDEC and the x and y position related to the initial angle. This transform process can be applied for the TARDEC data and subsequent

loading calculations. The angular rotation, θ , corresponding to the vertical displacement of 4.7 inch in the TARDEC is 19° .

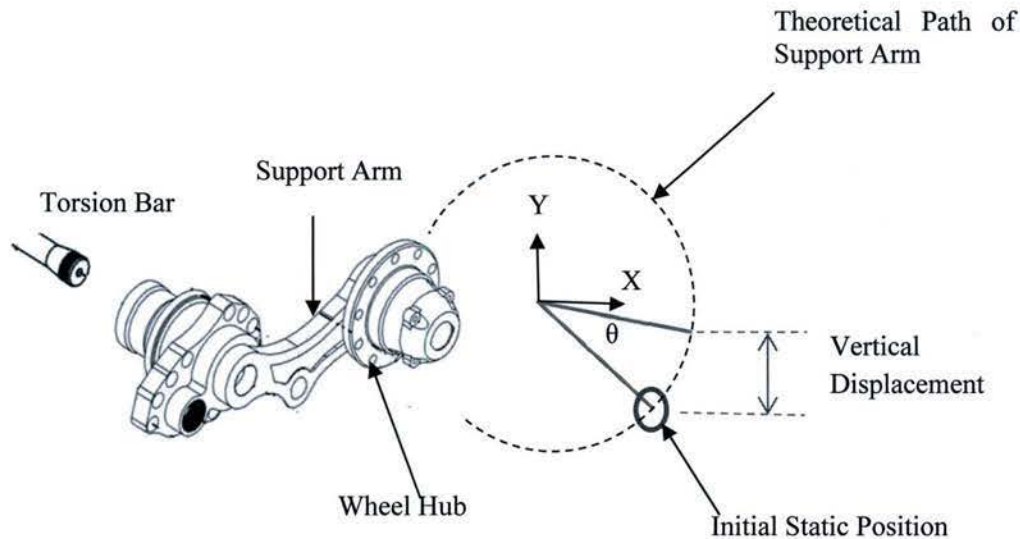


Figure 106- Depiction of Transform from Cartesian to Polar Coordinates

Using the same method employed to transform the TARDEC data, the change in the vertical displacement of the road wheel as witnessed during the brake and speed bump tests were transformed into angular rotations. This information was obtained from visually estimations by GIS engineers of the displacement during the testing of a refurbished AAV on an asphalt track at the Albany, GA depot in 2014. The displacements of 10 and 6 inches for the brake and speed bump test correspond to 46° and 24° of angular displacement, respectively. These values were for the wheels that had the greatest displacement during the test. The brake test resulted in the greatest angular rotation, 46° , when compared to the TARDEC and speed bump tests.

For the complete picture of the loading on the torsion bar and dynamic loads calculated from the brake test must be added to the angle of rotation resulting from the AAV static vehicle weight. To determine this static load, the first step was to obtain a value for the weight supported by each of the 12 torsion bars. Initially the value of 7,200 lbf was used based on available data from the hydropneumatic suspension report by Cadillac Gage Textron¹⁴ which assumed a 15% vehicle growth. Later in the project data was supplied for the AAV weight distribution¹⁵ for the AAV-1 MK 154 System T157 that provided the highest load of 7,660 lbf for axle number 2 on the port side. This force was then theoretically applied at the center of the 16inch support arm/hub to determine a torsional load of 122,560 lbf-inch. To begin the conversion of this

¹⁴ Susan Stack. Final Design Report In-arm Suspension Model Number 6kA1-AAV-0103. Cadillac Gage Textron, 1988

¹⁵ Test Record for the Physical Characteristics of the Assault Amphibious Vehicle (AAV) Baseline Testing. U.S. Army Test and Evaluation Command, Report No. AD-F-08-14; Sept 2014

load into rotation angle, a Solidworks finite element model was used to calculate a spring constant for the torsion bar. The formula relating torque to angle or rotation, $T=k\theta$, can be solved for the spring constant, k , given an input torque and measurement of the rotation. A 3D model of the torsion bar was drafted and a finite element analysis was applied to determine the spring constant for the entire bar. As a result of current limitations in Solidworks, the angular rotation had to be computed based on Cartesian displacements, refer to Figure 107. The procedure was to apply a torque of 6,000inch-lbf to one end of the torsion model and unite that end of the bar to an arbitrary arm for Cartesian measurement purposes. The opposite end of the bar was fixed. From this analysis a vertical displacement of 9.96E-2 inches was measured on a moment arm of 3.94inches from the center of the bar. This results in a spring constant of approximately of 2.4E-4 Degrees / (inch-lbf). This spring constant was employed to convert the 122,560 lbf-inch vehicle torsional load into an angular rotation of approximate value of 34.8° due to the vehicle weight.

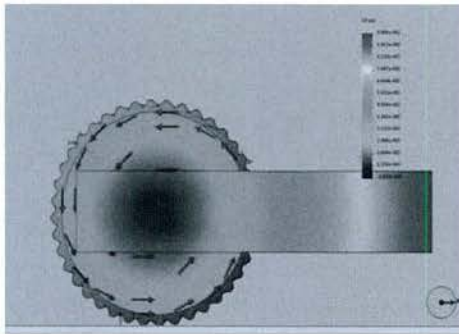


Figure 107- Spring Constant Model

The angular rotation resulting from combination the vehicle weight and brake test, 80.8° , was compared against the test requirements of Navy Drawing 7001119. A minimum life of 100,000 cycles is required for the endurance test under the Group D inspection criteria for 12° to 70° of cyclic rotation. Based on this drawing information three parameters can be extracted for analysis purposes: 1) The angular rotation calculated as 80.8° is more conservative than the 70° drawing requirement 2) After refurbishment and during use the bar should survive at least 100,000 worst case load cycles 3) A stress ratio, R, required for fatigue curves can be estimated as $12^\circ/70^\circ=0.17$. Loading data for the worst case operating conditions was compiled into a Use Profile for the component equal to 81° of maximum rotation with a stress ratio of 0.17. These values were used for subsequent modeling and laboratory experiments. Table 3 below provides a summary of the load scenarios from the TARDEC wall, speed bump, brake, and drawing endurance tests.

Table 3 - Load Scenarios

Torsional Load Scenario	Angular Displacement
Weight	35°
TARDEC Data	$19^\circ + \text{Weight} = 54^\circ$
Speed Bump Test	$24^\circ + \text{Weight} = 59^\circ$
Brake Test	$46^\circ + \text{Weight} = 81^\circ$
Endurance Test Requirement	12° to 70° (R= 0.17)

4.2.2.2 Bending Load

Aside for the torsion loading of the component, the other possible load on the torsion bar is a bending load that could occur during operation due to movement in the support arm bearing or flexure of the hull. Data was requested from ONR for detailed information related to distortion for the hull; however, this data was not available therefore another source of information was found. In 1988 a study the AAV was evaluated for potential upgrades to an aluminum and composite hull. As part of this study by David Taylor Research Center, the lateral distortion of the hull was calculated at several points along the length of the vehicle for various load scenarios. In one of the analysis scenarios employing higher loads, the distortion at the rear ramp and at the front profile were 0.416inch and 0.1 inch respectively, refer to Figure 108 - Hull Loading-Front View of Distortion. Based on the report the maximum lateral distortion at the rear hatch should be less than 0.5 inches to prevent binding between the ramp and the coaming. Unfortunately it is not clear whether or not the composite hull is stiffer than the current aluminum hull therefore the worst case value was employed in subsequent modeling task. Employed in the remanufacturing analysis was a deflection of 0.42 inch relative to the ends of the torsion bar that can be analyzed find determine the corresponding applied bending stress.

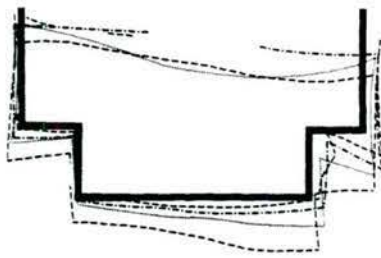


Figure 108 - Hull Loading-Front View of Distortion¹⁶

4.2.2.3 Residual Stresses

Using the preceding analyses, the angular displacements due to operational loading of the torsion bar can be employed for fatigue models; however, there are residual stresses purposefully added to the bar that must also be considered. Shot peening is applied to the surface to create a compressive residual stress layer at the surface of the component thereby reducing the effect of loading during operation¹⁷. Likewise, the torsion bar is preset during manufacturing to apply residual shear stress that effectively offsets the shear stress imparted in the same direction during operation¹⁸. Table 4 - Residual Stress from Preset, quantifies the angle that the bar is rotated during the preset operation and the angle remaining after release of the load used for the preset.

Table 4 - Residual Stress from Preset

Load Scenario	Angular Displacement
Preset Loading, minimum	169.4°
Residual Preset	80.5°
Elastic Region Remaining, min	88.9°

The preset effectively yields the torsion bar under shear stress, refer to Figure 109- Depiction of Torsion Bar Stresses, and upon release of the preset load a residual stress equivalent to 88.9° remains. The static and dynamic load of 81°, calculated in the preceding sections of this report, is less than the remaining elastic strain, Y_e , equivalent to 88.9° of rotation. To describe it differently, the operational loads fall within the elastic limit thereby allowable rotation without plastically deforming again.

¹⁶ Martin Marietta. Composite Hull for an Amphibious Vehicle. August 1988, available <http://www.dtic.mil/dtic/tr/fulltext/u2/a205213.pdf>

¹⁷ Verpoort and Gerdes. Influence of Shot Peening on Material Properties and the Controlled Shot Peening of Turbine Blades". Metal Behaviour and Surface Engineering, IITT-International 1989

¹⁸ Richard Budynas. Advanced Strength and Applied Stress Analysis, 2ed. McGraw-Hill Companies, Inc. 1999. Page 571

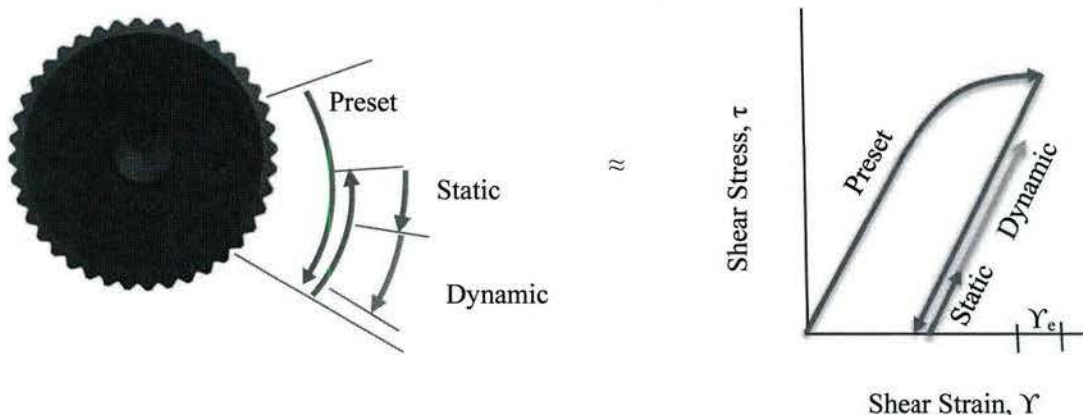


Figure 109- Depiction of Torsion Bar Stresses

4.2.2.4 Properties and Use Summary

Data on the component was obtained through details drawings and specifications provided by the AAV PM office. Sufficient detail on the geometry, material, processing, and acceptance tests were available within the specification to understand the original intent of the component design. Information on the use of the component, loads, and environment were supplied or gathered through investigation of the system operation.

4.3 Failure modes

Based on the current logistical data and anecdotal evidence from the depot for the AAV torsion bars, the failure modes are typically related to rejection of torsion bars during maintenance operations. An updated inspection procedure was put in place in 2005 according to PM AAV, after that time the depot is are not aware of any broken bars due to end of life issues. The updated inspection practice checks for pitting and peeling of the coating, and if either are detected the bars are rejected. Light rust at the splines that can be removed by manually wire brushing them is acceptable. It is possible that the worst case corrosion may occur in Hawaii or on storage ships where vehicles are subjected to salt water spray for longer periods of time. Alloy 300M is susceptible to stress corrosion cracking (SCC) in salt water¹⁹, hydrogen embrittlement, and decarburization²⁰. Based on this information the effect of corrosion on the AAV torsion bar must be understood to complete a robust remanufacturing assessment. The major potential failure modes for the torsion bar are overload, fatigue, stress corrosion cracking, and corrosion fatigue.

¹⁹ Prevey, Jayaraman, Ontko, Shepard, Ware, and Coate. *Mechanical Suppression of SCC and Corrosion Fatigue in 300M Landing Gear*. Proceedings of 6th Aircraft Corrosion Workshop, 2004

²⁰ Philip and McCaffrey. *Ultrahigh-Strength Steels*. Available www.asminternational.org

The potential failure modes associated with the torsion bar component are presented in the following sections and due to the commonality of the failures they are applicable to many other military and commercial components. Loading and environmental factors represent half of the equation for failure modes, the other half is related to the properties of the component. These properties will be explored in subsequent analyses and include heat treat, shot peen depth, residual stress depth, fatigue strength, and fracture toughness under corrosion.

4.3.1 Overload

Although less common for components that have already been employed in service but still an important failure mode is stress overload. If a refurbished component is to be used on a vehicle that has had capability upgrades since the original design then an overload analysis should be performed. Applying a load that exceeds the allowable limits of a component can result in undesired displacement, and fracture. Some designs that have tight tolerances between moving components may require limits on the amount of displacement the components exhibit during operation. This is intended to limit interference between parts that could result in binding or wear. On the other hand, overload fracture can occur when the material is stressed beyond its design limits and the strain on the material breaks the internal bonds which results in sudden failure.

Additional capabilities, such as up-armoring and mine resistance, have been added to the AAV design. The extra weight applied to the vehicle translates directly into the loading experienced by the torsion bars. Maximum weight per torsion bar, as shown in Section 4.2.2.1, has increased overtime therefore it is prudent to evaluate the potential for an overload scenario based on current loads. The increased vehicle weight along with the worst case bending and torsion load will be applied to the weakest section of the torsion bar to check for yielding of material. Having sufficient margin between the current yield point of the torsion bar and the operating loads will help prevent surface cracks forming from slip planes caused by yielding. The torsion bar is shot peened before and after the preset to assist in reducing the effects of slip planes on the outside of the bar where fatigue failures can initiate.

4.3.2 Background on fatigue

One of the most prominent failure modes associated with corrosion of metal components is fatigue that results in fracture of the component after it has been subjected to multiple cycles of use. When a component experiences cycles of varying load levels there is the potential for formation of cracks within the metal crystallography. Cracks may begin from voids within the metal lattice, dislocations, imperfections in material composition, and surface stress concentrators such as pits or scratches. It is estimated that 90% of structural failures are the result of fatigue mechanisms²¹.

As fatigue is considered a major failure mode for the corroded torsion bars, the refurbishment process focused heavily on this aspect. For the torsion bar example, the condition of the as-received bar must be evaluated then the effect of the environment and use must be comprehended through a combination testing and analysis. Exact material properties for components are often difficult to find and employ in analyses

²¹ Schaffer, Saxena, Antolovich, Sanders, and Warner. The Science and Design of Engineering Materials. 2ed. McGraw Hill Publishing Company, 1999. P.399

due to the effects of unique heat treatment, surface hardness, cold working processes and case carburizing. The approach implemented in this project was to replicate the material and manufacturing processes of the torsion bar and perform testing to understand the associated environmental and use factors.

Alloy 300M is an ultra-high strength alloy therefore the remanufacturing procedure must identify potential problems and solutions associated with this type of steel. In this case, alloy 300M is similar in composition to a more commonly used steel, AISI 4340, except for the silicon concentration (1.45% vs 0.2% for 4340) and the addition of vanadium in alloy 300M²². The heat treatment in accordance with Navy Drawing 7001119 is used to convert the austenite to martensite below a depth of 0.003 inches through a double tempering process. Martensite is a body centered tetragonal structure crystal structure of steel that locks the carbon atoms in position thereby blocking dislocation movement²³ and enhancing fatigue life. On the other hand, cracks and pits were observed by Murtaza and Akid to originate exclusively from non-metallic inclusions, such as silicon, in the bulk material. This mechanism becomes more significant for materials with a Rockwell hardnesses above 40C²⁴ (i.e. torsion bar). The non-metallic inclusions have different strain responses than other portions of the surrounding steel causing separation at the inclusion interface. Above a hardness of 40C the stochastic distribution of surface inclusions become a dominant factor in the fatigue limit as seen in the scatter within the data in Figure 110²⁵.

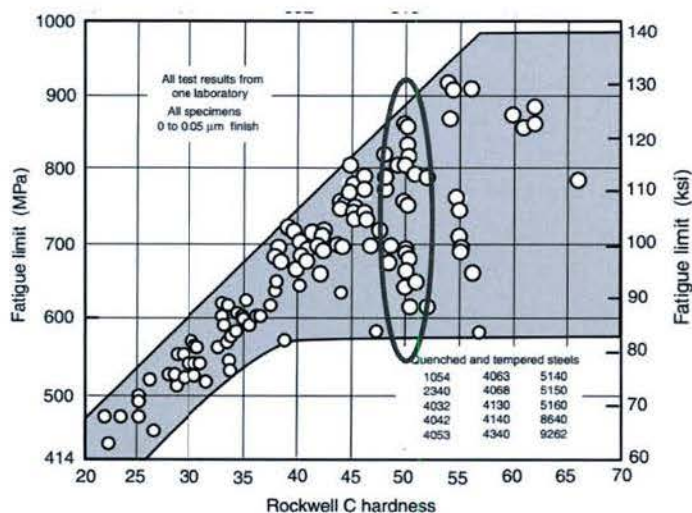


Figure 110 - Effect of Hardness on Fatigue Limit

The original equipment manufacturer's design of the torsion bar employs three main protective measures to reduce crack growth. The first protective measure is a polyurethane coating and corrosion inhibiting primer to mitigate the exposure of the steel to the corrosive environment. Second, the torsion bar is shot

²² C.S. Carter. "The Effect of Silicon on the Stress Corrosion Resistance of Low-Alloy, High-Strength Steels;" Boeing Commercial Airplane Division Report D6-23872; Sponsored by Advanced Research Projects Agency; March 1969

²³ Schaffer, Saxena, Antolovich, Sanders, and Warner. *The Science and Design of Engineering Materials*. 2ed. McGraw Hill Publishing Company, 1999. p310

²⁴ Murtaza and Akid. *Corrosion Fatigue Short Crack Growth Behavior in a High Strength Steel*. International Journal of Fatigue, Vol. 18, No. 8 p.557-566; 1996

²⁵ Pietro Paolo Milella. *Fatigue and Corrosion in Metals*. Springer Milan Heidelberg, 2013

peened with 200% coverage meaning that the entire surface should have been theoretically impacted twice. Shot peening works by strain hardening the surface (i.e. pinning dislocations), smoothing the rougher machined surface finish, and adding residual compressive stresses thereby reducing the mean fatigue stress²⁶. Third, the preset of the torsion bar adds residual compressive stress that reduces the net stress^{27,28}. For other examples, aside from the torsion bar, where components do not have sufficient material and mechanical properties to resist fatigue then engineers may consider adding these features during the recapitalization.

Extending the operating life of a product can force the onset of fatigue failures if engineers are not vigilant and identify related failure modes. For high cycle fatigue, defined as being greater than 1000 cycles, cracks typically propagate from the surface after completing a four phase process. The first phase is cyclic softening or hardening depending on the material, followed by a second phase where plastic slips lead to the formation of mechanically small cracks (MSC). Macro cracks form during the third phase and then grow to failure in the fourth phase, refer to Figure 111²⁹.

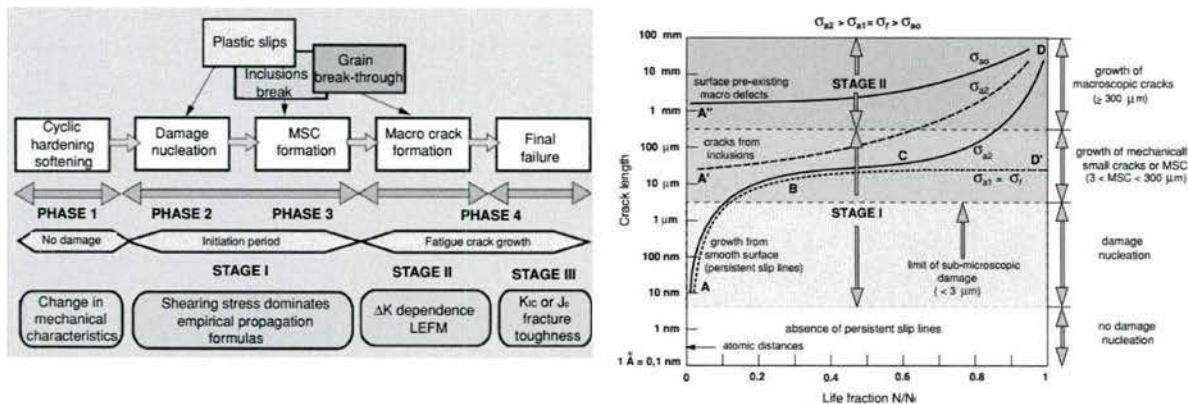


Figure 111-Stages of Crack Failure, a) 4 Phases b) Crack length for Stage I and II

Typically materials with ultimate strength to yield strength ratios of less than or equal to 1.2 soften because precipitates diffuse through the bulk material. Ratios greater than 1.4 typically harden and ratios between 1.2 and 1.4 are neutral. For quenched and tempered specimens of alloy 300M processed at tempering temperatures from 400°F to 600°F the ultimate to yield ratio ranges from 1.29 to 1.17 respectively³⁰. Using the samples prepared for this project the ratio is 320kpsi/258kpsi = 1.24 that indicates that the precipitates in the alloy 300M do not dissolve into the metal lattice thereby reducing the capacity to block dislocations and decreasing the fatigue resistance²⁹.

²⁶ Schaffer, Saxena, Antolovich, Sanders, and Warner. *The Science and Design of Engineering Materials*, 2nd edition. McGraw Hill Companies 1999.

²⁷ E.P. Popov. *Mechanics of Materials*. 2nd Ed, P 73. Prentice-Hall 1976

²⁸ Mocilnik, Gubelajak, and Predan. *Influence of Presetting on Fatigue Lifetime of Torsion Bars*. Procedia Engineering; 10 p.213-218, 2011

²⁹ Pietro Paolo Milella. *Fatigue and Corrosion in Metals*. Springer Milan Heidelberg, 2013

³⁰ Philip and McCaffrey. *Ultrahigh-Strength Steels*. Available www.asminternational.org

In high cycle fatigue, crack initiation typically occurs at a limited number crystal planes on the component surface. Surfaces crystal usually experience plain stress conditions and as a result there are fewer crystals impeding the dislocation of atoms on the exterior than within a material where tri-axial stress states occur. The organization of crystals within a metal is random with the orientation of the crystal formations in multiple directions. Cracks initiate on atomic planes within the crystal that are oriented in the direction of the maximum critical resolved shear stress³¹. Resolved Shear Stress, τ , is the equivalent stress resulting from a conversion from the tensile stress in the axial direction to the shear stress along a slip plane, refer to Equation 1, where ϕ is the angle of the slip direction on the slip plane and θ is the angle normal to the slip plane with respect to the specimen axis of symmetry³².

$$\tau = \sigma_{tensile} * \cos(\phi) * \cos(\theta)$$

Equation 1 – Schmid's Law: Stress Conversion

Resolved shear stress are shown in Figure 112 as it relates to the stages of crack growth. To prevent formation of large cracks the stress on the material must be kept below the fatigue limit, σ_f , so that nucleated cracks do not propagate through grain boundary barriers between crystals. The rate of crack growth is related to the stress intensity of the crack, K , that a function of the crack length, $\sqrt{\pi a}$, in fracture mechanics approach. In materials with larger grain sizes the crack length can form within the crystal and grow to a critical size that can propagate through the grain boundary causing fatigue failure. High cycle fatigue is typically transgranular compared to low cycle fatigue that is usually intergranular and converts to transgranular propagation.

³¹ Schaffer, Saxena, Antolovich, Sanders, and Warner. The Science and Design of Engineering Materials. 2ed. McGraw Hill Publishing Company, 1999. P150

³² Pietro Paolo Milella. Fatigue and Corrosion in Metals. Springer Milan Heidelberg, 2013. P34

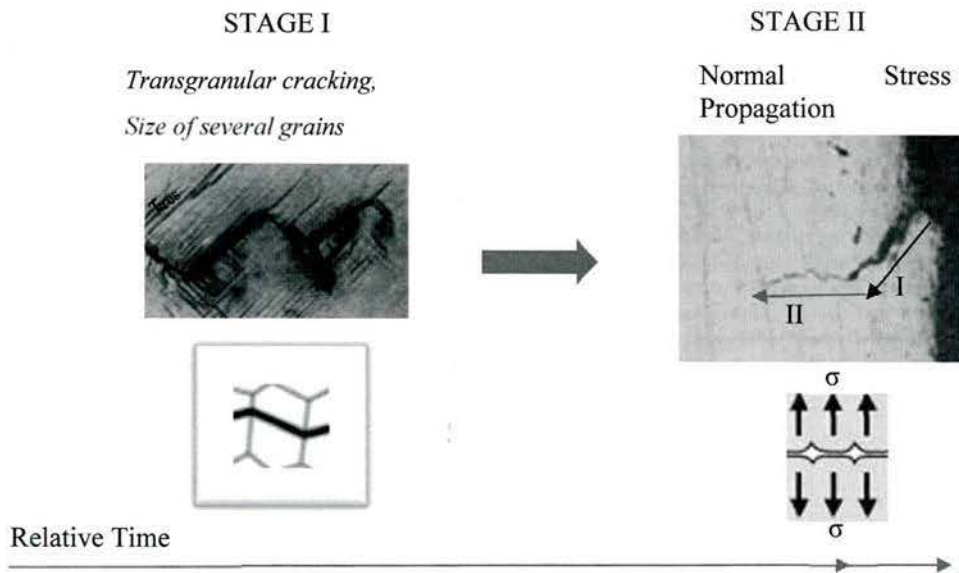


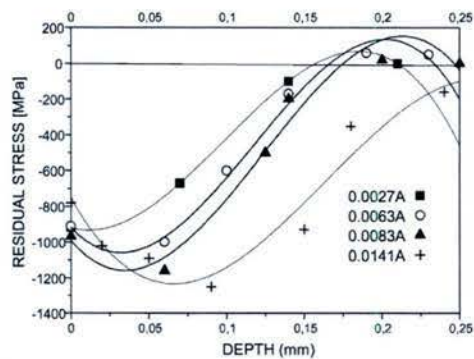
Figure 112 – Representation of High Cycle Fatigue³²

Shot peening has been shown to increase cycle life by 7 to 30% depending on materials and operating parameters for peening such as intensity and coverage^{33,34}. Shot peening creates residual stresses within the material that are compressive at the surface but become tensile at depths near 0.008 inches for AISI 4340 steel with a hardness of 50HRC therefore cracks can form beneath the initial surface layers of the part²⁹. Torres and Voorwald also showed that with cycling the compressive residual stress levels from peening were reduced overtime. This reduction is due to plastic deformation that restructures the stresses thereby reducing the residual compressive stress from the shot peening. Similar to the residual compressive stresses imparted by shot peening, the torsion bar is preset during manufacturing that applies residual shear stresses in the material. According to Budynas the residual stresses from presetting can be more effective than shot peening at reducing fatigue stresses. The offset shear stress imparted in the bar must be in the same direction as the stress during operation and the loading should be in one direction to be effective³⁵.

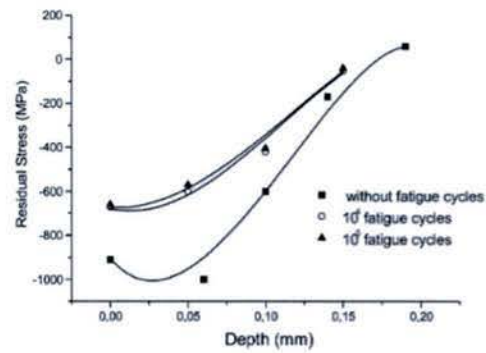
³³ Mattias Lundberg. *Residual Stresses and Fatigue of Shot Peened Cast Iron*. Linköping Studies in Science and Technology. Thesis No. 1622; 2013

³⁴ Torres and Voorwald. An Evaluation of Shot Peening, Residual Stress and Stress Relaxation on Fatigue Life of AISI 430 Steel. *International Journal of Fatigue*, 24, p 877-886, 2002

³⁵ Richard Budynas. *Advanced Strength and Applied Stress Analysis*, 2ed. McGraw-Hill Companies, Inc. 1999. Page 571



a)



b)

Figure 113- a) Effect of Shot Peening Intensity on AISI 4340 b) Cycling Effect of Residual Stress

4.3.3 Background on Stress Corrosion Cracking

Stress corrosion cracking (SCC) is another phenomenon related to degradation of materials caused by the application of a corrosion environment to components experiencing tensile stress. The material used in a component is generally only susceptible to certain corrosive environments, such as series stainless steel to sodium chloride solutions. Stress levels imparted on a component can be as low as a 10% of the materials yield strength to cause SCC failures³¹. The tensile stresses needed for SCC can be imparted by external loads or from the residual stresses within the material from processing. In the case of the torsion bar, alloy 300M is susceptible to SCC when introduced into seawater environments³⁶.

Three primary factors must be present for SCC to be considered as a failure mode. These factors are the simultaneous presence of tensile stress, a susceptible material, and a corrosive environment for the material of interest; refer to Figure 114. Through elimination of contact with the corrosive environment or reduction of tensile stress. Stress corrosion cracking typically initiates through two stages: First, pits of substantial size developed from dissolving of preferential elements within the metal and fatigue mechanisms allow SCC to begin; Second, the SCC process causes cracking to progress at a rapid rate³⁷.

³⁶ Kozol and Neu. "Stress Corrosion Susceptibility of Ultra-High Strength Steels for Naval Aircraft Applications;" Naval Air Warfare Center, Report No. NAWCADWAR-92018-60; 10 January 1992

³⁷ Judy and Goode. "Stress-Corrosion Cracking of High Strength Steels and Titanium Alloys." Welding Research Supplement Sept 1972. p 437-s

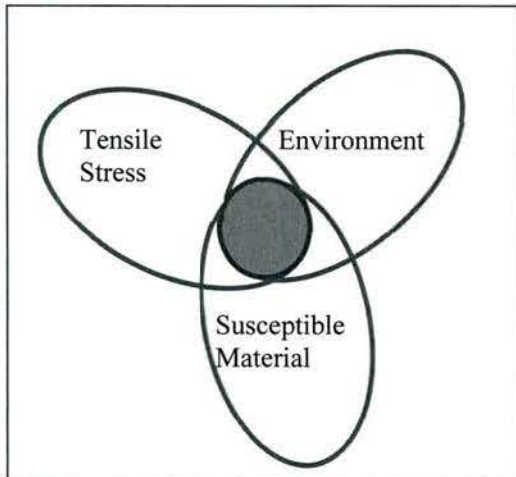


Figure 114 - Relationship for Stress Corrosion Cracking

Kozol and Neu presented results for the SCC threshold intensity factor (K_{ISCC}) determined for alloy 300M when loaded in a static bending fixture while exposed to a solution consisting of 3.5% sodium chloride in water. As can be seen in Figure 115, the slope of the curve for alloy 300M is much shallower than other high strength steels. This means a relatively small change in stress or crack length can result in substantial changes in the time to failure, i.e. 20% increase in stress can reduce the life by several orders of magnitude. Below a threshold stress intensity factor, K_{ISCC} , the growth rate of SCC cracks is negligible therefore a theoretical limit can be established through laboratory material testing. The type of material is one factor in the threshold; however, the resistance to SCC can also be influenced by the small changes in composition, work hardening, and microstructure³⁸. Precipitates or other elements of the micro-structure can make SCC transgranular, intergranular or a mixture of cracking modes.

³⁸ "Stress Corrosion Cracking". National Physical Laboratory, Crown Copyright 2000.

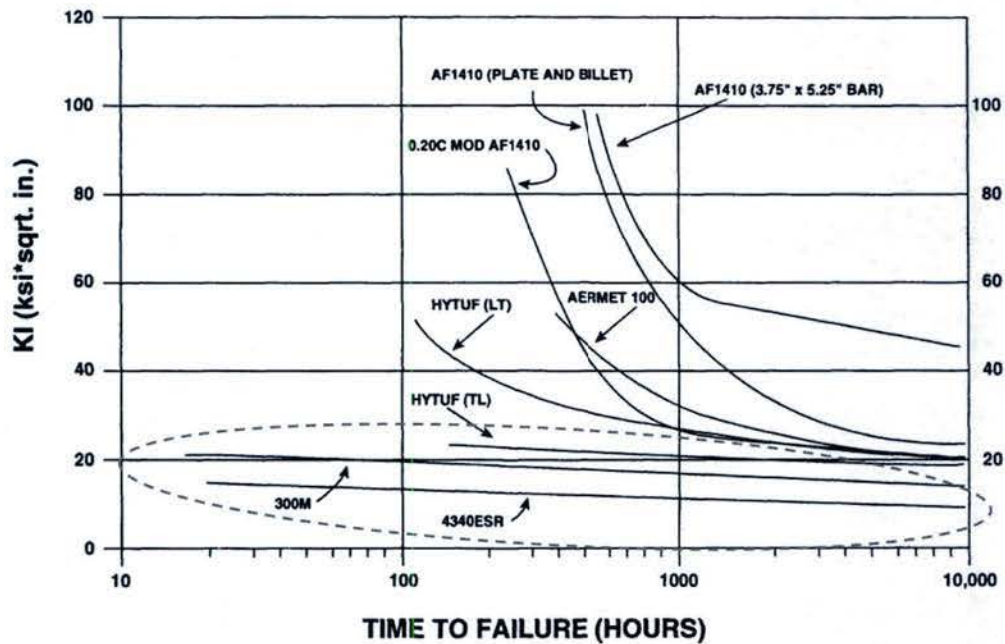


Figure 115 - Stress Corrosion Cracking 300M³⁶

Illustrations of effect of SCC on aluminum alloy under torsional loads and alloy 300M under residual bending stress are shown in Figure 116. Figure 116 – SCC of a) Aluminum under torsion. Although the aluminum specimen shown in the figure was subjected to a torsional load that results in shear stress the bar failed due to SCC. Applying Schmid's law for stress conversion, the maximum resolved tensile stress in the material would occur on a plane located 45° from the axis of the bar, similar to the failure recorded. The torsion bar is loaded in torsion but also has residual stresses due to the preset imparted during manufacturing. Residual stresses with tensile stresses above the stress intensity threshold can induce failure as exhibited in the 300M sample that was bent in a test fixture, removed from the fixture, and then periodically subjected to salt water over a course of three weeks. The crack was on the side of the specimen initially loaded in compression but resulted in residual tensile stresses once the load was removed. The crack propagated approximately halfway through the specimens until the tensile stress was minimized causing the crack to arrest. Based on these observations the torsion bar must be evaluated in multiple loading scenarios to account for operational loads and residual stress from preset.

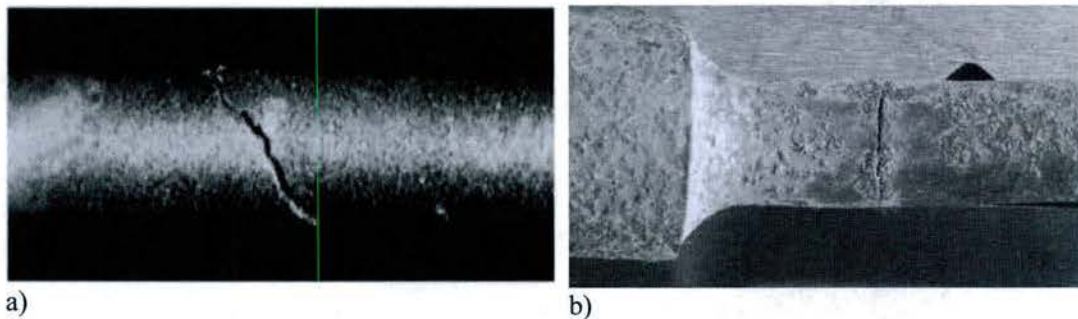


Figure 116 – SCC of a) Aluminum under torsion³⁹ b) Alloy 300M under residual bending stress at RIT

4.3.4 Background on Corrosion fatigue

There is a difference in the fatigue of metals that are cycled in a corrosive environment compared to inert and evacuated atmospheres. In corrosion fatigue tests, Murtaza and Akid also showed that stress levels below the endurance limit of steel were able to produce strain sufficient enough to break the surface oxide thus allowing pits and cracks to continue to increase in size. Corrosion fatigue, when compared to fatigue in a standard air environment, have many of the same characteristics but differ in several regards, cracks resulted from strain cracking of the protective oxide film allowing for dissolution and propagation due to tensile loading. Murtaza and Akid concluded that corrosion fatigue consist of three stages: pit development from dissolution, environment assisted short crack grow, and environment assisted long crack growth. Pits form at non-metallic inclusions through dissolving in the corrosive solution. Hydrogen embrittlement becomes a factor as the crack length increases and hydrogen adsorbs ahead of the tip; however, the crack growth in corrosion fatigue only occurs if the stress intensity factor exceeds a threshold stress level⁴⁰.

For 4340 in water vapor the a change in test frequency from 10 hertz to 0.1 hertz increased the crack growth rate, da/dN , by 20 times compared to similar tests in argon, refer to Figure 117. The load profile versus time also has an effect on the corrosion fatigue life with profiles that have shorter rise times being more damaging. Additionally, increasing ratios of minimum to maximum cyclical stress, R , increases the crack growth rate⁴¹. Corrosion fatigue can also result in the lack of an endurance limit for steels therefore engineers may not be able to take advantage of this characteristic during design as they would for non-corrosive environments⁴².

³⁹ Mears, Brown, and Dix. "A Generalized Theory of Stress Corrosion of Alloys;" ASTM STP64-EB; Paper Number STP42581S January 1945

⁴⁰ Rokhlin, Kim, Nagy, and Zoofan. *Effect of Pitting Corrosion on Fatigue Crack Initiation and Fatigue Life*. Engineering Fracture Mechanics 62 p 425-444 (1999)

⁴¹ Pietro Paolo Milella. *Fatigue and Corrosion in Metals*. Springer Milan Heidelberg, 2013. P790

⁴² Shigley and Mischke. *Mechanical Engineering Design*, 6th Ed. McGraw-Hill. 2001

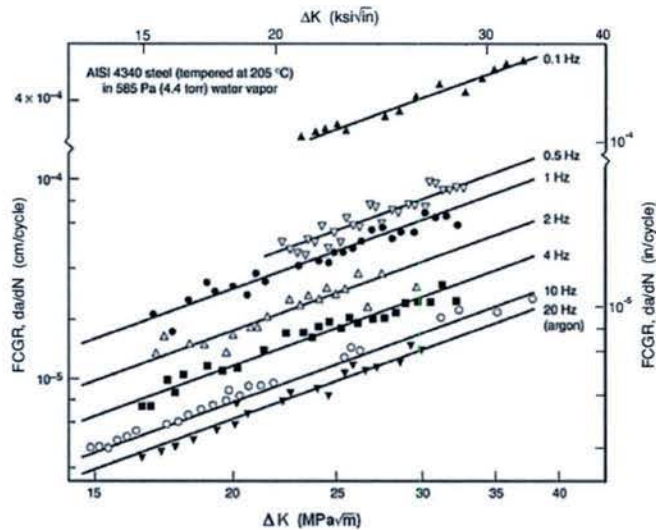


Figure 117 - Effect of Cycle Frequency on Corrosion Fracture⁴³

4.3.5 Coating delamination

As described in this report, the rejection criteria during vehicle inspection includes delamination of the coating from the steel. Many of the rejected bars at were examined at the depot showed separation of the polyurethane coating from the alloy 300M torsion bar. Upon further examination, it was observed that one failure mode was the separation of the primer layer between the coating and the metal without visual indication of corrosion products on the surface. The root cause of this failure mode could be the result of poor component preparation during manufacturing where the surface of the bar is not properly cleaned before the primer was applied or separation of the primer from the bar due to stress.

In order to evaluate the potential failure mode due to stress, the torsion bar was modeled in Solidworks finite element software and given a virtual coating with a thickness of 0.2 inches on the straight section of the bar. Near the base of the splines the coating thickness was modeled to taper to a thickness of 0.0625 inches. The material properties employed in the model for the coating were similar to Abcite X60 that has a modulus of elasticity of 511 psi (calculated from tensile test data). In Solidworks, the coating was assumed to be perfectly bonded to the bar and a 70 degree angle of twist was applied to one end of the bar while the other end was fixed.

⁴³ Pietro Paolo Milella. *Fatigue and Corrosion in Metals*. Springer Milan Heidelberg, 2013. P790

Two points of interest were examined: the inside surface of the coating on the straight section of the bar and the inside surface at the edge of the coating near the splines. Mathematical singularities at the edge of the coating prevented accurate analysis of the stresses at that location; however, at the location closet to the splines where the model converged the result for the maximum Von Mises stress was approximately 14 psi. The stress at the inside of the coating along the straight section of the bar was uniform at 5 psi. These results are not far off from hand calculations which approximated the bar as a uniform diameter rod, the results of which were 3.6 psi for the smaller diameter location and 4.3 psi for the edge of the coating.

Based on the analytical result of the coating analysis, the failure mode associated with the delamination of the coating is suspected to be caused by component material processing or environmental use factors. Environmental test for the replacement coating should be performed and a procedure for cleaning the bars before applying this new coating should be developed.

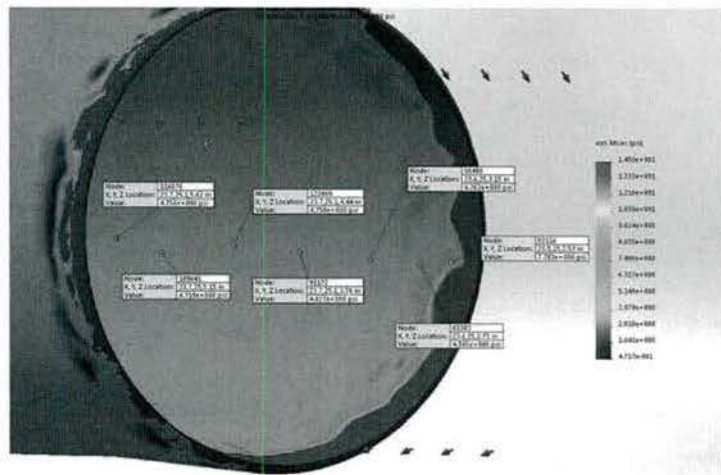


Figure 1: Adjusted Scale

Mike info-discrepancy in pull data in middle of the bar with clean spots beneath

4.4 Replication of Properties and Test Specimen

The physical size and limited number of available samples of the torsion bar precludes its use in testing requiring many replicates. As with many components the material properties are of equal interest to engineers as the test results with actual components. The reason for this stems from the ability to test components in a prototypical fashion and the speed at which results can be obtained from modeling. Knowing the material properties can allow for the development of models to simulate the effects of stress, temperature, fatigue, vibration, and electromagnetic fields on the component. Modeling does not replace testing of components; however, the modeling results can provide a method to screen the design for potential failures without the cost and time associated with testing of actual components. Additionally, testing of components that requires high levels of energy, such as pressure, force or rpm, can be dangerous to test technicians.

Properties of the alloy 300M material in the torsion bar were investigated and documented in the following sections of this report. Alloy 300M has been in use for several decades and generic mechanical properties, such as yield, elongation and fatigue curves, for the steel are available. When components are

used in critical functions, such as pressure vessels, the load scenarios and heat treatments should be considered in the test program in order to obtain properties related to the actual component. Test specimens were created to develop an understanding of the torsion bar properties and the effect that a salt water environment has on it.

4.4.1 Test Specimens

Several specimen types were created to allow for laboratory testing of the alloy 300M material that included: ultimate tensile tests, coating adherence, fatigue test, and corrosion tests. The heat treatment and shot peen information for the torsion bar example is partially available in the associated Navy drawing. With the information on the torsion bar material, heat treat, hardness, and surface preparation the properties of the bar material can be replicated for laboratory investigations. Minimum hardness requirements of the torsion bar after a quench and double temper are provided along with shot peen intensity. The drawing information was used to reverse engineer the temperatures and times for the heat treatment based on temperature-time diagrams for the steel.

The initial material properties of interest for the torsion bar example are the hardness measurements and composition of the microstructure. Alloy 300M material to AMS specification number 6257 was sourced from Aero-Vac Alloys & Forge, Inc. that matches the torsion bar specification. The tensile specimens were turned on a CNC lathe and wet polished with 400 and 600 grit sandpaper that was comprised of silicon carbide. Prior to shot peening the specimens were wiped to remove any contaminants from the surface. Round tensile specimens were machined in accordance with ASTM standards E8 and E466 for ultimate and fatigue specimen dimensions. The specimen dimensions are provided in Figure 118 for reproducibility of the results. Tensile specimens were then heat treated by austenizing in a vacuum furnace at 1600°F then quenching in oil and double tempering in an open furnace at 600°F. A minimum through hardness of 51C was targeted for the specimens to match the torsion bar drawing requirements.

Using AMS-S-13165, the shot peen vendor adjusted the intensity of the shot peen from the torsion bar requirements to a value that was suitable for the size of the tensile specimens. Owing to the smaller cross section of the test specimens as compared to the torsion, the shot peening intensity was reduced from the values stated in drawing 7001119 (e.g. 0.007C to 0.01C). Each specimen was shot peened with 200% coverage and an Almen range of 0.008 to 0.012A to obtain a compressive depth similar to the torsion bar. Of particular interest was the AMS standard states that shot peening is used to increase the fatigue life and improve resistance to stress corrosion cracking. The shot peening removed the surface roughness due to the manufacturing machining marks thus providing a more uniform finish that aids in the repeatability of the tests after rough machining operations.

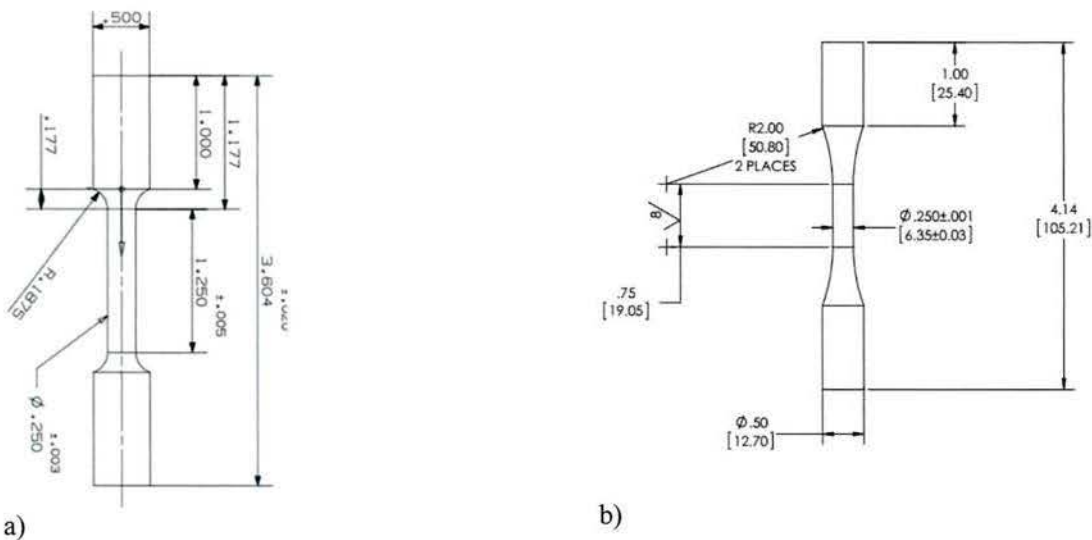


Figure 118 – a) Ultimate Tensile Specimen b) Fatigue Specimen

Test data for material properties could be collected once the ASTM tensile specimens had been prepared in a manner replicating the torsion bar properties. Micro-hardness tests and scanning electron microscopy were used to confirm the metallurgical properties of the specimens including the presence of retained ausenite. In order to evaluate the residual stresses in the specimens from shot peening the samples were sent for x-ray diffraction testing. The SAE standard HS-784 method to obtain the stress measurements except for a Modified-Psi diffract meter configuration was used instead of the traditional Omega or Psi configurations. The measurements for the torsion bar were performed on a section of the bar that had been wire brushed to remove corrosion therefore the surface layers of the shot peen may have been removed. Preset of the torsion bar creates additional tensile and compressive stresses within the bar therefore and stresses on along the axis are presented in Figure 119. The residual compressive stress of the smaller specimen are similar to the torsion bar.

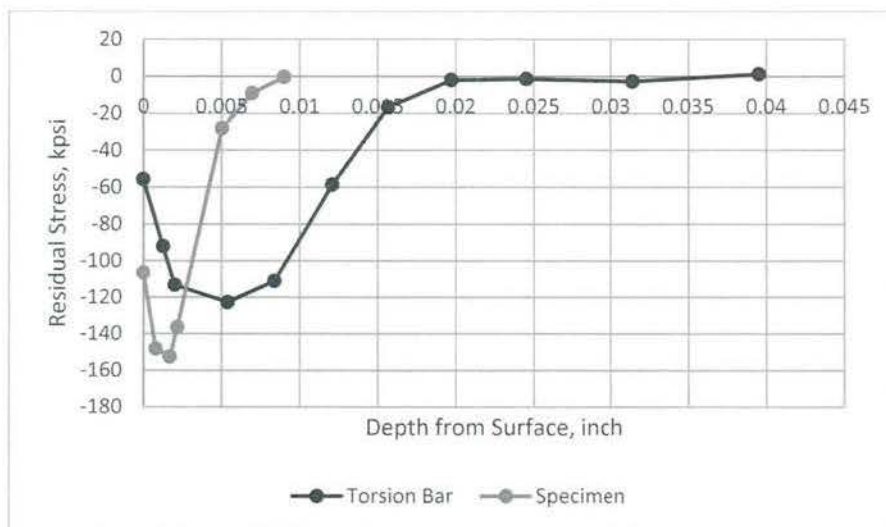


Figure 119- X-ray Diffraction Results

A test plan was developed after confirming the compressive stresses to allocate the appropriate number of specimens for the necessary screening and fatigue tests. Based on ASTM E739-10 for statistical analysis of fatigue data, the sample size and number of repetitions for each fatigue test were determined assuming Research and Development testing per the ASTM standard. A minimum of six (6) specimens and greater than 33% repetition is provided as a guideline in the specification where Percent replication equals $100*[1 - (\text{total different stress levels} / \text{total number of specimens})]$. Using this guideline, a target of six specimens to generate each fatigue curve and 3 stress levels (50% replication) was targeted.

4.5 Specimen Tests

The tensile and fatigue specimens that prepared for this project were designed for use on an Instron hydraulic testing system model 8801. The Instron is outfitted with a servo controlled hydraulic actuator, 20,000 lbf load cell, linear variable differential transformer (LVDT), hydraulic serrated v-grips, and an extensometer. The system is capable of controlling and recording data from ultimate and cyclical tests with cycle frequencies up to several dozen hertz. Several modifications to the test setup were performed in order to obtain repeatable data. The following section of this report describe in more detail the individual test setups and the results obtained from those tests.

4.5.1 Ultimate strength test specimens

The first tests performed on the Instron for this project were the ultimate strength tests on the alloy 300M that was heat treated but not shot peened. Initial test results showed the ultimate tensile strength of six specimens ranged from 236 to 300ksi. Final fracture of the specimens primarily occurred near the radius of the specimen on the 0.25inch diameter; however, the data between fractures at the center and radius are overlaid. Upon inspection of the samples with an optical microscope the machining marks from the lathe could be seen on the samples, refer to Figure 120. Unlike with most ASTM material test specimens these initial samples were intentionally not polished to remove effects due to surface flaws. The cause of the variability in the data is most likely due to the the combination of the hardness of the heat treated samples and rough machining marks. In addition to the ultimate strength, the calculated yield strength of 148ksi was also much lower than the anticipated value of 245ksi reported by Philip and McCaffrey. The lower yield strength was a function of both the surface flaws and the Instron's LVDT used during the test. Future tests employed the Instron's extensometer to correct this measurement.

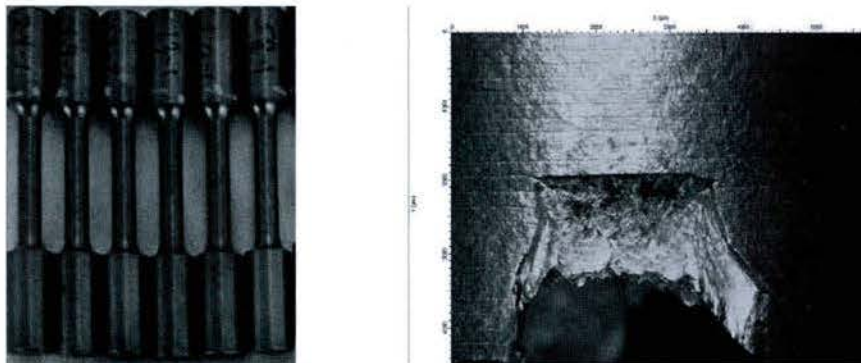


Figure 120 – Ultimate Tensile Specimens a) After Heat Treatment b) After fracture

The samples were sent to a shot peen vendor in Buffalo New York where coverage of 200% was applied to the gage section and radius of the samples. Ten new shot peened specimens were tested with a mean ultimate strength of 322.2 ksi and a standard deviation 2.8ksi, refer to Figure 121. Once repeatable data was obtained, the specimens could be used in subsequent tests to screen potential corrosion removal processes.

ASTM standard E11 provides measurement and calculation procedures to determine the modulus of elasticity, also known as Young's Modulus. Specifically mentioned in the standard is the use of an

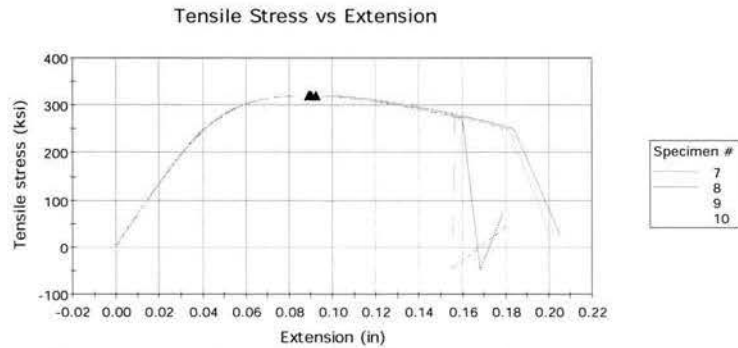


Figure 121 - Ultimate Strength Test of Shot Peened Specimens

extensometer to measure the strain in the gage section of the specimen. The difference in strain measurement between tests with the Instron's LVDT and the extensometer are provided in Figure 122 for reference. Using the LVDT data can cause errors if it is not corrected when determining the elastic modulus and yield strength. Strain from the extensometer was employed to determine the yield strength, 258 ksi, for the shot peened alloy 300M specimens. Although there are no visible signs of necking on tensile specimens, the specimens are considered ductile due to the elongation at rupture (9.7% on average, based on the elongation at rupture and original distance between the Instron grips) and the shape of the stress-strain curve.

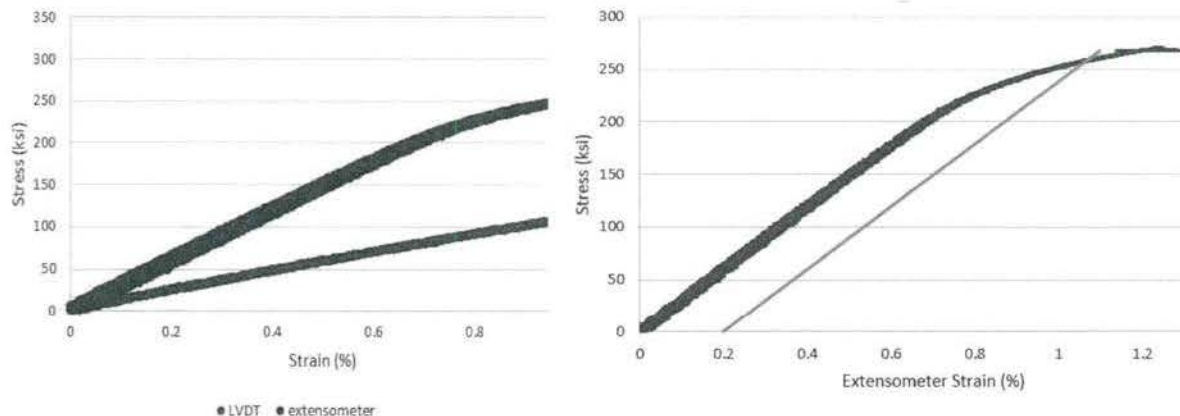


Figure 122 - Stress Strain Curves for Alloy 300M a) LVDT vs Extensometer Measurements b) 0.2% Offset Yield Data

Heat treatment has been reported to have an impact on the strength and elasticity of steel as shown in

Table 5. Fadare et.al. observed a reduction of 57% in tensile strength and a 43% decreased in Young's Modulus between the hardened and tempered states. Likewise, Phillip and McCaffrey noted that double tempering of 300M is recommended and that temperatures outside of the 500 to 600°F range could have severe effects on the material properties³². They also showed that the diameter of round bars can have an impact on tensile properties, e.g. the difference in tensile strength between a 1 and 3 inch diameter bar is approximately 3%. Published values for alloy 300M show an ultimate strength of 289 ksi for 1 inch bars tempered at 600°F which is similar to the 322 ksi result, when accounting for double temper and size, from testing of the ¼ of the diameter shot peened specimens.

Table 5 - Mechanical Properties of Heat Treated Steel (NST 37-2) ⁴⁴

Heat treatment	Mechanical properties						
	Tensile strength (N/mm ²)	Hardness (BHN)	Toughness (J)	Percentage Elongation (%)	Percentage Reduction (%)	Yield strength (N/mm ²)	Young modulus (N/mm ²)
Untreated	343.80	100.10	58.88	21.16	63.23	217.31	465.78
Annealed	325.42	95.95	64.10	23.24	71.94	209.47	562.00
Normalised	422.30	188.00	57.26	20.38	71.81	232.75	534.85
Hardened	678.70	460.50	24.67	8.42	41.14	288.05	1235.31
Tempered	385.42	131.00	60.70	21.00	76.92	228.52	535.17

4.5.2 Fatigue Specimen Results

Static load properties for the alloy 300M specimens were determined using the tensile specimens. To elucidate the properties related to the dynamic loading of the torsion bar an investigation into the effect of fatigue on the material was performed using fatigue specimens. The test program involved creating graphical load vs cycle curves, also known as an S-N diagram, for three sets of samples; similar to the processing characteristics of torsion bar, corroded samples, and samples that had the oxide layer removed during various cleaning processes. The intent of this testing was to provide data for modeling of the torsion bar and to understand the effect of the cleanup method on the fatigue life of the samples so that it could be related back to the torsion bar once reinstalled in a vehicle.

Initial testing of the fatigue samples resulted in fracture at the grip section of the specimen instead of in the gage section where it is desired. The cause of this failure was due to the serrated grips in the Instron test machine penetrating into the surface of the specimens. The cracks that were formed were severe enough that the stress concentrations at the grip were greater than the stress at the gage section. To solve the gripping problem, four shims made of 0.045 inch thick mild steel were placed on each face of the serrated v-grips. The shims dented through the entire thickness under the load; however, the deformation was not apparent on the fatigue specimens. This allowed the test to continue without the potential for the specimen to break at the grip or slip during the test.



As mentioned in previous sections of this report, the load ratio for the fatigue tests was chosen to be 0.17 based on the minimum and maximum rotation the torsion bars experience during the acceptance testing. This load ratio was used to develop constant amplitude fatigue diagrams for all of the test specimens. Each test specimen was heat treated, polished to an 8 μ m finish per ASTM E466, and shot peened as detailed in this report. The first tests performed were on the alloy 300M material that was polished and shot peened, refer to the results in Figure 123. The data was compared to S-N diagram for longitudinal and transverse specimens of alloy 300M at a loading ratio 0.2 and having an ultimate strength of 280 ksi⁴⁵. A line was manually drawn for the approximate endurance limit and the finite life region to encompass all of the data

⁴⁴ Fadare, Fadara, and Akanbi. "Effect of Heat Treatment on Mechanical Properties and Microstructure of NST 37-2 Steel." *Journal of Minerals & Materials Characterization & Engineering*, V.10, No. 3, pp299-308; 2011

⁴⁵ MIL-HDBK-5J January 2003

points since relatively few samples were tested. The lines in the following diagrams are for visual reference to help differentiate between the multiple testing parameters presented.

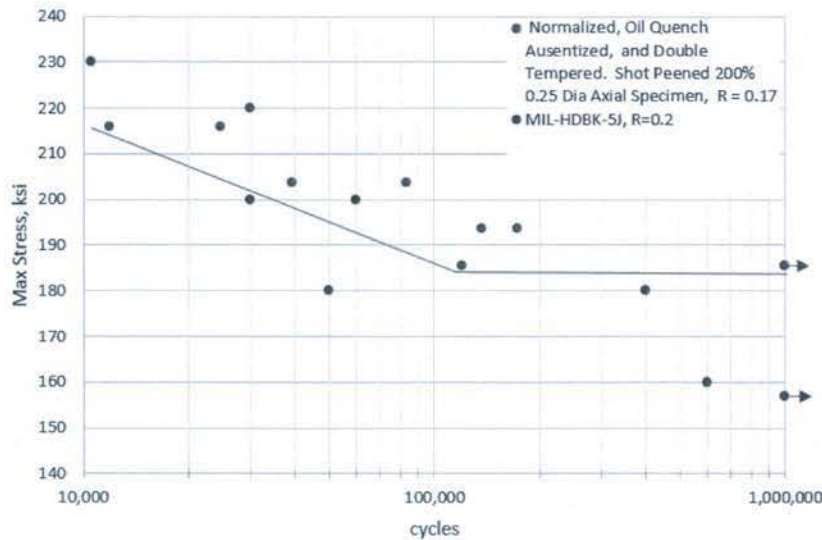


Figure 123 - Fatigue Data for Alloy 300M in Air, 20Hz

Many researchers have found that the effect of pitting corrosion on tensile specimens can reduce the number of cycles to failure up to an order of magnitude^{46,47} therefore the effect of pits on alloy 300M was investigated. Three sets of eighteen fatigue specimens were subjected to an ASTM B117 salt spray test for durations of 8, 24, and 72 hours. After the salt spray testing, the specimens were divided into groups of six that were organized based on the time exposed during salt test and the method used to remove the corrosion. The corrosion removal methods consisted of mechanical wire brushing and belt sanding. The specimens were cycled to failure or until reaching one million cycles using the same test conditions as applied in the non-corroded alloy 300M testing. Specimens that were wire brushed had the corrosion removed on an 8 inch benchtop grinder with knotted wire brush. The belt sanded specimens were processed with a 200 grit belt made by 3M on a Central Pneumatic 3/8" belt sander.

Based on scanning electron microscope images after corrosion removal using the wire brush, the pits on the samples in the 8 hour salt spray test had an aspect ratio of approximately 0.35 with a 0.0007inch depth and a 0.011inch width. Fatigue test results for the non-corroded, corroded, wire brushed, and belt sanded specimens are provided in Figure 124. As seen in the diagram, both the wire brushed and belt sanded specimens had improved cycle lives compared to the specimens that were left in the corroded state. Unlike the wire brushing process, the belt sanding did not seem to fully restore the fatigue properties of the samples. Several of the wire brushed samples survived a greater number of cycles than the non-corroded specimens at the same stress. A reason for the increase in cycle life of the wire brushed samples may be explained by the research performed by Fredj et.al. where they showed similar effects between the

⁴⁶ Sankaran, Perez, and Jata. "Effects of pitting corrosion on the fatigue behavior of aluminum alloy 7057-T6: modeling and experimental studies. Materials Science and Engineering; Vol 297 January 2001

⁴⁷ H. Guo, G. Li, X. Cai, R. Yang, and W. Yang. "Effect of Cyclic Loading on Cracking Behavior of X-70 Pipeline Steel in Near-Neutral pH Solutions." Journal of Material Science; Vol. 21 No. 4, 2005

compressive residual stress induced by wire brushing and those from shot peening⁴⁸. Additionally Fredj measured improvements in the surface roughness of the ground specimens once they were brushed. In regard to the wire brushing of the pitted alloy 300M specimens, the improved life could also be a result of material removal that would decrease the depth of the pit thereby lowering the aspect ratio and stress concentrations.

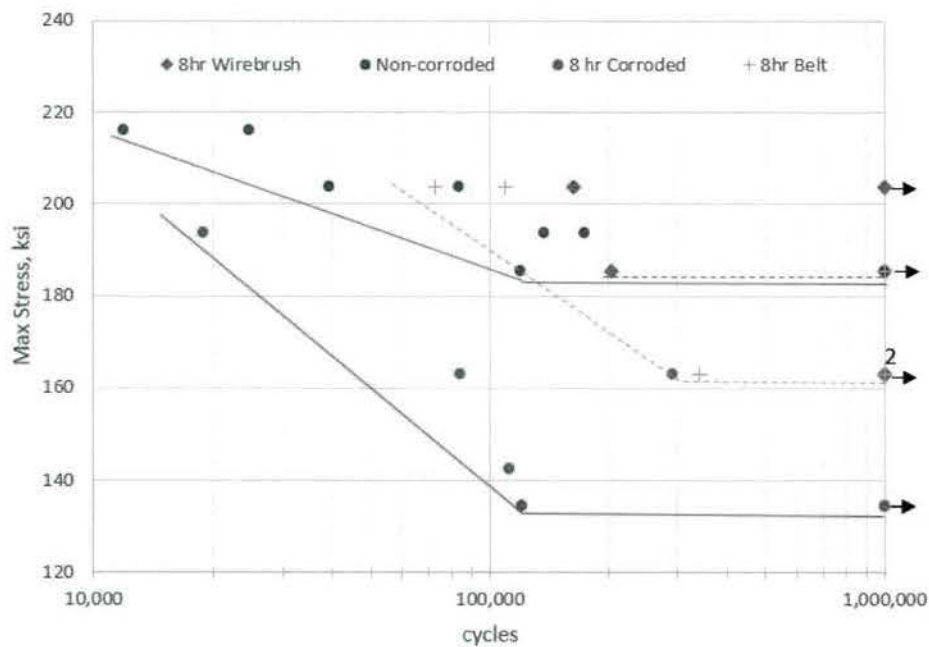


Figure 124 - 8 Hour Pitting Fatigue Test Results for Alloy 300M: a) Shot Peened b) corroded for 8hr c) corrosion removed with a wire brush and d) corrosion removed with a belt

The effect on fatigue life of additional compressive residual stresses from wire brushing is not consider a factor for the alloy 300M specimens in these tests based on x-ray diffraction measurements that were performed. Four tensile samples were sent to American Stress Technologies, Inc. for measurement of the residual stresses in the radial direction of the round samples. In Figure 125 the measurements for heat treated tensile specimens that were shot peened and then either wire brushed (1W), machined (1M) or belt sanded (1B) are shown with reference to the shot peened specimen (labeled 1Ten). As seen in the plot, the compressive residual stress of the shot peened specimens were more than double the stress in the other

⁴⁸ N. Fredj, M. Nasr, A. Rhouma, C. Braham, and H. Sidhom. "Fatigue Life Improvements for the ASIS 304 Stainless Steel Ground Surfaces by Wire Brushing". Journal of Materials Engineering and Performance. 2003

specimens. Compressive residual stress in the wire brushed specimen was a maximum of 400 MPa (58ksi) at approximately 0.03 mm (0.001inch) below the surface. This stress is similar to the 500MPa shown by Fredj et. al. for the stainless steel wire brushed samples in their test. The hypotheses for the decrease in residual stress from the shot peened state to the other mechanical processes is: 1st the material on the surface of the specimens was removed during processing and 2nd tensile stresses were added that partially offset the shot peening. If 0.004 of an inch was removed from the surface of the specimens this could account for the change in the stress state.

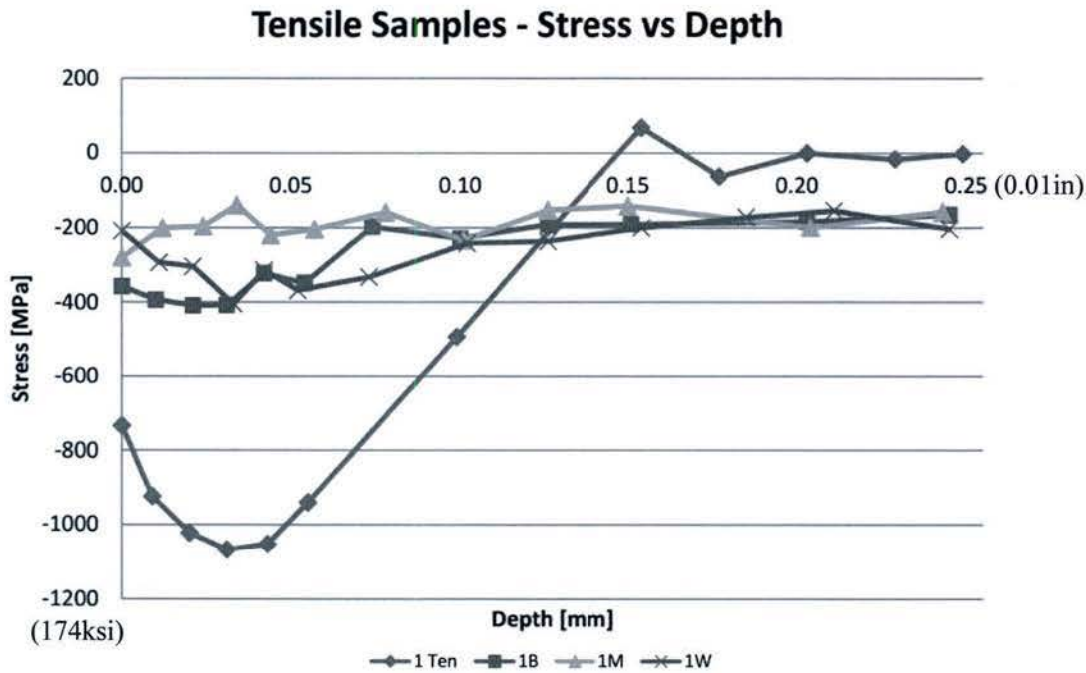


Figure 125 - X-ray diffraction results of tensile samples

A similar maximum compressive stress was observed in wire brushed torsion bar samples when compared to the wire brushed tensile specimens. Figure 126 shows the x-ray diffraction results for residual stresses from a wire brush cleaned torsion bar and a bar that underwent a laser ablation process to remove the polyurethane coating and surface rust. Using the stress data after laser process, where mechanical forces are not imparted on the surface, the bars cleaned using a mechanical wire brush were compared to the original torsion bar stress state under the assumption that the laser process had a minor effect on the residual stresses and minimal creep occurred during vehicle operation. Based on the figure, wire brushing of the torsion bar may enhance the fatigue resistance in the direction of deeper residual tensile stresses created during the preset operation. Although the maximum residual compressive stress is lower than the stress shown for laser cleaning, the worst case minimum compressive stress direction is also lower for the wire brushed bar.

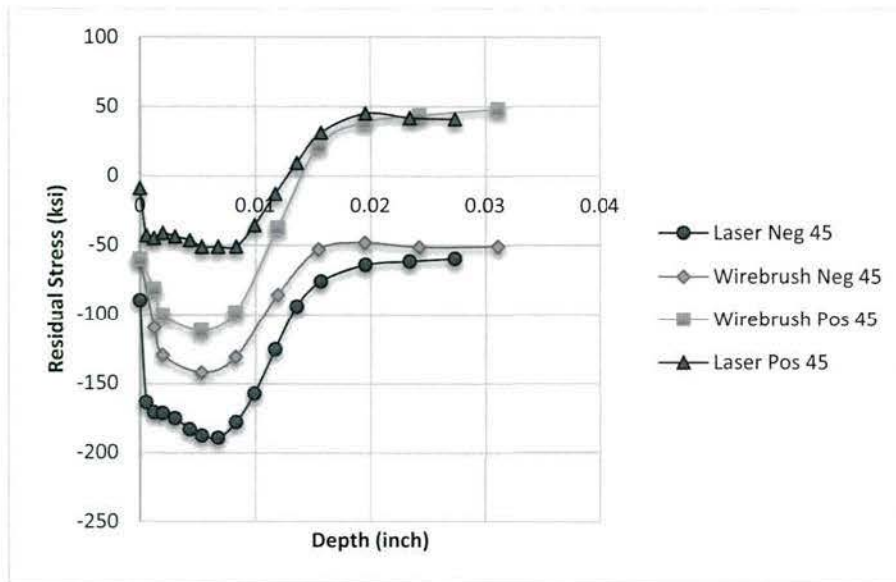


Figure 126 - Residual Stress from Laser Ablation and Wire brushing on the Torsion Bar

A similar result in decreased fatigue life was observed for specimens that were subjected to 24 hours of the salt spray testing. Corroded samples showed approximately a 15% decrease in the endurance limit based on the limited number of specimens tested. Both wire brushing and belt sanding improved the fatigue life but did not return the specimens to a conditional equivalent to the non-corroded state. The wire brushed samples had the greatest improvement but exhibited an 11% lower fatigue life than the non-corroded specimens, refer to Figure 127.

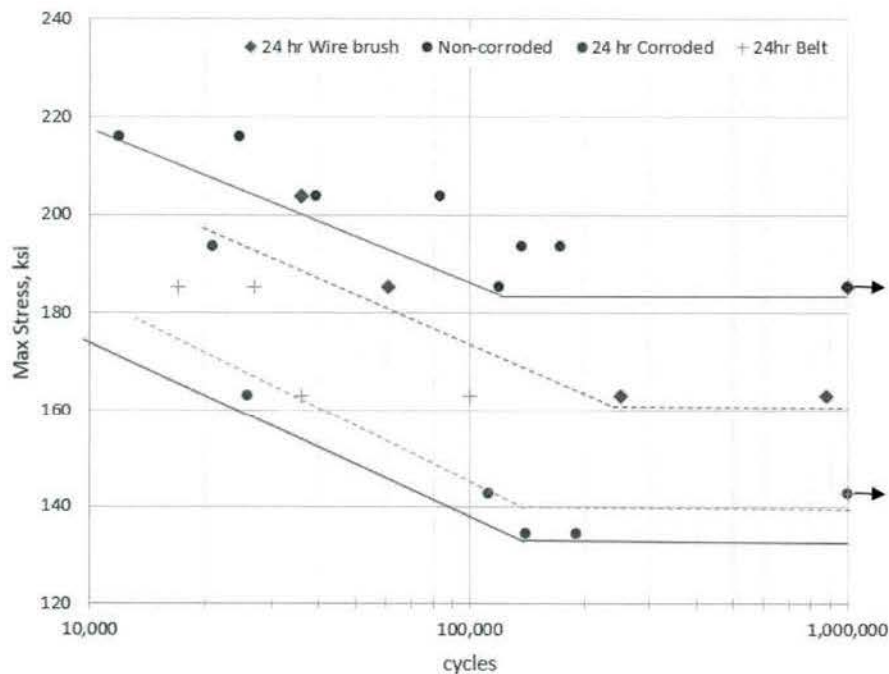


Figure 127- 24 Hour Pitting Fatigue Test Results for Alloy 300M: a) Shot Peened b) corroded for 8hr c) corrosion removed with a wire brush and d) corrosion removed with a belt

Specimens that had undergone 72 hours of salt spray testing showed the greatest change in fatigue life as compared to the non-corroded samples. The maximum stress employed during the testing of the 72 hour specimens was lower than for the 24 hour specimens; however, this stress was not low enough to identify the endurance limit for the corroded specimens. One corroded specimen was tested at a maximum stress of 70ksi to ensure an endurance limit was still obtainable and that effect of corrosion fatigue were not present after the samples were removed from the corrosive environment. Wire brushing and belt sanding showed slight improvements in fatigue life but other processes should be investigated for specimens and torsion bars that exhibit pitting of similar magnitude. The pit dimensions for one of the 72 hour corroded specimens was 0.007inch wide by 0.003 inches deep, refer to Figure 128.

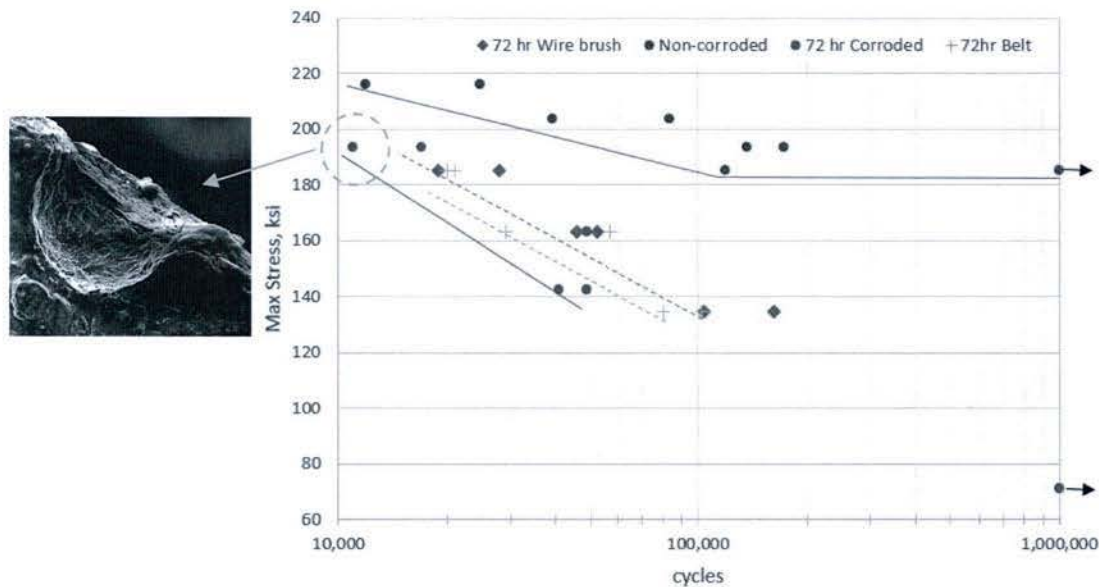


Figure 128- 72 Hour Pitting Fatigue Test Results for Alloy 300M: a) Shot Peened b) corroded for 8hr c) corrosion removed with a wire brush and d) corrosion removed with a belt

4.5.3 Corrosion Fatigue

After the corroded fatigue specimens were tested there were several wire brushed specimens that had reach 1million cycles without failure. These unbroken samples provided an opportunity to test the susceptibility of the shot peened alloy 300M specimens to corrosion fatigue. An investigatory experiment was setup to determine the fatigue life of the specimens while subjected to a corrosive solution of NaCl. Two samples were soaked in a salt water bath containing 4% by weight NaCl for 8 minutes and two other specimens for 80 minutes in advance of the fatigue testing to meet the intent of ASTM E1681. After being soaked the specimens were subjected cyclic testing while the gage section of the specimens were wrapped with a paper towel soaked in salt water and covered in a plastic wrap, refer to Figure 129. This method is similar to the

procedure performed by Hornback and Prevey for corrosion fatigue testing of alloy 300M for landing gear⁴⁹. They presented data on high cycle fatigue testing of spot peened specimens in air versus wrapped in a salt solution. The data for those two tests showed the fatigue life diverged near the endurance limit with the corrosion fatigue samples having lower fatigue lives.

The results from testing of the alloy 300M for the torsion bar showed similar results to the 8hr corroded specimens tested previously. Although the wire brushed specimens had survived 1 million cycles at 163 ksi they failed at ~400,000 cycles when exposed to a corrosive environment during cycling. The two samples cycled at a maximum stress of 134ksi reached 1 million cycles without failure as the corroded specimens had shown. These results are similar to the plots presented by Hornback and Prevey; however, a greater number of specimens could be tested for additional insight into the effect of corrosion fatigue on alloy 300M. The corrosion fatigue tests are considered precautionary in the event that the new abcite coating applied to the torsion bar delaminates leaving the alloy 300M steel exposed to salt water while being subjected to a high number of cycles.

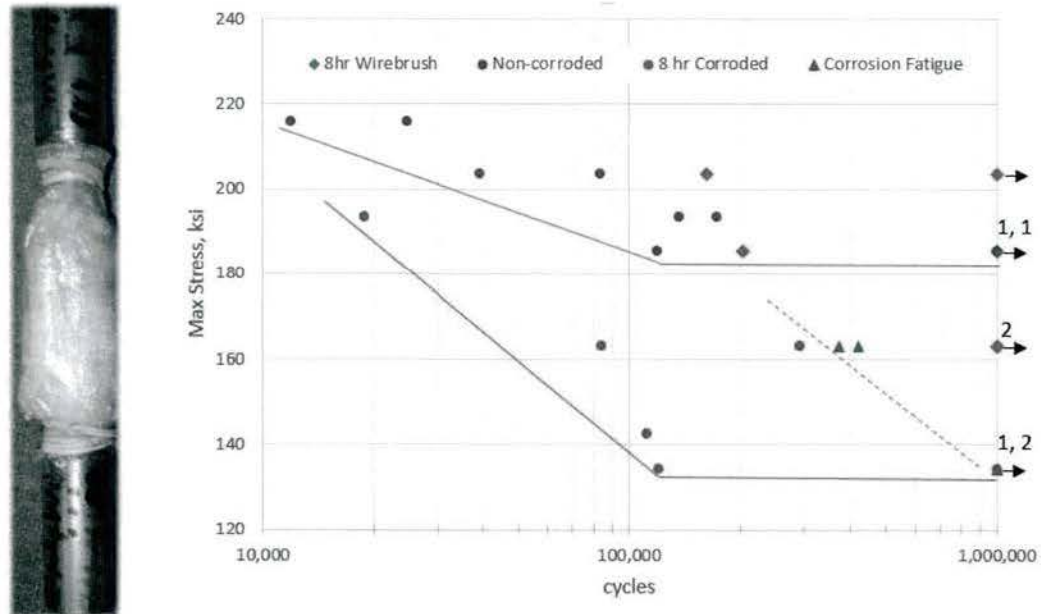


Figure 129 - Corrosion Fatigue Setup and Exploratory Results

4.6 Component Modeling

Once the use profile, material properties, component geometry, and specimen test results have been obtained then modeling of the component of interest can be performed. For structural models the primary methods of investigation are hand calculations and finite element analyses (FEA). Hand calculations of typically acceptable for geometries that can be reduced to analysis of simpler structures such as beams,

⁴⁹ D. Hornback and P. Prevey. "Reducing Corrosion Fatigue and SCC Failures in 300M Steel Landing Gear Using Low Plasticity Burnishing." Paper Number 07ATC-104; SAE International; 2007

plates, and rods. When components have irregular shapes or detailed features of interest then calculations using FEA software is advantageous. For evaluation of the torsion bar both hand calculations using spreadsheets and FEA were employed. Analysis of the pits and the neck/spline area of the bar were performed with the linear and non-linear Solidworks simulation packages.

The modeling effort consisted of primary 4 stages that will be reviewed in detail throughout the remainder of this report. The primary stages included pit modeling, fatigue specimen calibration, residual stress calculations, and superposition modeling. Each stage was used in the final determination of the acceptability for refurbishment of the torsion bar after experiencing corrosion pitting. The criteria for acceptability was based on the susceptibility to stress corrosion cracking and fatigue life of the component.

4.6.1 Pit size and modeling

An advantage of finite element methods is the ability to compute stresses with greater resolution especially at irregularities in a structure. For the torsion bar the effect of pitting was modeled in order to understand the stress concentrations affecting the fatigue life of the component. Stress concentration factors, such as pits, notches and splines, create localized strain and stress that is greater than in the surrounding bulk material. GIS sampled several torsion bars to quantify the dimensions and shape of the pits in order to model the stress concentration resulting from pits. The first quantification method involved using a laser scanning system from Keyence to measure a pit of a heavily corroded torsion bar. A two dimensional profile of the pit was created from the coordinates measured by the laser system and entered into computer aided design software, refer to Figure 130. From the profile a three dimensional model of the pit was created by revolving the shape.

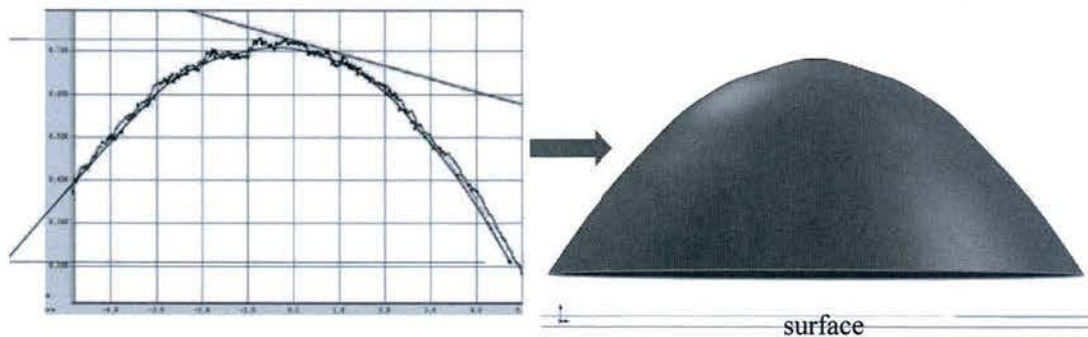


Figure 130 -a) Profile of a pit based on a laser scanning pit gage b) CAD model based on pit scan

When the model of the pit based on the laser scan was brought into the FEA software problems with singularities appeared. To create the pit model and 2D profile was brought into the CAD software and used to a guide for creating a spline that closely followed the path of the pit. Unfortunately the waviness of the spline created a point at the apex of the model which cause singularities when evaluating the stress distribution. To confirm the presence of a singularity, direct control of the mesh size was used to set the element dimensions over several runs of the analysis. The element dimensions differed by several orders of magnitude during the runs so that the resulting stress versus element size could be graphed on a

logarithmic scale, refer to Figure 131. As shown in the graph the stress consistently increases with large reductions in element size thereby confirming the presence of a singularity.

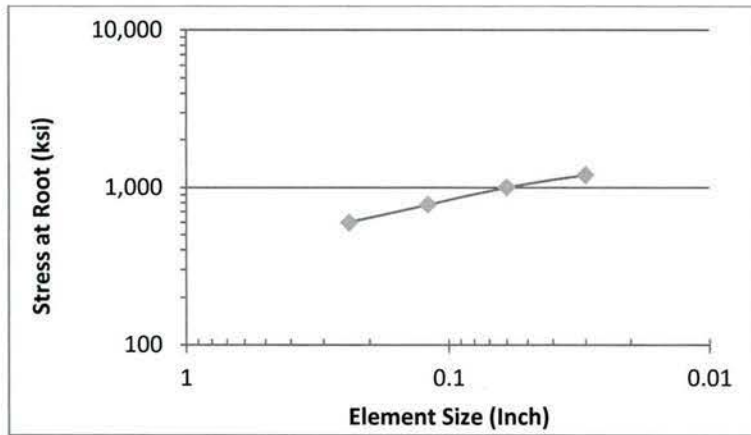


Figure 131 - Singularity Identification

To remove singularities associated with the pit model, a two dimensional image of a pit located on a fatigue sample was captured on a scanning electron microscope (SEM) and brought into the modeling software then used to set the radius of the pit instead of relying on a spline fit like previously attempted. The radius for the curvature of the pit was manually adjusted until it matched the SEM image. A change of 21% in the value of the pit's radius showed less than a 2% effect on the stress below the rim. For radii that result in a steep change of slope near the apex of the pit singularities occurred similar to the scanned model therefore pit models based on elliptical geometry were selected to avoid complications that arise with singularities. Integration of the pit model into the fatigue sample and torsion bar models completed successfully without indication of singularities. Variations of this model were employed in subsequent analyses for determining the stress concentrations resulting from pits in the component analysis.

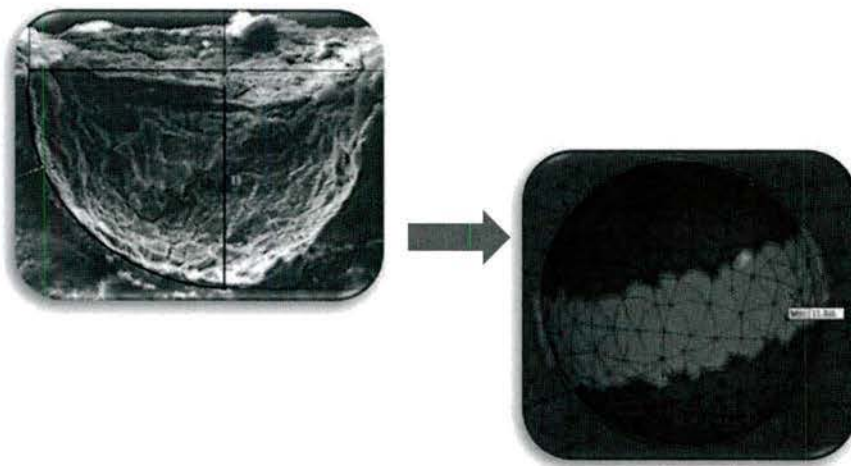


Figure 132 - Pit Modeling from SEM Image

4.6.2 Fatigue model calibration

Finite element analyses are helpful for predicting the effects of load and displacements on a structure; however, the models do not always anticipate variation in material properties, irregular features, and changes to chemical composition. To ensure that assumed extraneous parameters will not affect actual components the finite element analysis should be compared to test data. If experimental data and the models match the analyst has more confidence in the modeling results but understands the limitations of software tools for prediction of life for physical components. Models are simplifications of the physical component therefore assumptions have been integrated into the final result. For instance, radii created from the machining tools may not be accurately captured within the model or complex load states are introduced as point forces. Nevertheless it is important to obtain a sense of the potential failures associated with a design or refurbishment process before manufacturing a component and subjecting it to testing where damage to equipment or personnel could occur. Modeling also allows engineers to introduce worst case scenarios that may occur as a function of time but have not presented themselves yet.

Pitting within a component introduces stress concentrators that must be comprehended in the analysis of FEA models; however, this increases the model complexity due to increases in the mesh density around the feature and the potential for singularities. A comparison between fatigue sample data and the model was performed in order to check that the FEA models were able to reasonably predict the life of pitted components. The approach to this investigation involved cycling corroded fatigue specimens to failure then performing a post mortem analysis to identify the feature that initiated the failure. Once the initiation point was identified the dimensions of the feature could be recorded. In some cases the initiation points were at other irregularities within the microstructure and not from pits. An example of a post mortem analysis on a fractured surface is provided in Figure 133 that shows the pit as the point of the crack initiation.

To compare the experimental results to those of the model, pit sizes of different widths and depths were developed and analyzed. The estimated fatigue life computed by the model for the highest stress in the pit was plotted against the aspect ratio of the pit, depth/diameter. Information on the pit size from the SEM post mortem analysis was cross referenced to the fatigue data from the testing on the Instron for each particular specimen. The cycle to failure data was plotted against the aspect ratio of the actual pits and

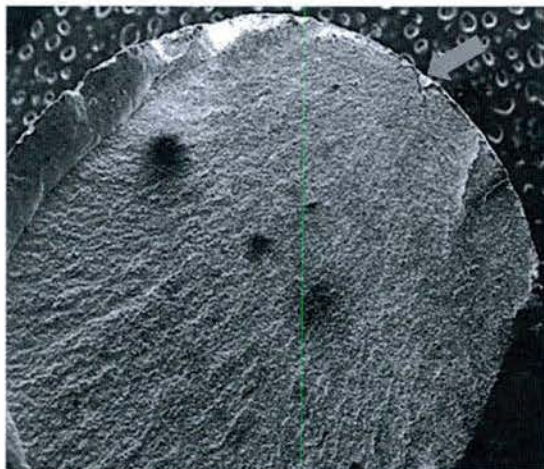


Figure 133 - Fractured Surface of Alloy 300M from Initiation at a Pit

compared to the model results, Figure 134. The findings of Cerit et. al. showed the main effect of pitting is the aspect ratio (depth/diameter) for fea models⁵⁰. Measuring dimensions of corroded pits is difficult due to oxide on the surfaces and the irregular shape of some pits. The data is further compounded because of the wire brush operation on the samples before salt spray which may have decreased the compressive residual stresses as observed in the x-ray diffraction measurements. The fatigue curve employed for the model was based on the high confidence level non-corroded shot peened samples therefore the model may overestimate the life of the specimens. Given additional data, a general trend between the model and experiment may emerge.

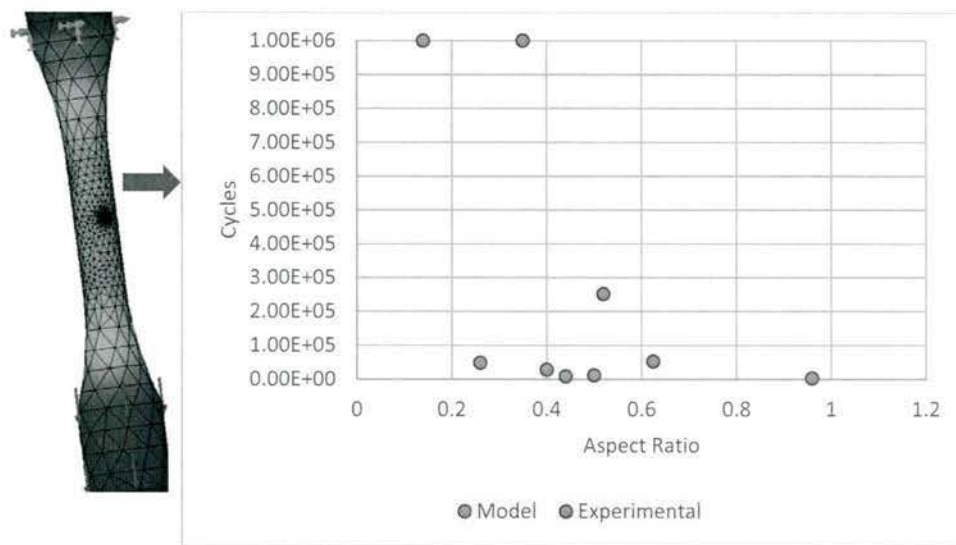


Figure 134 - Cycles vs Pit Aspect Ratio

4.6.3 Residual Stress

Residual stresses within the torsion bar that were applied during the presetting operation play an important role in the resistance of the alloy 300M material to fatigue and stress corrosion cracking. Unlike the compressive residual stresses at the shot peened surface of the torsion bar, the stresses imparted on the bar due to presetting are shear stresses from torsion. The torsional load deforms the material creating extension and contraction within the crystalline structure depending on the direction. If the torsion load generates stresses beyond the material's yield strength then residual stresses form when the load is relaxed. Strain created in the torsion bar while the preset load is applied results in tensile stress corresponding to the extension in the crystal while compressive stress form orthogonally in the bar. Once the load is removed the extended material that was initially under tension (+) rebounds thus creating compressive (-) residual stress, refer to Figure 135. The opposite is true for material initial under compression.

⁵⁰ Cerit, Genel, and Eksi. "Numerical Investigation on Stress Concentration of Corrosion Pit." Journal of Engineering Failure Analysis. Vol 16, issue 7; Oct 2009

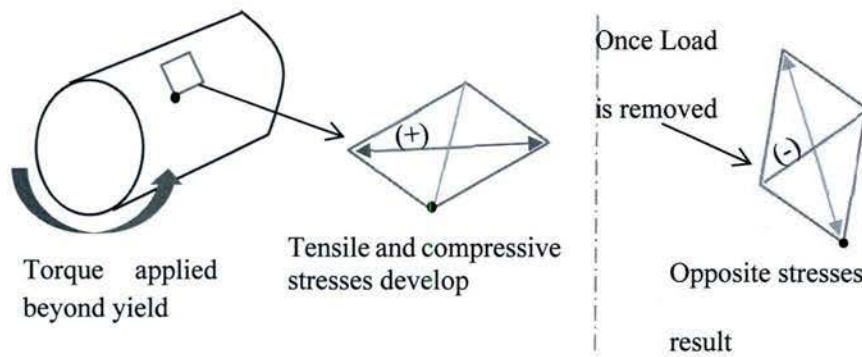


Figure 135 - Residual Stress

An important factor for materials susceptible to stress corrosion cracking is the presence of tensile stress in a component. The shear stress in cylindrical components, such as the torsion bar, can be resolved into principal tensile (σ_1) and compressive (σ_2) stresses using Mohr's theory. In the case of pure torsion the principal stresses are equal to the positive and negative shear stress. For pure torsion the principle stresses are oriented at 45° to the axis of rotation as shown in Equation 2.

$$\sigma = \tau_{xy} * \sin(2 * \theta)$$

Equation 2 –Stress Transform⁵¹

X-ray diffraction measurements of the torsion bar show three important aspects related to the residual stress in the bar. First, as seen in Figure 136, there are residual stresses from shot peen and preset of significant magnitude at a depth beyond 6mm (0.24 inch). Second, the compressive stress from shot peen occurs in all directions to a depth of 0.7 mm (0.03 inch) and overcomes the residual stress from the prior preset operation. Third, the stress in the positive 45° direction is tensile while the stress in the -45° direction is compressive which confirms the presence of residual stresses due to torsional preset. The direction of the torsional residual stresses will change depending on the part number for the torsion bar since bars on the opposite side of the vehicle rotate in in the opposite direction. The stress in the circumferential direction, shown as the red line in the figure, is not impacted by the preset operation therefore only the compressive residual stresses from shot peen are measured.

⁵¹ Shigley and Mischke. Mechanical Engineering Design. 6th Ed. McGraw Hill. 2001. P96

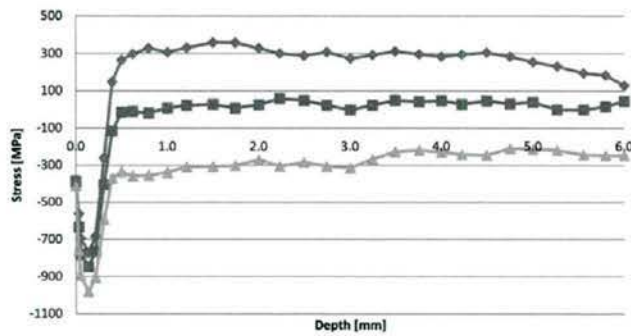


Figure 136- X-ray Diffraction Measurements, scan direction: Red =circumferential, Blue +45°, Green -45°

Computing the residual stress in a circular component is relatively straight forward with references in mechanical engineering textbooks. Popov provides a formula in his text for determining the residual shear stress in a circular cross section, $\tau_{residual} = \text{Torque} * \text{radius} / (2^{nd} \text{ polar moment of area}) - \tau_{yield}$. For components with complex and non-uniform cross sections calculation of the residual stress is more complex and must be computed at each different cross sectional geometry. To reduce the time required for the calculation of the residual stresses from preset it was beneficial to use non-linear finite element software for the straight section, neck region, and splined area. Especially in the spline region where bending of the spline teeth and twist from torsion are factors of the stress magnitude the software is very useful. Additionally, Popov states that linear elastic models tend to overestimate the stress concentration factor⁵².

Table 6 - Comparison of FEA and Textbook Calculations for Residual Stress

	Textbook	FEA
Radius of Elastic Core (inch)	0.37	0.33

For the straight section the text book calculations were compared to the results of the non-linear FEA model. A simple comparison between the radius of the elastic core calculated through the textbook equations and the radius from the FEA results is shown in Table 6. Given similar results between the modeling methods confidence was gained in the use of the non-linear FEA software, and use of the correct of input parameters and material properties. Non-linear models were then created for the remainder of the torsion bar with several models requiring computation time over multiple days.

Figure 137 shows the Solidworks simulation result for the reaction torque over the course of the torsion bar preset. At time step zero, the displacement angle applied at the free end of the bar is zero radians, but varies linearly to 3.104 radians at time step three. It can be clearly seen that the bar undergoes a transition in the amount of torque required to achieve an incremental increase in displacement. This curved section of the plot corresponds to the material reaching its yield point, where the stress strain curve of the material begins to flatten. As more volume of the bar reaches the yield point less torque is necessary to induce more strain.

⁵² E.P. Popov. Mechanics of Materials. 2nd Ed. Prentice-Hall 1976. p76

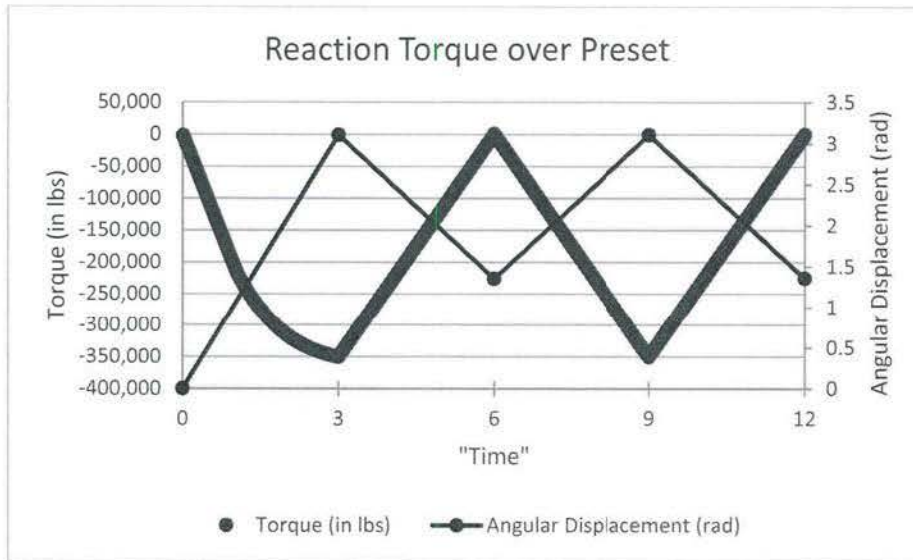


Figure 137: Simulated Reaction Torque During Preset

Between time step three and six, the displacement angle of the torsion bar is varied linearly between 3.104 radians and 1.353 radians. The 1.353 radians corresponds to the angle at which the outside forces on the bar reach approximately zero. Figure 137 shows that, for this section of time, the reaction torque varies linearly with angle, and demonstrates little to no further plastic deformation and a return to zero torque, as expected.

From time step six's 1.353 radians, the displacement angle is again returned to the maximum of 3.104 radians, then reduced to 1.358 radians at time step twelve. This second twist is performed as required in the torsion bar specification, but has little impact on the final preset angle in the simulation. It does serve to demonstrate the continued linear elastic behavior of the torsion bar when twisted between the final residual angle and the maximum preset angle.

Splines

In order to determine the resultant residual stresses inside the splines, it was necessary to perform a nonlinear simulation with the splines included. Several ways of applying resistance to the applied twist were considered, including fixing spline faces, adding a coupler and fixing its exterior, and fixing the peak of each spline. In previous simulations it was shown that the magnitude of the stresses experienced by the splines were similar in both the coupler and fixed peak cases, but with maximums located at different points along the spline root. Because the coupler added complexity and run time to the model it was decided that using the fixed peak condition would be used while providing accurate results at the root.

Attempts were made to simplify the model down to only four teeth, with an applied torque scaled down as appropriate for the fewer teeth. The results of those attempts showed that the stresses never reached expected values, and that modeling the whole splined end would be necessary for accurate results. The final model used the Solidworks non-linear FEA software to compute the stresses resulting from operation and presetting of the torsion bar. The rotation was applied to one end with the top surface of all of the teeth fixed as shown in Figure 138. The residual stress in the splines was a result of torsion loads as evidenced by comparison of Von Mises and equivalent shear stresses.

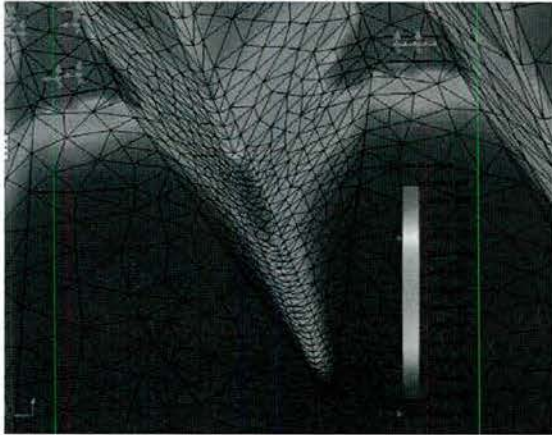


Figure 138 - Model of Splines

4.6.4 Superposition model

The Use Profile developed early in the process provides information needed for accessing the acceptance criteria for the torsion bar in a refurbishment process. There are many factors influencing the stress states of the torsion bar when it is in service therefore the use profile, manufacturing processing parameters, and corrosion effects must be combined into a single model. A superposition model was developed to combine the results of individual finite element models, x-ray diffraction results, and tensile tests. Two separate superposition models were

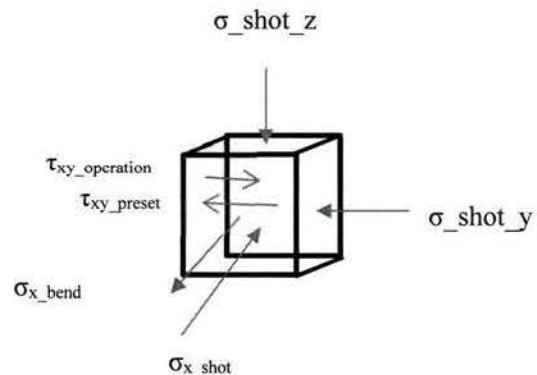


Figure 139 - Stress Element Diagram (showing non-symmetric representation)

developed; one for the straight section and one for the spline section of the torsion bar. The transition region between the smaller diameter straight section of the bar and the larger splined section was not specifically evaluated since the overall stress state in that region is lower than other sections as determined through observation. An excerpt of the superposition model is provided in Figure 140 for discussion purposes. Examining the columns in the model from left to right, the calculations include residual stresses due to preset, shot peen stresses, weight effects, loading during operation, and hull flexure loads.

The stress were transformed and combined in the worst case combinations to identify the maximum principal stress at the cross section of torsion bar being evaluated. The stress state was evaluated at incremental depths of 0.0005 inches from the outside of the torsion bar to 0.03 inches deep, and then at 0.1 inch increments to the center. Results from the finite element and conventional calculations were captured and reduced to an equation as a function of depth from the bar's surface. Similar to the preset stresses, the stresses from the shot peening operation were extracted into an equation through a curve fit of the x-ray diffraction data versus bar depth. Additionally, the remanufacturing analysis employed a hull deflection of 0.42 inch relative to the ends of the torsion bar that translates to a bending stress that contributes roughly 4% to the total stress.






		Residual Stress		Applied Stress					If crack initiated from fatigue or inclusion then static SCC could occur		Note: Don't double count shot peen	
												
Depth (in)	Radius (in)	Root Residual Shear Stress Due to Preset (psi)	Stress Due to Shot Peen (psi)	Shear Stress Due to Vehicle Weight (psi)	Shear Stress Due to Dynamic Loading (psi)	Stress Due to Hull Bending (psi)	Total Static Stress (psi)	Total Principal Stress Dynamic Without shot peen (psi)	Crack Size for SCC susceptibility Static (inch)	Corrosion fatigue Curve	Air Fatigue Cumulative Damage	
0	1.2125	-767,688	-55,694	125,194	30,319	2,833	-88,198	90,648	None	NA	0.12	
0.0005	1.212	-760,411	-72,589	125,133	124,371	2,832	-107,868	91,924	None	NA	0.12	

Figure 140 - Superposition Model

Two main results are obtained from the superposition model, the first is the susceptibility to stress corrosion cracking, and the second is the expected fatigue life. The combined static stress state based on preset, shot peen, and vehicle weight was compared to the stress corrosion cracking threshold intensity (K_{ISCC}) for alloy 300M, that has a similar heat treatment and hardness as the torsion bar, at 10,000 hours in 3.5% NaCl in water⁵³. The result is that tensile stresses within the torsion bar not large enough at rest are to initiate SCC generated cracks. Similarly, corrosion fatigue does not seem to be a factor for the torsion bar as the target of 100,000 cycles is above the endurance limit, the point where corrosion fatigue begins to have an effect.

Axial specimen test results obtained in this project for maximum fatigue strength for the shot peened and heat treated alloy 300M specimens were compared against the equivalent maximum principal stress calculated from a combination of the aforementioned stresses. As the test data and operating conditions have the same stress ratio (R) there were no modifications for equivalent mean stress. Additionally, the stresses from shot peening were not included in the fatigue calculation in order to prevent double counting their effect since the test specimens were peened. Evaluation of the fatigue life for brittle materials typically

⁵³ Kozol and Neu. "Stress Corrosion Susceptibility of Ultra-High Strength Steels for naval Aircraft Applications". Report No. NAWCADWAR-92018-60. 10 January 1992

employs the maximum principal stress theory in which the equivalent stress amplitude equals the maximum principal stress amplitude. Although McClafin and Fatemi showed this method to be a non-conservative approach for hardened spring steel until the endurance limit, test data from the Instron axial and torsion test fixtures at GIS showed the maximum principal stress method to be conservative for the alloy 300M specimens⁵⁴.

A limited sample size of torsional specimens were tested and shown to survive for a greater number of cycles before failure than axial tests with the same maximum principal stress value. Differences in frequency and strain versus load control could play a role in the test results as well, however, steps were taken to mitigate those potential effects. Likewise, shot peening theoretically has a greater benefit for components in torsion than axial fatigue tests since the torsional shear stress decreases radially unlike in axial test specimens. Based on this information it is believed that use of the axial fatigue data for determining torsional fatigue life is conservative. It is worth noting for posterity that the fatigue solution does not include a notch sensitivity (q) used in other fatigue calculations due to the material hardness and small size of the pits in the torsion bars.

4.6.5 Results at spline, neck, and straight sections

Results from the superposition models for the splines and straight section of the bar showed there is a theoretical opportunity for refurbishing the torsion bars. The margin for fatigue associated with the different use profiles is presented in the tables below for both locations of interest. The margin is defined as the value of the stress concentration factor caused by pitting that would indicate the torsion bar could experience fatigue failure at 100,000 cycles. Margin for the straight section under the 70° drawing specification requirements is 1.3 as shown in Table 7. Loading from the other scenarios would increase the margin for the same number of cycles.

Table 7 - Margin for the Straight Section of the Torsion bar

Location	Loading (°)	Source	Margin
Straight section	70°	Specification	1.3
Straight section	59°	Speed Bump	1.5
Straight section	54°	TARDEC	1.6

With an estimate for the margin available on the torsion bar we can identify the geometry of a pit that would decrease the margin to 1.0. Finite element models of pits with varying depths and aspect ratios were analyzed in order to relate the margin to acceptable pit geometries. Multiple pit depths were used in the models but the width of the pits was modified such that their aspect ratios were the same. The results of these analysis are provided in Figure 141 that shows a stress concentration factor of 1.3 corresponds to a pit aspect ratio of approximately 0.11. Within the theoretical bounds of this analysis the aspect ratio and not the pit depth are shown to be critical. The aspect ratio of the pits identified on the torsion bars, that were recently removed from the vehicle, range from 0.04 to 1.2 therefore the conclusion is that the pits should be removed from the straight section of the torsion bar to prevent potential fatigue failures, refer to

⁵⁴ McClafin and Fatemi. Torsional Deformation and Fatigue of Hardened Steel Including Mean Stress and Stress Gradient Effects. International Journal of Fatigue. 2004

Figure 141. Additionally, the fatigue specimens that were corroded for 8 hours were restored to original material fatigue properties after being wire brushed. The pits dimensions after wire brushing the specimens were 0.0007 inch deep by 0.002 wide for the 8 hour corrosion test and 0.002inch deep by 0.0038 wide for the 24 hour corrosion test. As fatigue properties of the 24 hour corroded specimens were not restored after wire brushing it is possible that the maximum pit size allowed before it has an effect on fatigue is between 0.0007 and 0.002 inches deep.

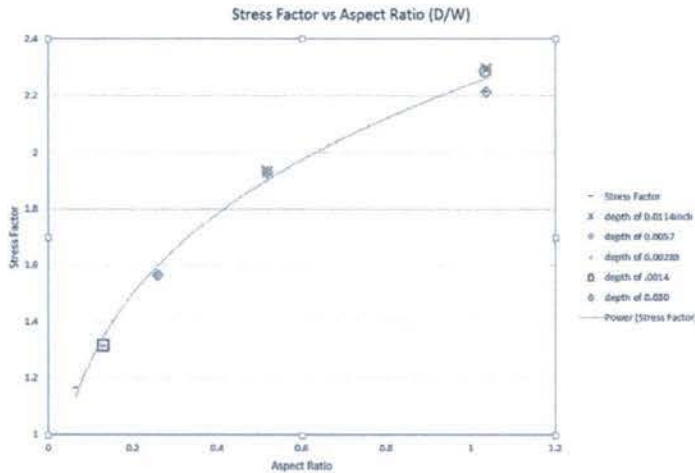


Figure 141 - Stress Concentration and Aspect Ratio

Margins at the splined section of the torsion bar are similar to those calculated for the straight section. Unlike the straight section there is a natural stress concentration within the bar caused by the presence of the splines at each end of the bar. This concentration is maximum at the root of the spline and impact the stress state not only at the surface but to a certain depth within the bar. Due to the splines the most susceptible point within the bar is approximately 0.020 inches below the surface of the roots. Based on inspection of the pits within the splines the deepest one was 0.003inches and the worst aspect ratio was 0.15. As a pit generates a stress affected zone that is greater than the depth of the pit itself, FEA models were used to estimate the depth affected by at 0.003 inch pit. From the model results at 0.003inch pit with an aspect ratio of 1 would have a stress field that dissipates to the stress of the bulk material at approximately 0.007 inches below the surface. The margin was calculated at 3 distinct depths at the splined section in order to capture the most relevant stress points within the bar, refer to Table 8. As fatigue is typically a failure at the surface and the pit depths observed are small, the margins at 0.007 inch below the surface should be of primary interest.

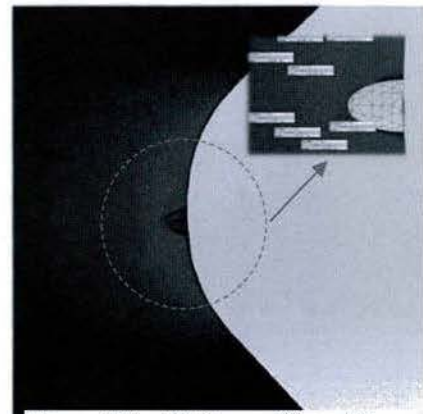


Figure 142 - Pit Stress Affected Zone

Table 8 - Margin at the Splines

Location	Loading	Margin	Loading	Margin	Loading	Margin
----------	---------	--------	---------	--------	---------	--------

Splines Surface	at	70°	1.3	59°	1.5	54°	1.7
Depth 0.007inch	of	70°	1.2	59°	1.3	54°	1.4
Depth 0.023inch	of	70°	1.0	59°	1.1	54°	1.2

Effect of pitting on the alloy 300M torsion bar may cause fatigue failure at the loading conditions employed in the analysis therefore a conservative option is to remove the pits. Removing the pits would require removing material in order to blend the pitted areas into the rest of the bar in an effort to minimize the stress concentration. The removal of material from the outer surface of the bar not only increases the stress but also affects the level of angular displacement of the torsion bar when it is loaded by the vehicle weight and dynamic load. The equation used for torsional deflection, in terms of the wheel support assembly angular rotation θ , is provided below:

$$\theta = 2 * (1 + \nu) \frac{TL}{JE} \quad \text{eqn 1}^{55}$$

Table 9 shows the relative effect of material removal on the AAV ride height as compared to the originally manufactured bar. The resulting decrease in ride height assumes all 12 of the bars on the vehicle have been modified in the same way. Modifying only 1 bar, at any axle, results in approximately 1/12 of the total loss in ground clearance because the front bars are clocked 12 degrees more during installation than rear bars to account for the extra weight up front, all bars are in the elastic region, and equivalent spring constant for parallel springs is the summation of the individual ones.

Table 9 -Ride Height Change

Material Removed, radial (inch)	Length of removed material per bar (inch)	Change in ground clearance [for all 12 bars] (inch)
0.010	Entire straight section	-0.4
0.020	Entire straight section	-0.7
0.020	25 inches total	-0.2
0.020	12 inches total	-0.1
0.020	2 inches total	0.0

⁵⁵ Richard Budynas. Advanced Strength and Applied Stress Analysis. Page 130

Based on these results it may be preferable to turn-down only a portion of the torsion bar length, e.g. 6 inches on either end of the bar. This would leave the majority of the torsion bar with the original diameter and therefore provide greater stiffness. Risk associated with modifying only a portion of the bar is there could be higher stress concentrations created than the pits if the bar is not blended well. If the depot uses a belt sander to remove the pits at a depth of 0.010 inch then a minimum radius of 5inch is required to keep the resulting stress concentration below 1.15. For a radial reduction of 0.040 inches over approximately 1 inch, with 5inch radial chamfer, the stress concentration is 1.21, refer to Figure 143.

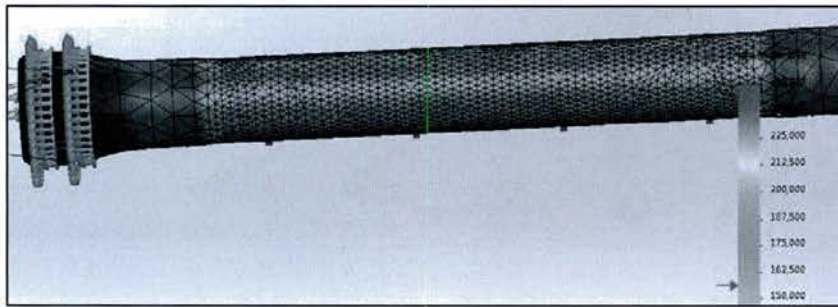


Figure 143 - Radial Reduction and Stress Concentration

4.7 Overall mechanical assessment for refurbishment

4.7.1 Inspection Acceptance Criteria

A robust methodology for assessing components for refurbishment was developed and characterized through an example based on the AAV torsion bar. Components similar to the torsion bar that have an unknown history of may be evaluated for remaining life using a combination of inspections for the current state of the material and estimates for future loading. There is pitting on the surface of the torsion bars that penetrates 0.003inch (84 μ m) deep as evidenced from the material evaluation of recently rejected bars from the Marine Corps depots. In order to determine acceptable refurbishment procedures, the pitted condition of the bars was evaluated in conjunction with load parameters obtained from specifications and testing.

The margins calculated for torsion bars in their original (new) condition seems to be adequate for use under the current vehicle weight and assumed loading conditions. For the corroded torsion bars, however, the aspect ratio of the pits theoretically dictates the maximum stress at the surface of the bars and therefore potentially limiting the loading conditions. Based on the sampling of pit size and aspect ratio gathered during the pitting inspection the conclusion is to remove the pitting from the surface before placing the bars in service. Care must be taken when removing the pits to have a smooth transition between the unworked surface and the sanded area in order to prevent creating stress concentrations that are greater than in the pitted bars. Shot peening should be applied after the corrosion is removed to add extra smoothing of the sanding areas and restore the compressive stress layer that aids in fatigue and stress corrosion cracking prevention.

The ride height of the vehicle will be affected by the material subtracted from the surface during the corrosion removal process. If all twelve torsion bars have material removed to a depth of 0.010 inches then the AAV will ride approximately ½ inch lower. The majority of the torsion bars inspected only require material remove for the first 12 inches from either end therefore the decrease in ride height would be closer 1/8 inch.

Analysis results presented in this report are theoretical therefore confirmation of the finding should be established through prototypic testing of a refurbished torsion bar. Testing should include the drawing requirements for the OEM first article inspection qualification.

5 Remanufacturing Process Development

5.1 Cleaning

This task has two objectives: Develop methods for removing:

1. Corrosion that has formed on the surface of the torsion bar, and
2. Polyurethane coating and primer from the entire surface of the torsion bar.

The processing for the torsion bar, especially the shot peening of the surface prior to the polyurethane coating, is designed to place compressive residual stresses on the surface. These compressive residual stresses improve both the mechanical properties of the 300M and, most importantly, prevent stress corrosion cracking in the 300M alloy⁵⁶, because the 300M alloy is very susceptible to stress corrosion cracking⁵⁷. For this reason, when removing the corrosion or the polyurethane or primer from the surface of the torsion bar it is very important not to damage the shot peened surface of the torsion bar.

5.1.1 Removing Corrosion

5.1.1.1 Research (Trade Study)

There are four general methods for removing corrosion from the surface of steel – abrasive blasting, mechanical removal, chemical removal, and laser⁵⁸. These methods were benchmarked and the processes most commonly used for each method that were applicable to the torsion bar were identified. These processes and their respective advantages and disadvantages of are listed in Table 10.

⁵⁶ Paul S. Prev  y and N. Jayaraman, MITIGATION OF SCC AND CORROSION FATIGUE FAILURES IN 300M LANDING GEAR STEEL USING MECHANICAL SUPPRESSION, Proceedings of the 6th Aircraft Corrosion Workshop August 24-27, 2004, Solomons, MD.

⁵⁷R. Padmanabhan and W. E. Wood (1985) Stress Corrosion Cracking Behavior of 300M Steel under Different Heat Treated Conditions. Corrosion: December 1985, Vol. 41, No. 12, pp. 688-699.

1 ⁵⁸William H. Cubberly; et al, Metals handbook. Vol. 5, Surface cleaning, finishing, and coating, American Society of Metals, cop. 1990.

Abrasive blasting methods have been used for many years to clean and remove rust, paint and corrosion. The abrasive methods benchmarked in this study included steel and ceramic shot blasting, slurry blasting, baking soda blasting and glass bead blasting. Steel or ceramic shot blasting are used for corrosion removal because these methods are relatively inexpensive and quickly remove the corrosion from the surface. However, they also will damage the surface. A newer process, slurry blasting combines chemical cleaning with shot blasting and depending upon the shot used, this method can also damage the steel surface. Baking soda blasting will not damage the steel surface, but it does not remove corrosion very easily. Glass bead blasting is an abrasive blasting method that can remove corrosion from a steel surface producing surfaces that are free of smears, contaminants, and media embedments; high points are blended and pores are sealed. The peening action of the media further acts to impart a layer of compressive stresses on the surface of the part. This increases fatigue life, decreases susceptibility of the part to stress corrosion, and enhances surface strength⁵⁹.

The three mechanical methods benchmarked for corrosion removal were abrasive woven belt, scotch-brite bristle brush and single point turning. All these methods are aggressive and quickly remove corrosion from the surface. Thus, they also cause various amounts of surface damage. Wire brushing is a less aggressive method of corrosion removal and only causes a minimal amount of surface damage. Both the scotch-brite brush and single point turning (machining) can cause surface damage.

One chemical removal method benchmarked, pickling, is commonly used and very effective for removing corrosion from steel strip. However, the torsion bar dimensions would make this process difficult to implement and it would also require the use and disposal of acid. Chemical cleaning, in combination of high pressure and temperature is another method used to remove corrosion. Again the size of the torsion bar is a negative for this process because it will require the fabrication of large, expensive cleaning equipment. In addition, chemical corrosion removal is typically a slow process.

Table 10 - Removing Corrosion from Torsion Bars

⁵⁹ R. Mulhall, N. Nedas, Impact blasting with glass beads, Metal Finishing, Volume 105, Issue 10, 2007, Pages 65-71

Cleaning Method	Advantages	Disadvantages
Abrasive Blasting		
Steel Shot	Quick effective corrosion removal method	Damage Surface, dusty process
Ceramic	Quick effective corrosion removal method	Damage Surface, dusty process
Glass Bead	Will not damage surface	Slower corrosion removal rate, difficult to remove corrosion from deep pits, dusty process
Slurry - media in water	Quick effective corrosion removal method	Damage surface, if not rinsed or dried properly, could cause corrosion or poor coating adherence, component size too large
Baking Soda	Ease of use	Will not remove corrosion
Mechanical Removal		
Abrasive Woven Belt	Very aggressive , very good wear, can conform to irregular shapes	Will grind and damage surface
Scotch-Brite Radial Bristle Brush	Good Wear, minimum surface damage, flexible- conform to irregular surfaces	Will grind and damage surface
Machining	Able to remove corrosion from surface Can be done using the same machine and set-up as for the coating removal	Will remove material from the surface so will affect the compressive residual stress on surface
Wire Brush	Will not damage surface, will remove light surface corrosion	Wear rate, slow process, could scratch surface
Chemical Removal		

Pickling	Will remove corrosion without damaging surface	Requires the use and disposal of acid Process must be closely controlled to obtain the proper removal rate. Surface after pickling will corrode quickly if not treated
Cleaning (Water plus Chemical)	Will only remove corrosion if used in combination of high pressure and elevated temperature	Could cause corrosion if not rinsed properly, large equipment required because of component size, longer time required for corrosion removal,

Another corrosion removal process that has been recently developed is laser ablation.⁶⁰ This process uses a short-pulse fiber-delivered focused laser beam to vaporize specific and targeted coatings or corrosion products on the surface. The short laser pulses create microplasma bursts and thermal pressure, which ejects and/or eliminates the corrosion from the surface of the substrate. Metal surfaces are ideally suited for this corrosion removal method because the temperature required to remove the organic contaminants and most oxides is lower than that which would damage the metal. The precise wavelength and pulse frequency for the laser processing can be chosen to only ablate the target materials without physically or intrinsically changing or harming the substrate material.

After reviewing the advantages and disadvantages of each of the corrosion removal processes listed in Table 10, the following processes were selected for further evaluation – glass bead blasting, chemical cleaning, abrasive woven belt, scotch-brite disk, machining (single point turning), wire brushing and laser cleaning.

⁶⁰ <http://www.photonics.com/Article.aspx?AID=56090>

5.1.1.2 Initial Cleaning Studies

A preliminary study was performed to determine the effect of wire brushing and glass bead blasting on the ability to remove the corrosion from the surface of the torsion bars that very excessively corroded. These two methods were selected for this initial trial because it was believed that they would do the least amount of damage to the component surface during corrosion removal. The glass beads used for this process are made from a lead free soda-lime type of glass.

The effect of the glass bead blasting on the ability to remove corrosion from the surface of torsion bar specimen 11 (from the initial Albany Ga, visit) are contained in Figures Figure 144. Figure 144, top shows that this shaft exhibited moderate to heavy corrosion. The optical photomicrographs in Figure 144 and SEM photomicrographs in Figure 145 showed that the surface after bead blasting had a similar physical appearance as the shot peened surface indicating that the glass bead blasting did not significantly damage the surface. However, the higher magnification SEM photomicrographs of the glass bead blasted surface contained in Figures Figure 146 and Figure 147 did show that the glass bead blasting did cause surface damage. Figure 147 shows that the glass bead blasted surface contained metal flakes that were partially bonded to the surface. The flakes developed because the bead blasting was performed at an angle to the surface.



Figure 144 - Torsion Bar Shaft 11" As Received" top, After Glass Bead Blasting, bottom (Mag. 50x)

The non-dispersive X-ray analysis and the higher magnification SEM photomicrograph (1923X) (Figures Figure 147 and Figure 148) showed that all the oxide was not removed by the glass bead blasting. The non-dispersive X-ray pattern in Figure 148, Region 1 shows oxygen as one of the elements present (See arrow). The present of the oxygen on the surface shows that not all the corrosion layer was removed during the glass bead blasting. It is interesting to note that the flakes that developed contained no oxide.

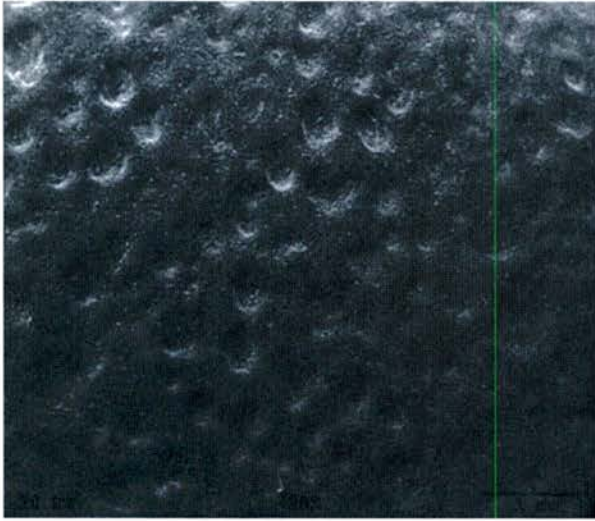


Figure 145- SEM Photomicrograph of Torsion Bar 11 After Glass Bead Blasting (Mag. 200x)



Figure 146- SEM Photomicrograph of Torsion Bar 11 After Glass Bead Blasting (Mag. 20x)



Figure 147 - SEM Photomicrograph of Torsion Bar Shaft 11 after Glass Bead Blasting (Mag 1923x)

Two methods of oxide removal were evaluated on Torsion Bar shaft 7 during the preliminary evaluation – wire brush and glass bead blasting. Both methods were performed using very light pressures in order to remove the surface oxide without imparting any significant amount of damage to the surface.

Prior to cleaning, Torsion Bar shaft 7 exhibited moderate to heavy corrosion. In addition, some pitting was observed (Figure 149). The wire brush cleaning revealed that there were a significant amount of pits on the surface under the corrosion (circled areas in Figure 149).

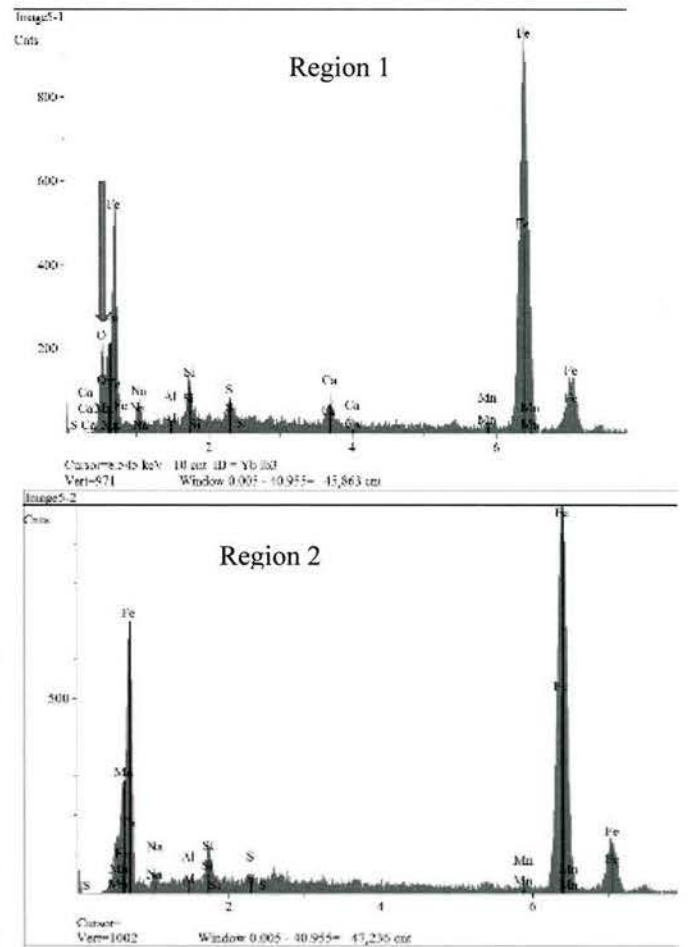


Figure 148 - Non-Dispersive X-Ray Analysis of the region Labeled in Figure 147

The SEM analysis of the wire brush cleaned surface showed that the light pressure did not remove all the corrosion from the surface (Figure 150). This was evident by the cracks observed on the surface (indication of a non-adherent oxide layer) and the large oxygen peak in the non-dispersive x-ray analysis (Figure 150, bottom).

The low magnification optical and SEM photomicrographs of the surface from Torsion Bar 7 after glass bead blasting again shows that the surface finish after blasting was very similar to

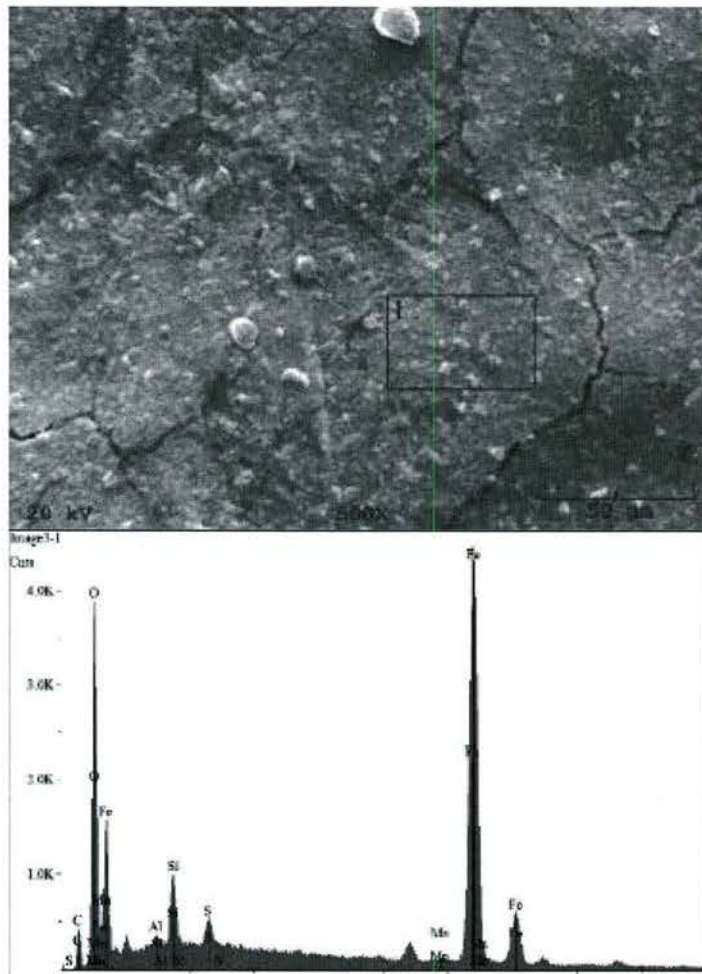


Figure 150 - SEM Photomicrograph of Torsion Bar 7, Top, Surface after Wire Brushing (Mag 500). Bottom, Non-dispersive X-ray Analysis of Region 1

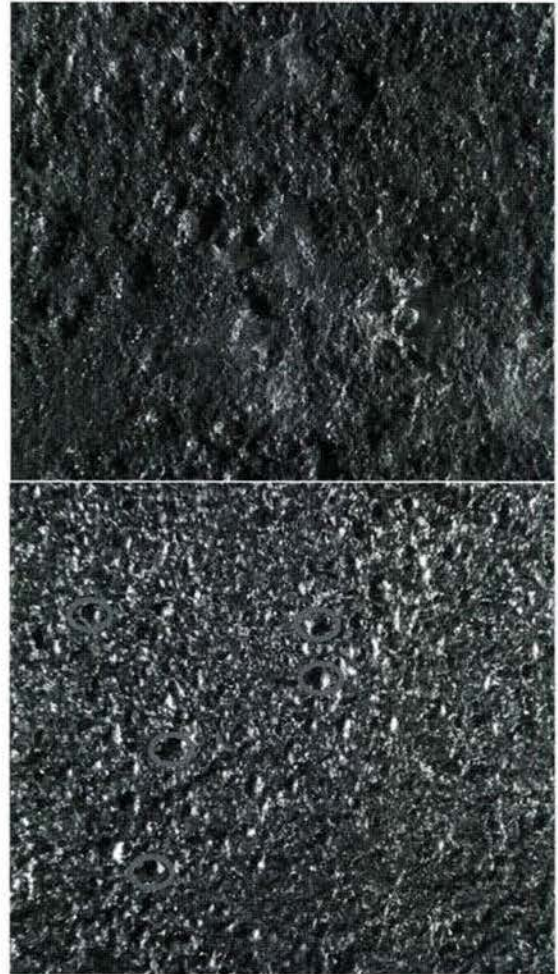


Figure 149 - Optical Photomicrograph of Torsion Bar 7, Top Corroded Surface, Bottom Surface After Wire Brushing (Mag 10x)

that of the shot peen surface (Figure 153). In addition, any pits that developed because of the corrosion were still present on the surface after the glass bead blasting (Figure 152).

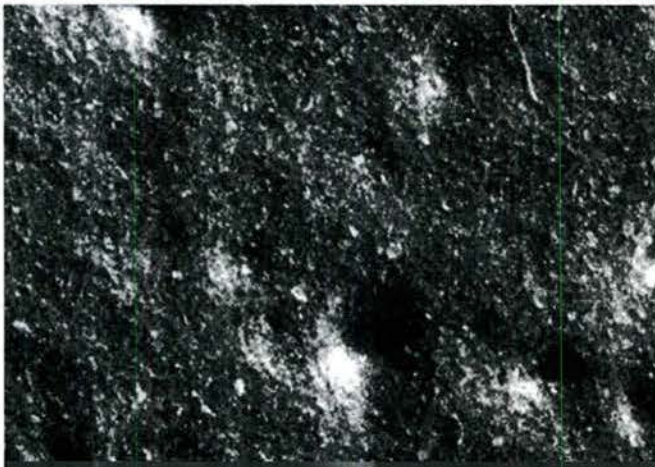
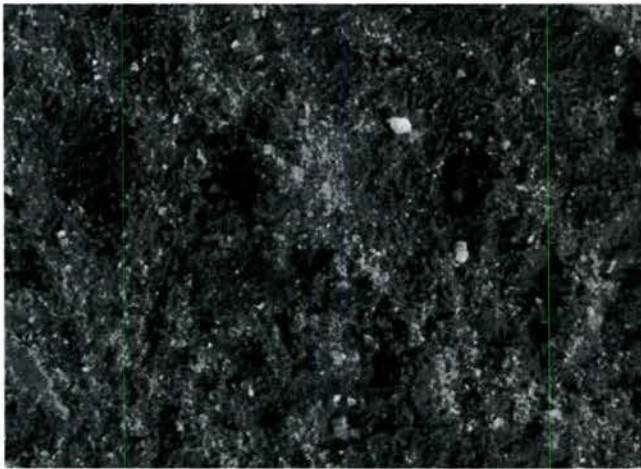


Figure 154 - SEM Photomicrograph of Torsion Bar 7 after Glass Bead Blasting (Mag 2000x)

Figure 151, a higher magnification view of the glass bead blasted surface, shows that the glass bead blasting, again because it was performed at a 45 degree angle from the surface, caused partially adherent metal flakes to develop on the surface (arrows in Figure 151).

The SEM analysis, shown in Figures Figure 154 and Figure 155 shows that after the light glass bead



Figure 152 - SEM Photomicrograph of Torsion Bar 7 after Glass Bead Blasting (Mag 20x)



Figure 151 - SEM Photomicrograph of Torsion Bar Shaft 7 After Glass Bead Blasting (Mag 200x)

blasting a thin corrosion layer was still present on the surface of Torsion Bar 7. Thus, a heavier amount of glass bead blasting is required to remove all the corrosion. Increasing the amount of glass bead blasting will also increase the amount of damage that occurs

on the torsion bar surface during corrosion removal. Finally, the non-dispersive X-ray analysis also showed that the partially adherence flakes were iron.

A laser was also evaluated for torsion bar corrosion removal. For this study, the coating was removed prior to laser cleaning. It should be noted that the

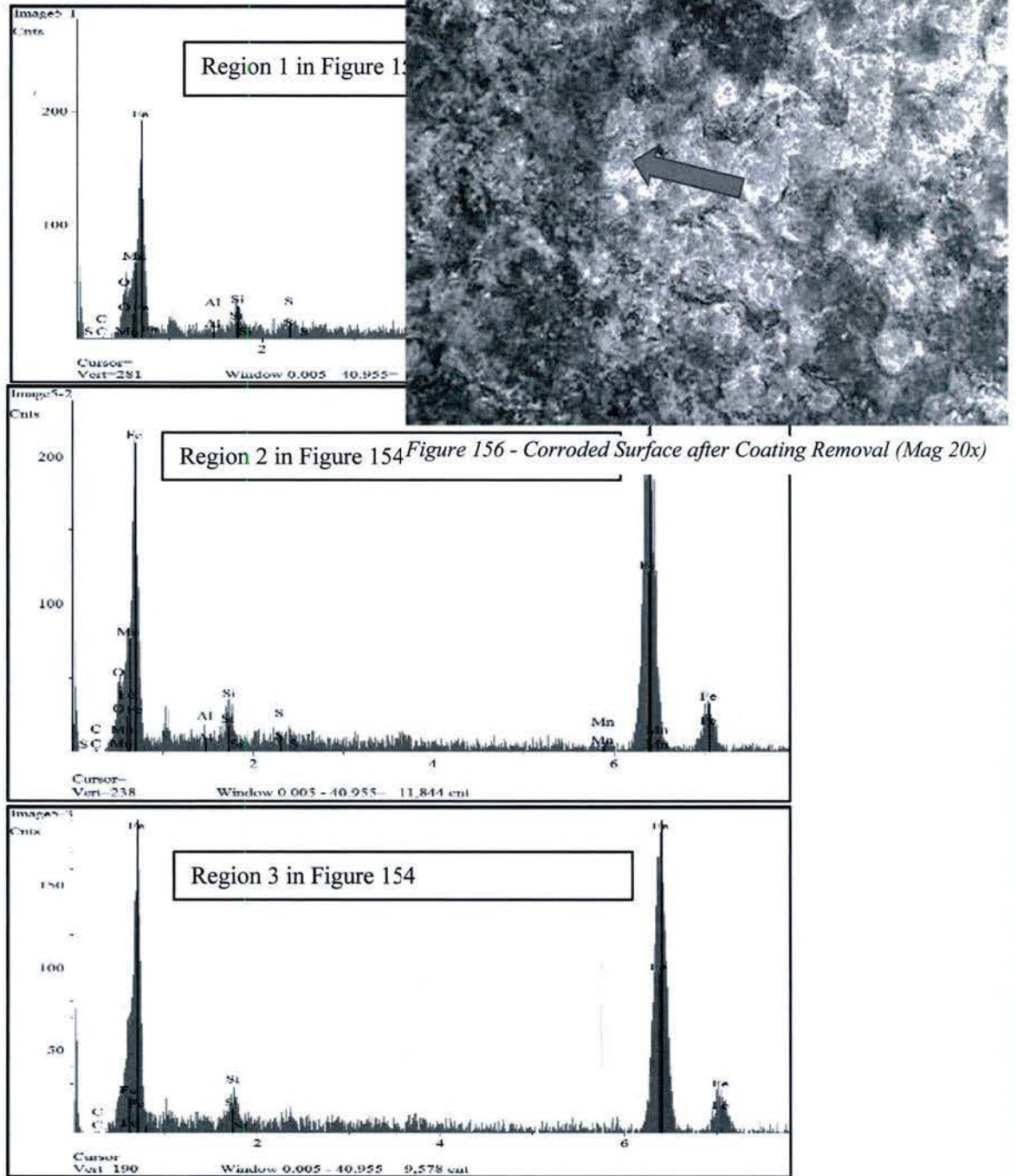


Figure 155 - Non-Dispersive X-ray Analysis from Figure 154

torsion bar section used for this study contained a significant amount of corrosion beneath the coating, which was poorly bonded to the torsion bar.

Optical photomicrographs of the torsion bar surfaces both prior to and after laser cleaning are shown in Figures Figure 156 and Figure 157. The 2D Surface roughness results are contained in Table 11 and Figure 158.

	Coating Stripped	Laser Cleaned
Ra (2D)	0.393 uM	0.307 uM
Rq (2D)	0.608 uM	0.508uM
Sa (3D)	21.12 uM	18.97 uM
Sq (3D)	28.96 uM	27.88 uM

Table 11 -

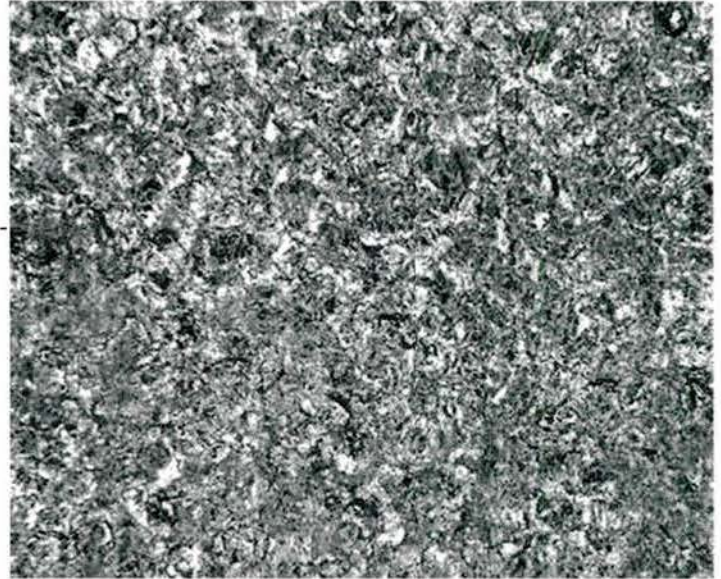


Figure 157 - Laser Cleaned Surface (Mag 20x)

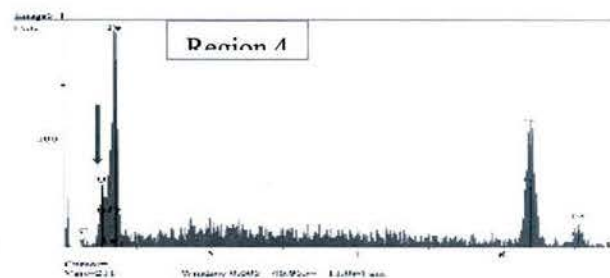
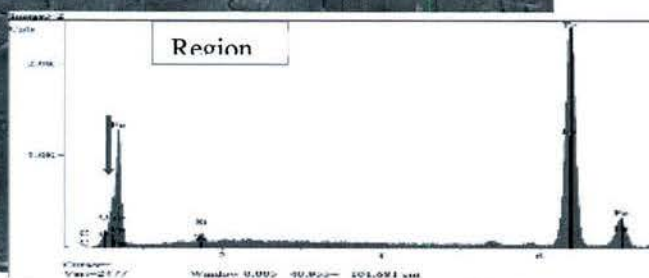
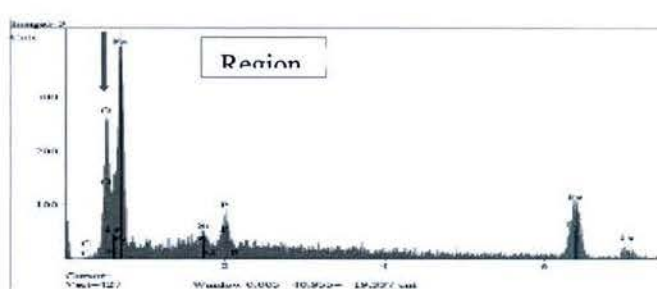
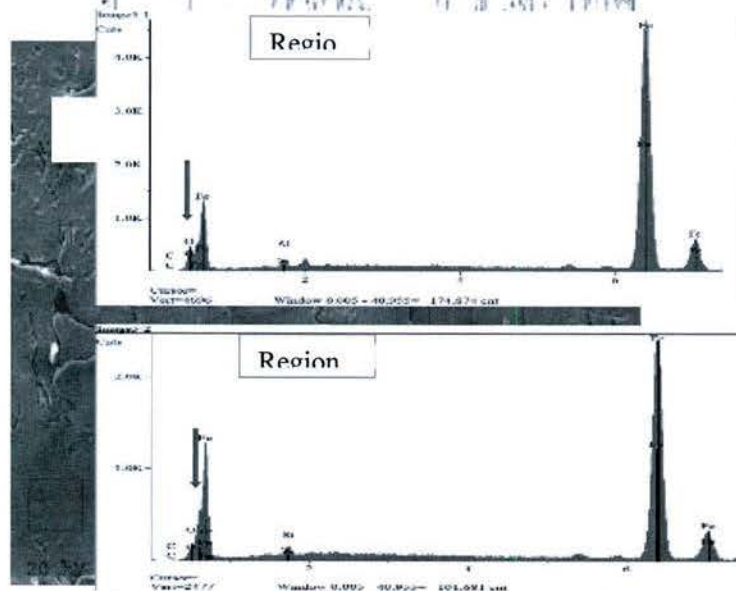
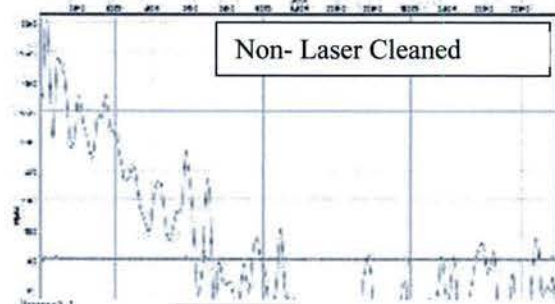
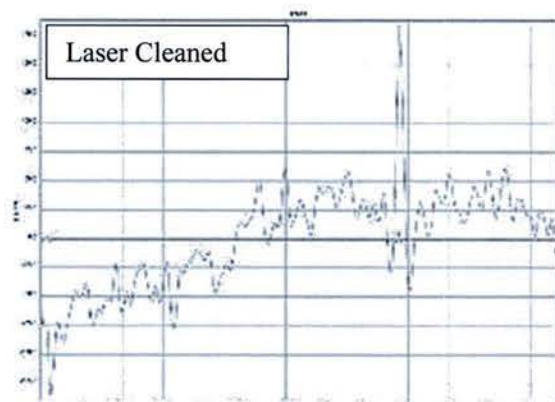


Figure 156 - Non-Dispersive X-ray Analysis of regions in Figure 159 (Mag 21)

The corrosion on the surface of the torsion bar prior to laser cleaning is shown in Figure 156 (see arrow). Figure 157 shows that after laser treatment no corrosion could be visually observed on the surface. The photomicrographs and the 2D and 3D surface analyses (Table 11 and Figure 158) showed that the laser cleaned region had similar surface finish as the non-laser cleaned region.

However, in figures Figure 159 and Figure 160, the SEM analysis of the laser cleaned surface, showed that the laser parameters used in this initial trial did not completely remove all the corrosion from the surface. This is evident by the non-dispersive X-ray analyses performed on the surface after laser cleaning that detected oxygen (blue arrow on trace) on the surface. The oxygen represents iron oxide on the surface.

While the initial laser cleaning trials were promising in that they showed that the laser could remove the corrosion from the surface of the torsion bar without damaging the surface, additional development is required to determine the optimum laser parameters to completely remove all the corrosion from the surface.

5.1.1.2.1 Tensile Specimens

After reviewing the results of the preliminary cleaning trials with the glass bead and wire brush a more in-depth study was performed to determine the effect of wire brush, scotch-brite disk, abrasive woven belt, chemical methods, glass bead blasting, and machining (turning) both corrosion removal and the mechanical properties of the 300M. In order to obtain the desired physical and mechanical properties from the 300M alloy for this application the 300M is heat treated, quenched, plastically deformed and shot peened to obtain a specific stress pattern within the 300M. Any cleaning method which removes material or damages the surface will adversely affect the stress pattern within the 300M and as a result will degrade its performance.

This second study began by exposing tensile specimens (ASTM E-8 B Size) to exposed to ASTM B117-3 salt, fog testing for 8, 72, and 336 hours. After testing the amount of corrosion after each time period was quantified. Then the corrosion was removed from the tensile specimens using the various methods and the tensile properties of the 300M were determined. For comparison the tensile properties of the 300M after shot peening and corroded prior to cleaning were also obtained. Finally after tensile testing the surfaces of the tensile specimens were examined to determine the effect of the cleaning method on the amount of corrosion removed and damage to the surface. The results of the tensile testing and surface examinations were used to select two cleaning methods that do not degrade the surface for the fatigue analysis.

Figure 161 shows the amount of corrosion that developed on the 300M during the salt, fog testing. As expected, increasing exposure increased the amount of corrosion on the surface. Figure 15 also shows how the corrosion developed on the 300M during this salt, fog test. Initially the corrosion develops within the bottom of the “dishes” that are present on the surface of the 300M because of the shot peening. These dishes trap the salt and moisture allowing for the initiation of the corrosion. As the exposure time increases the corrosion within the shot peened disks grow until a continuous corrosion layer is present on the surface of the 300M (72 hour surface). The oxide or corrosion layer that develops on 300M is very porous and non-adherent. For this reason when it reaches a certain thickness it spalls from the surface of the 300M and a new corrosion layer begins forming. The combination of the spallation of the corrosion layer and the growth of a new layer produce the very rough surface observed on the 300M after the 336 hours of testing (Figure 161).

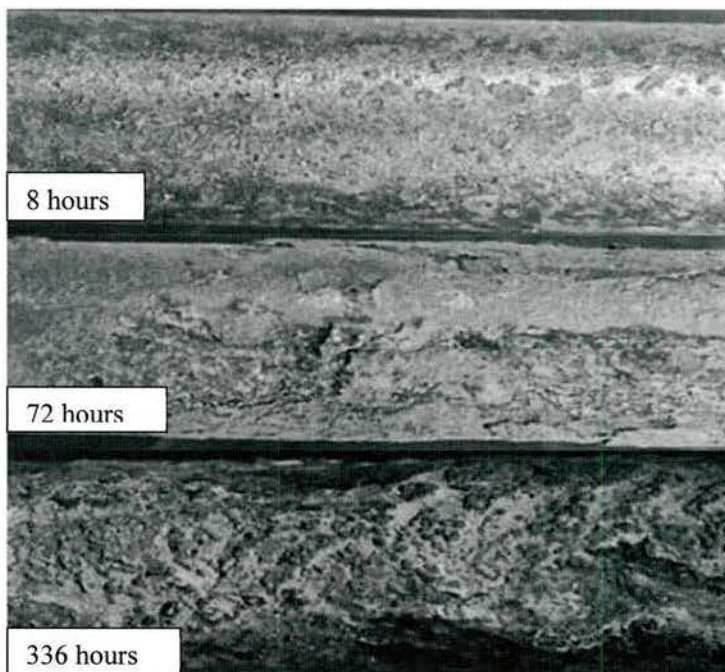


Figure 161 - Tensile Specimen Surfaces after Salt, Fog Testing (Mag 10x)

The results of the corrosion clean-up testing of the corroded, shot peened tensile specimens are shown in Figure 162-Figure 165. After 8 hours of salt, fog testing the corrosion that developed on the 300M specimens reduced the 300M tensile strength 2.5%, compared to the non-corroded shot peened specimens. Figure 162-Figure 165 also show that any method used to remove the corrosion from these 300M specimens reduced the tensile strength further. The corrosion removal method that had the least effect on the tensile strength was wire brushing. This method produced specimens with tensile strengths 3.1% lower than the shot peened specimens, which was only 0.6% lower than the “as corroded” specimens. Chemical and abrasive belt cleaning reduced the tensile values of the 300M specimens by 4.0 and 4.6%, respectively. The three cleaning methods which had the greatest impact on reducing the tensile strength were scotch-brite disk (-6.2%), glass bead blasting (-7.7%) and machining (-9.3%).

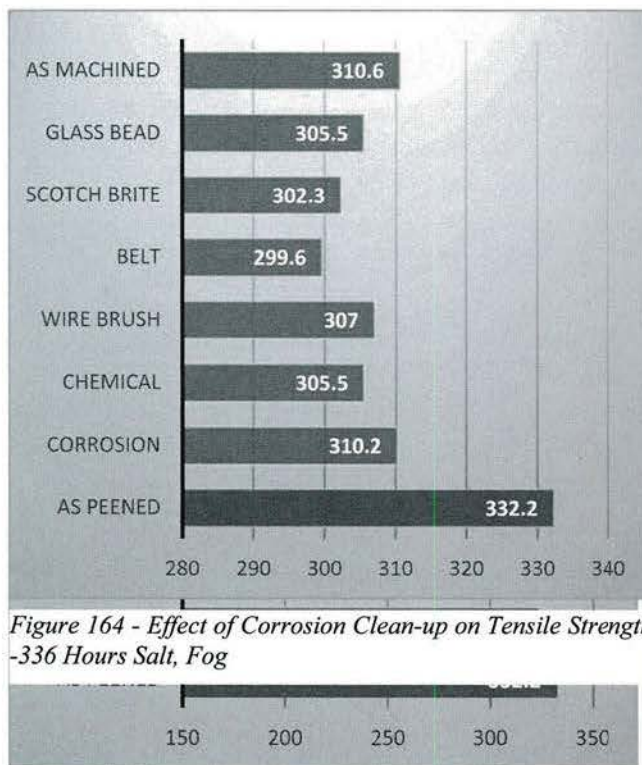


Figure 164 - Effect of Corrosion Clean-up on Tensile Strength - 336 Hours Salt, Fog

The 72 hour “as corroded” 300M specimens had a 4.0% lower tensile strength than the non-corroded, shot peened 300M. Thus, the increased amount of corrosion on these specimens reduced the tensile strength 1.5%.

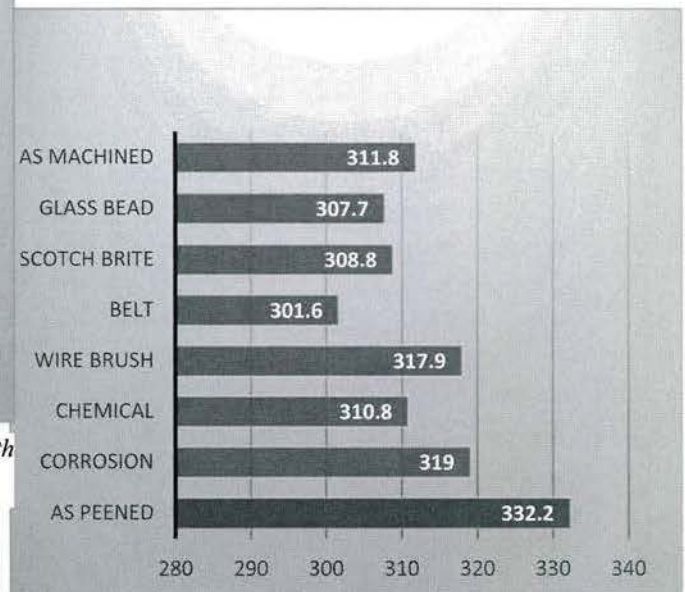


Figure 163 - Effect of Corrosion Clean-up on Tensile Strength - 72 Hour Salt, Fog

Again, using a wire brush for corrosion removal had the least effect on reducing tensile strength (-4.3%). In fact, the wire brush cleaned specimens had similar tensile strengths as the “as corroded” specimens (317.9 compared to 319 KSI). Figure 162-Figure 165 also show that any other corrosion removal method used significantly reduced the tensile strength of the 300M specimens.

The 300M specimens after 336 hours of salt, fog testing had a 6.6% lower tensile strength than the non-corroded shot peened 300M specimens. Again, the wire brush corrosion removal had the least effect on the tensile strength (-4.3%). On the other hand the abrasive belt, scotch-brite, and glass

bead corrosion removal methods had the greatest effect on the 300M tensile strength (-9.2%, -7.0%, -7.4%, respectively).

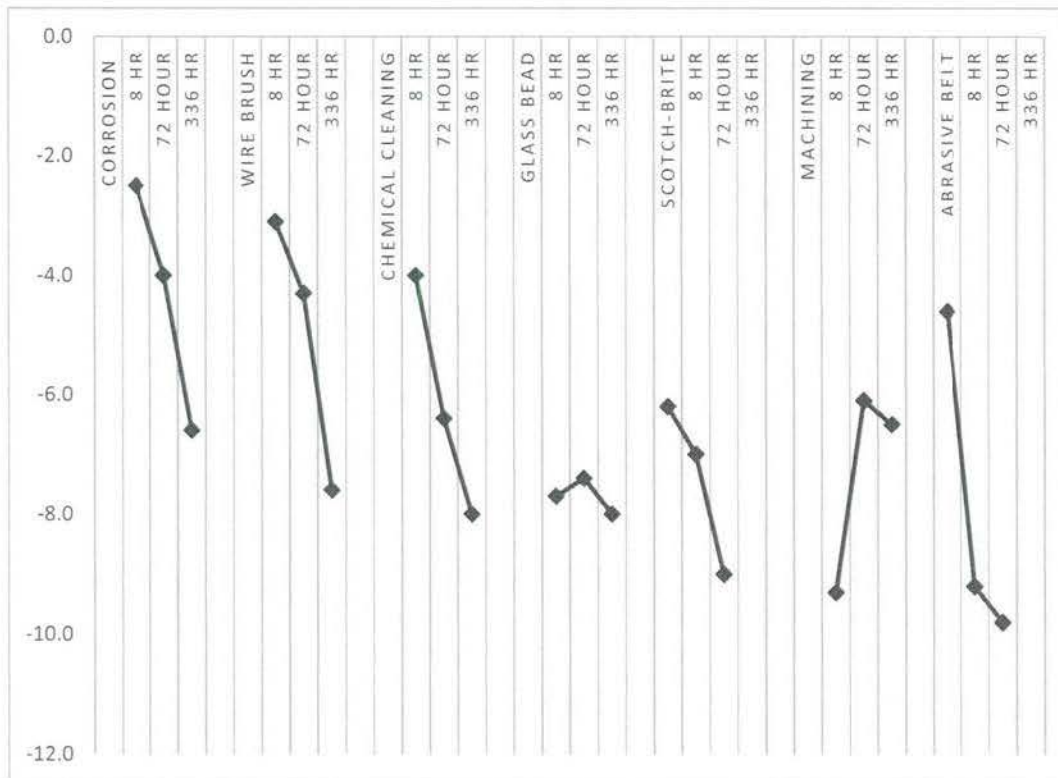


Figure 165 - Summary of the Effect of Corrosion Clean-up on Tensile Properties

The results of the tensile testing showed that corrosion on the 300M will reduce its tensile strength. After 8 hours of salt, fog testing the decrease in tensile strength was 2.5%, compared to a non-corroded 300M. The decrease in tensile strength for 72 hours of salt, fog testing was 4.0% and 6.6% after 336 hours of salt, fog testing. It should be noted that typically the torsion bars examined off the vehicles that have not spent a large amount of time in outside storage had significantly less corrosion than the specimens after 8 hours of salt, fog testing.

Optical photomicrographs of the surfaces of the 300M tensile specimens after corrosion removal are contained in Figure 166-Figure 170. The chemically cleaned specimens were placed in a Mart high pressure washer and cleaning with a detergent composition designed for rust removal. Figure 169 shows that there was a significant amount of corrosion remaining on the surfaces of all the tensile specimens irrespective of the salt, fog exposure time. Thus, the photomicrographs show that chemical cleaning could not remove all the corrosion from the surface of the 300M tensile specimens. However, the chemical cleaning did not damage the 300M surface.

Figure 167 shows the surfaces of the surfaces after wire brush cleaning. All the surfaces after wire brush cleaning did not contain any visible corrosion. In addition, there was no evidence that the wire brush significantly damaged the surface.

No visible evidence of corrosion was observed on the glass bead blasted tensile specimens (Figure 168). Unlike the preliminary trials for this corrosion cleaning study the glass bead blasting did not significantly damage the surface.

Scotch-brite corrosion removal removed all the corrosion from the surface of the tensile specimens but also polished the surface (Figure 166). However, while the surface was polished during corrosion removal the amount of material removed was not great enough to remove the pits that developed during testing on the surface.



Figure 169 - Optical Photomicrographs of Tensile Specimens after Chemical Cleaning (Mag 10x)

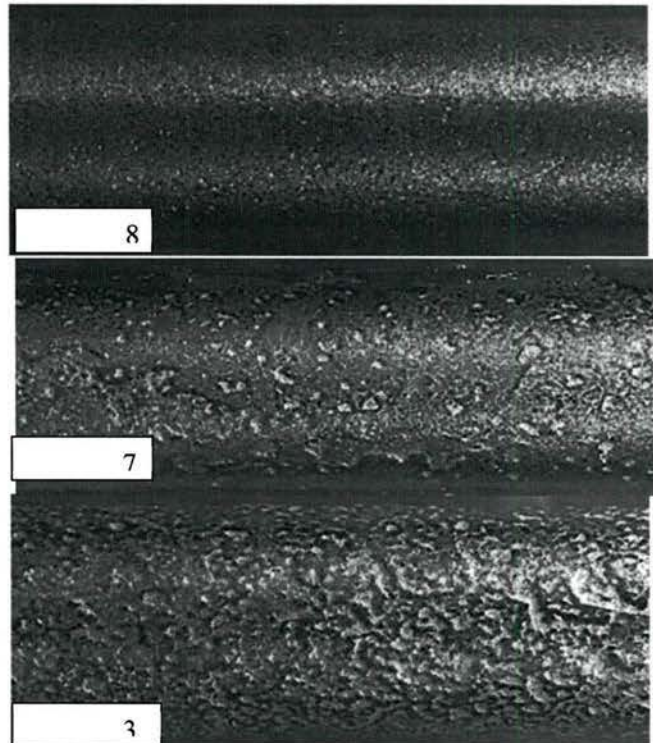


Figure 167 - Optical Photomicrographs of Tensile Specimens after Wire Brush Cleaning (Mag 10x)

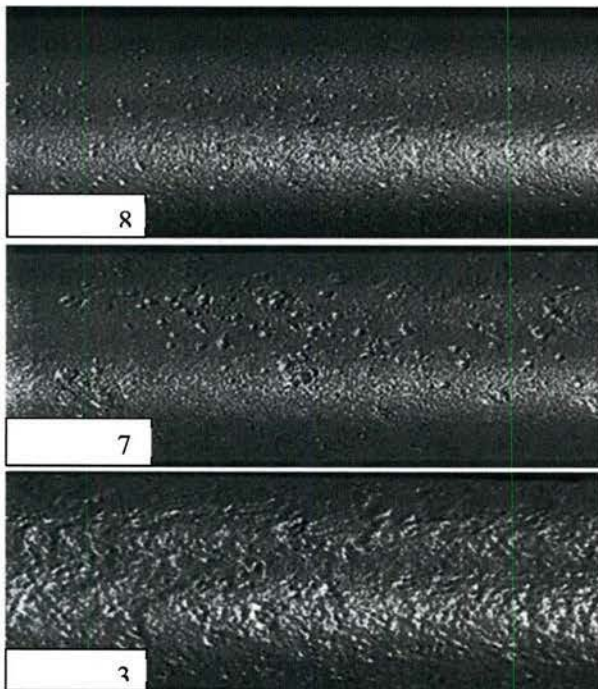


Figure 168 - Optical Photomicrographs of Tensile Specimens after Glass Bead Blasting (Mag 10x)

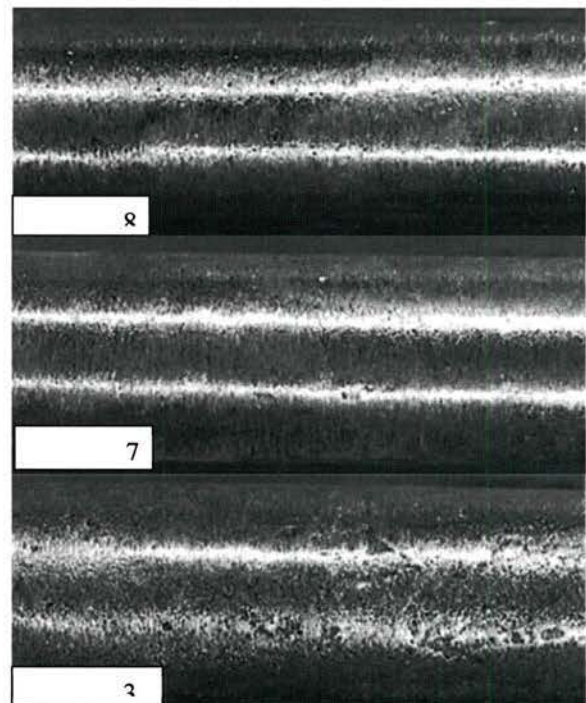


Figure 166 - Optical Photomicrographs of Tensile Specimens after Scotch-Brite Cleaning (Mag 10x)

Abrasive belt sanding and machining the surface removed the corrosion from the surface of the tensile specimens (Figure 170 and Figure 171). However, both methods cause a significant amount of surface damage. In addition, except for the deepest pits these methods removed most of the pits from the surface.

Summarizing the cleaning trials both the chemical and wire brush corrosion removal methods did the least amount of damage to the surface of the tensile specimens during corrosion removal. This was

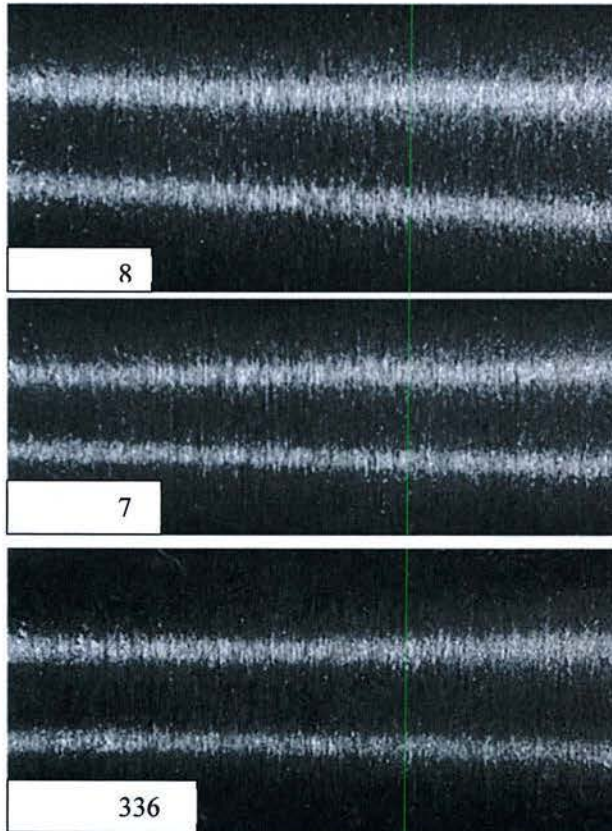


Figure 170 - Optical Photomicrographs of Tensile Specimens after Belt Sanding (Mag 10x)

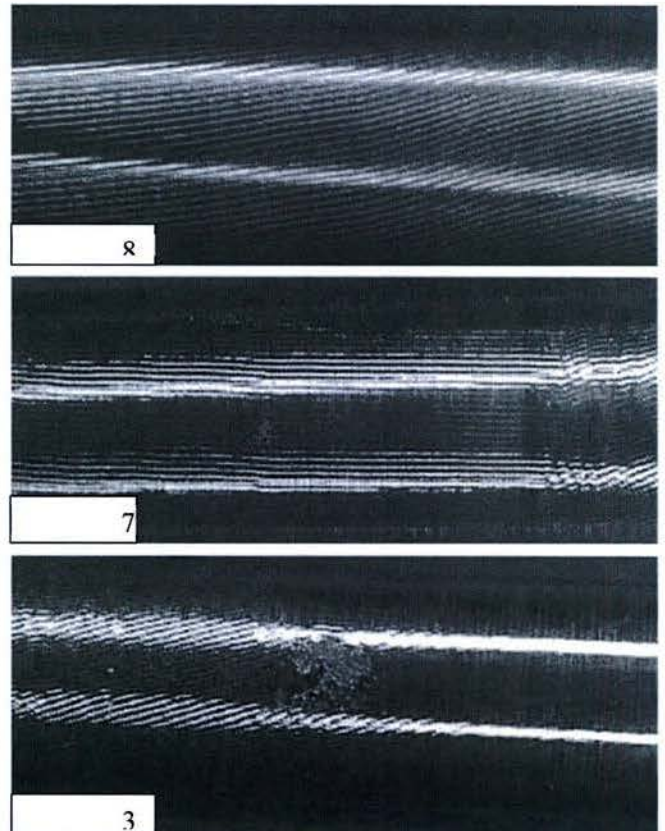


Figure 171 - Optical Photomicrograph of Tensile Specimens after Machining

confirmed by the tensile results (Figure 164) which showed that these two corrosion removal methods had the least effect on the tensile properties of the 300M. However, Scanning Electron Microscopy analyses of these cleaned surfaces showed that these methods did not remove the corrosion from the deep pits that developed on the surface. Although not visible, the tensile results showed that the glass bead blasting did damage the surface during corrosion removal. Finally, Scotch-brite, abrasive belt and machining all damaged the surface during corrosion removal reduce the tensile properties of the 300M. The Scanning Electron Microscopy analyses of these surfaces showed that removing the pits removed all the surface corrosion from the surface.

5.1.2 Coating removal

The objective of this task was to develop a process for removing the polyurethane coating from the torsion bar without compromising the compressive residual stresses imparted to the surface of the torsion bar from shot peening. Previous examination of the torsion bars have shown that the

polyurethane coating adherence is variable along the length of a torsion bar and between torsion bars. Thus, one section of a torsion bar could have excellent coating adherence while moving along the length of the bar three inches the coating adherence could be poor. In addition, the coating thickness, as allowed by the drawing can vary widely over the length and diameter of the torsion bar. Finally, because the torsion bars are twisted during processing they are not perfectly round and experience round-out of up to 0.005 of an inch randomly along the length of the bar.

Typically, thick coatings are removed from the surface of round specimens by placing the specimen on a lathe and then removing the coating using single point turning. However, because of the large amount of run-out on these bars this method was not successful for removing the entire coating from the surface. Figure 172 shows a machined torsion bar in which the surface was damaged by the single point turning and there was a significant amount of coating still on the bar on the opposite side of the bar.

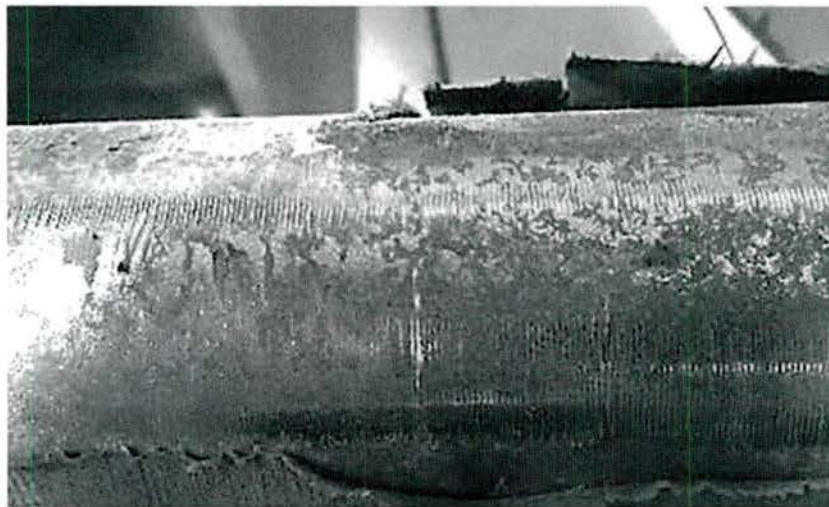


Figure 172 - Surface of Torsion Bar after Single Point Turning for coating Removal

During the cleaning of the bars for evaluation of corrosion at the beginning of the program, it was determined that wire brushing the torsion bar coating would adequately remove the coating. This process may require multiple passes across the part with each pass approaching the base 300M material. None of the other processes examined during the corrosion removal study were aggressive enough to remove the polyurethane coating.

A series of unsuccessful methods were evaluated for coating removal including the Scotch-brite flapper disk, nylon mesh sanding belts, and a 3M silicon carbide deburring disc. The Scotch-brite flapper disk was unsuccessful because it could not remove the coating. The nylon mesh sanding belt was able to remove the polyurethane coating but was not compliant and therefore, because of the run-out of the torsion bar, damaged the surface. Finally the 3M silicon carbide deburring disc was very aggressive in removing the polyurethane. However, it also damaged the surface of the torsion bar because it was not compliant.

Another method evaluated for coating removal was laser cleaning. This method was selected because it is a non-contact method that is being used to remove coatings on aircraft. Two torsion bar sections were sent out to have the coating removed by laser cleaning. After laser coating removal the effect of laser coating removal was determined by examining the surfaces using optical microscopy techniques to determine if the laser cleaning had any effect on the physical appearance or surface roughness of the torsion bar surface. Next, cross-sectional polished specimens were cut from one of the torsion bars to determine if the laser cleaning had any effect on the microstructure of the 300M. Any changes in microstructure caused by the laser cleaning could have a detrimental effect on the physical properties of the 300M. Finally, one laser cleaned surface was examined with a scanning electron microscope to determine the effectiveness of the laser cleaning on removing the coating, primer and corrosion from the surface of the torsion bar.

Optical photomicrographs of the surface both prior to and after machining and laser cleaning are shown in Figures 26 and 27, and 29 and 30. The 2D Surface roughness results are contained in Tables 1 and 2 and Figures 28 and 31.

For both torsion bar specimens the majority of the polyurethane coating was removed by machining (less than ¼ inch of coating remained on the surface after machining). Then the laser was used to remove the remaining coating and any corrosion on the surface. Removing the entire polyurethane coating with the laser would be a very time consuming and as a result expensive process. Therefore, to reduce processing costs it was decided to remove the majority of the coating by machining prior to laser cleaning. In addition, because the laser does not contact the torsion bar surface the variation in coating thickness or bar being out of round would not affect the coating removal or cause damage to the surface.

Table 12 - Surface Roughness Parameters for L-1 Prior to and After Laser Cleaning

	Coating Stripped	Laser Cleaned
Ra (2D)	0.378 uM	0.32 uM
Rq (2D)	0.611 uM	0.496 uM
Sa (3D)	18.4 uM	26.34 uM
Sq (3D)	17.66 uM	24.82 uM

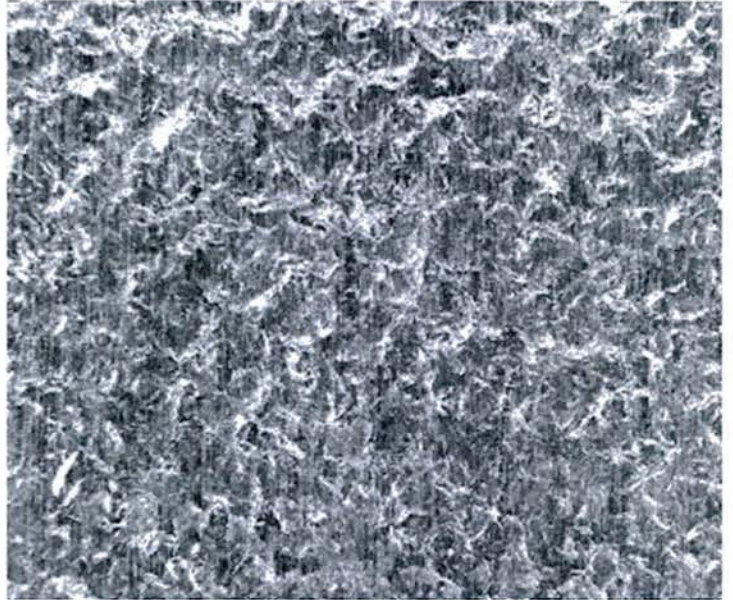


Figure 173 - First Non-Laser Cleaned Surface- Coating Removed Prior

Figure 173 and Figure 175 are optical photomicrographs of one torsion bar prior to and after laser coating and corrosion removal. Figure 176 and Figure 177 are optical photomicrographs of the second torsion bar prior to and after laser coating and corrosion removal. The removal of the coating on the surface prior to laser removal was obtained by wire brushing the surface.

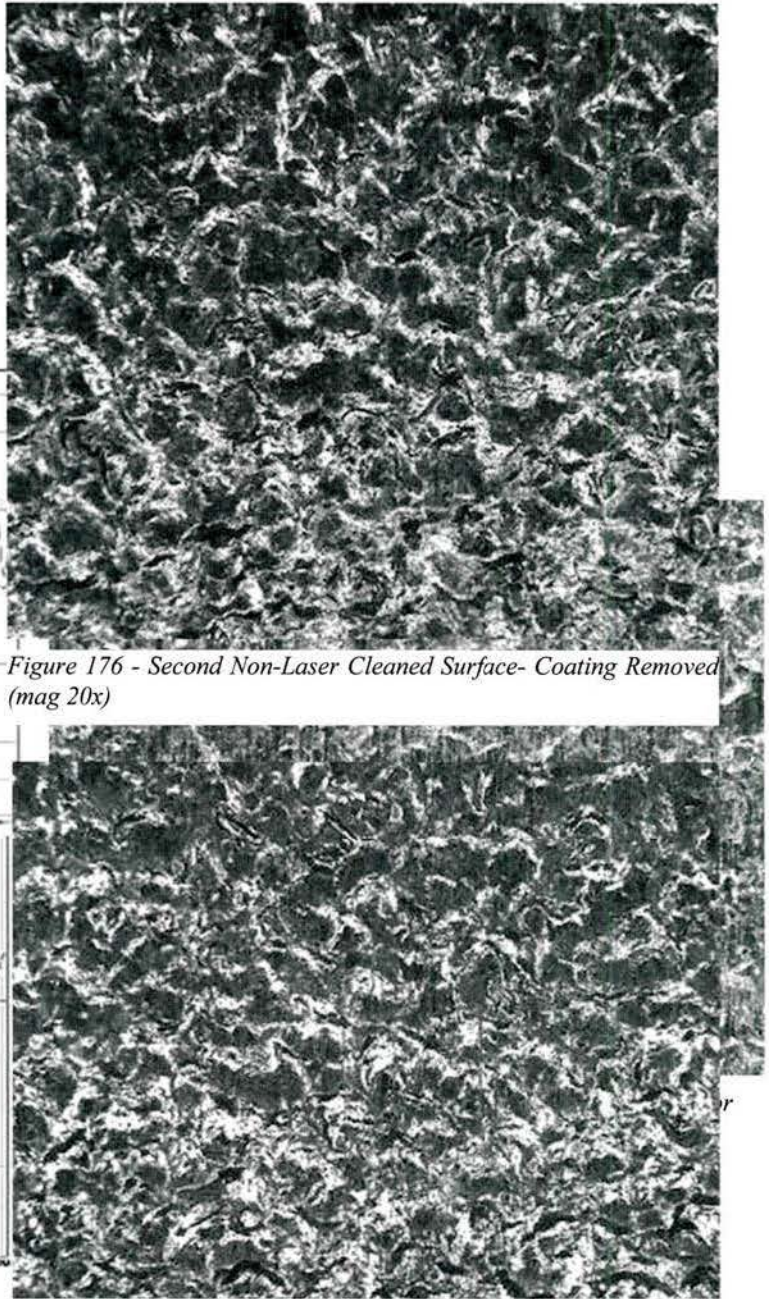
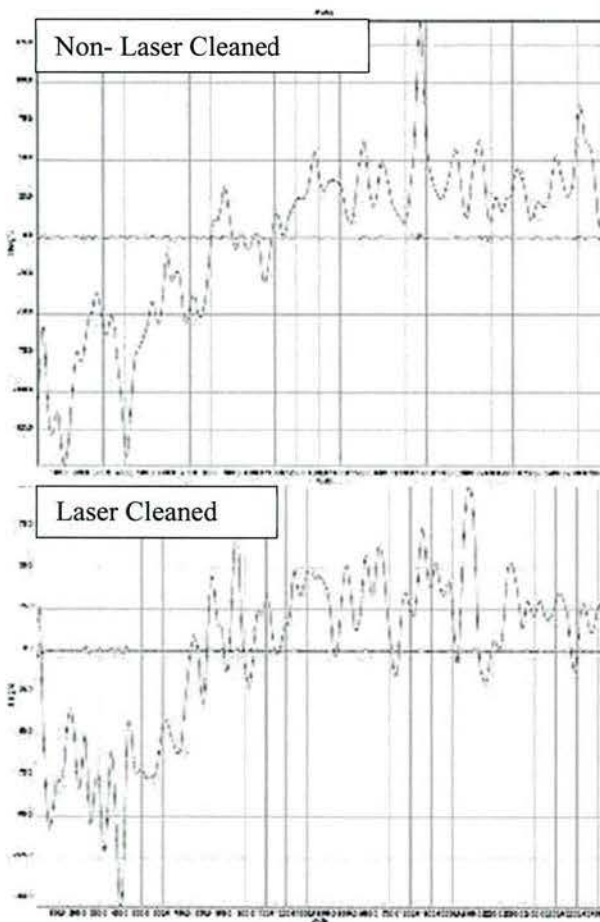


Figure 176 - Second Non-Laser Cleaned Surface- Coating Removed (mag 20x)

Figure 177 - Second Laser Cleaned Surface- Coating Removed (mag 20x)

Figure 174 - 2D Surface Roughness Traces (Mag 20X)

traces of the surfaces prior to and after laser cleaning. Comparing Figure 173 to Figure 175 and Figure 176 to Figure 177 (surfaces both prior to and after laser treatment), it can be seen that the laser cleaned surface had a similar physical appearance as the shot peened or non-laser cleaned surface. This was confirmed by the 3D surface roughness analysis which showed similar S_a and S_q values for each surface. (S_a is the mean height of the surface profile or peaks and valleys while S_q is the root mean square (RMS) of the roughness).

Table 13 - Table 13 - Surface Roughness Parameters for L-3 Prior to and After Laser Cleaning

	Coating Stripped	Laser Cleaned
Ra (2D)	1.314 uM	0.7912 uM
Rq (2D)	3.55 uM	1.331 uM
Sa (3D)	46.43 uM	43.88 uM

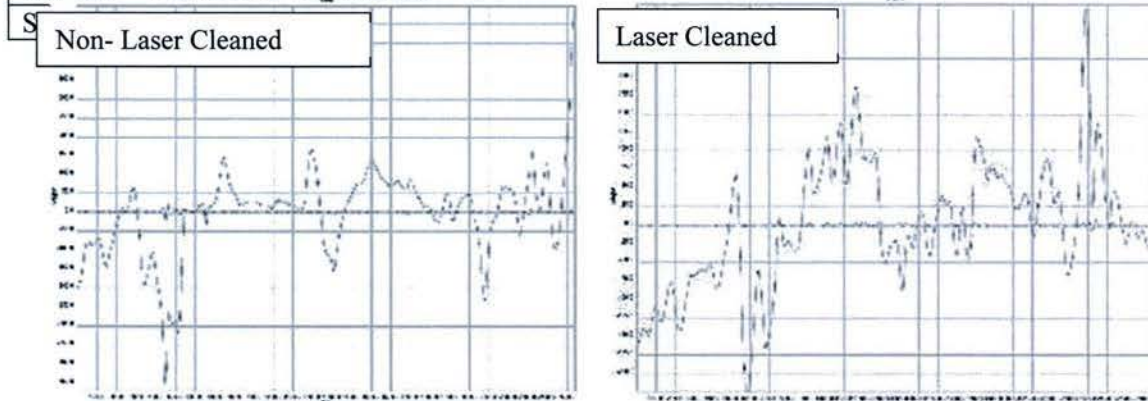


Figure 178 - 2D Surface Roughness Traces (Mag 20X)

Figure 179 and Figure 180 are cross-sectional optical photomicrographs showing the grain structure of the non-laser cleaned (Figure 180) and laser cleaned (Figure 179) 300M torsion bar. Both cross-sections were cut from the second torsion bar. The optical photomicrographs show that a similar martensitic grain structure was observed close to the surface for both the cleaned and non-cleaned specimens. Thus, the laser cleaning had no effect on the 300M grain structure close to the surface of the torsion bar. If the surface had been overheated during laser cleaning martensite would not be present on the surface.



Figure 180 - Cross-Sectional Optical Photomicrograph of Torsion Bar L-3 – Coating Removal Only- 2% Nital Etch (Mag 200x)

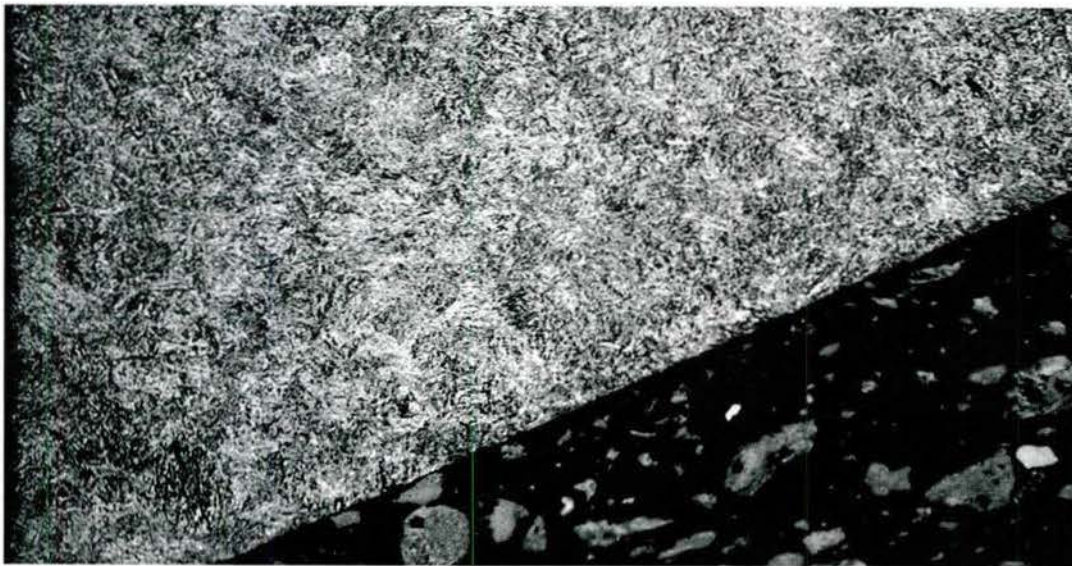


Figure 179 - Cross-Sectional Optical Photomicrograph of Torsion Bar L-3 – Coating Removal Plus Laser Cleaning- 2% Nital Etch (Mag 200x)

Figure 181 is a SEM photomicrograph of the surface of a torsion bar with the coating removed by mechanical means. The SEM photomicrograph and non-dispersive X-ray analyses performed showed that

there was both iron oxide (corrosion) and primer remaining on the surface after cleaning. The oxide is the discolored darker grey regions in Figure 181, while the black specks on the surface are primer

Figure 182 and Figure 183 are SEM photomicrographs of the torsion bar surface after laser cleaning. The SEM analysis showed that after the laser treatment there was small amount corrosion still remaining on the torsion bar surface (Figure 183).

Figure 182 shows that the laser treatment also did not remove all the coating from the surface of the torsion bar. The circles in Figure 182 are around some of the coating remaining on the surface after the laser treatment. The non-dispersive X-ray analyses in these locations confirmed that the particles within the circles are coating that had not been completely removed.



Figure 181 - SEM Photomicrograph of Non-Laser Cleaned Surface (Mag 268x)



Figure 183 - SEM Photomicrograph of Laser Cleaned Surface (Mag 234x)



Figure 182 - SEM Photomicrograph of Laser Cleaned Surface (Mag 76x)

5.1.2.1 Conclusion

It was shown that the laser could remove the entire polyurethane coating from the surface of the torsion bar but it would be a time consuming, expensive process. An alternative process is to single point turn off the majority of the polyurethane coating and then use the laser to remove the last 1/8th thickness of the polyurethane. This dual approach has the advantage of quickly removing the coating without damaging the surface of the torsion bar. The analysis showed that the laser cleaning did not change the surface roughness or grain structure of the 300M alloy. However, the analysis did show that the laser cleaning did not remove all the coating, primer and corrosion from the surface and additional laser process development is required to completely cleaning the surface.

A crimped wire wheel was used for coating removal. The wheel was mounted to a benchtop grinder attached to the lathe. Although it was a slow and dusty process it did eventually remove the entire polyurethane coating. In addition, because it was compliant to the surface and did not damage the surface the run-out of the torsion bar did not affect its performance. In efforts to speed up the process, a knotted wire wheel was used. This wheel was more aggressive than the crimped wire wheel and for that reason removed the polyurethane coating faster. Again, it was compliant to the surface of the torsion bar and did not damage the surface.

5.1.2.2 Recommendations

Both the laser and wire wheel were able to remove the polyurethane coating from the torsion bar. However, even using the knotted wire wheel both processes were relatively slow. For this reason it is recommended that the coating removal process consist of the following:

1. Remove the majority of the polyurethane coating using single point turning. The cutter should not make contact with the surface of the torsion bar.
2. Use the laser or knotted wire wheel to remove the remainder of the coating and any corrosion beneath the coating.

It is also recommended that further development be performed on the laser removal process to optimize the process in the hopes that it will be able to remove all the coating, primer and corrosion from the surface.

5.2 Coating Selection

The AAV torsion bars are currently supplied with a polyurethane coating. The purpose of the polyurethane coating is to protect the torsion bar from small chip and dents and prevent corrosion of the metallic surface. The small chip and dents and pitting corrosion on the torsion bar metallic surface will significantly degrade the mechanical properties of the torsion bar and could potentially cause torsion bar failure. Currently, the OEM air sprays the polyurethane coating onto the torsion bars after applying a primer to improve the adherence of the polyurethane. After coating application the coating is then dried and cured to obtain the desired coating adherence and physical properties. The OEM could also lightly grit blast the surface prior to coating to further improve the coating adherence.

The majority of the coating damage observed on the scrapped torsion bars inspected in this study was observed on either one end or both ends of the torsion bar. Typically, the coating disbonding was observed close to the splines on either end of the torsion bar. Once disbonded along an edge the disbond progressed towards the center of the torsion bar. Figure 184 shows the physical appearance of the majority of the coating disbands observed during the initial depot visit.

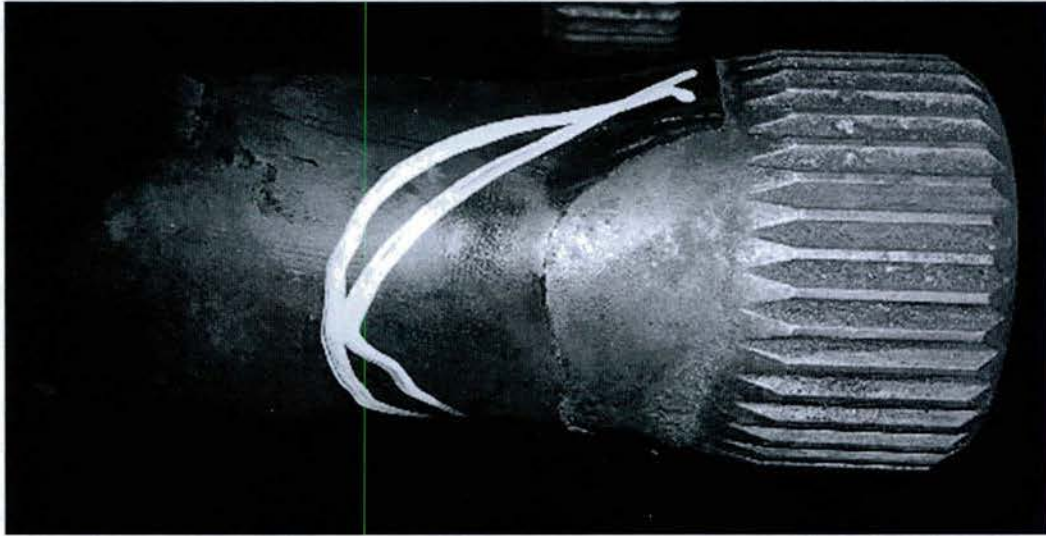


Figure 184 - Typical Coating Disbond on a "Scrapped" Torsion Bar

Additional coating defects noted were nicks and gouges in the coating near the center of the torsion bar and areas where the polyurethane coating was overheated during operation and the coating was "burned," creating a circular defect in the coating (Figure 185)

When developing a repair procedure for the AAV torsion bar it was concluded that the entire polyurethane needs to be removed because:

- The coating defects observed on the torsion bars removed from the AAV have been located in various locations along the length of the bar. While most of the coating defects occur at either end of the torsion bar, or in some cases at both ends, there are other locations where coating defects were observed along the length of the torsion bar.
- The coating adherence of the polyurethane coating was variable from torsion bar to torsion bar and along the length of a single torsion bar. In addition, there was no NDI technique identified that coating detect coating disbonds on the torsion bar

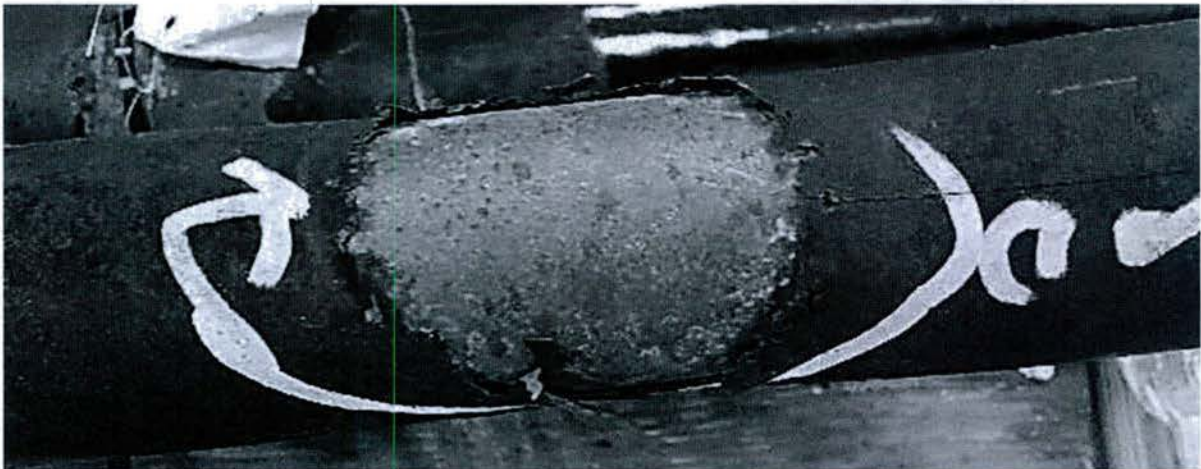


Figure 185 - Circular Defect on Torsion Bar from "Burning" Coating

5.2.1 Coating Application Method Selection

There are various methods that can be used for applying a coating to the AAV torsion bar. In order to determine the best method a research study was conducted. The evaluation criteria for coating application selection included: equipment and coating coats, the ability to coat entire torsion bar geometry and transfer efficiency. Transfer efficiency is a measure of the percentage of coating material that actually coats the product versus that wasted in the form of overspray. High transfer efficiency will not only reduce coating costs by allowing more of the coating to be applied to the part, it also provides a safer work place.⁶¹

The five application methods for applying a protective coating to the torsion bar investigated were brushing (painting), dipping, spraying (air and airless), flame spray and electrostatic. These methods were selected because they are the most commonly used methods for applying organic coating to metallic surfaces.

Brushing is a method where a wet coating to be applied and smoothed onto the metallic surface using brushes. Dip coating, in its simplest form, involves immersing products to be coated in a tank of coating material, draining off the excess in a solvent-saturated atmosphere and then drying or curing. It is a fast and efficient method that provides coverage in recessed areas. In general there are two types of spraying techniques – air and airless. Air-atomized spraying relies on the coating to be applied pumped under pressure to conventional spray guns, so that it mixes with a stream of compressed air either internally or externally. The compressed air breaks up the liquid stream or atomizes it, causing it to break up into droplets that form a spray. Airless spraying forces coating under pressure through a small orifice in the gun, atomizing it in the same manner as a nozzle attached to a garden hose atomizes water. Upon emerging from the orifice, the tremendous internal pressure causes the paint stream to blow apart into atomized droplets. Both dipping and air-atomized and airless spray processes spray a liquid which needs to be dried after application.

Flame spray melts a powder by injecting it into a flame.. After melting, the liquid is forced to the surface to be coated by air pressure. Once on the surface, the powder flows to form a continuous layer. During cool down the coating hardens. Finally, electrostatic spraying equipment charges coating droplets as they pass or contact an electrode. It relies upon the attraction of opposite electrical charges. Charged paint particles are attracted electrostatically to the surfaces of the products to be finished, which are usually at ground potential.

⁶¹ <http://www.pfonline.com/articles/todays-paint-application-methods>

contains the various corrosion control coating application methods considered for the remanufacturing of the AAV torsion bar as well as the advantages and disadvantages for each application method.

Brushing on coatings has the lowest capital cost of all the coating application equipment. However, it also has the highest labor costs and will require a drying oven. Dip coating is the most cost effective coating process, can be automated, and has no overspray. However, the large size of the AAV torsion bar makes this process unsuitable for this application.

Application Method	Advantages	Disadvantages
Brushing	Low capital cost No power requirement No overspray Easy Clean-up	High labor costs Difficult to control coating thickness Drying and curing required after coating
Dipping	Most cost effective coating process May be automated or manual High production capacities No overspray Able to coat inner and outer diameters	High capital costs Geometry and size of torsion bars no ideal for this application method - Uses large volumes of coating Coating tends to build up at bottom of article Drying and curing required – generation of VOC possible
Air and Airless Spray	Fast Application method Control of Film thickness Allows for use of fast drying coatings	Need an experienced operator Requires a special spray booth to limit overspray and protect operator Requires primer or surface treatment for improved adherence Drying and curing required –generation of VOC possible Equipment requires extensive cleaning after use Coating can build up on cap or in orifice during coating
Flame Spray	Fast Application method High transfer efficiency Able to control of Film thickness No drying or curing required No surface pretreatment required for adherence No or only small amount of overspray No spray booth required Quick clean-up	Limited amount of coating compositions available Article must be preheated to 150 to 200F Small open flame if use propane
Electrostatic	Dries Quickly High transfer efficiency Durable coatings	Very high start-up costs High VOC content –required spray booth to control build-up of toxic fumes Requires curing after application

Air and Airless Spray⁶² is a fast application method and allows for good coating thickness control. Table 14 –Coating Application Method Advantages and Disadvantages

On the other hand, spray coating requires a pretreatment of the surface to improve adherence, curing after coating, and a significant amount of cleaning and process control to prevent coating build-up on the gun cap. The depot in order to adapt this process will need to purchase a drying and curing oven. Finally, spray coatings can have high VOCs. Electrostatic coatings have high transfer efficiency and dry quickly, but require high capital costs for the electrostatic coating equipment. These coatings also require a curing oven and typically contain a high VOC content.

Flame spray coatings have high transfer efficiency and do not require:

1. Surface pretreatment for adherence,
2. Drying or curing after application,
3. A spray booth to control coating overspray or VOCs, and
4. Extensive clean-up.

The disadvantages of flame spraying is there is only limited amount of coating compositions available for spraying, the article needs to be preheated, sometimes up to 350F prior to coating application, and there is a small open flame on the spray gun if using propane. There are electric flame spray guns but the high capital costs for this spray gun makes it unsuitable for this application.

Using Table 14 as a guide it was decided to apply the repair coating to the AAV torsion bars using a flame spray process. This process is able to apply a corrosion control coating that will bond to the metallic without any surface preparation or primer. In addition, it does not require any post drying or curing. However, to optimize the bond strength of the applied coating preheating the torsion bar is required. Additional advantages of this process is it has one of the lowest capital costs because no drying oven is required and since it is not a liquid the clean-up is the easiest.

5.2.2 Coating Composition Selection

There are two main classifications for powder coatings: thermoplastic and thermoset. A thermoplastic powder coating melts and flows when heat is applied, but continues to have the same chemical composition once it cools into a solid coating. Thermosetting powder coatings also melt when exposed to heat. However, after they flow to form a continuous film, they chemically crosslink on additional heating. The final coating has a different chemical structure than the applied powder.

Comparing the application parameters for the thermoplastic and thermoset coatings^{63 64}, the thermoset coatings are typically applied by air spray, wet the surface better, have a longer self-life and are lower cost

⁶² http://www.altexboatpaint.com/ayb_application_methods

⁶³ Bauer, Stephen H.,EQUIPMENT MANUFACTURER LOOKS AT THERMOSETS VERSUS HIGH-PERFORMANCE THERMOPLASTICS, *Plastics Engineering*, v 33, n 12, p 28-30, Dec 1977

⁶⁴ Day, Forest B. Mills, Calvin C. APPLICATION OF THERMOPLASTICS FOR CORROSION CONTROL, *NACE*, p 1-12, 198

coatings than thermoplastic coatings. On the other hand the thermoplastic coatings when applied using flame spray do not require any pretreatment or post curing. In addition no VOCs are produced from the thermoplastic coatings when applied or during curing.

Comparing the physical properties of the thermoplastic and thermoset coatings the thermoplastic coatings have higher hardness, are less brittle (will flex with the torsion bar), demonstrate improved adherence, corrosion resistance, especially salt spray resistance, and the impact resistance than the thermoset coatings. For these reasons a thermoplastic coating was selected for the corrosion coating for the torsion bar.

Next, the thermoplastic coating composition needs to be selected. The initial selection was made by

Table 15 - Comparison between Thermoplastic and Thermoset coatings

						Thermoplastic	Thermoset
Application Parameters							
Safety Equipment required						xx	0
Mixing of Components at Gun						xx	0
Coating Shelf-life						x	xx
Wets Surface						x	xx
Drying time required						xx	0
Chemical Curing required						xx	0
Surface Pretreatment required for Adherence						x	0
Uniformly Applied						x	x
Depot Experience						xx	0
Cost						0	xx
VOC						xx	0
Coating Physical Properties							
Hardness						xx	xx
Brittleness						x	0
Adherence						xx	x
Corrosion Resistance						xx	x
Impact/Toughness						xx	0
Total X						25	11
Total 0						1	8
Ratings							
xx	Very good						
X	Good						
0	Poor						

comparing the properties of thermoplastic coatings listed on the each manufacture website or printed material and then compared to the properties to the coating specification for the torsion bar coating listed below:

- Hardness Shore Hardness between 70 type A to 60 type D
- Tensile strength 1 Ksi minimum
- Tear Resistance 125 lbf/in
- Pull-Off Adhesion 1000Psi
- Uniform Physical Appearance
- Heat Resistant to 220F

- Resistant to CARC paint thinner
- Compatible with diesel fuel, 10-40 motor oil, and a 50/50 blend of antifreeze and water

After comparing the properties of the available thermoplastic coatings to those in the torsion bar coating specification, the following coating compositions were selected for further evaluation – Abcite, PPA571 polyoefin, G-55, PP10 polypropylene, and G-17 polyethylene. Table 16 shows that except for the melt temperature for the Abcite coating all the coatings meet the torsion bar coating specification. The Abcite was kept in this study because it is currently being used in the Albany and Barstow Depots for remanufacturing Light Armor Vehicle drive shafts.

Table 16 - Thermoplastic Coatings Property Comparison

Table 3 Physical Properties of Thermoplastic Candidate Coatings	Abcite	Polyoefins PPA 571	Polypropylene G-55, PP10	Polyethylene G-17
Impact Resistance	Excellent	Excellent	Excellent	Excellent
Melt Point (F)	203	310	225	221
Hardness (Shore D)	50	63	53	55
Elongation at Break	580%	500%	900%	498%
Tensile Strength	16 MPa	18 MPa	14 MPa	24 MPa
Salt Spray Resistance	Excellent	No data	Excellent	Excellent
UV Resistance	Excellent	Good	Excellent	Excellent

After selecting the five (5) coating compositions the physical and mechanical properties of the “as sprayed” coatings were determined in order to verify that they meet the required coating specification. This was accomplished by spraying each coating composition on a 4 inch by 4 inch plate sprayed with mold release so the coating would not stick to the plate after spraying. After spraying the coating was removed from the plate and five (5) ASTM sub-size tensile specimens were machined from the coating. Then tensile strength and percent elongation were for each coating using an Instron 8801 tensile test machine. On addition the Shore D hardness was measured on the tensile bars.

Table 17 lists the coating parameters used for spraying the coating on the plates for the tensile specimens. Each of the coatings was sprayed to a thickness greater than ¼ inch so that the sub-size specimen could be machined to the ¼ inch thickness.

Table 17 - Coating parameters for Tensile Specimens

Coating Parameter	Abcite	PPA-571	G-55	PP10	G-17
Oxygen Psi	35	45	38	45	38
Propane Psi	25	25	30	25	30
Gun Air	45	45	45	45	45
Powder Air	10	10	10	10	10
Stand-off Distance	6.25 inches	4.5 inches	4 inch	4.5 inches	5 inches

The results of the testing on with these parameters are contained in Figure 186 - Ultimate Tensile Strength (MPa)-Figure 188. The tensile specification on Drawing 7010600 Rev A specifies a tensile strength of 1000 Psi or 6.9 Mpa. All the coating tensile strengths were significantly greater than the 6.9 MPa specification. However, comparing these coatings to the polyurethane coating none of their tensile strengths matched that of the polyurethane.

Comparing the tensile strength of the five candidate coatings the PPA polyolefin had the highest tensile at 41.3 Mpa, while the PP-10 polypropylene and the G-17 polyethylene had the lowest tensile strength at 19.3 Mpa. Again, it should be noted that these tensile strengths are still 3 times greater than the specification.

The torsion bar coating specification requires that the coating have a 60 percent elongation prior to break. Figure 187 shows three of the five candidate coatings meet the elongation specification. Both polypropylene coatings had elongations of 18-19 percent which is below the 60 percent elongation

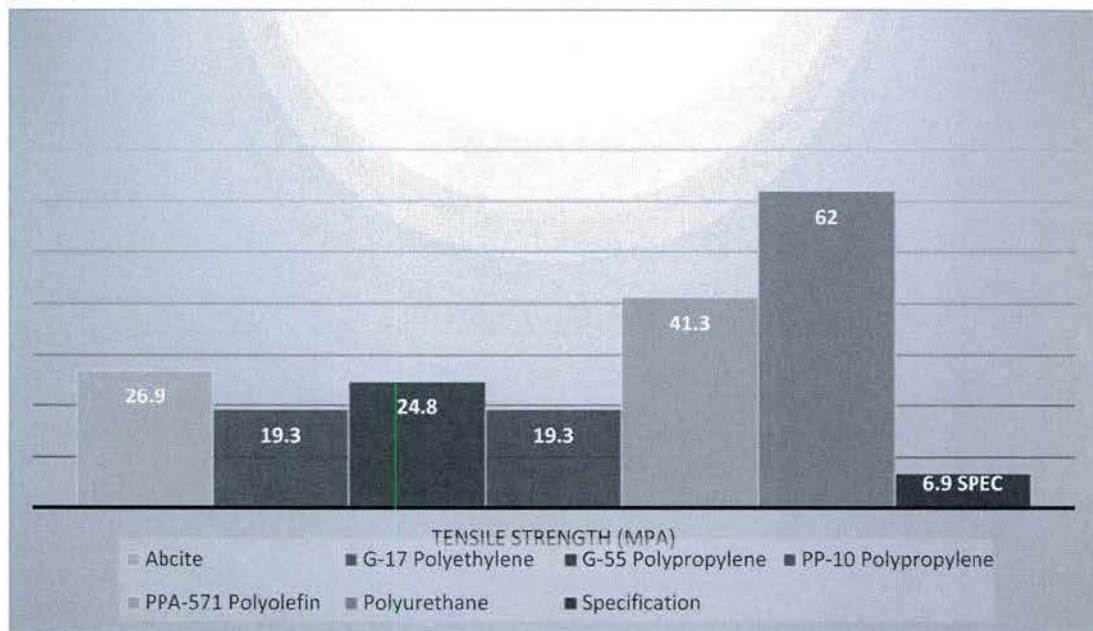


Figure 186 - Ultimate Tensile Strength (MPa)

requirement. The three remaining candidate coatings had elongations 2 to 3 times the specification. Again the highest percent elongation was recorded by the polyurethane coating.

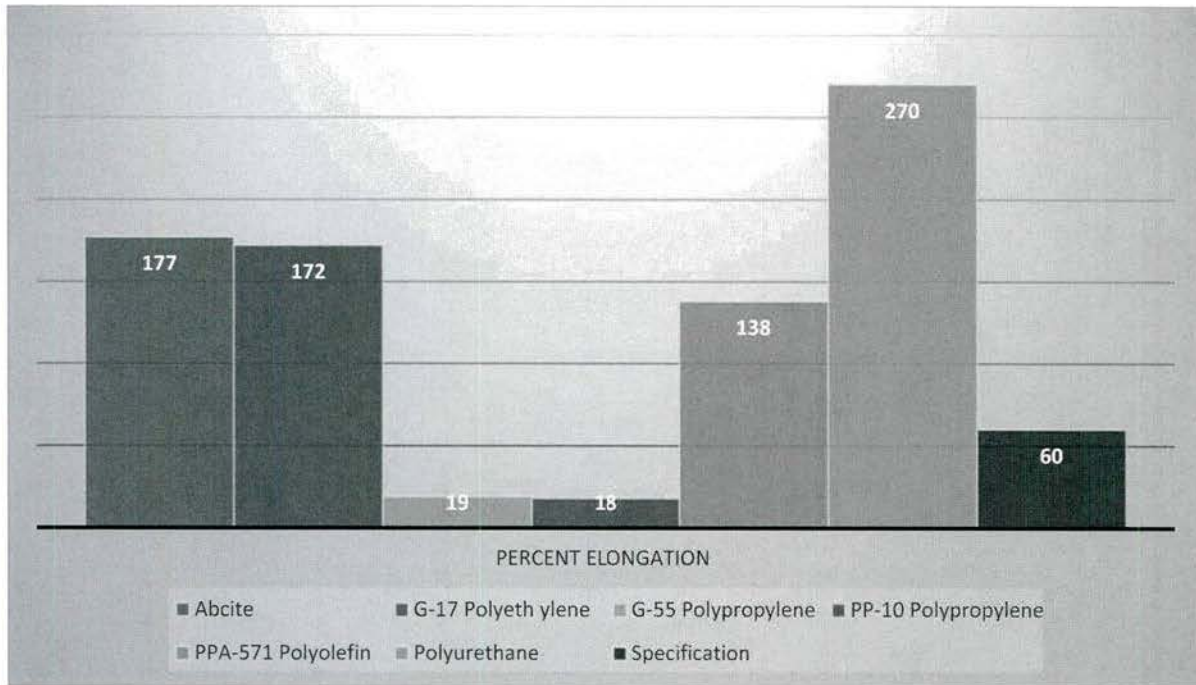


Figure 187 - Percent Elongation

The hardness specification for a torsion bar coating is a Shore Hardness of 70 type A to 60 Type D, or 22-60 Shore D. Figure 188 shows that all the candidate coatings except for the PP-10 meet the hardness specification. The PP-10 was 7 points above the maximum hardness specification.

Using the results of the tensile testing as a guide the three candidate coatings that will be take forward for the environmental resistance and salt spray corrosion testing are the Abcite, G-17 Polyethylene and the PPA-571 Polyolefin.

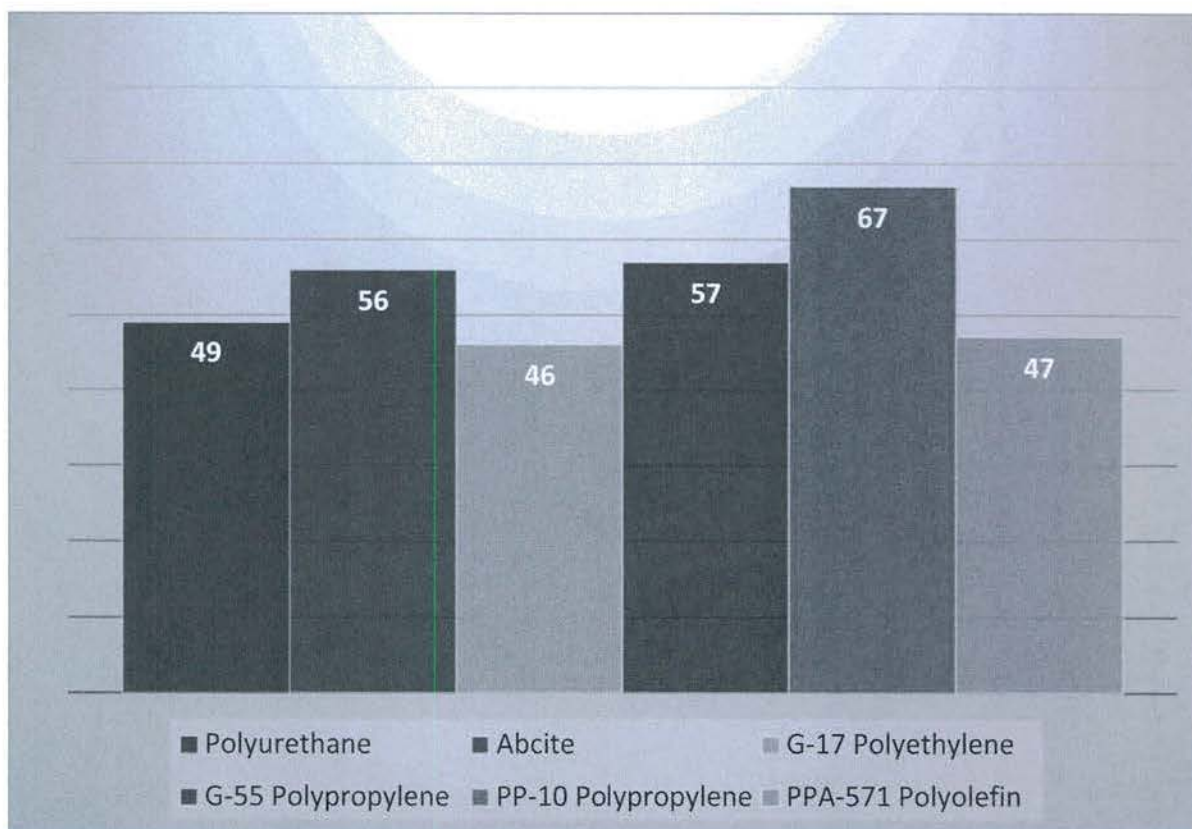


Figure 188 - Shore D Hardness of Candidate Flame Spray Coatings

After using the mechanical properties of the coating to downselect to the three selected coatings, they were subjected to environmental testing. The environmental testing consisted of immersing 5 by 5 inch panels coated with the Abcite, G-17 polyethylene and PPA 571 polyolefin for 72 hours in the following: diesel fuel, motor oil and coolant (50/50 mix with water). All this testing will be at room temperature (72F +/- 10F). In addition the plates also was subjected to an elevated temperature of 220 +/- 10F for 72 hours. The evaluation criteria for the coatings is meeting the Shore D hardness specification.

Another environmental test is the corrosion protection test. In this test a coating sample scored in the center 3-4 inches with a knife is subjected to a salt fog test (ASTM B117) for 336 hours. The evaluation criteria for this test is no more than 0.125 inch of corrosion beneath the coating around the scratch.

Finally pull-off adhesion testing was performed on the 5 by 5 inch flat panels coated with each candidate coating. The evaluation criteria is coating adherence greater than 1000PSI.

Table 18 lists the Shore D hardness values as coated and after immersion in oil, coolant (50/50 blend) and diesel fuel. The Abcite coating had the highest Shore D hardness after coating. The hardness was not effected by soaking in either motor oil of a 50/50 blend of antifreeze and water. The hardness of the Abcite dis decrease after soaking in the diesel fuel, but it was still above the minimum Shore D hardness value. Both the G-17 and PPA 571 increased in hardness slightly after soaking in motor oil and a 50/50 blend of antifreeze and water. Both these coatings had similar hardness prior to and after soaking in diesel.

Table 18 - Shore D Hardness Testing After Exposure

Coating	As Coated	Oil	Coolant (50/50)	Diesel
Abcite	56	53.5	54.2	47.6
G-17	46	50.1	52.2	45.3
PPA 571	47	53.7	54.0	49.5

After soaking 72 hours at 225F the Abcite Shore D hardness decreased approximately 10 points from 56 to 45.8. Again although the Abcite hardness decreased it was still we within the Shore D hardness specification. The hardness of the G-17 and PPA 571 did not change significantly after the 72 hour soak at 225F.

The coating adherence of the Abcite, G-17 and PPA 571 was measured after the environmental tests and soaking 72 hours at 225F. All the Abcite panels had glue failures which ranged from 1493 to 1995 PSI, all well above the 1000 PSI minimum for coating adherence. The G-17 had one coating failure below the critical limit, measuring 875 PSI, after soaking in a 50/50 blend of anti-freeze and water. All the remaining failures were glue failures ranging from 1155 to 1288 PSI. The PPA 571 also had one coating failure, 1005 PSI, after soaking in diesel fuel. The remaining tests were glue failures ranging from 1128 to 1512 PSI.

The both the G-17 and PPA 571 coatings peeled from the surface of the 300M plate after 336 hours of salt-fog testing. Corrosion was present under the both coatings. The Abcite coating did not disband during the salt-fog testing. In addition, there was not corrosion or coating peel-back around the scratch.

In summary all three of the coatings met the adherence and Shore D hardness specifications after coating. However, the Abcite hardness decreased approximately 10% after soaking in diesel and after the 72 hour soak at 225F. Nevertheless the Abcite's Shore D hardness was still significantly greater than the specification minimum. The G-17 and PPA 571 hardness values were not affected by any of the environmental testing.

Both the G-17 and PPA 571 coatings failed the scratch test. After 336 hours of testing both coatings completely disbanded from the 300M plate. The Abcite coating passed this test because there was no coating peel back after the 336 hours of testing. **Thus, the Abcite was the only coating to meet all the coating specifications.**

5.3 Recoating Process Development

Prior to beginning coating of the torsion bars, fixturing was developed to center the torsion bars on the lathe without allowing the flame spray gun to get too close to the spindle or the tailstock quill. To fixture the bar

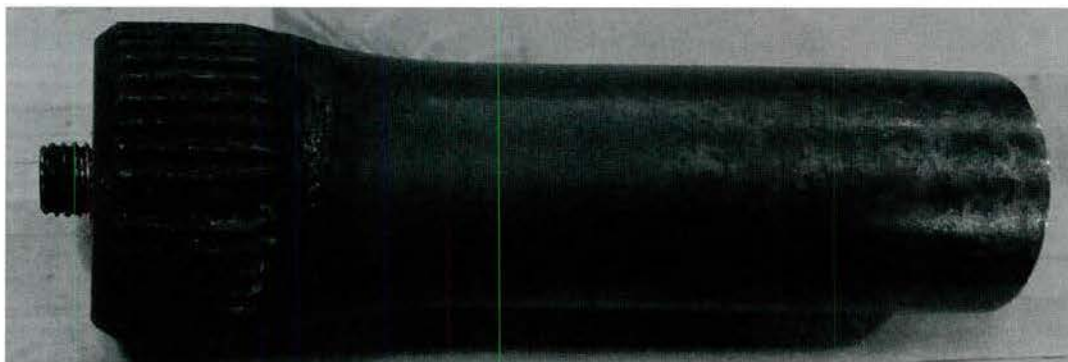


Figure 189 - Chucking Adapter

end into the spindle, a chucking adapter was made utilizing an existing end of torsion bar cut to

around 1' to 1.5' (Figure 189). A set screw is threaded into the end of the bar, allowing the full torsion bar to be screwed onto the adapter (Figure 190). This end of the torsion bar will be inserted into the chuck on the lathe.

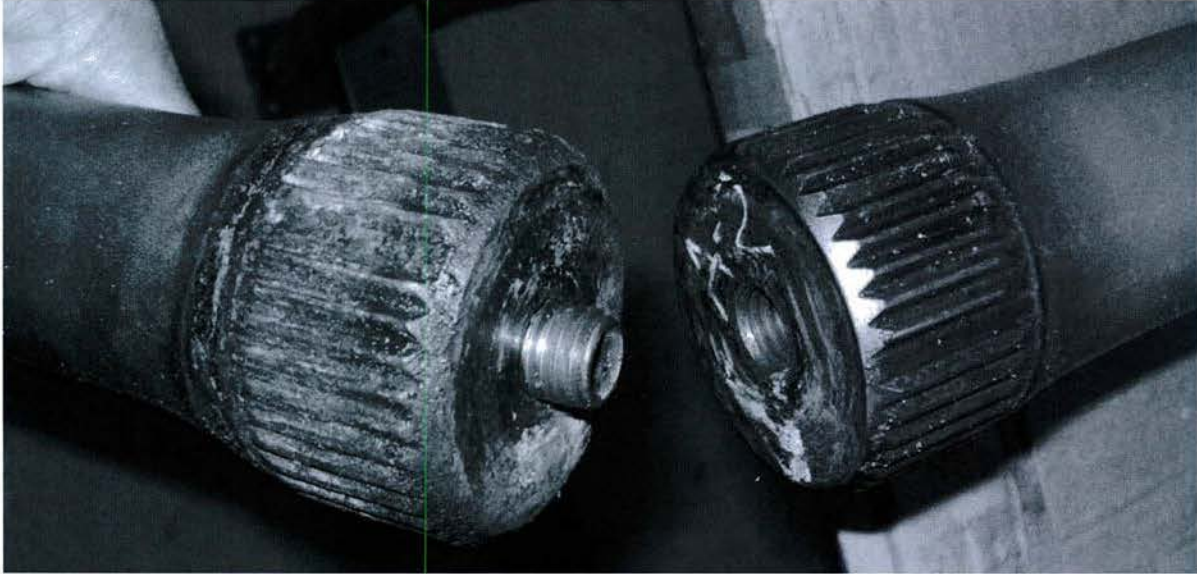


Figure 190 - Attachment of the chucking adapter

For the other end of the torsion bar, a Hex Head Cap Screw was utilized with sufficient length to stand the bar off from the tailstock quill. The center of the hex head cap screw was drilled to allow for engagement of the quill.

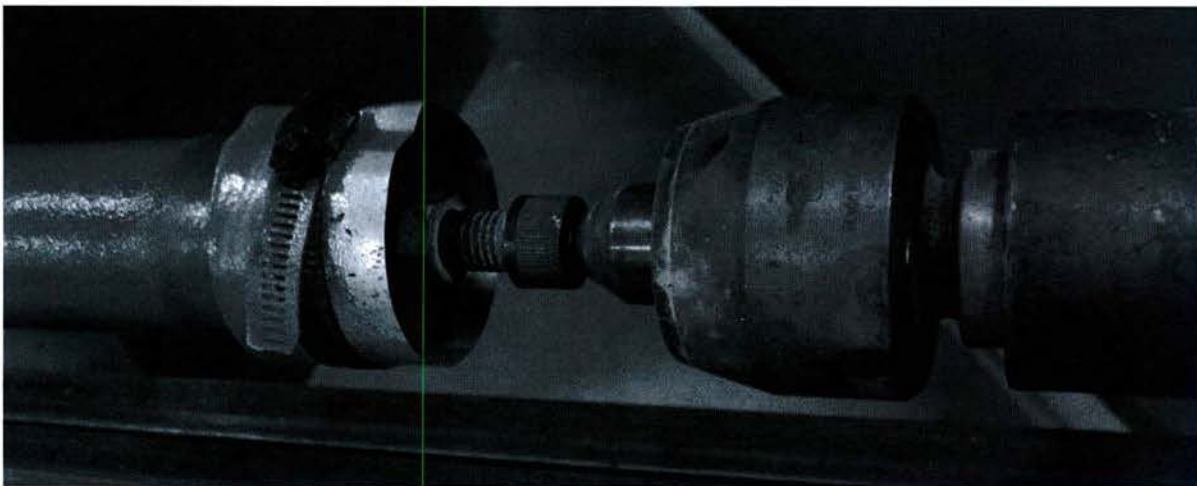


Figure 191 - Torsion bar to Tailstock adapter

Fixturing was also required to prevent the abscite from being deposited on the splines of the torsion bar. However, the distance from the splines to the coating can be no more than 0.188". A shadow mask was created close to the bar that will cover the splines. The mask consists of a thin sheet of metal wrapped around the splines and held in place by a worm drive hose clamp (Figure 192). The flame spray gun is then mounted onto the tool post with a custom designed fixture that allows the gun height and the distance to the torsion bar to be adjusted (Figure 193).

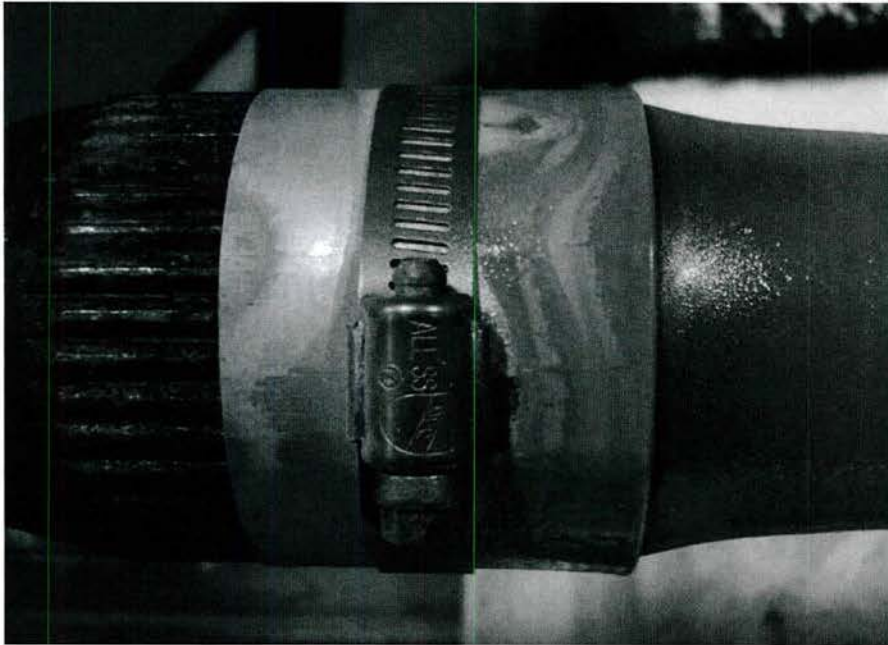


Figure 192 - Masked Spline Area

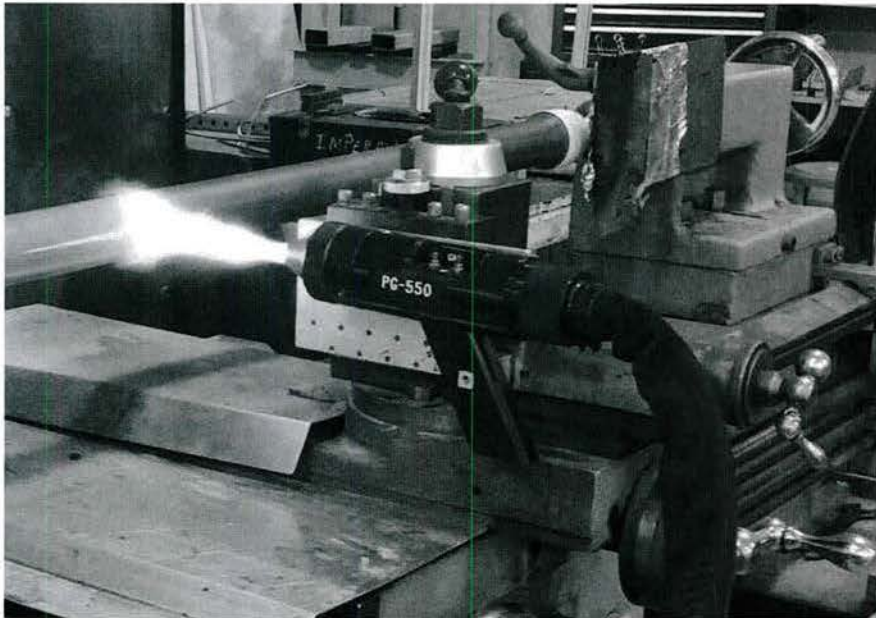


Figure 193 - Custom Flame Spray Gun Mount

Table 19 - Starting Torsion Bar Coating Parameters

Coating Parameter	Abcite
Oxygen Psi	35
Propane Psi	25

For the application of abcite onto a full-size torsion bar, the settings of the previous experiemtns are used as a starting point (Table 19). The goal when applying abcite is to produce an even , melted coating which is

Gun Air	45
Powder Air	10
Stand-off Distance	6.25 inches

usually indicated by a nice sheen of the coating

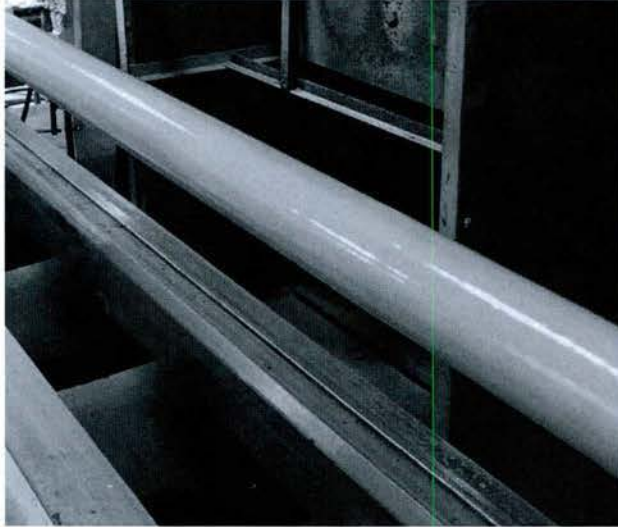


Figure 194 - A Nice Coating Sheen

Several trials were performed on torsion bars with varying degrees of success. One of the more important factors when applying a flame spray coating is the preheat temperature of the component. In our case, we heated the torsion bar with a rosebud until the center of the bar measures no less than 230°F and the ends reach a minimum of 250°F. Additionally, the optimal parameters for coating application on the torsion bar were identified as shown in Table 20 - Optimal Coating parameters for the torsion bar

Table 20 - Optimal Coating parameters for the torsion bar

Parameter	Setting
Oxygen regulator pressure	90 PSI
Propane regulator pressure	45 PSI
Shop/Compressed air pressure	90 PSI
Oxygen flow	35 CFM
Propane flow	25 CFM
Gun air pressure	45 PSI
Powder air pressure	18 PSI
Lathe RPM	219
Lathe traverse speed (IPM)	28
Nozzle distance to center surface of torsion bar	3.75"

The distinct process steps for coating are as follows:

- The torsion bar should be wiped down with alcohol to remove any contamination.
- The torsion bar should be spun at 219 RPM in the lathe.
- The torsion bar should be preheated so that the center of the bar measures no less than 230°F and the ends reach a minimum of 250°F (performed at RIT with an open flame, induction process should be implemented at the depot).
- The flame spray gun should be lit and started behind the shadow mask at one end of the torsion bar.
- The powder feed should be engaged, wait for a steady powder stream with consistent flame, and then engage the lathe traverse at 28 IPM. Approximately 0.18 inches was applied per pass.

- Once the spray is completely onto the shadow mask at the other end, the traverse shall be stopped and then restarted in the opposite direction.
- The coating was applied over 5 single passes. (In testing this applied to an average thickness of 0.96 inches))
- Once complete, the gun will be turned off and the bar will be left spinning while air cooling until the surface temperature checked with a laser reaches 110°F.
- Transfer the bar to the cooling racks without coming into contact with the coated surface.

5.4 Recapitalization Cost Model

A remanufacturing process is only beneficial if it meets two major criteria:

- 1) The remanufacturing process should meet or exceed all OEM manufacturing requirements.
- 2) The process must be cost effective

In the marine crops, a general rule of thumb is that if the component's remanufacturing process costs more than 60% of the new component cost, it is not cost effective. At the time of this study, replacement torsion bars range in price from \$1200 to \$1800. Therefore the target cost for the remanufacturing process is less than \$720 (utilizing the 60% * the lower price limit of \$1200).

Assumptions

In order to make an economic model for remanufacturing torsion bars, certain assumptions had to be made:

- 1) The labor cost at the depot is approximately \$65 per hour
- 2) The fixed capital costs of the lathe, spray equipment, grinder, shot peen booth and equipment, and belt sander are amortized over the number of units to be remanufactured.
- 3) Only bars passing the inspection criteria (pit size, etc.) will be recapitalized with a fallout rate of 13 based on estimates from the data collection at the depots.
- 4) Bars will only need to go through the recapitalization process once before retirement of the AAV.
- 5) Based on historical data, it is assumed that only 7 of the 12 bars on the vehicle will fail the IROAN inspection.
- 6) There are approximately 650 AAVs in service
- 7) Both Albany and Barstow will be performing the remanufacturing process

Based on these assumptions, approximately 3959 bars will need to be remanufactured in the next 7 years (650 vehicles x 7 bars per vehicle x 87% passing minimum inspection criteria).

Expected Capital Costs

Equipment	Estimated cost
PG-550 Thermal Spray Machine	\$12,950
120" Lathe	\$33,000
Shot Peen Booth & equipment	\$30,000
Belt Sander	\$2,000
Industrial grade tool post mount grinder	\$4,500
Total	\$82,450
Total for 2 depots	\$164,900

Amortizing the \$164,900 in capital costs over the number of bars to be remanufactured results in a cost of \$41.65 per bar.

Process Times and Costs

Process labor times were collected where applicable and estimated otherwise. The expected labor time for each bar is provide in Table 21. At the \$65/hr rate, the labor cost applied to remanufacturing a torsion bar is \$157.08.

Table 21 - Torsion Bar Processing Times

Process	Labor (minutes)
Loading	4
Cleaning	30
Inspection	10
Pit Removal	10
Shot Peen	30
Preheat	15
Coating	15
Cool Down	5
Unloading	2
Safety Factor (20%)	24
Totals	145

Cost Roll-up

The consumable material costs are what remains for the overall cost roll-up. Those cost estimates along with the amortized capital costs and labor costs are rolled up in Table 22. At \$328.86 per bar, the remanufacturing process fell far below the target cost of \$720.

Table 22 - Overall Cost to Remanufacture a Torsion Bar

Item	Cost Per Bar
Amortized Capital Costs	\$41.65
Cleaning Tools	\$1.34
Shot Peen Materials	\$4.00
Propane	\$2.43
Oxygen	\$0.11
Coating Material	\$122.25
Labor	\$157.08
Total	\$328.86

6 Conclusions

The torsion bar on the AAV is a relatively high cost item that fails IROAN inspection due to delamination of the polyurethane corrosion control coating. The bar is a highly stressed steel component that requires a corrosion control coating due to the potential for saltwater contamination during swim mode. Currently, the bars are scrapped when they are removed from the vehicle and no process exists for remanufacturing the component to OEM standards.

RIT worked through the various steps of the remanufacturing process on the torsion bar. RIT first evaluated the extent of the corrosion damage on the torsion bars. The corrosion damage information was combined with operating conditions to develop a Finite Element Analysis model that was used to understand how much damage could be repaired before a bar would need to be scrapped. The current recommendation is that pits of less than 0.010" may be removed through sanding but the repair needs to be blended into the area around the repair to prevent a build-up of stress in the component. Care must be taken to understand how much material is taken from each bar so that ride height is not affected by corrections to the torsion bar.

RIT evaluated multiple methods for corrosion and coating removal, with two processes showing potential. Laser ablation showed promise but would require additional development effort to ensure that all of the corrosion is also removed. A knotted wire brush was effective at cleaning off both the coating and the corrosion. RIT made effective use of a bench grinder mounted to the traverse of the lathe to clean off the bars. Once the bars are cleaned, the bar is visually inspected using a 10x eye loop to identify pits. The pitting is removed with a belt sander and bended into the rest of the bar.

RIT then evaluated various flame spray plastic and polymer coatings for their potential to prevent corrosion. The coatings were tested against the OEM standards and only the Abcite coating passed all of the tests.

Once confirmed as a suitable replacement coating, RIT adapted the spray process from the samples to a spray process for torsion bars. This process was evaluated and provided inputs to the cost model. It was determined that the remanufacturing process using Abcite coating was effective at meeting all OEM standards and could provide a significant savings (\$871.14) over the OEM torsion bar costs.

Additional research effort would be needed to implement the process at the both the Bartsow and Albany depots. In particular, the process would need to be optimized on site to achieve the best results.

Research Program 2:
Asset Life-cycle Management:
Data Needs and Data Gaps Assessment

This research was conducted under Office of Naval Research Grant N00014-14-1-0789.

Report Generated by:

Golisano Institute for Sustainability
Rochester Institute of Technology
190 Lomb Memorial Drive
Rochester, NY 14623
(585) 475-5101

Abstract

This report describes data analysis of vehicle maintenance data with the objective to determine whether current practices of periodic vehicle overhauls were effective and whether maintenance practices differ across the fleet with respect to their spatial and temporal dimensions. The challenges of inferring plausible values for missing, inconsistent, and conflicting maintenance records were addressed using probabilistic modeling. Several problems with data elements and pragmatic methods for pre-processing and interpretation of noisy data are covered in detail. The analysis results were integrated into a reliability model.

Chapter 1

Data Analysis of Vehicle Overhaul Effectiveness

1.1 Background

Equipment health and condition monitoring enables maintenance to minimize the effects of equipment degradation or failure. Building on existing concepts for predictive maintenance, *Reliability Centered Maintenance* (RCM) [1, 2] provides a formalism for *Condition-Based Maintenance* (CBM). Because it is based upon objective evidence of equipment degradation or impending failure, CBM has significant economic and safety benefits; it reduces incidence of unscheduled failures and downtime, and the occurrence of unnecessary or early scheduled maintenance.

Health or condition monitoring is the process of collecting asset data and extracting the information for CBM. Affordable sensors, data storage, and networking enable comprehensive monitoring of all types of assets. In order to make this data actionable for CBM, specific models are necessary to identify and characterize anomalies to relate the anomalous patterns to forward looking failure risk for decision making purposes (prognostics [3]). The models are typically classified as expert-system, physics-based, data-driven, or hybrid [4].

Health monitoring is generally an incremental process, as data is typically not available to develop comprehensive diagnostic and prognostic algorithms from the outset. Instead, the levels of *Prognostic Health Management* (PHM) capability grow over time [5, 6].

Consolidation of vehicle fleet data in a data warehouse provides an opportunity to develop CBM knowledge and algorithms incrementally. The scope of the present project was to determine the effectiveness of some of the current practices. Specifically, to determine the effectiveness of periodic overhauls and to propose a path towards condition-based overhauls based on the current existing data. The data for this project came from a family of military tracked vehicles. The approach was pragmatic, based upon the available data, and available expert knowledge.

1.2 Introduction

1.2.1 Best case scenario

The objective of this study was to test if a vehicle overhaul was effective. Informally, that means that vehicles require considerably less maintenance after this service. Clearly, maintenance needs depend on the context, defined by operating and environmental conditions a vehicle is subjected to. Thus, a careful analysis of vehicle overhaul effectiveness for a given vehicle must consider the context of use; however, this data was not recorded. Nevertheless, consideration of vehicles collectively has the potential to reveal the impact of overhaul on the continuous vehicle maintenance.

Figure 1.1 shows factors that contribute to the state of health of a vehicle. Two main classes of influence are identified as the operational history and the maintenance history.

Operational history is determined by usage, operating conditions, and environmental conditions. The usage is typically measured in miles, engine hours, or both. Operating conditions include in-use/storage patterns, braking, sudden accelerations, engine and vehicle speed distributions, and other similar parameters. Environmental conditions include terrain, humidity, exposure to salt water, dust, etc. The dominant approach for capturing usage data is the inclusion of *health and usage monitoring system* (HUMS), defined as a system of sensors, processes, and algorithms for prognostics, on the vehicle platform [7]. HUMS applications have been deployed only on the most expensive vehicles, such as fixed-wing aircraft [8] and rotorcraft [9, 10]. Tracked vehicles considered in this study were not equipped with HUMS. Maintenance history includes current issues, past repairs, and cost of maintenance over time.

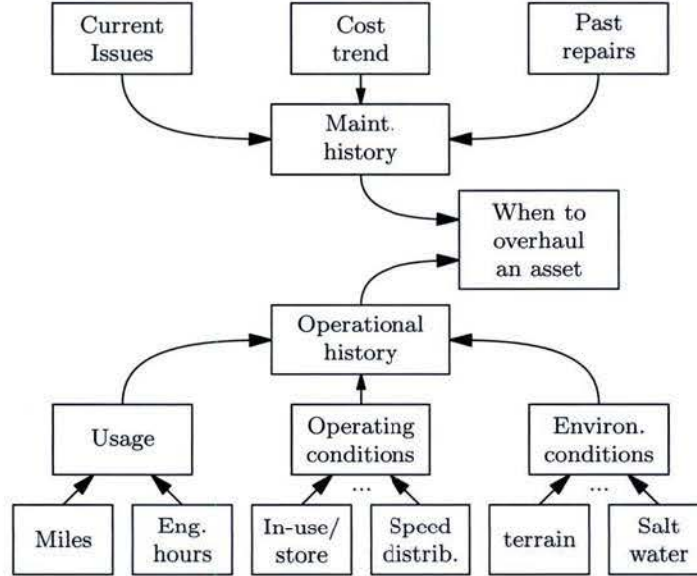


Figure 1.1: Data for making decisions on vehicle overhaul

1.2.2 Approach based on the available data

For the problem at hand, the maintenance history data is available, but the operation history is almost entirely lacking. While the knowledge of the operational history has the potential to greatly improve the decisions, the decisions must be made even when important data is absent.

A way to demonstrate effectiveness of previous vehicle overhaul using maintenance data alone is to look at the cost of maintenance over time. Figure 1.2 shows a hypothesized maintenance cost C_m as a function

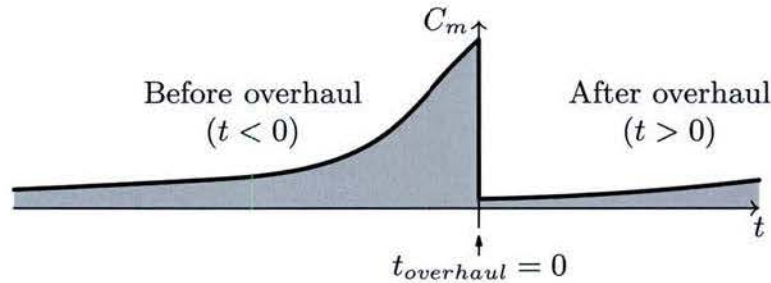


Figure 1.2: Sketch of expected maintenance cost before and after an overhaul assuming that the overhaul is effective

of time t , where cost of maintenance is computed as the sum of the cost of parts C_{parts} and the cost of labor C_{labor} , computed as the product of hourly labor rate HLR and labor hours LH

$$C_m = C_{parts} + \underbrace{HLR \times LH}_{C_{labor}} \quad (1.1)$$

The tacit assumption in this figure is that the usage and the general operating and environmental conditions do not change appreciably over the time considered. In practice, this assumption must be verified, as shown in Section 1.3. Within the existing database, parts cost was generally available. However, the number of parts replaced were sometimes misleading and the recorded labor hours were often missing. Section 1.4 describes estimating labor hours, and Section 1.6 identifies the issues with fields such as parts cost, quantity required and labor hours.

1.3 Usage estimation

Of all operational data, only usage data existed. However, usage data had many missing, inconsistent, and contradictory values. An illustration of this situation is shown in Figure 1.3, which plots cumulative usage over time. Cumulative usage $\sum_i u_i$ should be monotonically non-decreasing, except from a rare event of reset (e.g. after an engine replacement). However, the recorded usage data was non-monotonic, with only the trend appearing to adhere to the expected behavior.

The units of recorded usage were unclear at first. Due to the noisy nature of the data, they may have represented hours driven, or miles traveled. Further investigation of ordinance vehicle monthly and daily log-books strongly suggested the units of usage were hours. Of the 32 vehicle log-books provided for the project, several held records that precisely matched that of the database for the vehicle. The recorded units for those records were hours.

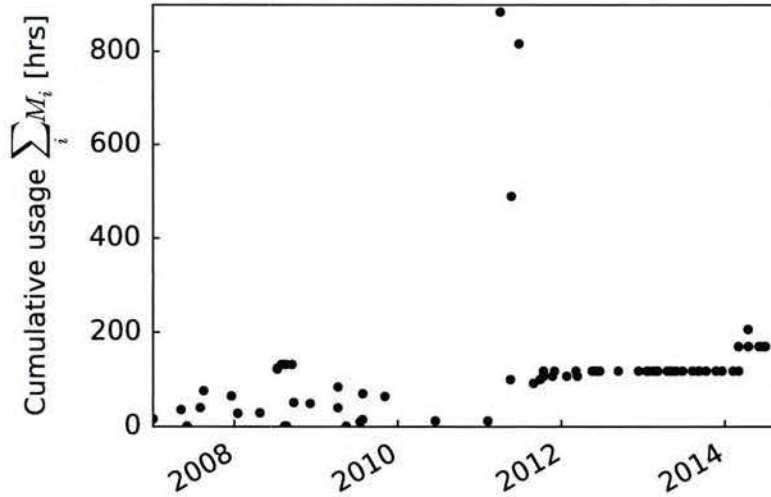


Figure 1.3: Usage data example: the values are not monotonically non-decreasing as expected

Two methods for estimating actual usage were considered: 1) development of a probabilistic model to reconcile the missing and inconsistent values, and 2) estimation of usage based on replacement of consumable parts. The two approaches are described in turn.

1.3.1 Probabilistic model for usage

This simple model is implemented in PyMC [11, 12], a probabilistic modelling library in Python. There are many alternatives including BUGS [13], JAGS [14], Church [15], Infer.NET [16], and Stan [17]. The PyMC library was selected because of its seamless integration with the open-source scientific Python ecosystem, which also includes NumPy [18, 19], SciPy [20], Matplotlib [21], with statistical Pandas [22], and machine learning tools such as Scikit-learn [23], and Theano [24]¹.

Markov chain Monte Carlo (MCMC) is a sampling method that draws likelihood measurements from simulated random data conditioned by some predefined observed data. It utilizes a high dimensional search space where certain positions (representing a set of parameter values for the variables being estimated) have a greater likelihood than others. In order to search the parameter space MCMC generates correlated random numbers from the current values by stepping to a new position of higher likelihood by use of the gradient field (or probability density). This requires an initial guess to start the chain and is part of the conditioning. Many test analyses were performed to condition the sampling parameters to the observed data. PyMC has sampling parameters such as number of iterations, burn-in, and thinning. The number of iterations represents how many times the program will step to a new position in parameter space. When computing with a large enough number of iterations one is guaranteed to eventually collect a set of numbers that look as if they are part of the original distribution of data. The burn-in parameter tells the program how many samples to remove from the beginning. This is useful for models that may take some sampling time to converge. Highly correlated variables (example $X + Y = 10$) spend more time in certain positions in the search space. Thinning reduces redundancy by removing every k^{th} sample, where k is the thinning parameter. In order to fine tune this process, intervals of observed data are tested using different sampling parameters and compared.

Figure 1.4 illustrates a simple probabilistic model. u_i and u_{i+1} are successive actual usages that are unknown, while M_i and M_{i+1} are the corresponding measurements, or observations. The observed variables are shaded, following the convention of [25]. The measurements were noisy versions of the usage, and noise was signified by n_i and n_{i+1} , and modeled as Uniform(0,50). This distribution was set as the standard deviation of the observed measurements, M_i , which was modeled as Normal(u_i, n_i). Noise that would distort an observation by more than 50 hours was not impossible, but less likely. Observed variables are held constant in probabilistic modeling. There is an unknown amount of usage between the two measurements. As the usage is assumed to be a non-negative function of time, we assume the following relationship between two subsequent samples

$$u_{i+1} = u_i + \beta_i \Delta t_i \quad (1.2)$$

where Δt_i is a known time interval between two samples, and β_i is an unknown usage factor which is known to be positive and limited. If time is measured in days, the usage factor cannot exceed 1. This usage factor was modeled as a uniform distribution, Uniform(0,1), because there was no consistent rule governing how long these vehicles were used and when. In practice the average usage factor over many days was typically a relatively small fraction of a day.

The model was constructed so that some actual usage values u_i , distorted by noise n_i , gave the observations M_i . If the actual values were known and some noise chosen, the values for M_i could have been generated. Instead of generating M_i values from its parameters u_i and n_i , the parameters are inferred from the observations. Inference is a reverse-generative process widely used in statistics and even more popular in the realm of probabilistic modeling. u_{i+1} was modeled as a deterministic variable equal to the sum of u_i and $\beta_i \Delta t_i$ as illustrated in Equation 1.2. In order for u_{i+1} to have been determined the i^{th} value had to be computed. This required an initial estimate for the first data point. The first data point was modeled as a normal distribution $u_1 \sim \text{Normal}(M_1, \frac{M_1}{2})$. Some extra measures were taken in order to prevent a bad first data point from offsetting the fit. Additionally, PyMC worked to maximize the likelihood of the entire fit and was not dependent on the initial estimate's accuracy as the number of samples increased. This is why an extreme outlier does not make the surrounding points' estimates less accurate, even given the limitations of the noise variable. PyMC assigns those values such a low probability that the average of the distribution remains near the rest of the data.

¹Stan also has an interface to Python

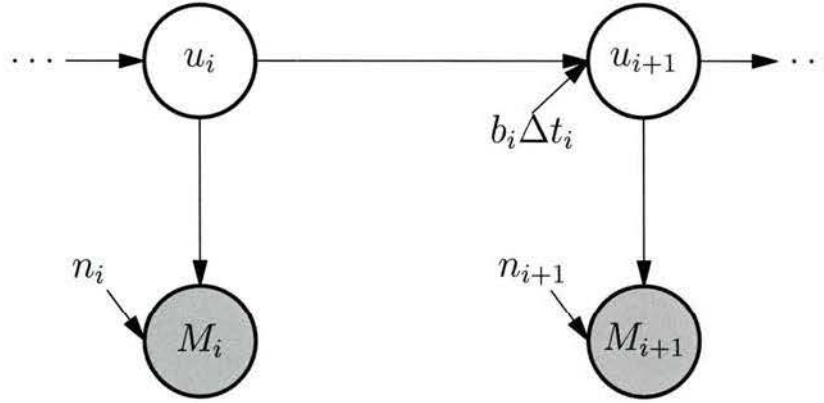


Figure 1.4: A simple probabilistic model

The results of an estimation using the simple model implemented in PyMC are shown in Figure 1.5

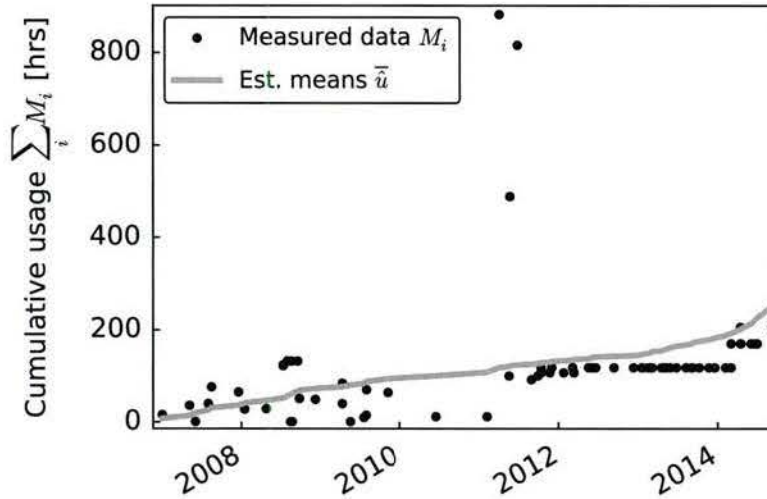


Figure 1.5: Usage estimation example

The orange line traces the means of the estimated distributions of usage u_i . After running the program, each observed data point had a probability density function (PDF) assigned to it, built by the model. Every value in the PDF represented one of the samples returned, according to the sampling parameters. Values that were returned most often represented the more likely values for that inference. The mean of these PDFs was chosen to represent the estimate because it denotes the average value of all the samples. The mode was considered but not used due to the possibility of a value that may not have accurately represented the best estimate to that point being the value that the stepping method hit more often. This was one example of how the thinning and burn-in sampling parameters were useful. Thinning reduced samples where the stepping method got stuck, so-to-speak, for a bit and burn-in removed early samples that may not have contributed to the final convergence.

These types of analyses improve on traditional probability measures by returning a full probability distribution for the data, known as the posterior, rather than a value with simple error bars. This allows for a much fuller understanding of the uncertainty of the results. In this case the PDFs for each observation were

those posteriors.

Probability was recognized as extended logic in the 1940s (see Cox [26, 27]) and greatly popularized by Jaynes [28] and others [29, 30, 31]. The problem with probabilistic models was their computational requirements. The MCMC method, that also originated in the 1940s [32], has become a standard tool for this computation. Probabilistic (graphical) models had notable successes in the sixties and seventies, but then fell out of favor to some other *artificial intelligence* (AI) approaches (e.g. fuzzy logic [33, 34], Dempster-Shafer evidence theory [35]). The renaissance of probabilistic modelling started in the late 1980s with theoretical development [36], but computational power did not allow the explosion of solutions witnessed in the very recent past. The graphical approaches will allow domain experts to take advantage of the framework. Many new applications including medical diagnostics, analysis of genetic and genomic data, speech recognition, natural language processing, analysis of market data, and fault diagnosis can be extended to reliability.

The potential of the probability networks has been recognized in the 1980s [37, 38]. More recently excellent tutorials (e.g. [39, 40]) and books (e.g. Jordan [41], Bishop [25], Barber [42], Koller and Friedman, [43], Gelman et al. [44], and Theodoridis [45]) have become available.

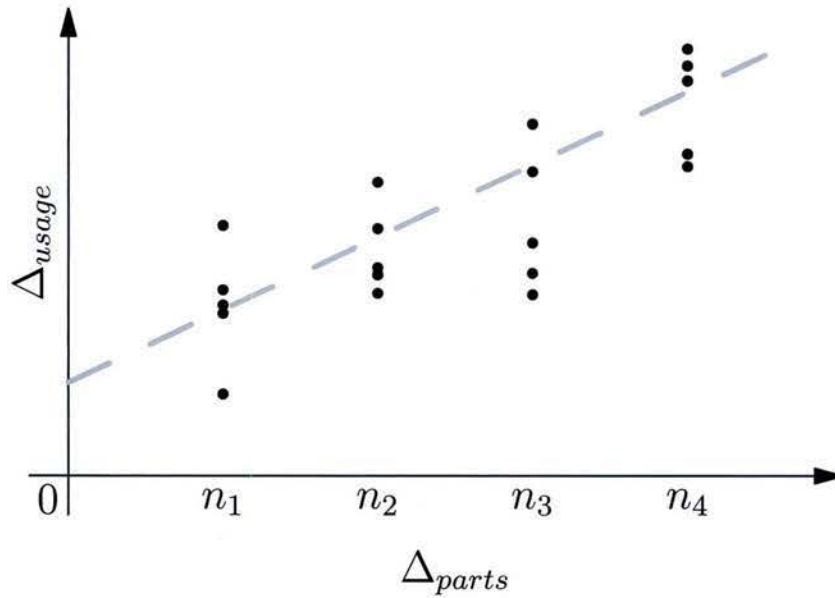


Figure 1.6: Hypothesized relationship for usage between maintenance events and number of replaced parts

1.3.2 Replacements of consumables

An alternative approach to determine usage was based on replacements of the consumable parts. Any ground vehicle has a set of parts that degrade as a function of usage: automobile tires, brakes, sprockets, etc. In military tracked vehicles, consumable parts include sprockets, road wheels, shock absorbers, track adjusters, support rollers, idler assemblies, etc. Replacement rates on a vehicle were expected to be proportional to usage rates, as illustrated in Figure 1.6.

Vehicle cost and maintenance histories were analyzed by sub-system (i.e a collection of components categorized by their collective purpose) and those with more weight in terms of usage, such as road wheels, were analyzed individually. Replacement frequency and failure rate differences among vehicles allowed testing for correlation of the consumable component's maintenance to the vehicle's usage.

Maintenance orders record the part replaced as well as the number of parts replaced. Figure 1.7 shows the cumulative replacement of road wheels over time and estimated cumulative usage. The inset plot on the top axis in Figure 1.7 shows the change in usage between maintenance over the change in number of

replacements. The correlation coefficient, ρ , was equal to -0.33 indicating these values did not support estimating usage based on replacements of consumables.

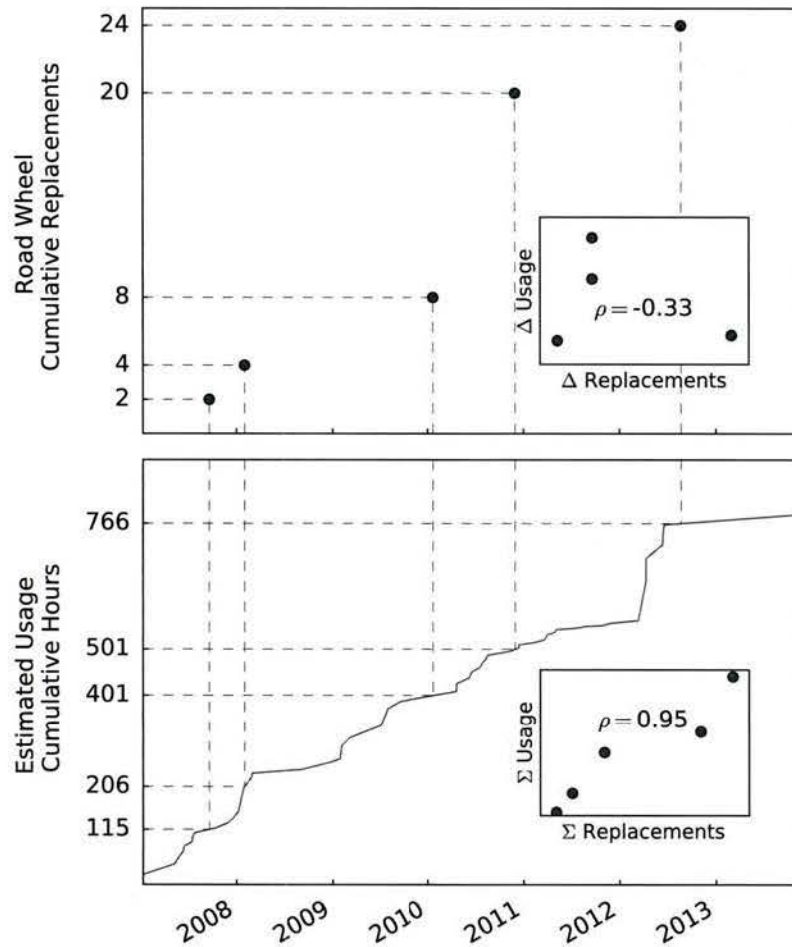


Figure 1.7: Cumulative replacement of road wheels over time and estimated cumulative usage. The two inset plots show the correlation between change in usage and change in replacements (top) and between cumulative usage by cumulative replacements (bottom)

Furthermore, the data for the number of replaced parts was inconsistent over the fleet. The majority of data for these vehicles contained very few maintenance records. The average usage between maintenance for the road wheel component example in the Figure 1.7 was approximately 230 hours. The average usage range for the part of the fleet that was analyzed (1,247 vehicles) was approximately 223 hours. Since the fleet average was less than the road wheel average it was expected that the majority of vehicles in the analysis contained data with no maintenance events during the usage period. This is illustrated in Figure 1.8.

Of the several consumable components, road wheels had the most replacement data. It was expected, however, that there be few replacements over the usage history of the vehicle. Because the usage was estimated with a probabilistic model that followed a piece-wise linear approximation between all usage events, the jagged edges of the usage estimation line in Figure 1.7 indicate where usage records existed. If there were replacements at each of those times the vehicle would have been under constant repair, indicating a larger underlying problem with the vehicle. This is why the change in usage to change in number of replacements did not correlate well. The inset plot on the bottom axis of Figure 1.7 shows cumulative usage over cumulative replacements. Here, the correlation coefficient was 0.95 indicating these values were highly

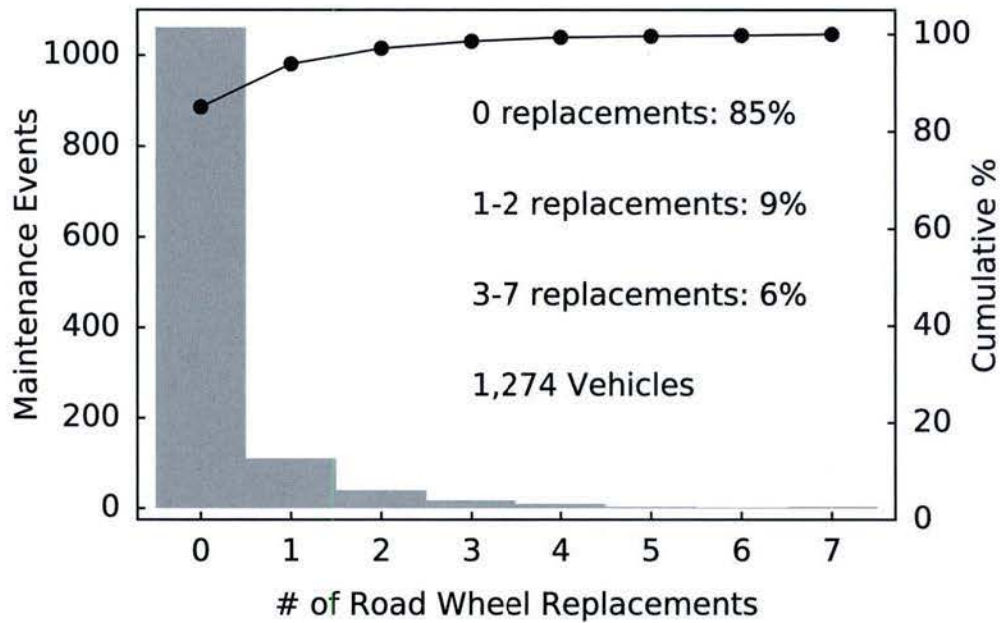


Figure 1.8: Number of maintenance events that contained a specific number of road wheel replacements. Only 15% of records for road wheels have one or more replacements associated with them

correlated. Overall, usage was indicated by the number of replacements when long term accumulation of data was observed. Figure 1.9 shows the computed coefficients for all vehicles that had usage records and replacements of road wheels. The sigma correlation also held for the following components: Shock Absorber, Track Pad, Track Adjuster, Sprocket. These are shown in Figures A.4, A.3, A.2 and A.1 in Appendix A but did not contain enough data to be including in the main analysis.

Replacements occurred during maintenance events but usage readings were based on logging from the vehicle operators and so replacements were expected to be entered with greater care. The vehicle shown in Figure 1.7 used the mean usage estimation from our probabilistic model in comparison to long term accumulation of replacements of the road wheel component. This was done for other vehicles as well. In Figure 1.7 matching usage and number of replacements in time is shown by dashed lines connecting the values between the axes. These pairs were used to generate the inset plots in that figure. Figure 1.10 shows cumulative (Σ) usage versus cumulative number of replacements for fourteen vehicles, including the first one that was shown by itself. The slopes of these lines varied considerably. In principle, one could use replacements of consumables to support usage estimation. There are several reasons for such variation in slope in this case. The usage estimation may not have been accurate due to bad data from the start for some vehicles. The replacement data may have been incorrect as well (this seems likely for the bottom-right line that goes out to 80 replacements after approximately 100 hours of use). The operating conditions of different vehicles may vary greatly depending on its location too. Referring back to Figure 1.1, unless the circumstances of usage are known, it is hard to relate to replacements. For example, if these vehicles operated under different location-based conditions, and this information is known, the user of the model could attribute the difference in slopes to the different conditions. If a set of vehicles were pre-classified by the relation between usage and replacements then replacement data for new vehicles, that are known to be part of a specific group, could aid in usage estimation. Using the slope for that class of vehicle would support likelihood estimates in the form of prior knowledge in the Bayesian usage estimator.

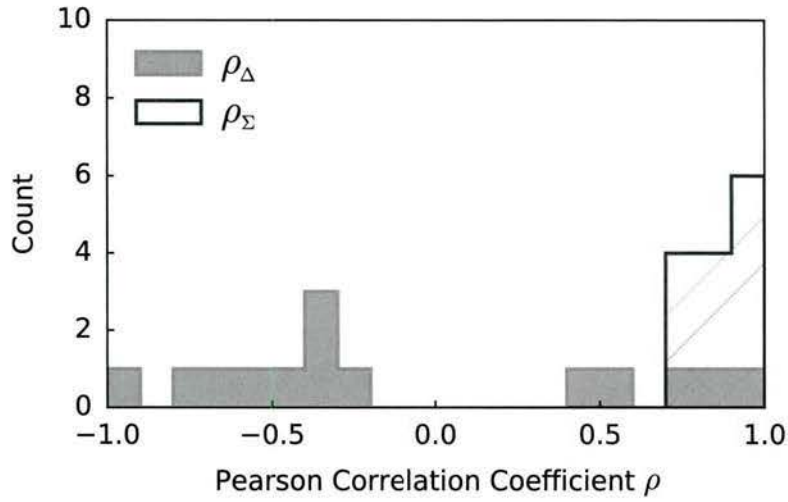


Figure 1.9: Computed coefficients for all vehicles that had usage records and replacements of road wheels. The average $\Delta\rho$ was -0.07 , and the average $\Sigma\rho$ was 0.87

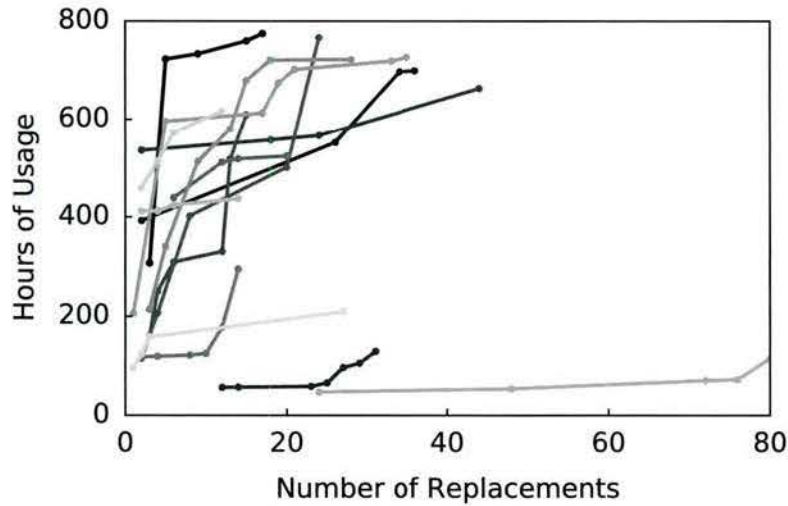


Figure 1.10: A comparison between hours of usage and number of road wheel replacements for fourteen vehicles

1.4 Labor estimation

Two approaches to estimate missing labor hours were considered. The first method was based on an assumption that the cost of labor was functionally related to the cost of parts. A scatter plot of labor hours and parts cost associated with many maintenance events was produced (see Figure 1.11) to test this assumption. The scatter plot suggested no functional dependencies, which was further verified by computing the Pearson correlation coefficient ρ (tests linear correlation) and *Randomized Dependence Coefficient* RDC [46] (tests more general, functional correlation). Both tests confirmed negligible interdependence suggested by the scatter plot, with values for ρ and RDC at 0.005 and 0.142, respectively.

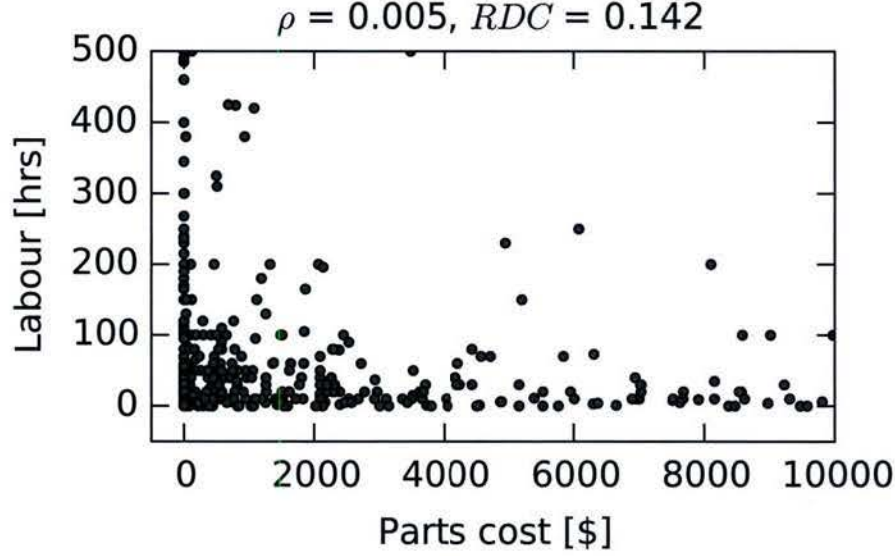


Figure 1.11: Labor hours vs. parts cost for different maintenance events. Log-log scale. The values for Pearson correlation coefficient and the randomized dependence coefficient are indicated

The second method inferred the labor associated with a particular part replacement based on multiple observation of maintenance events, where more than one part had been replaced. In the analysis n signified the number of maintenance events with observed labor hours and m the number of parts under consideration. The vector of observed labor hours associated with a maintenance event was denoted by $\mathbf{l}_{n \times 1}$ and the vector of labor hours contributed by parts was denoted by $\mathbf{p}_{m \times 1}$. The two vectors were related via a connectivity matrix $\mathbf{C}_{n \times m}$ as follows

$$\begin{array}{c} \text{connectivity matrix } \mathbf{C}_{n \times m} \quad \text{parts } \mathbf{p}_{m \times 1} \quad \text{labor } \mathbf{l}_{n \times 1} \\ \left[\begin{array}{cccc} c_{1,1} & c_{1,1} & \dots & c_{1,m} \\ c_{2,1} & c_{2,1} & \dots & c_{2,m} \\ \dots & \dots & \dots & \dots \\ c_{n,1} & c_{n,2} & \dots & c_{n,m} \end{array} \right] \left[\begin{array}{c} p_1 \\ p_2 \\ \dots \\ p_m \end{array} \right] = \left[\begin{array}{c} l_1 \\ l_2 \\ \dots \\ l_n \end{array} \right] \end{array} \quad (1.3)$$

The connectivity matrix indicated how many parts were replaced during a particular maintenance event. For example, if during an event i parts $p_1, p_{12}, 3 \times p_{25}$ were replaced, $c_{i,j} = 0$ for all j , except $j = 1, 12$, or 25 , where $c_{i,1} = c_{i,12} = 1$ and $c_{i,25} = 3$.

Once the connectivity matrix was assembled, it was used to compute the point estimates of the components labor associated with part replacement via a *maximum likelihood estimation* (MLE) by way of a regression, or used to estimate a probability distribution of the labor cost associated with the part replacement using a Bayesian formalism. We considered both.

The main challenge with this representation of the problem was that it was difficult to limit the list of parts to n *selected parts* that we were of most interest, because the maintenance events would inevitably include parts that were not on the list. This brought two options: 1) add more parts to the list, or 2) ignore the labor associated with the parts that were not on the list and model it as a noise vector $\boldsymbol{\nu}_{n \times 1}$ and the equation Eq. (1.3) became

$$\mathbf{C}\mathbf{p} + \boldsymbol{\nu} = \mathbf{l} \quad (1.4)$$

The first approach was problematic because the number of unwanted parts increased more quickly than the number of added (wanted) parts and the total number of parts was very high. Each order that contained parts considered also contained many unwanted parts and so adding one order of a specific type usually

added many parts that were not of interest. On the other hand, reducing the number of useful parts usually resulted in too few related parts making the matrix equation under-determined. The second approach was not well-suited for MLE estimation. Because both of these options had serious limitations, labor estimation based on replaced parts was not further investigated.

1.5 Overhaul effectiveness

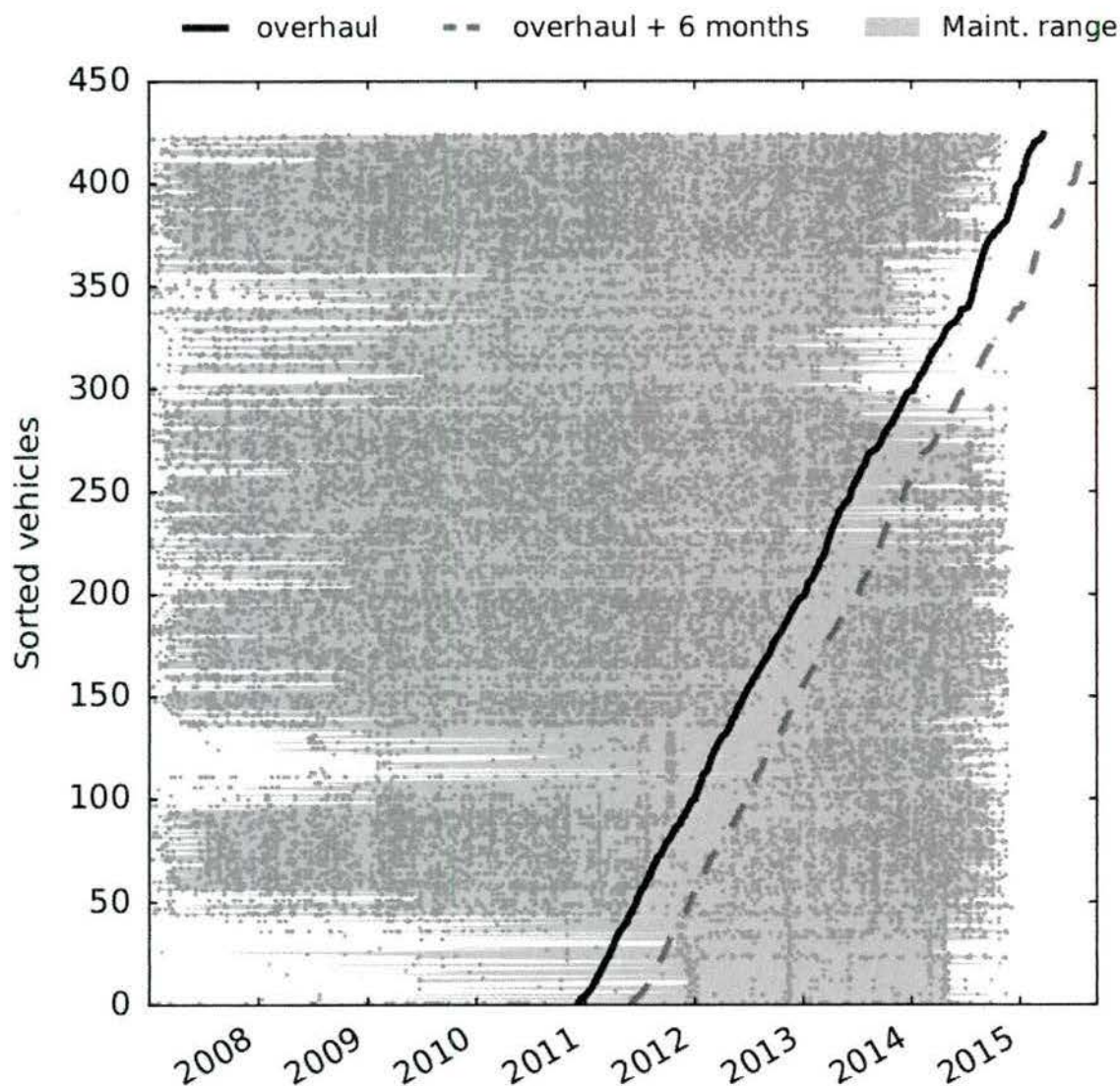


Figure 1.12: Overhaul (dark line) and maintenance events over time for a fleet of vehicles

In order to assess the effectiveness of current overhauls, data was arranged so that all the vehicles' overhaul dates aligned and cost records before and after could be compared. Vehicle cost and maintenance histories were analyzed by sub-system (i.e a collection of components categorized by their collective purpose). Components that were hypothesized to have the most influence by usage, such as road wheels, were analyzed individually. A cost analysis was done for the 425 vehicles that have been overhauled since 2007. Data was grouped by 90 day intervals. Total cost, available number of vehicles, cost per available number of

vehicles, and number of maintenance orders were plotted over time in Figure 1.13 for repair orders with non-zero costs. In order to avoid effects from the volatility of price variation over time, all costs shown in this plot were based on the 2014 unit prices found in the Current Parts Data table. For a comparison with the actual prices recorded in the database, refer to Figure B.1 in Appendix B. Cost values cannot be taken at face value when observing this many vehicles. It is the cost per vehicle that has meaning in these plots when considering the effectiveness of overhaul. The second subplot in Figure 1.13 shows the availability of vehicles. By taking the earliest and latest maintenance date for each vehicle, and the vehicle's overhaul date, the number of vehicles in the records was computed for each day. The gray region before, and blue line after the dotted line were the results of this calculation, however, not all vehicles that had seen an overhaul had maintenance records afterward. There were 132 vehicles that did not have maintenance records after their overhaul. This can be seen in the top right region of Figure 1.12, where there is no orange data points to the right of the blue overhaul line. This is also apparent in the second subplot of Figure 1.13, where a drop in available vehicles is seen where the gray region meets the blue line. In order to compensate for the absence of data for those vehicles when normalizing costs, a different approach was taken and is represented by the orange shade on the right side of the overhaul line. This was computed using the number of available vehicles based on the total number of days since their induction in overhaul. This was more effective for vehicle availability because it accounted for vehicles without maintenance records after overhaul that may still have been available.

1.5.1 High-level view

Figure 1.12 shows maintenance and overhaul activity on a fleet of vehicles: the dark blue line shows overhaul dates for 400+ vehicles, the orange patch signifies the time interval with recorded maintenance history corresponding to the overhauled vehicle, the orange dots denote maintenance events, and the dashed gray line marks six months after the overhauls. Note that there are generally few maintenances in the six months interval after overhaul.

1.5.2 Early failures

It is apparent from Figure 1.12 that during the first six months after an overhaul a vehicle rarely sees maintenance. There were 201 repairs done during this time on a total of 103 vehicles. The distribution of replacements in these vehicles is shown in Figure 1.14. The majority of overhauled vehicles did not see maintenance in this early period. There were very few vehicles that had more than one or two maintenance events.

1.6 Missing, incomplete, inconsistent, and contradictory data entries

The analysis of effectiveness has encountered many problems with respect to data quality. One of the principal objectives of the investigation was to determine the effectiveness of overhaul schedules. The cost estimation is the key metric that enables this evaluation. Noise in the maintenance records made the estimation of the cost elements in Equation 1.1 non-trivial.

1.6.1 Parts cost

The Parts table contained two fields, parts charge and quantity required, whose product was the cost of replacement. It was expected for cost of parts to increase over time but there was a noticeable spike in the year 2012. Figure 1.15 shows two examples of cost histories for parts that showed this behavior. The gray shade covers the entire year of 2012. Notice that there were cost records in this year that did not adhere to the price spike. The values inside this year were modeled using a bi-modal distribution and the ratio was computed using the larger of the two averages. This assured that non-spiked costs inside 2012 would not bring down the true spike's average. To summarize these findings many parts were analyzed. Figure 1.16

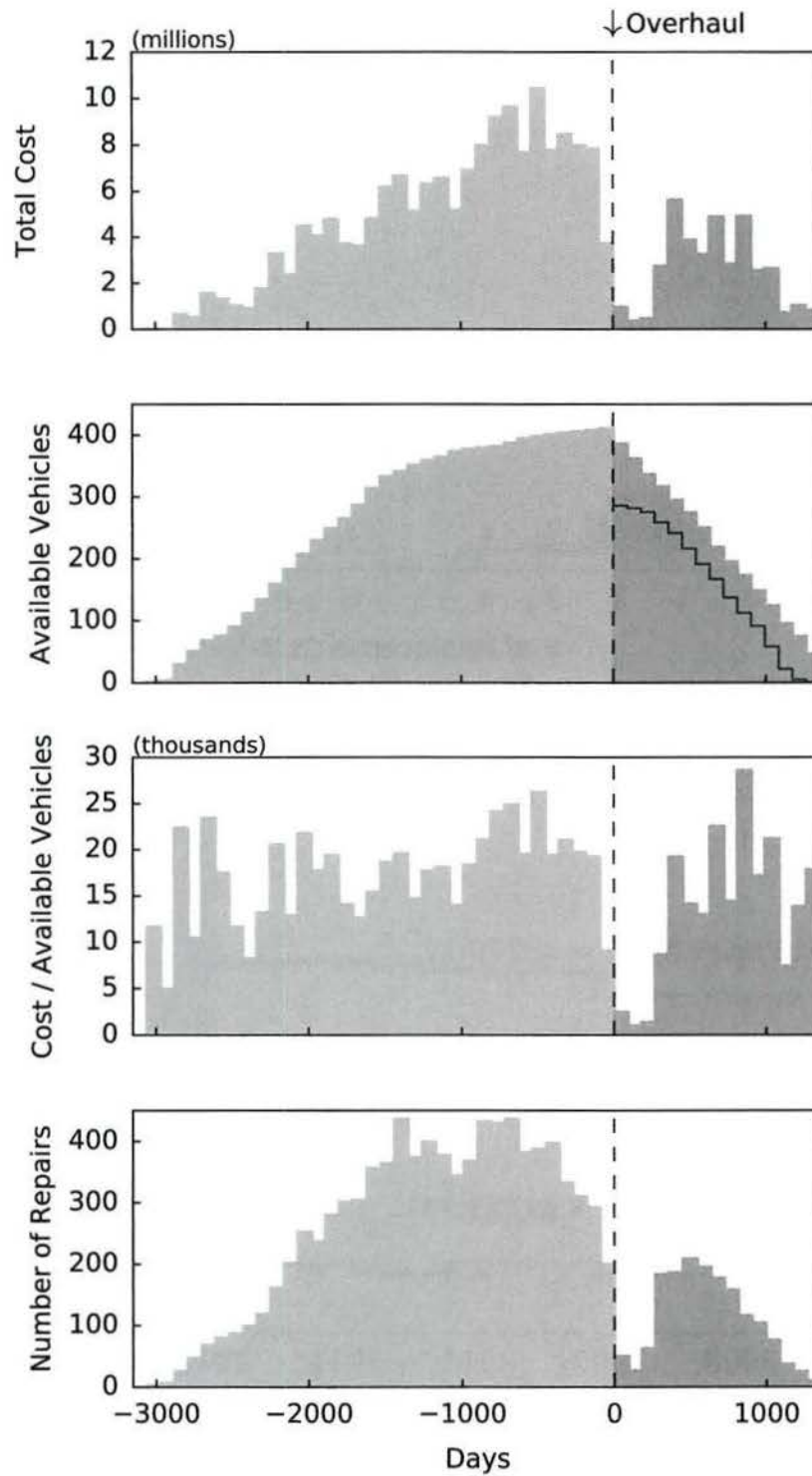


Figure 1.13: Vehicle information including cost, availability, and number of repairs with respect to each vehicles' overhaul date. Before overhaul is gray, and after overhaul is orange

shows a histogram of ratios for parts that had at least ten cost records, where at least five of those records existed in the year 2012.

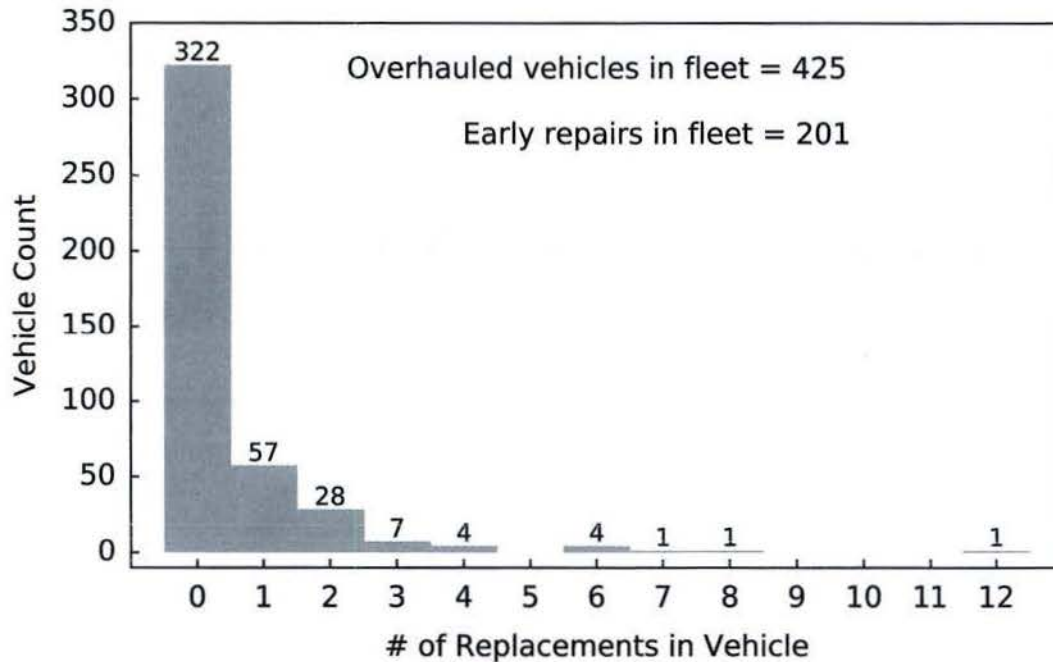


Figure 1.14: Fleet distribution of early repairs, within six months after the overhaul

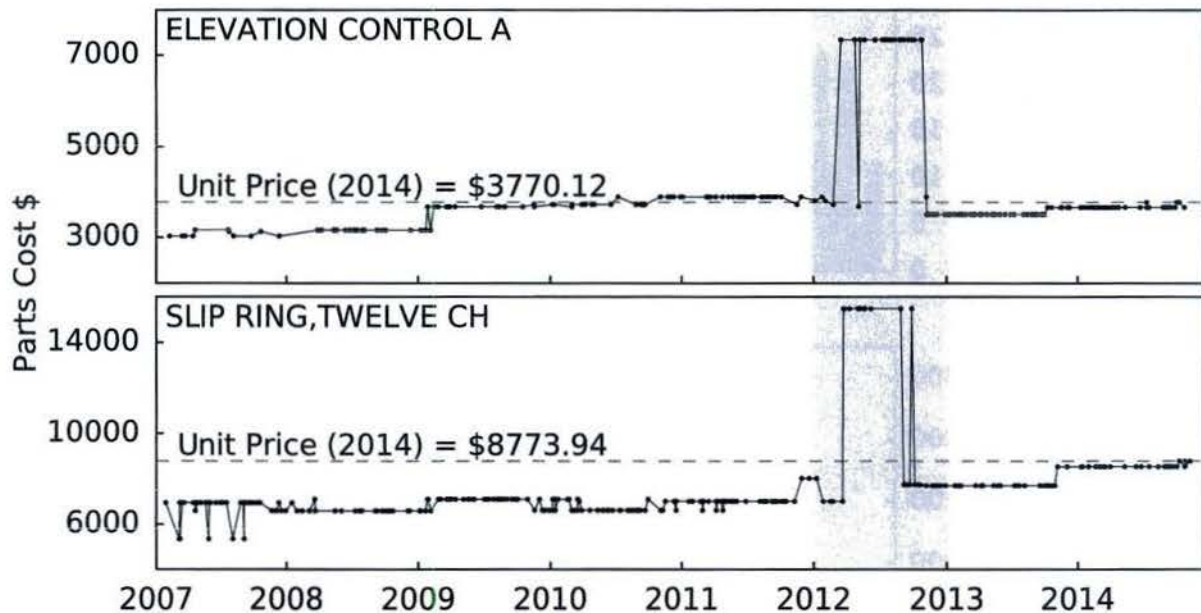


Figure 1.15: Two examples of cost histories for parts that showed anomalous behavior. There was a noticeable spike in price, primarily between 2012 and 2013, for many of the parts

Figure 1.17 shows the entire cost history for all records on a semi-logarithmic scale. Sometime near the beginning of 2011 records only held integer values on the interval $[1, 10]$. This trend is apparent above that interval as well but is not as clear. Furthermore, it seemed that after a certain time no charges were recorded below \$1.

There were a number of potentially erroneous records in the cost histories. Parts charge values for many components showed noticeable clusters of values almost entirely at $1/100$ th of the component's 2014 unit

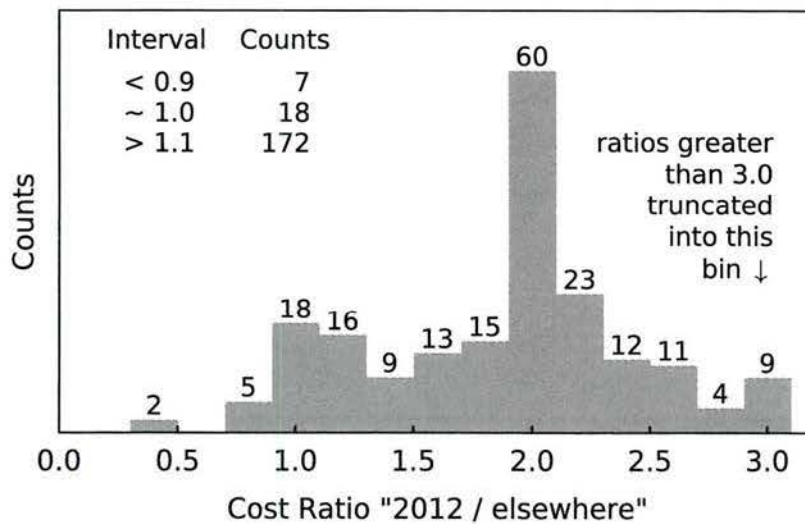


Figure 1.16: Histogram of ratios for parts that had at least ten cost records, where at least five of those records existed in the year 2012. For parts with cost records greater than \$100, 10 parts returned a ratio less than 1, 100 parts returned a ratio greater than 1 but less than 2, and 79 parts returned a ratio greater than 2 but less than 3

price. The majority of the other records for a component were at or around the 2014 unit price. Figure 1.18 shows a distribution of parts charge along the y-axis, for all unique parts sorted by unit price. The solid black line traces those unit prices and the very faint solid gray line traces 1/100th of the unit prices. The points that are along the gray line make up 6.931% of the total records suggesting there are a significant enough number of records with potential errors.

1.6.2 Quantity required

There were some unusual values in the Parts table for the quantity required field. There was a constant value representing the quantity per vehicle and was typically the upper limit on a specific part's order history. This was reasonable because it was not likely that everyone of a specific component would need replacing at once. There were cases, however, where the maximum quantity ordered at some time was far beyond the vehicles maximum requirement. The higher costing parts were considered first and more specifically the suspension components were focused on during these analyses. For example, according to the U.S Marine Corps Technical Manual for Assault Amphibious Vehicles (AAVs), a vehicle has six wheels on each side and each wheel contains two solid rubber wheel components, called road wheels. There were records of road wheels ordered in quantities of close to 150. This raised suspicion of incorrect records. In order to look into this issue a box and whisker plot was created which showed the distribution of quantity records for a selected number of components that raised suspicion. Figure 1.19 shows several components, including road wheels. For those parts that reached magnitudes higher in quantity, a log-scale was chosen to better illustrate the boxes. The boxes represent the inner quartile of data, or more specifically the middle 50% of data. The median is shown by a line that divides the box into two parts and the whiskers reach out to a range which contains 90% of data. Outliers were values that existed outside this 90% range and were plotted as points. Those components without boxes had very few records. The first two parts in Figure 1.19, 'Halon, Fire Ext' and 'Control, Intercommun', had some negative values in the records, and unreasonable high max values. 'Shock Absorber,Bump' is the next part down and there are eight of those per vehicle. On the plot, 8 is one of the outliers, suggesting all eight components in a vehicle were rarely replaced. The largest outlier for this part was 32 which seems unreasonably high. On the second axis, where a log-scale was used, component 'Track Shoe, Vehicula' reached values of close to 1,000. The number of these parts per side in a vehicle was

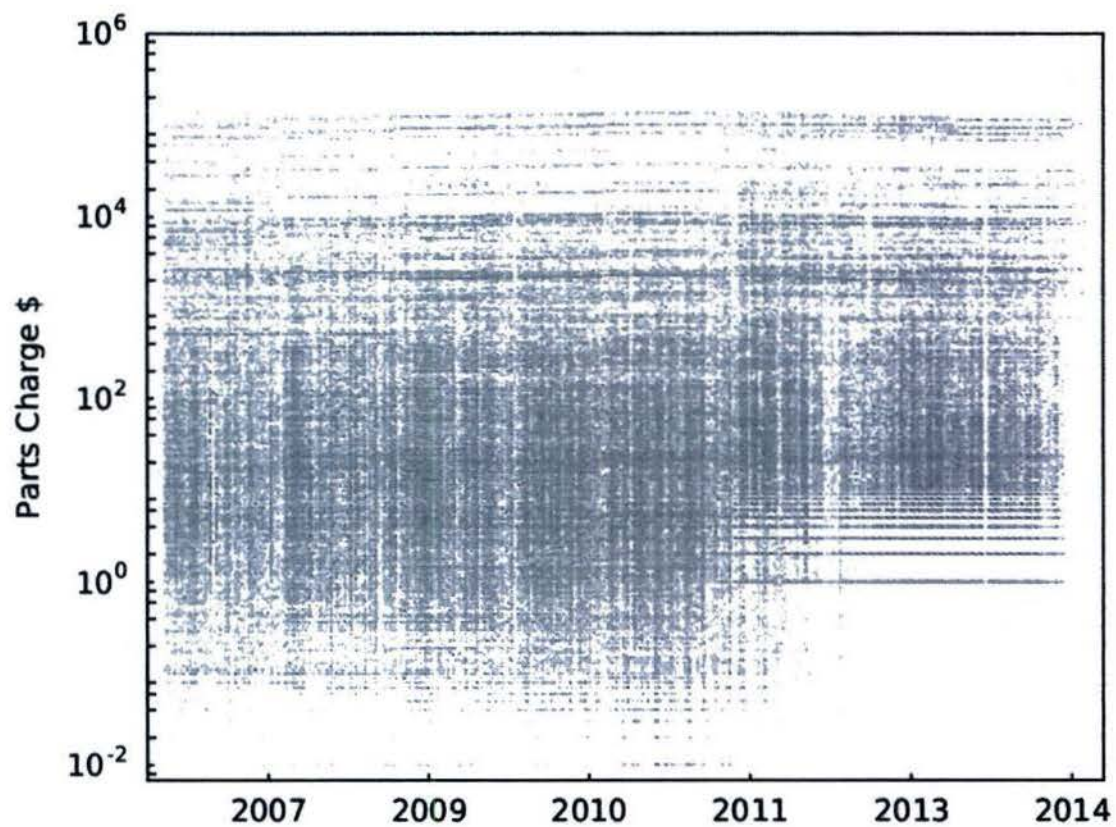


Figure 1.17: Entire cost history for all records on a semi-logarithmic scale. Every dot is a parts charge record. Notice the straight rows of dots and empty space after 2011

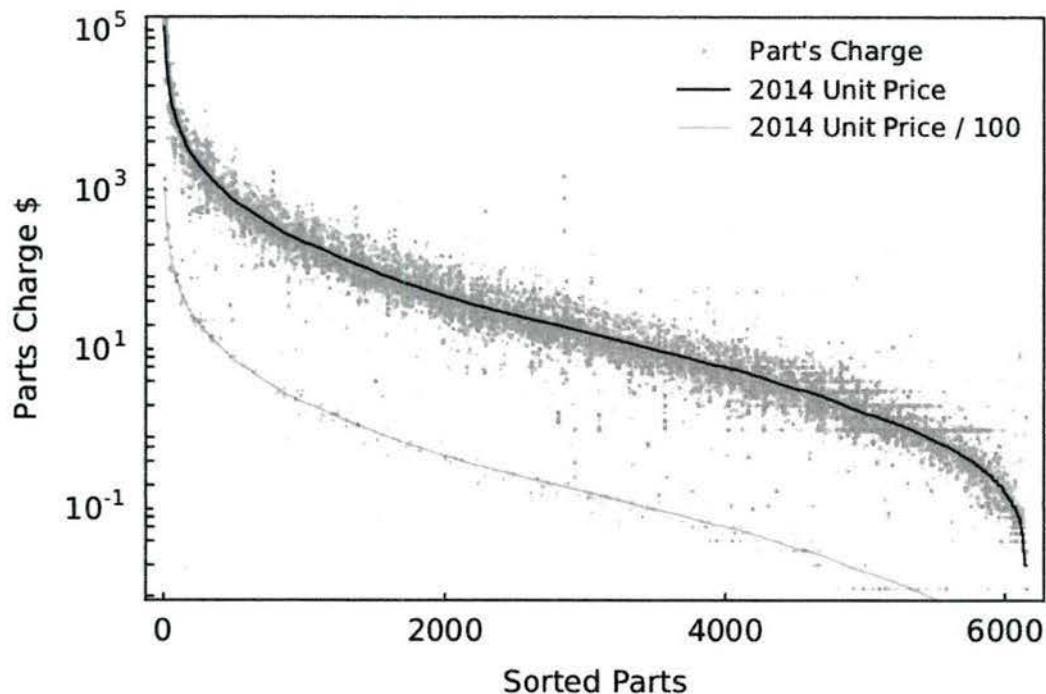


Figure 1.18: A distribution of parts charge for all unique parts sorted by unit price. Unit prices of parts show a faint but consistent line at a fraction of the majority of data

85, totaling 170 for the vehicle. That was the right end of the box and was not often expected in a work order. The values beyond that do not seem realistic at all.

1.6.3 Labor cost

Labor hours were the only factor other than parts charge in the cost of a repair. The cost of repairs were a key factor in determining the effectiveness of overhaul. Of the 65,560 recorded work orders in the Headers table, 18,430 (28%) did not contain a military labor hour value. Furthermore, 5,176 (8%) of work orders had a labor hour value of 0. That is over a third of the data. All percentages are rounded and should be interpreted within $\pm 0.5\%$ of their value. In order to illustrate the quantity of valid data Figure 1.20 shows work orders scattered by hours of military labor and hours in shop. A 1:1 line was plotted along the axes. Anything above this line is in a region where more hours were worked than hours spent in the shop. There were 4,886 (10%) work orders in this region. There were 47,130 work orders plotted in total. So of the 64% of non-null, non-zero military labor hours, 10% were in a region of suspicion. Military labor hours are defined as the total number of man hours expended for the complete maintenance action. Because of this, some of the work orders above the line were implausible but not impossible. If there were several people working on a vehicle in a day then it is possible to surpass 24 man-hours per day. Most of the data points in that region, however, are seemingly impossible. With 10% of the non-null, non-zero data potentially invalid that leaves 57.6% of all military labor hour data to be analyzed. Due to the large proportion of potentially invalid data, cost analyses were performed with the exclusion of all military labor hours.

There was an apparent change in military labor hours approximately after the beginning of 2012. As shown in Figure 1.21, there is a decrease in rate. The bottom center plot contains all work orders with military labor hours over time. They are plotted on a semi-log scale to demonstrate the magnitude of values. The median of data, before and after 2012, extend outwards to frequency plots for before and after 2012, respectively. The difference in these lines is approximately one order of magnitude.

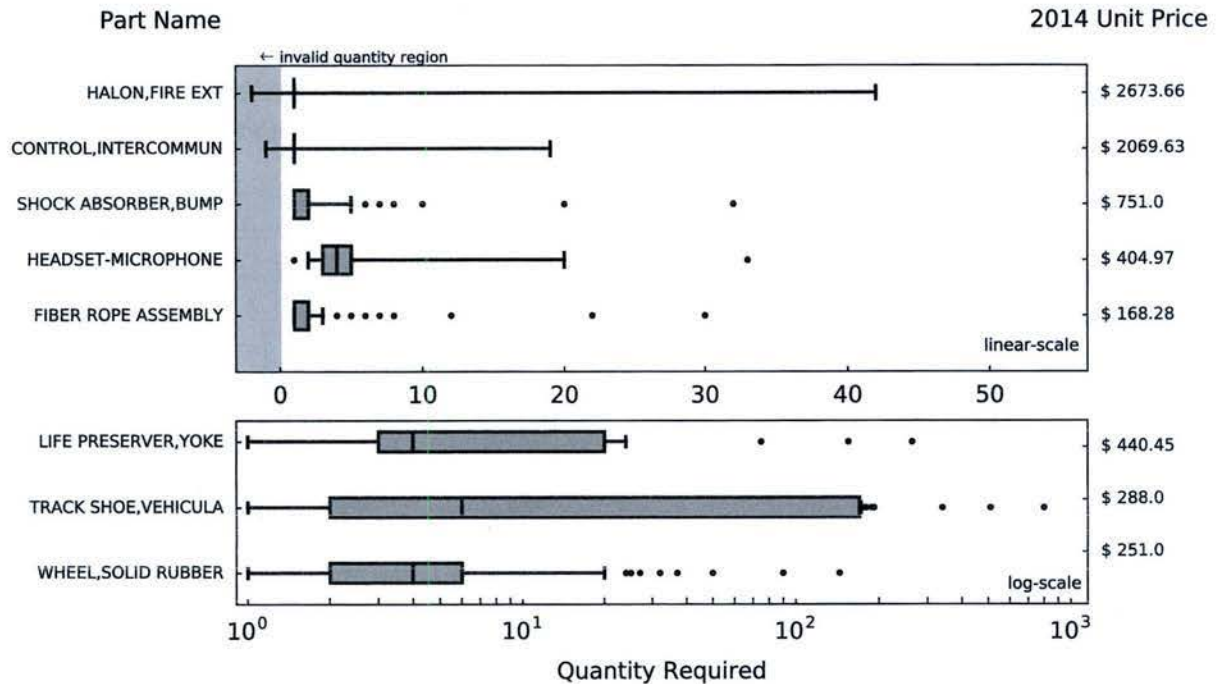


Figure 1.19: Some expensive components with suspicious quantity records

1.6.4 Issues in Unit Analysis

A unit is the home location of the owner of a vehicle; every unit has a collection of vehicles. The unit identifier code (UIC) is a number that identifies which unit a particular vehicle belongs to. The main database table that contained the maintenance event's general information, such as date received in shop or work-order number, also contained UICs in two forms. There was a home owner UIC, and the UIC of the unit doing the repair. From here forward, any reference to a UIC will imply the owner unit address code only. There was another table dedicated to holding a weekly summary of readiness information for the vehicles. This table contained more information on UIC's including the unit's name, maintenance level, supply rate, etc. There were fewer UICs in the Readiness table than the main maintenance event table. After reviewing individual cases, it became clear that some entries of units were suspicious in the maintenance event table. Two approaches for data cleansing were taken:

1. Remove suspect unit codes.
2. Remove single occurrence unit codes associated with a vehicle.

1. Suspect Unit Codes

To obtain a clearer picture, all UICs not been found in the Readiness table were removed. This table held more specific information and was less likely to have errors. For a list of UICs not found in the Readiness table please refer to Figure D.1 in Appendix D.

Assuming a vehicle was not owned by a single unit for the duration of the existing data, there was a distinct number of UICs for each serial number. The navy colored histogram in Figure 1.22 shows the distribution of unique UICs per vehicle. The orange histogram shows the same, after reducing the total unit codes by only considering those found in the Readiness table. The curved lines represent the cumulative total for each case. The orange plot shows that the number of distinct UICs per vehicle trended towards 1. This verified that UICs found in the Readiness table were generally more reliable, because owner unit codes were more likely to go unchanged throughout the maintenance history of a vehicle. Part of the goal was to identify habits in these owner units. This required that the vehicles spent some time at a particular unit.

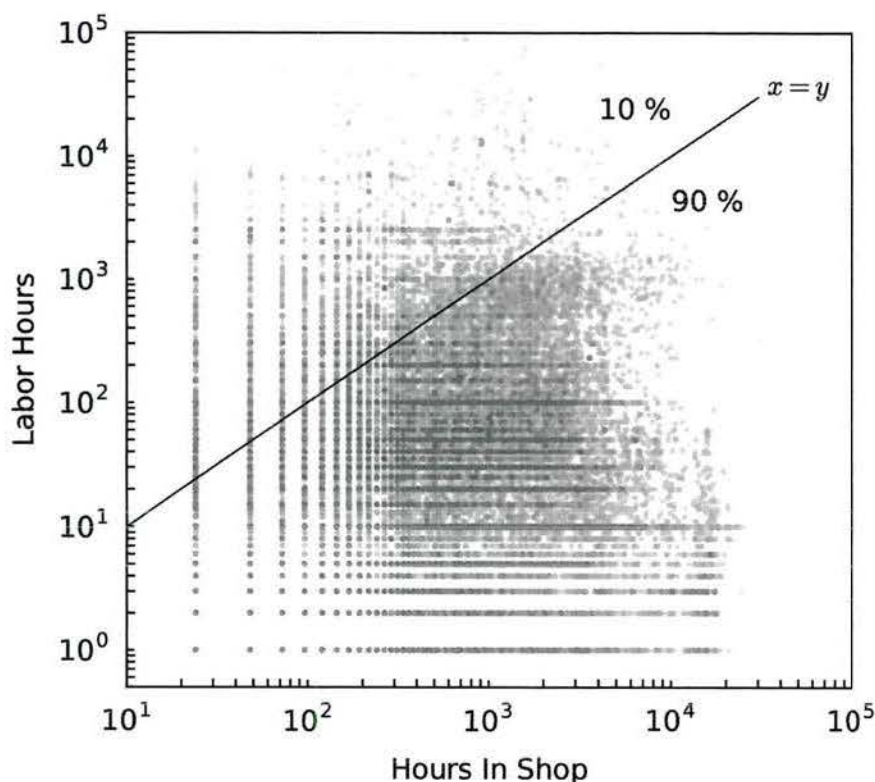


Figure 1.20: Work orders scattered by hours of military labor and hours in shop. The solid navy blue line represent the 1:1 relation between the two axis. Data points above the line had more labor hours than time spent in the shop. This is a sign of bad data. As mentioned above, however, there are some points that may be plausible since military labor hours refers to man hours worked. Much more than 24 hours a day is still unlikely. 10% of data existed above the line

2. Single Occurrence Unit Codes

For many vehicles, the majority of maintenance events occurred at a distinct unit. For some there were movements to another unit for only one maintenance. This is referred to here as a single occurrence unit code. It was expected to see this behavior in the records of the unit doing the repair, but not for the identifying owner unit. Figure 1.23 illustrates single occurrences for a selected vehicle.

Comparison of Units by Failure Rates

UICs not found in the Readiness table were kept in this part of the analysis for a fuller view. The plot in Figure 1.23 contains a shaded region representing these type of UICs. Single jumps happened quite often in the data. Failure rates were computed using the time between closed dates of maintenance. Observations at the vehicle/defect area level, when considering individual units, was not supported by enough data to be statistically significant. There were, however, a few units with a significant amount of data. Four UICs (21820, 21810, 34014, S3800) were considered and their expected mean time between failures (MTBF) were compared for a selection of defect areas. These were the most frequent UICs. A defect area, like a sub-system of components, is a collection of parts specific to an area. Figure 1.24 shows a histogram of the top ten occurring UICs.

The first two dominate the rest in number of date closed records, but the first four were compared.

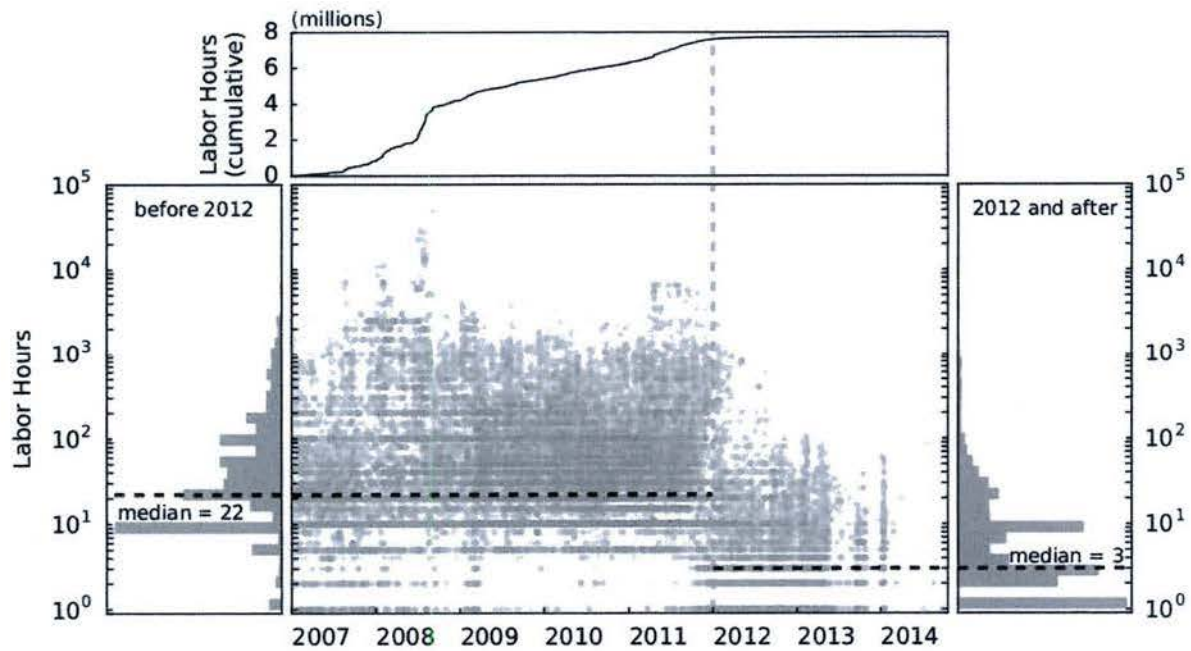


Figure 1.21: Detailed outline of labor hours over time. Labor hours show a shift in behavior after 2012

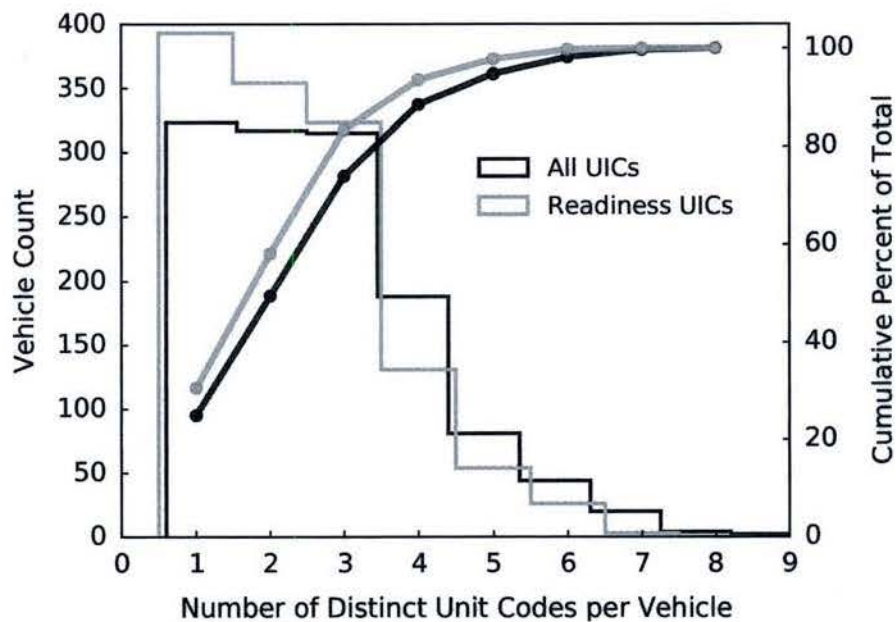


Figure 1.22: Comparing amount of data between two tables: Headers and Readiness

Deeper analysis showed that these four had the most data in the maintenance records when measuring failure rates by unit, vehicle, and defect area. After comparison it was evident that some units stood out in five specific defect areas. For those maintenance histories with only one date closed record, a value of

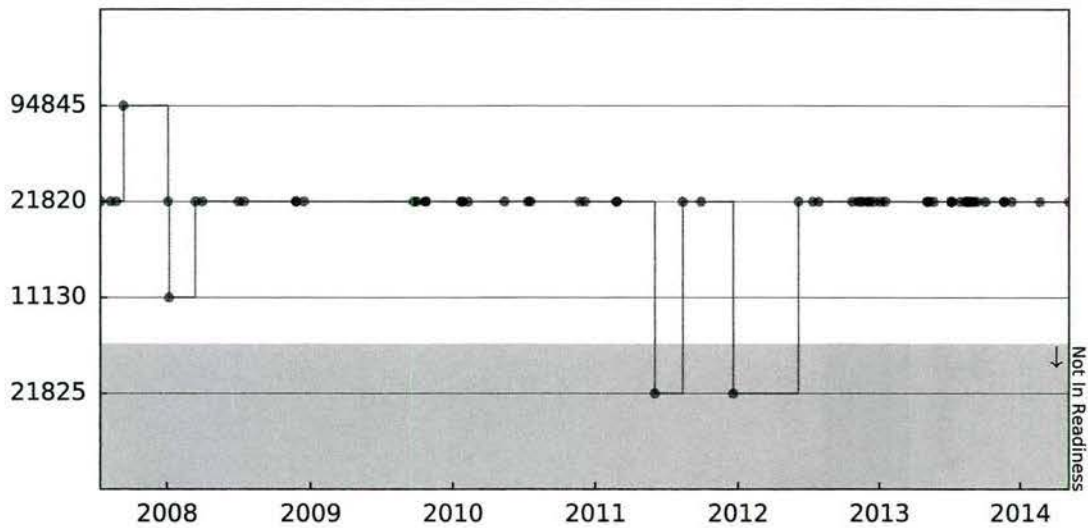


Figure 1.23: One vehicle's owner unit address code history for non-reduced unit codes

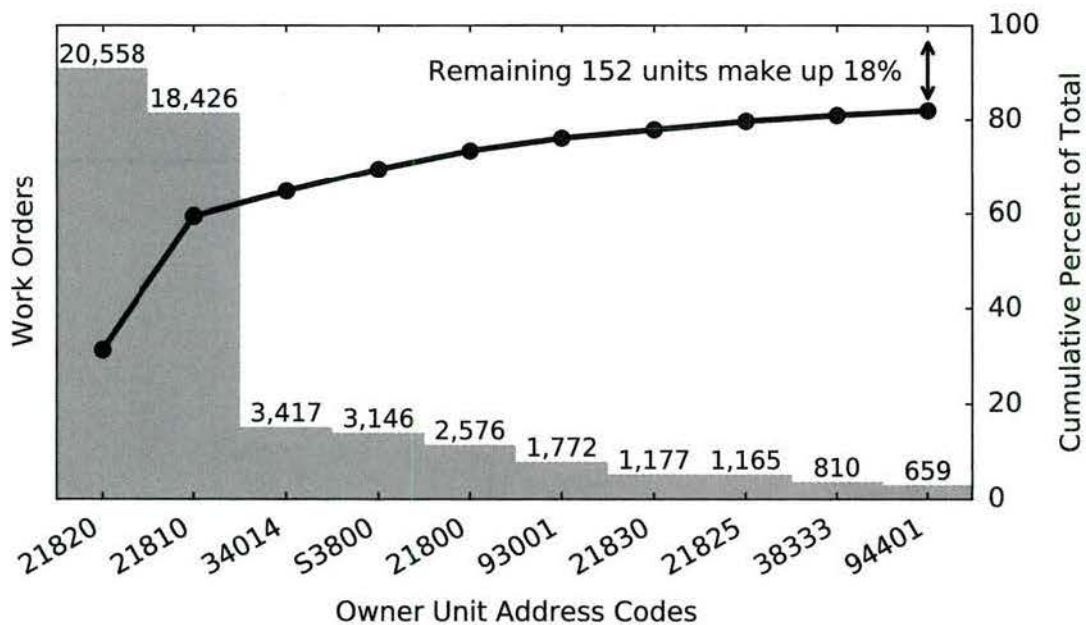


Figure 1.24: Number of work orders for specific owner unit addresses as a part of the total

2,555 days representing the full seven years of data was used as a simple approximation. These values were exempt when calculating the expected MTBF. Figure 1.25 shows a normalized failure rate distribution for the defect area 'Body, Frame, or Hull'.

The gray probability density function (PDF) is an aggregation of all unit's failure times. The blue PDF represents the unit with the best MTBF of the four and the orange represents the unit with the worst MTBF. Further investigation was needed when UICs like these differed from the MTBF of all UIC's failure times. Sub-populations of the failure rate distributions were generated and their means evaluated. Figure 1.26 illustrates the process of generating a distribution of means from a sample population of failure rate values.

This leads into Figure 1.27 which shows the expected MTBF for all four units and for the aggregation of

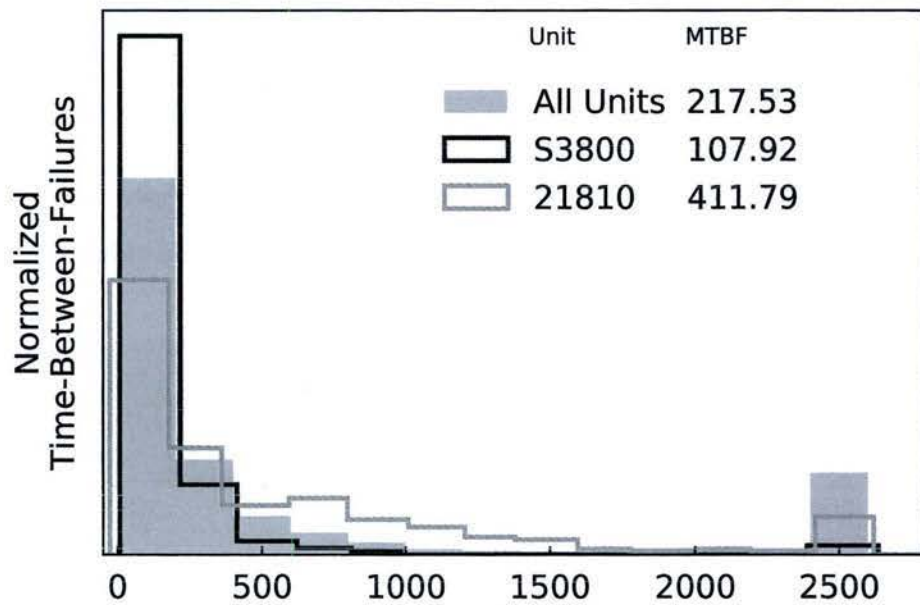


Figure 1.25: Normalized failure distribution for the defect area 'Body, Frame, or Hull'

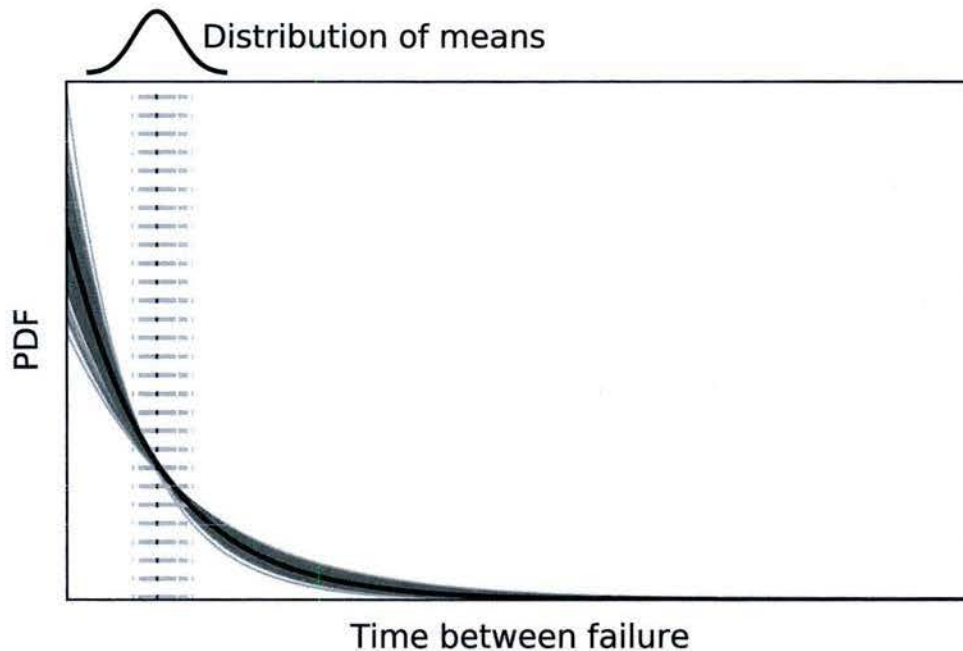


Figure 1.26: Illustration of how a distribution of expected means is computed from a single histogram of time-between-failure values

all units using the method illustrated in Figure 1.26. This figure shows the defect area 'Body, Frame, Hull' first, followed by the four other defect areas analyzed. The remaining four defect areas were: 'Suspension', 'Component', 'Electrical System' and 'Fire Control System' and can be found individually in Figures (D.2, D.3), (D.4, D.5), (D.6, D.7) and (D.8, D.9) respectively, in Appendix D.

1.7 Summary

The objective of this study was to examine maintenance data and use it to test if a vehicle overhaul was effective. In the process we improved methods in estimating long term accumulation of data that may be inconsistent or missing. Usage records were analyzed from military tracked vehicles and the approach to estimating usage based on noisy data was split into two parts. 1) development of a probabilistic model, and 2) estimation based on replacement of related consumable parts. The first method was a knowledge driven probabilistic model that estimated reasonable values for non-decreasing monotonic measurements that were inconsistent, incomplete, and sometimes missing in the data. The results were consistent for several cases of noise on the same data. The model was designed to estimate successive measurements and when applied to real usage data it was realized that noisy initial values biased the results. This was reconciled using an averaging method where the same data-set was sampled in a forward and reverse direction and the results averaged. This proved to significantly decrease the bias from a bad initial data point. The second approach was intended to estimate usage as well but was found to be only supplementary at best. For the road wheel component, correlation between usage and replacements of consumables was very close to 0 from the maintenance to maintenance perspective, however, long term accumulation of data showed high correlation. This suggests that cumulative records of replacements of consumable related to usage can be used to aid in the estimation of usage itself. One of the proposed methods was evaluated on our vehicle data and was shown to be ineffective at predicting usages because there was too much variation in regression parameters from vehicle to vehicle. In addition, we conducted detailed analysis of data quality and integrity and specifically pointed to several observed anomalies, including inconsistencies with data entries, temporary spikes in prices, and difficulties in tracking vehicle based on their unit membership.

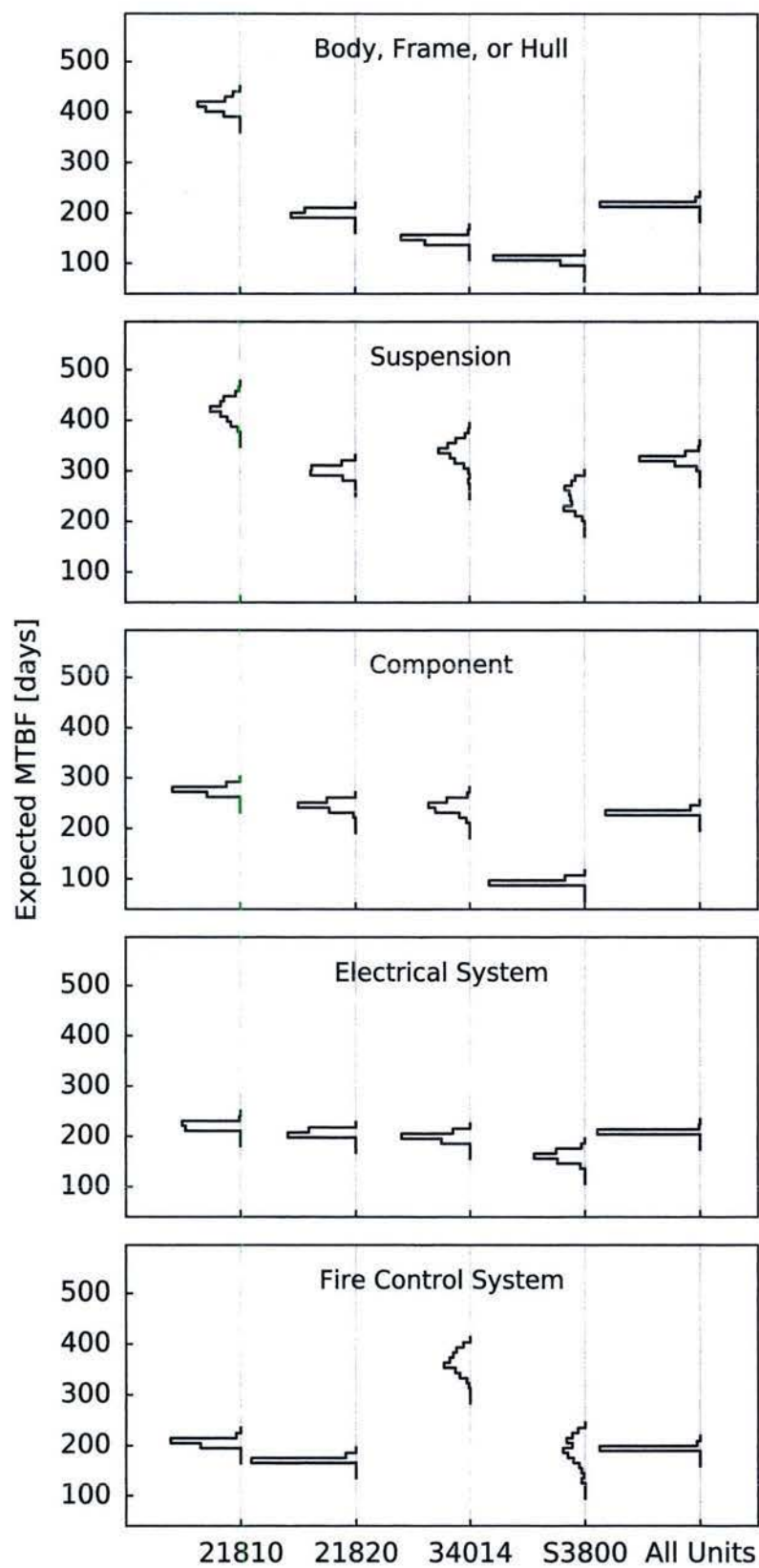


Figure 1.27: A comparison of expected means by unit, for the five defect areas analyzed.

Bibliography

- [1] F. Nowlan and H. Heap, "Reliability-centered maintenance," Tech. Rep. AD/A066 579, United Airlines, San Francisco, CA, 1978.
- [2] J. Moubray, *Reliability centered maintenance*. Industrial Press, 1997.
- [3] S. J. Engel, B. J. Gilmartin, K. Bongort, and A. Hess, "Prognostics, the real issues involved with predicting life remaining," in *Aerospace Conference Proceedings, 2000 IEEE*, vol. 6, pp. 457–469, IEEE, 2000.
- [4] G. Vachtsevanos, F. Lewis, M. Roemer, A. Hess, and B. Wu, *Intelligent Fault Diagnosis and Prognosis for Engineering Systems*. Wiley, 2006.
- [5] J. Z. Sikorska, M. Hodkiewicz, and L. Ma, "Prognostic modelling options for remaining useful life estimation by industry," *Mechanical Systems and Signal Processing*, vol. 25, no. 5, pp. 1803–1836, 2011.
- [6] H. E. Bussey, N. G. Nenadic, P. A. Ardis, and M. G. Thurston, "Case study: Models for detecting low oil pressure anomalies on commercial vehicles," in *Annual Conference of the Prognostics and Health Management Society 2014*, p. 13, PHM Society, <http://www.phmsociety.org/node/1466/>, 2014.
- [7] R. Heine and D. Barker, "Simplified terrain identification and component fatigue damage estimation model for use in a health and usage monitoring system," *Microelectronics Reliability*, vol. 47, no. 12, pp. 1882 – 1888, 2007. Electronic system prognostics and health management Thermal, mechanical and multi-physics simulation and experiments in micro-electronics and micro-systems (EuroSimE 2006).
- [8] C. Trammel, G. Vossler, and M. Feldmann, "Uk ministry of defence generic health and usage monitoring system (genhums)," *Aircraft Engineering and Aerospace Technology*, vol. 69, no. 5, pp. 414–422, 1997.
- [9] A. C. Gordon, "The development to production of an integrated health and usage monitoring system for helicopters," tech. rep., SAE Technical Paper 912093, 1991.
- [10] P. J. Ellerbrock, P. Shanthakumaran, and Z. Halmos, "Development of new health and usage monitoring system tools using a nasa/army rotorcraft," in *ANNUAL FORUM PROCEEDINGS-AMERICAN HELICOPTER SOCIETY*, vol. 55, pp. 2337–2348, AMERICAN HELICOPTER SOCIETY, 1999.
- [11] A. Patil, D. Huard, and C. J. Fonnesbeck, "Pymc: Bayesian stochastic modelling in python," *Journal of statistical software*, vol. 35, no. 4, p. 1, 2010.
- [12] C. Davidson-Pilon, *Bayesian Methods for Hackers: Probabilistic Programming and Bayesian Inference*. Addison-Wesley Professional, 2015.
- [13] D. J. Lunn, A. Thomas, N. Best, and D. Spiegelhalter, "Winbugs-a bayesian modelling framework: concepts, structure, and extensibility," *Statistics and computing*, vol. 10, no. 4, pp. 325–337, 2000.
- [14] M. Plummer *et al.*, "Jags: A program for analysis of bayesian graphical models using gibbs sampling," in *Proceedings of the 3rd international workshop on distributed statistical computing*, vol. 124, p. 125, Technische Universit at Wien, 2003.
- [15] N. Goodman, V. Mansinghka, D. Roy, K. Bonawitz, and D. Tarlow, "Church: a language for generative models," *arXiv preprint arXiv:1206.3255*, 2012.
- [16] T. Minka, J. Winn, J. Guiver, and D. Knowles, "Infer .net 2.5," *Microsoft Research Cambridge*, 2012.

- [17] A. Gelman, D. Lee, and J. Guo, "Stan a probabilistic programming language for bayesian inference and optimization," *Journal of Educational and Behavioral Statistics*, p. 1076998615606113, 2015.
- [18] T. E. Oliphant, *A guide to NumPy*, vol. 1. Trelgol Publishing USA, 2006.
- [19] S. Van Der Walt, S. C. Colbert, and G. Varoquaux, "The numpy array: a structure for efficient numerical computation," *Computing in Science & Engineering*, vol. 13, no. 2, pp. 22–30, 2011.
- [20] E. Jones, T. Oliphant, P. Peterson, *et al.*, "Scipy: Open source scientific tools for python, 2001-2008b," URL <http://www.scipy.org>.
- [21] J. D. Hunter, "Matplotlib: A 2d graphics environment," *Computing in science and engineering*, vol. 9, no. 3, pp. 90–95, 2007.
- [22] W. McKinney, *Python for data analysis: Data wrangling with Pandas, NumPy, and IPython*. " O'Reilly Media, Inc.", 2012.
- [23] F. Pedregosa, G. Varoquaux, A. Gramfort, V. Michel, B. Thirion, O. Grisel, M. Blondel, P. Prettenhofer, R. Weiss, V. Dubourg, J. Vanderplas, A. Passos, D. Cournapeau, M. Brucher, M. Perrot, and E. Duchesnay, "Scikit-learn: Machine learning in Python," *Journal of Machine Learning Research*, vol. 12, pp. 2825–2830, 2011.
- [24] J. Bergstra, O. Breuleux, F. Bastien, P. Lamblin, R. Pascanu, G. Desjardins, J. Turian, D. Warde-Farley, and Y. Bengio, "Theano: a cpu and gpu math expression compiler," in *Proceedings of the Python for scientific computing conference (SciPy)*, vol. 4, p. 3, Austin, TX, 2010.
- [25] C. M. Bishop, *Pattern recognition and machine learning*. springer, 2006.
- [26] R. T. Cox, "Probability, frequency and reasonable expectation," *American journal of physics*, vol. 14, no. 1, pp. 1–13, 1946.
- [27] R. T. Cox, *Algebra of Probable Inference*. John Hopkins University Press, 1961.
- [28] E. T. Jaynes, *Probability theory: the logic of science*. Cambridge university press, 2003.
- [29] G. L. Bretthorst, *Bayesian spectrum analysis and parameter estimation*. New York: Springer-Verlag, 1988.
- [30] D. S. Sivia, *Data analysis: a Bayesian tutorial*. Oxford university press, 1996.
- [31] P. Gregory, *Bayesian Logical Data Analysis for the Physical Sciences: A Comparative Approach with Mathematica® Support*. Cambridge University Press, 2005.
- [32] N. Metropolis and S. Ulam, "The monte carlo method," *Journal of the American statistical association*, vol. 44, no. 247, pp. 335–341, 1949.
- [33] L. A. Zadeh, "Fuzzy sets," *Information and control*, vol. 8, no. 3, pp. 338–353, 1965.
- [34] L. A. Zadeh, "The role of fuzzy logic in the management of uncertainty in expert systems," *Fuzzy sets and systems*, vol. 11, no. 1, pp. 197–198, 1983.
- [35] G. Shafer *et al.*, *A mathematical theory of evidence*, vol. 1. Princeton university press Princeton, 1976.
- [36] J. Pearl, *Probabilistic reasoning in intelligent systems: networks of plausible inference*. Morgan Kaufmann, 1988.
- [37] J. Pearl, "Evidential reasoning using stochastic simulation of causal models," *Artificial Intelligence*, vol. 32, no. 2, pp. 245–257, 1987.
- [38] S. Geman and D. Geman, "Stochastic relaxation, gibbs distributions, and the bayesian restoration of images," *Pattern Analysis and Machine Intelligence, IEEE Transactions on*, no. 6, pp. 721–741, 1984.
- [39] C. Andrieu, N. De Freitas, A. Doucet, and M. I. Jordan, "An introduction to mcmc for machine learning," *Machine learning*, vol. 50, no. 1-2, pp. 5–43, 2003.

- [40] P. Diaconis, "The markov chain monte carlo revolution," *Bulletin of the American Mathematical Society*, vol. 46, no. 2, pp. 179–205, 2009.
- [41] M. I. Jordan, *Learning in Graphical Models: [proceedings of the NATO Advanced Study Institute...: Ettore Majorana Center, Erice, Italy, September 27-October 7, 1996]*, vol. 89. Springer Science & Business Media, 1998.
- [42] D. Barber, *Bayesian reasoning and machine learning*. Cambridge University Press, 2012.
- [43] D. Koller and N. Friedman, *Probabilistic graphical models: principles and techniques*. MIT press, 2009.
- [44] A. Gelman, J. B. Carlin, H. S. Stern, and D. B. Rubin, *Bayesian data analysis*, vol. 2. Taylor & Francis, 2014.
- [45] S. Theodoridis, *Machine Learning: A Bayesian and Optimization Perspective*. Academic Press, 2015.
- [46] D. Lopez-Paz, P. Hennig, and B. Schölkopf, "The randomized dependence coefficient," in *Advances in Neural Information Processing Systems*, pp. 1–9, 2013.

Appendix A

Other Suspension Components

The Pearson Correlation Coefficient was computed for some of the more important suspension components in a comparison test of usage and replacements of consumables. Section 1.3.2 showed a histogram of this coefficient for both the individual changes in usage and replacements (orange), and cumulative change in usage and replacements (blue hatched). Figures A.1, A.4, A.3, A.3, A.2 show the same for Shock Absorber, Sprocket, Track Adjuster, Track Pad respectively. The sigma correlation between usage and replacements seemed to hold for all consumables shown in this appendix as well as the road wheel example in Figure 1.9.

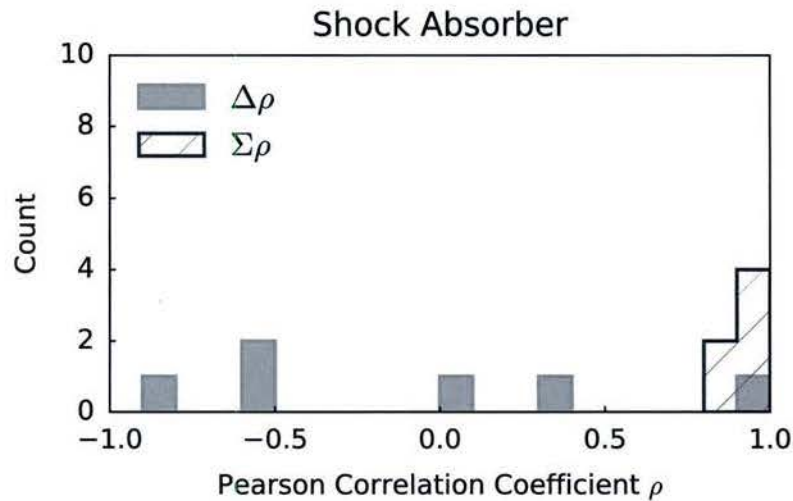


Figure A.1: Computed coefficients for all vehicles that had usage records and replacements of shock absorbers. 6 out of 470 repairs return values for correlating usage to replacements with shock absorbers

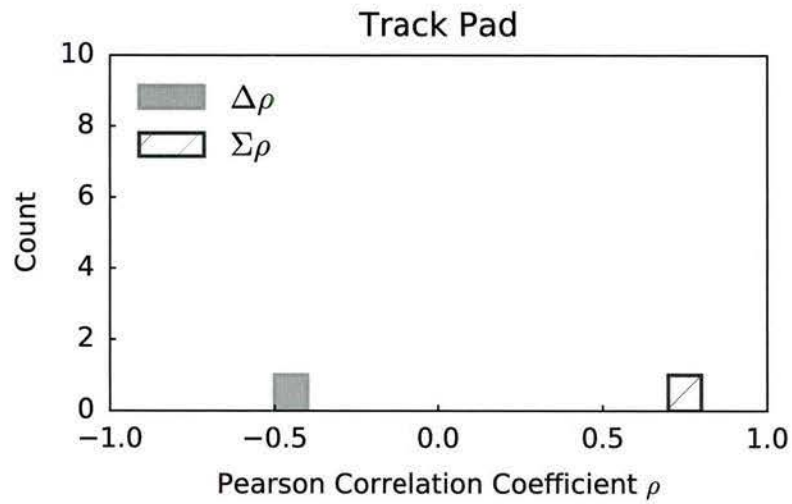


Figure A.2: Computed coefficients for all vehicles that had usage records and replacements of track pad. 1 out of 470 repairs return values for correlating usage to replacements with track pads

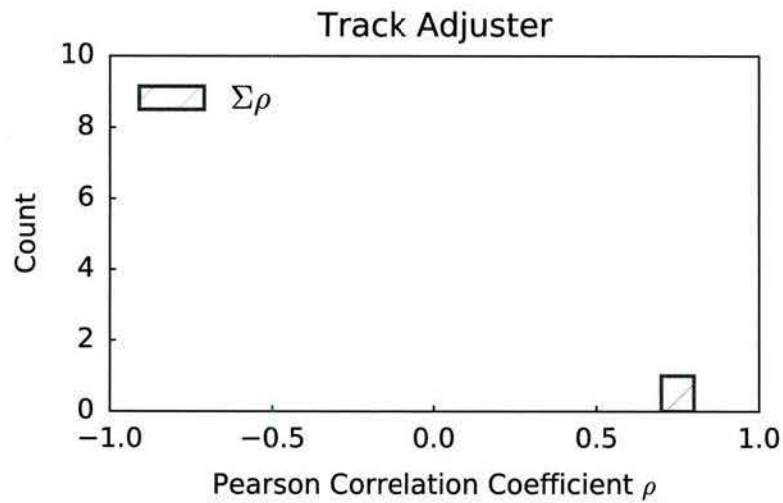


Figure A.3: Computed coefficients for all vehicles that had usage records and replacements of track adjuster. 1 out of 470 repairs return values for correlating usage to replacements with track adjuster

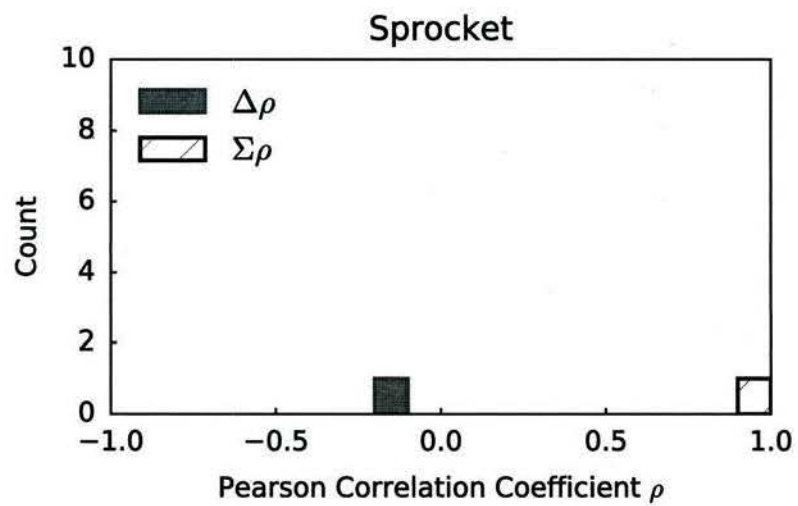


Figure A.4: Computed coefficients for all vehicles that had usage records and replacements of sprocket. 1 out of 470 repairs return values for correlating usage to replacements with sprocket

Appendix B

Before and After Overhaul

Figure 1.13 was shown in Section 1.5 and is repeated here as Figure B.1b for comparison with Figure B.1a, which shows the same plot with the actual recorded parts cost instead of the unit prices. The first and third subplots are different between these plots. The actual records had lower parts charges values than unit costs because parts charge generally increased over time. Using the unit costs removed the unknown factor of price variation over time.

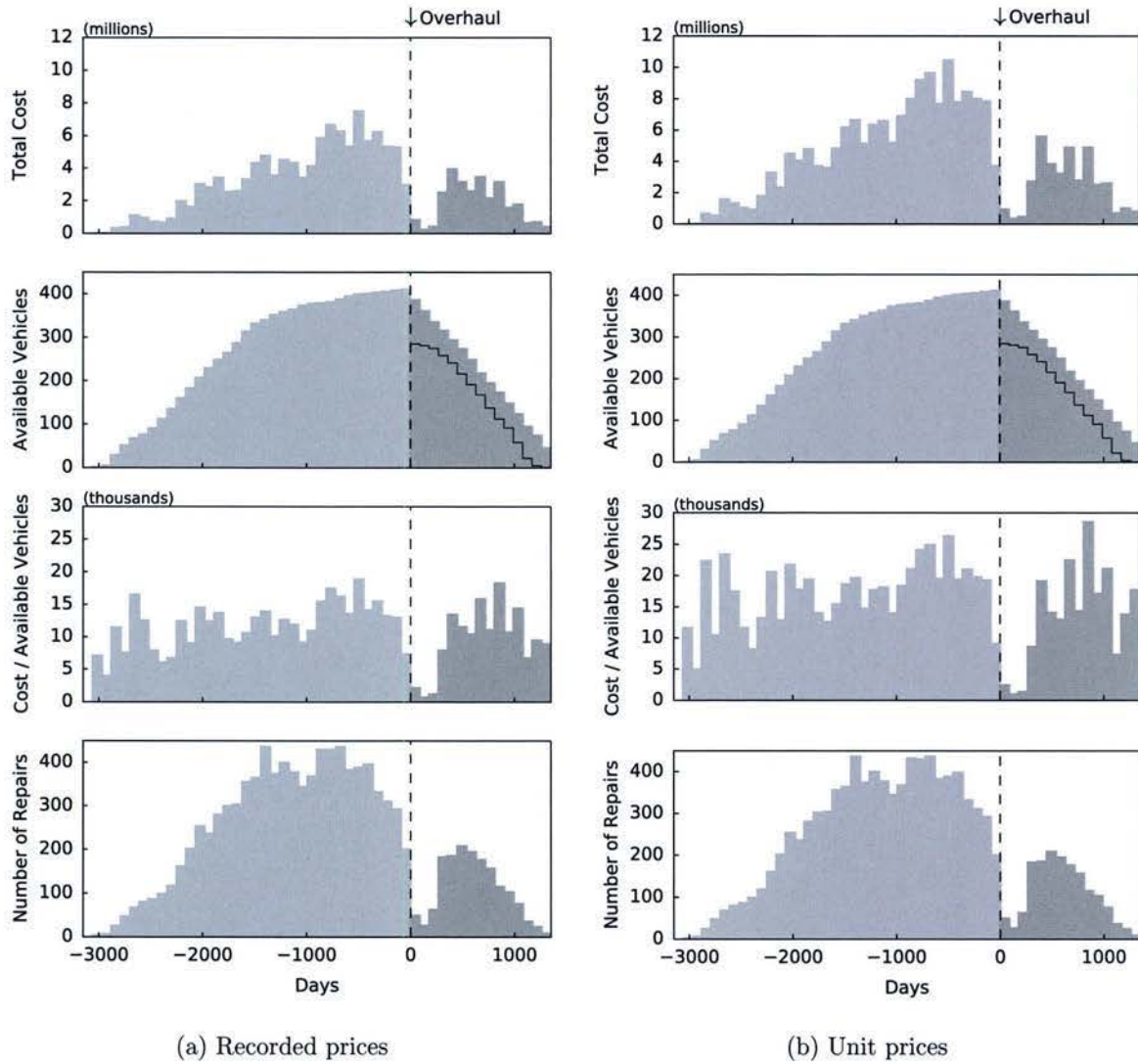


Figure B.1: A comparison between overhaul costs using the recorded values and unit prices of parts

Appendix C

Inconsistent Quantity Required

As described in Section 1.6.2, a number of parts records were observed for the field 'Quantity Required'. Figure C.1 is an extension of this section. The plot was generated using a logarithmic x-scale because there was a lot of variability in the range of quantities. 'Track Shoe,Vehicla' contains one record close to a thousand. The total quantity per vehicle for this particular part is 170. That is the right end of the box in Figure C.1 with unit price \$288. The dots indicate values that exist outside of 90% of records and for several of these examples there are dots magnitudes larger than the majority of records. There were also several low costing items that showed large values for the quantity required. They are tabulated in Figure C.2.

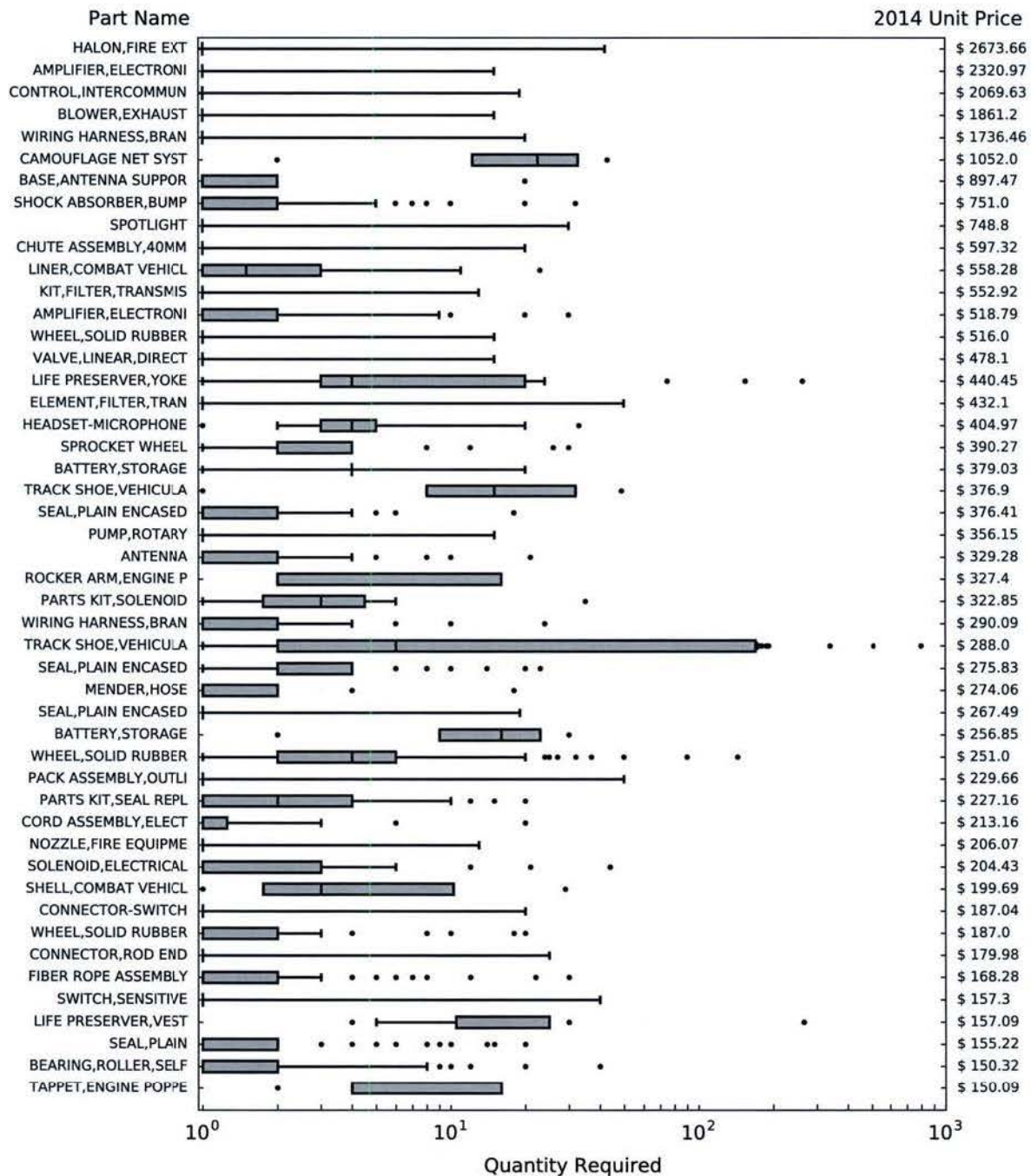


Figure C.1: Inconsistent quantity required records for parts with unit prices greater than \$150

Quantity	Part Name	National Stock Number	Unit Price \$
690	BELT,VEHICULAR SAFE	2540004015308	33.37
599	BELT,VEHICULAR SAFE	2540004015308	33.37
999	BRACKET,ANGLE	5340013956843	25.43
600	WASHER,FLAT	5310008095998	4.71
999	WASHER,LOCK	5310005845272	2.91
800	WHISTLE,BALL	8465002548803	1.96
600	NUT,SELF-LOCKING,HE	5310009826809	0.64
900	NUT,SELF-LOCKING,HE	5310009826809	0.64
999	NUT,SELF-LOCKING,HE	5310009826809	0.64
999	NUT,SELF-LOCKING,HE	5310009826809	0.64
999	NUT,SELF-LOCKING,HE	5310009826809	0.64
1080	NUT,SELF-LOCKING,HE	5310009826809	0.64
1080	WASHER,FLAT	5310008664418	0.49
561	SCREW,CAP,HEXAGON H	5305007247221	0.44
900	SCREW,CAP,HEXAGON H	5305007254183	0.38
948	SCREW,CAP,HEXAGON H	5305007168186	0.31
999	SCREW,CAP,HEXAGON H	5305007168186	0.31
999	SCREW,CAP,HEXAGON H	5305007168186	0.31
999	SCREW,CAP,HEXAGON H	5305007168186	0.31
811	SCREW,CAP,HEXAGON H	5305007168186	0.31
900	SCREW,CAP,HEXAGON H	5305001658098	0.28
600	SCREW,CAP,HEXAGON H	5305001658098	0.28
515	SCREW,CAP,HEXAGON H	5305008471159	0.28
600	SCREW,CAP,HEXAGON H	5305001658098	0.28
999	SCREW,CAP,HEXAGON H	5305002259091	0.27

Figure C.2: Low cost items with a large value for the quantity required. There were several low costing items that showed records with very large quantities

Appendix D

Unit Identifier Codes

The Readiness table was a weekly summary of each unit's progress in terms of fields such as number of items authorized/possessed/dead-lined, supply rate, readiness rate, etc. Only UICs from this table were considered in analysis. The total number of distinct UIC in the main maintenance table, Headers, was 162. 74 of those 162 UICs were found in the Readiness table and the rest are listed in Figure D.1 as UICs not found in Readiness. Almost half of UICs found in Readiness were not found in Headers. On the other hand, of the 65,560 rows of data in Headers, 62,347 contained information with UICs found in Readiness. So 95% of rows of data found in Headers were reliable. The remaining 5% of rows contained information with UICs not found in Readiness.

00207	00407	00880	00930	01283	01495	05172	11001
11104	11140	11330	11350	12009	12015	12190	12310
12660	13420	13700	14110	14151	20181	20252	20970
21410	21640	21670	21808	21814	21825	21834	27125
27127	27128	28301	28323	28327	28328	28331	28339
28360	29027	29028	29060	29071	29076	33800	35100
67700	69009	74746	92840	93002	93022	94142	94145
94216	94221	94321	94412	95101	95103	95104	95106
95111	95114	95305	95306	95310	95314	AB	BB
CV	MFAF5	MFAF7	MFAG2	MFAG8	MFAH7	MFAL1	MG801
MJ132	MR123	MR124	MR130	MSA90	MV123	MV444	X4002

Figure D.1: Owner unit identifier codes from the Headers table that were not found in the Readiness table

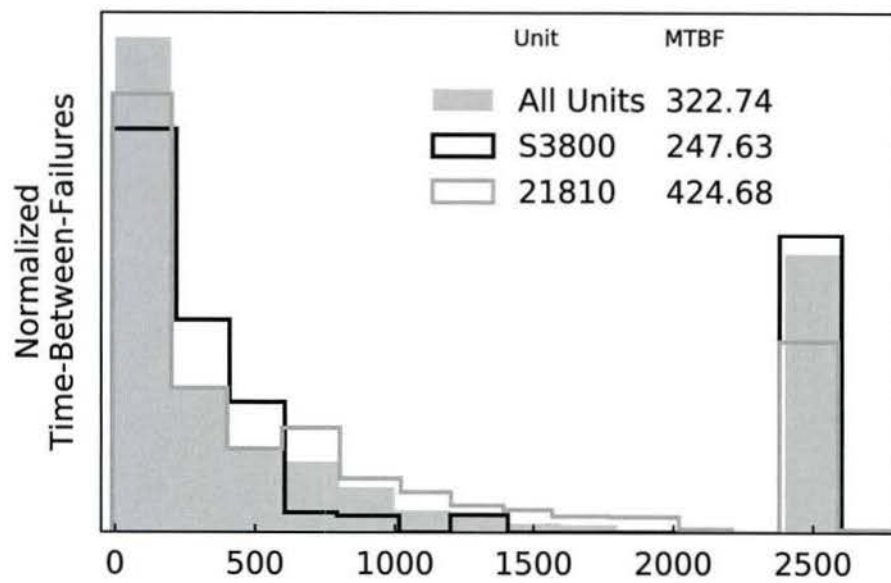


Figure D.2: 'Suspension'

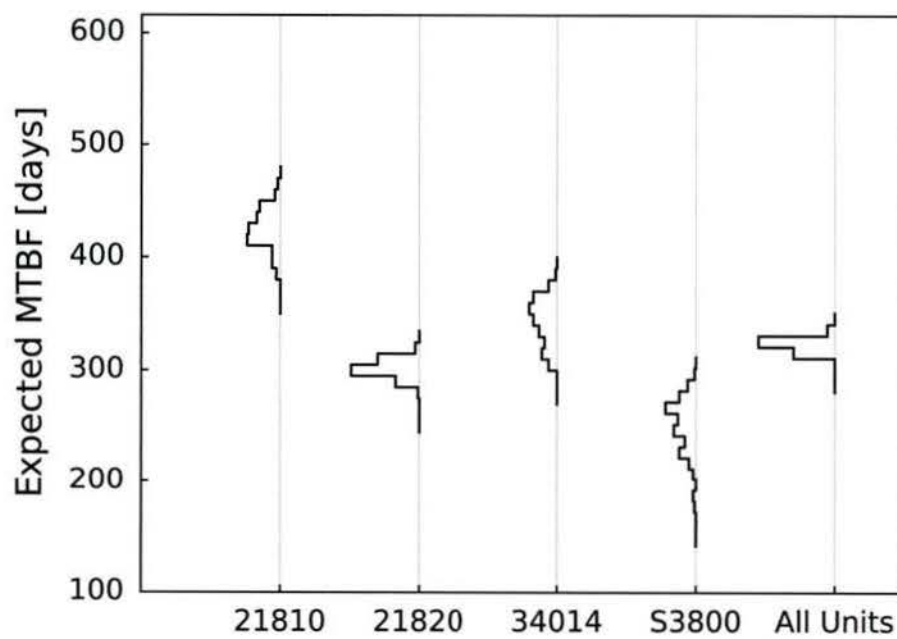


Figure D.3: 'Suspension'

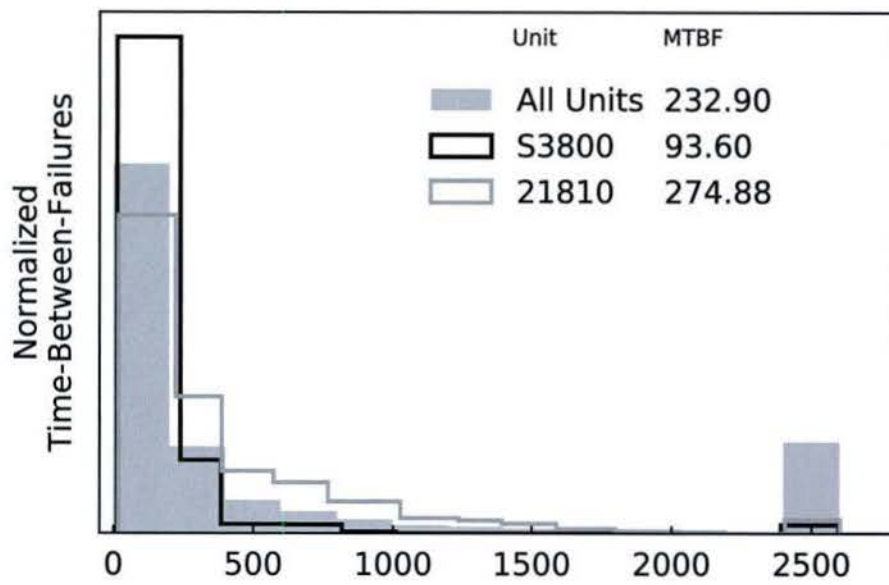


Figure D.4: 'Component'

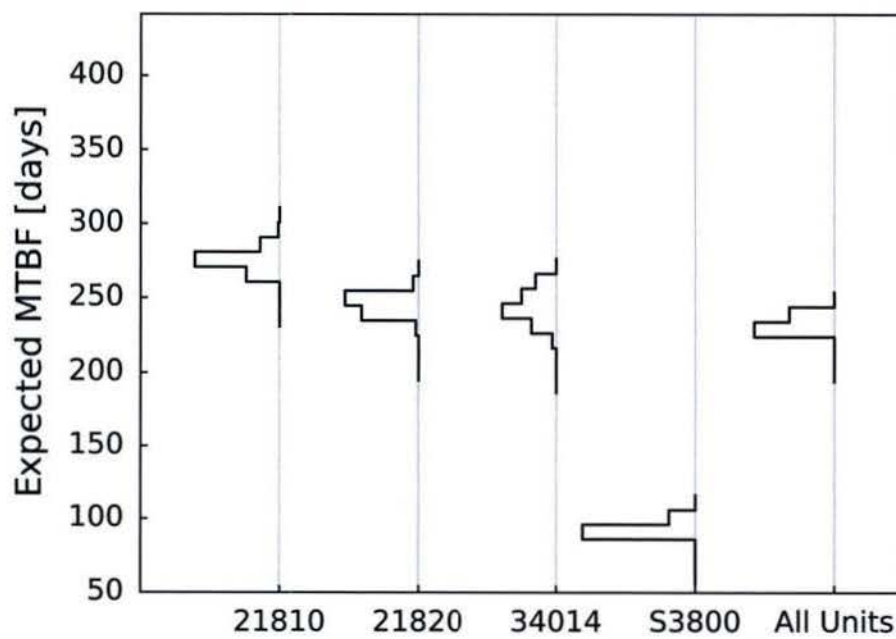


Figure D.5: 'Component'

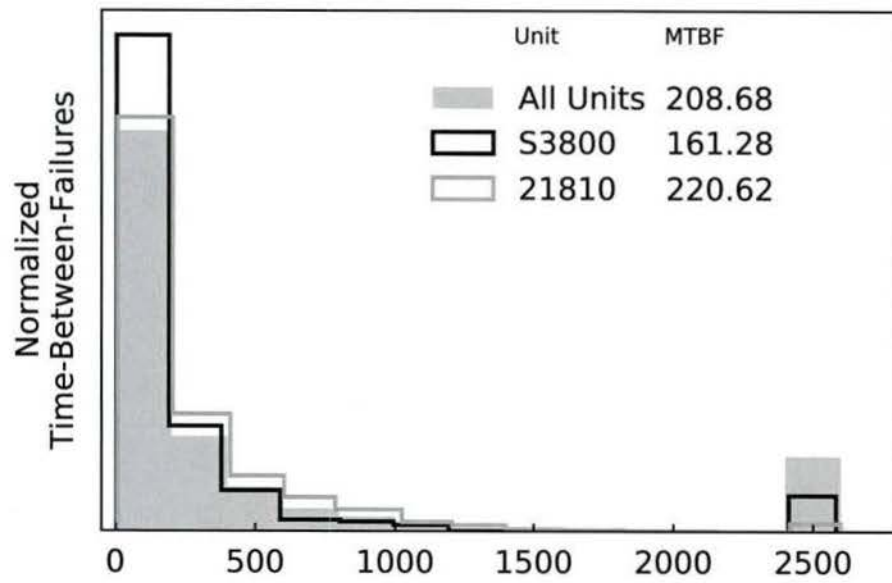


Figure D.6: 'Electrical System'

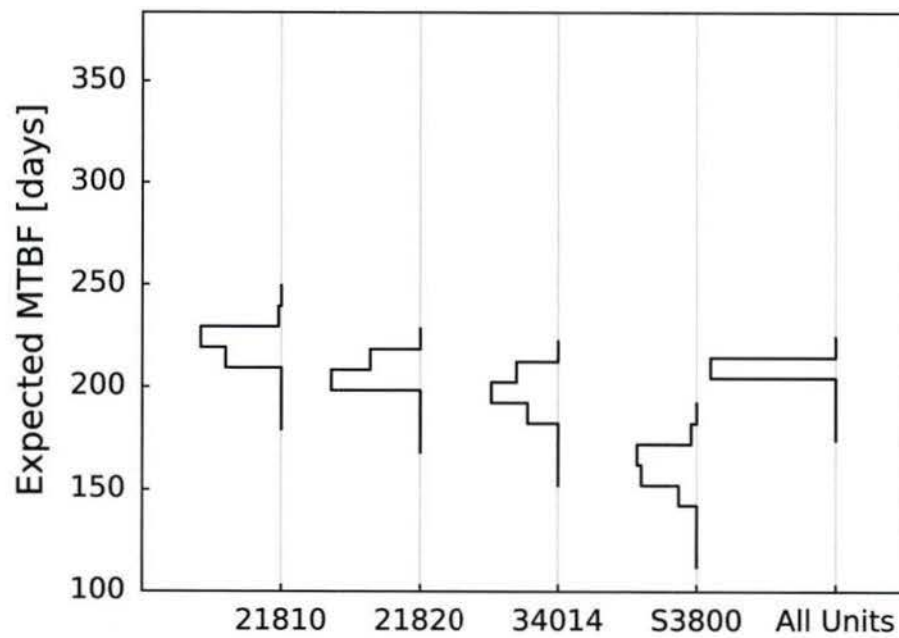


Figure D.7: 'Electrical System'

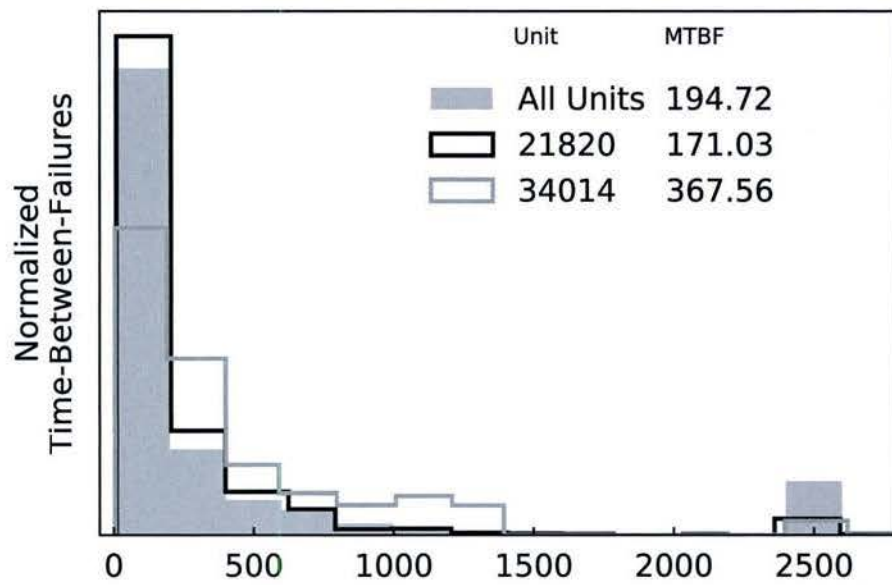


Figure D.8: 'Fire Control System'

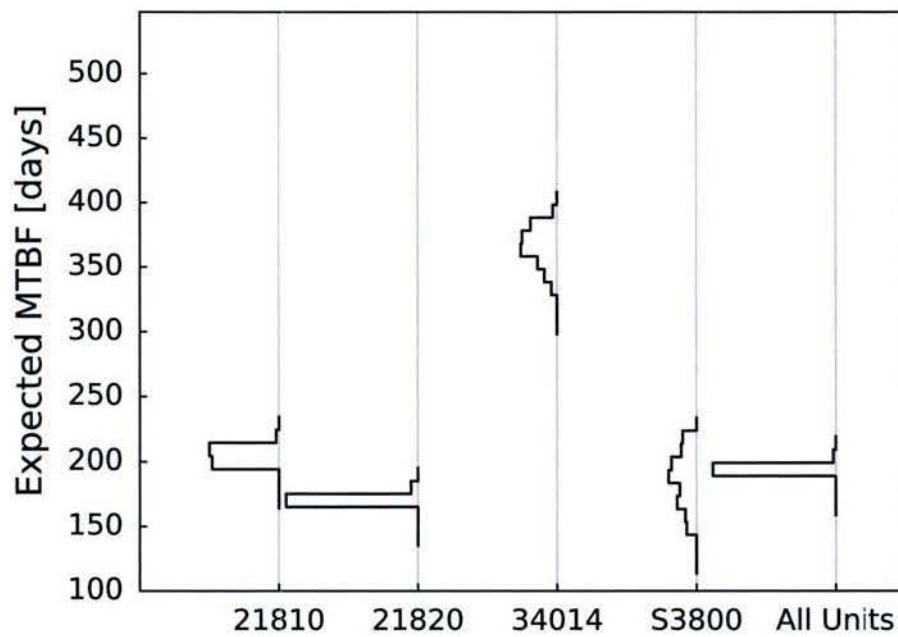


Figure D.9: 'Fire Control System'

Research Program 3:
Subsystem and Component Reliability Synthesis Methodology

This research was conducted under Office of Naval Research Grant N00014-14-1-0789.

Report Generated by:

Golisano Institute for Sustainability
Rochester Institute of Technology
190 Lomb Memorial Drive
Rochester, NY 14623
(585) 475-5101

Abstract

There are several existing bottom-up frameworks for reliability that enable the user to build a comprehensive reliability system. The systematic approach makes these systems very powerful, but populating all unknown parameters from bottom up often presents a significant challenge in practice. In contrast, we propose a simple top-down approach to reliability to facilitate the decision process based on the information that is more easily accessible to the decision maker. The uncertainties are all made explicit and accounted for in a principled way using the standard calculus of probabilities. While the approach can be broadly applied, this report describes it by the way of a specific example, viz. a torsion bar a part of vehicle suspension system. The implementation integrates existing open-source libraries primarily from the Python scientific ecosystem and Modelica. In addition to application of probabilistic calculus to decision making, this report employs methods of multi-criteria decision making using Pareto comparisons and computations based on genetic algorithms.

Chapter 1

Introduction

The ability to predict reliability, maintainability, availability, and life cycle cost for a new system during design phase, or a legacy system which is redesigned to operate in more demanding operating conditions, is essential. The redesigned systems have the potential to use the previous performance data and the information extracted from this data. However, more demanding operating conditions require that the underlying physics be taken into account. In this study we consider a specific component, the torsion bar, as it operates within its parent subsystem, the suspension.

Figure 1.1 shows a prototypical failure rate of a mechanical component as a member of a large population. Note that this is not a bathtub curve, because the simplicity of the design does not give rise to *infant mortality* type failures. It is common to expect the point of time when the failure rates start to increase, indicated by $t_{wearout}$. However, in many applications, this straightforward interpretation maps better on a suitable selected *usage* axis rather than the time axis.

The operational reliability and total ownership cost of high-value long-life assets change as they age. Required data are not always available to enable traditional reliability modeling approaches, and traditional approaches do not take into account the functional importance of different types of failures. The proposed approach rests upon the following two research hypotheses:

\mathcal{H}_1 : Disparate model types can be integrated into a single novel analysis framework that allows for synthesis or decomposition of asset reliability and functionality data.

\mathcal{H}_2 : System identification and estimating techniques, including probabilistic graphical networks, can be used to fill information gaps in reliability models.

The general approach will be illustrated on a torsion bar component of a vehicle suspension system. To facilitate reliability decisions one has to include performance, reliability, and cost parameters into consideration, as well as some interaction with other suspension subsystems.

Figure 1.2 shows a block diagram of the framework as applied to the specific problem at hand. Design parameters (torsion bar length, diameter, and material properties) are specified on the left. These input parameters are transformed into the three type of objectives.

A dynamical model receives its input parameters from analytic, closed-form, engineering calculations or

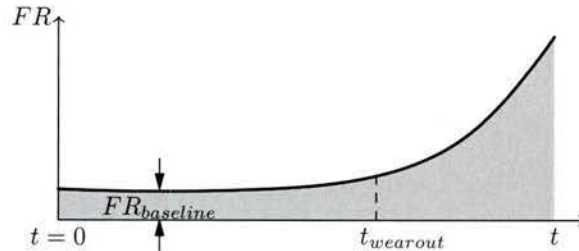


Figure 1.1: A typical wear out curve: the failure rates are approximately constant until a critical point of time $t = t_{wearout}$; after $t_{wearout}$, the failure rates increase exponentially

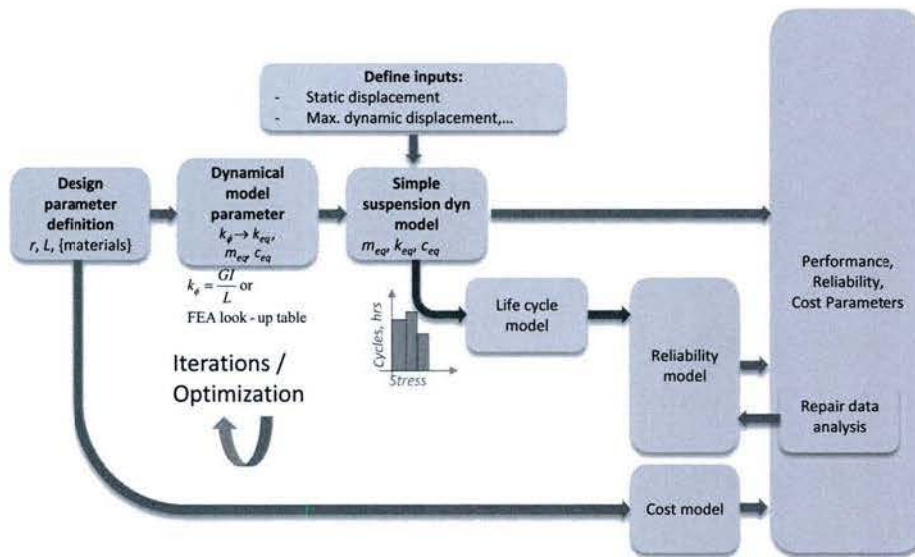


Figure 1.2: Block diagram of the framework

finite element analysis (FEA) and generates performance objectives. For example, performance objectives can be static and dynamic displacement that relate to static or dynamic clearance.

The dynamical model also feeds a life cycle model. The loading of the suspension are simulation inputs and displacements are simulation outputs. The output displacements are mapped into stresses. These stresses can be related to the stress-cycle life model.

The reliability model processes the outputs of the life cycle model with human inputs and exploits the observation from the field. Note, however, that in the case of redesign, field observations have to be appropriately transformed to reflect the change to more demanding operating conditions. This transformation has to include the underlying physics of failure.

The manufacturing cost can be considered as a separate branch. The total cost, on the other hand, must consider reliability to be able to anticipate its maintenance component.

Chapter 2

Background

2.1 Classical reliability approaches

Reliability modeling has a long history. The classical approaches include *reliability block diagrams* (RBDs), *fault tree analysis* (FTA), minimal cut-set methods, Petri nets, Markov models, and Monte Carlo simulations. They are briefly described in turn. The descriptions are at a very high level, with considerable simplifications. A similar review of some of these methods, with more details, is provided in [1]. References for more in-depth descriptions are provided in the subsequent sections.

2.1.1 Reliability Block Diagrams

A system can be considered as a network comprised of series and parallel connection of components or subsystems.

In a system that consists of a series connection of components, any component failure yields the failure; the reliability of the system is the product of reliability of components (subsystems)

$$R_{sys} = \prod_i R_{subsys,i}. \quad (2.1)$$

To illustrate this concept consider the drive train system, which consists of an engine, transmission, and suspension (see Figure 2.1): failure of any subsystem will give rise to system failure.

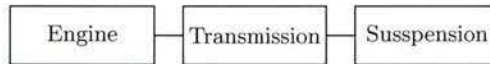


Figure 2.1: RBD: an example of a series connection of reliability components

In a system that consists of a parallel connection of subsystems, it is sufficient that only one of the subsystems be operational

$$R_{sys} = 1 - \prod_i (1 - R_{subsys,i}). \quad (2.2)$$

To illustrate this situation consider the suspension subsystem that consists of two torsional springs connected in parallel (see Figure 2.2): the system can survive for a limited time, with a single torsion bar.

In addition to series and parallel connection, and combinations thereof, another common type of system that can be analyzed using RBDs is the N -out-of- M system, where of M components N must be operational for the system to work. The block diagram looks like that of a parallel connection, but the system reliability is given as the binomial distribution:

$$R_{sys} = \sum_{i=0}^{M-N} \binom{M}{i} R_{sub,i}^{M-i} (1 - R_{sub,i})^i, \quad (2.3)$$

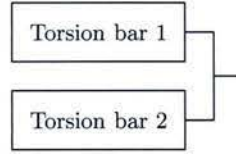


Figure 2.2: RBD: an example of a parallel connection of reliability components

which shows that any combination of less than M failures is sufficient. N -out-of- M systems are employed when there is a built-in redundancy to increased overall reliability.

A reliability block diagram is an effective tool for propagating probabilities of complex systems. However, the main challenge is to arrive at an accurate assignment of the reliability of the components at the bottom, before they can be propagated to the top. In addition, the uncertainties of the reliability values of the components are typically not included in the analyses, which may suggest to a practitioner unwarranted confidence in the results.

2.1.2 Fault Tree Analysis

Fault tree analysis is another graphical method for analysis of reliability and safety of complex systems. Initially developed by Bell Telephone Laboratories in 1962, FTA has been the workforce in the aviation industry. While RBD diagrams are more suitable to depict normal operation, FTA diagrams are more focused on failure paths. An illustration of an FTA model of a torsion bar is shown in Figure 2.3. The roll-ups, or propagation of reliability bottom up are covered quite well in fault tree models, but they also feature a large number of unknown parameters which can be difficult to assess and provide to the model.

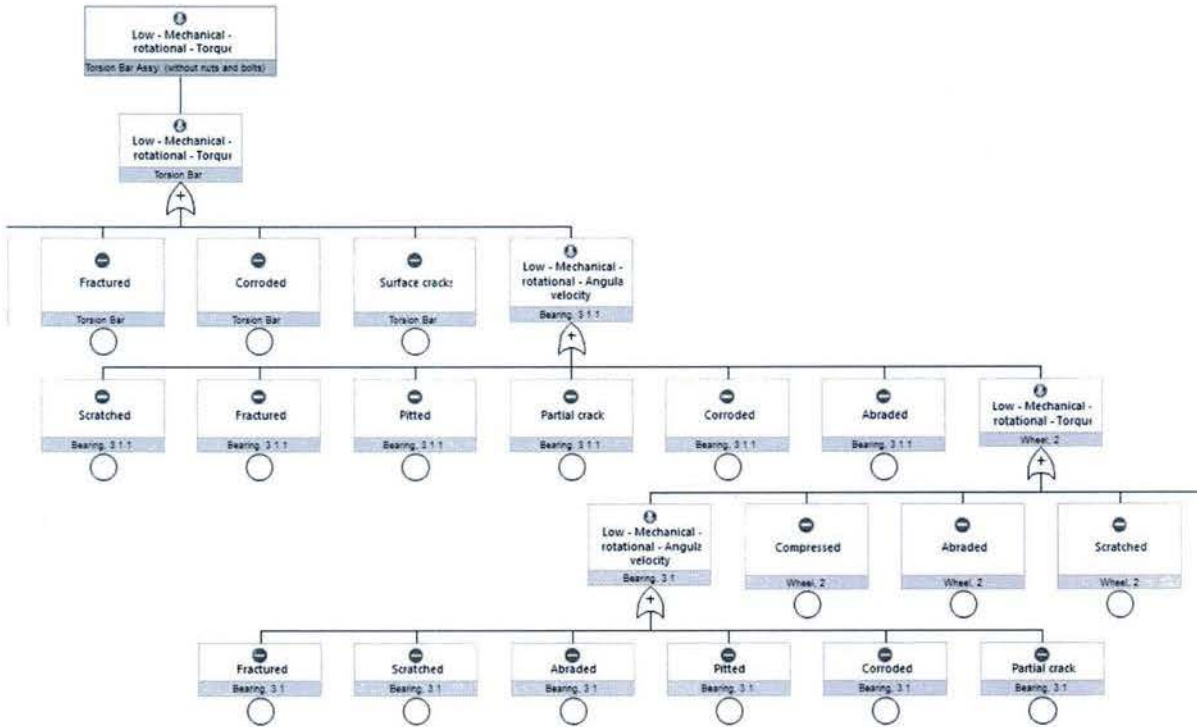


Figure 2.3: FTA: an illustrative example of a torsion bar system, using MAD^e

More details on FTA can be found in [2, 3]. *Maintenance-aware design environment* (MAD^e) [4, 5] is a

model-based software that implements both RBDs and FTAs.

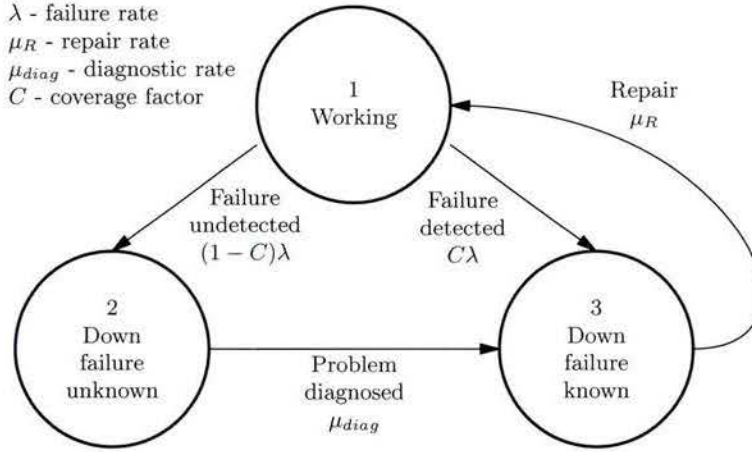


Figure 2.4: Markov Model state machine of a system

2.1.3 Markov Model

A Markov model employs state transition diagrams to model the time spent in each operational and non-operational state. Figure 2.4 illustrates the simplest case, with three states of health and repair:

1. working
2. down with an unknown failure
3. down with a known failure

Failure rate is denoted by λ ¹. Denoting the probabilities of the three states by P_i $i = 1, 2, 3$ ², repair rate by μ_R , diagnostic rate by μ_{diag} , and coverage factor (of known failures) by C , the states are described as follows (note that the equations can be read directly from the diagram of Figure 2.4):

$$\begin{aligned}
 \text{State 1 : } & -\lambda P_1 + \mu_R P_3 = 0 \\
 \text{State 2 : } & C\lambda P_1 - \mu_R P_2 + \mu_{diag} P_3 = 0 \\
 \text{State 3 : } & (1-C)\lambda P_1 - \mu_{diag} P_3 = 0
 \end{aligned} \tag{2.4}$$

Markov models assume that the processes of repair are stationary, that is that the behavior of the system is the same at each point of time and can be characterized by constant failure rate, repair rate, and diagnostic rate. A Markov model is another bottom-up method, that can be used to model different levels of hierarchy; they can be applied to model system, subsystem, or component reliability. For more detailed conceptual and intuitive description of uses in Markov model for modeling complex behavior of fault-tolerant systems, refer to Boyd and Lau [6].

2.1.4 Petri-Nets

Invented by Carl A. Petri ³, Petri Nets are a graphical and mathematical modeling tool for describing concurrent, asynchronous, distributed, parallel, non-deterministic, and stochastic information processing systems.

¹ λ is a typical parameter in exponential distribution $p(t|\lambda) = \lambda e^{-\lambda t}$ for $t \geq 0$ or Poisson distribution $p(n|\lambda) = \frac{\lambda^n}{n!} e^{-\lambda}$.

²Because these states are the only states defined, the probabilities are constrained as $P_1 + P_2 + P_3 = 1$

³This formalism was first described in his PhD thesis 1962, in German; one of the first publications of the key concept in English language can be found in [7]

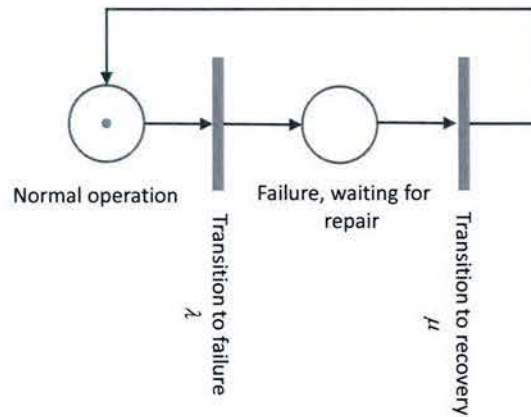


Figure 2.5: A simple Petri Net

A Petri net consists of a set of places, graphically represented as circles; set of transitions, drawn as bars; and a set of directed arcs, represented by arrows. Figure 2.5 shows a simplified example of a Petri net with two places; normal operation and failure, and two transitions; transition to failure and transition to recovery. This net can describe the failure and recovery of a simplex system or a component [1].

A comprehensive tutorial on Petri nets is provided by Murata [8]. Hierarchical models for system reliability, maintainability, and availability using generalized stochastic Petri nets is given by Ammar *et al.* [9].

2.2 Probabilistic decision making

When dealing with complex non-decomposable models where ballpark estimates of reliability suffice, stochastic simulation has been identified as a powerful technique for coherent inferencing [10]. The only principled way to handle uncertainty is using probabilities. Any betting system that goes against probabilities loses in the long run, Bruno de Finetti [11]. People think in terms of stories and probabilistic programming has the potential to unlock narrative explanations of data [12, 13]. Probabilistic reasoning has a solid epistemological foundation, it is compatible with human intuition, and it is amenable to network representation and parallel and distributed computation [14].

For example Figure 2.6 illustrates a typical reliability thought process where a decision can be influenced by the input from the manufacturer, expert knowledge, existing physics-based models and data.

Probability has been recognized as extended logic in 1940s (see Cox [15, 16]) and greatly popularized by Jaynes [17] and others [18, 19, 20, 21, 22, 23]. The problem with probabilistic models was their computational requirements. Markov Chain Monte Carlo (MCMC) method, that also originated in the 1940s [24], has become a standard tool for this computation.

Probabilistic (graphical) models had notable successes in the sixties and seventies, but then fell out of favor to some other AI approaches (e.g. fuzzy logic [25, 26], Dempster-Shafer evidence theory [27]). Their renaissance of probabilistic model began in the late 1980s, and started with theoretical development, but computational power did not allow the explosion of solutions that we have witnessed in the very recent past. The graphical approaches will allow domain experts to take advantage of the framework. Many new applications including medical diagnostics, analysis of genetic and genomic data, speech recognition, natural language processing, analysis of market data, and fault diagnosis, which can be extended to reliability.

The potential of the probability networks has been recognized in the 1980s [10, 28]. More recently excellent tutorials (e.g. [29, 30]) and books (e.g. Jordan [31], Bishop [32], Koller and Friedman, [33], Gelman *et al.* [34], and Theodoridis [35]) have become available. In the recent past there has been a great deal of development of software tools, including BUGS [36], JAGS [37], PyMC [38, 12], Church [39], Stan [40], Infer.NET [41], that facilitates the analysis and make it more mainstream.

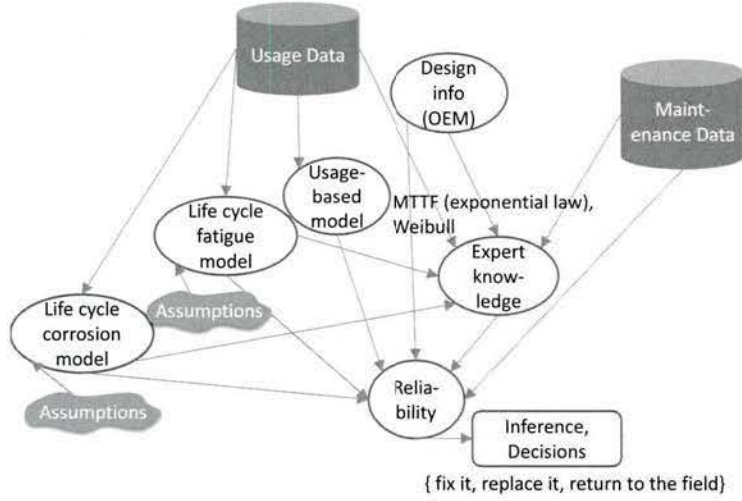


Figure 2.6: Example probabilistic decision

2.3 Multi-criteria optimization

The optimization problem that the framework faces can be classified as a nonlinear, multi-criteria optimization problem. The goal is to explore the space of input parameters denoted by $\mathbf{x} = \{x_1, x_2, \dots, x_n\}$ with respect to meeting a set of objectives $\mathbf{f} = \{f_1, f_2, \dots, f_k\}$. f_i are the objective functions that map the n -dimensional parameter space \mathbf{x} into real numbers $f_i: \mathbb{R}^n \rightarrow \mathbb{R}$.

The input parameters are typically design parameters that can be perturbed to arrive at the best three vectors, viz. performance parameters \mathbf{p} , reliability parameters \mathbf{r} , and cost parameters \mathbf{c} , are arranged in a single vector of objectives \mathbf{f}

$$\mathbf{f} = [\mathbf{p}^T \quad \mathbf{r}^T \quad \mathbf{c}^T]^T, \quad (2.5)$$

which is subjected to multi-criteria optimization.

The usual mathematical formulation of the problem is given as follows [42]

$$\begin{aligned} \min & \mathbf{f}(\mathbf{x}) \\ \text{s.t.} & \mathbf{x} \in \mathbb{S} \end{aligned} \quad (2.6)$$

where \mathbb{S} is the domain of the input parameters, defined by set of equalities and inequalities, i.e. $\mathbf{x} \in \mathbb{S}$ is defined as

$$\begin{aligned} g_j(\mathbf{x}) & \geq 0 \\ h_m(\mathbf{x}) & = 0 \\ x_{nL} & \leq x_n \leq x_{nU} \end{aligned} \quad (2.7)$$

Unlike real numbers, vectors cannot be ordered and their comparison can be made according to Pareto, which compares all components of \mathbf{f} . Decision vector \mathbf{x}^* and its corresponding decision vector \mathbf{f}^* are *Pareto optimal* if

$$\begin{aligned} \forall \mathbf{x} \in \mathbb{S} \wedge \forall i \in \{1, 2, \dots, k\}, \quad & f_i(\mathbf{x}^*) \leq f_i(\mathbf{x}) \\ \forall \mathbf{x} \in \mathbb{S} \wedge \exists j \in \{1, 2, \dots, k\}, \quad & f_j(\mathbf{x}^*) < f_j(\mathbf{x}) \end{aligned} \quad (2.8)$$

In other words, a Pareto solution is the solution that cannot be improved in one of the objectives without making other objectives worse.

An alternative to Pareto comparison is preference based multi-objective optimization where the user specifies the relative importance of the components of the objective vector via weights w_i (organized into

a vector $\mathbf{w} = [w_1 \dots w_n]^T$). In this approach the multi-objective optimization reduces to a single objective optimization where the single objective is the weighted average of the objectives [43].

$$\underset{\mathbf{w}}{\operatorname{argmin}} [\mathbf{w}^T \mathbf{f}] = \underset{\mathbf{w}}{\operatorname{argmin}} \left[\sum_{i=1}^k w_i f_i(\mathbf{x}) \right] \quad (2.9)$$

Single-objective optimization is generally faster than Pareto optimization, but preference-based optimization has an important limitation that the user must prescribe the relative importance in advance, relying on the user to properly guess at the trade-offs among conflicting requirements. By contrast, Pareto optimization allows the user to select the trade-offs after they have been observed.

In practice one needs good stochastic optimization tools to explore the parameter space, where one biases the search toward a region where a solution is plausible and allows randomness to guide the rest of the search [44]. The standard approaches to stochastic learning are simulated annealing (a Boltzmann learner), or evolutionary-based (genetic algorithm, genetic programming, or, more recently, particle swarming).

Evolutionary algorithms are gaining in popularity because of their natural acceleration by using parallel processing. Some of the key algorithms are SPEA 2 [45] and NSGA II [46] (and its recent improvement [47]).

The outcome of the optimization is a multi-dimensional surface, which can be examined for trade-offs by taking 2D projections (or if they are convex and smooth, 3D projections) which may require many plots – lots of pairs for many parameters; for 2D with n parameters there are $n(n-1)/2$ plots. More sophisticated projection tools are also emerging [48].

PyGMO [49] is a scientific library for easy distribution of massive optimization tasks over multiple CPUs. It is written in C++ and exposed in Python. In our experiments, PyGMO performed better than DEAP, which is a pure-Python library that also implements these algorithms and readily integrates into the framework [50].

AMPL [51] is a general purpose optimization tool that was briefly considered, but was not adopted because it does not naturally integrate into the framework based on the Python scientific ecosystem. The DAKOTA (Design Analysis Kit for Optimization and Terascale Applications) is a powerful toolkit with a flexible and extensible interface between simulation codes and analysis methods [52] and was carefully considered. However, the large the power of FMU paradigm and Python ecosystem have already been widely adopted and have great potential to further grow.

Pareto optimization has been applied to similar problems before. For example Jamali et. al [53] introduced the idea of crisp and fuzzy threshold values and how they can be used in genetic algorithms to find the best optimal solutions. Robust design optimization was used to reduce the effect of uncertainty in the parameters. Reliability-based design optimization includes metrics to determine probabilistic constraints to reduce the failure of meeting the design criteria. The emphasis was on meeting the design criteria and having the solution meet a predetermined failure rate. Deb et al. [54] addressed the issue regarding uncertainties in the design variables and the parameters and how to solve multiple different problems where this is inevitable. The solutions must fall within a specified range of probability of failure. Multiple ways to determine a solutions reliability are discussed and compared against each other. Methods to perform reliability based optimization are also explained and how to use them in unison with the determination of a solutions reliability. NSGA-II is implemented in the process for its ability to sort through solutions and is combined with the reliability optimization methods to produce the best set of solutions that fit the optimization criteria and also meet the minimum probability of failure.

Chapter 3

Framework description

This chapter discusses the main building blocks of the framework: the performance, reliability, and cost models. The inputs to the framework are design parameters, geometrical parameters of the torsion bar (length L and radius r), and material properties (modulus of rigidity G) of the torsion bar. In this section we describe the model in detail. The next chapter integrates the framework in a couple of relevant applications. Appendix D provides details on installation of the required open-source software libraries.

3.1 Performance model

Performance modeling is essentially modeling of the physical system. Because the torsion bar is a part of the suspension system, the physical model is that of vehicle suspension. The simplest suspension model is a single degree of freedom (SDF) spring-mass system

$$m_v \ddot{y}_{Chassis} + d_v (\dot{y}_{Chassis} - \dot{y}_{GND}) + k_v (y_{Chassis} - y_{GND} - h_0) = 0 \quad (3.1)$$

where m_v , d_v , and k_v denote effective mass, effective damping, and effective spring constant of the vehicle, respectively, while $y_{Chassis}$ is vertical displacement of the chassis and y_{GND} is the terrain profile (see Figure 3.1). The nominal height of the vehicles (without displacements due to gravity) is h_0 and is a constant. Defining the position u as (see Figure 3.1)

$$u = y_{GND} + h_0 - y_{Chassis}, \quad (3.2)$$

Eq. (3.1) becomes

$$m_v \ddot{u} + d_v \dot{u} + k_v u = -m_v \ddot{y}_{GND} \quad (3.3)$$

The model can be subjected to different performance test, e.g. step response (when a vehicle rolls over a step of a given height), or a periodic response to simulate a rough terrain.

The dynamical model is a single-degree of freedom (SDF) spring-dash-mass system. It employs an equivalent linear spring based on a torsion bar and nonlinear, direction-dependent, empirical model of the shock. Figure 3.9 shows the block diagram of the model.

3.1.1 Equivalent spring constant

The key component of interest of this study is the torsion bar. The first-order model of a torsion bar is a torsional spring k_ϕ . When connected to the arm and twist angle is transformed into a linear displacement it becomes a linear spring given by (see Appendix A for the complete derivation)

$$k_{eq} = \frac{k_\phi}{l_{arm}^2} = \frac{GI_p}{l_{arm}^2 l} \quad (3.4)$$

where G , I_p , l_{arm} , and l are modulus of rigidity, area moment of inertia, length of the arm that connects the torsion bar to the wheel, and length of the torsion bar, respectively.

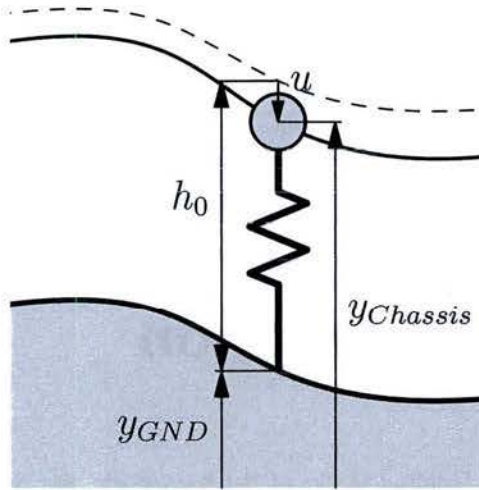


Figure 3.1: Positions and displacement

The effective vehicle suspension spring constant, with twelve torsion bars, is approximately¹

$$k_{veh} = 12 \frac{k_{\phi}}{l_{arm}^2} \quad (3.5)$$

The linear model of the torsional spring is implemented in Modelica, by using a simple kinematic transformation illustrated in Figure 3.2 (see also Appendix A).

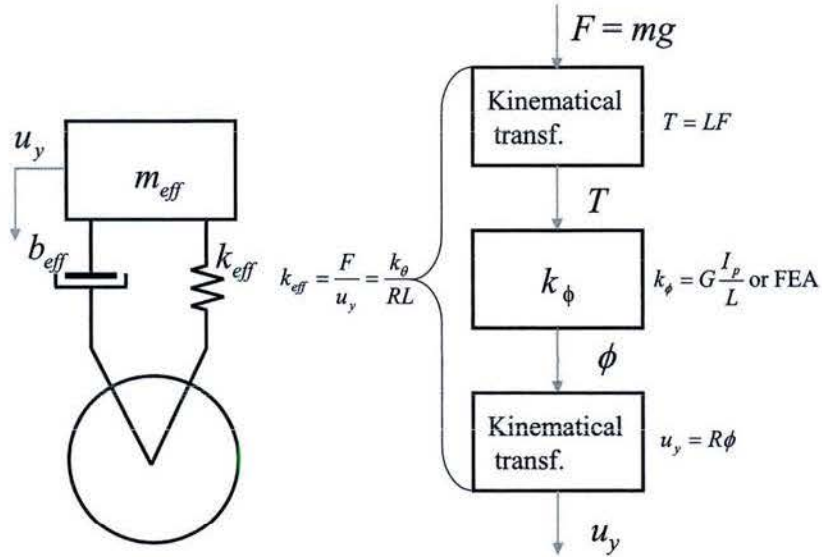


Figure 3.2: Kinematic transformation that converts torsional into a linear spring

Figure 3.3 shows a Modelica implementation of the composite spring, where Figure 3.3a displays the code for the built-in implementation of a linear spring and Figure 3.3b shows the modified code. The modified code includes rotational spring constant and an additional geometry parameter, the length of arm l_{arm} .

¹All vehicle configurations of interest employ more than one type of torsion bar, but for the first-order model, using the same torsion bar is a good starting point.

```

model Spring "Linear 1D translational spring"
  extends Translational.Interfaces.PartialCompliant;
  parameter SI.TranslationalSpringConstant c(final min = 0, start = 1) "Spring constant";
  parameter SI.Distance s_rel0 = 0 "Unstretched spring length";
equation
  f = c * (s_rel - s_rel0);

```

(a)

```

encapsulated model compSpring
  import Interfaces = Modelica.Mechanics.Translational.Interfaces;
  import SI = Modelica.SIunits;
  extends Interfaces.PartialCompliant;
  // constant SI.RotationalSpringConstant k_theta(final min = 0, start = 1) "Rotational spring constant";
  parameter SI.ShearModulus G = 80700000000 "shear modulus in GPa";
  parameter SI.Distance BarL = 2.203 "Torsion Bar Length in meters";
  parameter SI.Distance r = 0.02515 "Torsion Bar Radius in meters";
  parameter SI.Distance ArmL = 0.6 "Lever arm Length in meters";
  parameter Real N = 12 "Number of Springs";
  SI.MomentOfInertia Ip = 3.1415 * r ^ 4 "Area moment of Inertia";
  /* parameter */
  SI.TranslationalSpringConstant Klinear = G * Ip / BarL / ArmL ^ 2 "equivalent linear spring constant";
  //parameter SI.Distance H = 5 "Angle arm u = P*theta";
  // parameter SI.Distance L = 3 "Force arm T = L*F";
  parameter SI.Distance H = 2 "Vehicle Height";
equation
  // Ip = 3.1415 * r ^ 4 / 2;
  // Klinear = G * Ip / BarL / ArmL ^ 2;
  f = N * (Klinear * (s_rel - H));
  // f = k_theta / 18 * L * (s_rel - s_rel0);
  annotation(Documentation(info = "<html>
    <p>
      A <i>linear 1D translational spring</i>. The component is representative of a torsion Bar. The H parameter is representative of the vehicle's Height and
      is not a function of the linear representation of the torsional spring
    </p>
    </html>"), Diagram(coordinateSystem(preserveAspectRatio = true, extent = {{-100, -100}, {100, 100}}), graphics = {Line(points = {{-100, 0}, {-100, 65}},
    color = {128, 128, 128}), Line(points = {{100, 65}}, color = {128, 128, 128}), Line(points = {{-100, 60}, {100, 60}}, color = {128, 128, 128}),
    Polygon(points = {{90, 63}, {100, 60}, {90, 57}, {90, 63}}, lineColor = {128, 128, 128}, fillColor = {128, 128, 128}, fillPattern = FillPattern.Solid),
    Text(extent = {{-56, 66}, {36, 81}}, lineColor = {0, 0, 255}, textString = "s_rel", Line(points = {{-86, 0}, {-60, 0}, {-44, -30}, {-16, 30}, {14, -30},
    {44, 30}, {60, 0}, {84, 0}}, color = {0, 0, 0}}), Icon(coordinateSystem(extent = {{-100, -100}, {100, 100}}, preserveAspectRatio = true, initialScale =
    0.1, grid = {2, 2}), graphics = {Line(points = {{-60, -90}, {20, -90}}, Polygon(lineColor = {128, 128, 128}, fillColor = {128, 128, 128}, fillPattern =
    FillPattern.Solid, points = {{50, -90}, {20, -80}, {20, -100}, {50, -90}}), Text(lineColor = {0, 0, 255}, extent = {{-150, 90}, {150, 50}}, textString =
    "tname"), Line(points = {{-95, 0}, {-60, 0}, {-44, -30}, {-16, 30}, {14, -30}, {44, 30}, {60, 0}, {100, 0}}), Text(extent = {{-130, -45}, {150, -75}},
    textString = "c=k_phi / 18 * L * (s_rel - s_rel0)");
  end compSpring;

```

(b)

Figure 3.3: Implementation of the composite linear spring in modelica. (a) Default Modelica code for a linear spring (b) Modified code to model the composite spring

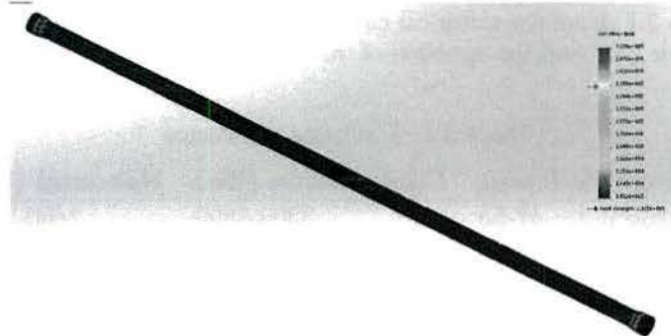


Figure 3.4: Deformed FEA mesh of a torsion bar

The dynamical model does not have to employ the first-order model for the spring constant. Alternatively, it can be based on the empirical data, or *finite element analysis* (FEA). Figure 3.4 shows a deformed mesh of a FEA model for the torsion bar.

The spring constant can be extracted from the numerical stress-strain curve, which can be scaled as a force-displacement, or, in this case, as torque-angle curve. Figure 3.5) shows torque T as a function of angle ϕ . The dashed arrows signify the direction of the simulation: the first loading takes place from point A to point B , then as the the magnitude of the torque is gradually reduced, the point traverses $B-C$ path on the torque-angle curve. During the next loading, the operating point moves from point C back to point B . The line $B-C$ is the actual pre-stressed operating point and the slope of this segment is used as the torsional spring constant k_ϕ .

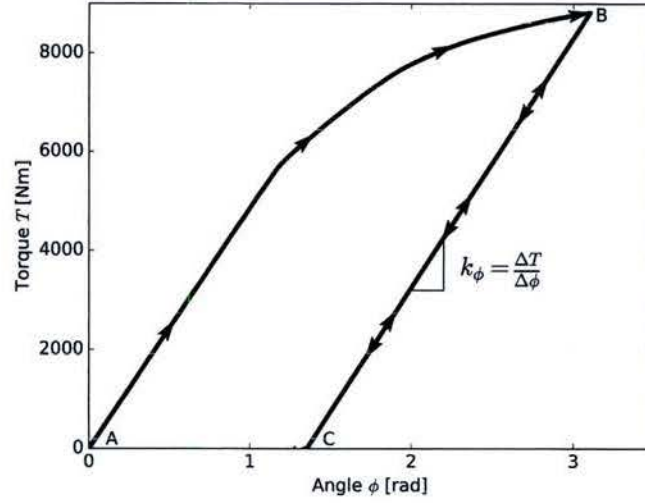


Figure 3.5: FEA-calculated torque-angle curve

3.1.2 Shock Absorber Analysis

In the first approximations, a shock absorber is modeled as a linear damper, that linearly relates force F and speed v

$$d = \frac{F}{v} \quad (3.6)$$

More accurate model of the shock is obtained from the empirical data from the original equipment manufacturer [55]. Table 3.1 shows the empirical data, where the cycling rate is given in cycles per minute (cpm) and force in pounds (lbs) and the direction of the force is distinguished as *compression* and *rebound*.

Table 3.1: Damping resistance

Cycling rate (cpm)	Compression (lbs)	Rebound (lbs)
47-53	3300-6800	2400-3300
94-106	5100-7100	2500-3600
141-159	5200-7300	2700-3900
282-318	5600-8200	3100-4700
564-636	6400-11100	3400-9400

The graphical representation of the data in Table 3.1, after converting to SI units, is shown in Figure 3.6. The data is shown as the black trace with error bars. The red dashed line signifies the fit. Table 3.2 shows the fitted piece-wise-linear model in a tabular form.

Table 3.2: Damping model

Velocity (m/s)	Damping (kg/s)
-0.79 to -0.07	21,703
-0.07 to 0.07	265,632
0.07 to 0.79	22,620

Modelica implementation of the shock model is shown in Figure 3.7 as the code.

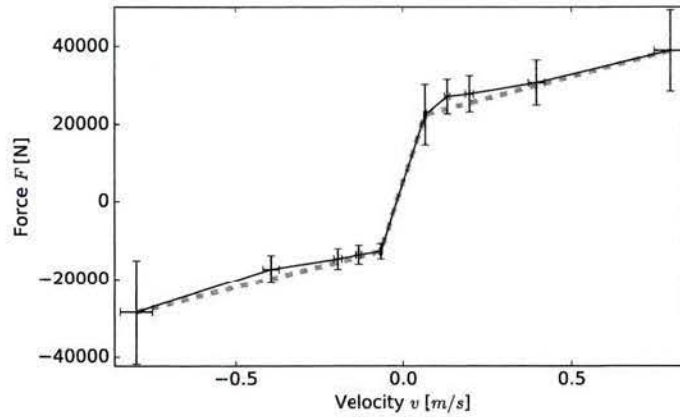


Figure 3.6: Damper characteristic

```

model nonLinDamp "Linear 1D translational damper"
extends Modelica.Mechanics.Translational.Interfaces.PartialCompliantWithRelativeStates;
parameter Modelica.SIunits.TranslationalDampingConstant d0 = 265632.3 "Damping constant in the linear range";
parameter Modelica.SIunits.TranslationalDampingConstant dM = 22620.01 "Damping constant for large rebound";
parameter Modelica.SIunits.TranslationalDampingConstant dP = 21702.98 "Damping constant for large compression";
parameter Modelica.SIunits.Velocity vM = 0.07 "velocity edge";
Modelica.SIunits.Force F1;
parameter Real N = 8 "Number of Dampers";
extends Modelica.Thermal.HeatTransfer.Interfaces.PartialElementaryConditionalHeatPortWithoutT;
equation
// z = d0 * v_rel;
F1 = if v_rel < (-vM) then dM * v_rel + (d0 - dM) * (-vM) else if v_rel > vM then dP * v_rel + (d0 - dP) * vM else d0 * v_rel;
z = F1 * N;
lossPower = z * v_rel;
annotation(Documentation(info = "<html>
<p>
<b>Nonlinear, velocity dependent damper</b>. The Nonlinear has 4 changeable input variables. the d variables are the dampening constant found for each
distinct part of the dampers curve. The vM term is the velocity at which the damping constant varies from the linear region. For this damper the vM is
both the upper and lower bound for the linear region.
</p>
</html>")));
end nonLinDamp;

```

Figure 3.7: Modelica implementation of the shock model.

3.1.3 Effective Mass

Effective mass is computed using distributed loads on individual loads. Figure 3.8 illustrates the distribution of loads for one vehicle configuration. There are three different vehicle configurations for the vehicles of interest. Their masses (in kg) are provided in Table 3.3.

In the Modelica implementation, described in the next section, the user can specify the mass as a parameter at the time of the execution of the simulation. In particular, the user can select a vehicle configuration and then choose whether to simulate an average model (total mass $m_{eff} = \sum_i m_i$ and total spring constant $k_{eff} = 2k_{tbar}$), or worst case model (highest weight per vehicle $m_{eff} = \max(m_i)$ and a torsion bar pair $k_{eff} = 2k_{ttbar}$).

3.1.4 Simulations

The model is implemented using the graphical user interface of OpenModelica Connection Editor ², with the spring constant and shock modified according to the code listing of Figure 3.3b and Figure 3.7, respectively.

²Refer to <https://www.openmodelica.org/>

Table 3.3: Distributed vehicle weight (kg) for three different configurations

Wheel	L1	L2	L3	L4	L5	L6	R1	R2	R3	R4	R5	R6
VCW	2095	3120	2935	1375	1120	690	1765	2935	2815	2255	1345	190
GCW	2710	2675	3030	1790	1515	1245	1910	2955	3170	2590	1835	810
MK	2030	3475	3105	1980	1670	1590	2090	3150	3160	2600	2150	1130

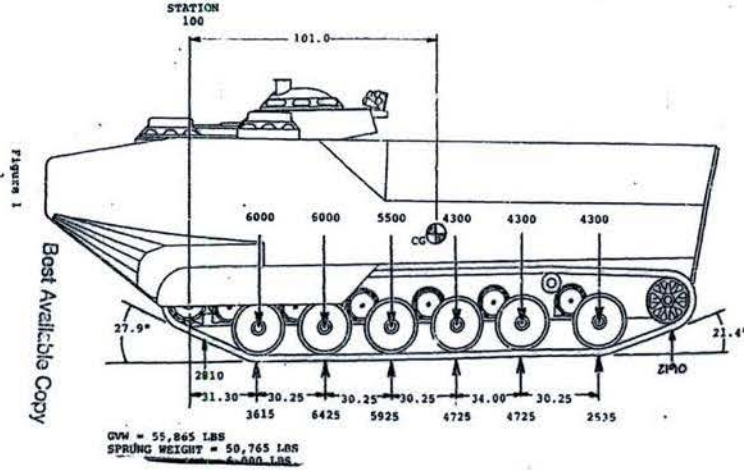


Figure 3.8: Illustration of distributed weight of a vehicle (lb)

Figure 3.9 shows the system level model. The force due to gravity is applied to the mass of the vehicle that is attached to the top of the spring. This force produces static displacements due to gravity. The displacement of a rough terrain is applied to the bottom of the spring.

The dynamical simulations are executed in the Python ecosystem's Jupyter Notebook, using JModelica's FMU/FMI interface between Modelica and Python (see Appendix D for installation details of Jupyter Notebook and JModelica).

Two types of displacement are considered: roll-over a step, or driving over a rough terrain. The vehicle can be simulated as a *single-wheel*, worst(best)-case model, or *average vehicle*. Figure 3.10 shows the simulation interface: the user can select the mass by using either the average vehicle mass, or single wheel and specifying the vehicle configuration; the user can adjust the number of springs and shock absorbers; and the height of the vehicle. Two types of simulations are implemented: the *step test*, where vehicle rolls over a step, and the *sine test*, where the rough terrain is approximated by a sinusoid. For the step test, the user can specify two parameters, the height and the offset; for the sine test, the user can specify the amplitude and the frequency. After displacements u are computed, they can be converted to twist angles ϕ according to

$$\phi = \frac{u}{l_{arm}}, \quad (3.7)$$

where l_{arm} is the length of the arm that connects a wheel and a torsion bar. For a given event, a step, or a cycle, the maximum displacement is the most important

$$\Delta\phi_{max} = \frac{|u|_{max}}{l_{arm}}. \quad (3.8)$$

The maximum twist angle is converted to maximum stress as follows (for a detailed derivation, see Appendix A)

$$\tau_{max} \approx G \frac{r \Delta\phi_{max}}{l}, \quad (3.9)$$

where G , l , and r are modulus of rigidity, torsion bar length, and torsion bar radius, respectively.

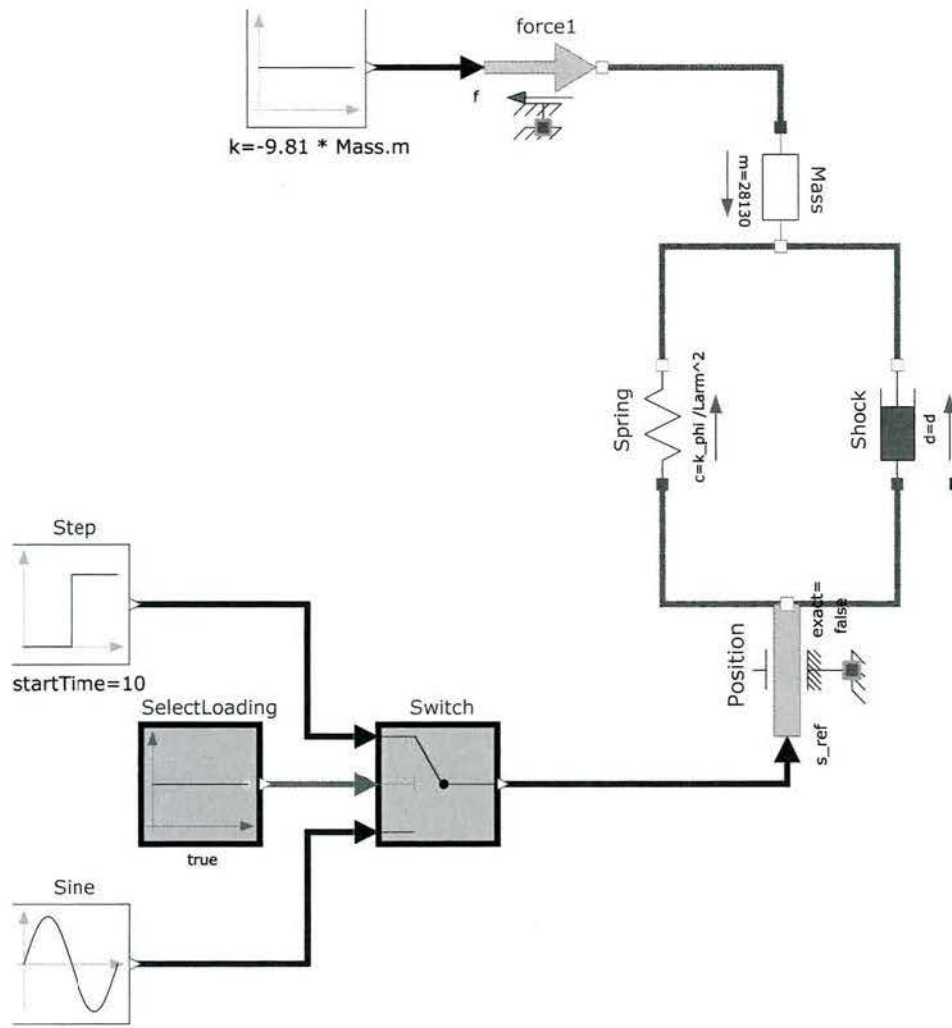


Figure 3.9: The model block diagram.

Once the maximum stress associated with an event (driving over a step, or over a bump) is estimated, it can be related to stress-cycle data, as illustrated in Figure 3.11. For this case of driving over a large step, with height $h = 1$ m, the maximum step is higher than the endurance limit and is expected to degrade the torsion bar's reliability. The next section will explore the fatigue life cycle model in detail. The relationship between the performance parameters, such as displacements u and the life cycle models will be revisited in the next chapter.

3.2 Reliability Model

3.2.1 Life cycle model

Life cycle model is based on empirical data obtained from *stress-cycle* (SN) curves³. Several sets of specimen were subjected to different conditions (e.g. no prior damage, different exposure to corrosion, different methods for corrosion removal) and obtained. For example, Figure 3.12 shows SN data of eleven samples that were not subjected to corrosion. The samples were subjected up to one million cycles. Thus, in this

³Sometimes referred to as stress-life curves.

Avg. Vehicle		Single Wheel		Step Test		Sine Test	
Veh Load Type		VCW		Step Height		-1	
Vehicle Height		1.5		Step Offset		1	
Num. of springs		12		position		-	
Num. of shocks		8		Simulate			

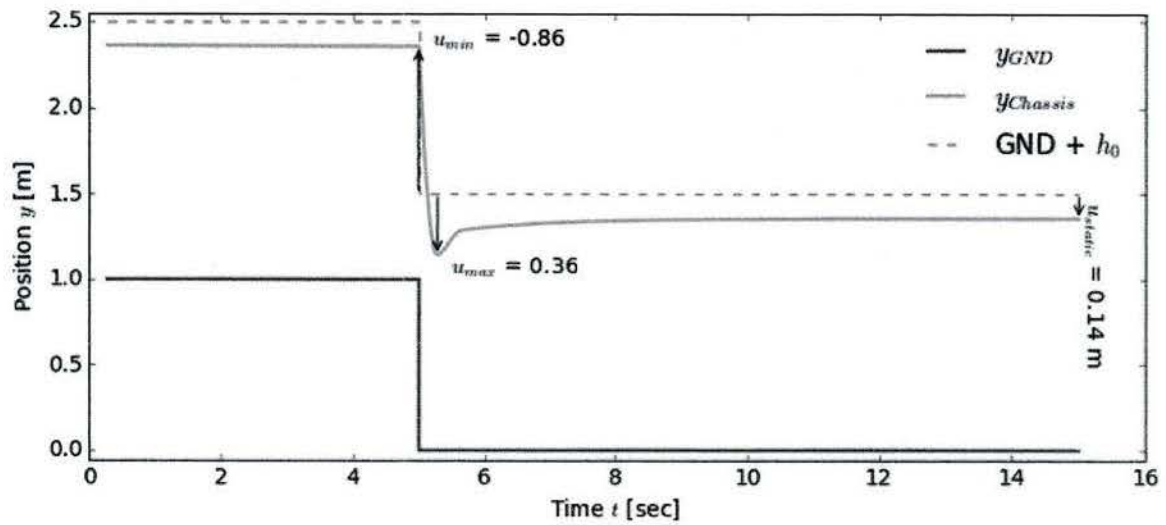


Figure 3.10: Simulation interface in Jupyter Notebook.

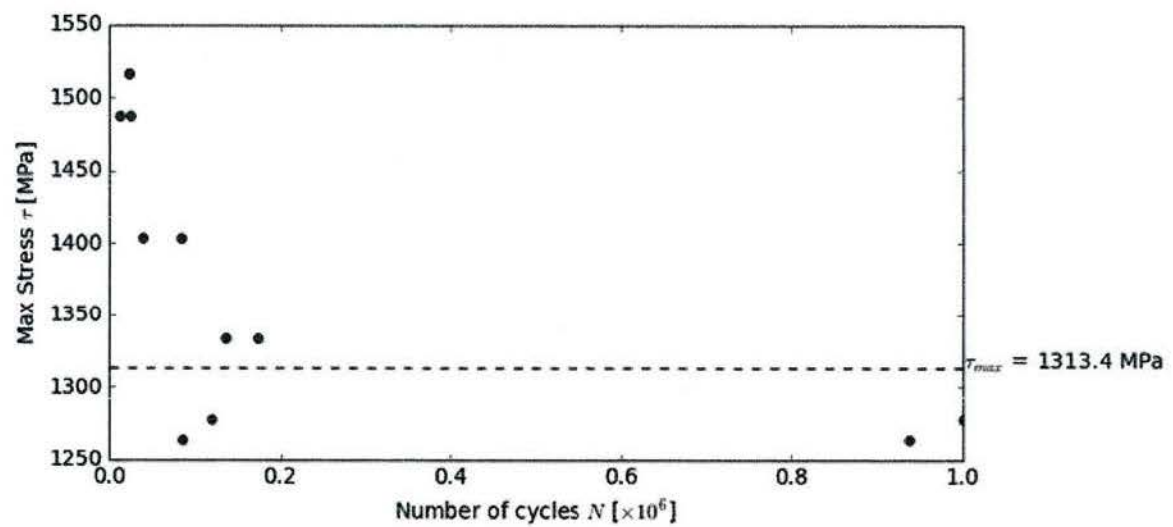


Figure 3.11: Maximum stress associated with a driving event on a stress-cycle data.

set, one point survived the test without failure.

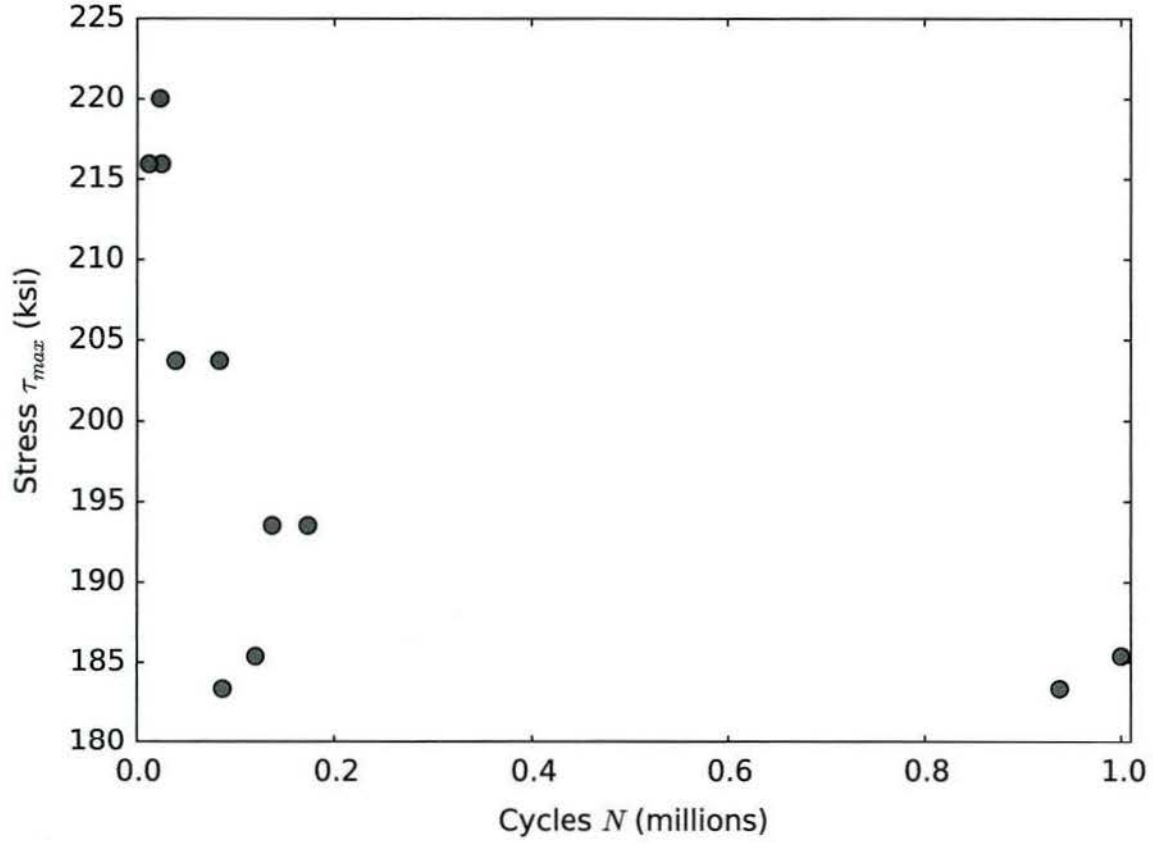


Figure 3.12: Empirically results SN data for uncorroded samples

Simple models stress-cycle model.

A simple hyperbolic stress-cycle model is postulated as follows

$$\tau = \frac{a}{N} + \tau_{\infty} \quad (3.10)$$

where τ and N denote stress and cycles respectively and τ_{∞} and a are model parameters, that are determined from the data. τ_{∞} is often referred to as the *endurance limit*. Exposure to stresses below the endurance limit is not expected to give rise to any damage, irrespective of the number of cycles.

An alternative model employs a piece-wise linear model with two regions

$$\tau = \tau^* + (N - N^*)b, \quad b = \begin{cases} b_0, & N \leq N^* \\ b_1, & N > N^* \end{cases}, \quad (3.11)$$

where the boundary point (N^*, τ^*) and the slopes, b_0 and b_1 , are model parameters.

Both models were fitted to data. The hyperbolic model has fewer parameters than the piece-wise linear model, two vs. four. Also, the hyperbolic model has the desired asymptotic property that captures the engineering view of the problem. Finally, when stress τ is expressed in terms of cycles N , the model is linear with respect to its parameters, and it naturally lands itself to simple data representation (linear regression).

A piece-wise linear model is intrinsically non-linear, but it is *symmetric*: the nonlinearity is the same when stress τ is expressed in terms of cycles N (3.11), or when it is inverted

$$N = N^* + \frac{\tau - \tau^*}{b}, \quad b = \begin{cases} b_1, & \tau \leq \tau^* \\ b_0, & \tau > \tau^* \end{cases}. \quad (3.12)$$

This section will examine fitting the hyperbolic model, given by (3.10), in detail. Similar analysis of the piecewise-linear model is provided in the Appendix B.

Fitting the life cycle models

Least-squares

The least-squares model is very simple to fit because the model is linear in parameters a and τ_∞ . We can prepare a design matrix in the form

$$\mathbf{X} = \begin{bmatrix} \frac{1}{N_1} & 1 \\ \frac{1}{N_2} & 1 \\ \vdots & \vdots \\ \frac{1}{N_n} & 1 \end{bmatrix} \quad (3.13)$$

so that

$$\boldsymbol{\tau} = \mathbf{X} \begin{bmatrix} a \\ \tau_\infty \end{bmatrix} \quad (3.14)$$

This problem has a closed-form solution,

$$\begin{bmatrix} a \\ \tau_\infty \end{bmatrix} = \mathbf{X}^\dagger \boldsymbol{\tau} \quad (3.15)$$

where \mathbf{X}^\dagger is the Moore-Penrose matrix (or pseudo inverse). The result is shown in Figure 3.13. This data model has a couple of limitations. First, the endurance limit runs well above the four points. This is not surprising because the model attempts to minimize the sum of squares, i.e. the cost function is given by

$$J = \sum_{i=1}^N (\tau_i - \hat{\tau}_i)^2, \quad (3.16)$$

where τ_i and $\hat{\tau}_i$ denote measurements and estimates of the measurements. Second, we would like to have some level of uncertainty associated with our estimates. The test standard [56] recommends that uncertainties should be provided: *a line is fitted by regression analysis or similar mathematical techniques to the fatigue data. If the data are fitted by regression analysis, the equation of the stress-life relation and concomitant statistical measures of dispersion (for example, stand error of estimate) should be presented.*

For this type of the model, errors are simply differences between the estimation and the measurement

$$\epsilon_i = \tau_i - \hat{\tau}_i, \quad (3.17)$$

and the distributions of errors, with the normal fit are shown in Figure 3.14. The curve fit with errorbars of one standard deviation of the fit error is shown in Figure 3.15.

Fit by Eye

The least square fit is not in the spirit of the model, because we expect that all the measurement points approach the endurance limit asymptotically from above. Just by adjusting parameters manually, one can arrive at a *fit by eye* similar to the one shown in Figure 3.16. It is immediately obvious that the fit by eye is closer to our intuitive interpretation of the data than the least-square fit. We next examine a couple of different approaches to arrive at this properties in a more objective manner.

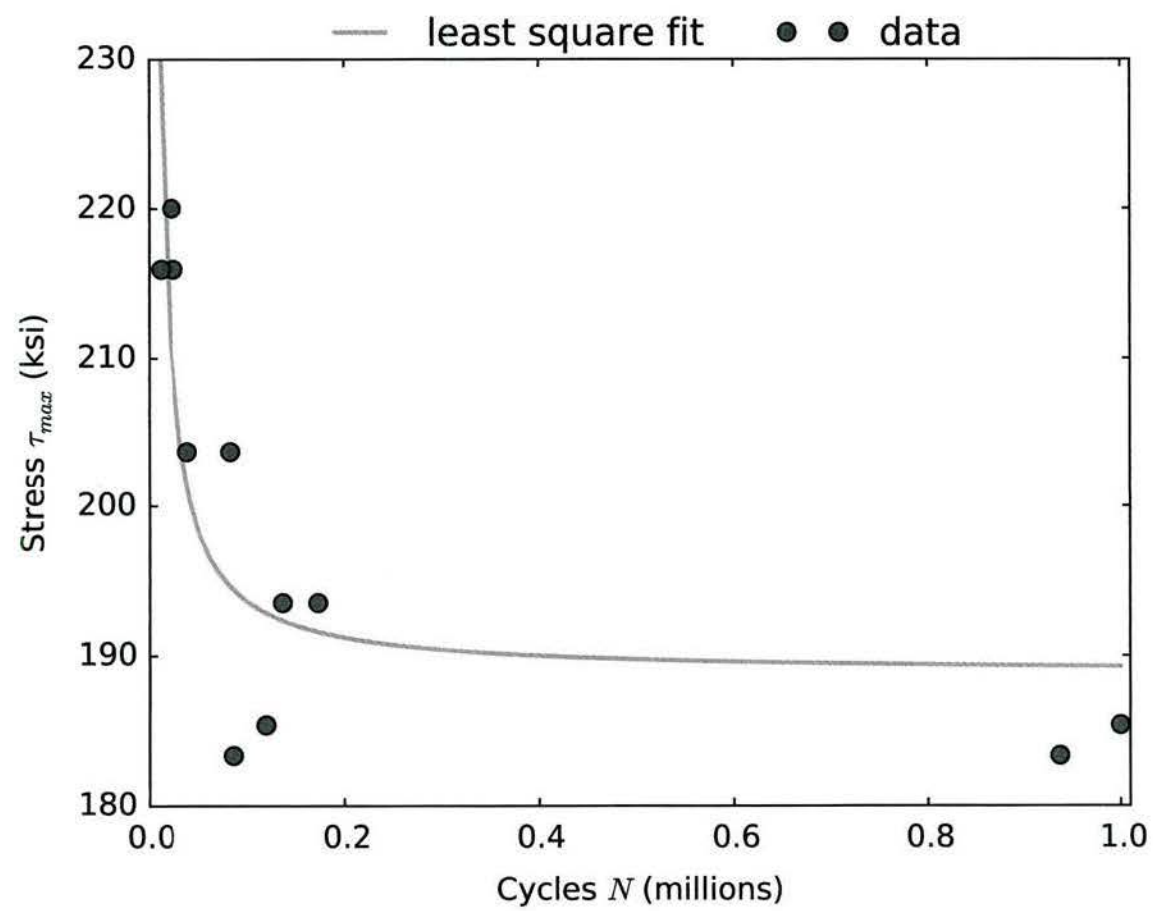


Figure 3.13: Least-square fit

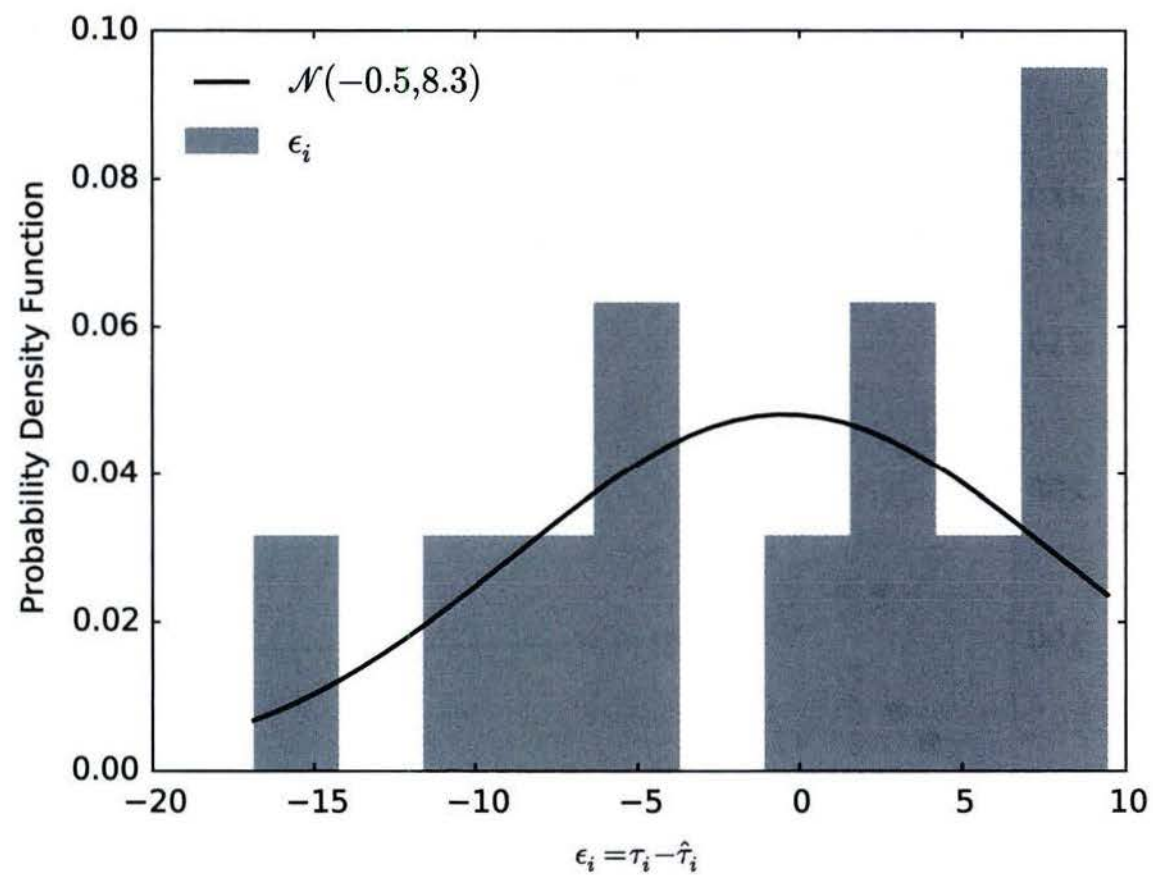


Figure 3.14: Distribution of errors associated with the least-squares fit, with associated normal fit

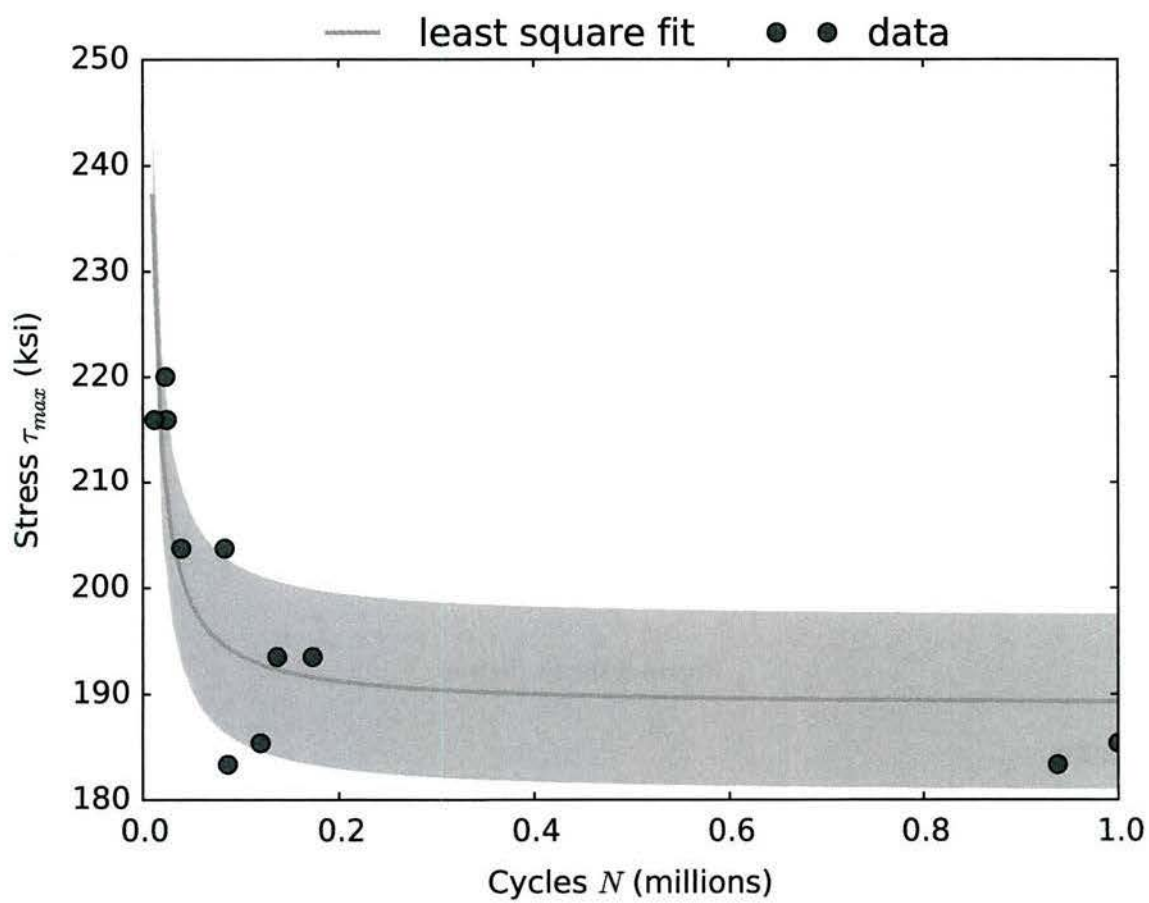


Figure 3.15: Least-square fit with error bars

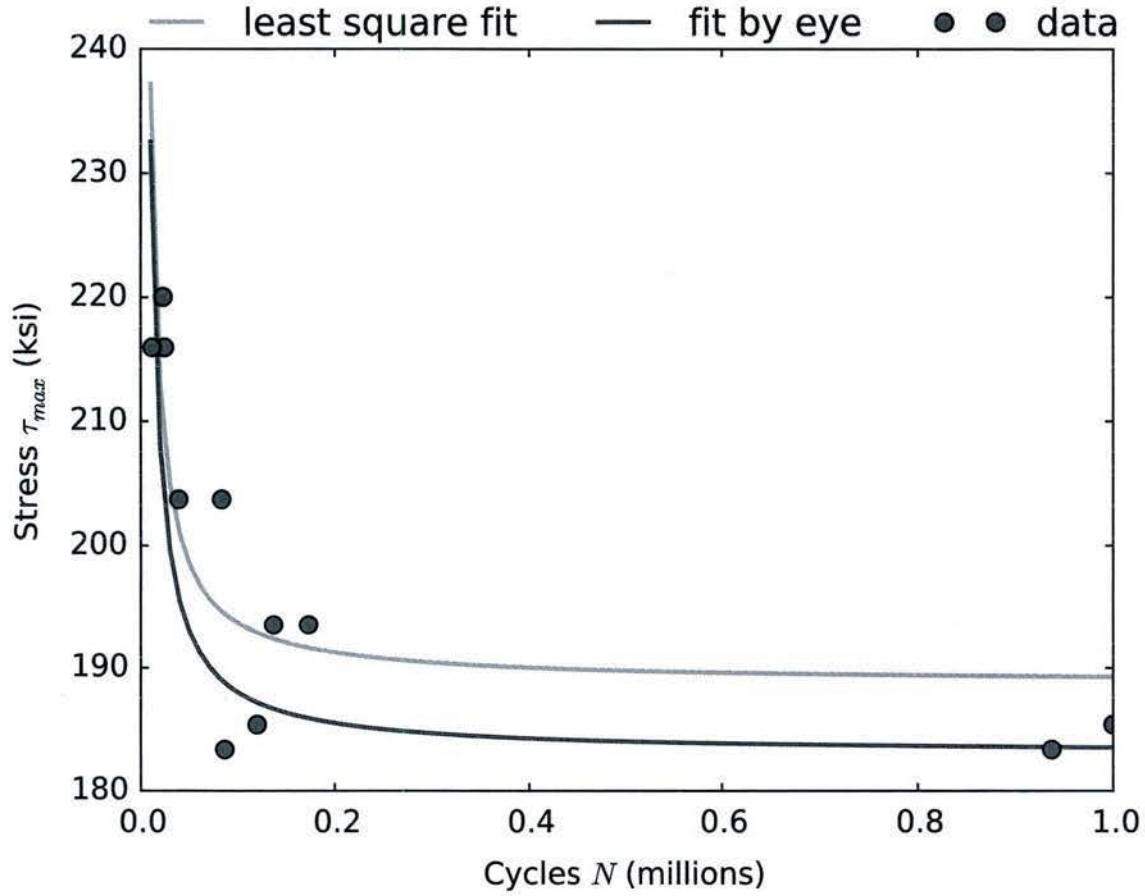


Figure 3.16: Fit by eye

$l = 1$ Fit

Different cost function

$$J = \sum_{i=1}^N |\tau_i - \hat{\tau}_i|, \quad (3.18)$$

This requires us to use an iterative optimization. $l = 1$ norm, or least absolute deviations regression is less affected by outliers in data, making it more robust than least squares. It gives equal weight to all observation's residuals, as opposed to least squares which emphasizes outliers in the data due to squared residuals. Also unlike least squares, there is no analytic approach to solving this. We use a gradient decent (GD) method to solve the regression.

Due to the iterative nature of the problem initial conditions are set. In this model the parameter a is set to ten thousand and τ_∞ to the minimum of the data. At every iteration the gradient of the cost function was evaluated and the following updates are made

$$\begin{aligned} a' &\leftarrow a - \eta \nabla_a J \\ \tau_\infty' &\leftarrow \tau_\infty - \eta \nabla_{\tau_\infty} J \end{aligned} \quad (3.19)$$

where the hash ' indicates the updated parameter and η is the learning rate. In practice it is useful to use separate learning rates for each parameter, especially for un-normalized data, as the learning rate can

be difficult. One that is too large can cause the loss function to jump around the minimum or even diverge. One that is too small can lead to an increasingly slower convergence. Scheduled learning rates can be used to adjust this value during training by pre-defined annealing. Two constant learning rates were used for this example.

Figure 3.17 shows the results of a mini-batch GD (i.e regular GD on subsets of the data, referred to as stochastic gradient decent) chosen at random each iteration.

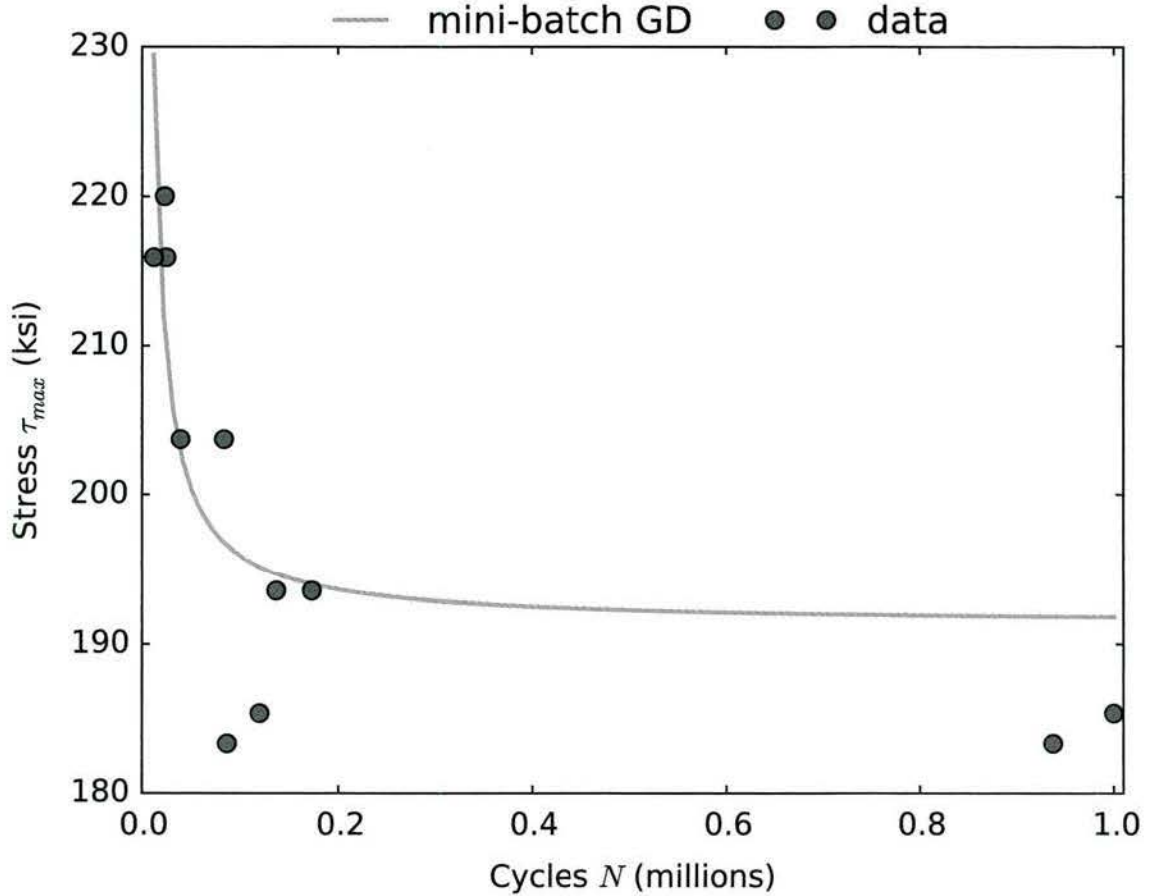


Figure 3.17: The mini-batch gradient decent method used here does not capture the essence of the features we are looking for. The endurance limit is not well interpreted here because data exists below the hyperbola

The above results is closer to our intuition than the least square, but endurance limit is inconsistent with the physics-based interpretation because it runs higher than 50% of points (which is consistent with the cost function and its gradient). There is a benefit to the iterative approach. We can encode our own criteria into the cost function to align with our desired features.

Modify the cost function

We can modify the cost function J to include penalty terms for any points that lie below the endurance limit

$$J = \sum_i |\hat{\tau}_i - \tau_i| + \lambda \sum_i (\tau_i - \tau_\infty)^2 [1 - \text{sign}(\tau_i - \tau_\infty)]$$

and the associated gradient is

$$\nabla_{\mathbf{a}} J = \left[\sum_i \frac{\text{sign}(\hat{\tau}_i - \tau_i)}{N_i} \quad \sum_i [\text{sign}(\hat{\tau}_i - \tau_i) + 2\lambda(\tau_i - \tau_\infty)(1 - \text{sign}(\tau_i - \tau_\infty))] \right]^T$$

The second term in the cost function penalizes values of $\tau_\infty > \tau_i$ by assigning a large error. When $\tau_\infty < \tau_i$ the second term is zero. λ is an arbitrary positive variable for conditioning. Figure 3.18 shows the results of this implementation.

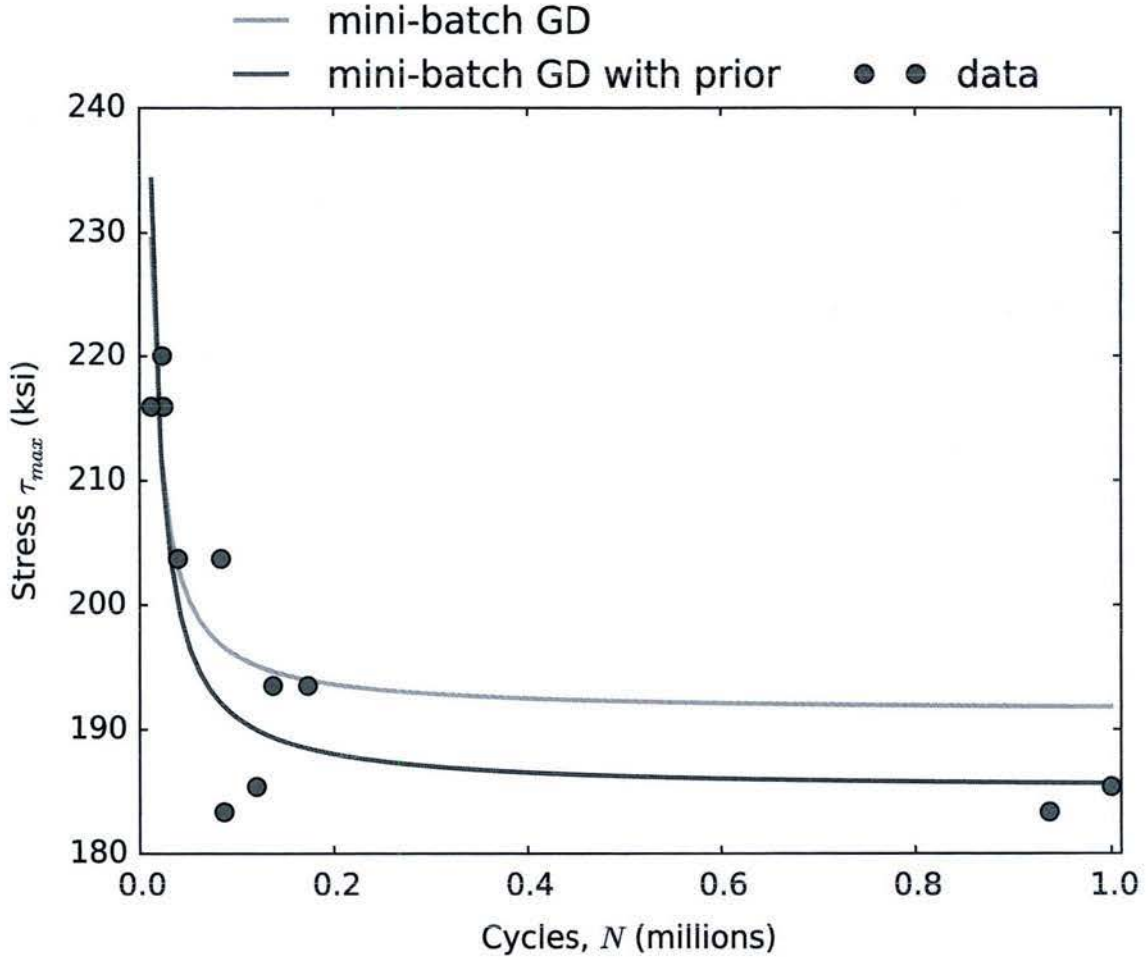


Figure 3.18: The use of prior knowledge encoded in the cost function leads the optimization in a direction more suitable without desired outcome as compared to the previous fit without a conditioned cost function

The piece-wise linear and hyperbolic fit gave way to point estimates with uncertainties. The distribution of solutions for a given estimate along these functions are governed by the uncertainty parameters. In the least squares and GD case it is convention to show the mean and standard deviations in the form of error bounds. Iterative methods like GD can outperform least squares by conditioning the cost function to emphasize features the analyst is looking to extract. In light of uncertainty it is more useful, however, to have a probabilistic distribution over a point estimate.

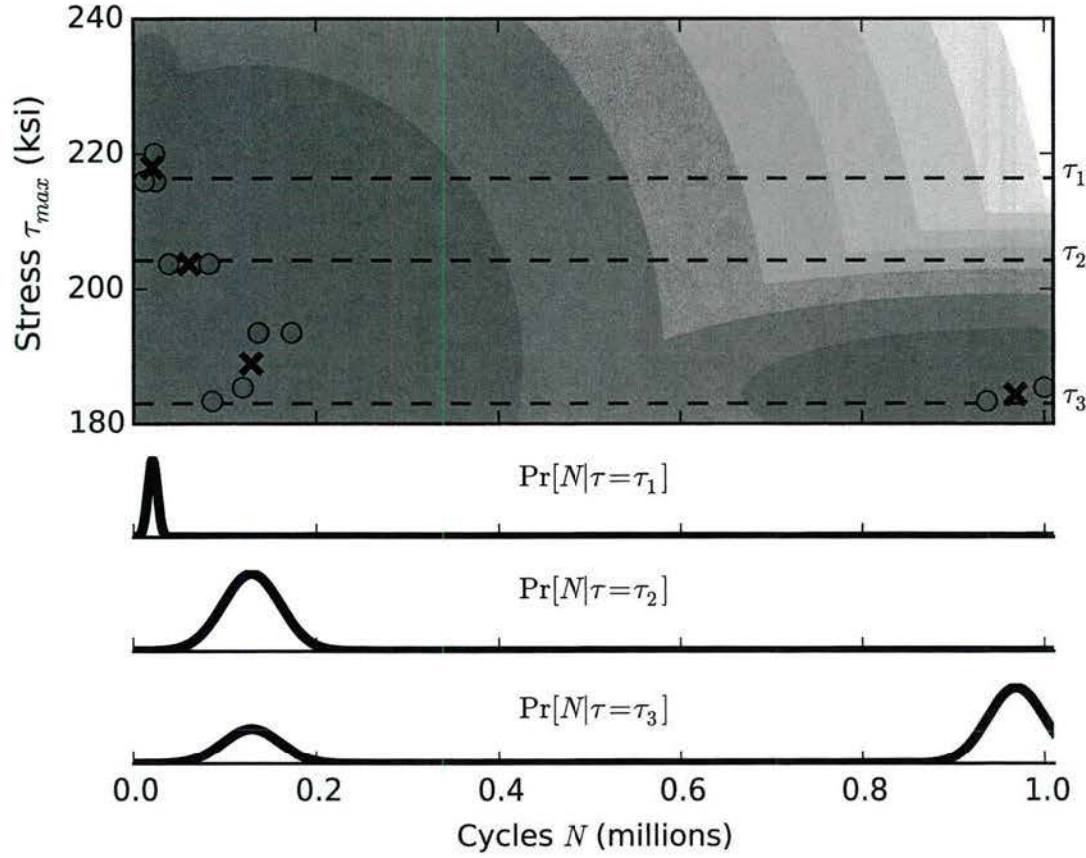


Figure 3.19: Slices of a Gaussian Mixture Model applied to the S-N curve

Data driven: Gaussian Mixture Model

Start with a purely data-driven model. *Gaussian mixture model* (GMM) can be defined as the joint distribution of τ and N

$$\Pr(\tau, N) = \sum_i \alpha_i \frac{1}{2\pi |\Sigma|^{1/2}} \exp \left[-\frac{1}{2} (x - \mu)^T \Sigma^{-1} (x - \mu) \right] \quad (3.20)$$

where x is the position in $[N, \tau]$ domain, $x = [N \ \tau]^T$ and μ is the mean of a cluster $\mu = [\mu_N \ \mu_\tau]$. α_i are cluster weights and they must sum up to one $\sum_i \alpha_i = 1$. The results are shown in Figure 3.19.

A purely data driven model, that does not apply to any domain knowledge, based on only few data points is not very informative. It does, however, show less certainty for lower values of τ . Three slices of stress are shown in the bottom subplots of Figure 3.19. To make this more sensible to what we are looking for we can normalize with respect to τ to get $\Pr[N|\tau]$ (Figure 3.20).

The nature of this model is a data-driven joint probability distribution. Distributions of N , when looking at slices of τ values, can be disjointed (Figure 3.19 bottom subplot and Figure 3.20). It does not make much sense to have a set of possible N values for a given τ , where a slightly different τ leads to a completely different distribution. The benefits of this model come with the uncertainty in the form of a distribution but the down-side is its non-continuous nature.

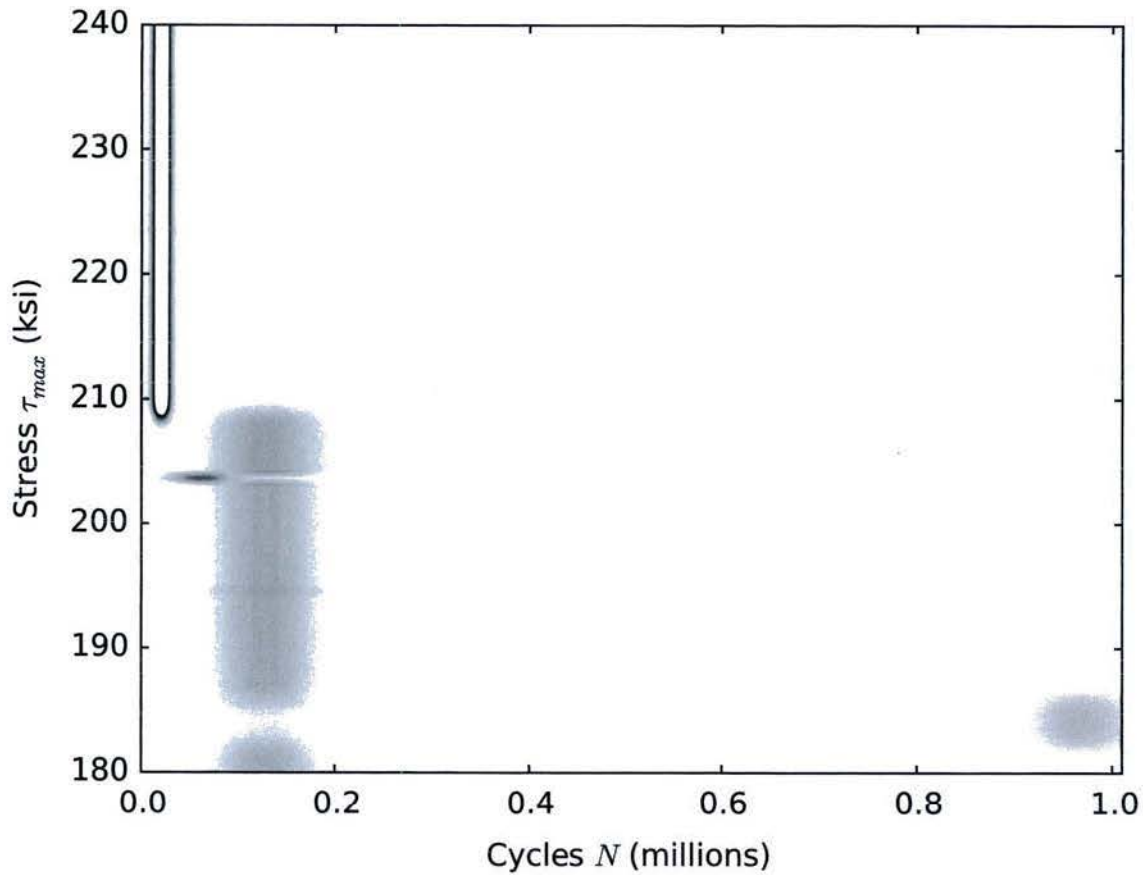


Figure 3.20: Illustrating the non-continuous nature of this modeling

The problems assessed by least squares, GD, and GMM can be summed up as follows. Ultimately we are looking for some distribution of N cycles given τ . Least squares and GD give solutions in the form of point estimates with uncertainty. GMM gives back the joint probability $\Pr(\tau, N)$ with uncertainty in the form of a distribution, however, these can become disjointed and impractical for life cycle assessment. We can do better by employing a Bayesian probabilistic approach. The nature of a Bayesian model is to input our own prior knowledge and update probability distributions by conditioning to the data.

Bayesian Model

As discussed in Section 2.2, probability is a powerful tool in decision making and modeling. The analyst can provide prior knowledge to the system in order to guide the model the right way. Some of the previous methods used, such as BGD or mini-batch GD are iterative processes that work to find the optimal fit given a model function. We can constrain loss functions to force certain outcomes when using these methods. This opens up the ability for the analyst to encode physical properties to the data estimates. Prior knowledge in the form of probability distributions can be assigned to variables and constraints can be directly applied to the model code as well as conditional statements (for instance, the piece-wise function with two conditional slopes can be handled easily in Bayesian modeling). There is no need to choose a loss function or evaluate gradients. The results are in the form of posterior probability distributions and the computed parameters in the form of a large number of samples can be used to directly observe uncertainty. This method maximizes the likelihood of the fit by a memory-less process of sampling. There are several methods to choose e.g.

Gibbs sampling, No U-Turn sampler, etc. No U-Turn sampler (see [34] for more details) was employed in this analysis.

The hyperbolic model shown in Eq. (3.10) is in the functional form $\tau(N)$. It is more natural to the problem to write the equation in terms of τ since that is our input.

$$N = \frac{a}{\tau - \tau_{\infty}} \quad (3.21)$$

A new variable N_{pred} is the predictor of N in Eq. (3.21). N is modeled as a normal distribution with mean N_{pred} and standard deviation σ ; $\text{Normal}[N_{pred}, \sigma]$. σ is a free variable constrained to be positive. The observed data, N , are held constant and it is N_{pred} and σ that are optimized. N_{pred} evaluations are results of parameters a , τ_{∞} , and observed data τ . a and τ_{∞} are in turn optimized to reach the maximum likelihood of the model formulation. This is called inference because the variables that determine N_{pred} , and in turn N , are inferred by the joint probabilities and observed data.

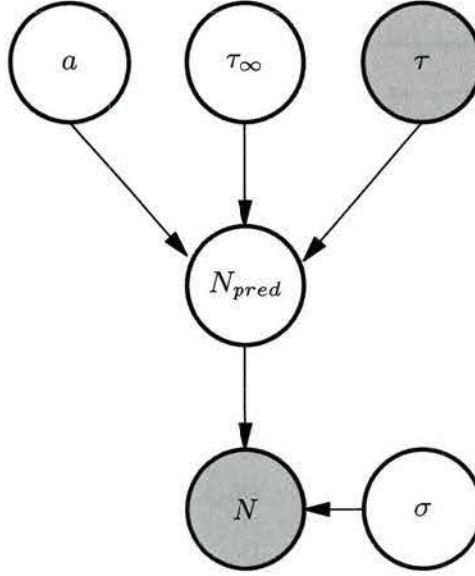


Figure 3.21: A graphical representation of the model

Sampling was done on the same data seen in the other methods and the results are shown in a few ways. Figure 3.22 shows the data as well as the average values of a and τ_{∞} evaluated within the domain of (N, τ) . There is a subplot below that shows the distributions of N evaluated with the posterior distributions of a and τ_{∞} . They resemble the results of the GMM fit, however, show no disjointed nature and include more detail. The GMM fit was an ordinary Gaussian fit which is a smooth curve. These distributions are formed by the evaluation of every returned sample of a and τ_{∞} and make more intuitive sense than the GMM results.

Figure 3.23 is a more complete way of looking it. Distributions of N were evaluated and a histogram was appended to a list for each τ value of evaluation. Then the results were put into a heat map that show the probability of cycles given stress. This plot aligns with our expectations because larger stresses lead to fewer cycles with greater certainty, and smaller stresses lead to more cycles with less certainty.

Multiple models

For a given stress, the model provides a probability distribution of cycles

$$\Pr(N|\tau)$$

This family of probability distributions (one for each stress level τ) corresponds to the case where no corrosion damage took place. This additional information can be encoded as a part of the condition as follows

$$\Pr(N|\tau, NC), \quad (3.22)$$

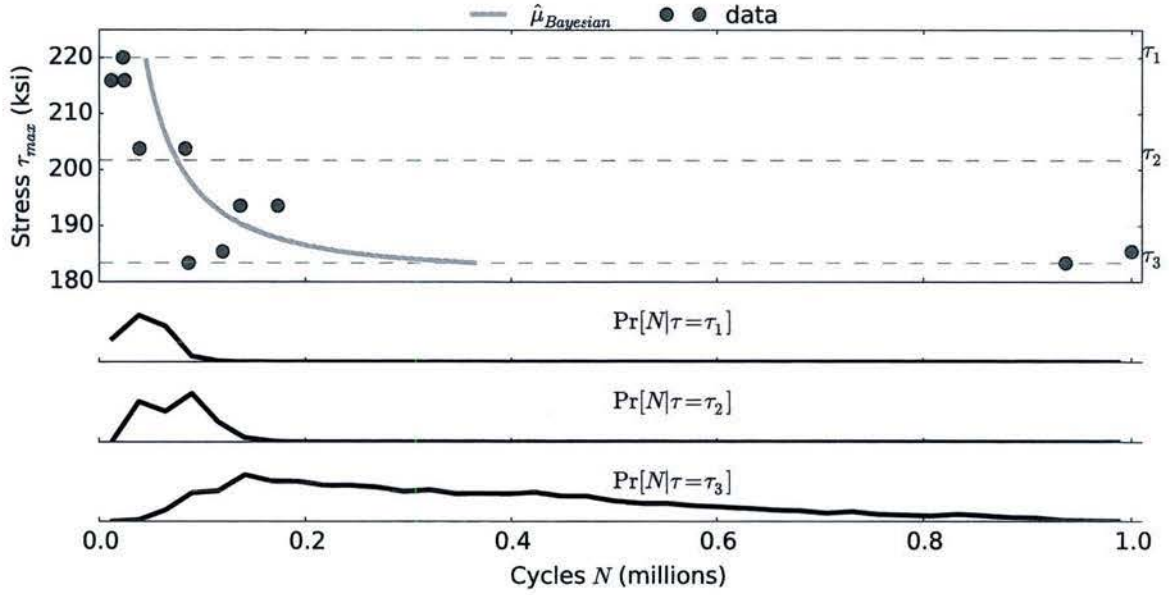


Figure 3.22: Illustration of the continuous nature of this modeling also shown in slices of stress levels

where *NC* stands for *no corrosion*.

Similar Bayesian model were developed for a few different test cases, that correspond to different levels of corrosion damage and different methods for damage repair, e.g.

$$\begin{aligned}
 & \Pr(N|\tau, DL_1) \\
 & \Pr(N|\tau, DL_2) \\
 & \Pr(N|\tau, DL_1, RM_1) \\
 & \Pr(N|\tau, DL_1, RM_2) \\
 & \dots
 \end{aligned} \tag{3.23}$$

where DL_i stands for i^{th} damage level, and RM_j stands for j^{th} repair method. Distributions of these models, with the explanation of damage levels and repair methods are provided in Appendix C.

Combining Bayesian Models

Sometimes the level of damage cannot be asserted with certainty. Given that our information and model dependence on damage is discrete and the model dependence on repair methodology is categorical, we can combine these models in a probabilistic sense when we are not sure about the level of the corrosion damage. For example, the user can provide a subjective belief that the actual corrosion damage is 30% DL_1 , 40% DL_2 , and 30% DL_3 . The model then combines these estimates as

$$\begin{aligned}
 \Pr(N|\tau) = & 0.3 \Pr(N|\tau, DL_1) \\
 & + 0.4 \Pr(N|\tau, DL_2) \\
 & + 0.3 \Pr(N|\tau, DL_3)
 \end{aligned} \tag{3.24}$$

More generally, the probability of remaining cycle, given stress level is

$$\Pr(N|\tau) = \sum_{i=0}^N \alpha_i \Pr(N|\tau, DL_i) \tag{3.25}$$

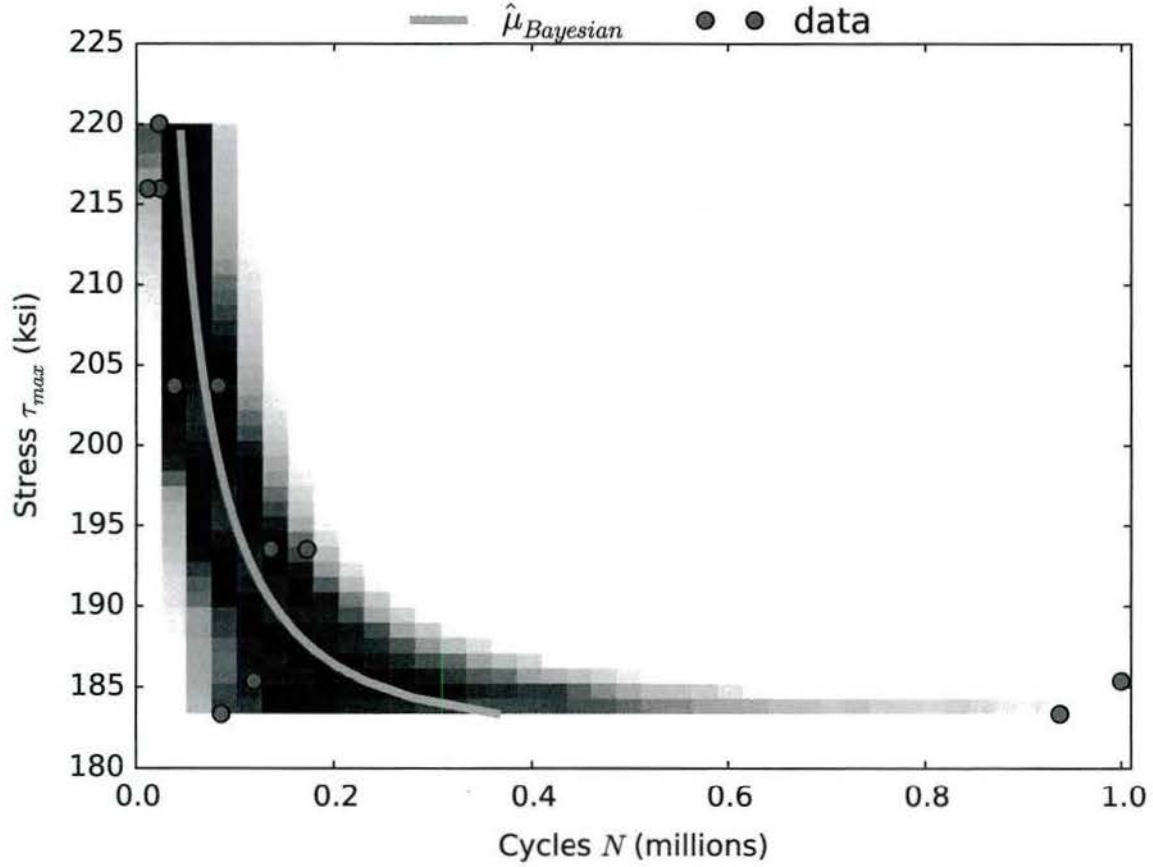


Figure 3.23: Heat map representation of Figure 3.22

To illustrate the model fusion, consider the case where the user is not sure about the level of damage and estimates it that it is *somewhere* between DL_1 and DL_2 , approximately 75% DL_1 and 25% DL_2 . The posterior distributions of cycles, given stress levels and beliefs of damage levels, $\Pr(N|\tau, DL = 0.75 \times DL_1 + 0.25 \times DL_2)$, are shown in Figure 3.24: the heatmap shows the histogram of the combined probability density function, and markers indicate observed data points from individual distributions (see Appendix 3.2.1 for more details of individual life cycle cases).

3.2.2 Database Model: Mean Time Between Failure (MTBF)

The life-cycle model so far has described methods of estimating failure rates based on empirical data from experiments with torsion bar samples. In order to tie this into the larger reliability model, cycle estimates must be related to actual usage. Repair data, such as the mean time between failures (MTBF) on the system, sub-system, and component levels can be used as a metric to link estimated cycles to usage data. Replacement rate data for system, sub-system and component analysis appeared to be distributed exponentially (ex. Figure 3.25). For single replacements, which had no time between replacements, the maximum day value was chosen. There were many instances of single replacements among components. Eq. (3.26) shows an exponential function with a single parameter.

$$\Pr[\text{replacement}] = \lambda e^{-\lambda t} \quad (3.26)$$

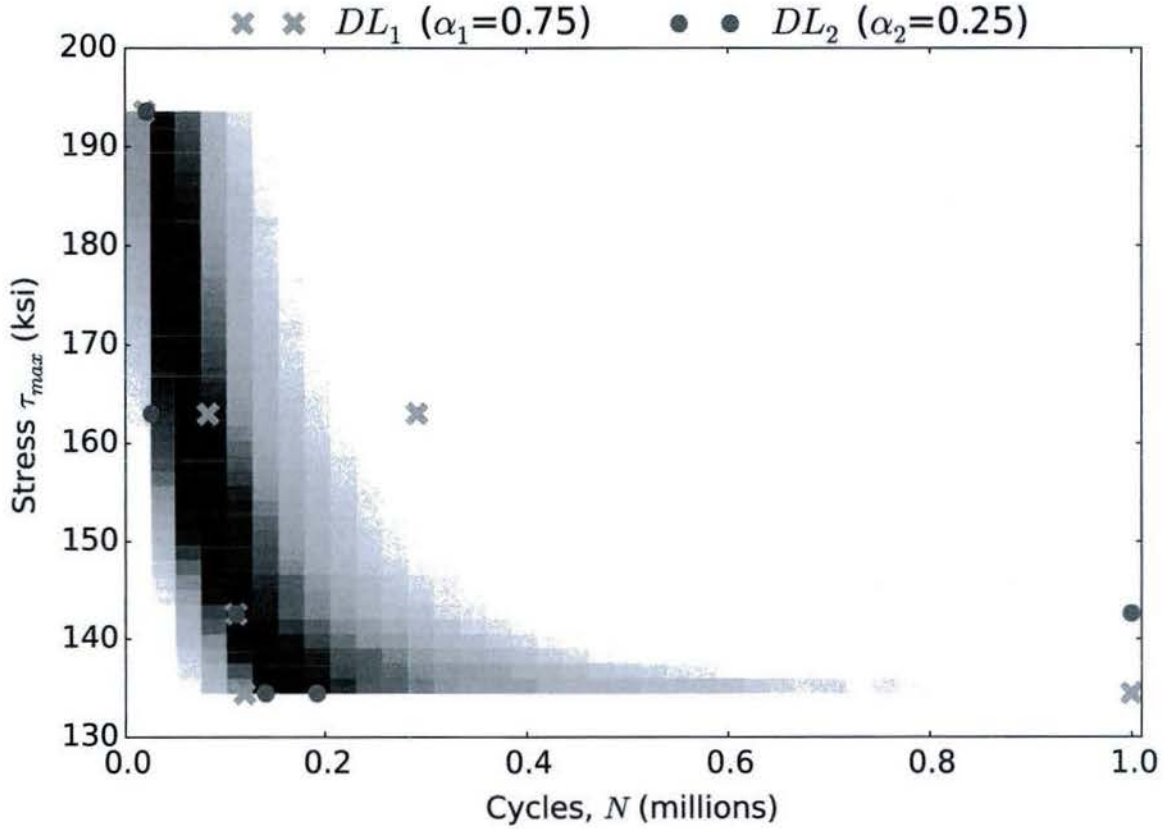


Figure 3.24: Data fusion of two levels of damage DL_1 and DL_2

where λ is a shape parameter. Evaluating the expectation value of this distribution at a component level gives $MTBF_i$

$$MTBF_i = \frac{1}{\lambda_i} \quad (3.27)$$

where i indicates the component. At the system level it is evaluated as

$$MTBF_{sys} = \frac{1}{\lambda_{sys}} = \frac{1}{\sum_i \lambda_i} \quad (3.28)$$

When calculating MTBF of a given component we are looking into many vehicles, usually with more than one of those components. We start with a single component on a single vehicle, which can be evaluated by averaging the time intervals between repairs, or more simply by dividing the total time of observation by the total number of replacements. This is shown in Eq. (3.29). The collected data ranges from 2007 to late 2015, approximately 3,199 days. For example, if a component was replaced once anywhere in that time interval it's MTBF would be approximated at 3,199 days. We still have to account for the number of components on a vehicle and the total number of vehicles. Consider a car with four wheels, observed for four days, over which time four replacements were made. Following Eq. (3.29) (only considering one wheel) gives an average of one replacement per day. Since there are four wheels, we can say that one wheel was replaced per day on average and the MTBF for a single wheel is increased by a factor of four, the number of wheels. This is shown in Eq. (3.30). The same logic applies to the number of vehicles. If two cars were observed from the start then the replacements would be distributed over both vehicles. It is as if one wheel

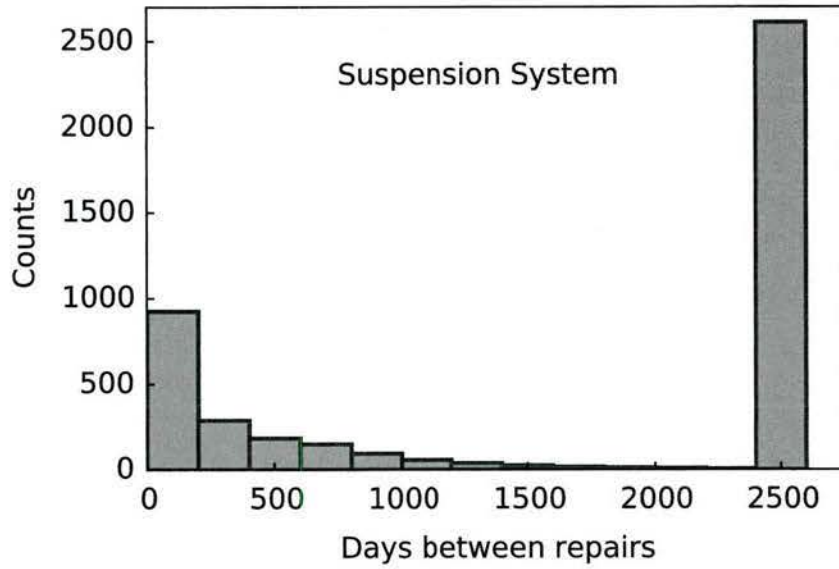


Figure 3.25: Time between replacements for the suspension system with last bin representing instances of single replacements over the observed time range. At the time this data was collected the observed time range was ~ 7 years or 2,555 days

was replaced per vehicle every two days instead of every day, and the MTBF has increased by a factor of two, the number of vehicles. By including the number of components per vehicle and the number of vehicles we have effectively averaged the time between replacements for a single component across all vehicles. This is shown in Eq. (3.31).

$$MTBF = \frac{(t_{start} - t_{end})_{fleet}}{\sum_i \text{Comp_replacement}_i} \quad (3.29)$$

add factor for quantity of component

$$MTBF = \frac{(\# \text{ Comp/Veh})(t_{start} - t_{end})_{fleet}}{\sum_i \text{Comp_replacement}_i} \quad (3.30)$$

add factor for number of vehicles

$$MTBF = \frac{(\# \text{ Veh})_{fleet}(\# \text{ Comp/Veh})(t_{start} - t_{end})_{fleet}}{\sum_i \text{Comp_replacement}_i} \quad (3.31)$$

There were 4 main torsion bar locations in the suspension sub-system; port-front, port-aft, starboard-front and starboard-aft. Each location had an associated component stock number, and there were three of each components in the sub-system, making a total of twelve torsion bars per vehicle. Using Eq. (3.31) we can evaluate the MTBF for all four components. Table 3.4, which was built from a database of information on vehicle system, sub-system and component maintenance data, shows the individual MTBFs for the four components in a table. Here is an example of how these values were calculated using Eq. (3.31) for the port-front torsion bars.

Table 3.4: MTBF in days for the four torsion bar components.

Location	Quantity	MTBF (days)
port-front	3	959,700
port-aft	3	812,054
starboard-aft	3	659,794
starboard-front	3	1,172,967

$$\begin{aligned}
 MTBF_{(port-front)} &= \frac{(1,100 \text{ vehicles})(3 \frac{\text{qty}}{\text{veh}})(3,199 \text{ days})}{11 \text{ replacements}} \\
 &= 959,700 \text{ days}
 \end{aligned}$$

Following Eq. (3.28) gives the MTBF for any given torsion bar in one of the four locations specified for all vehicles. Note that the factor of 3 accounts for there being three of each component torsion bar.

$$\begin{aligned}
 MTBF_{bars} &= \frac{1}{\lambda_{bars}} \\
 &= \frac{1}{\frac{3}{959,700} + \frac{3}{812,054} + \frac{3}{659,794} + \frac{3}{1,172,967}} \\
 &= 71,814 \text{ days}
 \end{aligned}$$

Figure 3.26 shows the recorded MTBF in days for several suspension components. Torsion bar is second with an average of 71,814 days between replacements. This method was used to compute the values in Figures 3.27 and 3.26. Due to the large number of vehicles in the fleet ($\sim 1,100$) these values are expected to be large, assuming replacements don't happen constantly.

3.3 Cost model

Table 3.5 shows the key factors in computing the cost of a nominal length (86.75") torsion bar. In addition to the costs listed in the table, torsion bar manufacturing requires a hardening process and torsional preset which do not depend on the geometry.

$$\begin{aligned}
 C_n &= C_{material}(r) \\
 &\quad + C_{machining}(r) + C_{shotPeening}(r) + C_{coating}(r) \\
 &\quad + C_{heatTreat} + C_{preset}
 \end{aligned} \tag{3.32}$$

Eq. (3.32) provides the total cost of a torsion bar of the nominal length C_n , as a function of the radius. The nominal cost is the sum of the costs listed in Table 3.5 and the geometry independent costs. The raw material costs $C_{material}$ were estimated based on a difference in cost to another alloy (300M vs 4140, with an estimated 75% premium applied to the 4140 prices found on MetalsDepot.com). Machining costs $C_{machining}$ depend on the difference between the standard bar stock diameter and the final diameter, which dictates the number of rough and finish passes. Shot peening $C_{shotPeening}$ and coating $C_{coating}$ costs were estimated based on previous experience and are dependent on surface area. Preset C_{preset} and heat treatment $C_{heatTreat}$ costs are estimated.

$$\begin{aligned}
 C(r, l) &= C_{material}(r, l) \\
 &\quad + \alpha(l) \left(C_{machining}(r) + C_{shotPeening}(r) + C_{coating}(r) \right) \\
 &\quad + C_{heatTreat} + C_{preset}
 \end{aligned} \tag{3.33}$$

Table 3.5: Cost table

Stock Diameter	Torsion Bar Diameter	$C_{material}$	$C_{machining}$	$C_{shotPeening}$	$C_{coating}$
2.250	1.97	553	170	125	165
2.250	2.00	553	170	125	167
2.250	2.05	553	135	125	170
2.250	2.10	553	135	125	173
2.250	2.15	553	100	125	176
2.375	2.20	606	135	125	179
2.375	2.25	606	100	125	182
2.375	2.30	606	100	150	185
2.500	2.35	666	135	150	188
2.500	2.40	666	100	150	191
2.750	2.45	798	170	150	194
2.750	2.50	798	170	150	197
2.750	2.55	798	135	150	200
2.750	2.60	798	135	150	203
2.750	2.65	798	100	150	206
3.000	2.70	944	170	175	209
3.000	2.75	944	170	175	212
3.000	2.80	944	135	175	215
3.000	2.85	944	135	175	218
3.000	2.90	944	100	175	221
inches ["]		dollars [\$]			

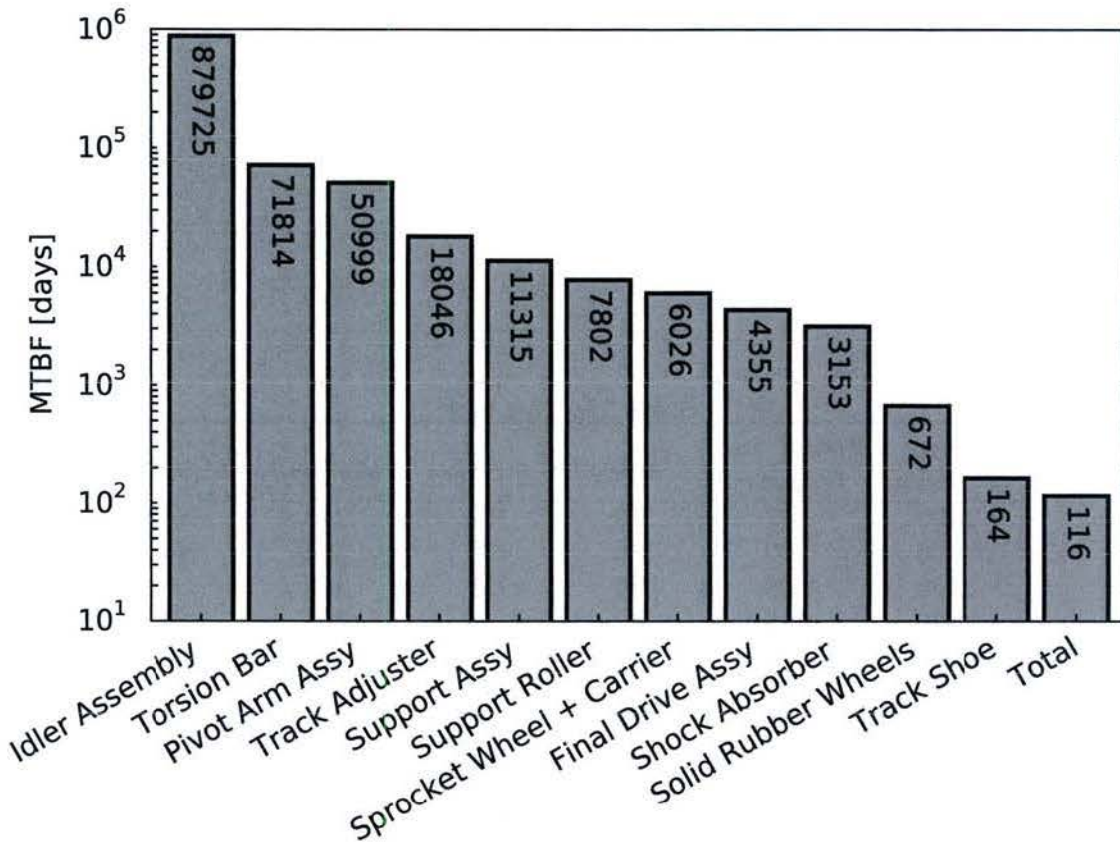


Figure 3.26: Several of the suspension components are shown with their MTBF values in days. The last bin shows the total MTBF of the sub-system, computed using Eq. (3.28)

Eq. (3.33) provides an updated cost C equation for torsion bars of other lengths. Cost estimates for other length torsion bars were created by updating the raw material $C_{material}$ costs and applying a scale factor, $\alpha(l)$, to the combined machining $C_{machining}$, shot peening $C_{shotPeening}$, and coating $C_{coating}$ costs. $\alpha(l)$, shown in Eq. (3.34), is the new bar length, l , divided by the full length, l_{full} , plus 0.1 which represents fixed costs that don't change based on length. The nominal preset and heat treating costs remained the same for the new length.

$$\alpha(l) = l/l_{full} + 0.1 \quad (3.34)$$

Figure 3.28 shows the cost C as function of the torsion bar geometry: length l and radius r . The cost surface is not a monotonic function of r length l . Often a torsion bar is cut from a thicker bar. When more is cut off the cost increases and there are tiers of initial diameters to cut from. So stepping up to center diameter 2.2" from 2.15" requires cutting from a 2.375" stock diameter, instead of a 2.50" stock diameter.

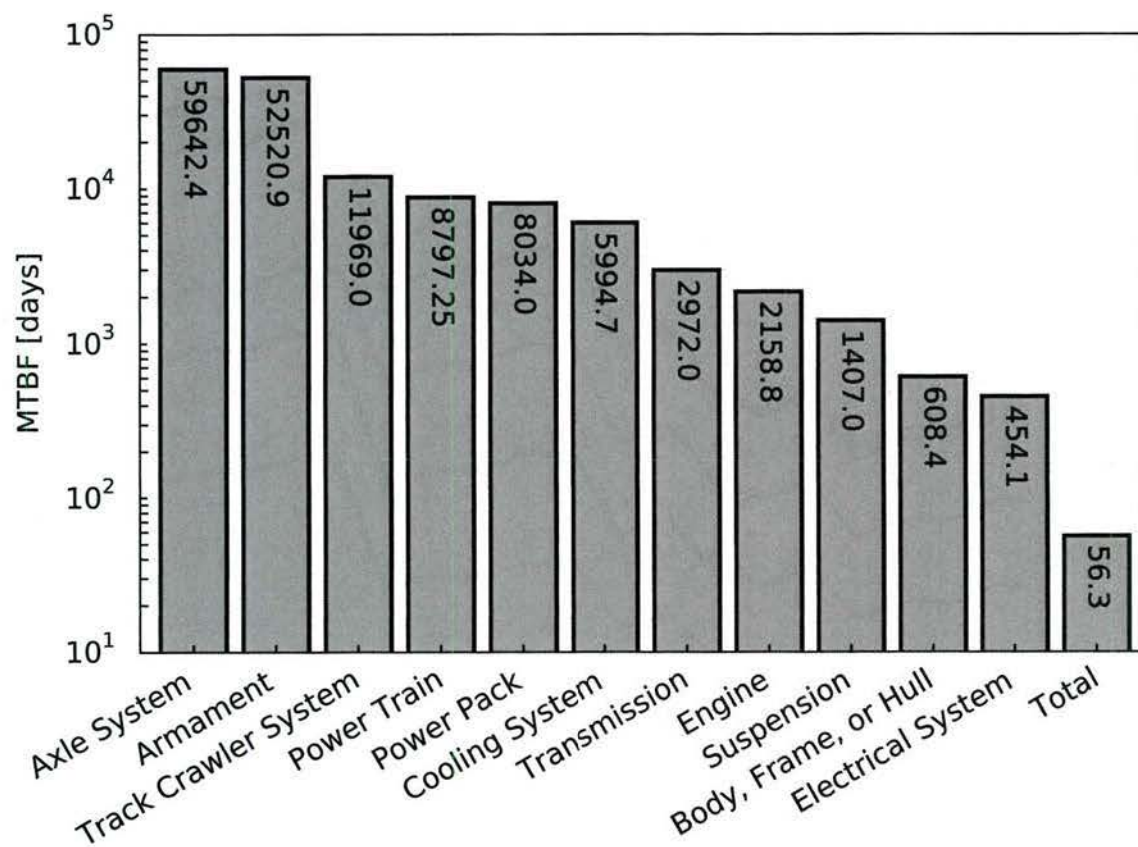


Figure 3.27: Several sub-systems are shown with their MTBF value in days. The last bin shows the total MTBF of the system, computed using Eq. (3.28)

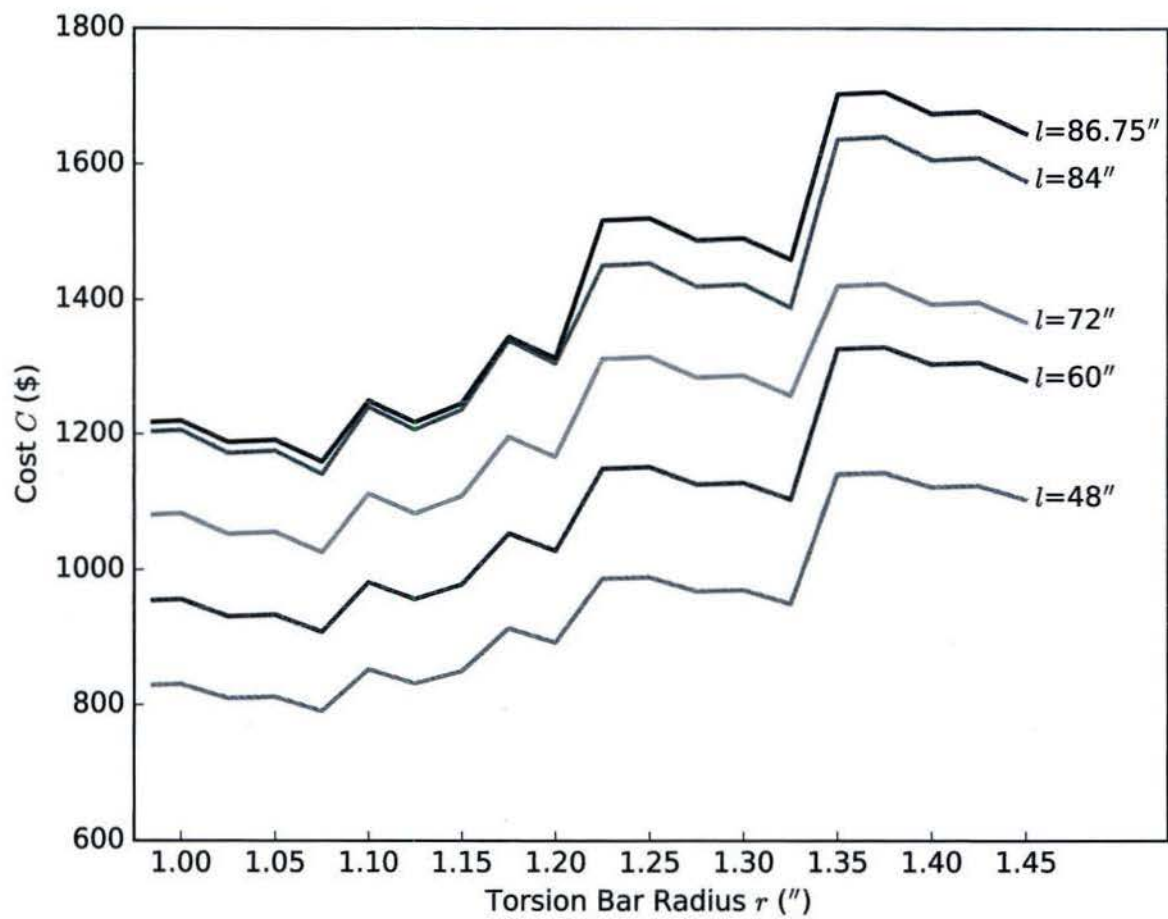


Figure 3.28: Cost of torsion bar by radius and length

Chapter 4

Applications

4.1 Reliability Assessment under Uncertainty

Pieces of the framework have been described separately so far. We considered an example scenario that integrates the performance and reliability model to guide decisions on torsion bar replacements for a given vehicle.

The dynamical model was designed to simulate part of the vehicle's suspension system under idealized terrain conditions. For this we used a sine wave to represent a rough terrain; The user would input amplitude, speed and cycle length in the form of probability distributions which were transformed into the model inputs, amplitude and frequency. Simulated stress levels that acted on the torsion bars were outputted in the form of a probability distribution. These stresses were then inputted into the life-cycle model which returned estimated cycles to failure in the form of a probability distribution. The user would have to input two more pieces of information; The total operational time of the vehicle in question, and the fractional time of operation on the specified terrain. Total operational time was approximated using the results of a Bayesian estimation of hours of operation given raw usage data (Figure 4.1). This, combined with the results from the life-cycle model, would allow for an estimate of the amount of lifetime experienced by the torsion bars. These inputs were also in the form of probability distributions and so the final result was a distribution of estimated lifetime of the torsion bars.

This process was accomplished using a Monte Carlo approach where a large number of stochastic sampling of input distributions generated output distributions. It followed that the uncertainty encoded by the user in the input distributions propagated through to the results. The more certain the inputs, the sharper the lifetime estimate. This is illustrated in Figures 4.2 and 4.3. We made assumptions on the conversion between hours of operation to miles traveled, miles traveled to cycles of stress, the physical parameters of the step and rough terrain (such as step height and sine wave amplitude), and the operational time of the vehicle. The output of the life-cycle model was used in a modified Miner's rule analysis to find the estimated percentage of torsion bar life remaining in the form of a probability distribution. The Miner's rule was altered a bit to add ratios of experienced life-time at a given stress to predicted cycles until failure at that stress by stochastic sampling, rather than point estimate inputs. The following sub-section describes the scenario from the user's point of view, giving realistic values and uncertainties. Figure 4.2 can be used as a guide for this next part.

4.1.1 Scenario with assumption

For this example a rough terrain was represented by a sine wave, for a vehicle with torsion bars that had experienced twenty-four hours of corrosion (damage level 2). The user inputs (top four nodes in Figures 4.2 and 4.3) were as follows: The speed of the vehicle, the length of a stress-cycle, the amplitude of the rough terrain, and the total time of operation at the time of analysis. These were all inputted in the form of probability distributions. For instance, the average operational speed of these vehicles on a rough or soft terrain was 10.5 mph (according to the vehicle's manual). So we represented speed as a normal distribution with a mean of 10.5 mph and a standard deviation of 1 mph. The distance between bumps (or troughs of the sine wave) was on average 9 feet apart with a standard deviation of 1 foot. This distance was analogous

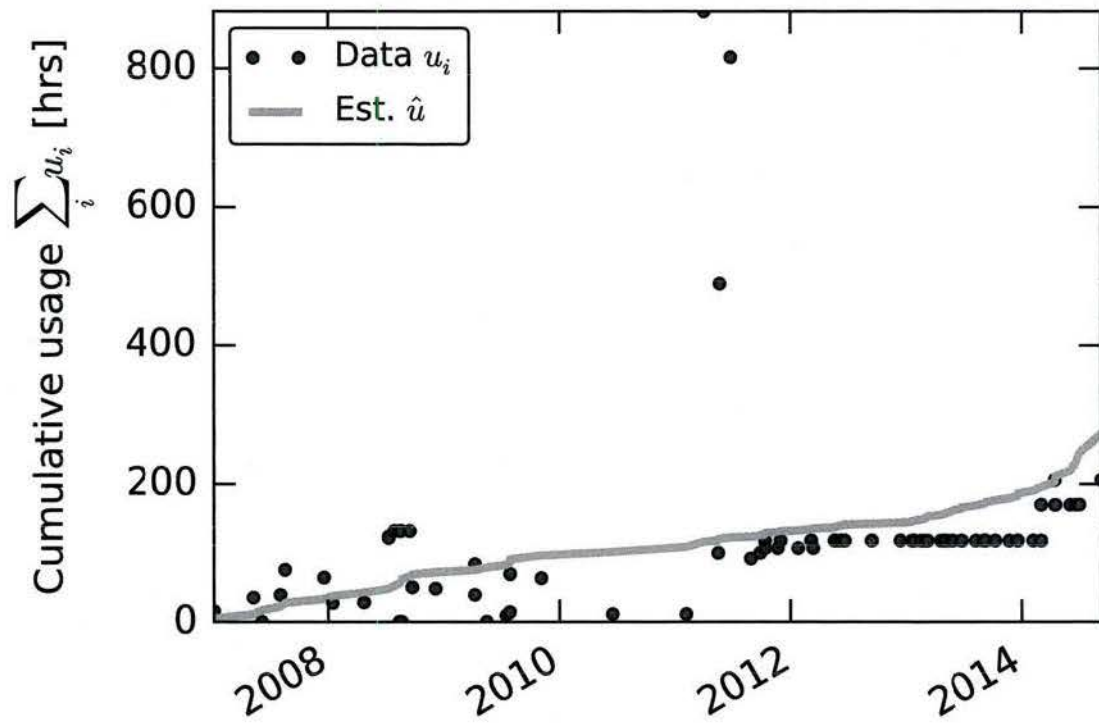


Figure 4.1: Example of usage estimator with Bayesian mean line (orange) over original noisy data (blue). This is the results of a scenario that the user might input into the framework

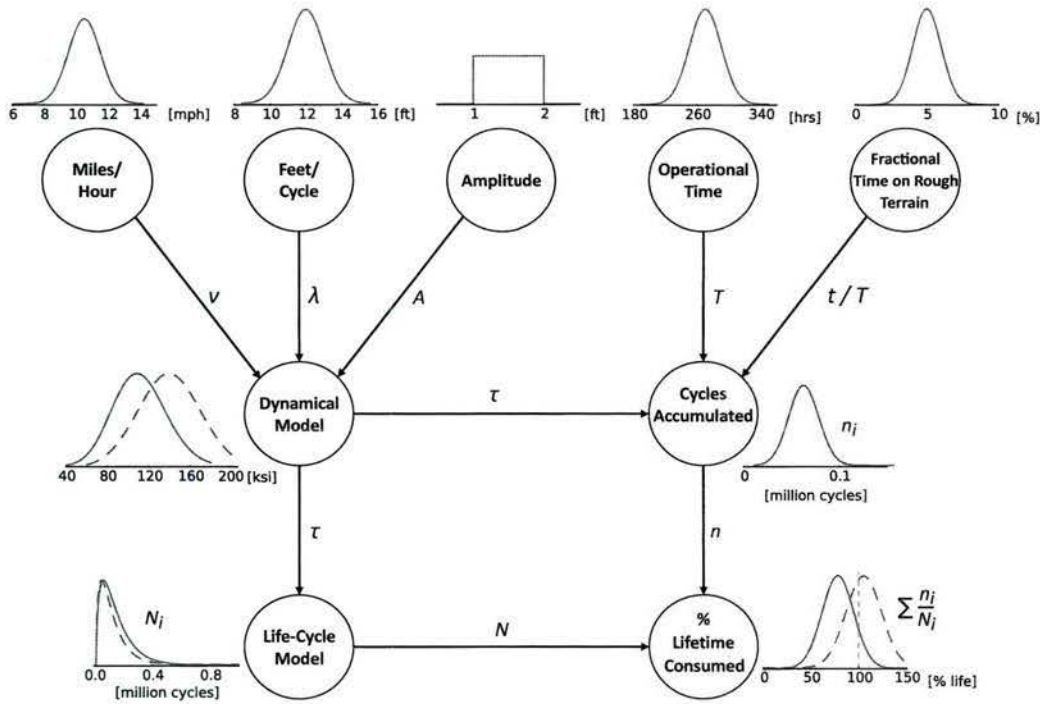


Figure 4.2: Graphical diagram of framework network with larger uncertainties

to the wavelength of the sine wave and was transformed into a frequency using the vehicle's speed, for use with the dynamical model. The amplitude of the bumps that formed the terrain were anywhere between 1 and 2 feet in height. According to our vehicle's usage data (Figure 4.1) there was approximately 270 hours of operation between the years 2007 and mid-2015 (based on the average Bayesian estimate), so we represented that as a normal distribution with a mean of 270 hours and a standard deviation of 20 hours. Realistically a vehicle was not driven for the entire time of operation, but rather was used on and off during that time. We assumed that 5% of the operational time was rough terrain driving and set that as the mean of a normal distribution with standard deviation of 1%. In other scenarios it would be up to the expert knowledge of the user to decide these values and uncertainties.

The bottom right node, labeled '% lifetime' showed the final results. In the first case where uncertainties were greater (Figure 4.2) the resultant distribution ranged from around 30% to over 120%. This would probably be interpreted as very close the end of the component's lifetime with a small chance it is past its expected lifetime. The second case where uncertainties were thinner (Figure 4.3) shows a resultant lifetime to be much less. This is a consequence of the specific model we built. Our life-cycle model is trained on Stress-Cycle (SN) curves and is represented by a hyperbolic function, whose offset value is interpreted as the endurance limit of the part. Values below the endurance limit are estimated at infinite cycles until failure. This is common practice with SN curves. For the second case, the output stress distribution from the dynamical model was thinner. Stress values below the endurance limit that were inputted into the life-cycle model returned infinite cycles to failure (the denominator of the summed ratios in Miner's rule analysis) and so these terms did not affect the results. A thinner stress distribution in this case meant less values above the endurance limit and therefore a smaller predicted lifetime as well as a thinner resultant distribution. The situational interpretation of these differences is that in the case of greater uncertainty, the vehicle spent more time experiencing stresses above the endurance limit than in the case with less uncertainty. This is an example of how uncertainties propagate through to the results.

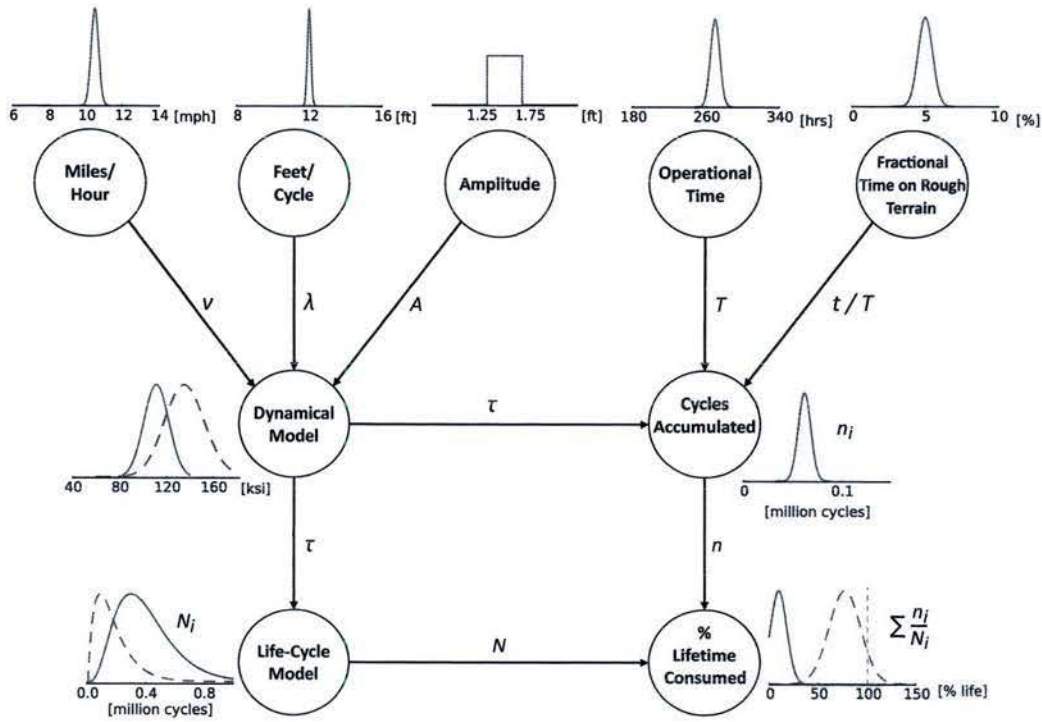


Figure 4.3: Graphical diagram of framework network with smaller uncertainties

4.1.2 Adjusting radius to recovery reliability in the added weight scenario

The reliability, R , of a torsion bar decreased when load mass was increased. Quantifying this allowed us to evaluate methods of recovering reliability loss in one of two ways; changing the radius r or changing the length l of the bar. We chose to change the radius because it was more effective in changing R which can be seen in Figure 4.10 where life consumed drops off quickly in the r direction and slopes down slowly in the l direction. In the framework stresses were simulated in a performance model with user inputted parameters for speed and terrain properties, which fed into a life-cycle model that estimated cycles to failure. By including more inputs such as operational time and fractional time on rough terrain, these life-cycle estimates were used to compute R . The inputs used in this section were the same as our framework example in Section 4.1. All inputs were in the form of probability distributions and were set using an average value, and standard deviation. The life-cycle model for a torsion bar with twenty four hours of corrosion was used as well. For stresses experienced below the endurance limit, returned cycle estimates were above 100,000 cycles and considered infinite lifetime for the torsion bar (reliability 1.0). In the added weight scenario where the vehicle's mass was increased by 20% the reliability was reduced from 61% to 33% for a radius of 0.95". Figure 4.4 shows R as a function of radius for this case. The grey dashed lines show the change in reliability of the same torsion bar when mass was increased. The dark line indicates reliability as a function of radius for the increased mass case. The plot is repeated right below it in the form of life consumed ($1 - R$) which coincides with the rest of the report. Point A indicates the initial reliability with no mass increase, point B indicates the reliability after mass was increased, and point C indicates the required increase in radius to recover the original reliability. The new radius value evaluated to 1.23" which was a change of 0.27" (28%). It was interpolated using the dark line in Figure 4.4. Stresses were initially stored in a look-up table so that simulations would not need to be run at the time of the assessment. In this case the interpolated radius was used to re-simulate stresses using the same input parameters. The orange line indicates this reliability distribution. We found that R was not entirely recovered at this new radius so R values were further evaluated about this point. Figure 4.6 shows stress distributions generated from the performance model for several radii near point C in Figure 4.4 along with a dashed line that indicates the endurance limit,

τ_{∞} , and connected average values to show the reduction of stresses as radius increases. Stress distributions were low enough that only the tails would reach above the endurance limit for radii near or greater than 1.3". This is an effect of the life-cycle model and is why we see a sharp drop off in the Figure 4.10. With our assumptions for the specific input and model parameters, one could achieve a reliability of 1.0 for this torsion bar by increasing the radius to 1.24".

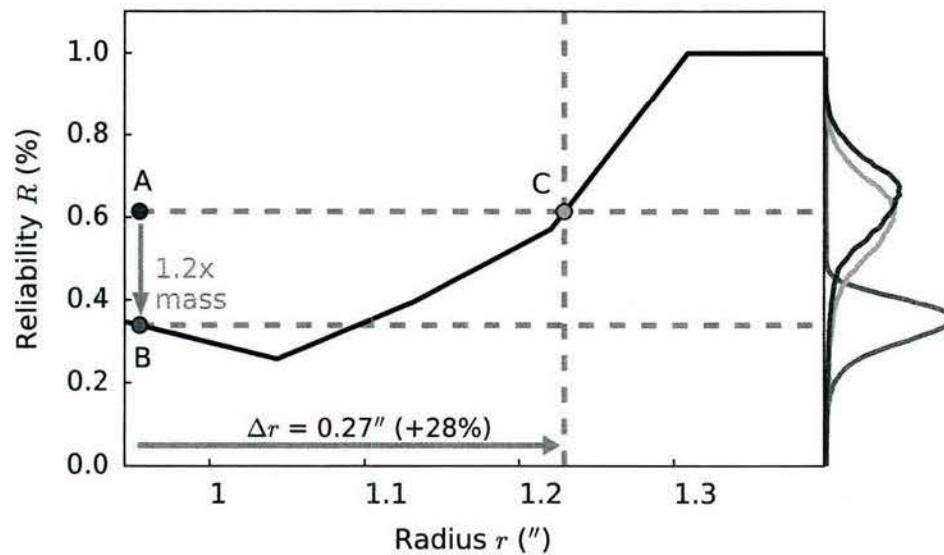


Figure 4.4: Recovering reliability by increasing radius

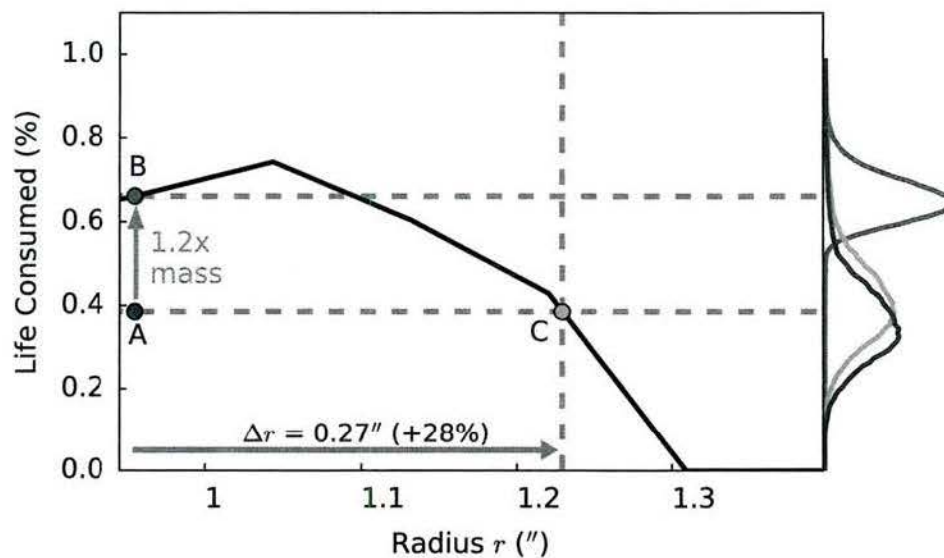


Figure 4.5: Life consumed ($1 - R$)

The increase in radius lead to a greater manufacturing cost. For this scenario, the price increase from the original radius was \$301. This number was only \$6 more than the initial attempt to recover R as shown

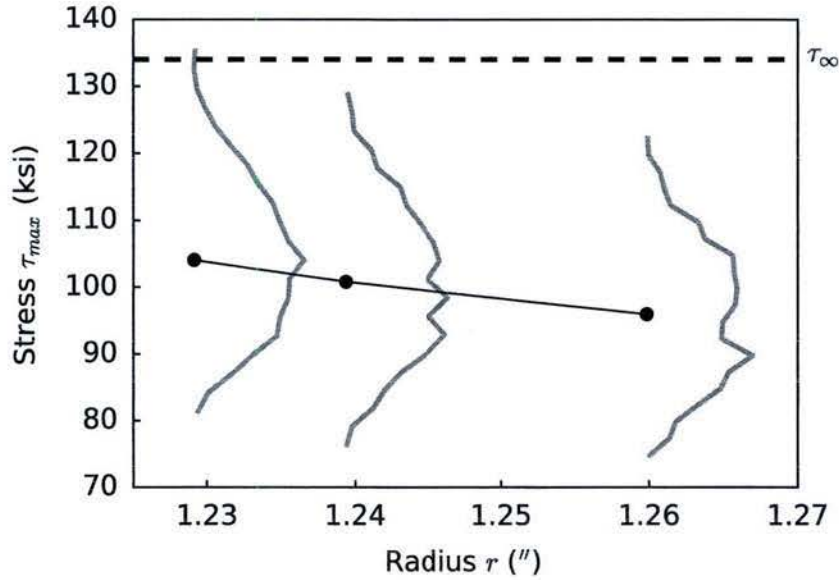


Figure 4.6: Stress distributions associated with different radii. The endurance limit, τ_{∞} is indicated by a dashed line. The stress distributions are shown in grey and the mean values for those stresses are plotted as connected points to show the reduction of stresses as radius increases

in Table 4.1 so the decision here would be to increase the radius to 1.24" and achieve the reliability of 1.0. This example naturally leads into the following section where optimization techniques were used to find pareto fronts indicating the best manufacturing parameters for these torsion bars based on a measure of user defined objectives.

Table 4.1: Cost of torsion bar with increased radius for reliability recovery.

Radius r	Manufacturing Cost C
0.95"	\$1,220
1.23"	\$1,515
1.24"	\$1,521

4.2 Optimization

The optimization problem is introduced by the way of a simple example of optimization of the spring design, with two geometric parameters, viz. radius r and length l of the torsion bar. The initial objectives were defined as minimization of material (expressed as mass) and maximization of clearance.

1. Minimize mass of torsion bar.

$$f_1 \triangleq m_{tbar} = \rho \pi r^2 l \quad (4.1)$$

where ρ was the mass density, r was the torsion bar radius, and l was the torsion bar length.

2. Maximize static clearance.

$$f_2 \triangleq \Delta_{eff} = (\Delta_o - u_{st}) \quad (4.2)$$

where Δ_o was initial clearance (before the springs were loaded) and u_{st} was the static displacement. Thus maximizing clearance was equivalent to minimizing static displacement u_{st} given by the ratio of the

force due to gravity, F , and the equivalent linear spring k_{eq}

$$u_{st} = \frac{F}{k_{eq}} = \frac{mg}{12k_{\phi}/L_{arm}^2} \quad (4.3)$$

The constraints were defined as maximum tolerable static displacement $u_{st_{max}}$, maximum allowable stress τ_{max} , maximum tolerable dynamic displacement $u_{dyn_{max}}$, and the following lower and upper limits for torsion bar radius and length.

1. Torsion bar radius range: $2.2 \text{ cm} \leq r \leq 4.0 \text{ cm}$
2. Torsion bar length range: $1.8 \text{ m} \leq l \leq 2.2 \text{ m}$
3. Static displacement is less than 73% of the initial clearance: $u_{st} < 0.73\Delta_o$
4. Maximum stress τ_{max} is less than maximum allowable stress τ_{lim} :

$$\tau_{max} = T \frac{r}{I_p} < \tau_{lim}$$
5. Maximum dynamic displacement is less than 86% of the initial clearance $u_{dyn} < 0.86\Delta_o$

For a full derivation of the simple torsion bar model, as well as some physical parameters and the relation between linear spring stiffness and torsional spring stiffness (k_{eq}), refer to Appendix A. This model was succinctly and naturally translated into the PyGMO framework, as shown in Figure 4.7.

4.2.1 Integration with Modelica Simulations

The focus of this sections is how dynamic simulations using Modelica's Functional Mock-up Interface (FMI) were included in the objectives and constraints along with two additional objectives; reliability in the form of life consumed, $(1 - R)$, and manufacturing cost of the torsion bar, C . Life consumed was evaluated using the reliability model from Section 4.1 and cost was evaluated based off Section 3.3. With the inclusion of dynamic simulations (a step down of 1 meter), dynamic clearance (defined as the minimum clearance during simulation) was maximized. Life consumed and cost were both minimized.

3. Maximize dynamic clearance. Dynamic clearance was defined as the minimum clearance during simulation.

$$f_3 \triangleq u_{dyn} \quad (4.4)$$

4. Minimize life consumed after rough terrain simulation. The same rough terrain simulation from Section 4.1.

$$f_4 \triangleq (1 - R) \quad (4.5)$$

5. Minimize manufacturing cost of torsion bar.

$$f_5 \triangleq C \quad (4.6)$$

f_1 and f_2 were algebraic expressions, f_3 and f_4 were simulation results, and f_5 was based on manufacturing costs. It is natural to think of static and dynamic clearance as similar quantities, however, their behavior was a little counter-intuitive because of the interplay between the spring stiffness and damper. Figure 4.8 illustrates four simulations for the minimum and maximum values of torsion bar radius r and length l . Positions were plotted over time and the subplots were arranged in a matrix where the bottom-left plot shows the results of inputs (r_{min}, l_{min}) and the top-right plot shows the results of inputs (r_{max}, l_{max}) . Within the subplots are three different lines. The grey dashed lines, labeled 'Initial vehicle height', represented the vehicle before it was influenced by the force due to gravity and the springs were not compressed. Once the vehicle was under the influence of gravity we saw a static displacement followed by dynamic displacements as the vehicle drove over the step. The vehicle height during this process was shown as a solid blue line, and the ground as a solid brown line. Notice how the static displacement, u_{st} , got smaller from the top left plot to the top right, but dynamic displacement, u_{dyn} , got larger. Due to the interaction between the springs


```

1 class Optimizer(base):
2     """
3     A multi-objective problem of a torsion bar with length and radius as inputs
4     and the total mass and torsional displacements as outputs
5
6     USAGE: torsionBar()
7     """
8
9     def __init__(self, dim=2):
10         # We call the base constructor as 'dim' dimensional problem, with 0 integer
11         # parts and 2 objectives.
12         super(Optimizer, self).__init__(dim, 0, 2, 2)
13         self.set_bounds((.02, 1.5), (.05, 3)) # ((lower1, lower1), (upper1, upper2))
14         # set the limits for the diameter and
15         # ((d_min, L_min), (d_max, L_max))
16         length [in meters]
17
18         self.best_x = [[.03, 2.5],]
19
20         # Reimplement the virtual method that defines the objective function
21
22     def _objfun_impl(self, x):
23         r = x[0] # Input1 = radius (chromosome)
24         L = x[1] # Input2 = length
25         f0 = rho*np.pi*(r**2)*L # Objective1 = the total mass (to be
26         minimized)
27         f1 = (m*g*(Larm**2)/
28              ((G*np.pi*(r**2))/(16*L))) # Objective2 = is clearance (to be maximized)
29         return (f0, f1, )
30
31     def _compute_constraints_impl(self, x):
32         r = x[0] # Input1 = diameter (chromosome)
33         L = x[1] # Input2 = length
34         c0 = (4*m*g*Larm**2 # Constraint1 = Max stress
35              / (np.pi*(r**3)) > sigma_max )
36         c0 = (r < .03)
37         c1 = (m*g*(Larm**2)/ # Constraint2 = Min clearance
38              ((G*np.pi*(r**2))/(16*L)) > Delta_min)
39
40         return [c0, c1]
41
42     # Add some output to __repr__
43     def human_readable_extra(self):
44         return "\n\t\tBar_1, with constraints"

```

Figure 4.7: PyGMO implementation of the simple problem

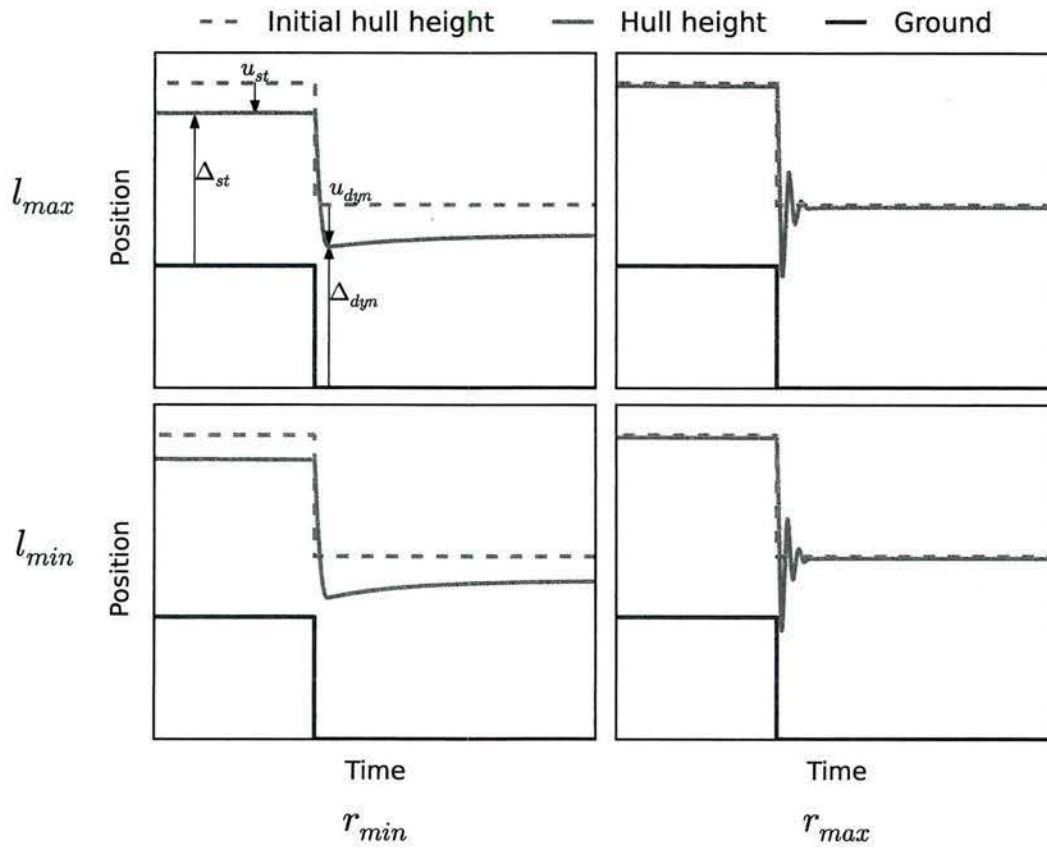


Figure 4.8: Vehicle position over time for the four cases: (r_{min}, l_{min}) , (r_{min}, l_{max}) , (r_{max}, l_{min}) , (r_{max}, l_{max}) . Due to the spring-damper interaction, static and dynamic displacements are not related

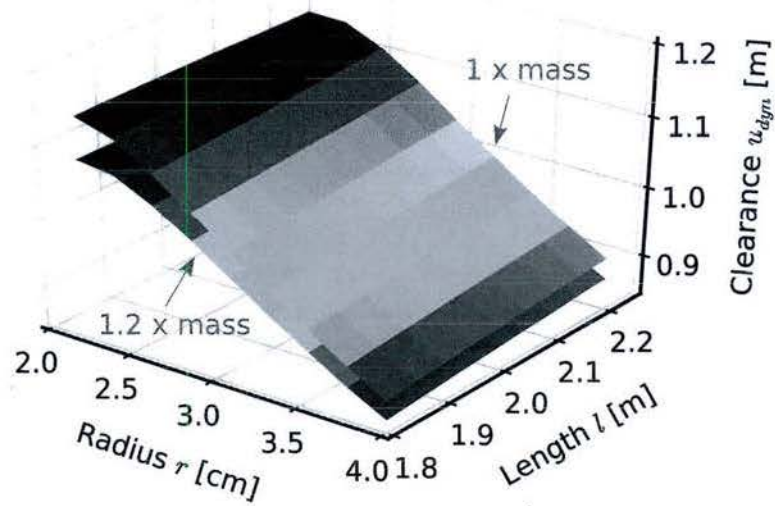


Figure 4.9: The surface plot for dynamic clearance with resolution 8

and the dampers, the resting (static) displacement and active (dynamic) displacement did not necessarily correlate.

Due to the stochastic nature of the dynamical and reliability models the evolutionary algorithm's runtime was greatly extended with the inclusion of these added objectives. Simulating outputs for every sample of every population in the EA increased the time greatly for even simulations that only took a few seconds. To reconcile this, simulation outputs were computed for many values of r and l once, and stored in a look-up table. When the optimizer generated a population of r and l values it used the table to look-up life consumed, performance, and cost factors and interpolate for r and l values not stored. Linear interpolation was sufficient for the performance output, dynamic clearance Δ_{dyn} , as indicated by Figure 4.9 which shows Δ_{dyn} for the parameter space of r and l for the two cases of mass. The same was sufficient for the reliability output, life consumed ($1 - R$), as shown by Figure 4.10 (the increased mass case was excluded from this plot). Notice the drop off after a certain level of r . These input values led to a lower experienced distribution of stress, the majority of which was below the endurance limit (this effect was explained in Section 4.1 with more detail). The simplest set of r and l values were the limits, which we called resolution one. Interpolation for all values in-between the limits was required of this case. Higher resolutions would allow for more values in between those points. The highest resolution needed was that which had interpolated values whose relative error, when compared to the exact values of the next resolution up, were small (Figure 4.11). A range of relative percent errors for the static clearance factor are shown in Figure 4.12 for several step-ups of resolution in the case of the performance output. Relative errors less than 0.5% were considered good enough for the needed accuracy, which corresponded to resolution 8. The same approximation was used for the reliability number as well.

After all the objectives were declared and the look-up tables generated, the optimizer was run for a population size of 500, with 100 generations. The final generation was plotted for output parameters, Figure 4.14, from input parameters, Figure 4.15. Each set of input parameters r and l mapped to the five output parameters. And each set of input-output matches were equal in decision weight. An orange X was placed in all plots to show the matching of the five output values from a given input set of r and l values.

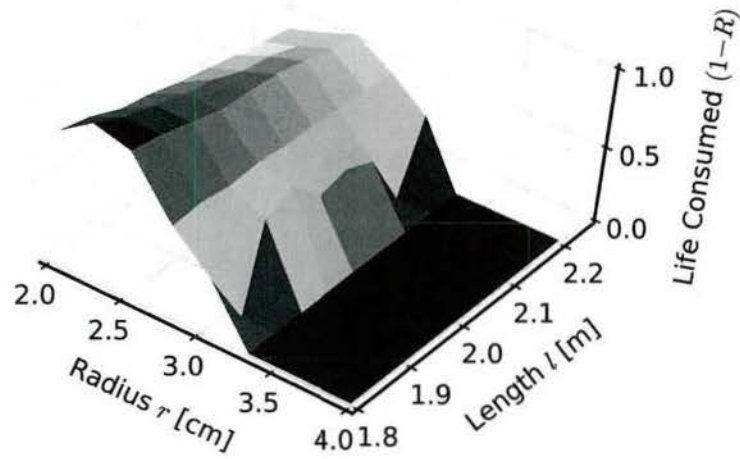


Figure 4.10: The surface plot for life consumed with resolution 8

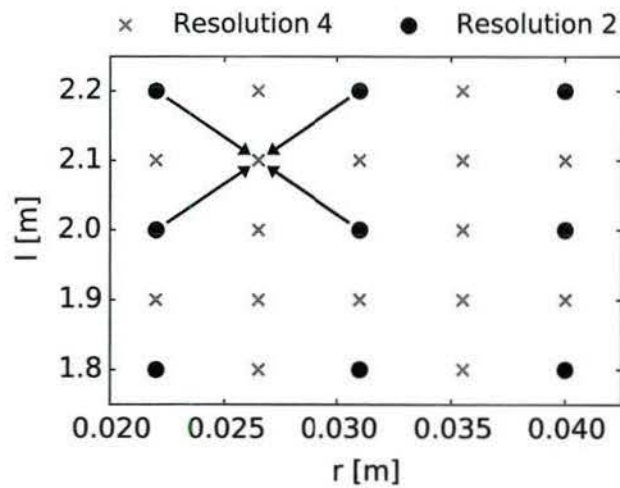


Figure 4.11: Illustration of the grid-space of input parameters r and l for two resolutions with arrows indicating linear interpolation

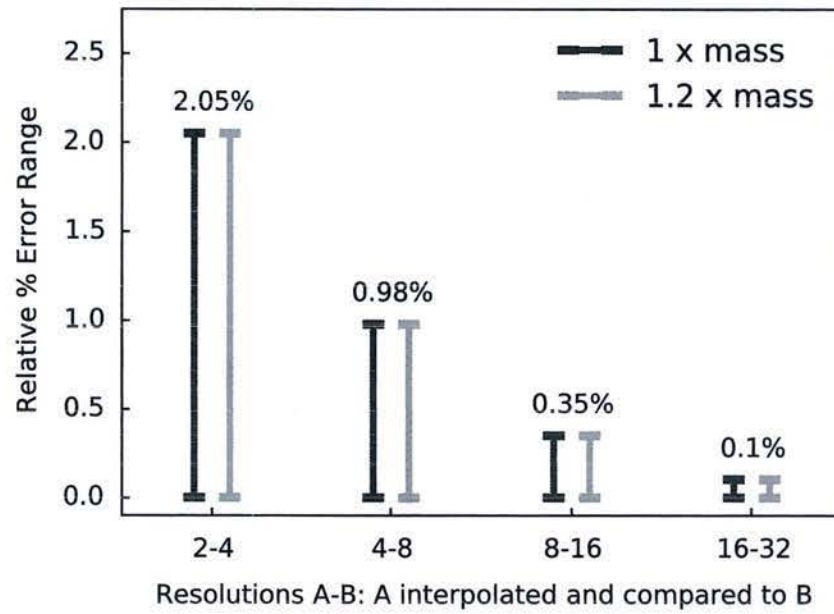


Figure 4.12: The minimum and maximum relative percent errors for several resolution step-up cases

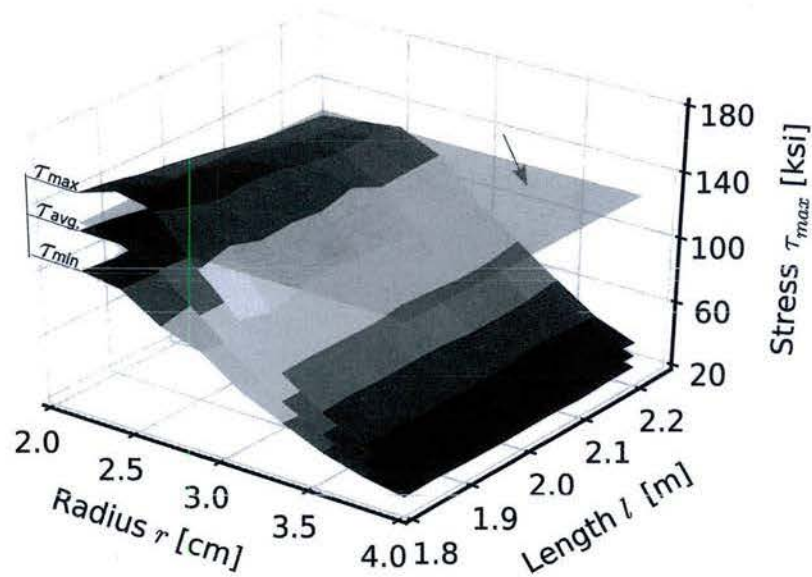


Figure 4.13: Three surface plots including the minimum, average, and maximum values of stress distributions at each value of r and l

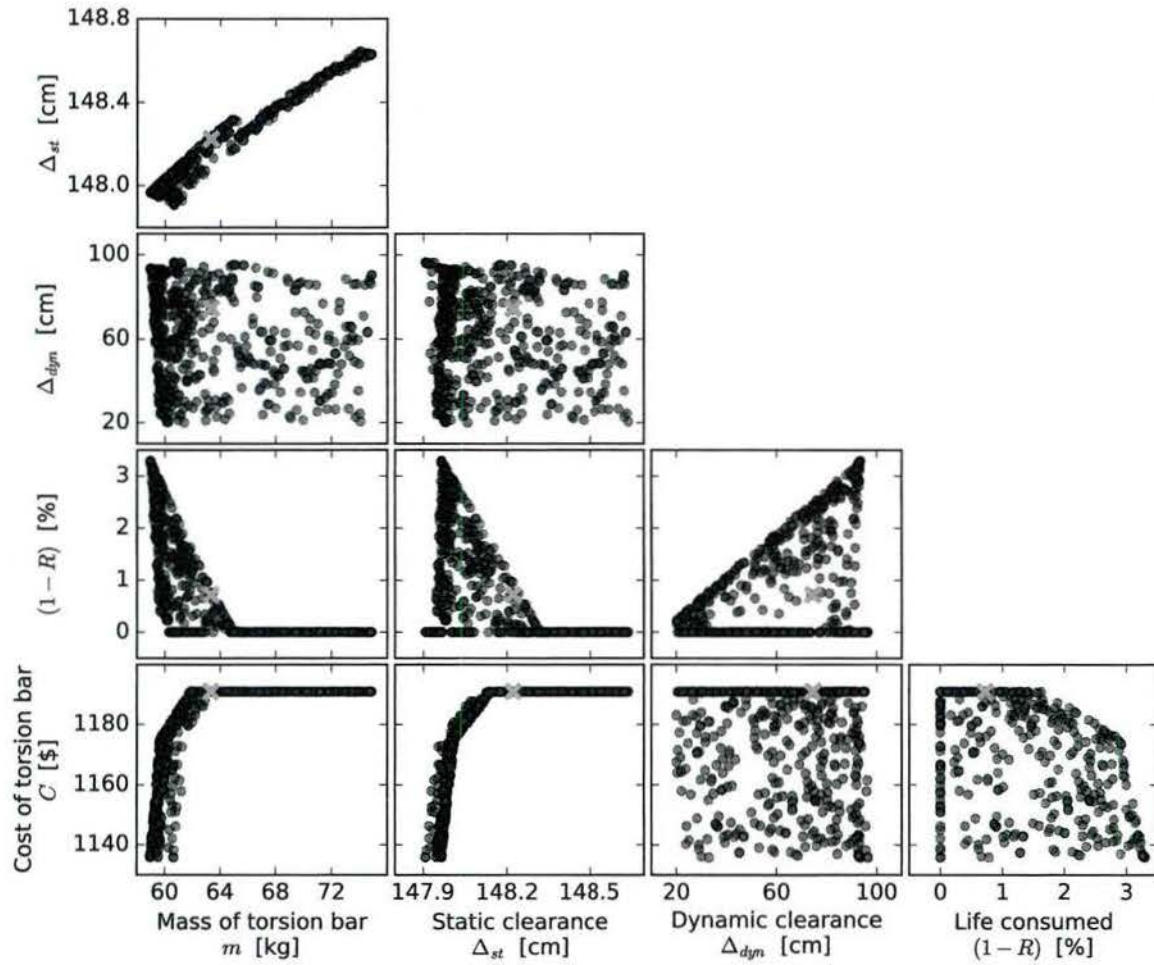


Figure 4.14: In order to view the results from the 5 objective optimization, cross-sections were plotted in a scatter matrix to show all slices of the Pareto fronts. A single set of input values from Figure 4.15 are shown as orange X's

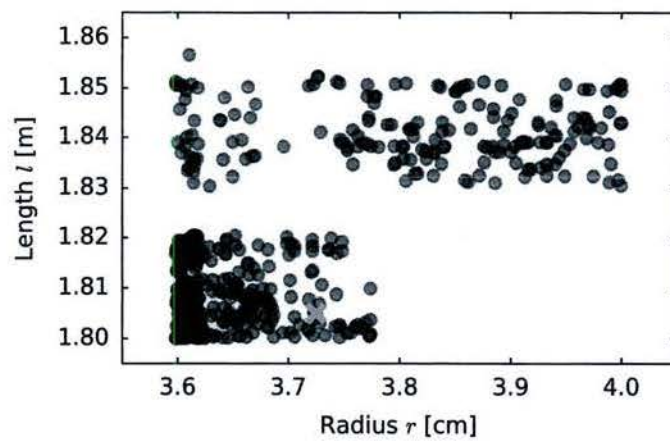


Figure 4.15: The final generation of the input parameters r and l . One value is shown as an orange X to show mapping of inputs in this figure to outputs in Figure 4.14

Bibliography

- [1] E. Bauer, X. Zhang, and D. A. Kimber, *Practical system reliability*. John Wiley & Sons, 2009.
- [2] R. E. Barlow, *Fault Tree Analysis*. Wiley Online Library, 1973.
- [3] W.-S. Lee, D. L. Grosh, F. A. Tillman, and C. H. Lie, "Fault tree analysis, methods, and applications a review," *IEEE transactions on reliability*, vol. 34, no. 3, pp. 194–203, 1985.
- [4] "PHM Technology." www.phmtechnology.com/products/made-phm.html. Accessed: 2016-07-24.
- [5] A. Hess, J. S. Stecki, and S. D. Rudov-Clark, "The maintenance aware design environment: Development of an aerospace phm software tool," *Proc. PHM08*, 2008.
- [6] M. A. Boyd and S. Lau, "An introduction to markov modeling: Concepts and uses," 1998.
- [7] C. A. Petri, "General net theory," in *Proceedings of the Joint IBM & Newcastle upon Tyne Seminar on Computer Systems Design*, 1976.
- [8] T. Murata, "Petri nets: Properties, analysis and applications," *Proceedings of the IEEE*, vol. 77, no. 4, pp. 541–580, 1989.
- [9] H. Ammar, Y. Huang, and R. Liu, "Hierarchical models for systems reliability, maintainability, and availability," *IEEE Transactions on Circuits and Systems*, vol. 34, no. 6, pp. 629–638, 1987.
- [10] J. Pearl, "Evidential reasoning using stochastic simulation of causal models," *Artificial Intelligence*, vol. 32, no. 2, pp. 245–257, 1987.
- [11] B. De Finetti, *Theory of Probability, volume I*. John Wiley & Sons, Ltd, 1974.
- [12] C. Davidson-Pilon, *Bayesian Methods for Hackers: Probabilistic Programming and Bayesian Inference*. Addison-Wesley Professional, 2015.
- [13] B. Cronin, "Why probabilistic programming matters." 2013.
- [14] J. Pearl, *Probabilistic reasoning in intelligent systems: networks of plausible inference*. Morgan Kaufmann, 1988.
- [15] R. T. Cox, "Probability, frequency and reasonable expectation," *American journal of physics*, vol. 14, no. 1, pp. 1–13, 1946.
- [16] R. T. Cox, *Algebra of Probable Inference*. John Hopkins University Press, 1961.
- [17] E. T. Jaynes, *Probability theory: the logic of science*. Cambridge university press, 2003.
- [18] G. L. Bretthorst, *Bayesian spectrum analysis and parameter estimation*. New York: Springer-Verlag, 1988.
- [19] D. S. Sivia, *Data analysis: a Bayesian tutorial*. Oxford university press, 1996.
- [20] S. F. Gull, "Bayesian inductive inference and maximum entropy," in *Maximum-entropy and Bayesian methods in science and engineering*, pp. 53–74, Springer, 1988.
- [21] T. J. Loredo, "From laplace to supernova sn 1987a: Bayesian inference in astrophysics," in *Maximum entropy and Bayesian methods*, pp. 81–142, Springer, 1990.

- [22] D. J. MacKay, "Bayesian interpolation," *Neural computation*, vol. 4, no. 3, pp. 415–447, 1992.
- [23] P. Gregory, *Bayesian Logical Data Analysis for the Physical Sciences: A Comparative Approach with Mathematica® Support*. Cambridge University Press, 2005.
- [24] N. Metropolis and S. Ulam, "The monte carlo method," *Journal of the American statistical association*, vol. 44, no. 247, pp. 335–341, 1949.
- [25] L. A. Zadeh, "Fuzzy sets," *Information and control*, vol. 8, no. 3, pp. 338–353, 1965.
- [26] L. A. Zadeh, "The role of fuzzy logic in the management of uncertainty in expert systems," *Fuzzy sets and systems*, vol. 11, no. 1, pp. 197–198, 1983.
- [27] G. Shafer *et al.*, *A mathematical theory of evidence*, vol. 1. Princeton university press Princeton, 1976.
- [28] S. Geman and D. Geman, "Stochastic relaxation, gibbs distributions, and the bayesian restoration of images," *Pattern Analysis and Machine Intelligence, IEEE Transactions on*, no. 6, pp. 721–741, 1984.
- [29] C. Andrieu, N. De Freitas, A. Doucet, and M. I. Jordan, "An introduction to mcmc for machine learning," *Machine learning*, vol. 50, no. 1-2, pp. 5–43, 2003.
- [30] P. Diaconis, "The markov chain monte carlo revolution," *Bulletin of the American Mathematical Society*, vol. 46, no. 2, pp. 179–205, 2009.
- [31] M. I. Jordan, *Learning in Graphical Models: [proceedings of the NATO Advanced Study Institute...: Ettore Majorana Center, Erice, Italy, September 27-October 7, 1996]*, vol. 89. Springer Science & Business Media, 1998.
- [32] C. M. Bishop, *Pattern recognition and machine learning*. springer, 2006.
- [33] D. Koller and N. Friedman, *Probabilistic graphical models: principles and techniques*. MIT press, 2009.
- [34] A. Gelman, J. B. Carlin, H. S. Stern, and D. B. Rubin, *Bayesian data analysis*, vol. 2. Taylor & Francis, 2014.
- [35] S. Theodoridis, *Machine Learning: A Bayesian and Optimization Perspective*. Academic Press, 2015.
- [36] D. J. Lunn, A. Thomas, N. Best, and D. Spiegelhalter, "Winbugs-a bayesian modelling framework: concepts, structure, and extensibility," *Statistics and computing*, vol. 10, no. 4, pp. 325–337, 2000.
- [37] M. Plummer *et al.*, "Jags: A program for analysis of bayesian graphical models using gibbs sampling," in *Proceedings of the 3rd international workshop on distributed statistical computing*, vol. 124, p. 125, Technische Universit at Wien, 2003.
- [38] A. Patil, D. Huard, and C. J. Fonnesbeck, "Pymc: Bayesian stochastic modelling in python," *Journal of statistical software*, vol. 35, no. 4, p. 1, 2010.
- [39] N. Goodman, V. Mansinghka, D. Roy, K. Bonawitz, and D. Tarlow, "Church: a language for generative models," *arXiv preprint arXiv:1206.3255*, 2012.
- [40] A. Gelman, D. Lee, and J. Guo, "Stan a probabilistic programming language for bayesian inference and optimization," *Journal of Educational and Behavioral Statistics*, p. 1076998615606113, 2015.
- [41] T. Minka, J. Winn, J. Guiver, and D. Knowles, "Infer .net 2.5," *Microsoft Research Cambridge*, 2012.
- [42] K. Deb, *Multi-objective optimization using evolutionary algorithms*, vol. 16. John Wiley & Sons, 2001.
- [43] K. Miettinen, *Nonlinear multiobjective optimization*, vol. 12. Springer Science & Business Media, 2012.
- [44] R. O. Duda, P. E. Hart, and D. G. Stork, *Pattern classification*. John Wiley & Sons, second ed., 2001.
- [45] E. Zitzler, M. Laumanns, L. Thiele, E. Zitzler, E. Zitzler, L. Thiele, and L. Thiele, "Spea2: Improving the strength pareto evolutionary algorithm," 2001.
- [46] K. Deb, A. Pratap, S. Agarwal, and T. Meyarivan, "A fast and elitist multiobjective genetic algorithm: Nsga-ii," *Evolutionary Computation, IEEE Transactions on*, vol. 6, no. 2, pp. 182–197, 2002.

- [47] H. Jain and K. Deb, "An improved adaptive approach for elitist nondominated sorting genetic algorithm for many-objective optimization," in *Evolutionary Multi-Criterion Optimization*, pp. 307–321, Springer, 2013.
- [48] O. M. Shir, S. Chen, D. Amid, D. Boaz, A. Anaby-Tavor, and D. Moor, "Pareto optimization and tradeoff analysis applied to meta-learning of multiple simulation criteria," in *Proceedings of the 2013 Winter Simulation Conference: Simulation: Making Decisions in a Complex World*, pp. 89–100, IEEE Press, 2013.
- [49] D. Izzo, "Pygmo and pykep: open source tools for massively parallel optimization in astrodynamics (the case of interplanetary trajectory optimization)," in *Proceed. Fifth International Conf. Astrodynam. Tools and Techniques, ICATT*, 2012.
- [50] F.-A. Fortin, D. Rainville, M.-A. G. Gardner, M. Parizeau, C. Gagné, *et al.*, "Deap: Evolutionary algorithms made easy," *The Journal of Machine Learning Research*, vol. 13, no. 1, pp. 2171–2175, 2012.
- [51] R. Fourer, D. M. Gay, and B. W. Kernighan, *AMPL: A mathematical programming language*. AT&T Bell Laboratories Murray Hill, NJ 07974, 1987.
- [52] B. M. Adams, W. Bohnhoff, K. Dalbey, J. Eddy, M. Eldred, D. Gay, K. Haskell, P. D. Hough, and L. Swiler, "Dakota, a multilevel parallel object-oriented framework for design optimization, parameter estimation, uncertainty quantification, and sensitivity analysis: version 5.0 users manual," *Sandia National Laboratories, Tech. Rep. SAND2010-2183*, 2009.
- [53] A. Jamali, A. Hajiloo, and N. Nariman-Zadeh, "Reliability-based robust pareto design of linear state feedback controllers using a multi-objective uniform-diversity genetic algorithm (muga)," *Expert systems with Applications*, vol. 37, no. 1, pp. 401–413, 2010.
- [54] K. Deb, S. Gupta, D. Daum, J. Branke, A. K. Mall, and D. Padmanabhan, "Reliability-based optimization using evolutionary algorithms," *IEEE Transactions on Evolutionary Computation*, vol. 13, no. 5, pp. 1054–1074, 2009.
- [55] "Critical item product function specification for shock absorber, direct action," Tech. Rep. 19207-12369332B, Bradley Fighting Vehicle Systems, 1990.
- [56] ASTM-International-ASTM-E468, "Standard practice for presentation of constant amplitude fatigue test results for metallic materials," 2011.
- [57] F. P'erez and B. E. Granger, "IPython: a system for interactive scientific computing," *Computing in Science and Engineering*, vol. 9, pp. 21–29, May 2007.
- [58] B. Carpenter, A. Gelman, M. Hoffman, D. Lee, B. Goodrich, M. Betancourt, M. A. Brubaker, J. Guo, P. Li, and A. Riddell, "Stan: A probabilistic programming language," *Journal of Statistical Software* (*in press*), 2016.
- [59] Stan Development Team. 2016. RStan: the R interface to Stan, Version 2.10.1. <http://mc-stan.org>.
- [60] Stan Development Team. 2016. PyStan: the Python interface to Stan, Version 2.9.0. <http://mc-stan.org>.

Appendix A

Torsion bar model

This section offers more detail on the simple torsion bar model. We utilize Hooke's law for shear and derive a few properties of the torsion bar as well as an interpretation between linear and torsional springs.

Hooke's law for shear is given by

$$\tau = G\gamma \quad (\text{A.1})$$

where τ is shear stress, G is shear modulus, and γ is shear strain.

A.1 Torsion of a rod

Taking an element along the length of the rod gives a disc of length Δx , as shown in Figure A.1.

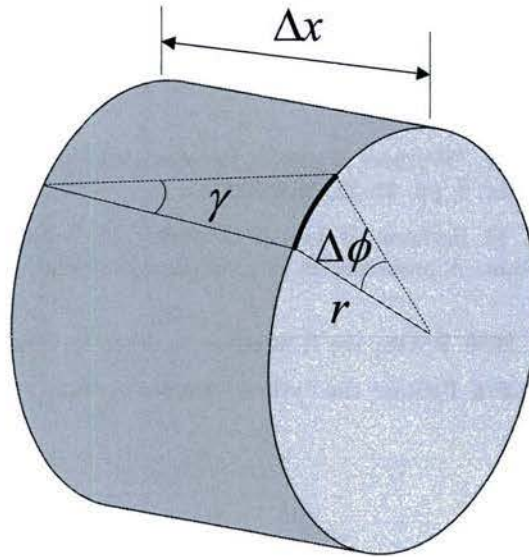


Figure A.1: Torsion of a rod element of length Δx

The dotted line represents the solid line after a torsional force is applied to the closer end. The two wedges share a common arc shown in bold. This gives a relation between ϕ , γ , r , and x .

$$r\Delta\phi = \gamma\Delta x \quad (\text{A.2})$$

Using this relation to solve for γ , and rewriting the Δ 's as differentials gives:

$$\gamma = r \frac{d\phi}{dx} \quad (\text{A.3})$$

Now the equation for γ can be used in Hooke's law for shear:

$$\tau = Gr \frac{d\phi}{dx} \quad (\text{A.4})$$

The total torque T on the end of the rod equals the integral of shear stresses crossed with the radius from the rod axis over the element dA , however the angle between τ and r is 90° so the integrand is simply the product of the two. The second to last expression subs in the expression for τ and the last expression calls the integral an area moment, I_p .

$$T = \int_A (\vec{r} \times \vec{\tau}) dA = \int_A r \tau dA = G \frac{d\phi}{dx} \int_A r^2 dA = G \frac{d\phi}{dx} I_p \quad (\text{A.5})$$

The maximum angle $\Delta\phi$ occurs at the end of the rod (attached to the arm) opposite of the rod's origin location. This requires an integration over the entire rod length, l .

$$\Delta\phi = \int_0^l \frac{T}{GI_p} dx = \frac{Tl}{GI_p} \quad (\text{A.6})$$

The importance of $\Delta\phi$ is its analogy to a linear displacement of a spring like object with some linear stiffness, and so $\Delta\phi$ is the torsional displacement, which is governed by a torsional stiffness.

The area moment is a function of the rod radius.

$$I_p = \int_A r^2 dA = \int_0^{2\pi} \int_0^r r^2 r dr d\phi = [\phi]_0^{2\pi} \left[\frac{1}{4} r^4 \right]_0^r = \frac{\pi r^4}{2} \quad (\text{A.7})$$

A.2 Torsional stiffness

Torsional stiffness (torsional spring constant) is given by the ratio of the applied torque T and the angle $\Delta\phi$:

$$k_\phi = \frac{T}{\Delta\phi} = \frac{T}{Tl/GI_p} = \frac{GI_p}{l} \quad (\text{A.8})$$

A.3 Equivalent linear spring

Figure A.2 shows an arm attached to the rod. The rod is rigidly affixed to the hull (schematically represented by the shaded wall) at the other side. For the sake of simplicity the connection between the arm and the rod is just a point in the center of the rod's cross-section. Realistically the arm would grasp the end of the rod around the circumference of the cross-section and twist the rod along that angular displacement.

The static displacement u_{st} is computed as

$$u_{st} = \frac{m_{veh}g}{k_{veh}} \quad (\text{A.9})$$

where m_{veh} is equivalent mass which makes contact at the point of applied torque in the above picture, g is the force due to gravity, and k_{veh} is the equivalent vehicle linear spring constant. If only a spring was placed vertically under the point of contact with the mass then k_{eq} would be that spring's stiffness.

This equivalent spring constant can be identified from

$$k_\phi = \frac{|\vec{T}|}{\Delta\phi} = \frac{|\vec{F} \times \vec{l}_{arm}|}{\frac{\Delta u}{l_{arm}}} = \frac{Fl_{arm}}{\frac{\Delta u}{l_{arm}}} = \frac{F}{\Delta u} l_{arm}^2 = k_{eq} l_{arm}^2 \quad (\text{A.10})$$

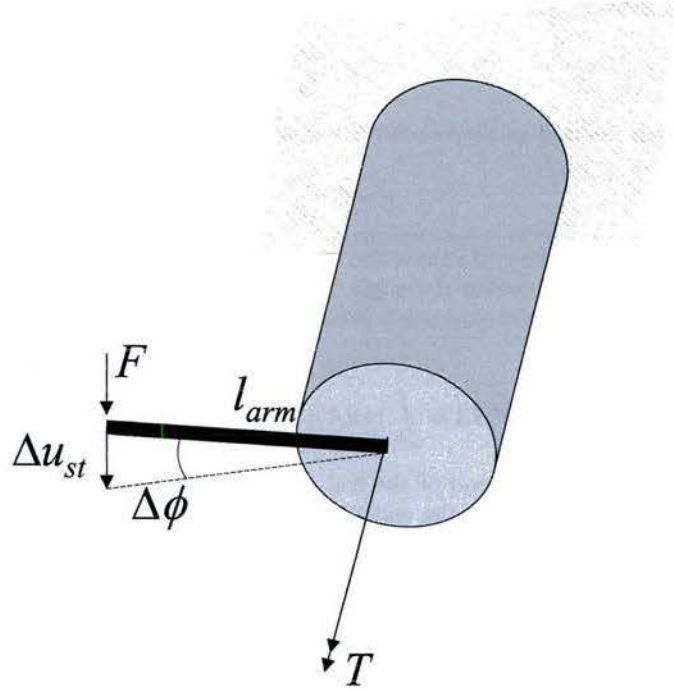


Figure A.2: Arm connected to torsion bar (which force acts on)

where l_{arm} is the length of the arm. The last expression in Equation A.10 has k_{eq} which is defined by the force applied, F , over the (linear) static displacement, u_{st} . Now taking the first and last expression above and solving for the effective linear spring constant (stiffness) of the rod:

$$k_{eq} = \frac{k_{\phi}}{l_{arm}^2} = \frac{GI_p}{l_{arm}^2 l} \quad (A.11)$$

The total equivalent spring of a vehicle k_{veh} , with 12 torsion bars is

$$k_{veh} = 12 \frac{k_{\phi}}{l_{arm}^2} \quad (A.12)$$

A.4 First order vehicle model for static displacements

A full expression for u_{st} can now be made with only dependence on the physical properties of the arm and rod, the mass of the what is forcing the arm down (in our case the vehicle mass m_{veh}), and the acceleration due to gravity on earth.

$$u_{st} = \frac{m_{veh}g}{k_{veh}} \quad (A.13)$$

or

$$u_{st} = \frac{m_{veh}g l_{arm}^2}{12 k_{\phi}} \quad (A.14)$$

Appendix B

Piece-wise linear model

As explained in Section 3.2.1 this section follows the same optimization techniques using a piece-wise function rather than the hyperbolic function. Equation 3.11, repeated here, gives the equation of two slopes

$$\tau = \tau^* + (N - N^*)b, \quad b = \begin{cases} b_0, & N \leq N^* \\ b_1, & N > N^* \end{cases} \quad (\text{B.1})$$

B.1 Batched gradient decent

The ordinary least squares approach is not suitable for this model because it is not linear. Instead, we used a batched gradient decent (BGD) method with an $l = 2$ fit. The cost function is the squared distance between the estimate, $\hat{\tau}$, and data point, τ_i

$$J = \sum_i (\hat{\tau}_i - \tau_i)^2 = \sum_i \epsilon_i^2 \quad (\text{B.2})$$

using the chain rule to solve for the gradient gives

$$\nabla J = 2 \sum_i \epsilon_i \nabla \epsilon_i \quad (\text{B.3})$$

the gradient of the error term is then

$$\nabla \epsilon_i = \left\langle \frac{\partial \hat{\tau}_i}{\partial \tau^*}, \frac{\partial \hat{\tau}_i}{\partial N^*}, \frac{\partial \hat{\tau}_i}{\partial b_0}, \frac{\partial \hat{\tau}_i}{\partial b_1} \right\rangle \quad (\text{B.4})$$

and partials are

$$\begin{aligned} \frac{\partial \hat{\tau}_i}{\partial \tau^*} &= 1 \\ \frac{\partial \hat{\tau}_i}{\partial N^*} &= - \begin{cases} b_0 & N \leq N^* \\ b_1 & N > N^* \end{cases} \\ \frac{\partial \hat{\tau}_i}{\partial b_0} &= (N - N^*) \quad N \leq N^* \\ \frac{\partial \hat{\tau}_i}{\partial b_1} &= (N - N^*) \quad N > N^* \end{aligned}$$

In training, each parameter is updated by the following assignment

$$b_0^{(k)} \leftarrow b_0^{(k-1)} - \eta \nabla_{b_0} J \quad (\text{B.5})$$

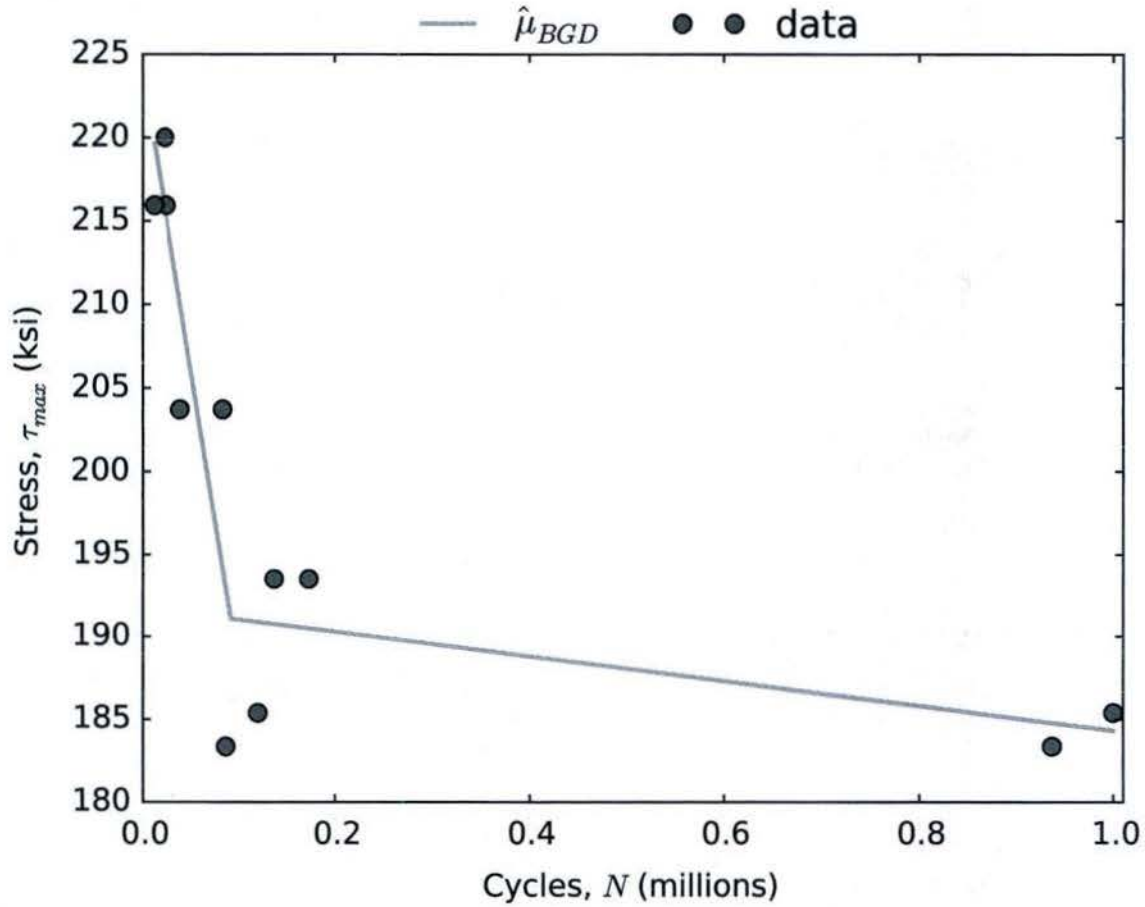


Figure B.1: Data with piece-wise linear model obtained by minimizing least square error using mini-batch gradient descent

where η is a learning rate, and k is the current iteration. The units of stress are in a thousand pounds per square inch (ksi). The parameters were initialized with a guess; $\tau^* = 195$ ksi, $N^* = 2 \times 10^5$ cycles, $b_0 = -1 \times 10^{-4} \frac{\text{ksi}}{\text{cycles}}$, $b_1 = -1 \times 10^{-5} \frac{\text{ksi}}{\text{cycles}}$. The results are shown in Figure B.1.

The GD method found the optimal fit, which appears to be very reasonable. This method is useful, however we can do better. There is more detail to explore in the uncertainty of this piece-wise linear model. A probabilistic approach, like the one performed on the hyperbolic model, was used for this model as well.

B.1.1 Bayesian model

The probabilistic model here follows the same trend as the hyperbolic Bayesian model, with adjusted equations to fit the piece-wise function shown in Equation 3.11. The four parameters, N^* , τ^* , b_0 , and b_1 were obtained by inference according to the following model (Figure B.2)

The results are shown in a heat-map (Figure B.3), where bins of τ values have associated probabilistic distributions describing the likelihood of cycles, N .

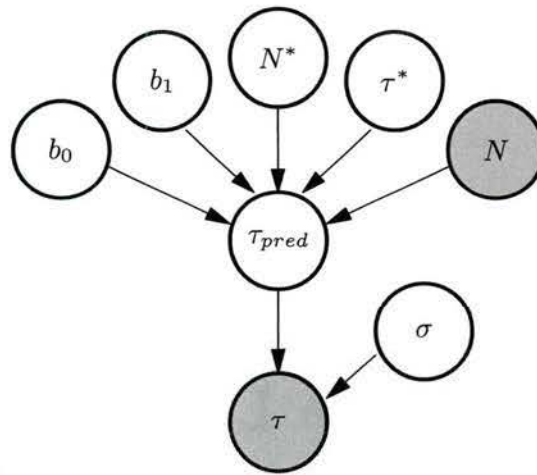


Figure B.2: A graphical representation of the model

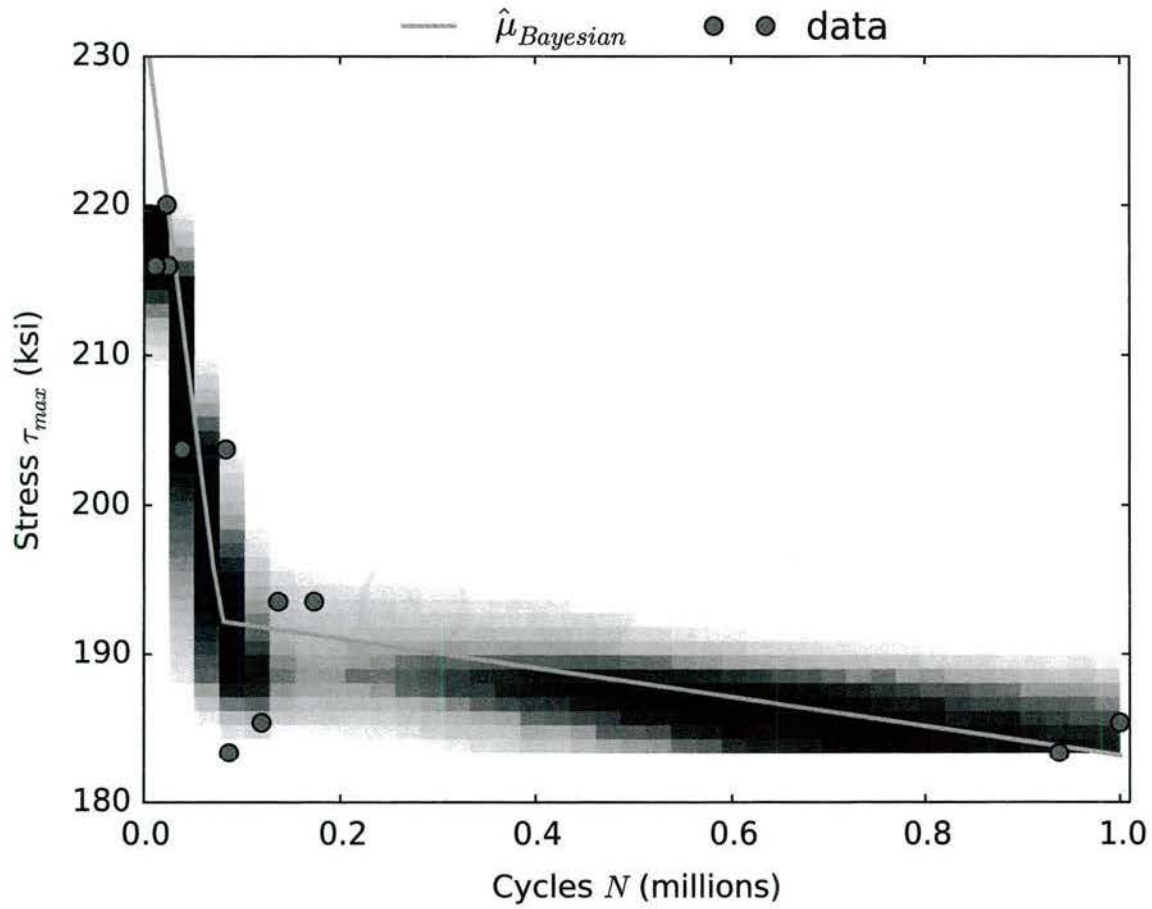


Figure B.3: Posterior distribution of cycles $\Pr(N|\tau)$ using a piece-wise linear model (dark areas indicate higher probability). The orange trace shows the model computed using the average parameters

Appendix C

Bayesian Models for Different Corrosion Damage Levels and Repair Methods

Section 3.2.1 describes a Bayesian modeling of life cycle data for the case of no corrosion damage. The analysis was repeated for different life cycle experiments and this appendix summarizes the results of the analyses, using the hyperbolic model defined by Eq. (3.10). A way to show this in a form of a probabilistic model is depicted in Figure C.1.

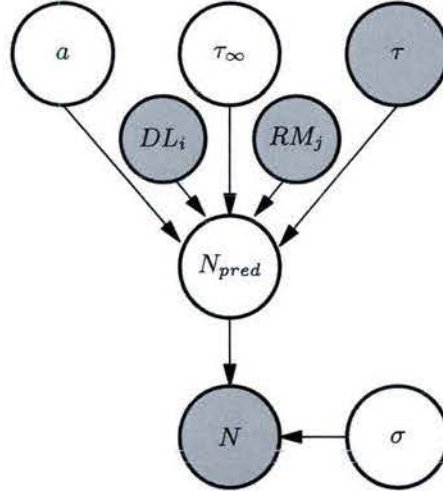


Figure C.1: A graphical representation of the model

C.1 Description of Life Cycle Experiments

Three level of damage and two repair methods were employed in the experiments. Table C.1 lists the damage level codes with the corresponding descriptions and Table C.2 lists the repair methods and their descriptions.

Table C.1: Description of Damage Levels

Damage Code	Damage Description
DL_1	Corroded 8 hr
DL_2	Corroded 24 hr
DL_3	Corroded 72 hr

Table C.2: Description of Repair Methods

Repair Code	Repair Description
RM_1	Belt
RM_2	Wire Brush

C.2 Bayesian Models for Different Damage Levels and Repair Methods

Stress-cycle (S-N) data for different corrosion damage levels and repair methods are shown in the subsequent subsections.

C.2.1 DL_1 : Corroded for Eight Hours

Figure C.2 shows the case where no repair was attempted: Figure C.2a shows the measurements (blue circles) and average Bayesian estimate $\hat{\mu}_{Bayesian}$ (orange trace) on top and three selected conditional probability densities of the life cycle in terms of cycles $\Pr(N|\tau, DL_1)$ (for three selected levels of stress τ); Figure C.2b shows a heatmap of the two-dimensional histogram of $\Pr(N|\tau, DL_1)$, where darker areas correspond to higher probabilities, with mean shown as orange trace and the data as blue circles.

C.2.2 DL_1, RM_1 : Corroded for Eight Hours, Repair Using Belt

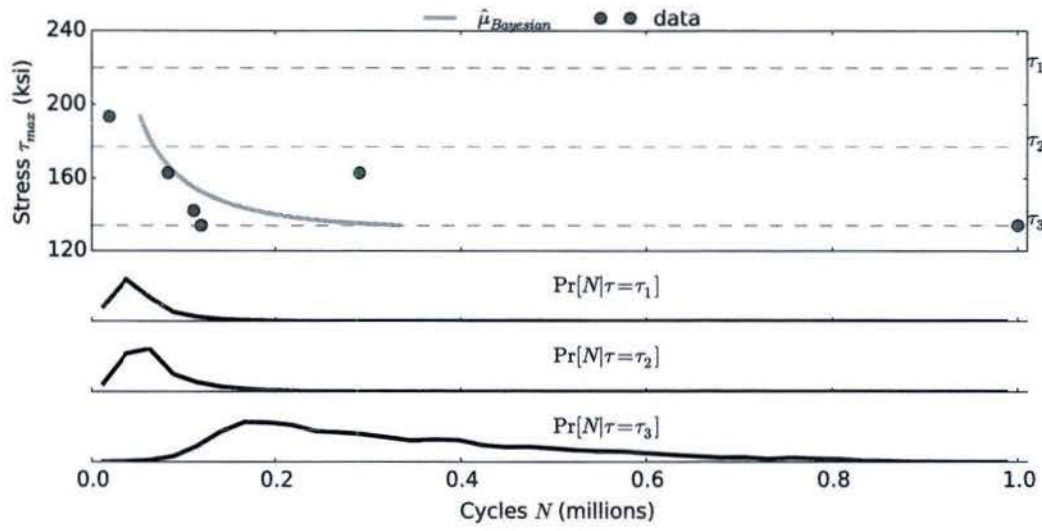
Figure C.3 shows the case of corrosion damage DL_1 followed by applying repair method RM_1 . As indicated in Table C.2, RM_1 consists of removing the layer of rust using a belt. The data points, marked with blue dots, show considerable variations among the samples. It is important to emphasize that samples that survived one million cycles did not fail.

The Bayesian model fit runs roughly through the middle of the data. The same variance σ was used as in other models (refer to Figure C.1). The measured samples exhibit considerable variability, which means that in this particular case larger variance σ could be used.

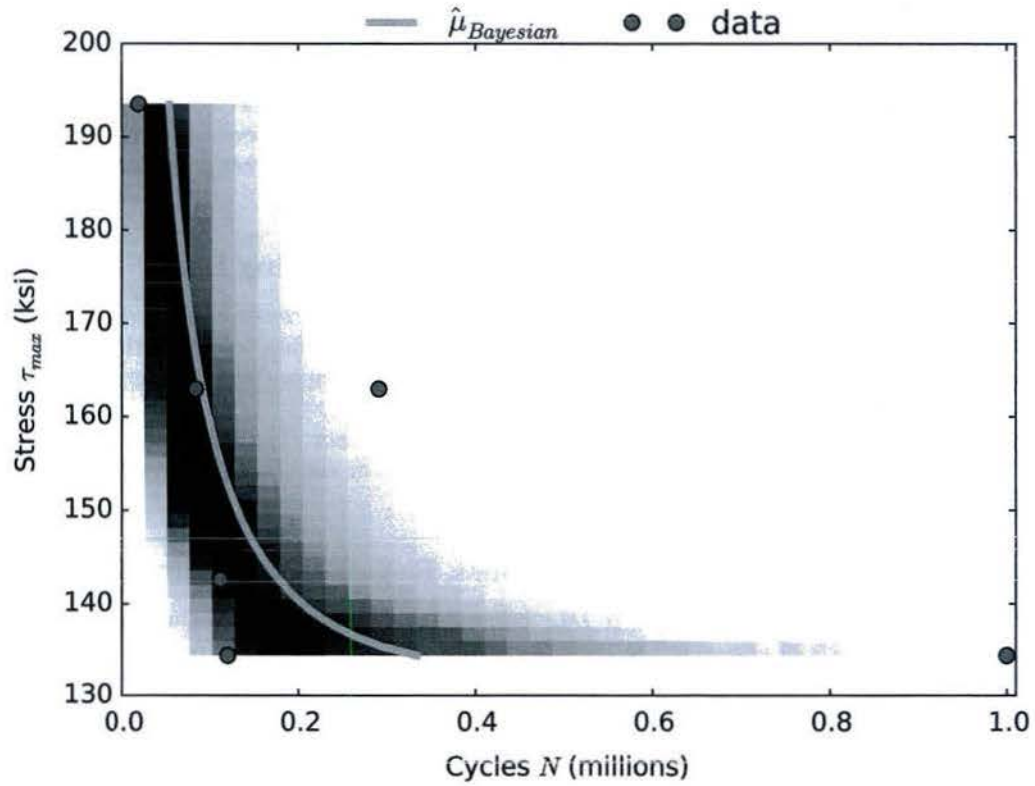
C.2.3 DL_1, RM_2 : Corroded for Eight Hours, Repair Using Wire Brush

Figure C.3 shows the case of corrosion damage DL_1 followed by applying repair method RM_1 . As indicated in Table C.2, RM_1 consists of removing the layer of rust using a belt. The data points, marked with blue dots, show considerable variations among the samples. Again, the samples that survived one million cycles did not fail.

For the two different stress levels, $\tau_{max} \sim 182$ ksi and $\tau_{max} \sim 204$ ksi, there are two considerably different samples: one that failed fairly early, similar to the untreated case at the same level of corrosion damage (shown in Figure C.2b), and the other survived one million cycles without failure. The mean estimate falls roughly in the middle because prior knowledge did not bias the estimate towards either of the two extremes. Testing additional samples would be valuable to determine if the distributions are simply wide, or there is a bi-modal behavior, where some samples were successfully treated and others were not.



(a)



(b)

Figure C.2: Posterior $\Pr(N|\tau, DL_1)$ with no repair attempted. (a) data and mean Bayesian fit (top) with three slices of the conditional pdf (b) heatmap of the conditional pdf

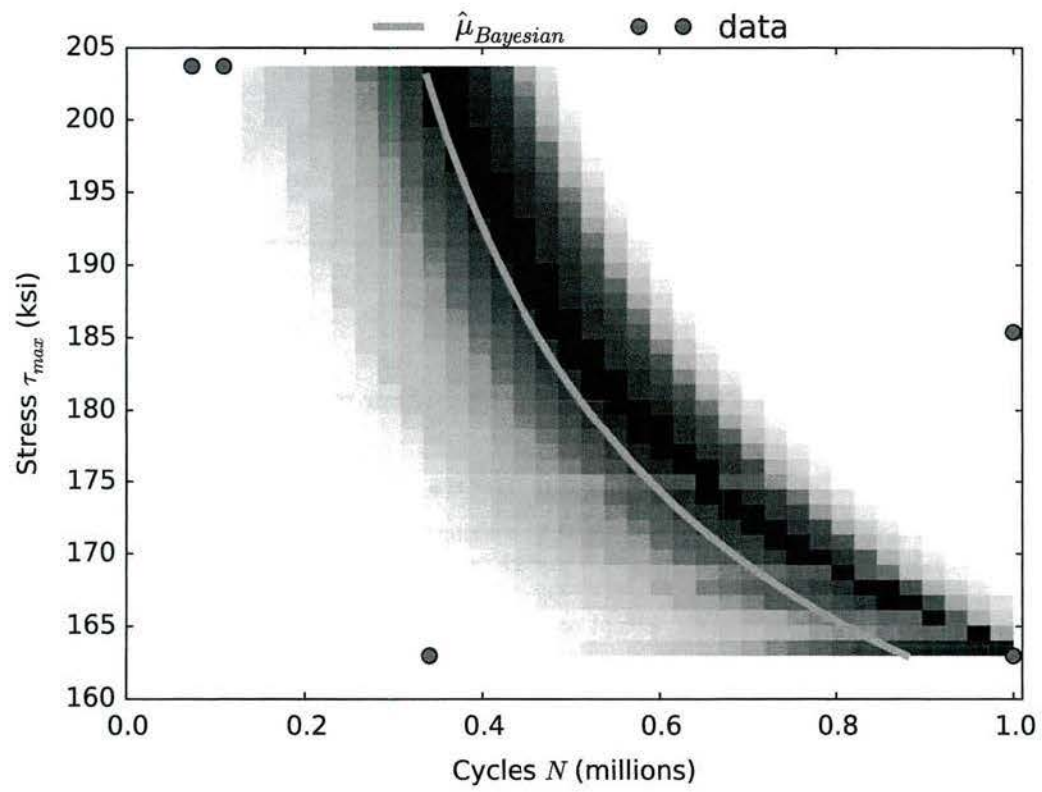


Figure C.3: Posterior $\Pr(N|\tau, DL_1, RM_2)$ after repair method RM_1 was applied

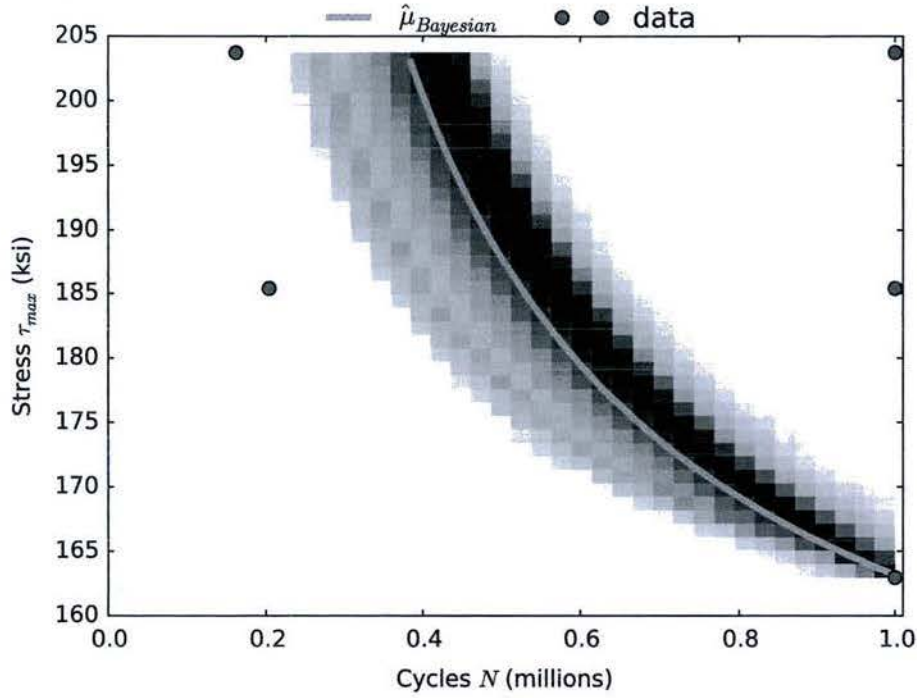


Figure C.4: Posterior $\Pr(N|\tau, DL_1, RM_2)$ after repair method RM_1 was applied

C.2.4 DL_2 : Corroded for Twenty Four Hours

The second level of corrosion damage was simulated by soaking the samples for twenty four hours. Figure C.5 shows the posterior probability distributions estimated from samples (blue dots) of cycles given different stress levels $\Pr(N|\tau, DL_2)$.

The samples are generally consistent, except one, which reached one million cycles without failure. This outlier reminds us of inherent uncertainty associated with life cycle estimates and shows that even higher exposure to corrosion can sometimes leave the life of a specimen unaffected.

C.2.5 DL_2, RM_1 : Corroded for Twenty Four Hours, Repair Using Belt

Figure C.6 shows the case of corrosion damage DL_1 followed by applying repair method RM_2 , which consists of removing the layer of rust using a wire brush. The data points, marked with blue dots, show considerable variations among the samples. It is important to emphasize that samples that survived one million cycles did not fail.

The Bayesian model fit runs roughly through the middle of the data. The same variance σ was used as in other models (refer to Figure C.1). The measured samples exhibit considerable variability, which means that in this particular case larger variance σ could be used.

C.2.6 DL_2, RM_2 : Corroded for Twenty Four Hours, Repair Using Wire Brush

Figure C.7 shows the case of corrosion damage DL_1 followed by applying repair method RM_2 , corrosion removal using a wire brush.

One sample subjected to considerable stress $\tau_{max} \sim 185$ ksi survived one million cycles but two samples failed at lower stress ($\tau_{max} \sim 163$ ksi) with 877,000 and 251,000 cycles. This particular case resulted in a higher endurance limit (signified by parameter τ_∞ in the model) than the eight hour corrosion with wire

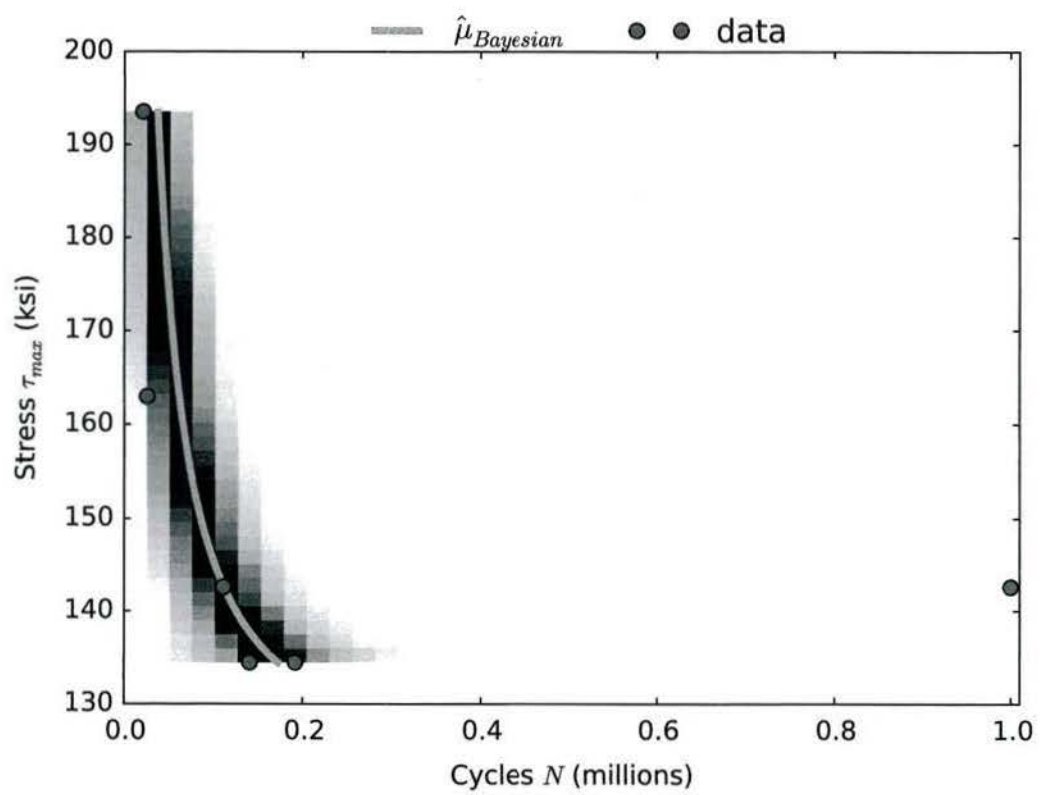


Figure C.5: Posterior $\Pr(N|\tau, DL_2)$ after repair method RM_1 was applied

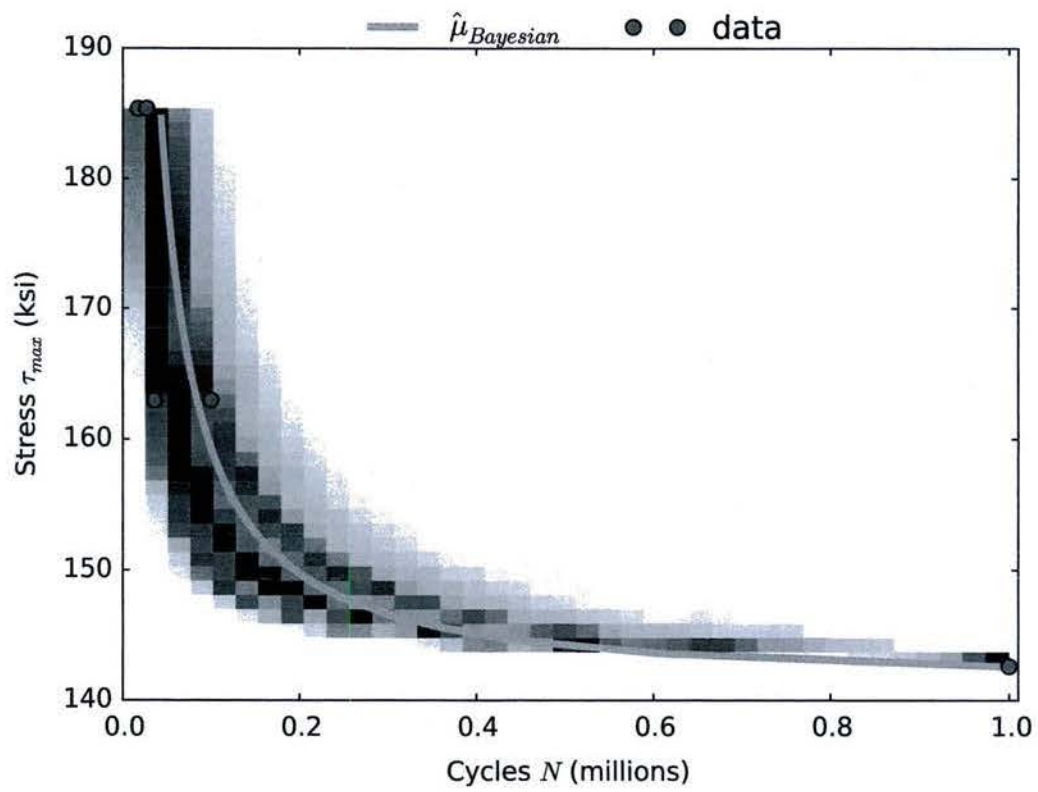


Figure C.6: Posterior $\Pr(N|\tau, DL_2, RM_1)$ after repair method RM_1 was applied

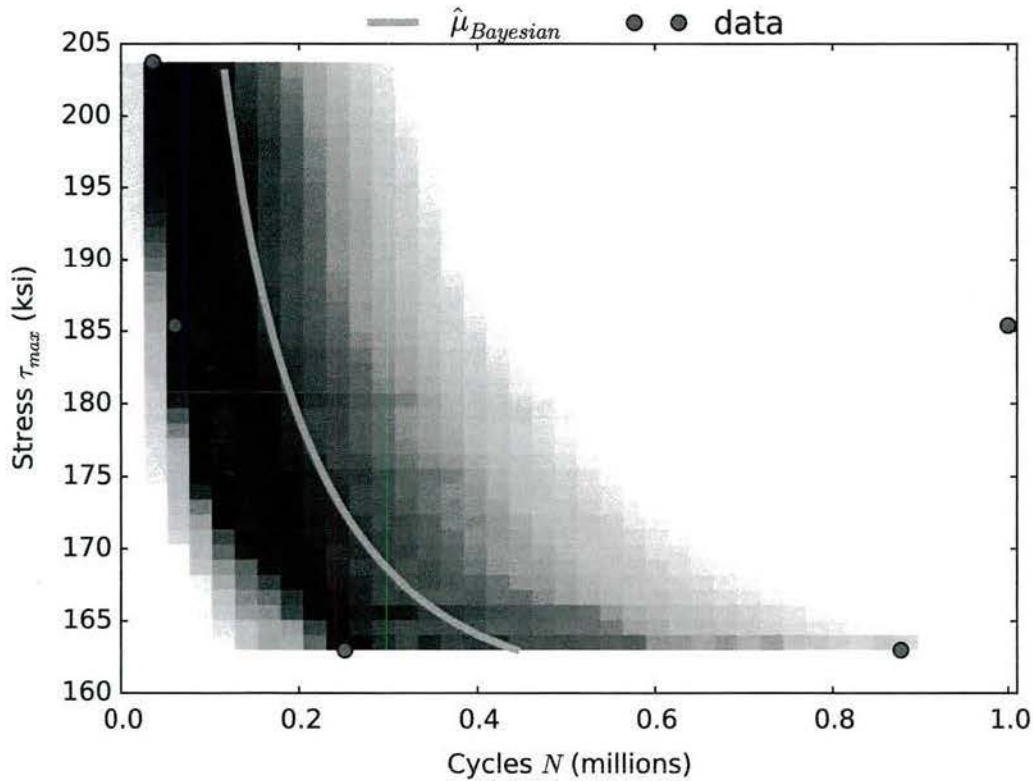


Figure C.7: Posterior $\Pr(N|\tau, DL_2, RM_2)$ after repair method RM_1 was applied

brush treatment. The outlying point at one million cycles in this case lead to a larger variance at higher stresses, relative to previous cases.

C.2.7 DL_3, RM_1 : Corroded for Seventy Two Hours, Repair Using Belt

Repair methods were used for all samples tested at damage level three. Figure C.8 shows the case for corrosion damage DL_3 followed by applying repair method RM_1 , corrosion removal using a belt.

This damage level was a more extreme case where the variance of estimated cycles was much smaller in comparison to lower damage levels. No samples survived to one million cycles. At the lowest stress $\tau_{max} \sim 135$ ksi, two samples failed at 80,000 and 102,000 cycles.

C.2.8 DL_3, RM_2 : Corroded for Seventy Two Hours, Repair Using Wire Brush

Figure C.9 show the case for corrosion damage DL_3 followed by applying repair method RM_2 , corrosion removal by wire brush.

Similar to Figure C.8, no samples survived to one million cycles. Two samples, at lowest stress $\tau_{max} \sim 134$ ksi failed at 104,000 and 163,000 cycles. Both cases of damage level three have narrow distributions associated with a given stress. The stress levels that are shown are almost all lower than those in the uncorroded case (Figure 3.23), and no samples survived more than 200,000 cycles. There are several ways to compare these two repair methods, both qualitatively and quantitatively. It is easier to qualitatively compare the two based on the figures alone. Considering only the mean estimate line at each damage level, the wire brush method did marginally better than that belt method.

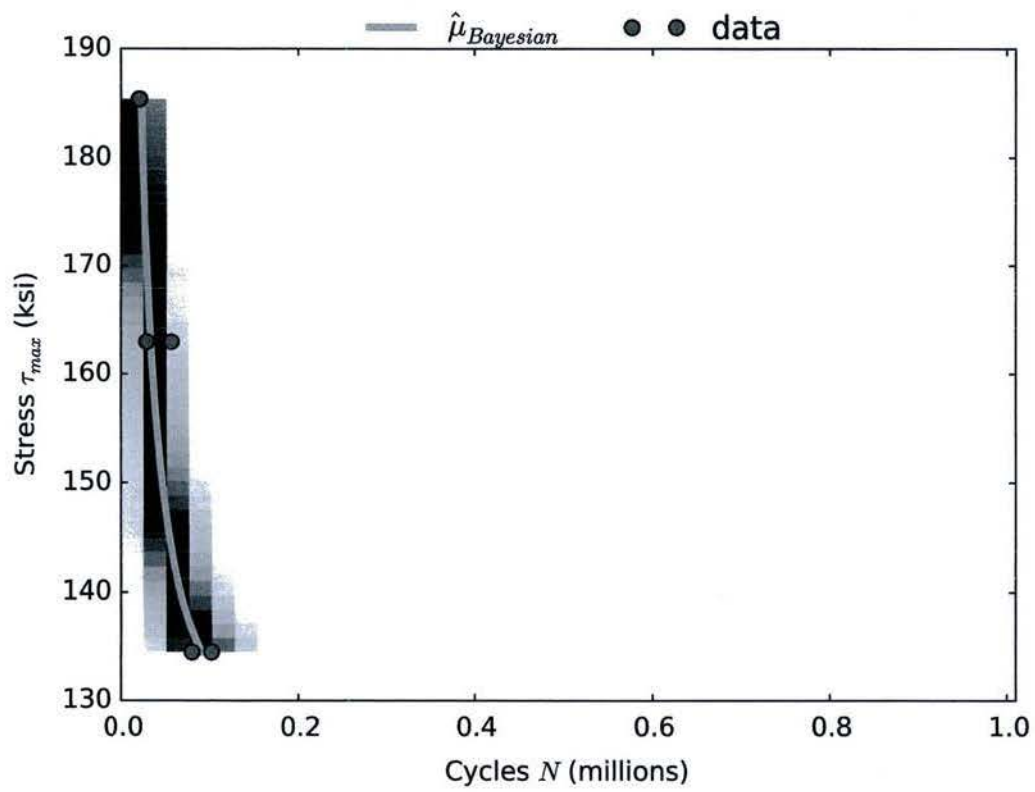


Figure C.8: Posterior $\Pr(N|\tau, DL_3, RM_1)$ after repair method RM_1 was applied

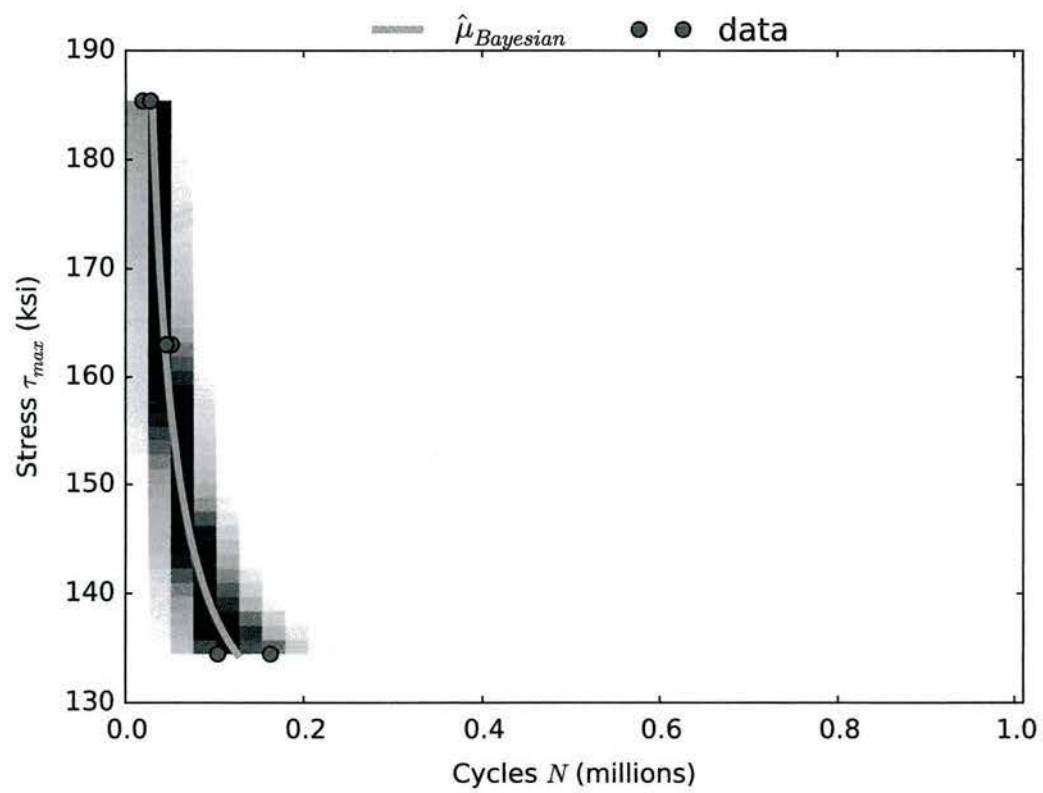


Figure C.9: Posterior $\Pr(N|\tau, DL_3, RM_2)$ after repair method RM_2 was applied

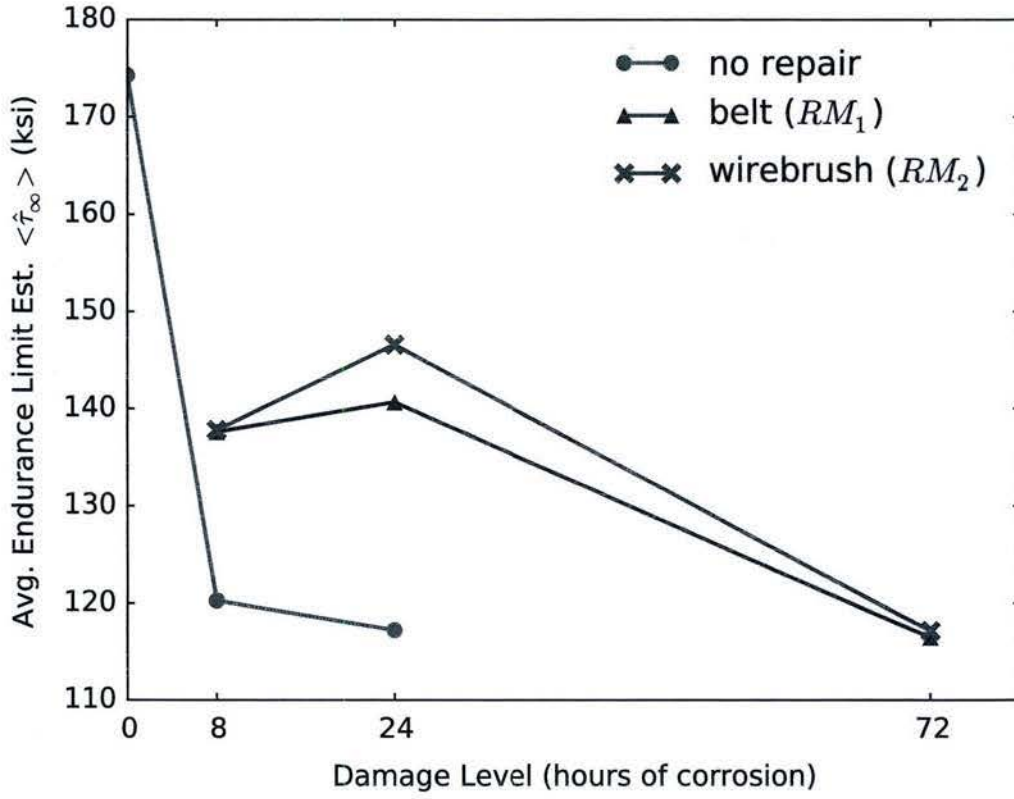


Figure C.10: For the three cases of repair method the model parameter τ_{∞} is plotted at each damage level. Damage level 0 indicates the uncorroded case

C.3 Comparing Repair Methods at Different Damage Levels

The parameter τ_{∞} is interpreted as the endurance limit. Theoretically, stress below this limit yields infinite cycles. The higher the endurance limit the stronger the sample. Figure C.10 shows the average value of τ_{∞} at different damage levels for the corroded only, corroded then repaired with belt, and corroded then repaired with wire-brush cases. The green points are cases of corrosion with no repair. Zero corrosion had the largest endurance limit, coherent with expectation. The seventy two hour corrosion with no repair method (what would be a green marker at damage level value 72) was omitted from analysis due to a lack of enough data. The twenty four hour case (DL_2) shows anomalous behavior because the endurance limit improved where samples were corroded for longer. The seventy two hour case (DL_3) had endurance limits that were much smaller, as expected.

The endurance limit is a good parameter to consider when comparing different repair methods, however it should not be the only factor in comparison. Our framework so far is a life-cycle model based on inputs of stress τ_{max} , damage level DL_i and repair method RM_i in order to output a data-driven prediction on the number of cycles until failure. The complicated micro-structure of these samples were not included in the model and we have seen effectively random outcomes from it (ex. Figure C.4 and the DL_2 case in comparing endurance limits in Figure C.10). In Figure C.4 there are four data points that reach one million cycles. Two of which are at the same point, stress $\tau_{max} \sim 163$ ksi, and the other two are at larger stresses, $\tau_{max} \sim 185$ ksi and $\tau_{max} \sim 204$ ksi. At $\tau_{max} \sim 185$ ksi there were two failures; one at 204,000 cycles and the other, one million. At $\tau_{max} \sim 204$ ksi there were also two failures; one at 162,000 cycles and the other, one million.

In Figure C.10 we saw the anomalous improvement of endurance limit at twenty four hours of corrosion (DL_2) from the eight hour corrosion (DL_1) samples, which went back down to a lower endurance limit for the seventy two hour (DL_3) case. This behavior suggests that the micro-structure contributes largely to test results. The wire brush repair method (RM_2) did marginally better than the belt method (RM_1), even with the suspicious increase in endurance limit for the twenty four hour case. In order to compare these cases more concisely, Figure C.11 was generated to show the average Bayesian estimate along with data for all cases. Each subplot shows a different damage level. Within each subplot there are three lines and sets of data. Green indicates the uncorroded and no repair case, blue indicates the first repair method, and red indicates the second repair method for that damage level. Underneath each legend label are data on the endurance limit estimate ($\langle \hat{\tau}_\infty \rangle$) with units of ksi, and the number of samples that survived to one million cycles (N_∞). In all cases the wire brush repair method was marginally better.

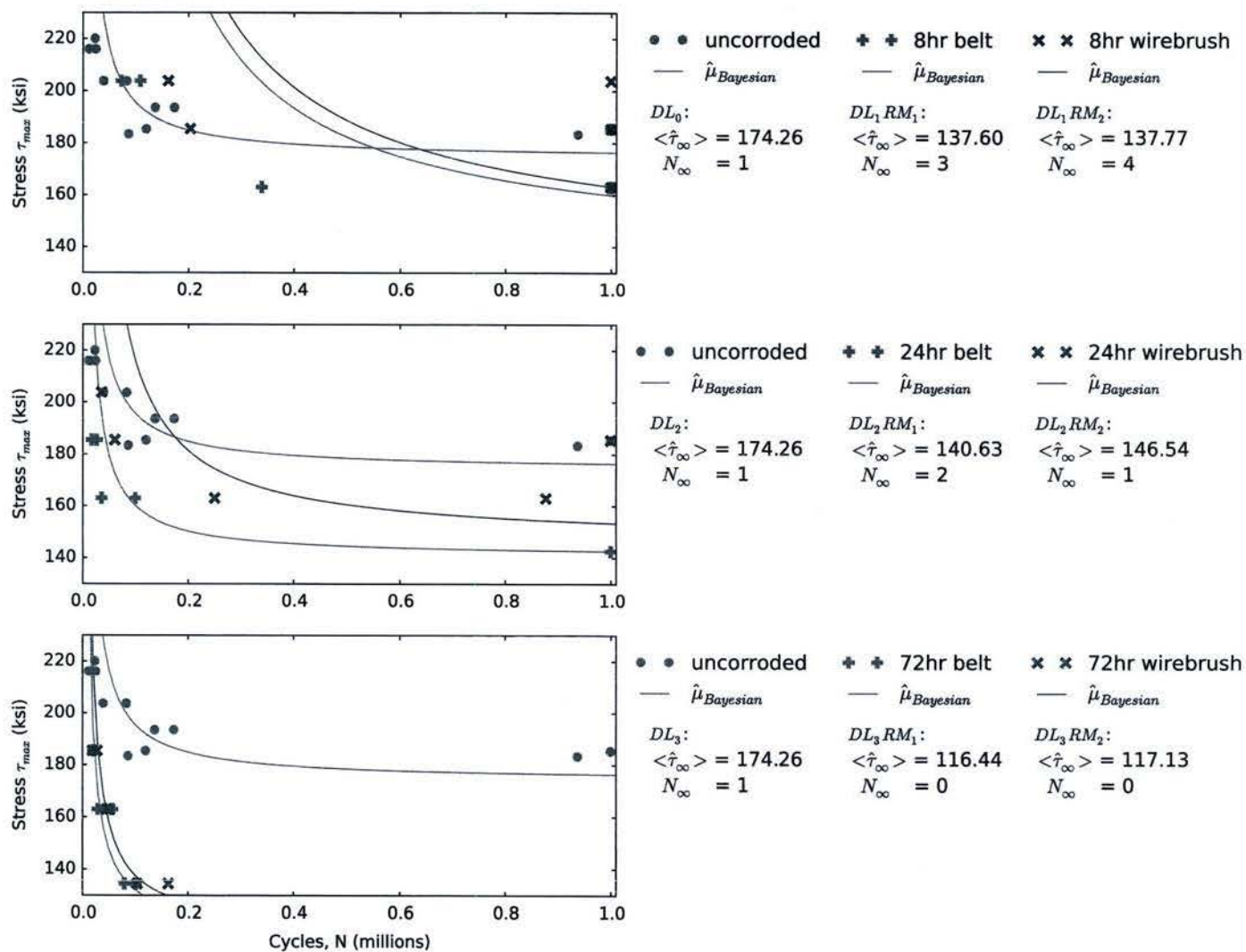


Figure C.11: For each damage level (subplot) the uncorroded case is compared with two repair methods (columns to the right of subplots) by looking at the average endurance limit estimate ($\langle \hat{\tau}_{\infty} \rangle$ ksi) and the number of samples that survived to one million cycles (N_{∞})

Appendix D

Software

Several different pieces of software we employed in building this framework. This section details the installation and integration process of these software. It is important to emphasize that all links and references in this section alone are of the time this was written and may have changed.

D.1 Environment - Anaconda

Our programming environment was Anaconda from Continuum Analytics (<https://continuum.io>). The root environment is obtained by downloading and installing the appropriate version. It is available with Python 2.7 or 3.5 for 64-bit Mac and 32/64-bit Windows or Linux. We used the Windows 64-bit graphical installer with Python 2.7. Anaconda is made easier by giving the user the ability to install and work between different environments. For example, if the user's root environment is a 64-bit implementation of Python 3.5 he/she can install a 32-bit implementation of Python 2.7 within that and use it when needed. All environments are kept in a folder named 'env' in the root environment and the commands for installing, naming, and switching between these environments along with further documentation are detailed here: <http://conda.pydata.org/docs/using/envs.html>. There is an Anaconda cheat sheet, containing many useful commands for command prompt (http://conda.pydata.org/docs/_downloads/conda-cheatsheet.pdf). An alternative to using the 'conda' command is to use 'pip' which comes with the Python package (see documentation: <https://packaging.python.org/installing/>).

D.1.1 Spyder

Spyder is an integrated development environment (IDE) for scientific programming in Python and comes with Anaconda. It was used for database access with use of the module pyodbc (current source: <https://github.com/mkleehammer/pyodbc>). Like most Python libraries in Anaconda installing is as easy as typing 'conda install pyodbc' in the command prompt and pressing 'y' when asked to continue with installation. Spyder was also used to generate a toolbox of functions for database access, make figures and tables, and store data.

D.1.2 Jupyter Notebook

Project Jupyter (<http://jupyter.org/index.html>) spawned from the IPython Project[57] and has evolved into an open source interactive data science tool. Jupyter notebook gives the user the ability to design individual cells of code or markdown to create an interactive notebook where cells could be run individually, in groups, or all together. This notebook was more useful than the Spyder IDE because we could generate detailed reports that were written along with interactive code cells making it an all-in-one tool. It utilizes LaTeX markup code making an easier transition from notebook to finalized paper/report.

D.2 Probabilistic Programming

D.2.1 Stan

Stan[58] is a library for statistical modeling and data analysis. The language manual can be found at <http://mc-stan.org> along with an installation guide and section on getting started. Stan has several implementations available including RStan[59] for R users, and PyStan[60] for Python users. PyStan provides an interface to Stan, where some model code is written in *C++* and implemented in Python (Figure D.1). A *C++* compiler is required to be available to Python during installation and at run-time. We used a Linux machine to run the probabilistic code because at the time it was most reliable.

```
1 usage_model = """
2 data {
3     int N; //number of observations
4     real M[N]; //observed usage of dimension N [hours]
5     real<lower=0> dt[N-1]; //delta time of dimension N-1 [delta days]
6     int F; //forward-reverse condition
7 }
8 parameters {
9     real<lower=0,upper=1> b[N-1]; //usage factor [usage/days]
10    real M0;
11    real<lower=0,upper=40> sigma0; //initial noise
12    real<lower=0,upper=40> sigma[N]; //noise
13    real n_outlier; //conditional noise parameter for large outliers
14 }
15 transformed parameters {
16     real u[N]; //estimated (real) usage
17
18     u[1] <- M[1] + M0;
19     for (i in 2:N) {
20         if (F==1) {
21             u[i] <- u[i-1] + b[i-1]*dt[i-1]; //forward case
22         }
23         else if (F==0) {
24             u[i] <- u[i-1] - b[i-1]*dt[i-1]; //reverse case
25         }
26     }
27 }
28 model {
29     M0 ~ normal(0,sigma0); //First data point
30     b ~ uniform(0,1);
31     for (i in 2:N) {
32         if ((M[i]-M[i-1])/dt[i-1])>1) {
33             M[i] ~ normal(u[i], n_outlier); // for clear outliers
34         }
35         else {
36             M[i] ~ normal(u[i], sigma[i]);
37         }
38     }
39 }
40 """
41 # Compile model
42 m = pystan.StanModel(model_code=usage_model)
43 # Run Sampler
44 fit = m.sampling(data=data, iter=10000, chains=4)
```

Figure D.1: Stan code example with PyStan implementation

D.2.2 PyMC/PyMC3

PyMC is a Python module for probabilistic programming (PyMC3 is its successor). It utilizes several Markov chain Monte Carlo (MCMC) sampling algorithms. We did not use PyMC or PyMC3 for final results but developed some models with it in the early stages of this framework. Ultimately we chose Stan because PyMC3 required extra steps in order to utilize the computer's graphics processing unit (GPU) when compiling and sampling models (newer GPUs only). This utilization can be extremely useful and speeds up computation time immensely, but was not necessary for our type of model, and data size. Theano is a numerical computation library in Python with a forte in tensor expressions, is required to use PyMC3. The installation instructions along with many examples and full documentation on how to operate these libraries are found here, PyMC: <https://pymc-devs.github.io/pymc/>, PyMC3: <https://pymc-devs.github.io/pymc3/>.

D.3 Decision Making

D.3.1 PyGMO and DEAP

The Python Parallel Global Multi-Objective Optimizer (PyGMO) was used in the decision making chapter of this framework. Documentation can be found here: <http://esa.github.io/pygmo/>. Installing PyGMO was made easy in the Anaconda environment by executing the command 'conda install pygmo' in the command prompt.

D.4 Dynamical Model

D.4.1 Modelica

JModelica

In order to run the JModelica compiler with a Jupyter notebook, the notebook needs to be initiated in a Jmodelica environment. This is accomplished, for example, with the following batch file which was created in notepad++ (Figure D.2)

```
1 @echo off
2 call C:\JModelica.org-1.17\setenv.bat
3 if %errorlevel% neq 0 pause
4 "C:\Anaconda2\Scripts\jupyter-notebook.exe" %*
5 if %errorlevel% neq 0 pause
```

Figure D.2: Code example of initiating a Jupyter notebook in the Jmodelica environment with a batch file

Research Program 4:
Evaluation of Material Properties and Repair
Procedures in Aluminum Parts with Thermal,
Impact and Environmental Stresses

This research was conducted under Office of Naval Research Grant N00014-14-1-0789.

Report Generated by:

Golisano Institute for Sustainability
Rochester Institute of Technology
190 Lomb Memorial Drive
Rochester, NY 14623
(585) 475-5101

1. Introduction

This document provides a summary of an investigation into sensitization of high strength aluminum alloys through a case study on the cracking failure mode witnessed in components on the U.S. Marine Corps' vehicles and provides options for mitigation of future failures. The fleet of vehicles studied is susceptible to compromised structural integrity due to crack propagation in the alloy 5083-H aluminum material used in a seal component. This problem is not limited to vehicles as evidenced by reports that reference cracking in other Navy applications. Although results of this investigation may lend themselves to other applications, the specific failure mode investigated in this case study is the transverse crack propagation that primarily occurs in the corner of the seal groove of the component. The approach applied to this investigation involved research on known effects of temperature and corrosion for series 5xxx aluminum alloys, analyzing fracture surfaces on the component, measuring operational temperatures and strains, and identifying protective coating options for series 5xxx alloys through laboratory testing.

Aluminum 5083-H is a strain hardened alloy that exhibits high strength, corrosion resistance in moderate environments and offers good weld capability. Results of this investigation on cracking of the aluminum alloy 5083-H components revealed that stabilization techniques and surface coating with pure aluminum did not adequately protect specimens when subjected to a corrosive environment while experiencing fatigue loading. Applying a protective coating of anti-corrosion polymer extended the corrosion fatigue life of the aluminum substrate at high load ratios by preventing development of surface pits. Due to the difficulty in detecting cracks in components, it is not recommended that the components be refurbished if signs of degradation in the protective paint layer or pitting are present. Future design modifications may be warranted to extend the typical life of high strength aluminum alloys by applying thick anti-corrosion polymer layers at regions of high stress intensity before pitting occurs.

Contents

1. Introduction.....	279
2. Background.....	281
2.1 Component review	281
3. Failure Analysis	286
3.1 Fractograph Analysis	287
3.2 Optical Analysis.....	290
4. Operating Conditions	291
4.1 Test 1 – Tightening	292
4.2 Test 2 – Stationary Temperature.....	292
4.3 Test 3 -Driving.....	293
5. Mechanical Simulation	294
6. Usage & Sensitization.....	298
7. Stress Corrosion Cracking	299
8. Fatigue Evaluation	300
8.1 Stabilization Process	301
8.2 Flame Spray Coating Process	302
8.3 Twin-wire arc Process.....	303
8.4 Fatigue Testing in Air	303
8.5 Corrosion Fatigue Testing.....	305
9. Conclusions.....	307
10. References.....	308

2. Background

Marine Corps vehicles are designed to transport Marines from sea through the littoral zone onto land. The vehicle experiences a multitude of service conditions throughout its operating life, including seawater and arid temperature regions. These conditions along with the stressors imparted during operation affect the material characteristics of components. One of the functions of the component of interest is to prevent water infiltration during swim operations. The component is comprised of several welded parts including a main plate with a seal surfaces. The seal is engaged by two finger latches holding the component in place. Both the component and mating parts have seals that fit into dovetail shaped grooves thereby creating a labyrinth seal to decrease the potential of leakage. The seal groove naturally traps water, debris, and residual salt from evaporation of seawater.

Over the last several years, the maintainers at the Marine Corps' depots have identified cracks in the component on aging vehicles. These cracks either had gone unnoticed previously or had finally grown sufficiently large as to be easily detected at this time. Figure 1 shows a crack that formed at a step in the seal groove on a media blasted component pulled from service. Several complete component assemblies rejected during inspection were checked to determine if a specific location along the crack groove could be pinpointed as the source of the crack initiation. Unfortunately, the cracks extended along almost the entire perimeter of the seal groove preventing identification of a common source. Of the components inspected during a visit to the depot, all showed crack openings at the seal groove extending toward the center of the component and one showed a crack on the outside edge of the component with the opening facing outside the part.



Figure 1 - Crack in Component

2.1 Component review

Anecdotal evidence from maintainers suggested that cracking in the Aluminum 5083-H is a recent occurrence and predominantly at the seal interface of the component and adjacent parts. The cracking on the component was noticed during Inspect and Repair Only as Necessary (IROAN) cycles at one of the depots starting around 2013. The depot has begun cutting off the component main plate and machining a replacement part that is subsequently welded to the other assembly parts. The failure warranted research on the material and the environmental conditions associated with use of the component in order to determine the root cause of the failure mode and potential solutions to mitigate future cracking issues. The material of fabricated is aluminum alloy 5083-H which includes magnesium (Mg) at 4.3% and manganese (Mn) up to 1%. The alloy obtains its strength from these solutes and strain hardening; therefore, it generally has a good strength, weld capability, and corrosion resistance but is non-heat treatable.

The aluminum alloy is strengthened similar to steel alloys, movement of dislocations through the metal matrix are impeded by the addition of alloying elements such as Mg for 5xxx series aluminum [1]. Series 5xxx alloys achieve the highest strength of non-heat treatable aluminum alloys from Mg added to the composition [2]. Reboul and Baroux identified the maximum hardening results from coherent precipitates that are uniformly distributed in the aluminum matrix, refer to Figure 2 [2].

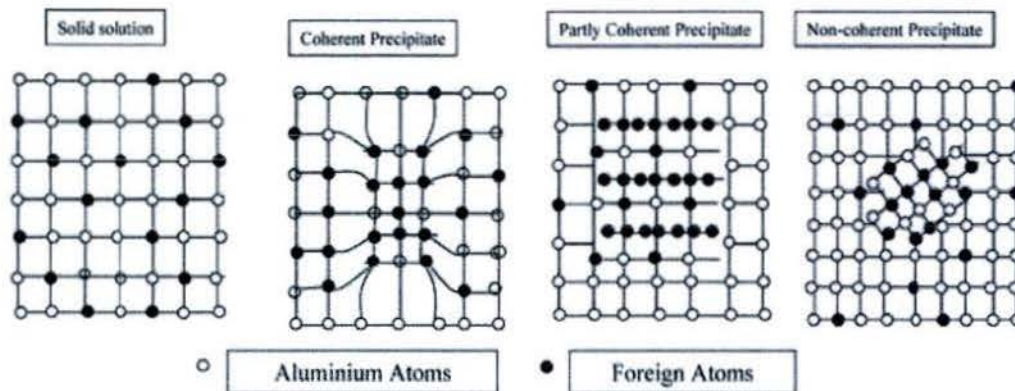


Figure 2 - Matrix of Aluminum [2]

A literature review showed that hydrogen charging decreased the ductility of aluminum alloy 5083. In a study by Panagopoulos and Georgiou, wrought 5083 that had undergone cathodic hydrogen charging resulting in brittle transgranular fracture at its surface layers while ductile intergranular fracture was observed in the deeper layers. Hydrogen charging can result from welding and corrosion processes, both of which are present for the seal component. The additional concentration of hydrogen can result in formation of a hardened region or micro-cracks [3]. It has also been determined that there are various reasons cracking or micro-cracking may occur. One study by Mutombo et al. shows that through welding processes alloy 5083 aluminum can be susceptible to cracking along the weld interface. The heat affected zone from the weld can cause the material properties to reach an altered state which creates a crack at the grain boundary between the welded materials [4]. Likewise, a study by Lippold, Nippes, and Savage noted cracking among the grains featured in the fusion zone, specifically at the solid-liquid interface. Their investigation states that the two main causes of cracking for their situation were fusion zone cracks and heat affected zone cracks. Fusion zone cracking is associated with crack formation at grain boundaries due to forced segregation from rapid solidification of welds. Heat affected zone cracks are associated with the forced micro-segregation at grain boundaries in materials that had been introduced to a heat source, which caused partial melting or a change in material microstructure [5]. In the case of the seal component, it is plausible that the existence of micro-cracks and segregation could be present and worsened due to repetitive thermal expansion or applied stresses.

Aluminum alloys that contain a magnesium content greater than the equilibrium solubility limit are susceptible to sensitization [6]. For alloy 5083 aluminum, low temperature heat sources can change the material properties and weaken the material. As explored by Kaibyshev et al., alloy 5083 aluminum experiences decaying strength as temperature increases. At temperatures at or above 550°C it is believed that the dissociation of lattice interfaces are the reason for the significantly deteriorated strength properties [7]. When heated, the alloy's precipitates are allowed to relocate and the material becomes susceptible to grain growth, recrystallization, and uncontrolled development of grain boundaries [2]. It is therefore common to see reduced hardness in heat affected zones. In a study by Perez-Bergquist et al. [8], the impact of heat on 5059, 5083, and 7039 aluminum alloys is detailed. As determined by their study, the material strength of all of these alloys begins to fall off at temperatures upwards of 100°C, refer to Figure 3. When examined using transmission electron microscopy (TEM) in the "as received" condition and at 300°C, the change in alloy 7039 can be established through the release of precipitates as temperature rises. This allows for a correlation to be confirmed, as temperature rises the recrystallization and release of precipitates is detrimental to the strength properties of 5xxx and 7xxx series aluminum alloys above 100°C. Shown in ASM International [9], 5083 Aluminum displays a decrease in strength properties as temperature rises when under a tensile loading. In addition,

the material elongation increases as temperature increases. The microstructure of cold worked parts will deform to resemble the contours of a part surface.

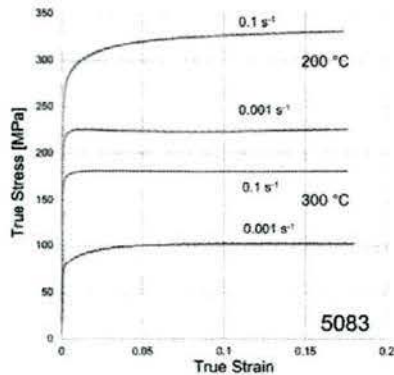


Figure 3 - Temperature Effects on Compression of Alloy 5083 [8]

Aluminum alloys with Mg concentration greater than 3.5% are susceptible to stress corrosion cracking throughout a range of temperatures due to precipitation of a reactive β phase (Al_3Mg_2) along grain boundaries. The β phase is anodic compared to the aluminum matrix; therefore the grains, refer to Figure 4, are susceptible to stress corrosion cracking when exposed to stress and a corrosive media, such as seawater [10]. Studies have also shown that the stress corrosion cracking initiates at grain boundary junctions on the alloy's surface and propagates into the alloy along the grain boundaries when the β phase particles are either anodically dissolved or converted into Al_2O_3 by salt water. After dissolution or conversion, the crack, aided by the external stress being applied, will propagate through the voids created by the dissolution of the particles or will transverse through or around the Al_2O_3 particles. In addition, it has also been shown that the crack growth between the β particles was caused by hydrogen uptake at the grain boundaries [11]. Burleigh stated that the surface during stress corrosion cracking usually appears corrosion free even when the component is near failure [12].

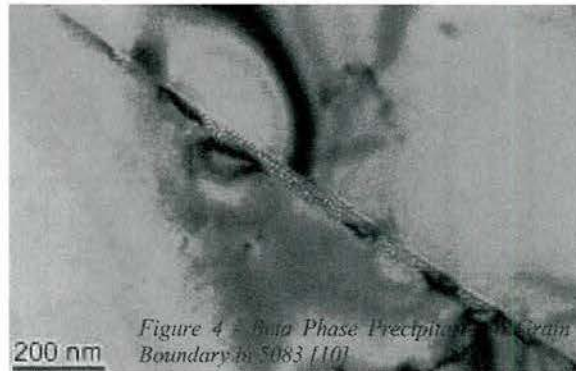


Figure 4 - beta Phase Precipitation along Grain Boundary in 5083 [10]

A comprehensive report on sensitization of alloy 5083 at low temperatures was published by Crane and Gangloff in 2015 [13]. They investigated intergranular stress corrosion cracking (IGSCC) of 5083-H in a NaCl solution and determined that threshold stress intensity decreases as a function of mass loss

for sensitized aluminum at temperature

conditions of 60°C to 100°C.

The microstructure of 5083-H is anisotropic with grain size measured at an average 200 μm in longitudinal-working (L) direction, 100 μm

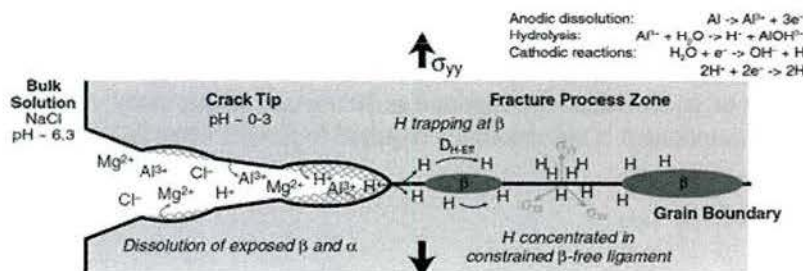


Figure 5 - Illustration of IGSCC Mechanism

in the transverse direction, and 30 μ m in the short-transverse (S) direction. Crane and Gangloff proposed a model of the grain boundary in NaCl at low temperature sensitization while loaded in the S direction with crack growth in the L direction, refer to Figure 5. Aqueous and corrosive environments degrade the normally occurring oxide layer that protects the underlying aluminum alloy. Then interaction with the environment allows for hydrogen production, anodic dissolution, and embrittlement. The illustration shows dissolution of the β particles and hydrogen uptake along the grain boundary. Scanning electron microscope fractographs showed flat brittle surfaces of IGSCC through the material and round cupped surfaces of adjacent ductile fractures. They concluded that alloy 5083 is only slightly susceptible to IGSCC in NaCl solutions, but sensitization at or above 60°C can make the material more susceptible under S-L orientation loading. Crane and Gangloff showed the stress intensity threshold for unsensitized 5083-H in a salt solution was measurably greater than the aluminum after sensitization for several days at temperatures of 60, 80, and 100°C, refer to Figure 6. Furthermore, crack growth rate curves elucidate the correlation between the stress intensity threshold and degree of sensitization (eg. specimens with 30 mg/cm² show greater crack growth at lower stress intensities).

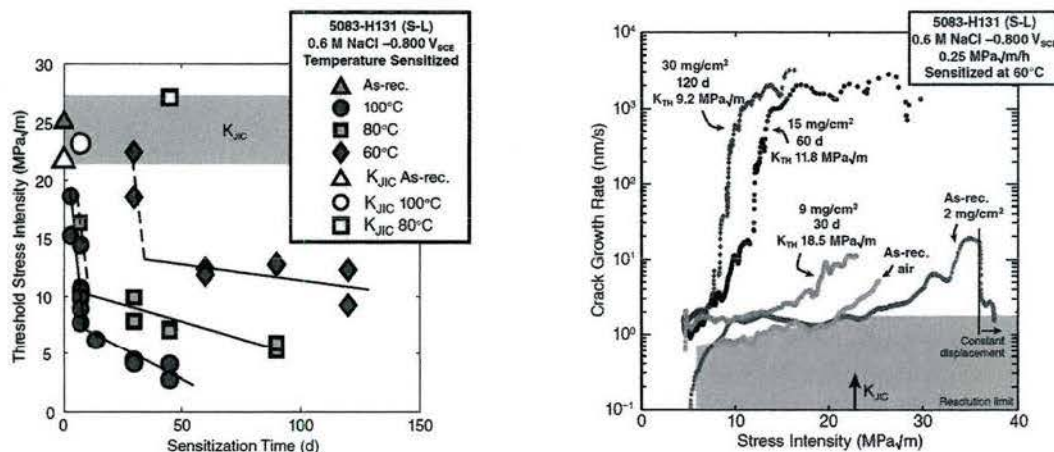


Figure 6 - Comparison of Sensitized and Unsensitized 5083-H [13]

Although there has been significant research around stress corrosion cracking of aluminum alloys, Holtz et al. highlight the lack of published information on corrosion fatigue of sensitized alloy 5083-H [14]. They showed sensitization creates semi-continuous regions of the β -phase at the grain boundaries when aged at 100°C for 72 hours. Furthermore, a continuous layer of the β -phase at the grain boundaries was identified at 240, 1080, and 3000 hours for 175, 100, and 70°C respectively. In their experiments, the S-L load/crack orientation was studied at 10Hz, load ratio (minimum stress over maximum stress) of 0.85, 1% NaCl solution with passivation inhibitor, mass loss of 27 mg/cm², and a sinusoidal profile per ASTM E647. The standard defined the stress intensity amplitude at a crack growth rate of 1x10⁻¹ m/cycle. Concentrations of NaCl above 1% were found to have a negligible impact on the experiment results, while the load ratio played a significant role. Holtz and colleagues concluded it is the degree of sensitization, not the temperature of sensitization, that impacts the corrosion fatigue threshold, refer to Figure 7. The critical degree of sensitization was reported as 30 mg/cm² in this study; therefore, the temperature-time history of the component is not absolutely required to predict when failure may occur.

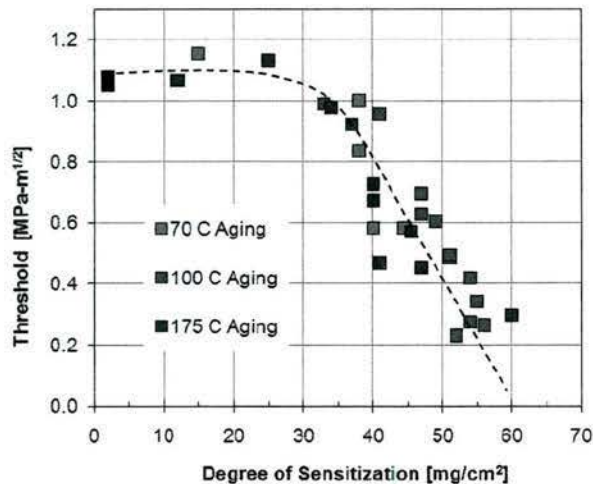


Figure 7 - Cracking Threshold vs Degree of Sensitization [14]

In another study, Holtz and collaborators focused on the corrosion-fatigue behavior of 5083-H131 under various load ratios and corrosive environments. Experiments were performed in vacuum, air, and salt water after sensitizing the aluminum at 175°C for varying lengths of time. They found for degrees of sensitization below 30mg/cm² there was no measurable degradation to fatigue properties at load ratio of 0.85 in air; however, higher degrees of sensitization did affect fatigue properties in a salt solution. Additionally, the distinction between crack growth rates for highly sensitized and annealed specimens only became apparent at high load ratios and high fatigue stress intensities [15].

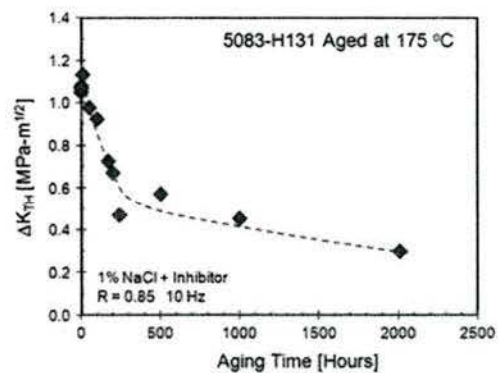


Figure 8 - Fatigue Crack threshold for 5083-131

Similar to fatigue crack growth behavior of 5083-H131 is corrosion fatigue behavior of 5083-H111 researched by Mutombo and du Toit [4]. They specifically focused on effects of weld zones on the aluminum properties; however, many results are transferrable to other sensitization mechanisms. Phases of aluminum and magnesium, such as Al₂Mg₃, are anodic with respect to the aluminum-magnesium matrix; therefore, the phases preferentially dissolve in aqueous environments forming pits. It is suggested that aluminum alloy pitting at grain boundaries consisting of β-phase lead to higher stress concentrations in fatigue than pits by themselves. In fatigue tests, pits formed from corrosion or defects resulting from welding reduced the fatigue life of the specimens compared to unwelded samples, refer to Figure 9. Pit width to depth ratio was approximately 0.60 for 1440 hours and 0.53 for 2160 hours of exposure to a 3.5% NaCl solution. Furthermore, the fatigue load profile and cyclic frequency can affect the corrosion fatigue properties. Higher frequencies lower the reaction time of the fluid environment with the material at the crack tip thereby lowering the crack propagation rate per cycle. Other findings showed welded tensile specimens exhibited brittle failures while as-supplied materials had ductile fracture surfaces.

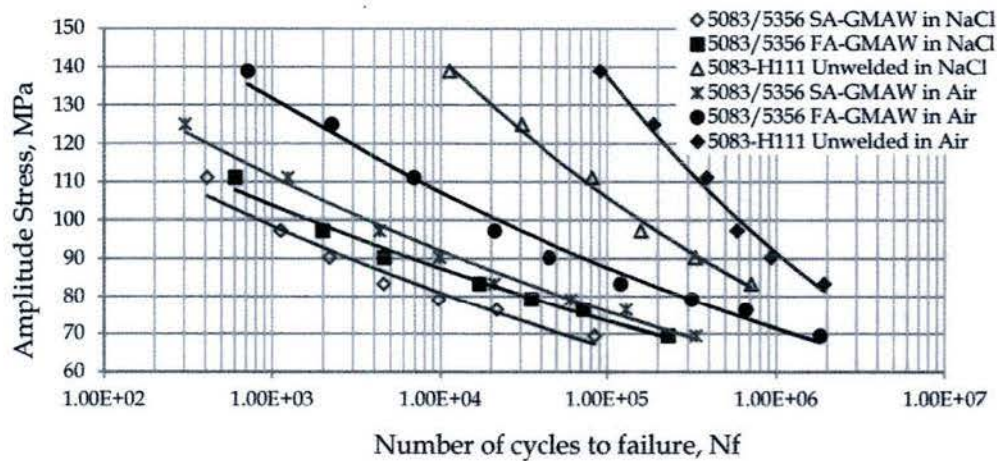


Figure 9 - Fatigue Testing of Alloy 5083 in NaCl Solution at 1 Hz [4]

3. Failure Analysis

Mechanical and metallurgical testing was performed to confirm the hypothesis that failures of the seal component were a result of sensitization. Figure 10 shows a section of the component sent for analysis from the Marine Corps depot. Figure 11 shows that a large continuous crack developed along the entire seal interface.

After imaging the exterior crack, a prying method was employed to break open the crack in order to expose the fracture surfaces, refer to Figure 12. Next, the fracture surface of the separated section was analyzed using scanning electron microscopy (SEM) techniques. In addition, B sized ASTM tensile specimens were machined from the section, both parallel and perpendicular to the aluminum plate rolling direction. Finally, an optical microscopy examination of the 5083-H grain structure was performed.



Figure 10 - Component Section Received



Figure 11 -Left- cracking around the seal groove. Right- High Magnification Photograph of Crack along the Edge



Figure 12 - After Breaking Open the Crack

3.1 Fractograph Analysis

The results of the SEM analysis are contained in Figure 13 to Figure 15. These three figures show that the fracture was intergranular – meaning cracking occurred between the individual aluminum grains.

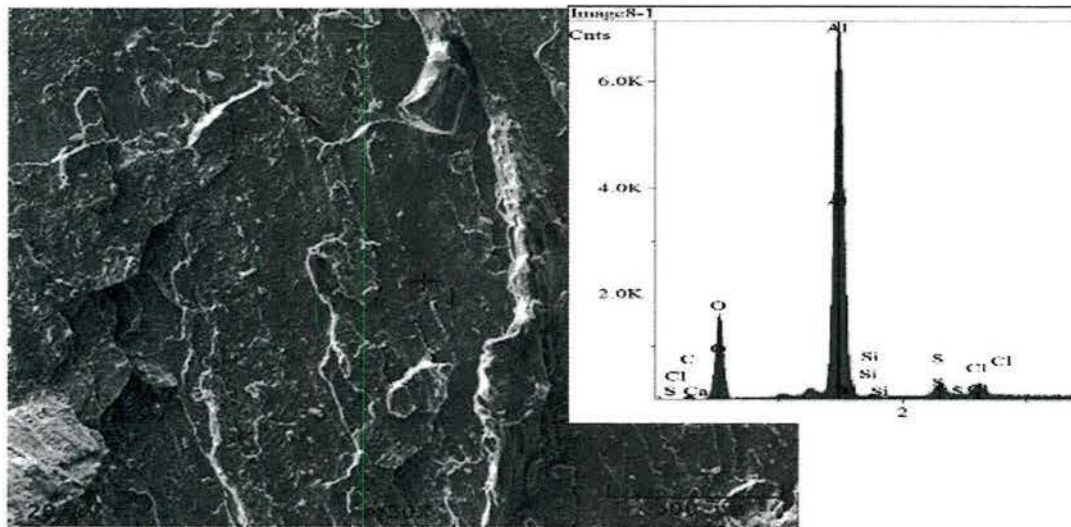
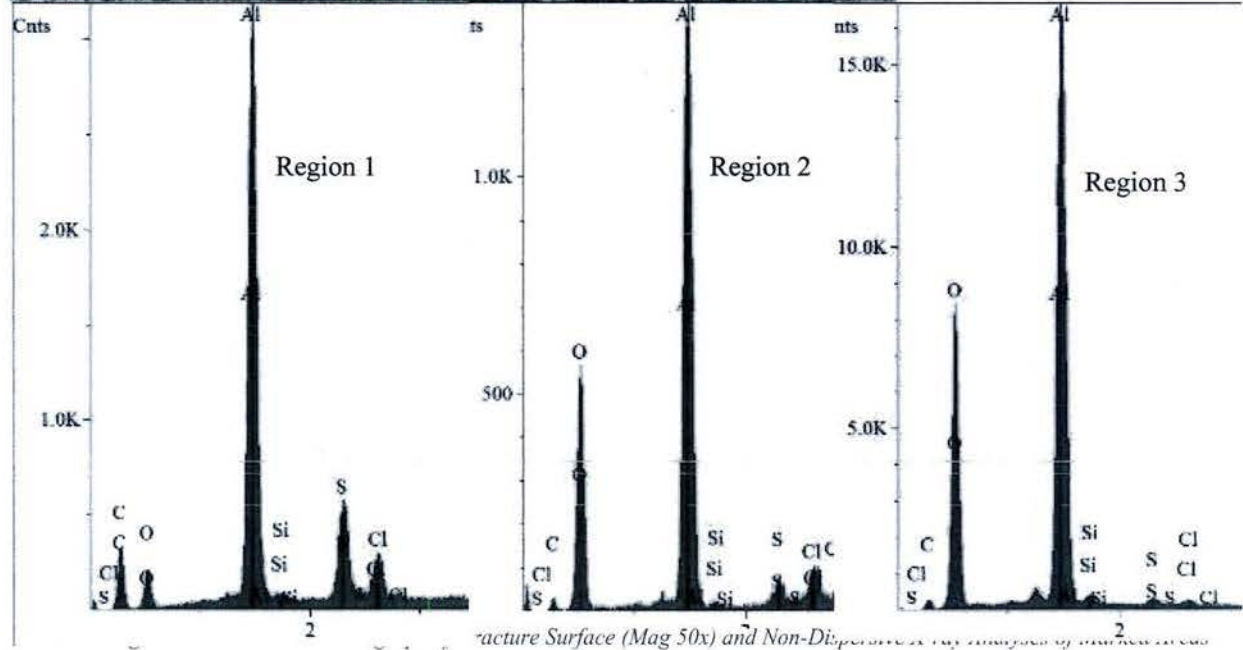
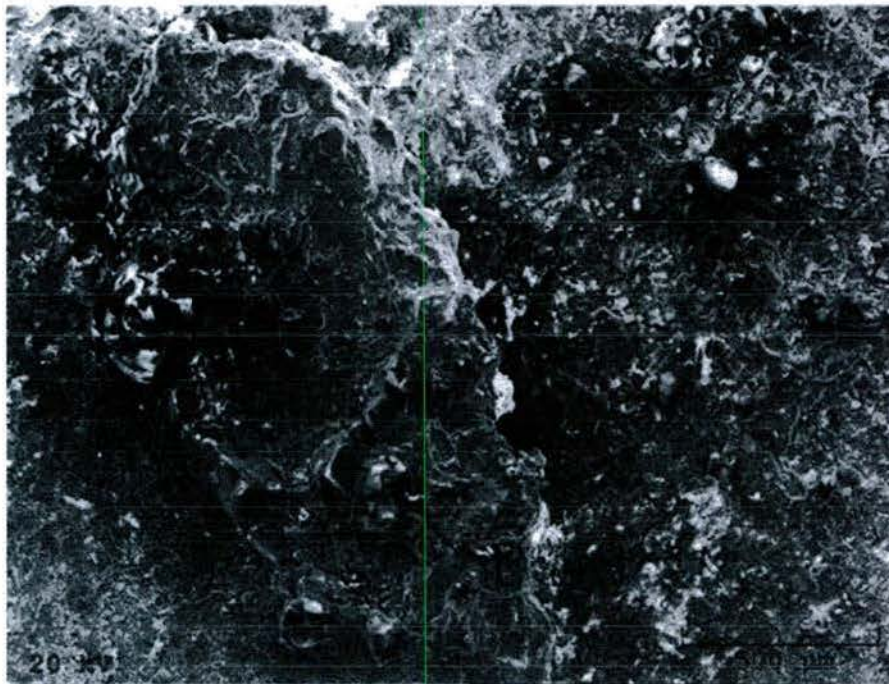


Figure 13 - SEM Photomicrograph of Fracture Surface – Area1 (Mag. 50x) and Non-dispersive X-ray Analysis of Region 1

This fracture mode is typical of 5083-H that has been sensitized as found by previous researchers [10] [11] [13] [16]. In addition, all the non-dispersive x-ray analyses showed that the fracture surfaces consisted of aluminum, magnesium, chlorine, oxygen, and sulfur. The hypothesis is the chlorine came from the seawater trapped in the seal while the sulfur was leached from the seal by the seawater. The oxygen could be from aluminum and magnesium oxides. The presence of the Mg on the fracture surface is another indication that sensitization of the 5083-H occurred on this component during service.



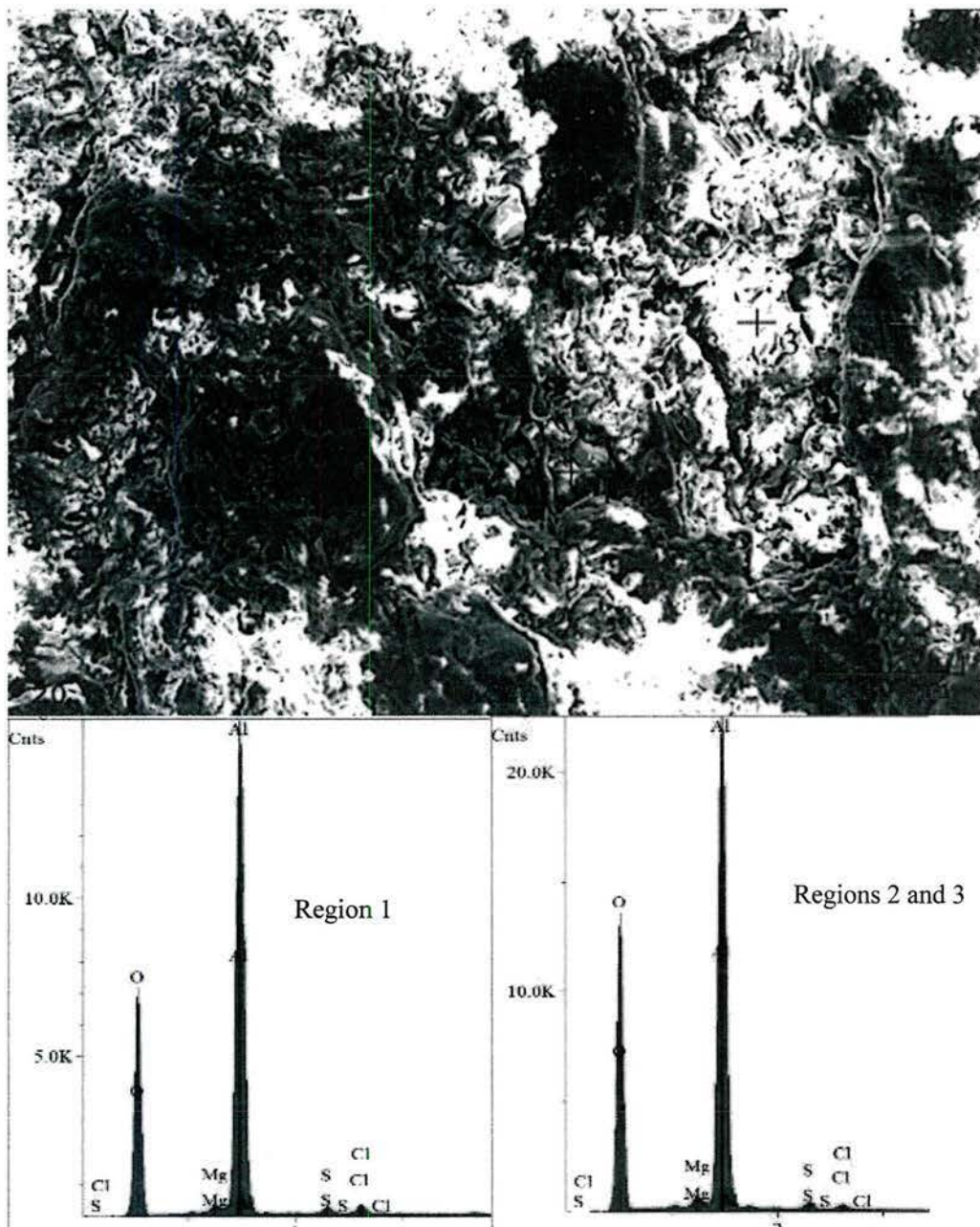


Figure 15 - SEM Photomicrograph of Fracture Surface (Mag 169x) and Non-dispersive X-ray Analysis of 3 Regions

3.2 Optical Analysis

Metallographic samples cut from the sectioned component were prepared in accordance with ASTM B928/B928M-15. A longitudinal section perpendicular to the rolling direction was cut and prepared for metallurgical examination. After polishing, the sample was micro-etched using a solution of 40% reagent grade phosphoric acid (85% concentration) and 60% distilled water, by volume, for approximately 3 minutes at 95°F.

The metallographic examination, per the ASTM specification, was conducted at 500x magnification. The results of this examination, contained in Figure 16 and Figure 17, showed a semi-continuous β -



Figure 17 - Optical Photomicrograph -5083 Microstructure, Region 1 after 40% Phosphoric Acid Etch (Mag 500x)



Figure 16 - Optical Photomicrograph -5083 Microstructure, Region 2 after 40% Phosphoric Acid Etch (Mag 500x)

phase precipitate at the grain boundaries. According to the ASTM specification, these samples were

rated as a moderate amount of sensitization (above 25 mg/cm²), beyond the critical degree of sensitization identified by Holtz et al.; therefore, the temperature-time history of the component is not necessarily required to predict that failure will occur given detrimental loading but may indicate which operations impart sensitizing temperatures. Tensile tests were performed on an Instron test system to determine the mechanical properties in the rolling direction and perpendicular to the rolling direction, refer to Figure 18. Both sample sets had an ultimate tensile strength of 57 ksi, a yield strength of 40 ksi, and an elongation of 13%. These values are within the range of values listed in ASTM B928 for various tempers of alloy 5083; ultimate tensile 41-56 ksi, yield strength > 29 ksi, and 10-12% elongation.

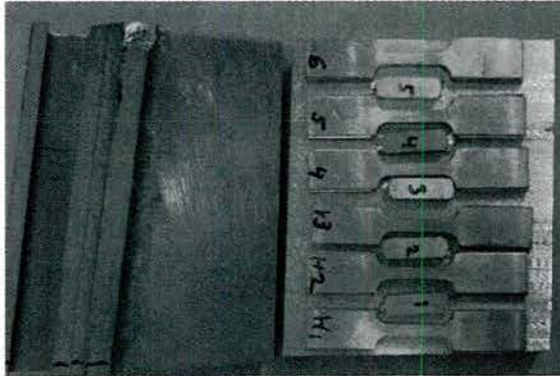


Figure 18 - Tensile Samples from received seal component

4. Operating Conditions

RIT researchers set out to confirm the operating temperatures of the vehicle were consistent with degree of sensitization observed in the single sample provided. To collect the data for evaluating the seal component cracking failure mode, measurements of temperature and geometry were recorded in situ. Although temperature measurements were the primary concern, strain measurements were also captured for additional information on the loading experience by the component. The researchers traveled to an engineering and technical services contractor in Virginia in order to collect data on a vehicle while in operation. A total of five strain gages and four thermocouples were strategically placed on the inside and outside of a seal component. An additional thermocouple was placed on the mating part between the exhaust pipe and the component. Sensor locations were identified through preliminary FEA modeling that identified the areas of concern. Strain gages of quarter bridge configuration were attached to the component using cyanoacrylate, and the thermocouples were attached using epoxy. A data acquisition system was setup to capture the real-time data of the vehicle while driving and idling. It was noted that various particles and debris were found in the component seal groove along with water and salt like residuals.

Testing to the test plan was limited due to inclement weather conditions – lower temperatures and restricted driving conditions prevented maximum temperature and strain measurements. Additionally, a water splash test onto a hot seal component was not performed due to potential damage to the vehicle. Initially it was desired to capture data when seal component was being dropped into place; however, this could cause serious damage to the vehicle and typical opening-closing of the component is performed using a ratchet strap to control the descent. A summary of the test results are provided in Table 1 below.

Table 1 – Vehicle Test Data

<i>Test</i>	<i>Measurement</i>
-------------	--------------------

Revving
Driving

160°F (71°C)
2500 μ strain

4.1 Test 1 – Tightening

Three strain gauges were used to collect data as the finger clamps contacting the component were tightened. A pneumatic impact wrench was used to tighten the two clamps while the strain gauges recorded change in the strain readings. The data in Figure 19 shows the component in the lowered state and the bolts being tightened. The first two seconds of data in Figure 19 show a change in strain as the first of two clamps were tightened. A maximum change of 25 micro-strain was recorded on Strain gage #1.

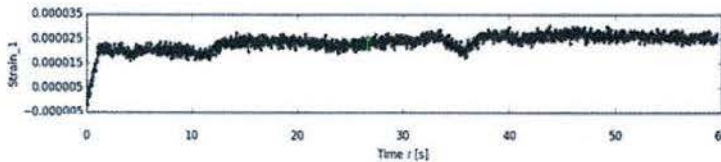


Figure 19 - Tightening Seal Component Finger Clamps

Data shows a relatively minor change in strain; therefore, it was concluded that the component fit securely within the hull without tolerance issues and was verified with a feeler gage around the edge of the component. Upon finishing the test, the other strain gauges and thermocouples were attached to the top of the component.

4.2 Test 2 – Stationary Temperature

Once all instrumentation was attached, the vehicle was stationary while the engine was revved so that the temperature profile could be recorded. For reference, the ambient temperature was 55°F (13°C) with light rain and overcast skies. The temperature profile shows large peaks and valleys for inside thermocouple #0 as the vehicle transitioned multiple times between “driving mode” and “swim mode”. The peaks correspond to the “swim mode”, while the valleys correspond to “driving mode”, refer to Figure 20. Since the vehicle was not in water during the testing, time in each swim mode was limited to prevent damage to the vehicle. Thermocouple #2 was the only sensor on the outside and showed a decrease in temperature as a result of detachment from the component, rain, and evaporation.

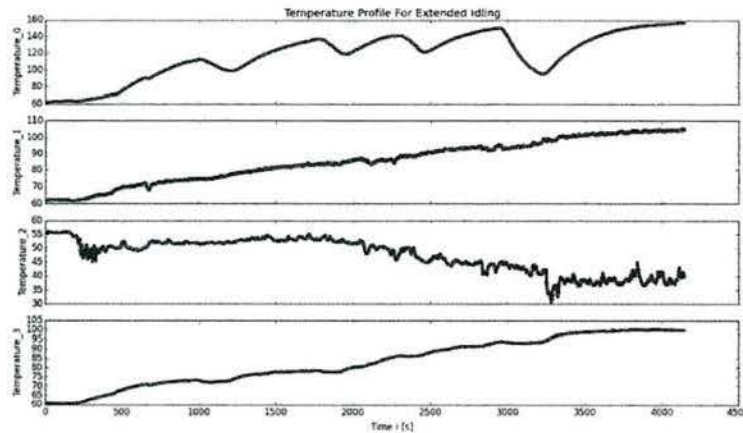


Figure 20 - Temperature profile (°F) for the extended revving time in land and swim modes

Since the vehicle did not undergo a typical warm up period equivalent to 3 hours, the interior temperature data was further extrapolated to estimate a peak temperature during revving. The extrapolated peak temperature was calculated to be approximately 172°F (78°C) in these ambient conditions.

4.3 Test 3 -Driving

Heavy rain on the day prior to the test prevented use of the normal vehicle test track; therefore, several sections of 6x6 dimensional lumber were setup in a gravel parking lot and driven over with one track making contact at a time. Large spikes in the data can be seen in Figure 21 as the vehicle drove along the improvised test track. Strain 2 was orders of magnitude higher than the other gages and the time corresponded to when researchers noted a large bump was hit by the vehicle. The large increase in strain gauge #2 provided evidence that the seal component was experiencing high stresses due to the stress concentration on the underside of the plate at that location.

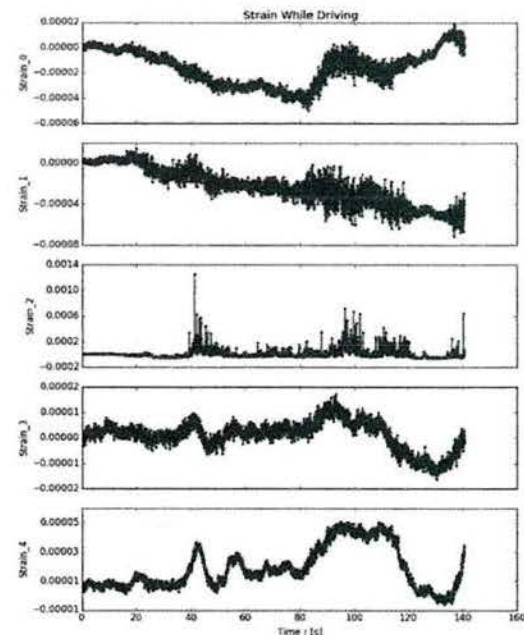


Figure 21 - Strain data collected on the first driving test collection

Apart from the loading evidence, sufficient information was obtained using the thermocouples while driving. Since sensitization was an area of major concern, monitoring the temperature and its affects were the highest priority.

Figure 22 shows temperature changes as the vehicle began to drive after the rev test. Since the vehicle drove without the use of “swim mode”, the various temperatures either remained constant or dropped significantly as the vehicle drew more air through the engine compartment. While most temperatures maintained at a steady value, thermocouple #0 decreased drastically as the vehicle began driving. Several tests were performed to determine the repeatability of the results and each test yielded similar temperatures and strain values. Based on this evidence, the greatest area of concern occurs when the vehicle is in “swim mode” and is stationary without sufficient cooling from the contact cooler.

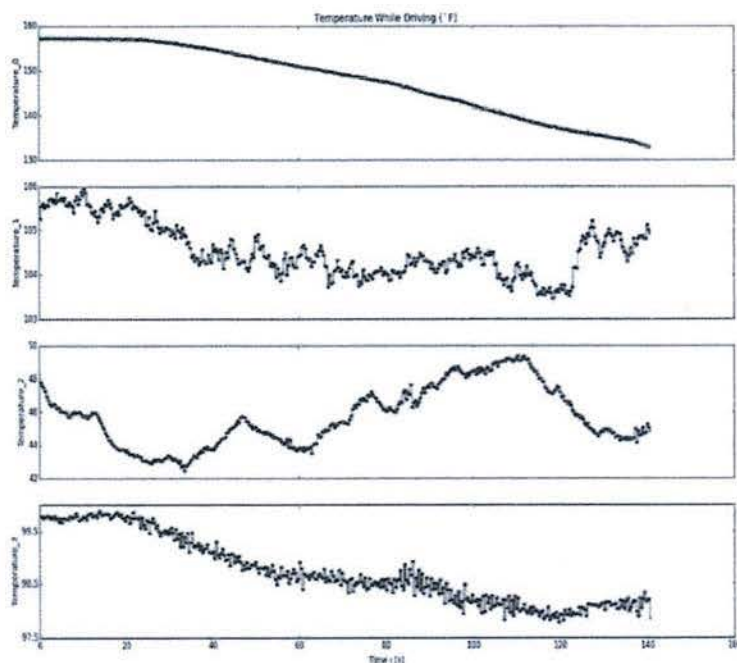


Figure 22 - Temperature (°F) changes in the component during the first driving test. Thermocouple #2 shows reasonable evidence of damage or separation.

Since the outside thermocouple, #2, seemed to be relaying inaccurate data, additional measurements were captured for the temperature using a handheld infrared pyrometer calibrated to emissivity of the rough paint. The infrared measurements recorded after testing, when it was safe to exit the vehicle, showed a temperature of 144°F (62°C) where the air crosses the component via convection, and 102°F (39°C) measured on the component near thermocouple #2. This confirmed the suspicion that thermocouple #2 had poor contact with the component or was damaged, and the measurement should be discarded.

5. Mechanical Simulation

After completion of experimental testing and materials examination, a computer aided three dimensional model was created from the component drawings. A finite element analysis (FEA) was then performed to analyze the strain imparted in the seal component under various theoretical loading conditions. The experimental data previously collected was employed to relate results between actual and modeled strain values. These values were comparable to one another and offered validation by showing accurate strain values during driving. The highest modeled strain value occurred in the corner of the groove section near the spotter, which was on the opposite side of the main plate from strain gauge #2.

The FEA model consists of loads and boundary conditions; the component hinges are fixed from translating but are allowed to rotate to represent the pin interface. The edge of the component, on both sides of the seal groove, are fixed from translating vertically, but are allowed to expand or contract

within the plane of the component. This is an assumption based on the observed gap between the edges of the component and the frame. Custom material properties were entered into the software for the 5083-H alloy as outlined in Table 2. Depending on the scenario, the loadings consist of gravity, forces from the door, applied acceleration, and thermal stress.

Table 2 -5083 Aluminum Material Properties for FEA [17]

Property	Value	Units
Elastic Modulus	10.3	Mpsi
Poisson's Ratio	0.33	-
Thermal Conductivity	3.02e-6	Btu/(in*sec*°F)
Mass Density	0.096	lb/in ³
Specific Heat	0.331	Btu/(lb*°F)
Thermal Expansion Coefficient	1.322e-5	°F ⁻¹

The mass of the actuator and door were estimated from dimensions recorded during the operational testing. In the cases where the seal component door is closed, an additional pressure is applied to the internal seal groove. The magnitude of this pressure was calculated by assuming an evenly distributed hydraulic force applied by the actuating cylinder over the entire groove area. Information on the actuating cylinder was found in the maintenance manuals. From the information, it was estimated that the component door exerts an upward pressure on the internal component seal of 19 psi. The gravitational effects are applied at the center of gravity under the acceleration corresponding to the scenario under analysis. Estimates for the weight of the component door and actuating cylinder were applied to the internal hinges and acted with a magnitude scaled to the vertical acceleration of the vehicle in the scenarios.

Due to the complexity of the completed model, the FEA was performed using a blended curvature mesh, as neither a standard nor curvature mesh could be individually created for the entire model. Mesh controls were used to refine the mesh in the area of interest and the influence of mesh size on results was investigated. The radius section of the seal groove was selected as the primary location of interest due to the high stresses and various mesh sizes were studied. The maximum stress values appear to have little dependence on the mesh size smaller than 0.1 inch, refer to Figure 23. In order to verify the accuracy of the simulation, a hand calculation was performed to check if the simulation results were reasonable, refer to Equation 1. The hand calculation was intended to be a rough estimate and approximated the component shape as a rectangle. Only gravitational force was included in the hand calculation for comparative purposes to FEA and the formula assumed a flat rectangular plate of uniform thickness with two edges fixed and two simply supported [18].

Equation 1

$$\sigma_{MAX} = \frac{-\beta q b^2}{t^2}$$

Where $q = F/(a*b)$, a = long dimension, b = short dimension, t = thickness, β is found in Roark Table 11.4.

The component was approximated to be a 2.5" thick, 40" wide, and 45" long rectangular plate. The maximum stress resulting from the hand calculation was located at the center of each long edge. Replicating the same conditions (ignoring thermal load and the load from the component door) the FEA results showed a maximum stress within 13% of the hand calculation at the same location. The agreement of these values and the strain readings lent confidence to the accuracy of the simulation.

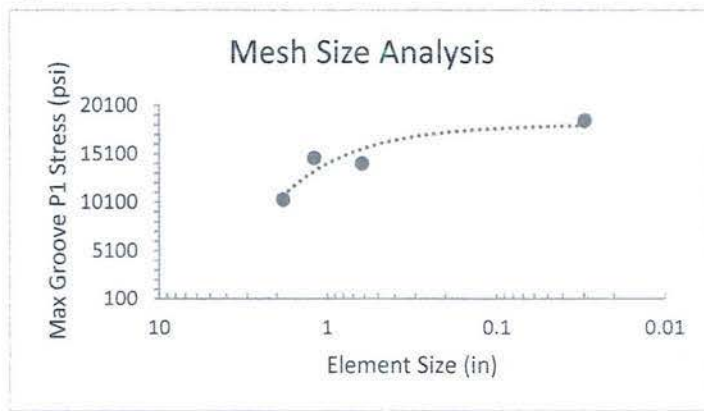


Figure 23- Mesh size analysis for maximum groove stress

Based on usage information reported by the depot, ten different potential loading scenarios were simulated. Table 3 contains the simulated Von Mises stress values for selected scenarios. The points referenced in the table are the three points where the highest stresses were typically found to occur in the model. There are a number of factors that influence the simulation results: g-forces acting on the component, the position of the component door, and the thermal profile. The thermal effects proved to have the greatest impact on stresses, as there are scenarios that involve a significant thermal gradient between the top and bottom of the component.

Table 3- Summary of Selected FEA Results

Scenario #	Description	Door Position	G-Forces	Inside Temp (F)	Outside Temp (F)	Point 1 Stress (psi)	Point 2 Stress (psi)	Point 3 Stress (psi)	Location of Max Stress

1	Parke d inside	Clo sed	1g	70	70	26 1	55 5	33	Poi nt 2
3	Idling	Op en	1g	19 0	19 0	90	63 7	20	Poi nt 2
6	6g on land	Op en	6g	15 0	14 0	26 61	46 24	22 76	Poi nt 2
9	Drivi ng betwe en water ways	Clo sed	3g	20 0	18 0	43 24	30 72	46 47	Poi nt 3
11	Splas h w/ 3g	Clo sed	3g	20 0	10 0	24 20 4	13 70 5	23 26 1	Poi nt 1

The first scenario (Scenario 1) modeled the vehicle parked inside. In this scenario, no thermal effects were considered as the inside and outside of the component are at equilibrium. The component door is closed while the vehicle is parked to prevent debris from entering. The second scenario (Scenario 2) was for the vehicle parked outside. This case was the same as the first with the addition of thermal effects. A 10°F gradient between the outside and inside faces of the component was assumed to be caused by solar heating. This approximation is based on an assumed gradual increasing rate of heat transfer from the sun, which allows time for the entire component to heat somewhat evenly.

The third scenario (Scenario 3) was the vehicle parked at idle. This scenario had the component door open. It was assumed that the vehicle was idling at steady state and that there was no temperature difference between the inside and outside of the component. This assumption is only true once the vehicle has had ample time to warm up and the component has come to equilibrium. The next case (Scenario 4) was with the vehicle driving on a smooth surface. While the vehicle runs on land, the component door is open to allow heat from the engine to vent to the outside. In this case, an approximate difference of 10°F between the inside and outside of the component was assumed based on the temperature data recorded. This scenario was repeated with the component experiencing 3g, 6g, and 10g to replicate all different types of terrain (Scenario 5,6,7). The accelerations were based on recorded values during testing and results from the dynamic model for the suspension system. The torsion bar model by Nenadic et al. indicates rough terrain creates a maximum acceleration of 10g over 12 inch bumps for a maximum speed dictated by the operator's manual.

The next scenario (Scenario 8) was for the vehicle operating in calm water. The component door was modeled as closed while in swim mode to keep water out of the engine compartment. The component door being closed creates a larger thermal gradient in the component as the engine is not allowed to cool as much, approximated as a 20°F difference assuming the contact cooler is operating in water. Based on information about typical training drills, simulations of the loading associated with the vehicle exiting one body of water and entering another were evaluated. There were two scenarios associated with this - driving on land in swim mode, and splashing the vehicle into the water- both have the component door shut. Driving in swim mode has a similar simulation to floating with the only change being the gravitational effects, which are set to 3g to allow for mildly rough terrain in between waterways (9). The splash is the scenario with the largest stresses and is modeled by a large thermal shock to the component. This thermal shock is modeled by simulating a 100°F difference between the

inside and outside of the component based on assumed water temperature and nominal operating temperatures measured. Splashes were modeled at both 1g and 3g (Scenario 10,11) to allow for a smooth or rough transition into the water.

The stress analysis showed the largest stresses typically occurred in the groove where the components are failing. The geometry of this groove causes a large stress concentration, which offers confirmation on the area of concern and the causation of the cracking. Adding thermal effects to the simulation increased the stresses substantially on all parts, especially in the groove of interest. The measured and modeled stresses observed, even in the worst case scenario - a rapid change in temperature, are below the yield strength of 5083-H aluminum; however, possible manufacturing defects and corrosion pitting were not evaluated. The combination of mechanical stress, thermal stresses, corrosive environment, and sensitization of the aluminum is believed to be the root cause of the crack observed in the location of interest.

The stress extrapolation method tested by Han et al. was used to estimate the stress intensity value at the corner of the seal groove in the seal component under Scenario 11 [19]. This method estimates the stress intensity at the surface by plotting stress intensity values against the corresponding distances from the surface, refer to Figure 24. The values were extrapolated through the point where it crosses the ordinate in order to identify the stress intensity at the surface that would otherwise decrease to zero as the distance approached the surface. The mesh size was refined to 0.01 inch, 8 elements across radius, in order to capture a sufficient number of points within the vicinity of the groove. The resulting stress intensity was estimated to be 1.6 MPa $\sqrt{\text{m}}$. This stress intensity value for the worst case loading evaluated is near the threshold stress intensity and alternating stress intensity values report in literature that cause measureable crack growth rates at moderate degrees of sensitization. Manufacturing defects, restoration processes, and pitting at the groove surface would add stress concentrators that further increase the stress intensity. Additionally, the stress measured during operation indicates the stress values may be twice this result when shock loads are imparted on the vehicle.

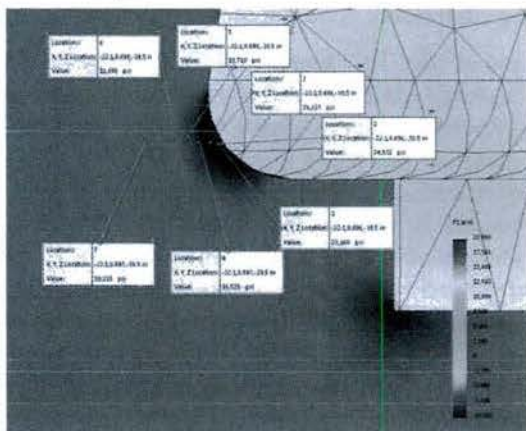


Figure 24 - First principal stress values for stress intensity determination – Scenario 11

6. Usage & Sensitization

Seeking to better understand the life cycle of the seal component, usage data from the depot was paired with sensitization curves. By comparing the temperatures recorded and calculated maximum stress intensity value to published sensitized material data, it was possible to estimate how long it takes the seal component to sensitize. The typical measured operating temperature of the seal component, 160°F (71°C), falls within the sensitization section of the diagram for aluminum magnesium concentrations

[16]. This temperature is also above the 70°C result that Holtz et al. showed would cause sensitization after 3000 hours in their study [15]. For vehicles with extended service lives, this time requirement for sensitization is possible and matches the estimates for the degree of sensitization from micrographs of the seal component.

Sensitization is typically measured by mass loss, and a threshold for sensitization classification is between 15 and 30 mg/cm². Sensitization beyond this threshold causes greater susceptibility to stress corrosion cracking. Figure 25 shows the time for 5083 aluminum to sensitize at various temperatures. Based on the temperature data discussed above, the periods of most concern for thermal effects are during high idling and during swim mode. As Crane et al. show, the time needed to sensitize 5083 aluminum decreases as the temperature of the component increases. Even at the peak extrapolated temperature for data collection of 172°F (78°C), the component could sensitize beyond the critical threshold in as little as 200 hours of operation.

Usage data from the depot indicates operation of vehicle for approximately 13,000 hours over an 8-year service cycle. The majority of the time, about 80%, the vehicle is operating in land mode, which may not apply high enough temperatures to cause sensitization in mild climates (40°C vs 60°C). However, while the vehicle is running in swim mode or idling, the temperatures do reach a high enough level to cause sensitization. Even if these conditions are only met 20% of the time the vehicle is being used, the component can sensitize within a single 8-year IROAN cycle.

Once the seal component is sensitized, corrosion resistance is reduced, which leads to the potential of stress corrosion cracking or corrosion fatigue. Stress corrosion cracking requires the presence of a corrosive compound, in this scenario seawater or soil. Holtz et al. concluded that sensitized material does not have any noticeable changes in fatigue behavior in air and sensitization is only a factor in stress corrosion cracking when a corrosive environment is present [15]. The presence of salt inside the component's seal groove indicates that seawater is able to leak through the seal and can become trapped in the groove for a significant period of time.

7. Stress Corrosion Cracking

Based on operating temperatures recorded and micrograph assessment of samples from cracked components, sensitization can occur within a maintenance cycle and reach a degree of sensitization with a mass loss above 35 mg/cm². In solutions replicating seawater, 0.6M NaCl (3.5% by wt), aluminum 5083-H131 has a stress corrosion cracking (SCC) threshold of 2.5 MPa√m or lower for the degrees of sensitization experienced by the seal component, refer to Figure 26. Higher degrees of sensitization may lower the threshold sensitivity further and align the the stress intensity value calculated based on the finite element analysis. Additional corrosion pitting that occurs on the surface would further increase the stress intensity, elevating it beyond the threshold for crack growth. Given the potential for pitting of the aluminum 5083-H due to dissolution at the sensitized grain boundaries, the stress intensity could be high enough to enable crack growth rates, refer to Figure 6, that would manifest in cracks the size seen in the components over years of operation.

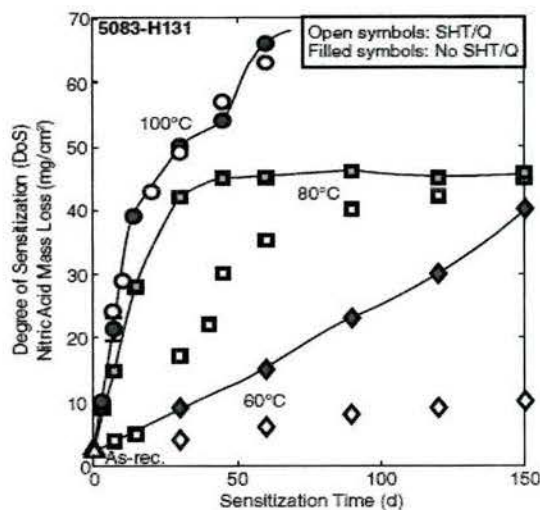


Figure 25 - Mass loss for various sensitization times and temperatures [13]

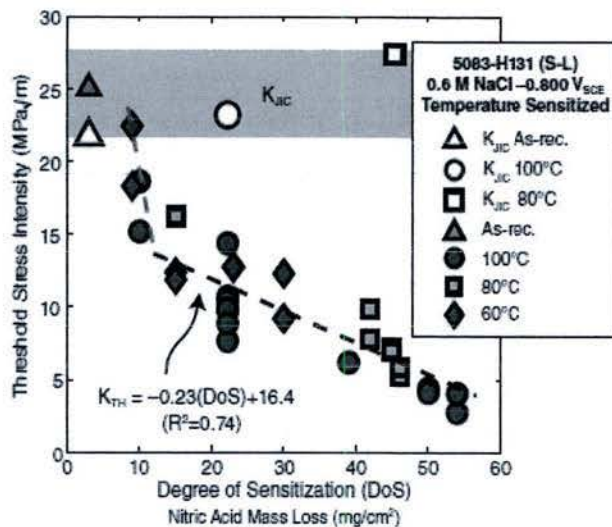


Figure 26 - Relationship showing decreasing SCC stress intensity threshold with greater degrees of sensitization [13]

8. Fatigue Evaluation

Stress corrosion cracking of high strength aluminum components is one potential failure mode for applications with high static loading; however, the seal component cycles through those load conditions. Based on the cyclic nature of the seal component loading, other potential failure modes, such as fatigue and corrosion fatigue, are likely possibilities. Although there are similarities between each failure mechanisms, the differences can significantly shorten component life depending on the combination of environment, material, and load-time profile. Two sets of tests were conducted to assess the impact in this case study – 1) Fatigue testing in air after a 500 hour salt spray exposure and 2) Corrosion fatigue in NaCl solution after a 500 hour salt spray exposure. The objective of the study was to identify the number of cycles to failure for a number of material modifications including potential solutions to prevent fatigue of high strength aluminums, e.g. 5083-H material, after years of exposure in corrosive atmospheres.

The solutions investigated were a flame spray coating, twin-wire arc coating, and material stabilization. The first two potential solutions, flame spray and twin-wire arc, operate on the principle of applying a protective coating to prevent the corrosive elements from reaching the underlying sensitized aluminum. Stabilization is a process of heating the aluminum beyond its sensitization temperature for a short period of time, then cooling it under controlled conditions. This stabilization causes the magnesium, which precipitates out of solution during sensitization, to diffuse back into solution, theoretically restoring the alloy to near its original properties.

To perform the study, fatigue specimens were machined from commercially available Alca 5 alloy and from 5083-H aluminum samples extracted from the seal component samples. Alca 5 and 5083 have identical compositions and similar material properties, although 5083-H has twice the ultimate strength and a flattened grain structure due to processing conditions. Specimens were machined to ASTM E466

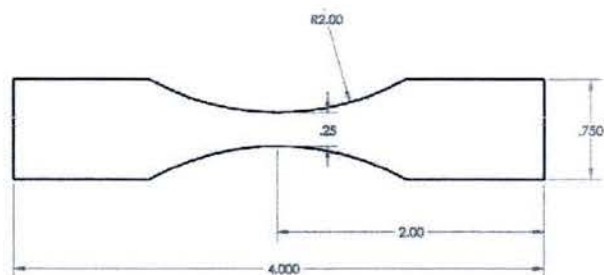


Figure 27 - Nominal dimensions of fatigue specimens

specification parameters and dimensioned as shown in Figure 27. The surfaces of fatigue specimens were prepared by sanding sharp edges and polishing the gauge section smooth. Polishing was completed in the longitudinal direction with 400 grit sandpaper per the ASTM standard. The samples were then split into five batches. Batch A was a control group that was neither sensitized nor treated. Batch B was sensitized and then stabilized at 240°C for 60 minutes. Batch C was sensitized then flame sprayed with a polymer containing corrosion inhibitors, Abcite x60. Batch D was sensitized then twin-wire arc sprayed with commercially pure aluminum, grade 1100, with the cross sectional area under the coating equaling the other specimens. Batch E was sensitized and not treated further. Batches B-E were sensitized at 175°C for 48 hours and each batch consisted of six specimens machined from Alca 5 and one specimen machined from the seal component sample, Table 4. A total of 40 samples were sent out for 500 hours of salt spray exposure in accordance with ASTM B117-16 – sufficient time for appreciable mass loss and pitting of the susceptible specimens. The coated samples had the coating interface of the sample covered in wax to prevent corrosion at the grips. Samples were loaded into an Instron fatigue test system, taking care that the specimens were parallel with the load direction to prevent bending stresses.

Table 4 -Fatigue Specimen conditions

Batch	Blast Surface Prep	Sensitized	Stabilized	Abcite Coating	Aluminum Coating	Salt Spray
A – As-supplied	x	x	x	x	x	✓
B – Stabilized	x	✓	✓	x	x	✓
C – Abcite	✓	✓	x	✓	x	✓
D – Aluminum	✓	✓	x	x	✓	✓
E – Sensitized	x	✓	x	x	x	✓

8.1 Stabilization Process

Figure 28 shows the sensitization and stabilization temperature regions for Al-Mg alloys. Aluminum alloy 5083, containing 4.5% Mg can become sensitized and prone to corrosion when exposed to temperatures in the blue region of the figure [20]. Additional factors that affect the amount of sensitization and stabilization are the exposure times at temperature, the amount of cold work in the alloy, and the amount of recrystallization.

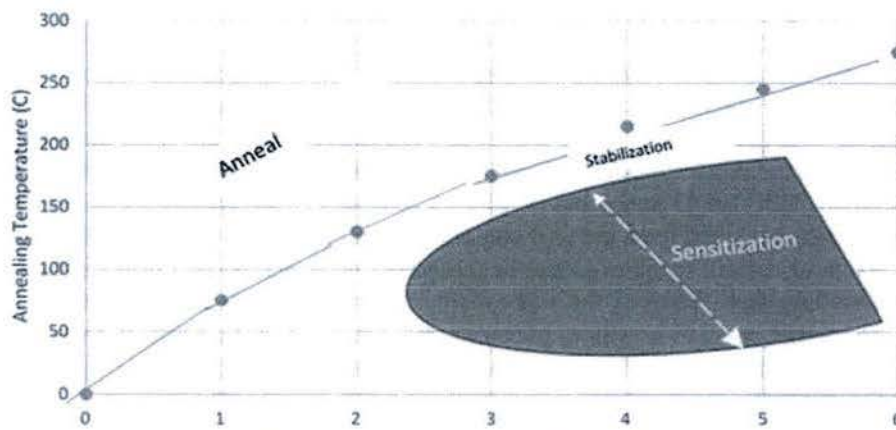


Figure 28 - Temperature Effects on Al-Mg Alloys [16]

Adapted from Kramer

Figure 28 also shows that if the aluminum alloy is heated in a range greater than the sensitization temperature but below the annealing temperature, the alloy will become stabilized, that is, the Al_2Mg_3 that had precipitated to the grain boundaries will diffuse back into solution and the sensitization will become reversed. Thus, one method to reverse the effects of the sensitization is to heat the alloy between 240 and 300°C [16]. Heating above 300°C causes a significant decrease in mechanical properties, because the alloy begins to recrystallize [21]. The reverse sensitization process in this experiment consisted of placing selected samples into the oven preheat at 240°C for 60 minutes. Although the stabilization process reduced the degree of sensitization, there was still precipitates at the grain boundaries as shown with phosphoric acid solution etching, Figure 29.

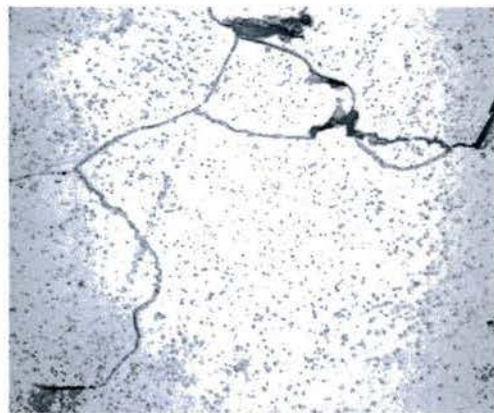


Figure 29 – Semi-Stabilized Alca 5

8.2 Flame Spray Coating Process

Specimens in batch C were sensitized then subdivided into two subgroups, 1- glass bead and 2- SiC grit blasting, to evaluate effects of surface preparation techniques prior to coating with the Abcite x60 polymer. Immediately before spraying, the specimens were preheated to a surface temperature of 104°C with the propane flame from the flame spray system. The Abcite spraying process consisted of spraying one pass on each side (no return passes), rotating 90 degrees, and spraying the next side.

Subgroup C1: The glass bead used was of medium size Ballotini glass bead media at 100psi, 3" distance, 2 passes (one vertical and one perpendicular pass across all sample), and propelled with 100 psi air to achieve a surface roughness between 3.5 μm and 4 μm . The flame spray fuel mixture used was 50 mm oxygen, 25 mm propane, and 45 psi air. The Abcite x60 powder feedstock was fed at 8 psi on the Alamo Spray System. After all four faces were coated the powder feed was shut off and all four faces underwent a "flame only" pass. The coating thicknesses ranged from 0.015 to 0.027 inch.

Subgroup C2: The material was prepared with 36 grit SiC blasting at 43 psi, 9" distance to achieve a surface roughness of 4 μm . The flame spray fuel mixture was set to the same parameters as group C1,

except the powder feedstock was fed at 5 psi on the Alamo Spray System. The thickness values for the four samples were all consistently around 0.022 inch.

8.3 Twin-wire arc Process

Similar to corrosion protection techniques referenced by Golumbfskie et al. where series 5xxx alloys were clad with 75% Mg coatings, specimens from batch D were coated with aluminum to evaluate twin-wire arc as a possible means of corrosion protection [6]. Before spraying, the specimens surfaces were prepared using the same two procedures as the Abcite coating. A Thermach AT-400 twin wire arc system was used to spray commercially pure aluminum onto the specimens. The feedstock for the coatings was 1/16 inch diameter wire of 1100 grade commercially pure aluminum. The spray used a voltage of 30 V, current of 70 A, air pressure of 48 psi, traverse rate of 150 mm/s, and a standoff distance of 4.5 inch. These parameters were chosen to minimize porosity by depositing many thin layers of coating. Traverse rate and standoff distance were kept constant using an industrial robot. In order to achieve the desired coating thickness of 0.050 inch, 20 layers of coating were deposited on each face of the part. Layers were deposited using two passes per side before rotating the specimen. All faces were then milled to remove the top 0.025 inch of coating, leaving only the smooth coating beneath with sufficient thickness to prevent continuous pores from allowing water to attack the underlying surface. Final polishing was performed using a series of sand paper and coolant with 220, 320, and 400 grit paper.

To determine the properties of the twin-wire arc sprayed coating, the aluminum was sprayed on a 3/8inch thick steel plate covered with a light coating of mold release. The aluminum coating was milled flat, hammered off from plate then milled and sanded to shape (ASTM B size specimen). The Instron system was used to measure the tensile properties of the aluminum 1100 coating for future reference, refer to Table 5.

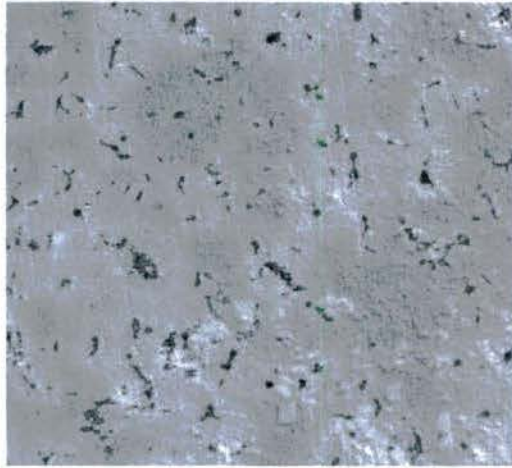
Table 5 - Measured Properties of Twin-wire Arc Sprayed Aluminum 1100 Material

	Yield Strength (ksi)	Ultimate Strength (ksi)
Specimen 1	8.9	11.5
Specimen 2	10.3	11.1
Specimen 3	10.3	11.8
Average	9.9	11.5

8.4 Fatigue Testing in Air

The objective of the fatigue testing was to determine the effectiveness of the different corrosion resistance methods on surface that had already experienced corrosion pitting. As expected, the 500 hours of salt spray produced numerous pits on the surface of the Alca 5 specimens, refer to Figure 30. Under the Abcite coating the surface was comparatively rough due to the surface preparation procedures required for the coating to properly adhere but did not show evidence of pitting after the salt spray test. The as-supplied Alca 5 appeared to have a higher density of pitting than the stabilized samples possibly due to the mild degree of sensitization in the as-supplied material. The pit aspect ratio

(W/D) was estimated to be 9:1 for an average width of 0.06 inch and depth of 0.007 inches (177 μ m), was determined using non-destructive optical measurements after 500 hours of salt spray testing. Owing to the non-destructive nature of the measurement, the pit depth may have been deeper than the visual estimates allowed. There was minimal pitting on the surface of the 1100 aluminum alloy deposited during twin-wire arc.



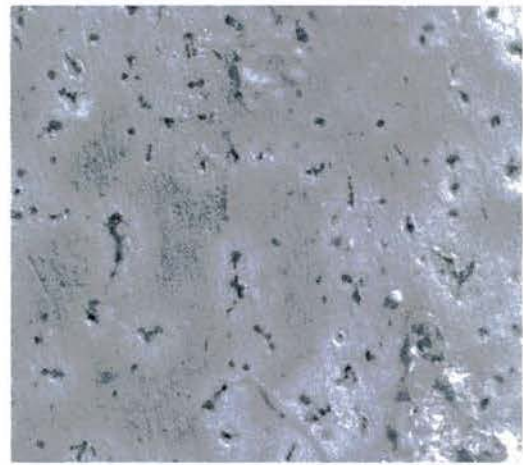
As-Supplied



Stabilized



Aluminum Coating



Sensitized

Figure 30 - Optical images of Alca 5 surface after salt spray for 500 hours

The specimens were loaded such that the maximum stress in the gauge section cycled between 32 ksi and 16 ksi, load ratio = 0.5, at a frequency of 20 Hz. Although the cross sectional dimensions of the specimens were equal for the Alca 5 material, the outer dimensions of the Abcrite and pure aluminum materials were greater. Due to the stresses applied, the aluminum coating cracked circumferentially around the entire specimen and delaminated at the gage section on the first cycle thereby reducing the influence of the extra material on the stress imparted on the Alca 5. The thickness and elastic modulus of the Abcrite material was applied in a FEA to confirm negligible impact on the Alca 5 stresses.

Based on a limited data set, the resulting fatigue measurements showed the As-supplied Alca 5 fractured after fewer stress cycles than the other groups, refer to Figure 31. This is due to the degree of sensitization of the Alca 5 material that came from the vendor and was identified through optical micrographs of etched samples. The Abcrite coated and Stabilized specimens completed approximately

the same number of cycles on average, whereas the twin-wire arc and sensitized specimens outlasted the other groups. In general, the results were relatively close considering the probabilistic nature of fatigue and varying degrees of sensitization among the specimen types. The degradation of the aluminum surface required for the Abcite coating appeared to have a detrimental effect on fatigue. The sensitized, stabilized, and as-supplier specimens had similar degrees of sensitization; therefore, they had similar pitting and fatigue lives. Stabilization and twin-wire arc aluminum coatings did reduce pitting; however, fatigue typically initiates at the greatest stress concentrator therefore any pitting makes the material susceptible.

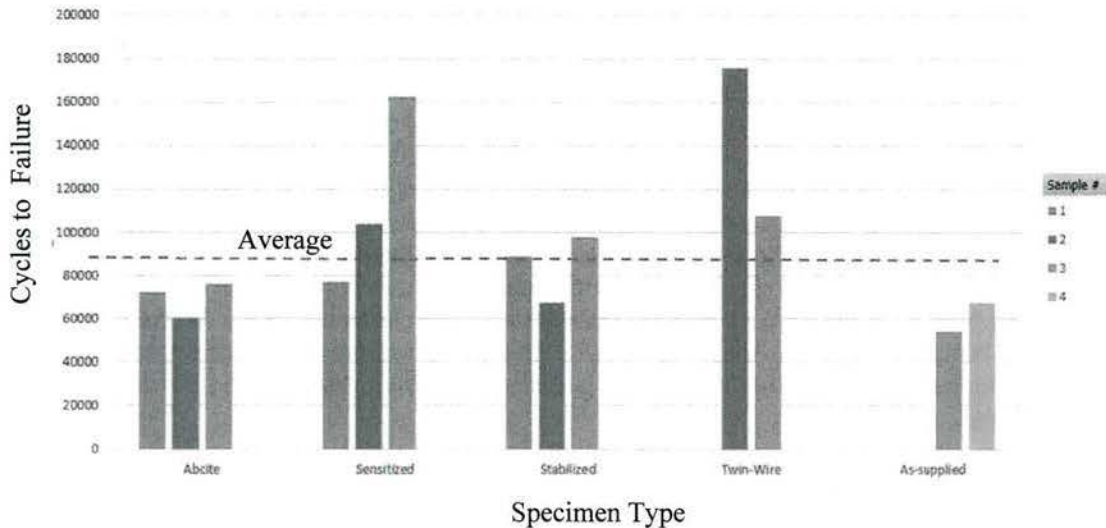


Figure 31 - Fatigue Life of Alca 5 in air after 500 hours of Salt Spray; $R=0.5$, 20 Hz

8.5 Corrosion Fatigue Testing

Another potential failure mode for high stress aluminum materials is corrosion fatigue, which differs for general fatigue conditions because specimens are continuously subjected to a corrosive media during testing. As presented earlier by Holtz, higher load ratios (R) allow for additional contrast between degrees of sensitization; therefore, a load ratio of 0.85 was selected for studying the effects of corrosion fatigue on Alca 5 and 5083-H in this experiment. The remaining Alca 5 specimens from the 500 hour salt spray exposure and four 5083-H samples extracted from the seal component were tested in a corrosion fatigue environment.

Before fatigue testing, each specimen was exposed to a 3.5% by wt. NaCl solution consisting of deionized water and table salt (simulating seawater) for 20 minutes immediately before loading to help break the protective oxide layer. ASTM G31 for immersion corrosion testing was referenced for preferred test solution volume to specimen surface area ratios; however, the guide was not strictly followed due to limitations of the test apparatus. During the fatigue cycles, the specimens were continuously exposed to the NaCl solution by sealing the lower gage section with heat shrink tubing and caulk before filling it with the solution. Although not a perfect solution, the method was effective at creating a pocket of fluid around the section while protecting the Instron hydraulic fatigue system.

Yield strengths for Alca 5 and 5083-H differ significantly, 18 and 37 ksi respectively [22]; therefore, the maximum stress selected for the Alca 5 corrosion fatigue tests was set at 17ksi to allow for high cycle fatigue similar to what the seal component experiences. A maximum stress of 32ksi was applied for the 5083-H specimens. The maximum force applied to the aluminum sprayed specimens was reduced compared to the other specimen types in order to prevent cracking of the coating during cycling which would cause the corrosive fluid to attack the Alca 5 substrate. The yield strength of the aluminum coating was 10ksi with a lower elastic modulus compared to Alca 5. Using finite element analysis, the geometry of the as sprayed fatigue specimens was subjected to a load that resulted in 17ksi in the Alca 5 substrate and less than 10ksi in the coating/substrate interface, refer to Figure 32. This allowed the aluminum coated specimen to experience the same stress as the other sample types while maintaining the integrity of the coating.



Figure 32 -
FEA Al.
Coating

Test results for corrosion fatigue showed the Abcrite coating survived the longest of the specimen types, refer to Figure 33. This is partly due to the protection from the NaCl solution provided by the polymer coating during salt spray and corrosion cycling. The aluminum twin-wire arc specimens varied with the final result being similar to the sensitized and stabilized specimens. The stabilized specimens did not show any improvement beyond the sensitized samples. The average cycles to failure for the Abcrite coated specimens was 279,415 compared to the 63,915 cycles average for the other specimen types. The effect of glass bead versus SiC grit blasting of the Alca 5 substrates for the Abcrite and aluminum sprays did not show an effect on fatigue life in this data set. Additionally, the 5083-H samples from the seal component showed similar results to the Alca 5 trends with the Abcrite coated samples outlasting both the stabilized and sensitized specimens.

Due to similar degrees of sensitization, the pitted specimens, as-supplied, stabilized, sensitized and aluminum coated, failed at similar cycle values, whereas the Alca 5 that was protected from pitting during salt spray and corrosion fatigue survived beyond the other specimen types. From optical inspection and test data, the Abcrite coating appeared to protect the glass bead and grit blasted surfaces from corrosion in salt spray and corrosion fatigue. Given the protection afforded by the polymer coating, the fatigue and corrosion fatigue tests were effectively the same, equating to a non-corroded state. It is hypothesized the Abcrite coated specimens failed earlier than the corroded specimens in the air fatigue test due to higher in surface stress concentrations from grit/bead blasting. At the higher load ratios in the NaCl solution, where the effect of sensitization becomes apparent, the unprotected aluminum specimens experienced faster crack growth therefore failed sooner than the Abcrite coated specimens.

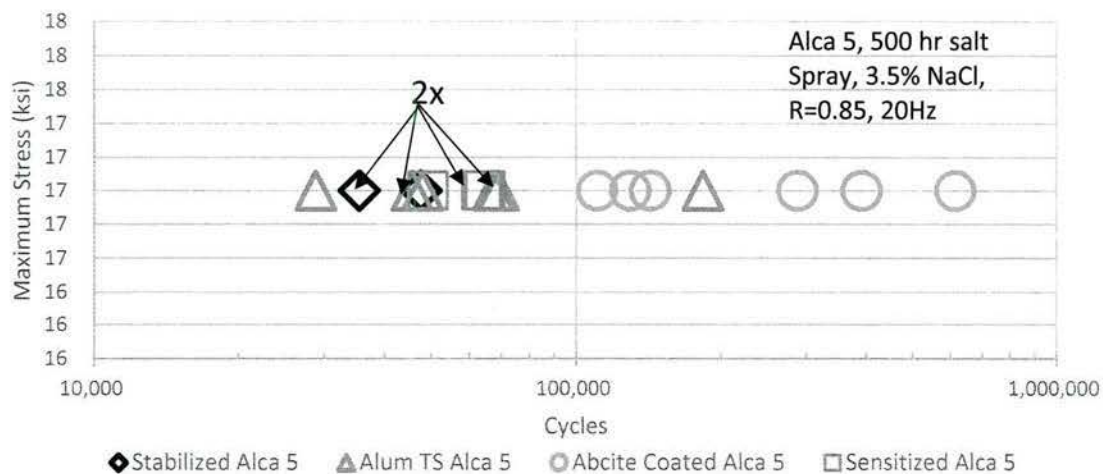


Figure 33 - Corrosion Fatigue of Alca 5: 500 hour Salt Spray Followed by Fatigue in NaCl Solution

9. Conclusions

High strength aluminum alloys, such as 5083-H used in the selected seal component of a Marine Corps vehicle, are susceptible to pitting and corrosion crack growth that can result in early component failure. The root cause failure analysis on the sample section provided showed that the 5083-H aluminum was sensitized during service conditions above 71°C. The resulting β -phase in the component was dissolved by the chlorine in the seawater that became trapped in the seal groove and ultimately aided in crack formation along the S-L plane. Both stress corrosion cracking and corrosion fatigue failure modes were possible given the degree of sensitization and the stress concentration factors formed at the radius of the seal groove.

The stress intensity factors calculated for worst case loading conditions exceeded the threshold stress and alternative stress intensities for degrees of sensitization above 30mg/cm². Although reducing the applied stresses could potentially eliminate or reduce the corrosion induced cracking of the component, that would require redesign and testing. Results from this study showed that stabilization and pure aluminum coatings did not extend the life of components with existing corrosion pitting. Applying a corrosion inhibiting polymer coating, such as Abcite, extended the fatigue life of the material at high load ratios in corrosive environments by preventing pitting of the aluminum. Due to the difficulty in detecting S-L cracking in parts like the example seal component, it is not recommended that the components be refurbished if signs of degradation in the protective paint layer or substrate pitting are identified. In components where the material selection cannot be changed, it is recommended that stress concentrations near weld zones and sensitized regions be avoided, and protective coatings be applied to mitigate the potential for pitting and subsequent corrosion cracking.

10. References

- [1] European Mill Products, "5xxx Plate," [Online]. Available: https://www.arconic.com/mill_products/catalog/pdf/general_engineering_plates/en/5xxx_en.pdf. [Accessed 2017].
- [2] M. Reboul and B. Baroux, "Metallurgical aspects of corrosion resistance of aluminium alloys," *Materials and Corrosion*, vol. 62, pp. 215-233, 2011.
- [3] C. Panagopoulos and E. Georgiou, "The Effect of Hydrogen Charging on the Mechanical Behaviour of 5083 Wrought Aluminum Alloy," *Corrosion Science*, vol. 49, no. 12, pp. 4443-4451, 2007.
- [4] K. Mutombo and M. Du Toit, "Corrosion Fatigue Behaviour of Aluminum 5083-H111 Welded Using Gas Metal Arc Welding Method," <http://www.intechopen.com/books/arc-welding/corrosion-fatigue-behaviour-ofaluminium-5083-h111-welded-using-gas-metal-arc-welding-method>, 2011.
- [5] J. C. Lippold, E. F. Nippes and W. Savage, "An Investigation of Hot Cracking in 5083-O Aluminum Alloy Weldments," 1977. [Online]. Available: https://app.aws.org/wj/supplement/WJ_1977_06_s171.pdf. [Accessed 2017].
- [6] W. Golumbski, K. Tran, J. Noland, R. Park, D. Stiles, G. Grogan and C. Wong, "Survey of Detection, Mitigation, and Repair Technologies to Address Problems caused by Sensitization of Al-Mg Alloys on Navy Ships," *Corrosion*, vol. 72, no. 2, pp. 314-328, 2016.
- [7] R. Kaibyshev, Musin, E. Avtokratova and Y. Motohashi, "Deformation Behavior of a Modified 5083 Aluminum Alloy," *Materials Science and Engineering*, pp. 373-379, 2005.
- [8] S. J. Pérez-Bergquist, G. Gray, E. K. Cerreta, C. P. Trujillo and A. Pérez-Bergquist, "The Dynamic and Quasi-static Mechanical Response of Three Aluminum Armor Alloys: 5059, 5083 and 7039," *Materials Science and Engineering*, pp. 8733-8741, 2011.
- [9] J. G. Kaufman, "Properties of Aluminum Alloys: Fatigue Data and the Effects of Temperature, Product Form, and Processing," ASM International, 2008.
- [10] R. Jones, J. Vetrano and C. Windisch Jr, "Stress Corrosion Cracking of Al-Mg and Mg-Al Alloys," *Corrosion Science*, vol. 60, no. 12, p. 1144, 2004.
- [11] R. Jones, V. Gertsman, J. Vetrano and C. Windisch Jr, "Crack-Particle Interactions During Intergranular Stress Corrosion of AA5083 as Observed by Cross-Section Transmission Electron Microscopy," *Scripta Materialia*, vol. 50, pp. 1355-1359, 2004.
- [12] T. Burleigh, "The Postulated Mechanisms for Stress Corrosion Cracking of Aluminum Alloys, A Review of Literature 1980-1989," *Corrosion Science*, vol. 47, no. 2, pp. 89-98, 1991.
- [13] C. B. Crane and R. P. Gangloff, "Stress Corrosion Cracking of Al-Mg Alloy 5083 Sensitized at Low Temperature," *Corrosion Science*, vol. 72, no. 2, pp. 221-241, 2015.
- [14] R. Holtz, P. Pao, R. Bayles, T. Longazel and R. Goswami, "Corrosion Fatigue of AL 5083-H131 Sensitized at 70, 100, 175°C and Relation to Microstructure and Degree of Sensitization," [Online]. Available: https://www.researchgate.net/publication/266873274_CORROSION_FATIGUE_OF_AL_5083-

H131_SENSITIZED_AT_70_100_AND_175_o_C_AND_RELATION_TO_MICROSTRUCTURE
_AND_DEGREE_OF_SENSITIZATION.

- [15] R. Holtz, P. Pao, R. Bayles, T. Longazel and R. Goswami, "Corrosion-Fatigue Behavior of Aluminum Alloy 5083-H131 Sensitized at 448 K (175C)," *Metallurgical and Materials Transactions*, vol. 43, no. 8, pp. 2839-2849, 2012.
- [16] L. Kramer, M. Phillippi, M. T. Tack and C. Wong, "Locally Reversing Sensitization in 5xxx Aluminum Plate," *Journal of Materials Engineering and Performance*, vol. 21, no. 6, pp. 1025-1029, 2012.
- [17] "Matweb.com," [Online].
- [18] W. C. Young and R. G. Budynas, *Roark's Formulas for Stress and Strain*, New York: McGraw-Hill, 2002.
- [19] Q. Han, Y. Wang, Y. Yin and W. , "Determination of stress intensity factor for mode I fatigue crack based on finite element analysis," *Engineering Fracture Mechanics*, vol. 138, pp. 118-126, 2015.
- [20] E. H. Dix, W. A. Anderson and M. B. Shumaker, "Influence of Service Temperature on the Resistance of Wrought Aluminum-Magnesium Alloys to Corrosion," *Corrosion*, vol. 15, no. 2, pp. 55-62, 1959.
- [21] R. Zang, S. Knight, R. Holtz, R. Goswami, C. Davies and N. Birbillis, "A Survey of Sensitization in 5XXX Series Aluminum Alloys," *Corrosion*, vol. 72, no. 2, pp. 144-159, 2016.
- [22] *MIL-DTL-46027*.
- [23] G. Scamans, "Stabilisation of AA5xxx Alloys," Innoval Technology Limited, 2008.

Research Program 5:
Evaluation of Additive Manufacturing for
Dimensional Restoration of Cast Iron
and Alloy Steel Components

This research was conducted under Office of Naval Research Grant N00014-14-1-0789.

Report Generated by:

Golisano Institute for Sustainability
Rochester Institute of Technology
190 Lomb Memorial Drive
Rochester, NY 14623
(585) 475-5101

Additive Manufacturing Final Report

Contents

1	Problem Statement	314
2	Problem Background	316
2.1	Discussion of sample geometries, base materials	316
2.2	Additive Materials Trade Study	317
3	Analytical Approach	318
3.1	Microstructure & Hardness	318
3.2	Adhesion	318
3.3	Wear	318
4	Twin Wire Arc	319
4.1	Program Objectives	320
4.2	Background (literature review)	320
4.2.2	Preliminary Process Development	325
4.2.3	Optimization Experiment	335
4.3	Conclusions	342
5	Cold Spray	343
5.1	Cold Spray Objectives	343
5.2	Cold Spray Background	343
5.2.1	Introduction	343
5.2.2	Cold Spray Benefits	346
5.2.3	Main Types of Cold Spray Systems	346
5.3	Coating Selection – powder trade study	350
5.4	Process Development	352
5.4.1	Introduction and Objective	352
5.4.2	Equipment and Process used in the Experiments	353
5.4.3	Process Development Experiments and Results	354
5.4.4	Baseline Data Collection for the RIT Low Pressure Cold Spray System	354
5.4.5	Surface preparation optimization	356
5.4.6	Understanding mixed material coatings for the restoration of hard surfaces	357
5.4.7	Evaluation of 420 SS based low pressure cold sprayed coatings	358
5.4.8	Evaluation of 420 SS mixed with Ni-5% Al alloy binder material	360
5.4.9	Evaluation of Cu for use as a binder material for 420 SS	362
5.4.10	Evaluation of theory 1 - 420 SS blended with Cu (85% Cu / 15% SS 420)	364

5.4.11	Evaluation of theory 2 - 420 SS blended with Cu (85% 420 SS / 15% Cu)	366
5.5	Conclusions and Recommendations for Future Development	372
6	LENS Coating Development	373
6.1	Program Objectives	374
6.2	Background (literature review)	374
6.3	Process Development	375
6.3.1	Equipment	375
6.3.2	Screening Tests	376
6.3.3	Mounting and Polishing Samples	377
6.3.4	Surface Preparation	377
6.3.5	Set-up of the Initial Design of Experiments	379
6.3.6	Bead Width and Bead Height	381
6.3.7	Layer to Layer Interaction	382
6.3.8	Definition of DOE Output Measurements	384
6.4	DOE Results and Discussions for Ductile Iron Substrate	386
6.4.1	Deposition Efficiency	387
6.4.2	Porosity	388
6.4.3	Hardness	391
6.4.4	Summary of the Ductile Iron Substrate DOE	393
6.4.5	Optimization for Wear	394
6.5	DOE Results and Discussion for 9310H Alloy Steel Substrate	396
6.5.1	Design of Experiments	396
6.5.2	Results	397
6.6	Further Measurements on optimal Coatings	406
6.6.1	Wear Resistance	406
6.6.2	Tensile Strength	409
6.7	Conclusions	411
7	Overall Research Conclusions	411
8	References	413
9	Appendices	417
9.1	Appendix A - Ductile Iron Trade Study Data Summary	418
9.2	Appendix B1 – 9310 H Trade Study Data Summary	419
9.3	Appendix B2 – 9310 H Trade Study Data Summary continued	420

1 Problem Statement

Components can degrade because of corrosion or wear. The consequences of corrosion are variable, but its effects on the safe, reliable and efficient operation of equipment or structures are often more serious than the simple loss of a mass of metal. Failures can occur even though the amount of metal destroyed is quite small because the corrosion causes a reduction of metal thickness leading to loss of mechanical strength and structural failure or breakdown. In addition, when the metal is lost in localized zones to give a crack like structure, considerable weakening may result from quite a small amount of metal loss [1].

Contamination of machine-element contacts by solid particles caused by either corrosion or wear is a serious problem and can significantly reduce the performance of a seal or bearing and eventually lead to failure. Particles ranging in size from nanometers to micrometers are responsible for increased wear and for even catastrophic failures of bearings, gears, seals [2]. The wear such contaminants can cause is abrasion, surface indentation, flaking, and even scuffing, depending on the operating conditions and the mechanical properties of the particulates.

During equipment rebuilding sealing surfaces are often machined or lapped to restore flatness or to improve the surface finish. When these surfaces are machined several times some of the component's dimensional tolerances can fail out of specification. When this occurs the component needs to be scrapped.

One method to restore worn, corroded or out specification components to the original OEM specifications is to use additive manufacturing techniques. There are a variety of different additive processes that are used for repair of components such as welding, stitching, cold spray, thermal spray and epoxy filling [3-6] however there is very limited scientific information in the literature that compare the mechanical and material properties of the different repair processes. In addition, some recently developed "additive manufacturing" processes offer some new alternatives.

The twin wire arc process applies a voltage between two wires. This voltage causes the wires to melt and form droplets. These droplets are then propelled to a substrate by compressed air or nitrogen.

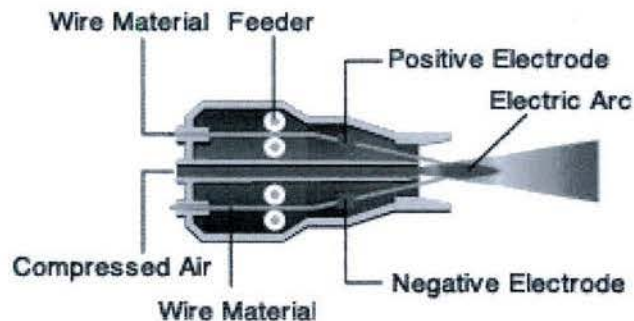
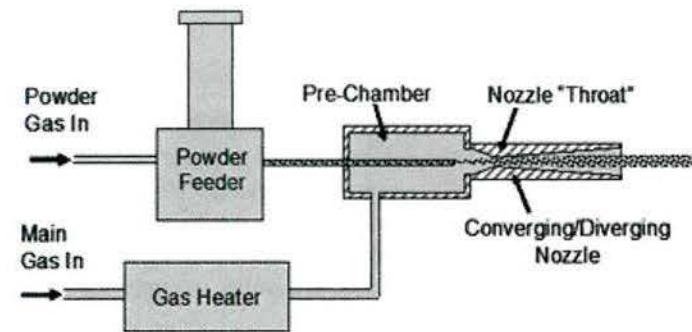


Figure 1: Twin-wire electric arc spray system

Cold Spray is a relatively new additive manufacturing process. It is an innovative coating technology mainly based on the high-speed impact of metallic particles on different substrates. Through the employment of low-temperature gases (air, He, N₂), spray particles (usually 1–50 μm in diameter) are accelerated to a high velocity (typically 300–1200m/s) that is generated through a convergent-divergent de-Laval-type nozzle. Severe plastic deformation of particles impacting the substrate occurs at temperatures well below the melting point leading to the unique mechanical properties experienced by such kinds of coatings.



Source: Sandia National Laboratory

Figure 2: Cold Spray System Schematic

Laser Engineered Net Shaping (LENS®) process may be characterized as a “disruptive additive process” that may be utilized for a variety of repairs and freeform fabrications. One advantage of this process is it combines excellent material properties with near-net-shape, direct-from-CAD, part building and repair. Another advantage of this additive process is, that since it is a melt process, the material forms a metallurgical bond to the surface to which it is deposited and the deposited layer contains very little porosity.

Selection of an additive manufacturing process for component restoration is difficult because there is no data that compares the physical, mechanical, and microstructural properties of the additive layers produced with each additive process. There is a need to develop this data to enable the proper selection of the right additive manufacturing process for each component.

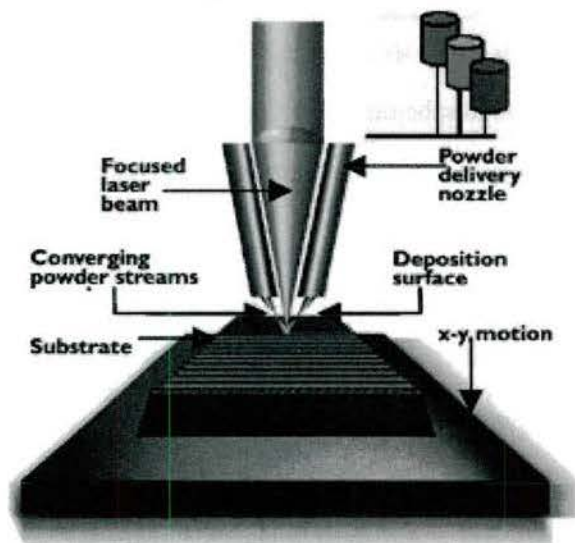


Figure 3: LENS system

2 Problem Background

2.1 Discussion of sample geometries, base materials

The Amphibious Assault Vehicle (AAV) is an aging tracked amphibious landing vehicle used to transport troops by the United States Marine Corps. This platform has been in service for 45 years and has proceeded through multiple life extension and survivability upgrade programs. With aging platforms, a lack of source of supply for components becomes an ever more challenging problem. Two components were selected from the AAV as sample geometries and materials based on the inability to obtain replacement parts. One of the major considerations in selecting components was the ability to apply the research to other industries.

The first component was a pump housing manufactured from Grade 80-55-06 ductile Iron per ASTM A-536. The component being evaluated is a casting that experiences wear caused by rotation from two mating components that were identified as C92700 Lead Tin Bronze. Details on the material and properties were unavailable therefore micro hardness measurements, micrographs, and x-ray analysis were obtained to determine the composition of the component. The component had an average micro hardness of 237HV and based on the composition, and microstructure, refer to Figure 4 below, believed to be equivalent to grade 80-55-06 ductile iron per ASTM 536.

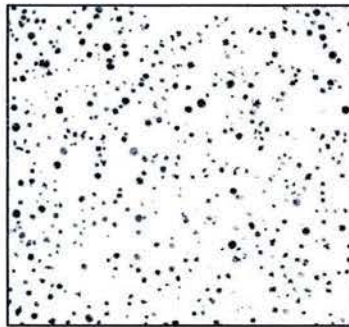


Figure 4: Micrograph of the Component

Micrographs of the component showed spheroids of carbon within the alloy which is typical of ductile iron. The X-ray analysis returned a composition similar to values expected for ductile iron but picked up traces of copper from the mating components. The recorded elements from the X-ray scan were 96% Fe, 1.4% Si, 1.2% Cu, 0.64% Mn, 0.38% Ni, 0.20% S, 0.04% P, and 0.04% Cr.

Operating conditions of the components were estimated from the manuals and drawings. An FEA model was developed to estimate maximum stresses on the component. Maximum stresses were identified at the ports in the casting where differential pressure occurs. Maximum stress values of 14,000 psi were recorded for bending at the ports. These results inform the types of technologies can be applied to repair worn surfaces because the stresses near the surface of this part exceed the adherence strength of many additive processes. Care must be taken to understand the application and operating conditions before selecting an additive repair process.

In this study, the ductile iron component requires a robust surface that can withstand relatively high stresses during operation. In industry, 80-55-06 ductile iron is equivalent to SAE J434c Grade D5506 ductile iron. Ductile iron is used in many components, including brakes, gear boxes, pumps, compressors, and municipal castings.

The second component was a drivetrain gear which was suffering corrosion failure at a seal surface. The gear is fabricated from 9310H alloy steel and required repair on a shaft surface. 9310H alloy steel is a typically used in gears and crankshafts in heavy duty trucks and some aerospace components due to its high core hardness and fatigue strength.

2.2 Additive Materials Trade Study

A trade study was performed to identify the optimal materials to be added to both of the selected components. A survey of available powders to be used for the Cold Spray and LENS processes was conducted. Similarly, the available wires for the twin-wire arc process were identified. The material characteristics of the ductile iron and 9310H alloy steel were compared to published values of the additive materials, when available; otherwise, wrought property values were used. For the LENS process, welded property values were also evaluated.

Stainless steel coatings are desirable in many applications due to their corrosion and wear resistance. This study focuses on grade 420 stainless steel coatings applied to both 9310H steel and ductile iron substrates. Grade 420 stainless steel was selected as the preferred coating because of its relative strength, wear and corrosion resistance, elastic modulus, and thermal expansion coefficient compared to the substrates.

A summary of the material properties of these materials is provided in Table 1. The full table of materials evaluated is provided in Appendix A.

Material	Hardness - Rockwell B (HRB)	Yield Strength (Elastic Limit) (Mpa)	Young's / Elastic modulus (GPa)	Shear modulus / modulus of Rigidity (GPa)	Ultimate Tensile strength (MPa)	Meltin g Pont (°C)	Thermal expansion (CTE @ 20 - 100 C) µm/m-°C	Corrosion resistance	Machinability
Wrought Ductile iron 80-55-06	98		159		552		11	Not good	39
Welded Ductile Iron 80-55-06	93				581				
9310 Annealed	97	450	190	80	820	1427	11.5	Good	51
420 SS Annealed	100	345	200	77.2	655	1450	10.3	12	45
420 SS Hardened & Stress Relieved	117	1365	200		1580		10.9		
420 SS Cold Spray - as sprayed	109		183.3						
420 SS wire - as sprayed	111								

Table 1 - Additive Material Study Properties

3 Analytical Approach

In order to identify the optimal coating solution for each of the base materials, 9310H and ductile iron, the overall quality of the coatings was assessed by investigating the adhesion, hardness, wear, and microstructural characteristics of each specimen. Adhesive strength measurements were collected using a portable adhesion tester. Hardness and microstructure were both assessed by evaluating cross sections of the specimens that had been potted and polished using Struers equipment. Hardness values were measured using a Struers DuraScan hardness tester with a Vickers indenter. Images of the samples were gathered using optical microscopes between 10 and 500 times magnification. Wear testing was performed on a custom built reciprocating wear fixture and dimensions of the wear scars were measured using a Zeiss 3D optical microscope.

3.1 Microstructure & Hardness

Metallographic specimens were prepared following ASTM E3-11 and ASTM E1920-03 [7, 8]. Cross sections were cut using a Struers Discotom 5 cutting saw with cutting wheel 60A25. Sections were mounted in black phenolic mounting compound using a Struers LaboPress 3. Sections were then ground against 220 grit and 450 grit sandpaper, then polished against 9, 3, and 1 μm polishing disks using diamond suspension on a Struers RotoForce 4 polishing system. Etching was not required to obtain images. The microstructure was then viewed using a Zeiss 3D optical microscope. Porosity, oxides, interface voids, and layer boundaries were the primary characteristics of interest within the coating. Microhardness data were collected using a Struers DuraScan-20 hardness tester, following ASTM E384 using a Vickers indenter [9]. The Vickers hardness test was performed with a maximum load of 1 kg and a 12 second full load dwell time.

3.2 Adhesion

To test the adhesion of the coating to the substrate, ASTM D4541 was utilized while incorporating elements of ASTM C633 concerning surface preparation [10], [11]. FM1000 adhesive was used to adhere the dolly to the coating, see Figure 5 for adhesion test setup. A DeFelsko PosiTest AT-M adhesion tester was used for the adhesion test. The maximum measurable adhesion utilizing the PosiTest is 10,000 PSI when used with a 10mm dolly.



Figure 5. Adhesive Specimen Setup

3.3 Wear

Wear testing was only performed on specimens that were selected for optimization from the original design of experiments. For comparative purposes, coated and substrate material specimens were tested under ball-on-flat lubricated reciprocating wear conditions against both bronze and steel balls. The coated specimens were ground to a finish of 16 micro-inches to remove the top 0.020" of coating, in order to provide a smooth

coating 0.030" thick for wear testing. ASTM G133 was followed for guidance and the wear volumes of both the specimens and the balls were quantified [12]. Samples were tested with a stroke length of 8.25 mm for 25,000 cycles (412.5m total distance) at 45 Hz, which equated to a total test time of approximately 90 minutes. The fixture incorporated a 20 kg mass to press the ball down onto the specimen. The oil used in the wear testing was Shell 15W40 non-synthetic engine oil that was heated to 250°F. The wear balls were ¼ inch diameter and made of either M50 tool steel or 260 brass with hardness values of 60 Rockwell C and 75 Rockwell B, respectively.

After testing, the wear scars were measured with the SmartScope and Zeiss 3D microscope to find the wear volume of both the specimen and the ball. The wear volume of the balls was found by measuring the flat area created by wear. This was used to calculate the volume removed. 50x images of the wear scars were recorded. These images were used to calculate the wear volume of the coatings or uncoated substrates.

4 Twin Wire Arc

Twin-wire arc spraying is a form of thermal spray that feeds two electrically charged wires through opposing sides of a spray nozzle producing an electrical arc as the wires converge which melts the wires. Compressed air expelled from behind the wires atomizes the molten material and accelerates the particles onto the work surface. Bond strengths of approximately 9,000 pounds per square inch (psi) are achievable with this process and with twin-wire arc spray. One significant advantage to the twin-wire arc thermal spray process is a relatively large selection of coating materials commercially available in wire form.

Twin-wire arc thermal spraying is a process within the family of thermal spray technologies that converts solid feedstock into a molten spray that condenses back into a solid form upon impact with the target substrate. The flexibility of this additive process allows for a multitude of applications for twin-wire arc spray including:

- Restoration of worn parts to their original dimensions for a lower cost than replacing with a new cast or machined part.
- Enhanced longevity of parts by making them more resistant to wear, abrasion or corrosion.

The economic and environmental benefits of using twin-wire arc thermal spray processes to repair components that would otherwise be scrap are significant. Components that no longer meet dimensional requirements are prime candidates for remanufacturing with twin-wire arc spray and other additive manufacturing processes. Many opportunities for remanufacturing of worn surfaces include components comprising of steel or ductile iron as both materials find uses in wear applications because of their resistance.

Deposition of twin-wire arc coatings with substantial thicknesses, high wear resistant and toughness are possible. They are being extensively applied in oilfield drilling and production applications to coat wear surfaces on drill pipe and downhole tools, to create stabilizer or centralizer ribs for casing, drilling and running, and to create internal end stops for bow-spring centralizers [13]. The alloy coatings have been applied to steel, aluminum, nickel alloys, and nickel copper substrates and the process has been found to be highly cost effective as compared with traditional alternatives. The coatings have been tested extensively for fatigue, shock, wear, friction, casing wear, and metallurgical changes to the base material.

First, this study evaluated surface preparation methods to achieve a suitable surface profile for further experiments. Next, effect of the following coating parameters on the coating microstructure, physical, and mechanical properties were studied using a fractional factorial experimental design: air pressure, voltage between the wires, current (which is tied to wire feed rate), traverse rate, and stand-off distance. A single parameter set was chosen as the most promising and then a second design of experiments was conducted to optimize the coating. These coatings were evaluated for adhesion, hardness, porosity, and oxide content to select a single optimal coating. This optimal coating was tested for wear.

4.1 Program Objectives

4.2 Background (literature review)

A 2011 investigation by the International Trade Commission found that the national production of remanufactured goods in the United States exceeded \$43 billion annually and was responsible for 180,000 American jobs [14]. The investigation also reported that the average cost of remanufactured goods was typically between 25% and 50% less than the cost of the equivalent newly fabricated goods. While the material cost of remanufacturing is very small, the labor costs and time requirements are often equal to or greater than that of new parts. Furthermore, the environmental benefits of remanufacturing often outweigh the economic benefits because the amount of energy and raw material necessary for remanufacturing are typically less than half of what is necessary to manufacture new parts [14]. These findings are generally true for thermal spray coated parts because the mass of the raw material added is small with respect to the part undergoing remanufacturing.

Cooke and co-workers investigated the use of iron-chromium-boron wire arc coatings to improve the wear resistance of new cast iron parts. They found the system parameter that had the greatest impact the coating wear resistance was the air pressure [15]. Other parameters, such as current, voltage and offset distance, also made significant contributions to the wear characteristics. The results of the wear tests are shown in Figure 6, where a smaller mass loss indicates superior wear resistance.

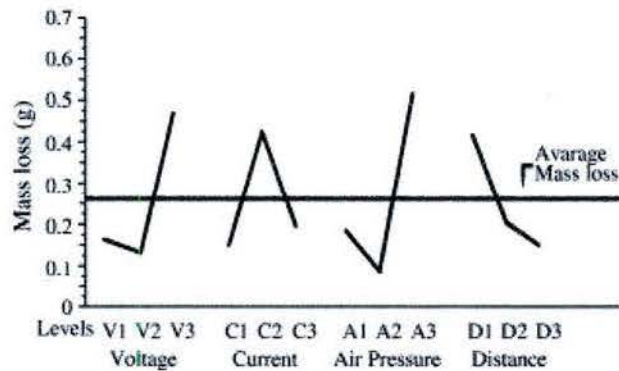


Figure 6. Relationships between Spray Parameters and Wear Behavior [15]

An extensive study performed by Wilden et al. on the thermal and flow profiles of sprayed chrome particles in twin-wire arc sprayed coatings showed the effect of process parameters on metallurgical properties. This study used high speed imaging to characterize the particle velocity, particle temperature, and spray plume geometry. It was concluded that an increase in the voltage setting created larger particles and higher particle temperature. It was also found that increasing the air pressure and decreasing the voltage both produce an increase in particle velocity that effects impact behavior. Lower temperatures also maintain the composition of the alloy feedstock by limiting burn-off of components [16].

Research by Tillman, Vogli, and Abdulgader sought to relate movement of the spray gun, relative to the positive and negative charged wire tips, to differences in coating properties - this study concluded that there was a significant relationship between the traverse direction and thickness per pass as well as the resulting porosity. The least porosity was observed when moving the spray gun in the direction of the positively charged wire, while alternating spray directions produced the greatest porosity. The reason for this was hypothesized to be differences in the particle size produced from each wire. The same study showed a relationship between traverse direction, hardness, and adhesion strength [17].

Varacalle et al. studied the effects of varying current, traverse speed, and stand-off distance in spraying aluminum coatings using twin-wire arc [18]. This study investigated hardness, layer thickness, and porosity by utilizing a fractional factorial design experiment. The researchers found that increasing current,

physically tied to wire feed rate, resulted in increased layer thickness. Porosity could be reduced by increasing the current and air pressure simultaneously. This study also measured the deposition efficiency and found that shorter stand-off distances were correlated to higher deposition efficiencies. By combining all of the relationships that were found, an optimal parameter set for aluminum coatings was selected to achieve low porosity, low roughness, high hardness, and high deposition efficiency [18].

Newbery and Grant studied the effects of oxidation of plain steel coatings during twin-wire arc spraying. The coating selected in this study was plain carbon steel and the substrates were mild steel. This study tested the effects of varying the oxygen content of the atomizing gas as well as in the spray environment. As expected, it was found that the oxygen content of the coating increased as the oxygen content of the atomizing gas increased. Newbery and Grant's inverse relationship between the oxygen content of the atomizing gas and coating hardness is provided in Figure 7. The study concluded that a larger oxide content in the atomizing gas leads to improved adhesion to the substrate at the expense of hardness [19].

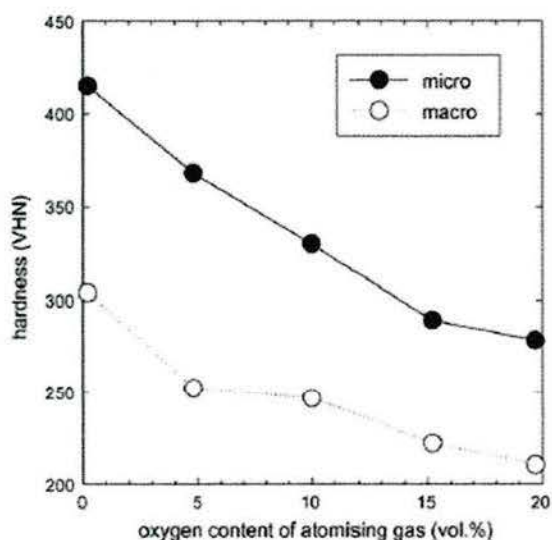


Figure 7. Relationship between Hardness and Gas Oxygen Content [19]

Likewise, Jandin et al. studied high carbon steel coatings produced by twin-wire arc. Jandin's study sought to relate the input parameters of pressure, current, and type of atomizing gas to mechanical coating properties such as hardness and elastic modulus. This experiment studied the use of both compressed air and nitrogen as the atomizing gas. It was found that the coatings produced with nitrogen contained consistently fewer oxides than those produced using compressed air. In both cases, however, increased gas pressure caused increased oxide content. The study was able to conclude the hardness and oxide content were directly related to each other. The relationship between hardness, current, and gas flow rate is shown in Figure 8. A relationship between increased current and decreased hardness was also noted. Elastic modulus of the coating was measured with a novel cantilever method. It was found that the use of nitrogen as an atomizing gas creates coatings with consistently higher moduli of elasticity. Elastic modulus results are shown in Figure 9 [20].

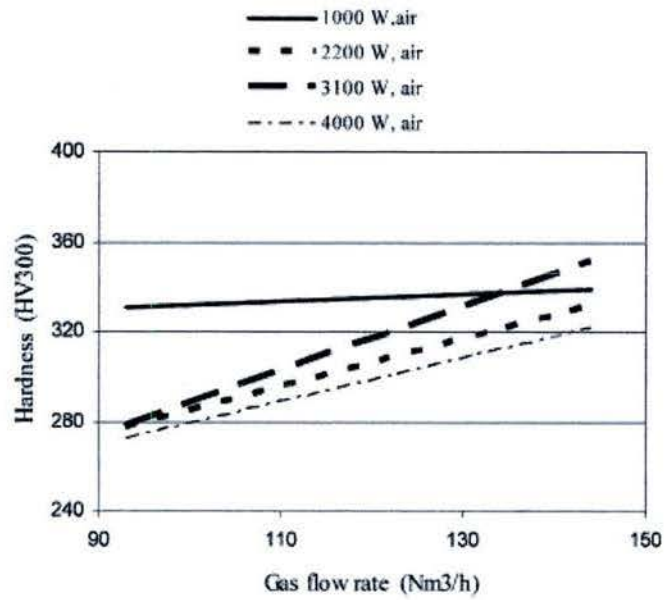


Figure 8. Relationship between Gas Flow Rate and Hardness [20]

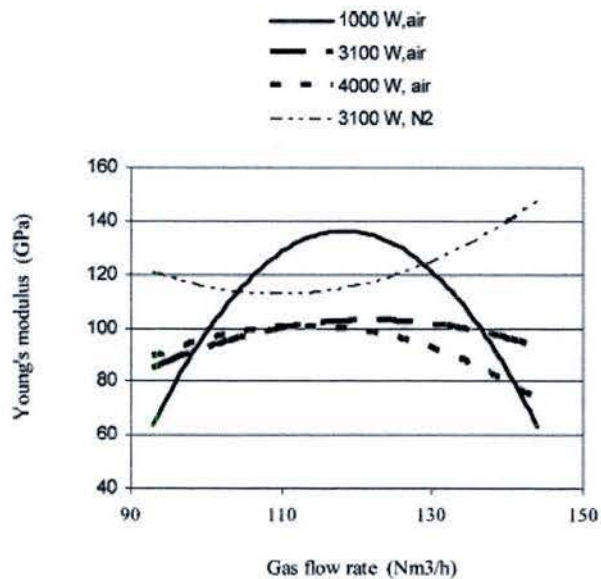


Figure 9. Relationship between Gas Flow Rate and Elastic Modulus [20]

The research performed under this report set out to expand on previous works by investigating further parameter interactions, such as voltage and surface preparation, combined with the a more comprehensive design of experiments. This work sought to resolve discrepancies in the results found by previous researchers while creating a more thorough understanding of the coating quality through testing of adhesion, hardness, porosity, and wear resistance. In this work, a wide range of mechanical and metallurgical

properties were studied in order to develop a full set of parameters optimized to create robust coatings of alloy 420 stainless steel on 9310H steel and ductile iron substrates.

4.2.1.1 Equipment

A Thermach AT-400 twin wire arc spray system was attached to an ABB IRB 1600 robot to control the application of the alloy 420 stainless steel coating to the substrates. The AT-400 spray unit allowed for control of voltage, current, and air pressure settings during the experiments. The range of voltages for the trials performed was 10 to 38 DC Volts. Experimentation showed that a consistent arc was difficult to achieve at voltage settings less than 30 Volts. The spray unit allowed current settings between 0 and 400 amps, however, the spray began to sputter at currents below 60 amps. While the spray gun was running the current fluctuated ± 10 amps due to variations in the length of the arc between the wires. The air pressure at the system was measured by a pressure gauge on the front of the spray unit and developed an airflow of up to 83 SCFM, as measured by a flowmeter attached to the compressed air supply. While the spray gun is rated for pressures of up to 140 psig, the facility compressed air supply limited the maximum air pressure while flowing to 105 psig for the tests. The industrial robot was essential for consistent and repeatable traverse speeds, stand-off distances, and pattern overlaps. A Donaldson Torit dust collection system with variable frequency drive was used to capture a significant amount of dust and fumes created as a byproduct of the wire arc spray process; however, the air to cloth ratio of the filters was marginal for this process.

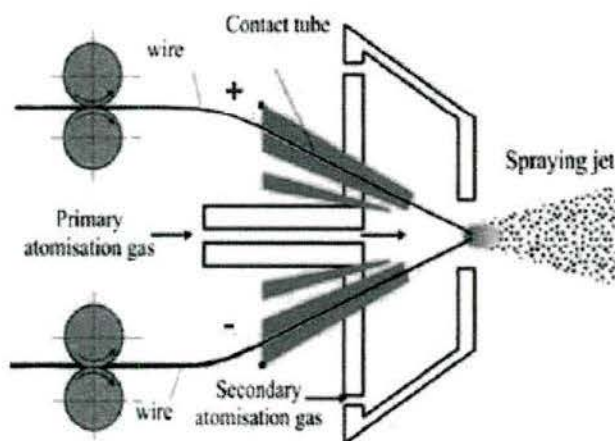


Figure 10. Schematic Drawing of Twin-wire arc Process [17]

The elemental makeup of each material used in this study was collected for reference, refer to Table 2. The wire selected was grade 420 stainless steel with a 1/16 inch diameter for similar mechanical properties and enhanced corrosion protection of the substrates.

Table 2. Elemental Composition of Substrates and Coating Material

Material	Ductile Iron (%)	9310H Steel (%)	420 Stainless Steel (%)
C	2.5 - 4.3	0.08 - 0.13	0.15
Cr	0.01 - 2	1 - 1.4	12

Cu	0.01 - 1.5	--	--
Mn	0.01 - 2	0.45 - 0.65	1
Mo	0.01 - 0.5	0.08 - 0.15	--
Ni	0.01 - 3	3 - 3.5	--
P	--	0.025	0.04
S	--	0.025	0.03
Si	1 - 4	0.02 - 0.035	1
Sn	0.01 - 0.3	--	--
Ti	0.01 - 0.5	--	--
Fe	Balance	Balance	Balance

4.2.1.2 Set-up

The twin-wire arc spray gun was held by an ABB IRB 1600 robot to ensure consistent and repeatable stand-off distances and traverse speeds, refer to Figure 11. The spray gun was held vertically, perpendicular to substrates. The robot's maximum payload of 6 kg was exceeded by the weight of the spray gun and the cables connecting the spray gun to the wire feeding unit therefore the cables were suspended from the ceiling of the spray booth using a pulley and counterweight. This offset a sufficient portion of the weight and allowed the robot to function normally.

The coatings were applied to 2" diameter substrates with a thickness of 0.35" that were clamped horizontally against a fixture during coating. The spray pattern was controlled by ABB code programmed into the robot. The entire spray system and robot were enclosed within the spray booth equipped with a dust collection system. The spray process was controlled entirely from outside the spray booth to ensure the safety of operators.

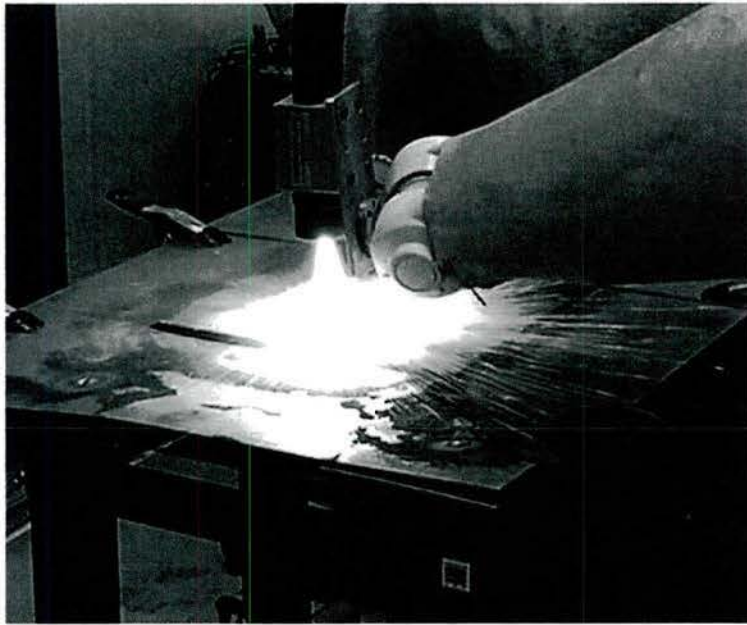


Figure 11 - Twin Wire Arc Setup

4.2.2 Preliminary Process Development

4.2.2.1 Surface Preparation Study

Adhesion of the twin-wire arc coatings is due to mechanical bonding between the substrate and the coating. For this reason, the surface roughness or topography of the substrate was an important parameter for obtaining a thermal spray coating with good adherence. Two studies were performed to select the proper process parameters and equipment modifications. First, a cursory study was performed to ascertain the effects of different grit blasting parameters on the resulting adherence strength of the coatings. After investigation into the desired grit spray angle and distance to the substrate, the effect of grit blasting pressure on the surface roughness of a ductile iron specimen was studied along with the effect resulting adherence of a twin-wire arc sprayed alloy 420 stainless steel coated specimen. The grit blasting parameters tested were:

- 36 grit aluminum oxide, 90 psi air pressure, 4-inch stand-off distance, 200% coverage, size 5 nozzle, 90° spray angle (perpendicular pass pattern)
- 36 grit aluminum oxide, 40 psi air pressure, 4-inch stand-off distance, 200% coverage, size 5 nozzle, 90° spray angle (perpendicular pass pattern)

This study began by grit blasting a ductile iron surface using the two parameter sets listed above. After grit blasting, the surface roughness was determined using a portable Starrett SR100 Surface Roughness Tester and a Surface Form Talysurf surface profiler by Taylor-Hobson was used for additional surface profile data. After measuring the surface roughness, an alloy 420 stainless steel coating was applied to the surface of the ductile iron substrate using the following twin-wire arc spray procedure: 7 layers, 30 volts, 60 psi, 180 amps, 4.5 inch stand-off distance and 6 inch/s traverse rate. The top 0.020 inch of coating was removed with a mill to provide a smooth, 0.030 inch thick coating for adhesion testing. Once the sample was prepared and cleaned, the adherence strength of the coating to the substrate was determined using ASTM D4541, the pull test procedure described in Section 3.2 of this report.

Using the portable Starrett surface profiler, the surface roughness for the ductile iron substrate was found to be 3.5 micron (138 μin) and 5.5 microns (217 μin) for the 40 and 90 psi grit blast pressures, respectively. Next, surface roughness profiles for each substrate was obtained using the Taylor-Hobson surface profiler, refer to Figure 12 and Figure 13.

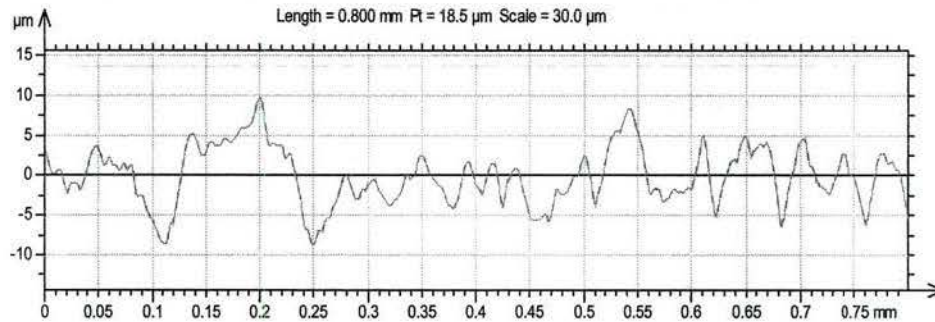


Figure 12 - Surface Profile of 40 psi Grit Blasted Surface

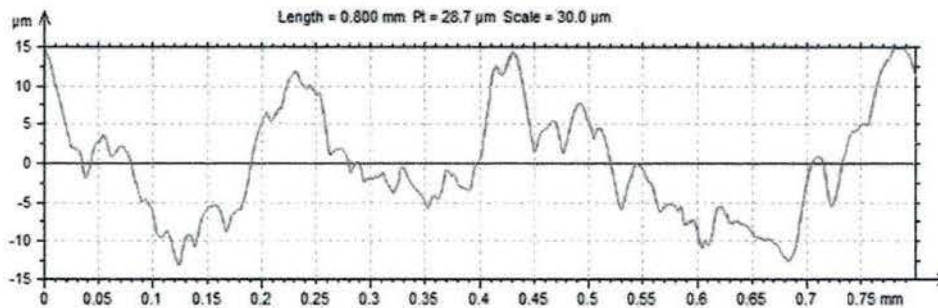


Figure 13- Surface Profile of 90 psi Grit Blasted Surface

In order to further characterize the grit blast surfaces, the profiles in Figure 12 and Figure 13 were analyzed for R_a (the average of all the peaks and valleys). The results were:

- 40 psi -- $R_a = 2.4 \mu\text{m}$ (94 μin)
- 90 psi -- $R_a = 3.4 \mu\text{m}$ (134 μin)

The analyses of the grit blasted surfaces showed that increasing the pressure during grit blasting increased the R_a value for the blasted surface by approximately 30 percent. This difference was deemed to be insignificant because the desired surface roughness was near $7.6 \mu\text{m}$ (300 μin).

After grit blasting, alloy 420 stainless steel coatings were applied to the iron substrates using twin-wire arc spray. The bond strength of the stainless steel coating to the ductile iron substrate was determined for four specimens, refer to values below. This testing showed that both grit blasted surfaces provided a coating adherence greater than the 6000 psi. The surface grit blasted at 40 psi showed an average coating adherence 1004 psi greater than the surface grit blasted at 90 psi. This confirmed the results from the surface profile that indicated the 40 psi samples exhibited a more consistent surface with a larger quantity of smaller peaks and valleys compared to the 90 psi grit blasted surface.

- 40 psi grit blasted surface – 7460 and 6888 psi
- 90 psi grit blasted surface – 6144 and 6196 psi.

Cross-sectional optical micrographs of the applied twin-wire arc thermal spray coatings are contained in Figure 14 and Figure 15. The stainless steel coating had a laminar structure because it was built from

multiple passes of metallic splats that develop during the melting of the wire. In the micrographs the coating-substrate interface was highlighted with arrows with the alloy 420 coating above the interface and the ductile iron below.

The micrographs show that the roughness at the 40 psi grit blasted interface was similar to the roughness at the 90 psi grit blasted interface. This was expected as the two surfaces had only slightly different R_a and R_z values. The major difference, however, between the two interfaces was the 90 psi surface consisted of alternating large peaks and valleys while the 40 psi interface consisted of an increased number of smaller peaks and valleys. Since both coatings had adherence values greater than 6000 psi using standard spray parameters, either preparation method would provide acceptable coating adherence for many applications. The surface preparation technique using 40 psi air pressure was selected for the Screening Experiment.

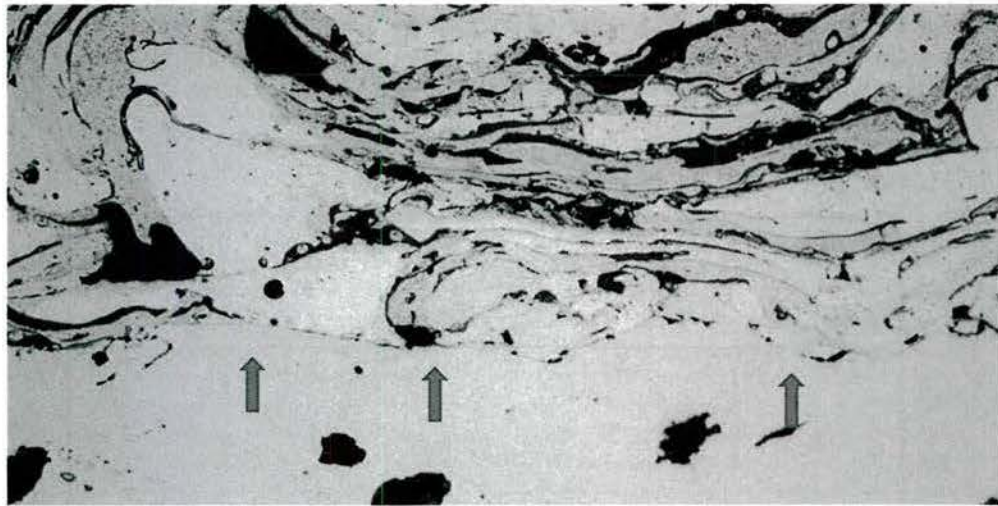


Figure 14- Cross-sectional Photomicrograph of Thermal Spray Coating on 40 psi Grit Blasted Surface, 500 x

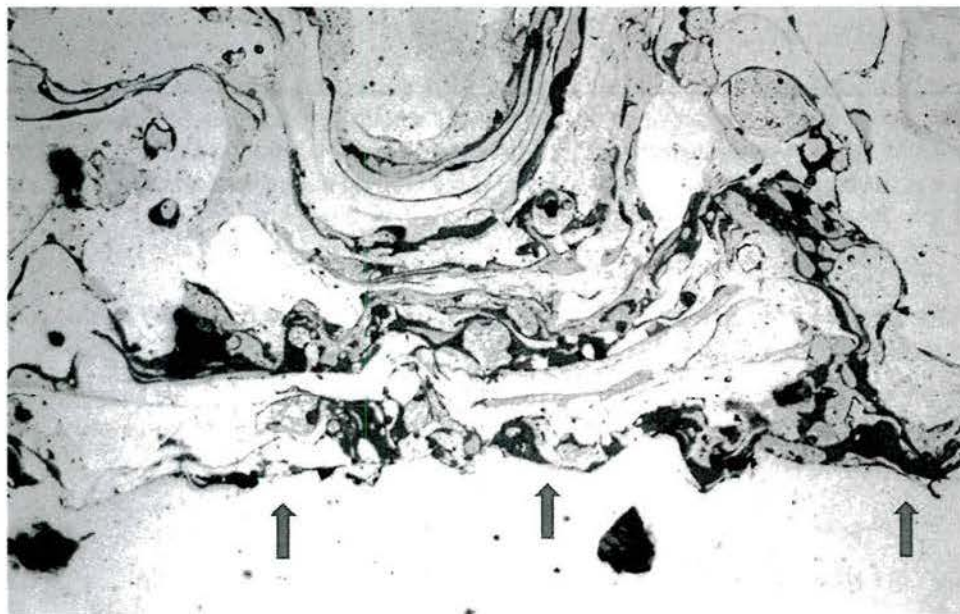


Figure 15- Cross-sectional Photomicrograph of Thermal Spray Coating on 90 psi Grit Blasted Surface, 500 x

A second experiment was performed in an attempt to create rougher substrate interfaces after several coatings sprayed during the Screening Experiment showed highly inconsistent adhesion results. Based on the work of Varacalle et al., the bond strength generally increases as surface roughness is increased [21]. Their study showed steel grit of 16 and 40 provided high R_a and R_z values that increased the adhesion strength of the twin-wire arc coatings. Optimal pressure and working distance were found to be at intermediate settings. Informed by this, the second grit blast experiment focused on obtaining the highest R_a value possible. This was achieved by fitting the grit blaster with size 6 orifice and a longer nozzle to increase the velocity of the grit. With recommendations from the equipment vendor, a new grit blast technique was utilized. The parameters used were: 36 grit aluminum oxide, 4" stand-off distance, 100 psi, 15° from perpendicular, spiral pattern from outer edge toward center. Using this technique, R_a values of greater than 7.5 μm (300 μin) were consistently obtained. An example of the surface profile for a ductile iron substrate is shown in Figure 16. Similar to findings by Varacalle et al. this surface preparation technique that yielded higher roughness values and increased adhesion strength by 23%. This surface activation technique was utilized in the Optimization Experiment (Section 4.2.3).

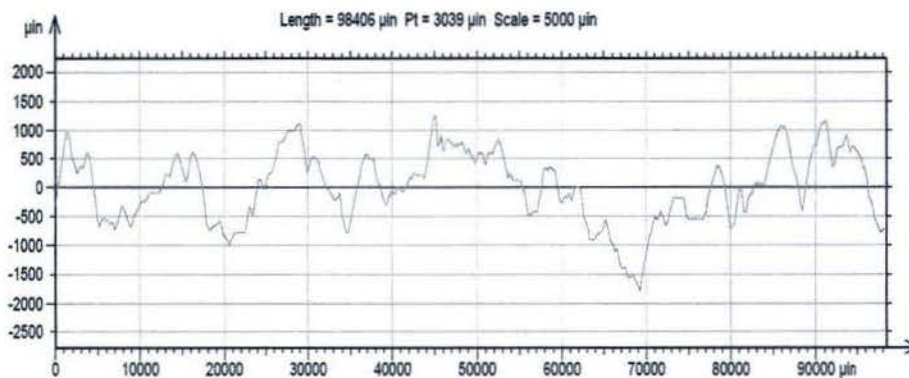


Figure 16. Surface Profile for Improved Grit Blasting Procedure

4.2.2.2 Factorial Experiment for Process Development

Two sets of experiments, Screening and Optimization, were performed to develop a robust coating of alloy 420 stainless steel for wear applications on ductile iron and steel substrates. The Screening Experiment was based on a partial factorial design for the various levels of the user controlled settings. The Optimization Experiment was developed to hone the twin-wire arc spray coating parameters selected from the Screening Experiment in order to achieve a wear resistant, high strength coating.

4.2.2.3 Screening Experimental Procedure

The test matrix created for the first partial factorial design of experiments included 9 unique spray settings with 3 replicates of each, the parameters and levels tested are provided in

Table 3. The design of experiments set input parameters at low, mid, and high levels based on manufacturer recommendations for the AT-400 twin-wire arc spray unit and the alloy 420 wire feedstock. Runs were performed in a randomized order throughout the experiment.

Table 3. Design of Experiments Matrix

Replicate Group #	Run #	Stand-off Distance (in)	Voltage (V)	Amperage (A)	Air Pressure (psi)	Traverse Rate (in/s)
-------------------	-------	-------------------------	-------------	--------------	--------------------	----------------------

1	1,14,27	6	34	90	75	4
2	2,21,23	3	30	60	105	10
3	3,12,22	9	30	60	50	1
4	4, 7, 11	9	30	120	50	10
5	5, 18, 25	3	38	60	50	10
6	6, 13, 15	3	38	120	50	1
7	8, 17, 24	9	38	60	105	1
8	9, 10, 20	9	38	120	105	10
9	16, 19, 26	3	30	120	105	1

In each run, a pair of substrates was coated simultaneously, one ductile iron and one 9310H steel. The substrates were saw cut from 2 inch round stock material at a thickness of approximately 0.4 inch. Each sample was milled flat to a thickness of 0.35 inch to remove the tool marks from saw cutting. Immediately prior to spraying, the substrates were grit blasted with aluminum oxide using the first technique discussed above (40 psi to achieve 3.5 μm R_a). The surface roughness R_a value was measured using a Starrett surface profile tool in four positions on the sample face and the results were averaged together to verify that the roughness was above the 3.5 μm target. To prevent lifting from the spray, the parts were held in place with dowel pins as shown in Figure 17. The 9310H samples were slightly smaller than the ductile iron samples, so a wedge was used to aid in securing the steel substrates. After fixing the parts, the surfaces were wiped with isopropyl alcohol. 9310H steel and ductile iron samples were coated following the red spray path shown in Figure 17. Each step in the pattern was 0.24 inch (6 mm), chosen to create an approximately 50% overlap of the twin-wire arc spray diameter. The substrates were coated to a minimum thickness of 0.050 inch to allow for a 0.030 inch coating after final machining. If the coatings did not meet the minimum thickness, the parts were loaded back into the fixtures and more layers were added.

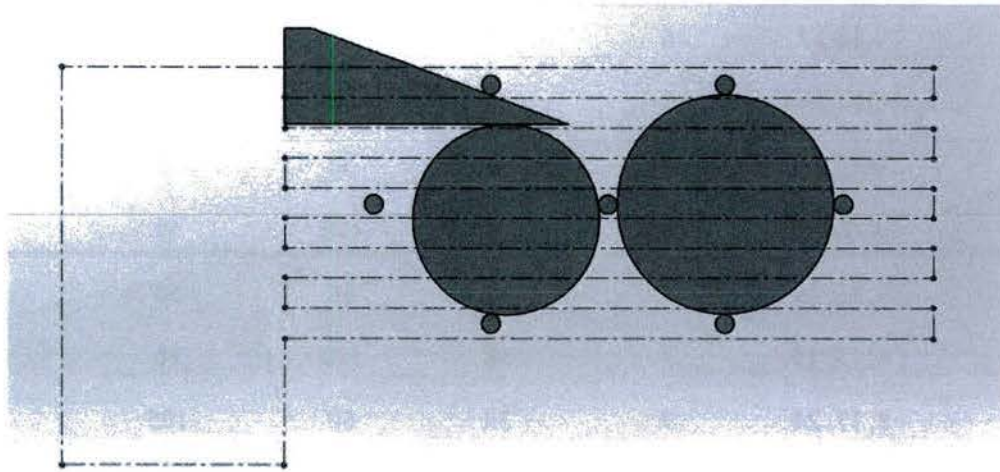


Figure 17 -Spray Coverage Pattern, steel sample on left and iron sample on right

4.2.2.4 Screening Experiment Results (hardness, adherence and microstructure)

4.2.2.4.1 Adhesion Results

Adhesion pull tests were to be performed on the specimens, however, the coating did not adhere to several specimens during the spray process preventing testing. In total, eight of the 27 pairs of coatings did not adhere to the substrates and three only adhered to one of the two substrates in their group of 3 replicates. The eight coatings that failed immediately were from Group 7, Group 9, and two of the runs from Group 2. For coatings that were subjected to adhesion tests, the adhesive failures all occurred at the interface between the coating and the substrate, indicating that the bond strength was weaker than the coating's tensile strength. An ANOVA analysis was not possible on this data due to the groups of failed coatings. The data presented in Table 4 shows that pressure was highly influential.

Table 4. Adhesion Results for Experiment 1

Replicate Group #	Run #	Mean Iron Adhesion (psi)	Iron Adhesion Standard Dev.	Steel Adhesion (psi)	Steel Adhesion Standard Dev.
1	1, 14, 27	6579	366	4620	2274
2	2, 21*, 23*	7836	N/A	7116	N/A
3	3, 12, 22	6696	602	5257	481
4	4, 7, 11	5487	351	5609	683
5	5, 18, 25	6055	418	5585	675
6	6, 13*, 15	6147	491	5956	311

7	8, 17, 24	N/A*	N/A	N/A	N/A
8	9*, 10, 20*	5764	566	3634	3386
9	16, 19, 26	N/A*	N/A	N/A	N/A

*Incomplete spray adhesion

The coatings sprayed at 105 psi either displayed very strong adhesion or failed to adhere. The specimens coated at 50 psi were consistent, but did not display adhesion values as high as Group 2, which were created at 105 psi. As a result, air pressure was studied further in the Optimization Experiment in order to create consistently successful coatings at high pressure. Results also showed lower current produced consistently higher adherence values than the high current settings. The effect of stand-off distance was unclear from this experiment therefore stand-off distance was also chosen to be studied in the Optimization Experiment. Voltage and current seemed to have little effect on the coating adhesion.

The two substrate materials displayed similar responses to changing parameters, however the adhesion to the ductile iron substrate was consistently stronger than the adhesion to the steel substrate. This may be due to the difference in thermal conductivity between the two materials; 24 W/m*K and 52 W/m*K for ductile iron and steel, respectively. The higher thermal conductivity would remove heat from the coating quicker causing higher residual tensile stresses. The difference in adhesion may also be due to differences in the surface activation of the substrates. While there was no discernable difference between the R_a values of the different materials, it is possible that the surface profiles were different.

4.2.2.4.2 Hardness Results

Experimental test results from micro-hardness measurements, provided in Table 5, were taken on the alloy 420 stainless steel coating. As above, an ANOVA analysis was not possible due to the groups with an entire set of failed coatings.

Table 5 - Micro Hardness Alloy 420 on Ductile Iron and Steel

Replicate Group #	Run #	Mean Iron Hardness	Iron Hardness Standard Dev.	Mean Steel Hardness	Steel Hardness Standard Dev.
1	1, 14, 27	286	47	298	48
2	2, 21, 23	357	N/A	349	N/A
3	3, 12, 22	321	11	324	34
4	4, 7, 11	274	41	333	12
5	5, 18, 25	299	50	284	18
6	6, 13, 15	314	40	285	1
7	8, 17, 24	N/A	N/A	N/A	N/A
8	9, 10, 20	297	7	297	34
9	16, 19, 26	N/A	N/A	N/A	N/A

In a publication by Jandin and collaborators, it was theorized that hardness was correlated with higher oxide content resulting from higher air flow rates [20]. This experiment found that the hardest coating (Group 2) was produced with high pressure (equating to more air flow and generally smaller particles) and traverse rate, which supports findings by Jandin et al. Use of inert gas such as nitrogen or argon would affect these results as would changes to the dwell time of the molten melt drops in the air stream. It was clear that the hardness was consistently higher with a higher traverse rate. It was theorized that this was due to the fact that increased traverse rate was directly tied to an increased number of layers in order to achieve the same final coating thickness. Layer interfaces were observed to have a greater proportion of hard oxides than the bulk material. Therefore, the specimens with more layer boundaries were expected to be harder than those with few layer boundaries. A general trend was observed between higher hardness in the steel samples and lower voltage. Stand-off and amperage did not indicate any significant trends when compared to hardness. The substrate material did not influence the relationship between parameters and hardness and there was no evidence that the coatings on one material were consistently harder than on another.

4.2.2.4.3 Microstructure Results

Each specimen was viewed and imaged under 50x and 200x magnification to better understand the microstructure of stainless steel coatings. Specimens having the least porous microstructure, absence of interface voids, and general intra-layer consistency were considered for the optimization experiment. The microstructure of the samples was reviewed for oxide content and it was discovered that samples with higher hardness levels exhibited greater oxide content.

Figure 18 through Figure 24 show the optical micrographs of a selection of specimens at 50x magnification for the groups that passed adherence testing. Ductile iron specimens were presented in the left hand image and 9310H steel samples in the right hand image. Each image was presented with the substrate shown below the interface region and the black potting compound above the sample. Black spots in the coating are porosity or artifacts of specimen polishing, dark grey areas are oxides, and light areas are alloy 420 stainless steel. The coatings have a laminar structure. The micrographs reveal that specimens using a slow traverse rate have thicker lamellae. The micrographs confirm that oxide content and specimen hardness are related. This is best seen with the micrographs of the hardest (Figure 19) and least hard (Figure 21) specimens, which reveal that the harder coating contains significantly more oxides (grey areas) than the less hard specimen does. All of the specimens show little porosity.

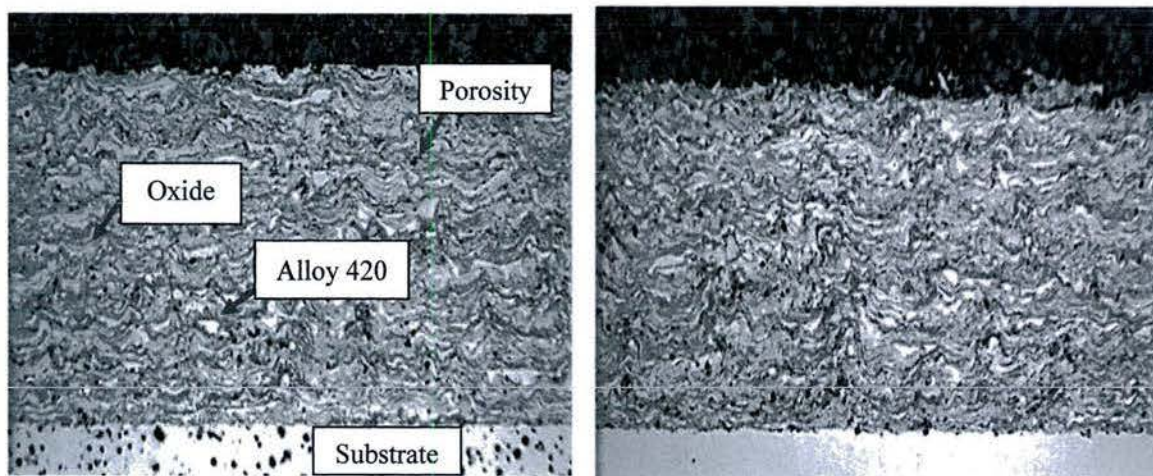


Figure 18. Micrograph of Group 1 Specimens

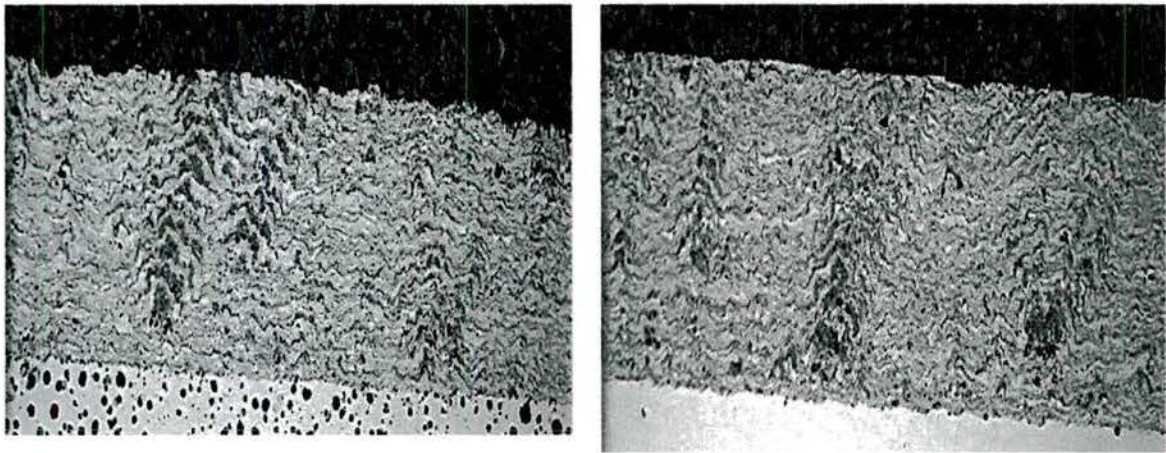


Figure 19. Micrograph of Group 2 Specimens

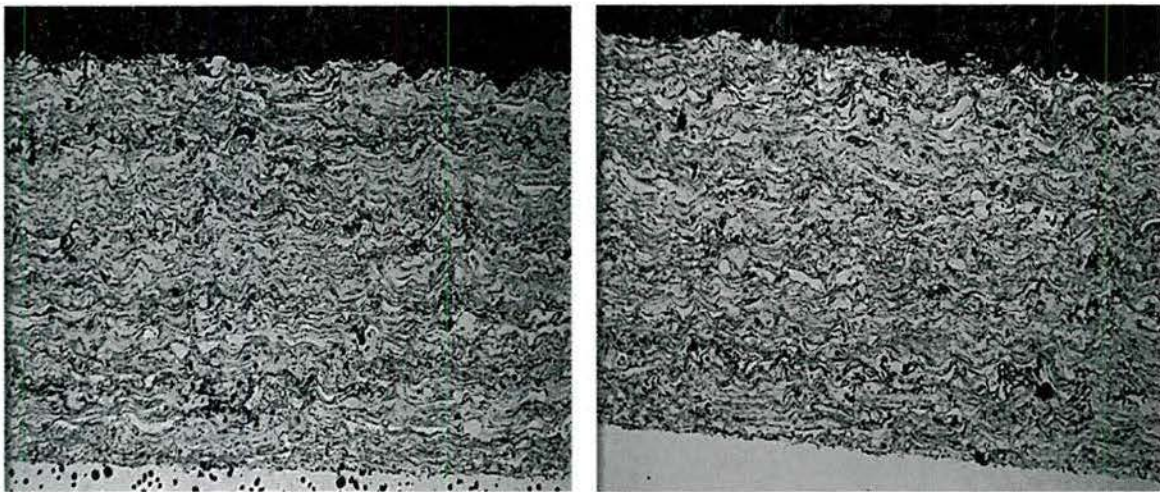


Figure 20. Micrograph of Group 3 Specimens

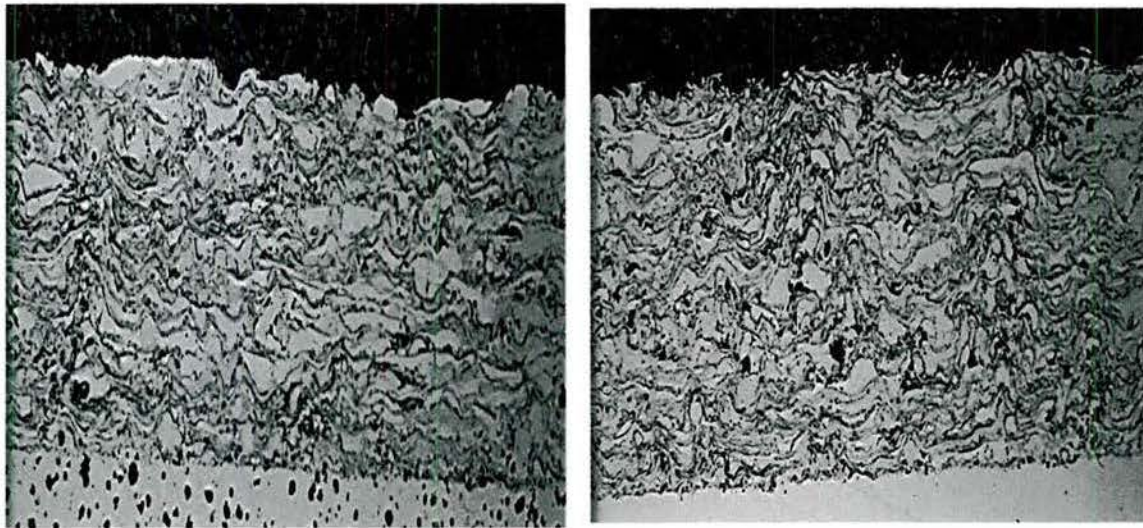


Figure 21. Micrograph of Group 4 Specimens

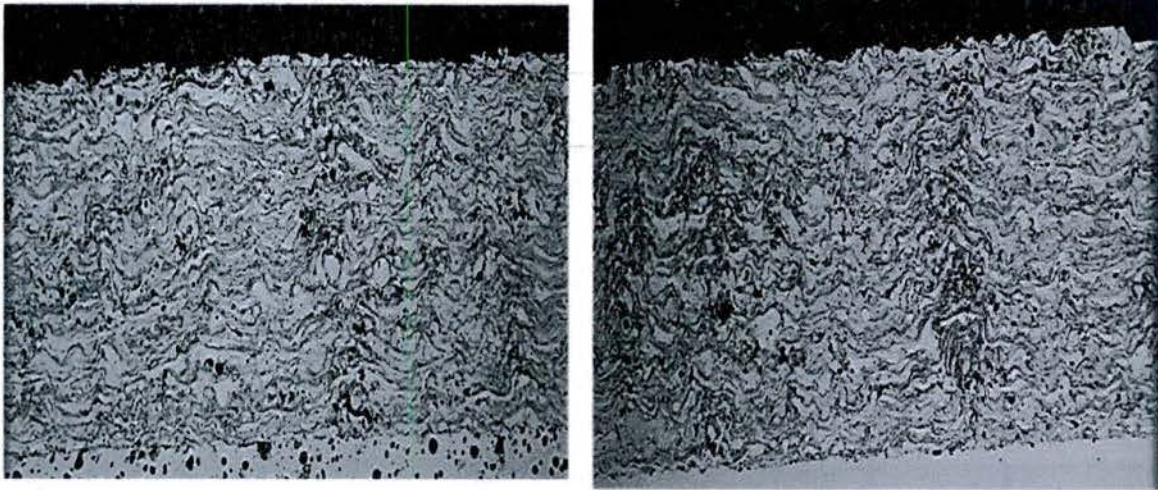


Figure 22. Micrograph of Group 5 Specimens

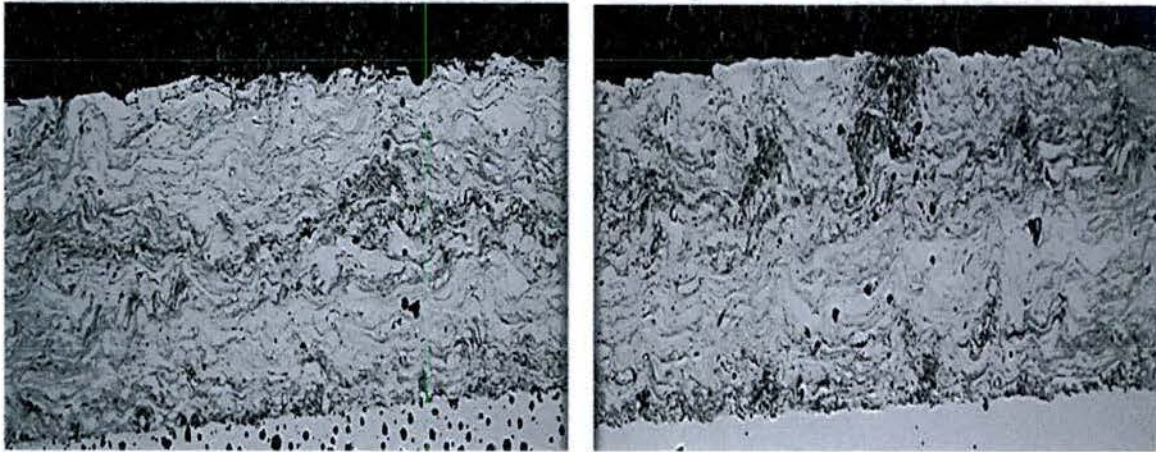


Figure 23. Micrograph of Group 6 Specimens

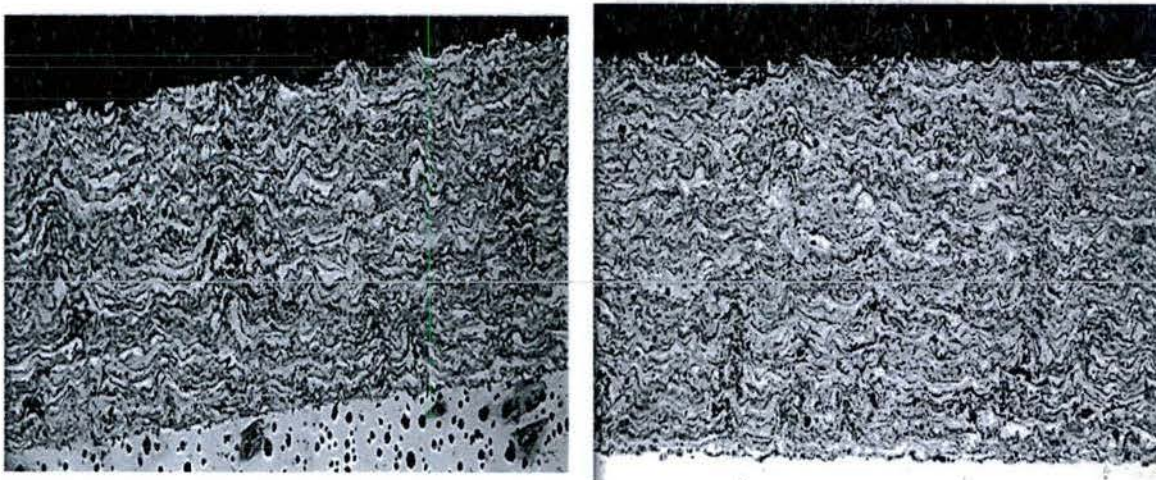


Figure 24. Micrograph of Group 8 Specimens

4.2.2.5 Preliminary Coating Process Selection

4.2.3 Optimization Experiment

Based on the results of the initial fractional factorial experiment, a second experiment was designed to further improve the quality of the coating. This second experiment was a 2^2 full factorial design that varied the air pressure and stand-off distance while keeping traverse, voltage, and current constant. The grit blast procedure was also modified as described in the Surface Preparation section of this report. In the Screening Experiment, current was found to have a significant impact on the layer thickness, and showed a trend of higher adhesion with lower current therefore the low current (60 A) setting was selected for the Optimization experiment. Additionally, the amount of dust and fumes produced by higher current settings caused strain on the dust collection equipment. Likewise, lower voltage appeared to produce a harder coating therefore the setting was held constant at 30 V in this experiment and provided the additional benefit of reduced power consumption. Pressure and stand-off were varied because these factors were some of the most influential to the results of the Screening Experiment. While traverse was also found to be influential, the slow traverse speed produced consistently lower adhesion and softer coatings than the fast traverse speed. Therefore, only the fast traverse was used in the optimization experiment.

4.2.3.1 Experimental Design

The experimental design for the optimization experiment was performed with 5 replicates of each parameter set and run in randomized order, refer to Table 6. Group A was the set of parameters that was chosen as the baseline from the initial set of experiments. This initial group of parameters (3" stand-off, 30 V, 60 A, 105 psi, 10 in/s) was chosen because the successful pair of coatings showed low porosity, the strongest adherence, and the greatest hardness of any specimens tested. These settings are identical to Replicate Group 2, which was applied in Runs 2, 21, and 23 of the Screening Experiment. Of those three Screening Experimental runs, only Run 2 produced a successful coating. The modification to the surface preparation method for the Optimization Experiment, see section 4.2.2.1, was based on the conclusions of Varacalle [21] and was an attempt to address the observed adhesion failures. In the Optimization Experiment, Groups B, C, and D varied the air pressure and stand-off distance around the Group A parameter set in an attempt to further improve the robustness and repeatability of the coating.

Table 6. Optimization Experiment Matrix

Replicate Group	Run #	Stand-off Distance (in)	Voltage (V)	Amperage (A)	Air Pressure (psi)	Traverse Rate (in/s)
A	11, 13, 14, 15, 20	3	30	60	105	10
B	1, 5, 8, 9, 19	5	30	60	80	10
C	2, 4, 6, 12, 16	5	30	60	105	10
D	3, 7, 10, 17, 18	3	30	60	80	10

The Optimization Experiment closely followed the experimental procedure outlined in the Screening Experiment except for differences in the surface preparation and the number of layers sprayed. As the current and traverse rate, the two factors that influence layer thickness, were kept constant in the Optimization Experiment, the number of layers sprayed was kept constant at 20. Additionally, pauses between layers in the Screening Experiment were removed to reduce variability in the coatings.

4.2.3.2 Results

4.2.3.2.1 Adhesion Results

The procedure for adhesion testing was altered slightly between the first and second experiment. In the Screening Experiment, specimens were milled after coating to flatten the surface prior to gluing the dolly in place. This caused excessive wear on the mill's cutters and posed potential damage to the bond. For the Optimization Experiment, the specimens were sanded instead of milling. This procedure still conformed to ASTM C633, which stated that "only a rough grinding or machining step is needed, to provide a final coating thickness that does not vary by more than 0.001 in." [11]. Adhesion and micro hardness measurements were performed on each of the replicates, refer to Table 7 and Table 8. After selecting the parameter set with the most promising adhesion, hardness, and microstructure, further samples were produced for wear testing.

Three of the five specimens created for each group were allocated to adhesion testing with the remaining two samples used in wear testing. The adhesion results are provided in Table 7.

Table 7. Optimization Experiment Adhesion Results

Group	Mean Iron Adhesion (Psi)	Iron Adhesion Std. Dev. (Psi)	Mean Steel Adhesion (Psi)	Steel Adhesion Std. Dev. (Psi)
A	9627	332	8330	1137
B	8329	503	8267	170
C	9269	589	9373	453
D	8376	893	8993	211

All of the adhesion values for Group A exceeded those observed in the Screening Experiment, confirming that the higher surface activation from the more aggressive grit blasting procedure improved the adherence. The main effects on adhesion from the ANOVA analysis (refer to Figure 25) showed that the ductile iron and steel substrates responded differently to changing stand-off distance. In both cases, the samples with the highest individual adhesion were from Group C; however, the Group A on ductile iron show the highest average adhesion. For both substrates the higher air pressure produced stronger mechanical bonds at the interface suggesting higher shear of the splats at impact. Higher pressure increases the particle velocity thereby lowering the time for the particles to cool and results in higher temperature upon impact. It was witnessed during the Screening Experiment that overheating of the substrate during coating led to high residual stresses due to differences in coefficients of thermal expansion and reduction in adhesion. The fast traverse rate, used in all groups for the Optimization Experiment, appears to have eliminated overheating problems.

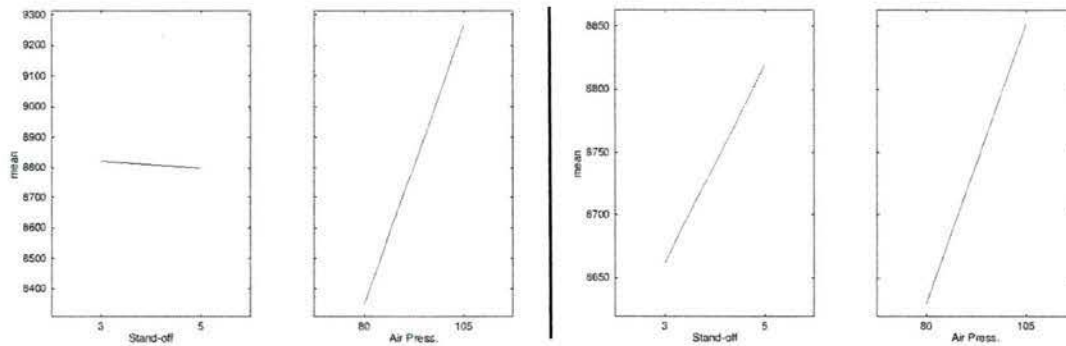


Figure 25. ANOVA Main Effects Plot for Adhesion: Ductile Iron (Left) and Steel (Right)

4.2.3.2.2 Hardness Results

After specimens were tested for adhesion, they were cross sectioned and tested for hardness in several locations throughout the coating layer. The mean hardness for each group of specimens is shown in Table 8.

Table 8. Optimization Experiment Hardness Results

Group	Mean Iron Hardness	Iron Hardness Std. Dev.	Mean Steel Hardness	Steel Hardness Std. Dev
A	318	9	336	4
B	320	30	336	20
C	340	11	344	18
D	288	7	287	9

The results were analyzed using ANOVA and the results are shown in Figure 26. Group C was found to have the greatest mean hardness for both the ductile iron and steel substrates. Figure 26 shows the relationship between stand-off, air pressure, and hardness. The parameters for Group C were the combination of the higher air pressure and the furthest stand-off distance. This group was the hardest due, in part, to the molten spray particles being subjected to a greater relative flow air, hence more oxygen, for a longer dwell time between melting and impacting. This resulted in a greater proportion of hard oxides, primarily iron oxide with trace quantities of manganese oxide [19], in the coating that formed predominantly between oxygen and iron in the alloy 420 stainless steel.

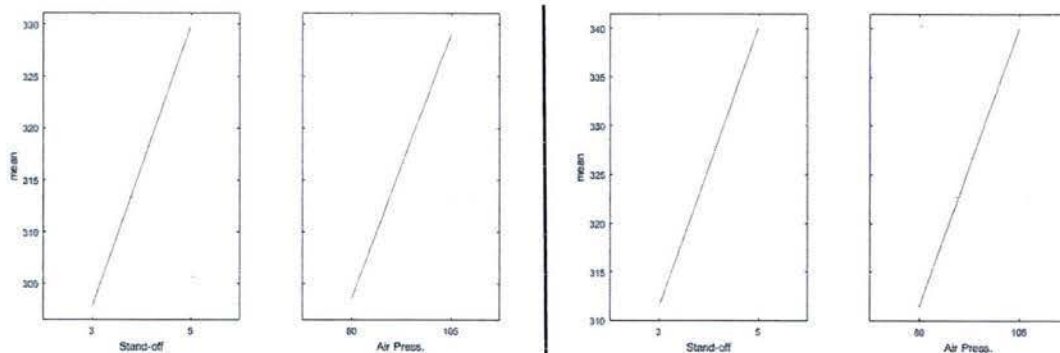


Figure 26. ANOVA Main Effects Plot for Hardness: Ductile Iron (Left) and Steel (Right)

4.2.3.2.3 Microstructure Results

As seen in Figure 27 through Figure 30, the porosity for all specimens was within the expected range for thermally sprayed coatings, 2 to 5%. Oxides are present in varying quantities in the coatings. This parameter set applied to the twin-wire arc process produced a lamella structure consisting of individual layer thicknesses of 0.0025 inches. The only visible effect of changing standoff distance and air pressure on microstructure was a change in the amount oxides in the microstructure.

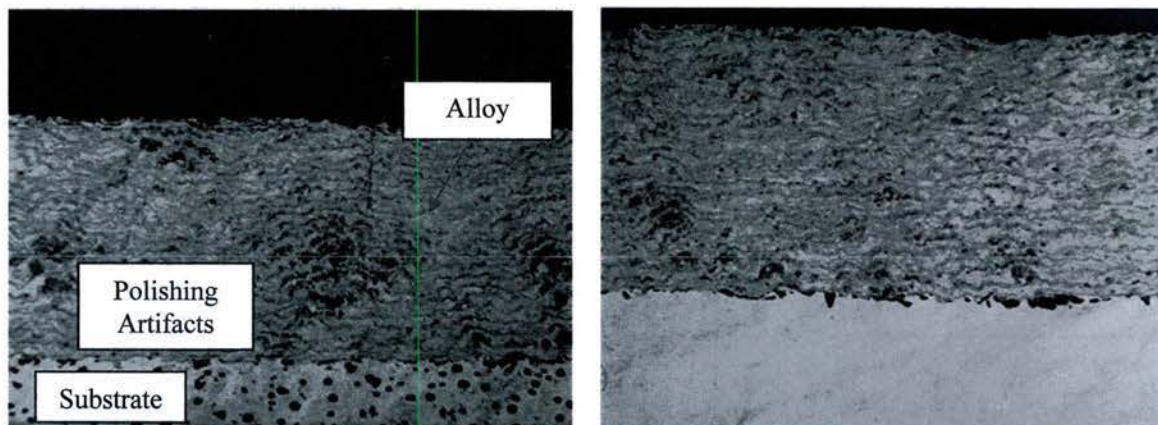


Figure 27. Micrograph of Group A Specimens (Ductile Iron on Right, Steel on Left), 50x

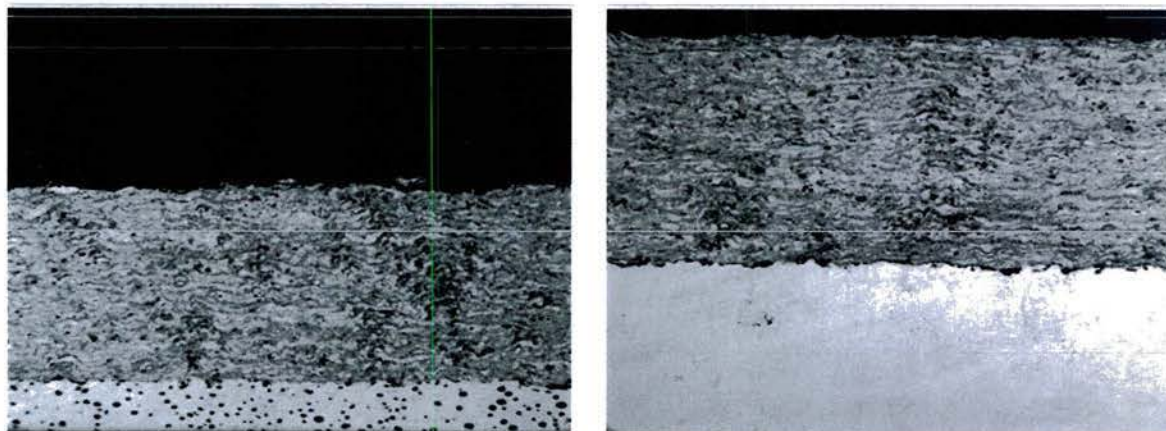


Figure 28. Micrograph of Group B Specimens (Ductile Iron on Right, Steel on Left), 50x

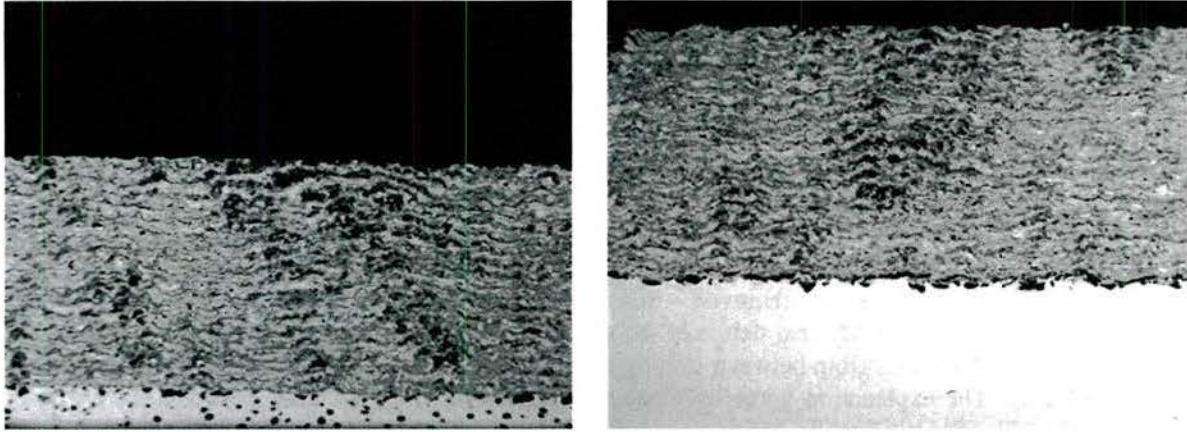


Figure 29. Micrograph of Group C Specimens (Ductile Iron on Right, Steel on Left), 50x

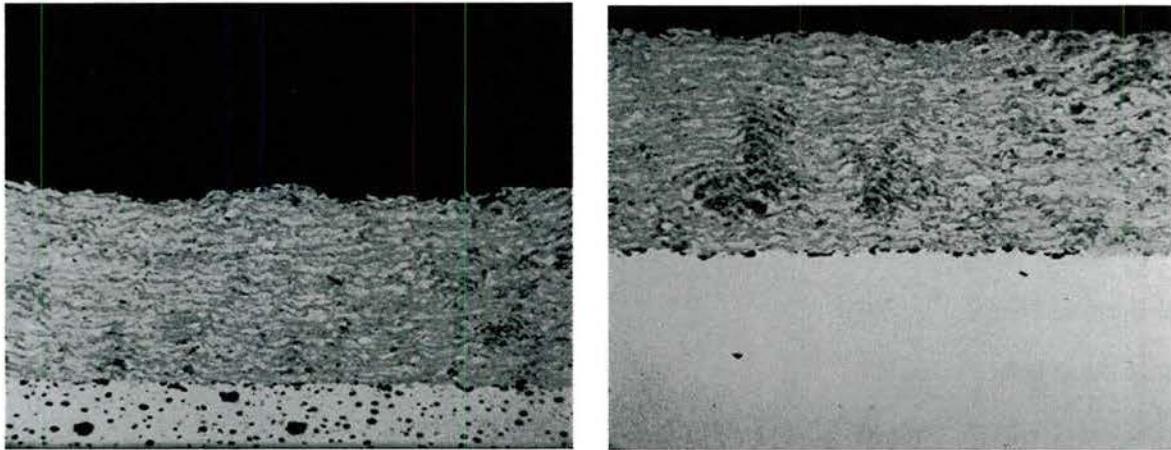


Figure 30. Micrograph of Group D Specimens (Ductile Iron on Right, Steel on Left), 50x

4.2.3.2.4 Wear Properties

The preceding tests showed Group C, having the highest air pressure and stand-off distance, exhibited the most oxide in coating (between layers) and the highest hardness. Conversely, Group D, having the lowest standoff distance and air pressure, exhibited the least amount of oxides in coating and lowest hardness. Based on the test results, Group C was selected as the best candidate for wear testing based on the microstructure, adhesion, and hardness results from the Optimization Experiment. Three pairs of specimens were created with the Group C parameter set, the surfaces ground and polished, and mated against both steel and brass balls in wear tests. The results were compared to baseline wear measurements obtained from the iron and steel substrates without coatings. Mechanical properties of the materials tested are provided for reference, refer to Table 9. The tensile strength of the alloy 420 was not obtained because the necessary coating thickness could not be reached. Wear was measured in volume of material removed, where a greater loss of volume indicated the sample had poorer wear resistance. The volume of material removed from the specimen and mating ball was recorded, refer to Table 10. The test specimens showed no measurable material removal from wearing against brass balls. This was an expected result considering the large difference between the hardness values of brass and the 3 specimen types (steel, ductile iron, and alloy

420). Micrographs of the wear scars from steel balls against each type of flat surface were captured; refer to Figure 32 and Figure 33. The specific wear rate for each specimen against the steel balls was then calculated, see Figure 31. The twin-wire arc coatings demonstrated higher wear rates compared to the untreated substrates and showed brittle fractures compared to ductile fractures and galling in substrates. Furthermore, the mating steel balls also experienced greater wear as a potential result of debris formed at the interface as the coatings degraded [22].

It appears from the micrographs that the twin-wire arc 420 coatings' wear scars are wider than the wear scars on the base material. This may be due to the coatings being more brittle than the substrate materials. The ductile substrate materials experienced localized deformation from the wear ball while the more brittle coating experienced localized fractures. Additionally, oxides in the thermal spray coatings caused body wear after some of the coating was removed – this did not occur with the base metal because hard oxide particles were not present in the wear debris of the substrate. These findings match those of Cooke et al., who found an inverse relationship between coating hardness and wear resistance of iron chromium boron sprayed coatings. The explanation given by Cooke is that the hard, brittle oxide particles are prone to breaking off and tearing out coating during wear testing, leading to a higher wear rate [15]. The relatively high contact stresses imparted by the balls onto the substrates in this alloy 420 testing would increase the potential for cracking of the coatings.

Table 9. Comparison of Material Properties of Coating and Substrates

Property	Hardness (HV1)	Tensile Strength (ksi)
Ductile Iron	240	55
9310H Steel	255	119
As Sprayed SS 420	340	-
Brass Wear Ball	137	50
Steel Wear Ball	697	175

Table 10. Mean Wear Volumes for Optimized Samples

Sample Material	Brass Ball Wear Volume (mm³)	Puck Wear Volume from Brass Balls (mm³)	Steel Ball Wear Volume (mm³)	Puck Wear Volume From Steel Balls (mm³)
420 Coated Ductile Iron	4.462	0	0.132	1.604
420 Coated 9310H Steel	4.987	0	0.148	1.841
Uncoated Ductile Iron	1.093	0	0.010	0.233
Uncoated 9310H Steel	0.727	0	0.014	0.253

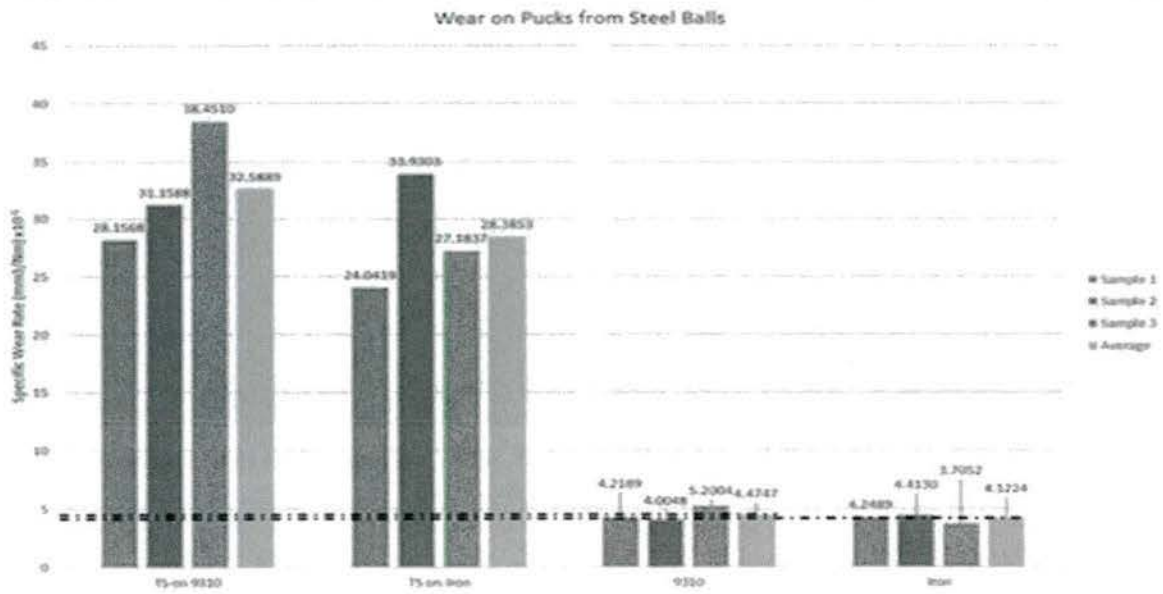


Figure 31. Comparison of Specific Wear Rates of Substrate Materials and Thermal Sprayed Alloy 420 Coatings

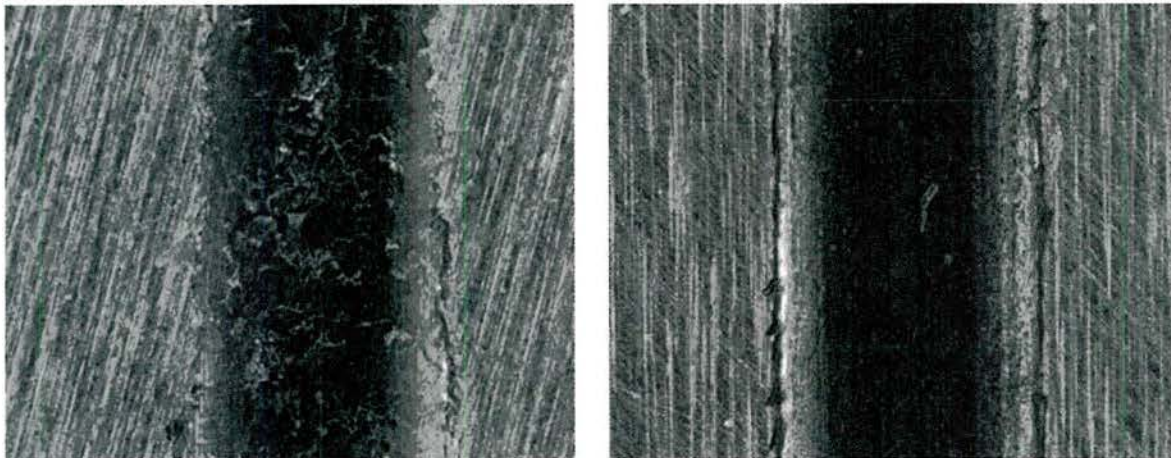


Figure 32. Wear Scars of Steel Ball against Untreated Iron (left) and Steel (right) Substrates, 50x

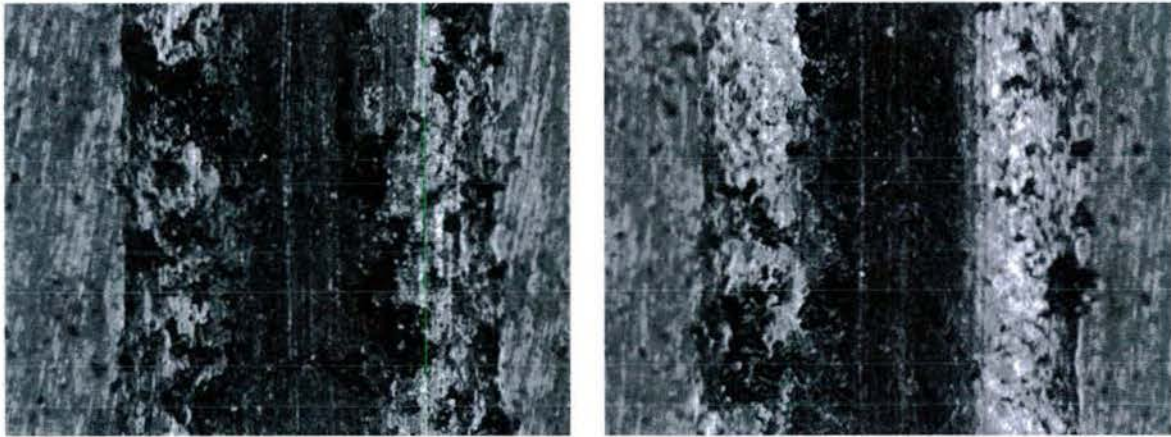


Figure 33. Wear Scars of Steel Ball against 420 Stainless Steel Coating on Iron (left) and Steel (right) Substrates, 50x

4.3 Conclusions

A robust process was developed to repair worn surfaces by restoring them to their original dimensions using alloy 420 coating sprayed with twin-wire arc spray technology. Alloy 420 stainless steel was selected for this work based on the alignment of its thermal expansion and elastic modulus values with those of the ductile iron and 9310H steel substrates. The void of publically available information on alloy 420 coatings spray with the twin wire arc process led to the need for investigation into process settings. A robust alloy 420 coating for wear applications was optimized by investigating the relationships between the process parameters (air pressure, voltage, current, standoff distance, and traverse rate) and the resulting coating properties (hardness, adhesion strength, microstructure, and wear rate). The following conclusions were drawn from the experimentation and results:

- Rougher substrates enhanced the adherence between the coatings and substrates. Comparing two surface preparation techniques showed that the more aggressive preparation led to adhesion values approximately 1,500 psi higher than the less aggressive preparation. The surface preparation did not appear to have an effect on any other coating properties.
- Atomizing air pressure was the factor with the greatest impact. In general, increased air pressure lead to improved adhesion through hotter particles at impact and higher hardness due to higher oxide content. For adhesion, this was contingent upon the substrate being sufficiently roughened, as the high air pressure settings required more surface preparation to achieve a well bonded coating.
- Stand-off distance was also a critical factor in producing the best possible coating. Stand-off distance can be correlated to the thermal energy into the substrate, closer being hotter. Many coatings failed to adhere when applying close stand-off distances which likely overheated the substrate. Increased stand-off distance in general improved adhesion and hardness.
- Current and voltage had little impact on the coating quality. It is recommended that the current is set to the lowest setting possible while still achieving a steady spray to reduce the amount of ambient dust. Higher traverse speeds produce higher quality coatings, specifically with improved hardness, but require more layers to achieve a desired thickness.
- There was negligible wear of the alloy 420 coating against brass balls, however, the coatings exhibited higher wear rates when mated against harder steel balls as compared to the wear of the substrates.
- Low porosity alloy 420 stainless steel coatings on steel and ductile iron substrates with excellent adherence were provided for enhanced wear against brass components. These relationships matched results from previous research performed for other coating materials and substrate pairs.

Based on these findings, the optimal parameter set for this process was: 5 inch stand-off distance, 30 Volts, 60 Amps, 105 psi air pressure, and a 10 inch/sec traverse rate.

5 Cold Spray

5.1 Cold Spray Objectives

The objective is to investigate the restoration of iron and steel materials via low pressure cold gas dynamic spray (aka cold spray or LPCS). The project investigates the cold spraying of 420 SS onto 9310H steel and ductile iron substrates.

The selection of the substrate materials of interest, 9310H steel and ductile iron, and their material properties were described previously in this report (Sections 2.1 and 2.2). 9310H steel is used in applications requiring good wear resistance, but that do not require corrosion resistance. Ductile iron is a ferrous casting material which has increased tensile strength, yield strength, and ductility (elongation) as compared to grey cast iron. Spherically shaped graphite (carbon) nodules are a notable trait of ductile iron.

There is a lack of published research which investigates cold spraying 420 series stainless steel coatings. 420 SS is a commonly used material in thermal spray (e.g. twin-wire arc spray), with applications including restoration of iron and steel parts, however, it is challenging to cold spray because of the material strength and hardness.

5.2 Cold Spray Background

5.2.1 Introduction

Cold spray is a thermal spray process which uses a heated accelerating gas to apply coatings from small-sized powdered materials (<100µm in diameter). Cold spray is also referred to as supersonic or kinetic spray.

In cold spray, a pressurized gas is heated and flows through a converging – diverging de Laval nozzle, which causes the gas to accelerate. Different from other thermal spray processes (e.g. high-velocity oxy fuel, twin-wire arc, and plasma spray) which melt particles to aid deposition, cold spray temperatures typically are below the particle melting point. Instead of melting particles, cold spray uses particle kinetic energy to apply coatings, allowing for a wide range of powders which can be cold sprayed including plastics, ceramics and metals. Very thick coatings are possible with cold spray [23].

A selection of cold spray coating materials are shown in Table 11 [24].

Table 11: Selected cold spray coating materials

Sampling of cold spray coating materials	
Pure metals	Aluminum, copper, zinc, nickel, titanium
Alloy steels	316 / 316L
Nickel based alloys	Inconel, Hastelloy
Aluminum alloys	6061
Cermet's (ceramic-metal composite)	Aluminum + aluminum oxide, WC-Co

Low pressure systems are less expensive than high pressure systems; \$80,000 - \$250,000 for low pressure vs. over \$500,000 for high pressure, not including robots, material handling, or powder dust collection systems. Low pressure systems typically use compressed air or nitrogen as the working gas, are smaller than high pressure systems, require significantly less power, and may be portable. High pressure systems typically use helium and nitrogen as the working gas and nitrogen or argon for the powder feeding gas, and are not portable.

A discussion of the two main types of cold spray systems; low pressure, and high pressure, is presented later in section 5.2.3.

Cold spray systems are ideal for the restoration and remanufacturing of components:

- They do not impart a significant amount of heat into the component. This limited heat transfer is particularly important in applications where stress-corrosion cracking or cold cracking is common.
- They do not require elaborate masking due to the close standoff distances and the fact that overspray powder is solid and not molten (e.g. splatter).
- They perform well in applications where the coating is under compressive stresses. Applications which involve tensile stresses should be avoided or carefully evaluated for the effects on coating adhesion and other properties.
- They are often used to form conductive and anti-corrosion coatings. Applications include restoration of corroded surfaces or repair of stress-corrosion cracks, and the deposition of coatings to change the electrical or thermal conductivity of a substrate material.
- They may be used to grit blast the substrate surface, prior to applying.

Cold spray can trace its history back to a 1900 U.S. patent by Thurston for a system of applying metal to a metal surface. No other applications are seen until 1958 when a patent was issued for a pressurized spray system which used a de Laval nozzle to accelerate air [25]. The development of cold spray in its current forms may be traced to its accidental discovery in Russia during the 1980's by rocket scientists. Aluminum powder (1-100 μ m in diameter) is added to solid rocket propellant to increase the temperature of the burn and decrease pressure oscillations, however, when exhausted unburnt it can damage rocket systems. To determine the effects of these unburnt Aluminum particles on rocket systems, wind tunnel experimentation was conducted by scientists at the Institute of Theoretical and Applied Mechanics of the Siberian Branch of the Russian Academy of Science (ITAM SB RAS). During these experiments the scientists observed a new phenomenon – the deposition of Aluminum in a ‘cold’ flow (7°C) with particle velocities above 400 m/s [23].

The prevailing theory for how cold spray builds coatings is that the particles impact the surface at high velocity and plastically deform, leading to adhesion (particle to substrate) and cohesion (particle to particle) bonding. Ductile particles will compress at impact, or splat, generating a rapid increase in temperature and strain at the interface, followed by a rapid decrease in temperature and stress [26]. Non-ductile materials, e.g. aluminum oxide and tungsten carbide, require a ductile binder to form cold spray coatings [27-32]. As much as 90% of the deformation energy is quickly transferred to heat [26] in the particle and substrate, softening the particle and sometimes the substrate, which aids bonding [33]. The impact generated heat also reduces stresses and reduces work hardening within the coating, which aids cohesion [34].

In cold spray the powder is introduced into the working gas stream and accelerated, reaching particle velocities of 350 – 1375 m/s [35]. When the particle velocity at impact, or V_p , rises above a material specific velocity referred to as the critical velocity, or V_c , particles deform plastically allowing for adhesion to occur [36, 37]. These deformed particles form a dense coating with low oxidation levels [37].

Critical velocity is influenced by the powder material properties and size [36, 38, 39], some general relationships are shown below in Table 12.

Table 12: Effects of material characteristics on particle Critical Velocity

Powder Particle Characteristic	Change in characteristic	Effect on Critical Velocity (V_C)
Mass	↑	↓
Density	↑	↓↓
Diameter	↑	↓
Hardness	↑	↑
Ultimate Tensile Strength	↑	↑
Melting point	↓	↓

Critical velocities for various ductile materials were modeled and experimentally measured, varying from a low of approximately 150 m/s for tin to 700 m/s for titanium [40]. The density of the material was shown to have the largest effect on critical velocity.

Particle morphology has been shown to effect particle velocity, with irregularly shaped particles achieving higher velocities compared to spheroidal shaped particles of the same material type and size due to a reduction of drag forces [41].

In addition to particle characteristics and morphology, process parameters influence the particle velocity (V_P) at impact. Typical cold spray process parameters include;

1. accelerating gas type and gas pressure [42, 43]
2. gas pre-heat temperature
3. nozzle standoff distance
4. nozzle design
5. traverse speed
6. powder feed gas type and gas pressure (if pressurized powder feeder is used)
7. powder pre-heat temperature (if heated powder feeder is used)
8. powder feed rate

Previous work has investigated the relationship between particle velocity, critical velocity, and erosion velocity. The work explored how these relationships effect the coating and substrate [40, 44], and is summarized in Table 13.

Table 13: Relationship of Particle Velocity (V_P) to Critical Velocity (V_C) and Erosion Velocity (V_E) for a given particle size and material type in cold spray

Velocity relationships	Effects on the coating & substrate
$V_P < V_C$	Peening or grit blasting
$V_C \leq V_P \leq V_E$	Deposition and bonding (adhesion, cohesion)
$V_P \sim 2V_C = V_E$	Erosion

When particles impact below critical velocity, they will not adhere, however, in certain cases the non-adhering particles have been shown to increase coating hardness by acting topeen or work harden the coating layers [27]. Adhesion and cohesion occur when the particle velocity is between the critical velocity and erosion velocity. Erosion of the coating and substrate occurs when the particle velocity is approximately two times the critical velocity.

Process optimization in cold spray centers on increasing the particle velocity of enough particles in the accelerating gas jet to increase the deposition efficiency of the process. Deposition efficiency (D.E.), or the ratio of how much spray material is deposited to how much was sprayed, is an important metric for all spray processes. Since cold spray powder is up to 10x the cost of other forms of thermal spray feedstock (e.g. wire), it is especially important to have a high D.E. while cold spraying.

Previous research of copper sprayed onto aluminum examined the effects of gas pressure, gas pre-heat temperature, powder feed rate and nozzle SOD on coating characteristics [45]. The authors determined that the (4) studied process parameters effected the conductivity, microhardness and porosity of the coatings by varying degrees. With some parameters having little effect on a particular coating properties, while others having significant effect. Gas pre-heat was consistently the most influential process parameter.

Experiments at RIT and previous cold spray research has shown that powder feed rates and particle size can effect D.E. The particle density in the middle of the spray jet is up to 3x greater than at the rim of the jet [44] and the particles in the center of the jet tend to be larger and slower [46, 47]. Because of this, having too high a particle feed rate prevents many particles in the center of the jet from reaching critical velocity (V_c), reducing D.E. Spraying too large a particle size may reduce D.E. because the larger particles are slower and may not reach the critical velocity (V_c) to deposit.

These effects highlight the need to optimize the powder feed rate and particle size distribution in order to reduce powder costs. Powder feed rate effects are explored in section 5.4. Particle size distribution optimization is discussed in more detail in section 5.3.

5.2.2 Cold Spray Benefits

Cold spray has numerous benefits compared to other thermal spray processes, including [33]:

- Low temperature process, eliminating or minimizing microstructural changes in the substrate
- Low coating oxidation levels, often the same as the raw powder [37], which allows for spraying oxidation sensitive materials such as copper and titanium
- Ability to spray very small particles (nanophase)
- A variety of materials can be deposited - plastics, metals, ceramics and composite materials
- Solid state process, no melting occurs, eliminating the segregation of alloying elements common in other thermal spray processes when the coating solidifies
- Reduced tensile residual stresses in the coating due to the fact that the material is solid when deposited and does not shrink during solidification as in other thermal spray processes
- Peening effect of impacting particles can introduce beneficial compressive stresses in the coating
- Low porosity <2%
- Thick coatings – potentially unlimited thickness because cold spray coatings are formed with solid or semi-solid particles, thus avoiding compromised material properties often found in other thermal spray and welding processes due to embrittling of the coatings

5.2.3 Main Types of Cold Spray Systems

The two main types of cold spray systems are the low pressure and high pressure designs.

Figure 34 shows examples of both low and high pressure systems. Low pressure systems typically operate at or below 10 bar (150 psi) gas pressure, with high pressure systems above 20 bar (≥ 300 psi). Low pressure systems may be portable or fixed installations, high pressure systems are typically fixed installations. All cold spray processes use a de Laval nozzle, which converges and then diverges the flow of the heated accelerant gas causing an increase in velocity 350 – 1375 m/s (Mach 0.6 – 4) [35, 48].

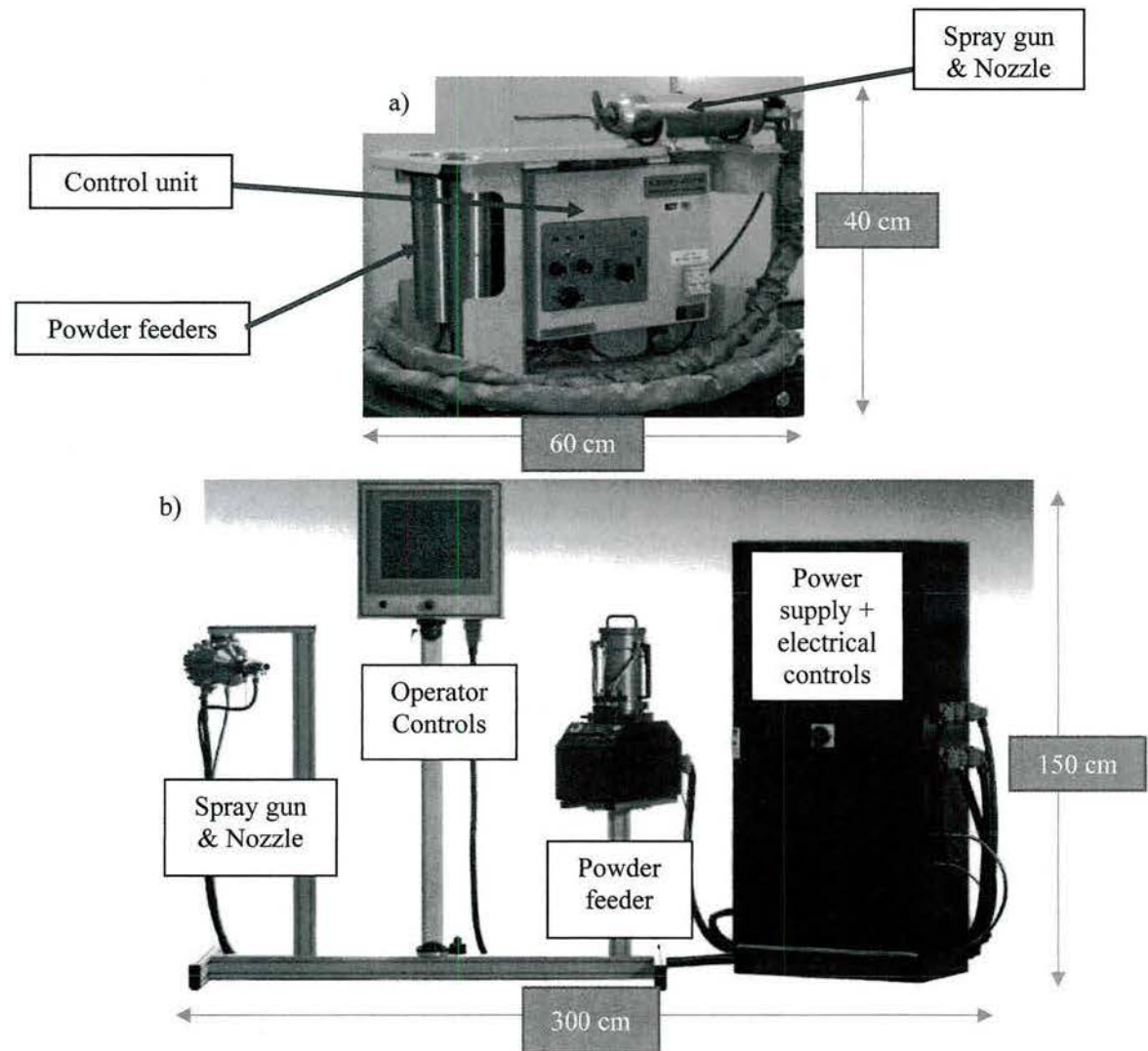


Figure 34: a) RIT cold spray system b) Example of high pressure cold spray system (ASB Industries)

There are distinct differences between the performance characteristics of low pressure and high pressure system designs, as summarized in Table 14 [35, 49].

Table 14: Typical cold spray System Parameters

Control Parameter	Low Pressure Cold Spray (similar to RIT system)	High Pressure Cold Spray
Working gas	air (typical), N ₂ , He	N ₂ (typical), He, air

Gas pressure operating range – MPa (psi)	0.5 – 1 (73 - 145)	0.5 – 7 (73 – 1000)
Gas preheat - °C (°F)	20 – 600 (70 – 1112)	20 – 1200 (70 – 2192)
Gas flow rate – m ³ /min (SCFM)	.45 – 1 (16 - 37)	.45 – 3 (16 – 106)
Maximum Gas Velocity Mach # (f/s)	1 – 3 (1125 - 3375)	1 – 4 (1125 - 4466)
Powder flow rate - g/min (lbs/hr.)	5 – 25 (0.67 – 3.3)	5 – 75 (0.67 – 9.9)
Powder particle size diameter - μm (in)	< 50 (0.002)	< 100 (0.004)
Power - kW	2 - 8	17 - 47
Standoff distance – mm (in)	5 – 25 (0.2 – 1)	10 – 60 (0.4 – 2.4)

Another key difference, beyond the obvious differences in operating pressures, between the low pressure and high pressure systems is how the powder is fed into the system (Figure 35, adapted from MIL-STD-3021) [35]. In the high pressure systems the powder is introduced into the heated accelerating gas stream ahead the nozzle by the use of a pressurized powder feeder (which may be heated as well). The low pressure system introduces the powder into the nozzle, where it mixes with the accelerating gas. Low pressure systems may use either a gravity or pressurized powder feeder.

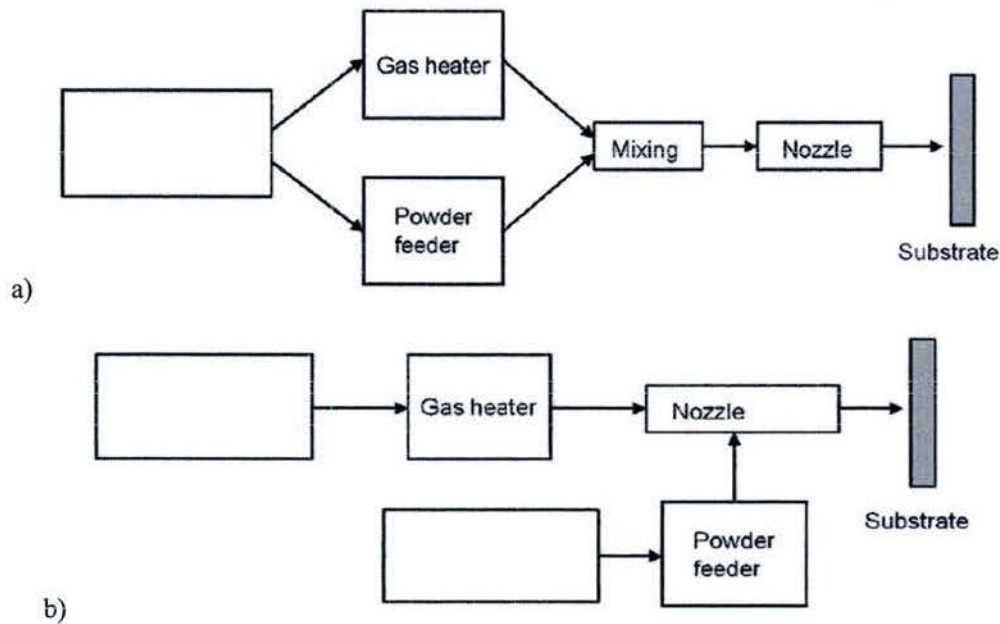


Figure 35: High Pressure Cold Spray (a), and Low Pressure Cold Spray (b) system diagrams

The RIT low pressure system uses a gravity powder feeder; powder is fed into the nozzle by suction created when the accelerating gas flow passes the powder feed tube. RIT system powder feed rates are roughly controlled by varying the vibratory rate of the hopper.

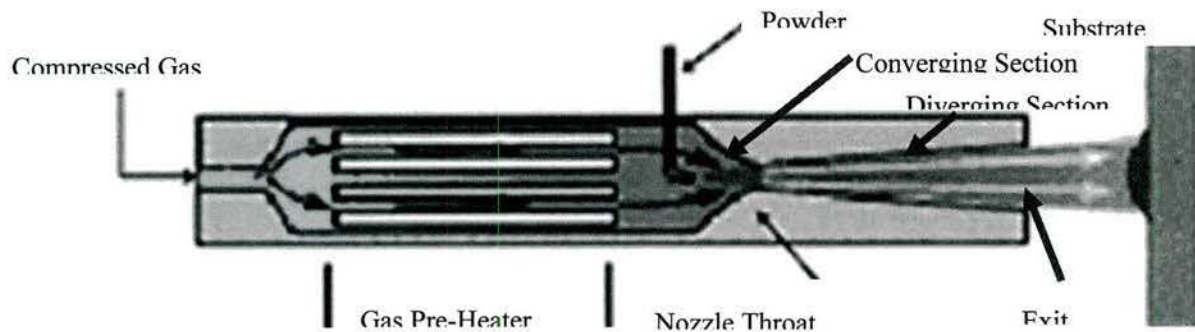


Figure 36: Schematic of RIT Cold Spray system [50]

Nozzle geometry is critical to the success of a cold spray system. Stoltenhoff, et al., conducted research to compare nozzle geometry, showing it impacted D.E. up to 20% [37]. In related research, it was shown that the shock zone of compressed gas above the substrate (which slows particles as they pass through) is directly proportional to the size of the nozzle throat, limiting the size of the throat and nozzle length that may be used in cold spray [51].

Key challenges for all cold spray processes [23, 52]:

- The availability and cost of suitable powders, which is discussed in more detail in section 5.3.
- Certain powders (e.g. pure Aluminum) are explosive / fire hazards
- Nozzle clogging occurs for very ductile metals (e.g. pure aluminum) when sprayed with steel nozzles, forcing the need to use WC-Co and composite nozzles in these applications.
- Cold spray cannot directly fill cracks. A groove must be machined where the crack is and then built back up. This is because cold spray requires the angle of the spray jet to the substrate surface to be close to 90° to maintain optimal particle impact trajectories.
- Line of sight from the nozzle to the deposit location is also required, making internal surfaces difficult to spray.
- Using helium as the accelerating gas has been shown to increase both the particle velocity and D.E. in cold spray as compared to nitrogen or compressed air [47]. However, the scarcity of helium has led to high costs, limiting its use to those applications where the increased velocity and D.E. are cost justified.
- Slower deposition rates than other thermal spray processes (e.g. HVOF, twin wire arc).
- Substrate ductility effects bond strength, with typically lower bond strengths for less ductile materials.

5.2.3.1 High Pressure Cold Spray and its Applications

In high-pressure systems, the input pressure of the working gas is typically between 20 – 70 bar (290 to 1015 psi). The gas is heated to between 100 – 1000° C and then flows into the converging section of the nozzle where it mixes with the powder before entering the throat. The powder is fed from a pressurized feed system and may be pre-heated as well. A broader range of materials may be sprayed due to the higher velocities achievable with high pressure colds spray systems, but this comes with higher equipment and operating costs. These systems are also typically not portable, limiting their applicability to do field repairs and maintenance. Current applications of high pressure cold spray systems have included:

- Structural repair of aluminum (A2024-T6) aircraft panels with aluminum alloy (A6061). Fastener holes became elongated in service and were repaired with cold spray [23, 52].

- Structural repair of high nickel alloy (Inconel) aircraft nose-wheel steering actuator barrels. The barrels are exposed to dirt and water and corrode over time, a nickel-based cold spray powder was used to repair them and return them to service [23, 52].
- Crack repair of CA6NM (ASTM A743) cast martensitic stainless steel with 316 stainless steel. Cold spray was compared to TIG welding in this study [53], with the main benefits that cold spray doesn't require post-weld heat treatment and had a higher coating microhardness.
- Cermets (ceramic-metal composite) coatings for energy applications, including Ni-Al₂O₃ coatings for gas turbine sealants [54]

5.2.3.2 Low Pressure Cold Spray and its Applications

In low-pressure systems, the input pressure of the working gas is typically between 5 – 20 bar (73 to 290 psi). The gas is heated to between 100 – 1000° C and then flows into the converging section of the nozzle. The powder is fed under atmospheric pressure or from a pressurized feed system and is introduced to the gas jet inside the nozzle.

One disadvantage of the low-pressure system is that particle velocities cannot go as high as in the high-pressure systems, which limits the materials that may be sprayed. To get around some of these limitations, novel materials and material blends (e.g. hard material combined with a binder material) have been and continue to be developed. Suitability of materials for low-pressure cold spray is discussed in more detail in section 5.3. Current applications of low-pressure cold spray have included:

- Pure aluminum coatings on magnesium components to improve electrical conductivity [55].
- Structural repair of a worn aluminum (A7149) helicopter mast using Al-Al₂O₃ and a nickel alloy repair of a worn cast iron engine block [52].
- Replacement of hexavalent chrome wear resistant coatings using tungsten-carbide with copper and tungsten-carbide with aluminum cold spray coatings [29].
- Development of tungsten-carbide with nickel corrosion and wear resistant coatings to mitigate the effects of high pH, temperature and pressure induced flow-accelerated corrosion in the nuclear industry [56].

5.3 Coating Selection – powder trade study

Coatings used to restore worn parts or structurally repair damaged parts must have good wear resistance, tensile strength and approximate the hardness of the original part surface. Additionally, for remanufactured parts, the ability of a coating to match the appearance and machinability of the original part surfaces is critical for many customers and applications [52].

As previously detailed in the Materials trade study section (section 2.2) 420 stainless steel was selected for its similar hardness and machinability to 9310H and Ductile Iron. A thorough cold spray literature review was conducted and limited work has been documented for cold spray applications using stainless steel, and no references were found for 420 stainless. Stainless steel (316L, 420) is used for restoration and repair in many thermal spray processes, e.g. twin-wire arc spray, see Table 15.

Table 15: Thermal Spray feedstock properties - SS 420

Feedstock properties	Twin-Wire Arc Spray	High-velocity Oxy Fuel (HVOF)	Atmospheric Plasma Spray (APS)	Cold Spray*
----------------------	---------------------	-------------------------------	--------------------------------	-------------

	316L	420	316L & 420	316L & 420	316L & 420
Product	Wire	Wire	Powder	Powder	Powder
Form / Morphology	Spool or reel	Spool or reel	Spherical or Irregular	Spherical or Irregular	Spherical or Irregular
Size range	1/8", 1/16"	1/8", 1/16", 2 & 2.3 mm	15 – 75 μm	15 – 105 μm	5 – 50 μm

*Powder Sieving may be required

Previous research by Irissou [27], Sacks [32], Nunthavarawong, et al.[57], and Melendez, et al. [30, 31], has shown that successful cold spraying of hard materials often requires the addition of ductile binder material(s) to the coatings. As previously described in the additive materials trade study, section 2.2 of the report, 420 SS was selected as the primary (hard) coating material in the present study. Due to the hardness and yield/tensile strength of 420 SS, it is theorized that the addition of ductile binder material(s) is required to produce low pressure cold sprayed coatings.

It has been shown that low pressure cold spray systems achieve improved results when mixing ductile and hard powders in coatings, e.g. the metal matrix composites Al-Al₂O₃ [27, 58] and WC-Ni [29-32, 56, 57, 59, 60]. During bonding in cold spray, ductile particles work harden, making it more difficult for subsequent layers to build [59, 61]. The theory as to why mixing ductile and hard powders improves coating results is that the addition of a harder material to a ductile powder or “binder”, e.g. alumina added to aluminum, has two beneficial effects; by roughening the previous coating layer, which reduces the work hardening effect in the ductile material, and by increasing overall micro-hardness of the coating [30].

As discussed in sections 5.2.3.1 and 5.2.3.2, cold spray applications for ceramic-metal (cermet) or metal matrix composites coatings (MMC) have included coatings for steel components (WC-Ni) used in nuclear piping [56] and the repair of worn or damaged castings (Al-Al₂O₃) [52]. In the above examples, the coatings exhibit a mixture of hard and ductile materials with the ductile material acting as binder for the harder material. The current research includes the low pressure cold spraying of WC-15%Ni and Al-85% Al₂O₃ onto a steel substrate to understand the behavior of the RIT system with respect to:

- Optimized surface preparation to produce high adhesion strength of hard/ductile powder produced coatings
- Optimized process settings to maximize deposition efficiency of hard/ductile powder produced coatings

The WC-Ni and Al-Al₂O₃ research was conducted to determine the effects of the lower heating capacity (lower power) of the RIT system vs. the systems used in published work (Centerline SST). These experiments are detailed in section 0.

The first ductile material studied in a mixture with 420 SS is nickel-5% aluminum. The use of nickel-5% aluminum as a twin-wire arc spray bond coat (wire form) is a common application, and nickel-5% aluminum powder is a lower cost option than pure nickel powder. The current research explores the cold spray of Ni-5%Al powder mixed with the harder 420 SS. The theory being investigated is that the Ni-5%Al powder will create a matrix which incorporates the harder 420 SS in a coating, improving the hardness and tensile strength as compared to pure Ni-5%Al coatings.

An additional ductile material blended with 420 SS is also investigated. Copper is a well-studied and understood cold spray powder. It has been successfully applied in a variety of cold spray applications and is widely available in cold spray powder formulations [45, 62-66]. The current research explores the cold

spray of Cu mechanically mixed with 420 SS. The theory being investigated is that the Cu powder will create a matrix which incorporates the harder 420 SS material in a coating, improving the hardness and tensile strength as compared to pure Cu coatings, and improving the machinability and deposition efficiency (D.E.) as compared to pure SS material.

The morphology of thermal spray powder particles is determined by the manufacturing (atomizing) process, and a commonly used process, gas atomization, typically produces spheroidal particles. Previous cold spray research has shown that irregularly shaped or angular particles perform better in cold spray when compared to spheroidal powders of the same size diameter and material type [41], under the theory that reduced drag forces increase the particle velocity. For certain materials, the only powder morphology available is spheroidal, which may require process parameter adjustments to insure particle velocities are sufficient to deposit.

There are two major challenges in selecting coating materials for cold spray; the cost of the powders, and the availability of the powder in the optimal size or “cut” for cold spray [23]. Cold spray powders are more expensive to produce than the wire used in the traditional processes of welding or twin-wire arc spray. For example, the stainless steel powders used in the current cold spray study ranged from \$20 to \$36 per lb., compared to \$3 to \$4 per lb. for 420 SS wire used in twin-wire arc spray, or 7 to 12 times the cost per lb. Cold spray also requires smaller particle size distributions than HVOF or APS, and due to its relatively small market size, powder manufacturers haven’t created many formulations optimized for cold spray. In many cases sieving of powder is required to achieve particle size distributions, which adds to the cost.

In the current work, the copper, Ni-5%Al and 420 SS powders were not available within recommended particle size distributions (PSD) provided by the equipment manufacturer, necessitating the extra step of sieving material down to the recommended PSD. To determine suitability of each powder for cold spray, small quantities of perspective materials were obtained, sieved and test sprayed. Sieving to achieve the desired particle size distribution increased the material costs by 20-100%, depending upon the material.

The as received powders were sieved using a Gilson US Mesh #450 (-32 μm) 8 inch diameter sieve and Meinzer sieve shaker. The sieving yield, which is the ratio of powder that passes through the screen divided by the total powder sorted, was tracked for each lot of material. The yield was used to determine order quantities for each powder and to determine the cleaning frequency for the sieve. Periodic sieve cleaning was performed via ultrasonic washing in an aqueous solution.

To determine the powder particle size distributions used in the experimentation, samples were analyzed using a COULTER COUNTER from each lot of material, after sieving if applicable. The results from the particle size analysis are shown in the process development section (section 5.4).

Details on the supplier and formulation, along with SEM images, are provided for each powder used in the cold spray study in the process development section 5.4.

5.4 Process Development

5.4.1 Introduction and Objective

The objective of the cold spray process development phase was to investigate the feasibility of using LPCS produced coatings to restore ductile iron and 9310 H. As discussed previously in sections 5.2.4, 5.2.5 and 5.3, successful coatings have been created which combine both ductile materials, acting as a binder, and hard materials which work to increase the hardness of the coatings. The work included the development of novel material blends, which mated the harder 420 SS with ductile copper or Ni-5%Al, and the optimization of process parameters to spray them. A series of experiments were conducted to evaluate the novel coatings. The present work investigates two differing theories to produce coatings of 420 SS combined with ductile binder material(s):

- Theory 1 – Blending a high mass fraction of a ductile binder material with less of a hard material – e.g. 85% Cu + 15% 420 SS or % 420 SS + 15% Ni-Al, produces hard coatings.
- Theory 2 – Blending a high mass fraction of a hard material with less of a ductile binder material – e.g. 85% 420 SS + 15% Ni-Al or 85% 420 SS + 15% Cu, produces hard coatings.

The mass fraction of a single material is the percentage by weight of that material in the powder blend.

The experiments were designed to evaluate the coating characteristics for each material, and followed the same sequence:

1. Measure Deposition Efficiency (D.E.) - determine the process settings that yield acceptable D.E. D.E. is simply the amount of powder in the coating divided by the amount of powder sprayed.
2. Next, measure coating thickness to determine material build-up rates per layer (or pass).
3. Next, analyze microstructure, microhardness and porosity of coatings. Select the high performing process settings for the next round of experiments.
4. Next, optimize coatings to minimize porosity and increase adhesion strength. Select the high performing process settings for the next round of experiments.
5. Last, optimize coatings for wear and corrosion resistance.

If a coating material did not successfully produce a coating at any step in the above sequence, it was not pursued for further experimentation.

5.4.2 Equipment and Process used in the Experiments

The experiments were conducted using a commercially available Low Pressure Cold Spray system model K-205/407R supplied by RS Technologies, Inc. The spray system has a round spray nozzle which is approximate 155 mm long. The distance between passes of the spray gun was set to 3mm, or 50% of the spray spot size. Compressed air was selected as the accelerating gas due to its availability, safety and cost compared to other options such as nitrogen and helium. Spray powder is fed under atmospheric pressure from a vibratory feeder. Powder feed rates are adjusted manually by setting the agitator frequency. The spray system is mated to an ABB model IRB 1600-6/1.45 robot with 1.45 m of forward reach and a 6 kg payload capacity, see Figure 37.

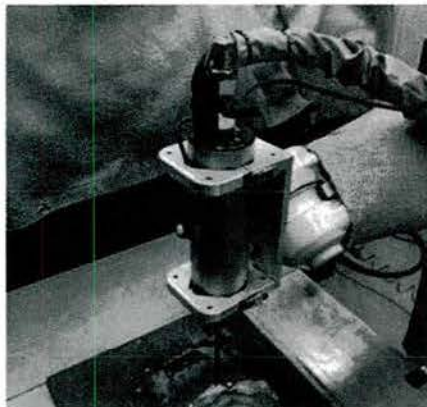


Figure 37: Cold Spray Setup for Robot Controlled Motion

All experiments were conducted within an enclosed 12 x 12 x 10 ft. spray booth built by Marathon Finishing Systems (Harbor City, CA), and overspray powder was collected via a Donaldson-Torit (Minneapolis, MN) Torit® Downflo® Workstation DWS-4 dust collector but not reused. The spray booth and cold spray system were purchased under the Defense University Research Instrumentation Program (DURIP) and installed during the summer of 2016.

Powder particle size data were collected using a Beckman Coulter Multisizer™ 3 COULTER COUNTER® particle size analyzer. The COULTER COUNTER measures the volume of particles, then returns a calculated diameter under the assumption that the particles are spherical. All particle size data are reported using calculated diameters and the percentile of particles by mass; with D10 = 10th percentile diameter size, D50 = 50th percentile, and D90 = 90th percentile.

Prior to spraying, some powder materials required sieving to achieve recommended or targeted particle size distributions that were smaller than available from the powder manufacturer. The sieving was done to meet size recommendations from the cold spray system supplier, RS Technologies, Inc., and was performed at RIT using a Meinzer II sieve shaker and 8" diameter test sieves from Advantech Manufacturing.

An Amray 1830 SEM from Amray, Inc. was used to capture images during the powder and coating chemical composition analysis. Chemical composition analyses were performed using an EDS (Energy-Dispersive X-Ray Spectroscopy) detector model IXRF 550r and analysis software Iridium Ultra from IXRF Systems. Graphite powder was used on SEM specimens as needed to reduce electron beam charging effects, allowing for clearer images. Optical microscopy of sections and surfaces were performed with a Zeiss model AXIO Zoom.V16 with an AxioCam MRc5 camera and ZEN pro 2012 image capture and analysis software.

5.4.3 Process Development Experiments and Results

To determine an equipment baseline for the experiments, a series of measurements were taken to document the force of the compressed air jet, compressed air flow rate and jet temperature in the spray nozzle over a range of pressures (5 to 10 bar) and gas pre-heat settings (0 to 600°C). Once these baseline data were established, a series of experiments were designed to determine optimal process settings, including surface preparation and spray settings, to investigate novel material blends to achieve successful coatings, and to optimize the physical properties of coatings.

5.4.4 Baseline Data Collection for the RIT Low Pressure Cold Spray System

The RIT cold spray system was commissioned during the summer of 2016. As such, a series of data collection tests were performed to assess the baseline conditions for the equipment. These tests were conducted without spraying powder and measured:

1. Compressed air mass flow rate
2. Gas temperature in the diverging section of the nozzle, and
3. The force of the compressed air jet on a precision scale, over a range of typical pressures and gas pre-heat conditions.

Equipment verification is a key process control check for spray systems. Baseline air flow rate data were collected at various gas pre-heat temperatures and input pressures, along with gas force at the substrate. These baseline data are an important part of the RIT process checks as they allow for comparison to a standard for future experiments and allow for evaluation of hardware changes (e.g. compressed air fittings). Additionally, the data were used as inputs for a separate project which used Computational Fluid Dynamics (CFD) to model the RIT low pressure spray system. This model will be used in future research to tune process parameters for optimized coatings.

Compressed air consumption was measured using a Hedland flow meter connected inline to the supply line. Gas flow rate measurements were taken at varying pressures from 5 to 8 bar (73 to 116 psi) with no gas preheat, see Table 16. The flow rate increases at approximately 82 L/min per 1 bar change in pressure. The flow rate data may also be used to estimate the cost of the process gas (air, nitrogen, helium) for any potential cold spray project.

Table 16: Air Consumption at Various Pressures, no preheat = gas at room temperature, 20°C

Input Pressure - bar (psi)	Compressed Air Flow Rate - L/min (scfm)	Force - N (lbf)
5 (73)	453 (16)	1.77 (.398)
6 (87)	538 (19)	-
7 (102)	595 (21)	-
8 (116)	708 (25)	-

The cooling effect of increasing input pressure (with associated increase in gas flow) on gas jet temperature in the nozzle was also of interest. The gas preheat chamber was set to setting 5, which is designed to be 600°C, and the nozzle gas temperature was measured using a thermocouple positioned in the diverging section of the spray nozzle, see Table 17. The results show the nozzle exit gas jet temperature drops significantly as the pressure increases. The decline of nozzle gas temperature ranges from 29 to 43°C per 1 bar change according to a curve fit of the data, increasing slightly as the pressure increases from 5 to 10 bar. These data are useful in the design of experiments where control of substrate and coating temperature are important.

Force measurements were taken by placing a precision scale, Sartorius model ED8201, beneath the spray gun nozzle, adding a thick steel plate to disperse heat, and measuring the change in the scale reading under varying conditions, see Table 17. Force measurement is used as a proxy for air velocity.

Table 17: Compressed Air Jet Force and Jet Temperature within the Nozzle at Various Input Pressures, Gas Preheat = 600°C

Input Pressure - bar (psi)	Force of air - N (lbf)	Nozzle gas temperature - °C (°F)
5 (73)	2.08 (.468)	515 (959)
5.5 (80)	2.24 (.504)	500 (932)
6 (87)	2.55 (.577)	510 (950)
6.9 (100)	3.19 (.717)	-
7 (102)	3.09 (.695)	470 (878)
8 (116)	3.81 (.857)	-
8.3 (120)	3.97 (.893)	360 (680)
9 (131)	4.27 (.960)	-
9.5 (138)	-	330 (626)
9.75 (141)	4.91 (1.104)	-
10 (145)	-	285 (545)

The results show that input pressure has a significant impact on the forces, more than doubling the measured force (2.08 to 4.91 N, 136%) with a change from 5 to 9.75 bar. Also of note, the 600°C gas pre-heat increased the force by a small margin (1.77 to 2.08 N, 17%) at 5 bar when compared to no pre-heat (see Table 16, gas at room temperature, 20°C). Of note, the increase in pressure from 5 to 10 bar significantly reduced the nozzle gas temperature, indicating the heater is not able to maintain higher temperatures at the higher pressures and correspondingly higher compressed air mass flow rates. This reduced temperature can act to reduce D.E. by lessening the softening of particles seen with higher temperatures.

5.4.5 Surface preparation optimization

Adhesion of cold sprayed coatings is due to the plastic deformation of impinging particles onto the substrate creating both mechanical fastening and metallic bonding between deformed particles [33, 34, 36]. For this reason, surface preparation of the substrate is a critical factor in creating acceptable coatings. Grit blasting is used to create favorable conditions for bonding by both reducing the oxide film and increasing the roughness (and contact surface area) of the substrate [33, 63].

The cold spray equipment vendor recommended an average substrate surface roughness (R_a) of approximately ≥ 7.5 microns to increase adhesion. The original RIT grit blast equipment (orifice, nozzle, and tubing) achieved an average surface roughness (R_a) of 3.5 – 5.5 microns using #36 aluminum oxide grit in studies conducted for the twin-wire arc spray ONR additive manufacturing project, section 4. To increase the surface roughness to cold spray vendor recommended levels, experimentation was conducted as described below.

Previous research on changes to the substrate surface roughness have yielded contradictory adhesion results on cold sprayed aluminum alloy and titanium alloy substrates [67]. Research from Sharma, et al. [68], showed increased adhesion strength (>38 MPa vs. 24.5 MPa) for commercially pure Al sprayed onto roughened (R_a of 5 – 6.3 microns) AA2024 -T351 substrate as compared to the un-roughened base substrate. It is theorized that the increased adhesion strength is due to a reduction in surface oxides and an increase in surface area on the roughened surface, providing a clean and increased surface area for bonding to occur. The AA2024 has a similar hardness to the 1018 CRS substrate in the present work. Blast pressure, standoff distance, number of passes and blast time were not provided in the Sharma [68] study, and the #24 aluminum oxide grit used is larger than the RIT system can process. Marrocco, et al. [69], show that for Ti coatings on Ti6Al4V substrate, aluminum oxide grit blasting (R_a of 2.7 microns) decreased adhesion when compared to smoother sanded (R_a of 0.2 microns) substrates. To address these conflicting results, the present work shows the effects of differing levels of surface roughness on adhesion and microhardness of Al-Al₂O₃ coatings.

Experiments were conducted to determine optimal surface roughness values and grit blast process parameters to produce high adhesion strength cold spray coatings. The experiments investigated the effects of surface roughness on coating adhesion and microhardness at two levels of average surface roughness (R_a); <5.5 microns (RIT original technique), and >7.5 microns (RIT improved technique).

- Referencing the Sharma, et al. [68], work, the original RIT grit blast system was used to create the <5.5 micron samples. These samples are referred to as the original technique.
- Referencing the spray equipment vendor recommendations for surface roughness, a third party (Heany) was used to create the >7.5 micron samples. This company used the parameters as shown in Table 18. These samples are referred to as the improved technique.
- All surface prep was conducted using aluminum oxide #36 grit (305 - 762 micron grit size).
- Surface roughness and coating adhesion results were compared to published research from Sharma, et al., and Irissou, et al. [27, 68] to evaluate the RIT system performance, see Table 18.

Both the original and improved surface preparation techniques were used to prepare 1018 CRS substrates. These substrates were then cold sprayed with 85%Al-15%Al₂O₃ powder using nominal spray parameters

provided by the material vendor. All samples were built to approximately 750 μm (.030") thickness and milled flat for adhesion testing. Coating samples using the original technique and improved technique were sectioned for microstructure and SEM analysis. Coating microhardness was found to be in the range of 64-97 Vickers for the original and improved techniques, which is higher than pure aluminum (hardness 34 to 70 Vickers) [68]. The higher microhardness in the coating is expected due to work hardening during cold spray and the inclusion of Al_2O_3 in the coating.

Table 18: Comparison of Grit Blast Parameters, Surface Roughness and Coating Results for (2) Techniques and Previous Research

Parameter	RIT Original Technique	RIT Improved Technique	Previous Research
Pressure - bar (psi)	6.2 (90)	6.9 (100)	-
Stand-off Distance - cm (in)	10.2 (4)	10.2 (4)	-
Angle from Normal - °	0	15	-
Blasting Time - sec	90	30	-
Orifice Size	#5	#6	-
Coverage	200%	100%	-
<u>Surface roughness results:</u>			
Roughness R_a - μm (μin) [27, 68]	3 – 4 (118 – 156)	6 – 9 (276 – 354)	5 – 6.4 (200 – 250)
<u>Coating Results:</u>			
Adhesion of Al- Al_2O_3 - MPa (psi) [27]	37 – 41 (5,400 – 5,900)	54 (7,884)	49 – 57 (7,107 – 8,267)

As a result of the experiments, new grit blast equipment was installed based upon the improved coating adhesion strength. The experiments determined the optimum process settings, orifice size and technique for grit blasting steel substrates to achieve the spray vendor recommended surface roughness. The new equipment and improved technique were used on all subsequent cold spray experiments.

5.4.6 Understanding mixed material coatings for the restoration of hard surfaces

The use of hard materials mixed with ductile materials to form cold spray coatings was detailed in section 5.3. In order to better understand how cold spray coatings are formed using combinations of hard and ductile materials, a series of experiments were conducted using materials from prior research to evaluate the two different theories detailed in section 5.4.1:

- Theory 1 – combine a high mass fraction of ductile binder with less of a hard material
- Theory 2 – combine a high mass fraction of a hard material with less of a ductile binder

To evaluate theory 1, a powder with a high mass fraction of aluminum (ductile binder) combined with aluminum oxide, 85%Al-15%Al₂O₃, was sprayed onto 1018 CRS. Commercially pure aluminum + aluminum oxide powder, supplied by RS Technologies was used in the present study. The powder was mechanically mixed by the supplier, and had a mean particle size diameter of 9.3 microns.

Previous work with these coatings has shown the feasibility of depositing very hard materials via cold spray [5]. Including Al₂O₃ in the powder blend reduces nozzle clogging experienced when spraying pure Al, along with reducing the oxide film and increasing the roughness of the surface [11]. Al-Al₂O₃ coatings were shown to improve coating microhardness and adhesion compared to pure aluminum in previous LPCS research [5], [36]. Al-Al₂O₃ is commonly used for repair/restoration of aluminum castings and for corrosion protection coatings on steels, however, it is not hard enough for use in restoration of hard substrates such as ductile iron or 9310H.

To inform the design of experiments using a high mass fraction of ductile binder (copper or Ni-Al) combined with hard material (420 SS), an evaluation of the effects of process parameters on microstructure, adhesion and D.E. was performed. Results were reviewed and optimal parameter settings were used in the design of experiments in sections 5.4.7 to 5.4.11.

The evaluation of theory #2 used a proprietary mixture of a high mass fraction of WC-Ni (~70%) and low mass fraction of Cu-Zn-Al₂O₃ (~30%) powders which were mechanically blended and manually applied to 1018 CRS substrates. Particle size analysis showed a mean (D₅₀) of 6.6 μ m (D₁₀ = 3 μ m, D₉₀ = 25 μ m) for the powder as received.

Previous research from N.M. Melendez, et al., [8], [9] showed the effects of different percentages of the hard composite material WC-12%Co blended with the ductile material Ni on the microhardness, porosity and retained WC in the coatings. They showed a wide range of microhardness values, and theorized that the variation is due to the non-homogeneity of the WC dispersion in the coating and fracturing of the WC particles during deposition. P. Nunthavarawong, et al., [35] showed the effects of varying powder feed rates on the microhardness, retained WC, and porosity of WC blended with 5%Ni coatings. D. Lioma, et al., [37] studied varying levels of Ni added to both WC-12%Co and WC powders. They compared the effects of varying compressed air pressure and gas pre-heat temperature on hardness, porosity and %WC retained in the coatings. WC based coatings are often used for hard-facing applications such as slurry abrasion resistant coatings for industrial piping [56] or to protect blades on earth- and snow-moving equipment (plows, dozers, etc.) [70]. WC based coatings are not appropriate for restoration of components with sliding wear as the embedded WC dislodges and increase the wear rate. Also, the WC content makes the coatings difficult to machine for dimensional restoration applications.

The effects of process parameters on the microstructure and D.E. of the WC blend were evaluated. The results were reviewed and optimal parameter settings were used in the design of experiments in sections 5.4.7 to 5.4.11.

5.4.7 Evaluation of 420 SS based low pressure cold sprayed coatings

As previously detailed in the additive materials and powder trade study sections (sections 2.2, 5.3), 420 SS was selected as the primary material of interest in the present work. There is a lack of published research on 420 SS cold spray coatings. To address this knowledge gap, RIT investigated the cold spraying of 100% 420 SS and 420 SS blended with binder materials.

Referencing the work of Schmidt, et al., [40, 49] the critical velocity, or material specific minimum particle velocity required to bond via cold spray, was estimated for 420 SS. Critical velocity is estimated from material properties of the powder; density, tensile strength, specific heat, and melting temperature and impact temperature of the particle. The minimum particle velocity was estimated using the Schmidt, et al., equations 1 and 8, and varied between 589 – 867 m/s for un-annealed 420 SS adhesion. The RIT equipment

supplier literature lists a wide range of achievable particle velocities between 150 – 800 m/s for all spray materials (polymer, ceramic, metal).

With estimated 420 SS critical velocities approaching or exceeding the upper limit of the RIT system, a screening experiment was conducted to determine if the RIT system could achieve high enough particle velocities for bonding of 420 SS particles without the use of a ductile binder. The substrate for these experiments was 1018 CRS, grit blasted with alumina as described in section 5.4.5. Commercially available 420 SS powder, Diamalloy 1002, supplied by Oerlikon-Metco (Westbury, NY), was sieved to below 32 microns using a US Standard #450 sieve. Particle size analysis of the sieved powder shows a mean (D50) of 7.6 μm (D10 = 4.6 μm , D90 = 11.2 μm). SEM analysis shows the 420 SS particles are irregularly shaped, see Figure 38.

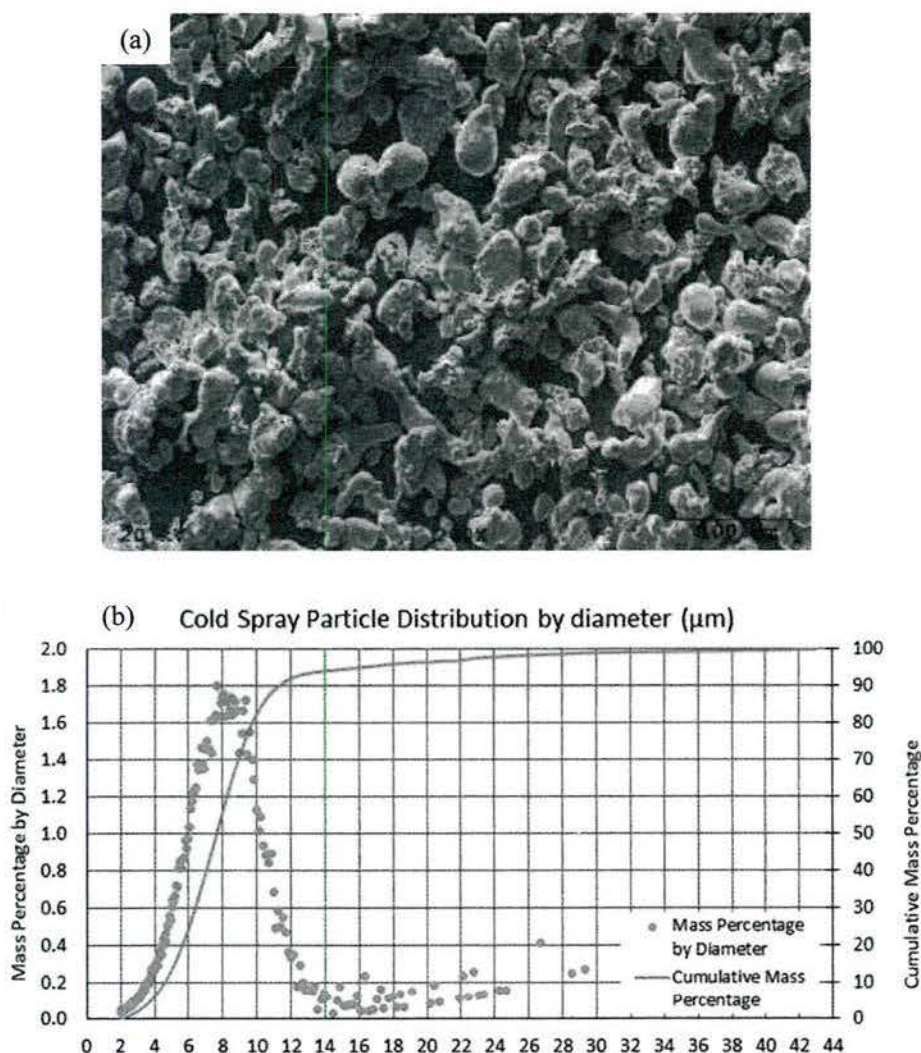


Figure 38: (a) SEM image of 420 SS particles, 200x, (b) Particle size distribution of 420 SS

Initial randomized experiments investigated the effects of input pressure, traverse speed, standoff distance and gas pre-heat on coatings, see Table 19.

Table 19: 420 SS sprayed onto 1018 CRS experimental settings

Parameter	Settings
Input Pressure - bar (psi)	5.5 – 9.7 (80 – 140)
Traverse - mm/s (in/s)	5 – 20 (.20 - .79)
Stand-off Distance - mm (in)	5 – 15 (.20 - .60)
Gas Preheat Temperature - °C (°F)	480 – 600 (896 – 1,112)

To evaluate the effects of substrate pre-heat, oven drying of powder, and the annealing of powder on coatings, three small screening experiments were conducted. For each of these three experiments, no coatings were produced beyond an initial layer, typical results are shown in Figure 39. The 420 SS acted to reduce the surface roughness, when compared to the as prepared grit blasted surface (R_a of $>12\text{ }\mu\text{m}$ as blasted vs. $<10\text{ }\mu\text{m}$ in the sprayed areas).

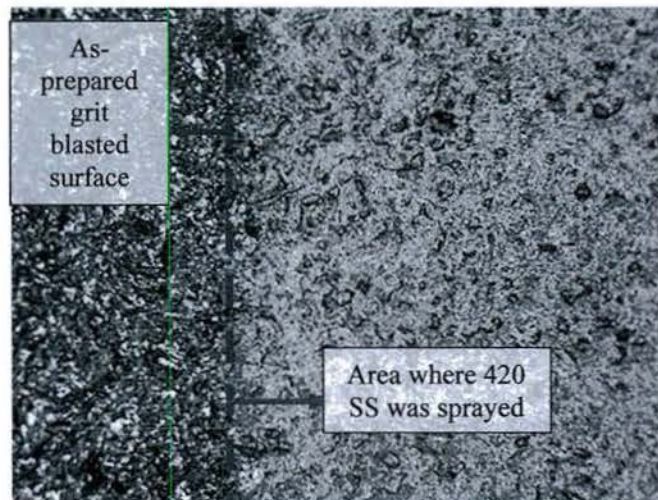


Figure 39: Comparison of grit blasted surface (left) and 420 SS spray area (right)

Since the 420 SS material did not produce coatings when used on its own, further experimentation was conducted to determine if blending it with ductile binder materials could successfully produce coatings. A nickel alloy, Ni-5%Al, along with commercially pure copper (99% Cu) were selected for investigation as described in sections 5.4.8 and 5.4.9. The experimentation followed the sequence as described in section 5.4.1.

5.4.8 Evaluation of 420 SS mixed with Ni-5% Al alloy binder material

Based on previous low pressure cold spray research conducted on WC + Ni low pressure cold spray coatings [30-32, 57, 59, 60], and the use of Ni or Ni based alloys as bond coats in twin wire electric arc spray applications, Ni and Ni alloys were investigated for use with 420 SS in a mixed material coating. A small material trade study was conducted to review available thermal spray Ni and Ni alloy powders (HVOF, cold spray) and wire materials (twin wire electric arc). The Ni-5%Al alloy was selected over pure Ni powder, as it has a lower hardness, tensile strength and melting temperature, and is less expensive than pure

Nickel powder. Ni-5%Al alloy is a commonly used as a bond coat in wire form, and is self-bonding in twin-wire electric arc thermal spray applications [71].

A series of screening experiments were conducted to determine if the RIT system was able to deposit coatings of Ni-5%Al alloy powder blended with 420 SS on 1018 CRS substrate. Since Ni-5%Al alloy + 420 SS coatings have not been reported in previous research, vendor recommended process settings for Ni based powder blends were used as nominal parameter settings in the present work. The effects of the mass fraction of steel in the powder blends on coating performance were evaluated. A control trial of 100% Ni alloy powder was conducted, along with 15%, 50%, and 85% Ni alloy powder blended with 420 SS.

Commercially available Ni-5%Al alloy powder, Diamalloy 4008, from Oerlikon Metco, was sieved to below 32 microns using a US Standard #450 sieve. Particle size analysis of the sieved powder shows a mean (D50) of 11.1 μm (D10 = 7.1 μm , D90 = 16.3 μm). SEM analysis shows the Ni-5%Al alloy particles are spheroidal, see Figure 40.

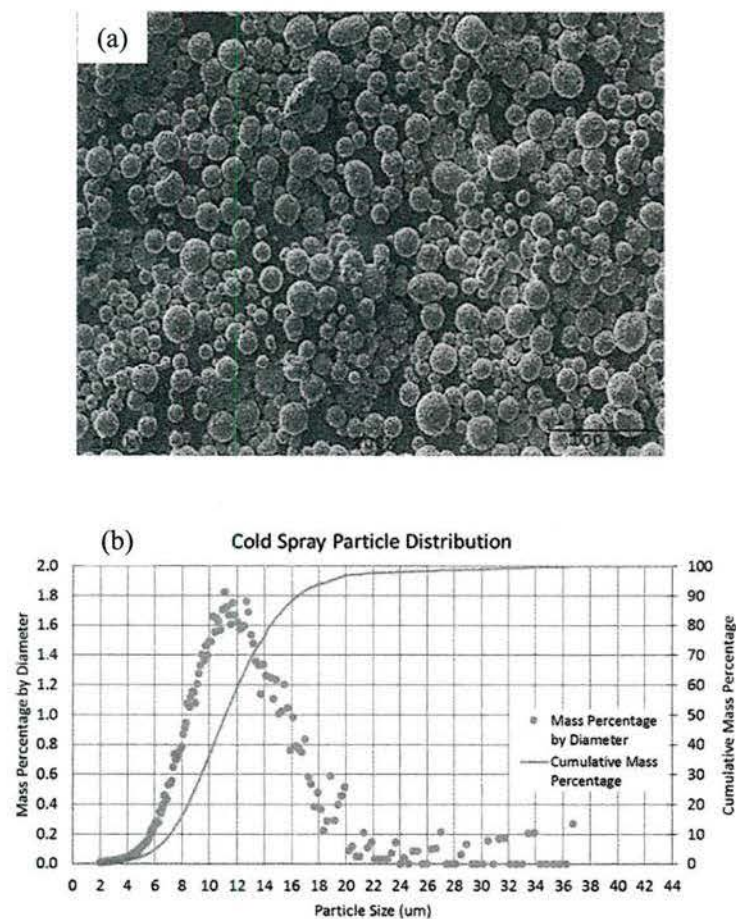


Figure 40: (a) SEM image of Ni-5%Al alloy particles, 200x, (b) Ni-5%Al particle size distribution

Blends with the Ni-Al alloy at 100%, 85%, 50%, and 15%, with the balance 420 SS, were cold sprayed onto 1018 CRS substrates grit blasted with alumina as described in section 5.4.5. The randomized experiments investigated the effects of input pressure, traverse speed, standoff distance and gas pre-heat on coating adhesion, and spot size, see Table 20.

Table 20: Ni-Al sprayed onto 1018 CRS experimental settings

Parameter	Settings
Input Pressure - bar (psi)	6.9 – 8.3 (100 – 120)
Traverse - mm/s (in/s)	5 – 40 (.2 – 1.6)
Stand-off Distance - mm (in)	5 – 125 (.2 – 4.9)
Gas Preheat Temperature - °C (°F)	600 (1,112)

No coatings were produced in these experiments beyond an initial layer, typical results are shown in Figure 41. Evidence of peening effects (craters) caused by subsequent layers may be seen in the Ni-Al portion of the specimen. Ni-Al based materials were not investigated further based upon these results.

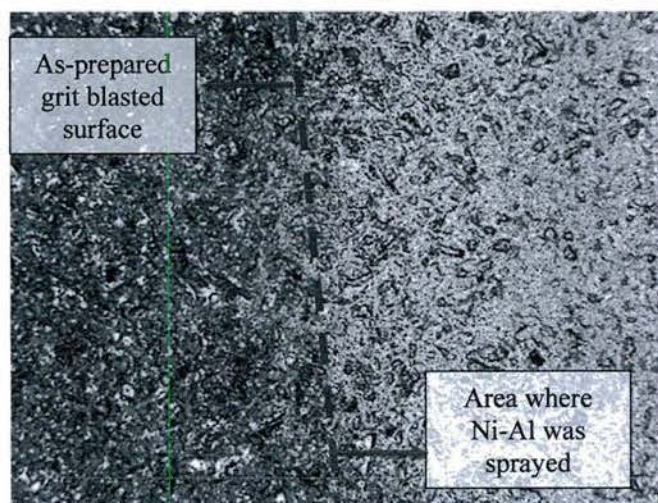


Figure 41: Comparison of Grit Blasted Surface (left) and Ni-5%Al Coating (right)

5.4.9 Evaluation of Cu for use as a binder material for 420 SS

Upon conclusion of the 420 SS with Ni-5%Al experiments (section 5.4.8), a search was conducted to find a more effective binder material for use in 420 SS mixed material coatings. RIT reviewed the material properties of pure aluminum and copper, both of which are the subject of published cold spray research. When creating coatings of dissimilar materials, e.g. copper and steel, materials with anodic indexes which are within 0.25 of each other inhibit galvanic reactions (i.e. corrosion) in the coating in normal applications [72]. Cu was selected because it is a readily available cold spray material, and has an anodic index less than and similar to 420 SS (0.35 vs. 0.60). Aluminum was ruled out because its anodic index is greater than and dissimilar to 420 SS (0.95 vs. 0.60). 100% mass fraction of Cu content was used for these experiments.

99% pure copper powder, HA4155-4, from HAI Advanced Material Systems, was sieved to below 32 μm using an US Standard #450 mesh sieve. Particle size analysis of the sieved powder shows a mean (D50) of 10.8 μm (D10 = 6.3 μm , D90 = 30.5 μm). The Cu particles exhibited both irregular and spheroidal shapes, see Figure 42.

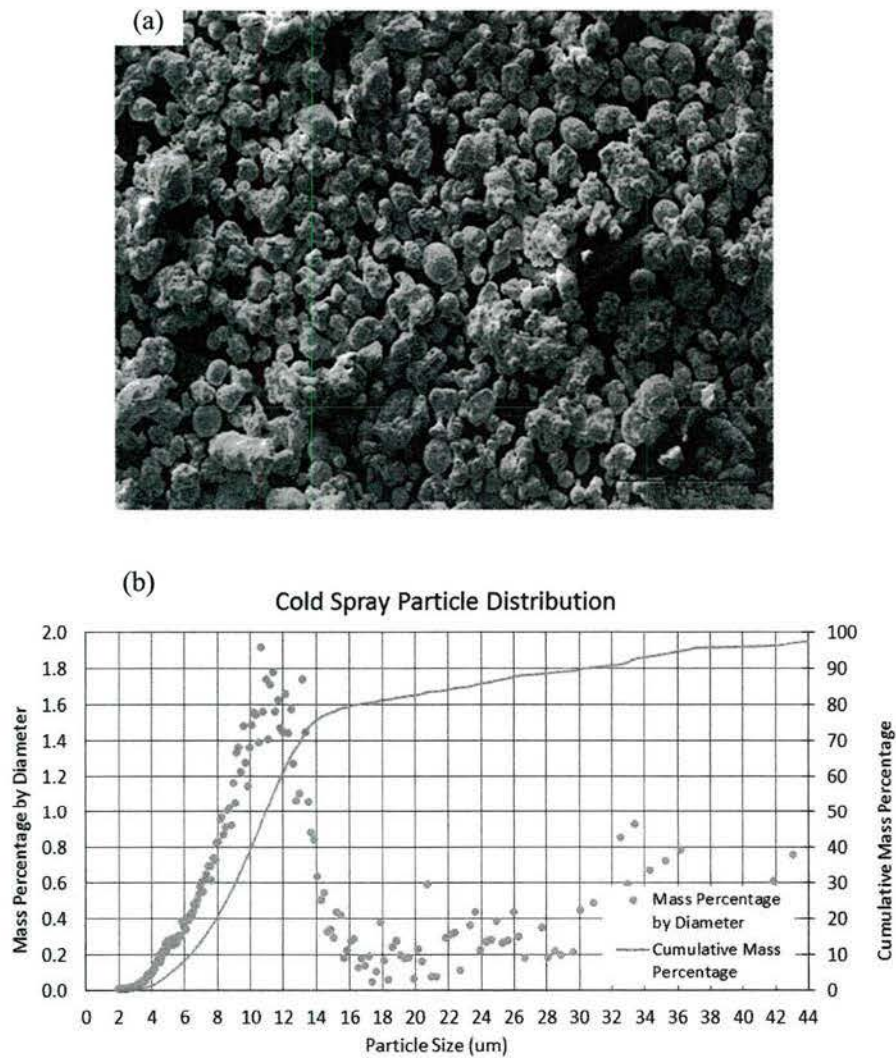


Figure 42: (a) SEM image of Cu particles, 250x, (b) Cu particle size distribution

Pure copper was cold sprayed onto 1018 CRS substrates with a minimum average surface roughness of $R_a = 7.5 \mu\text{m}$. The experiments investigated the effects of input pressure, traverse speed, standoff distance and gas pre-heat on coating adhesion, spot size, and oxidation of the coating, see Table 21.

Table 21: Cu sprayed onto 1018 CRS experimental settings

Parameter	Settings
Input Pressure - bar (psi)	4.8 – 9 (70 – 130)
Traverse - mm/s (in/s)	Manually controlled, spraying for approximately 30 seconds

Stand-off Distance - mm (in)	5 – 25 (.2 – 1)
Gas Preheat Temperature - °C (°F)	480 - 600 (896 – 1,112)

Minimal thickness coatings were produced in these experiments. Heat induced color changes (red, purple, etc.) due to oxidation of the Cu are evident for those areas where the nozzle traverse was slow or stopped, typical results are shown in Figure 43.

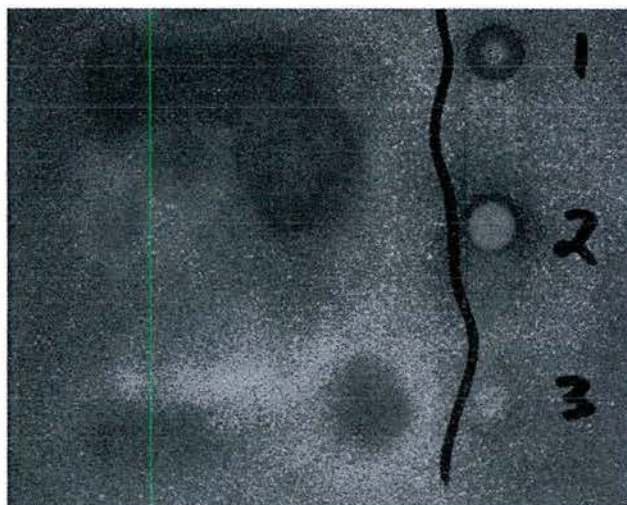


Figure 43: Cu sprayed onto 1018 CRS

Cu produced minimal coatings on its own. The process parameters which produced at least a minimal coating and had evidence of little to no oxidation were used to inform further experimentation. Future experiments were conducted to determine if improved adhesion occurs when Cu is blended with 420 SS in various ratios, see sections 5.4.10 and 5.4.11.

5.4.10 Evaluation of theory 1 - 420 SS blended with Cu (85% Cu / 15% SS 420)

Building on the previous work with 100% copper, section 5.4.9, and Al-Al₂O₃, section 5.4.6, a ductile to hard material ratio of 85% Cu / 15% 420 SS was used. Material from the same lots as previously investigated were used in these experiments. All blends were mechanically mixed. Particle size analysis of the blended powder shows a mean (D50) of 9.3 µm (D10 = 5.4 µm, D90 = 46.6 µm), see Figure 44.

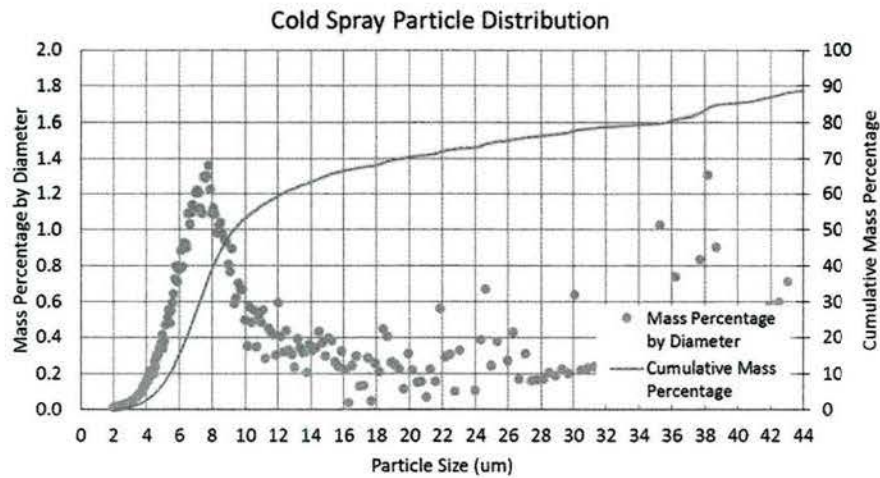


Figure 44: 85% Cu + 15% 420 SS powder blend particle size distribution

This blend was sprayed onto 1/8" thick 1018 CRS substrates with a minimum average surface roughness of $R_a = 7.5 \mu\text{m}$. The experiments investigated the effects of input pressure, traverse rate and standoff distance on coating adhesion, spot size, and oxidation of the coating, see Table 22.

Table 22: 85% Cu + 420 SS powder blend experimental settings

Parameter	Settings
Input Pressure - bar (psi)	6.9, 8.3 (100, 120)
Traverse - mm/s (in/s)	Manually controlled
Stand-off Distance - mm (in)	10, 15 (0.4, 0.6)
Gas Preheat Temperature - °C (°F)	600 (1,112)
Vibratory Powder Feed Rate	#2, approximately 24-30 g/min

The parameter set which produced the highest amount of deposition was:

- Gas pre-heat temperature = 600°C
- Input Pressure = 8.3 bar
- Standoff distance = 10 mm
- Traverse rate = manual, approximately 1 – 3 mm/s; robot control at 1 mm/s
- Offset between passes = manual; robot offset at 3 mm
- Vibratory powder feed rate = #2, approximately 24-30 g/min

The coatings exhibited high levels of porosity and oxidization, see Figure 45. The 85% Cu + 15% 420 SS powder blend was not investigated further based upon these results, however, the parameter settings which produced coatings were used to inform the design of future copper blend experiments.

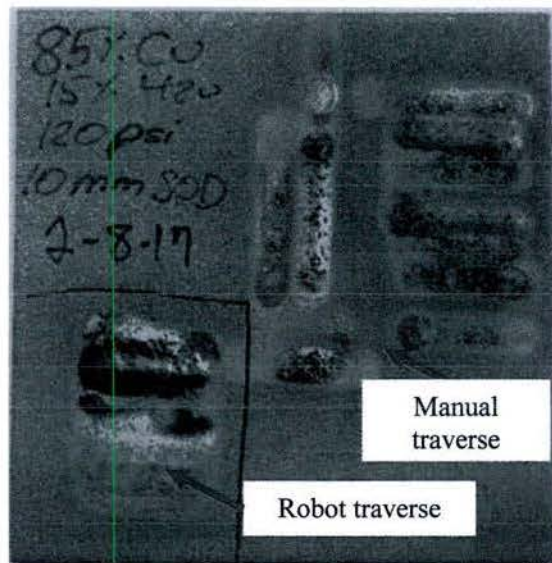


Figure 45: 85% Cu + 15% 420SS Specimen Overview

5.4.11 Evaluation of theory 2 - 420 SS blended with Cu (85% 420 SS / 15% Cu)

Referencing the WC-Ni blend experiments (section 0), the hard to ductile ratio of 85% / 15% was used as a guideline for the 420 SS mixed with Cu experiments. Material from the same lots as previously investigated were used in these experiments. All blends were mechanically mixed.

Both the Diamalloy 1002 420 SS (Oerlikon-Metco) and the HA4155-4 Cu (HAI) powders were sieved to $-32\ \mu\text{m}$ prior to blending. Particle size analysis of the blended powder shows a mean (D50) of $8.6\ \mu\text{m}$ (D10 = $5.1\ \mu\text{m}$, D90 = $24.6\ \mu\text{m}$), see Figure 46.

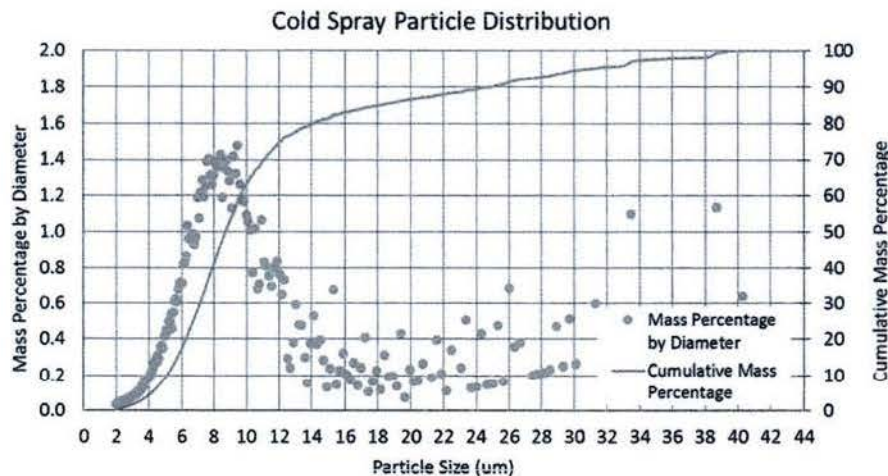


Figure 46: Particle Size Distribution of 85% 420SS + 15% Cu Powder Blend

This blend was cold sprayed onto 1018 CRS with a minimum surface roughness of $7.5\ \mu\text{m}$ in all of the following designed experiments (DOE's).

5.4.11.1 Iteration 1

The first set of experiments (iteration #1) was a small manually controlled screening test to investigate the effects of input pressure and standoff distance on coating adhesion and oxidation of the coating. Manual traverse speed, gas pre-heat of 600°C, and powder feed rate #2 were used for all samples, see Table 14. The maximum input pressure achievable with this equipment is 9.7 bar (140 psi).

Table 23: Iteration #1 settings and results

Sample #	Input Pressure - bar (psi)	Standoff Distance - mm (in)	Coating Produced?
1	8.3 (120)	10 (0.39)	Yes
2	9.7 (140)	10 (0.39)	No
3	9.7 (140)	25 (0.98)	Yes
4	8.3 (120)	25 (0.98)	Yes

Sample 2, which did not produce a coating, was observed to deposit material initially, but consecutive layers eroded the initial deposition. The parameter sets from samples 1, 3, and 4 were investigated further, as described below.

5.4.11.2 Iteration 2

In these experiments, the parameter sets from samples 1, 3, and 4 were rerun with a robot controlled traverse of 5 mm/s in an approximate 20 x 30 mm pattern onto 1018 CRS. Each sample was sprayed with 12 layers and a powder feed rate of 2 (approximately 24-30 g/min). The experiments investigated the effects of input pressure, gas pre-heat and standoff distance on coating microstructures and microhardness. The experimental design for iteration #2 and results are shown in Table 24.

Table 24: Iteration 2 settings and results

Sample #	Input Pressure - bar (psi)	Standoff Distance - mm (in)	Gas Preheat Temperature - °C (°F)	Coating thickness - mm (in)	Average Hardness HV1
10	8.3 (120)	10 (.39)	600 (1,112)	0.76 (0.030)	154
11	9.7 (140)	25 (.98)	600 (1,112)	0.54 (0.021)	-
12	8.3 (120)	25 (.98)	600 (1,112)	0.45 (0.018)	-
13	9.7 (140)	25 (.98)	480 (896)	0.59 (0.023)	156

Samples 10 and 13 were selected for microhardness testing because they had the thickest coatings. The average hardness values in the coatings are higher than those for pure copper (HV1=100) and mild steel (1018 CRS, HV1=131), indicating the inclusion of stainless steel in the coatings. SEM image analysis

indicates dispersion of 420 SS (darker regions) within a Cu matrix (lighter regions), see Figure 47. EDS analysis of the elemental makeup of the samples shows ~20% 420 SS in the coatings.

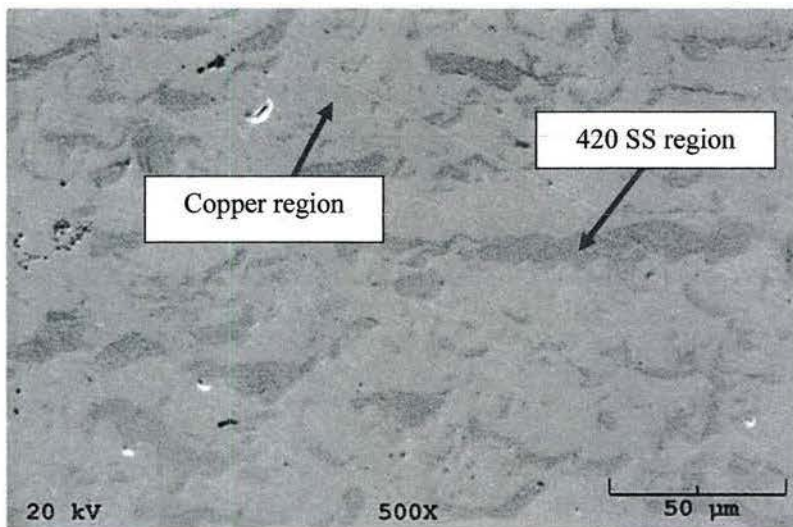


Figure 47: SEM image of 85% 420 SS + 15% Cu coating sample #13, 500x

All specimens had visibly uneven surfaces with varying degrees of surface pores. Optical microscopy revealed that these pores extended down to the substrate, see Figure 48.

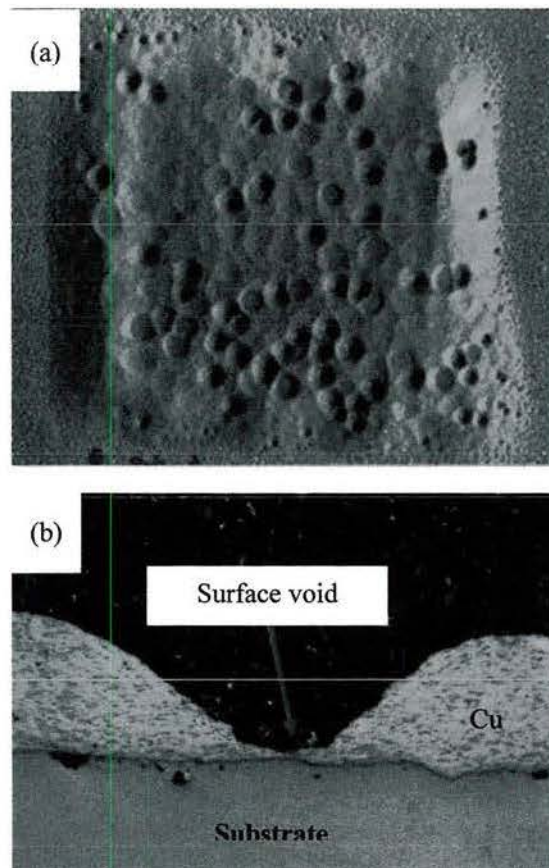


Figure 48: (a) Top view of sample, (b) image at 50x showing voids

It was theorized that the large pores were a result of localized overheating of the copper particles, causing excessive softening and preventing adhesion when impacting by the harder 420 SS particles. Therefore, the next set of experiments sought to reduce the suspected overheating of the copper by controlling the gas preheat heat, standoff, and traverse. Based upon visual inspection of the surface conditions and microhardness data, the input pressure from sample #13 (140 psi) was selected as the basis for the next set of experiments.

5.4.11.3 Iteration 3

These experiments investigated the effects of gas preheat, standoff and traverse on the surface porosity and microhardness. The design of experiments carried forward the settings from sample #13 as a baseline and also investigated several theories for reducing the suspected localized overheating of the copper:

1. Increasing the standoff distance will reduce the temperature of the particles due to longer cooling time outside of the nozzle, reducing surface pores.
2. Increasing the traverse rate will reduce dwell time over the substrate and previously coated layers and reduce heat concentrations in the coating, reducing surface pores
3. Reducing the gas pre-heat will reduce the temperature of the particles, reducing pores.

Each 1018 CRS sample was cold sprayed with 12 layers at a powder feed rate of 2 (approximately 24-30 g/min) and air pressure of 140 psi. The experimental design for iteration #3 and results are shown in Table 25. Coating thicknesses varied from 0.10 - 0.54 μm (0.004 – 0.021 in.).

Table 25: Iteration 3 experimental design and results

Sample #	Stand-off Distance mm (in)	- Gas Setting	Preheat - °C (°F)	Traverse Speed - mm/s (in/s)	Coating thickness mm (in)	Average Hardness - HV1
14 (repeat of #13)	25 (.98)	480 (896)		5 (.20)	.54 (.021)	-
15	25 (.98)	240 (464)		5 (.20)	.18 (.007)	183
16	50 (1.97)	240 (464)		5 (.20)	-	-
17	50 (1.97)	480 (896)		5 (.20)	.23 (.009)	163
18	50 (1.97)	480 (896)		20 (.79)	.10 (.004)	173
19	50 (1.97)	240 (464)		20 (.79)	-	-
20	25 (.98)	240 (464)		20 (.79)	-	-
21	25 (.98)	480 (896)		20 (.79)	.10 (.004)	161

Samples 15, 17, 18 and 21 were selected for microstructure and hardness evaluation based upon the low surface porosity exhibited as compared to the baseline sample shown in sample 14, Figure 49(a), and are denoted with an * in Figure 49. Sample 21 exhibited the lowest level of surface pores and was selected for further investigation (Figure 49 (h)).

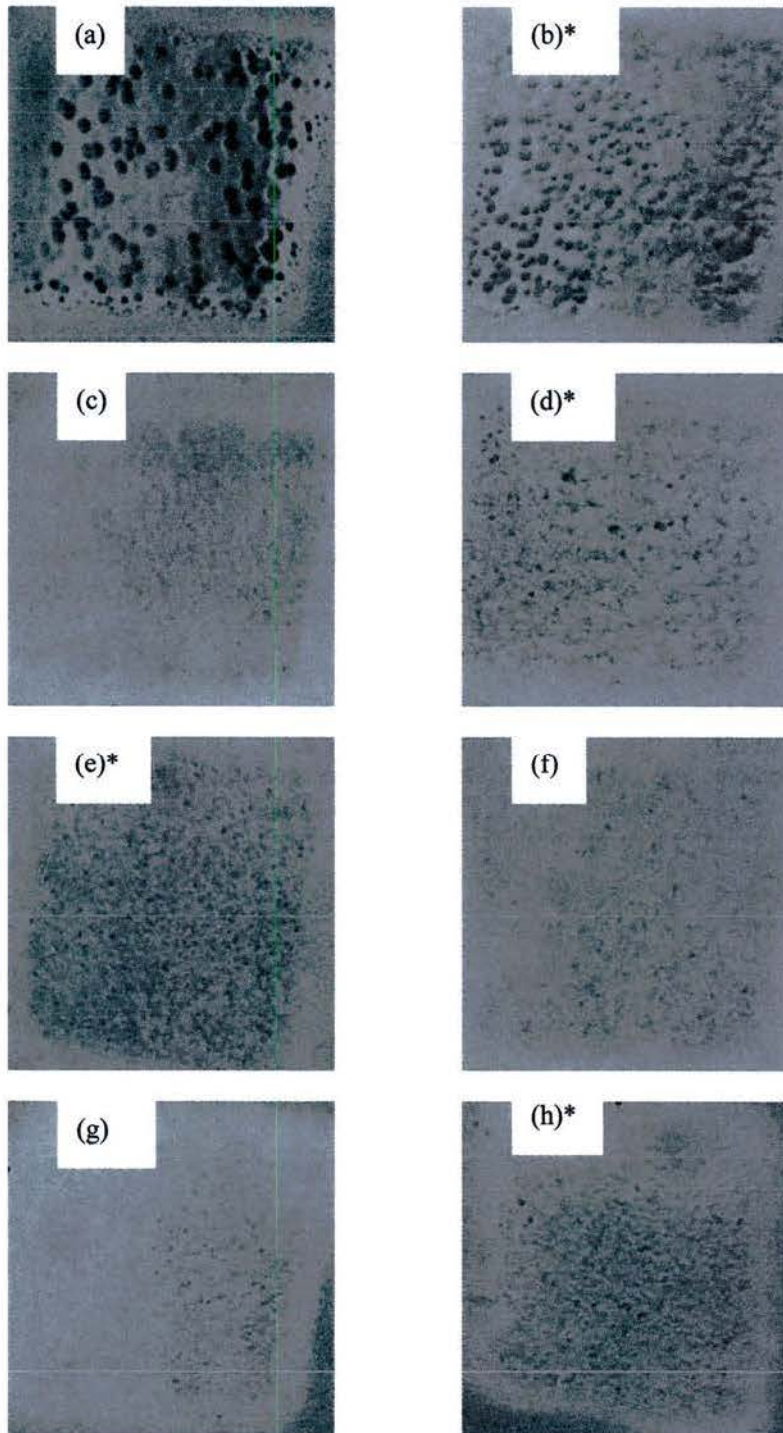


Figure 49: Iteration 3 coatings (a) #14-25mm SOD, 480°C, 5mm/s (b) #15-25mm SOD, 240°C, 5mm/s (c) #16-50mm SOD, 240°C, 5mm/s (d) #17-50mm SOD, 480°C, 5mm/s (e) #18-50mm SOD, 480°C, 20mm/s (f) #19-50mm SOD, 240°C, 20mm/s (g) #20-25mm SOD, 240°C, 20mm/s (h) #21-25mm SOD, 480°C, 20mm/s. Items with an * were selected for evaluation.

Sample #21 was determined to have the lowest level of surface pores and the most complete coverage of the spray pattern area, but was relatively thin at 0.1 mm. The settings which produced sample #21; 25mm SOD, 480°C, 20mm/s, 140 psi (Figure 49 (h)) were selected for one additional experiment.

5.4.11.4 Iteration 4

Using the settings from previous sample #21, an experiment was conducted to determine the effect of thicker coatings on porosity; 120 layers were sprayed, with a coating thickness of 0.71 mm. The additional sample exhibited surface porosity which grew in size as additional layers were built, indicating that the initial coating – substrate layer was not consistent, as shown in Figure 50.

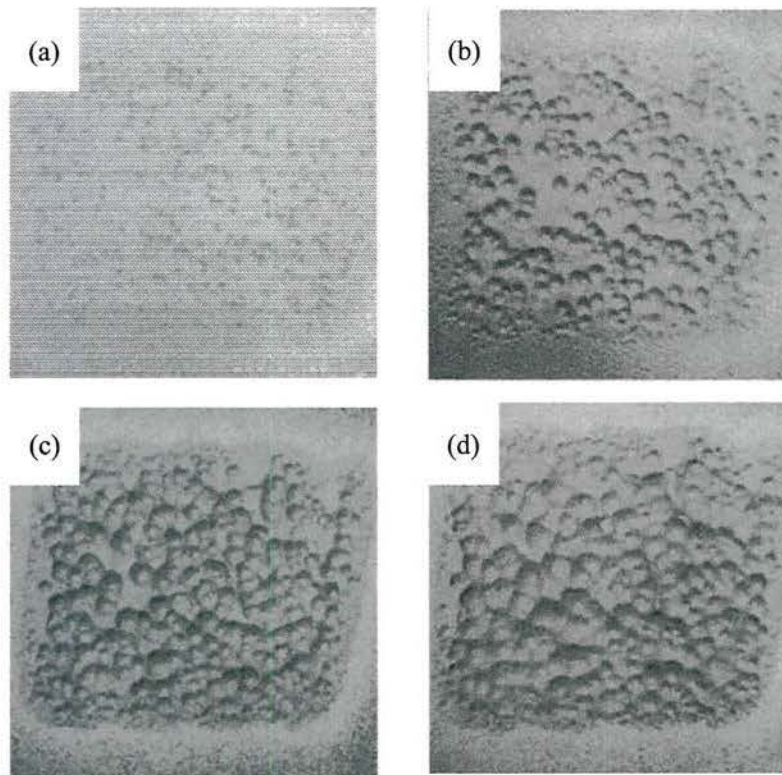


Figure 50: Progressive layers of coatings for 25mm SOD, 480°C, 20mm/s, 140 psi, powder feed of 2 (a) 30 layers (b) 60 layers (c) 90 layers (d) 120 layers

In these experiments the lower gas pre-heat temperature of 240°C did not produce coatings, and the traverse rate had a minimal impact on reducing surface pores for the 85% 420 SS / 15% Cu material blend. The experiments also showed the importance of creating a consistent initial coating bond to the substrate.

5.4.11.5 Iteration 5

One final experiment was conducted for the 85% 420 SS / 15% Cu material blend to investigate the effects of lower input pressure on the initial coating layer, under the theory that lower input pressures would allow more Cu to bond in the initial layer, creating the necessary binder for the harder 420 SS.

The experimental design for iteration #5 and results are shown in Table 26. The two runs (#1, 4) which employed low pressure were failures and no material deposited. Sample 2 was sufficiently thick to obtain

hardness measurements, with an average hardness of 170 HV. Both samples 2 and 3 were porous, though less so than in previous experiments.

Table 26: Experimental Design and results for 85% 420SS - 15% Cu Iteration 4

Sample #	Input Pressure - bar (psi)	Traverse Speed - mm/s (in/s)	Coating thickness - mm (in)	Average Hardness HV1
1	4.8 (70)	5 (.20)	-	-
2	6.2 (90)	5 (.20)	.40 (.016)	170
3	6.2 (90)	20 (.79)	.08 (.0032)	-
4	4.8 (70)	20 (.79)	-	-

The runs which deposited materials, samples 2 and 3, are shown in Figure 51.

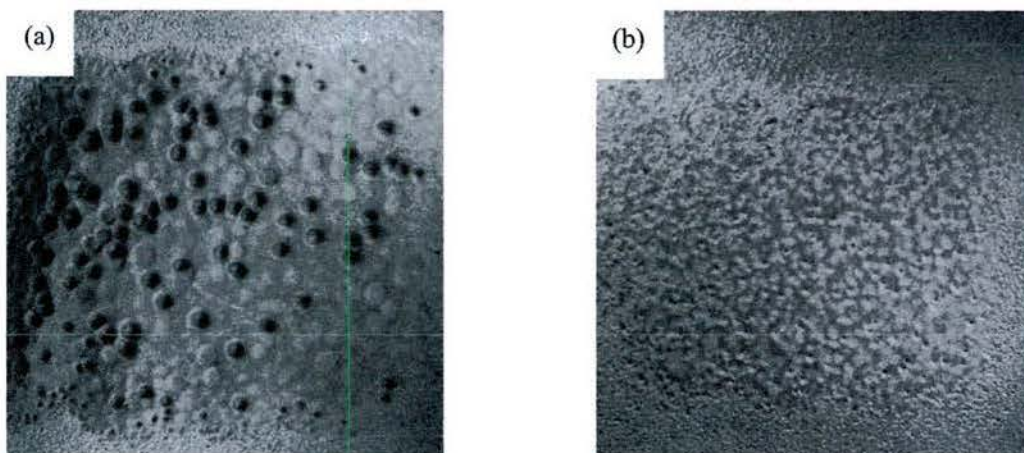


Figure 51: 6.2 bar input pressure samples (a) #2 at 5 mm/s traverse, and (b) #3 at 20 mm/s

The use of copper as a binder for 420 SS was investigated and found to produce coatings which exhibited a dispersion of 420 SS within a copper matrix (see Figure 47), yielding coating hardness values in excess of pure copper (Table 25, Table 26). However, optimization of coatings was not achieved and the deposits had high levels of surface pores.

5.5 Conclusions and Recommendations for Future Development

In the process development phase of the project, using LPCS to coat hard surfaces was investigated. To establish a baseline for the new equipment setup at RIT, a series of tests were conducted to determine the working ranges of the compressed air mass flow rate, gas temperature after pre-heat and gas force. The effects of surface preparation on adhesion results was evaluated, and determined a minimum surface roughness to optimize adhesion results.

Based upon the powder trade study, section 5.3, Ni-Al alloy and copper powders were selected for use as a binder for the 420 SS. Two theories were investigated on how to produce mixed material coatings; blending

a high mass fraction of a ductile binder with less of a hard material (theory 1), and blending a high mass fraction of a hard material with less of a ductile binder material (theory 2).

The results from testing theory 1, which investigated cold spraying a mixture of 85% of the ductile metals copper or Ni-Al blended with 15% of the harder 420 SS, did not produce coatings. The specimens exhibited signs of a shot peening effect, as the surface roughness of sprayed areas was reduced when compared to the as prepared grit blasted surface, indicating the LPCS system was not able to accelerate the particles high enough to produce coatings.

Theory 2 was investigated using 85% of 420 SS blended with 15% of the ductile metals Ni-Al or copper. Experimentation of SS 420 blended with Ni-5%Al did not produce coatings. Coatings were produced with SS 420 and copper blends. The coatings produced did show dispersion of the 420 SS within the copper binder, and the hardness values for the coatings were well in excess of pure copper coatings. However, voids were seen in the coatings and some oxidation of the copper was observed under certain spray conditions.

The results of the 420 SS experiments in the current work show the difficulty in successfully depositing 420 SS and 420 SS blends via cold spray onto steel and cast iron substrates. Some recommendations for future work include:

- Investigation of other novel blends, for example, cermet or ceramic metal blends containing 420 SS.
- Determining the effects of annealing or tempering 420 SS powders on coatings.
- Understating the effects of substrate pre-heating on 420 SS powder blend coating performance.

6 LENS Coating Development

Many components that are candidates for remanufacturing require repair or replacement of surface coatings for wear applications. For the ductile iron component, a fusion bonding process was evaluated to produce a coating with high substrate adhesion and sufficient inter-coating strength. To create fusion bonds, a directed light fabrication additive manufacturing process was chosen for this research based on its applicability for remanufacturing a wide variety of metallic components. The relatively new hybrid vertical milling center with laser sintering capability from Optomec® was employed to apply a stainless steel surface coating to ductile iron and steel substrates (as selected in Section 2.1) that are typical in remanufacturing applications.

An initial design of experiments (DOE) was implemented to research the effects of the operating parameters related to directed light fabrication processes on coatings for remanufacturing worn components. A partial factorial experiment was performed with five factors at two levels in order to determine the optimal combination of factors to produce robust coatings for remanufacturing wear surfaces. The factors studied were laser power, traverse rate, powder flow rate, laser focal point, and substrate preheat temperature. Performance was assessed based on metrics from the microstructure, hardness of the printed material, build efficiency, and coating porosity. Upon completion of the initial design of experiments, the optimal settings resulting in the most robust microstructure and hardness were selected for additional wear and tensile testing. All experiments were performed using alloy 420 Stainless Steel powder for the coating on grade 80-55-06 cast iron and alloy 9310H steel substrates.

Results were compared to observe the effects substrate properties may have on performance. It was found that substrate properties had a significant effect on the properties of the coating. Not only did the thermal properties of the substrate play a part, but the volume and shape of the substrate did as well. The ductile iron substrate samples built more efficiently than the 9310H alloy steel substrate samples. Consequently, the two sets of samples also had different resulting optimal settings as well. It was found that the optimal settings for ductile iron were 800W laser power, 10 inches/min traverse rate, 0.2302 grams/second powder feed rate, 0.425 inches vertical offset, and 572F substrate preheat temperature. The corresponding optimal

settings for 9310H alloy steel were 800W, 20ipm, 0.2676 g/s, 0.425 inches, and 72F. Deposition pattern was not found to have a significant impact on the material properties.

6.1 Program Objectives

6.2 Background (literature review)

The Hybrid Laser Engineered Net Shaping (LENS) machine is a directed light fabrication process and is a relatively new technology for fabricating fully solid 3D parts with the concurrent ability to subtract material through conventional milling techniques. Griffith, et al. showed that the LENS process can produce parts with X and Y dimensions accurate to ± 0.005 inches and Z dimensions accurate to ± 0.015 inches, with further improvements possible with optimization of process parameters [5]. The LENS process can also build with a maximum angle of 30 degrees for single width deposition, and 15 degrees for solid parts. Fabricated parts can have material strengths significantly superior to annealed materials and comparable to wrought materials [5]. In addition, the LENS process allows for all this to be created in a single step, eliminating needs for dies and molds, capital equipment, and space associated with the additional processes required for conventional manufacturing processes [2].

Although the Hybrid LENS machine has been primarily used to build parts from scratch, its use can also be extended to rebuild and repair applications. A worn part can be setup inside the machine, and the profile of the part can be modeled and uploaded so that the machine will build up the worn surface. The surface can then be machined back down to its original dimensions without removing the part and setting it up in separate machining center. For the application of remanufacturing and repair of wear components, the LENS process must be optimized towards producing a strong coating. The width and height of the printed beads are determined by powder size, laser power, powder feed rate, and traverse speed [1]. Lewis and Schlienger did work that revealed that porosity within the coating can be improved by increasing laser power, lowering traverse speed, or creating thinner layers [2]. Unocic and DuPont found that deposition efficiency is dependent on processing parameters and their control over the melt pool, and that deposition efficiency increases with laser power, and decreases with feed rate and traverse speed [4]. Krishna and Bandyopadhyay also discovered that a vertical offset of 9.525 mm from the part gave the best combination of microstructure and hardness [3]. Aside from fabricating 3D parts from scratch, the LENS process can also be used for surface modification via laser surface-melting. Vamsi Krishna and Amit Bandyopadhyay showed that with the right process parameters, laser surface-melting with the LENS can significantly increase the surface hardness of AISI 410 martensitic stainless steel by reducing the retained austenite [3].

Another factor that was shown to affect coating properties is the substrate material properties that the coating is printed on. The LENS process is primarily a heat transfer process, thus the thermal properties of the substrate will be significant in shaping the characteristics of the resulting coating. All experiments will be performed on two different substrates, 80-55-06 ductile iron, and 9310H alloy steel, to show the effects of substrate properties on coating quality.

In order to apply the most effective repair that yields parts equivalent in mechanical properties to the original component, a combination of settings that result in the best material properties for the specific application must be determined. In this study, a two level partial factorial experiment with five factors was implemented to understand the effects of the LENS parameters on material properties. With this understanding, the experiment is then refined to a full factorial experiment with only the factors that have the biggest impact on the quality of the coating to obtain an even greater understanding on how to print the strongest coating.

A two level partial factorial experiment with five factors involves five independent settings with a high and a low level for each setting. For example, based on the literature, the laser power was determined to be one of the primary factors affecting the quality of LENS component therefore it was selected as one of the five

settings to manipulate. The laser power is controlled by setting the wattage of the beam from approximately 200 to a maximum of 1000W therefore the high level chosen for this study was 800 Watts, while the low level chosen was 400 Watts. The factorial experiment provided insight on how each setting affects the metrics of performance measured, within the range of the high and low levels chosen. While a full factorial experiment would have involved every permutation of high and low levels for each setting, a partial factorial experiment reduced the number of trial runs, allowing for replicates. In addition to the high and low levels for the experiments, a set of nominal, or midpoint, levels were also included to give more insight into the shape of the trend.

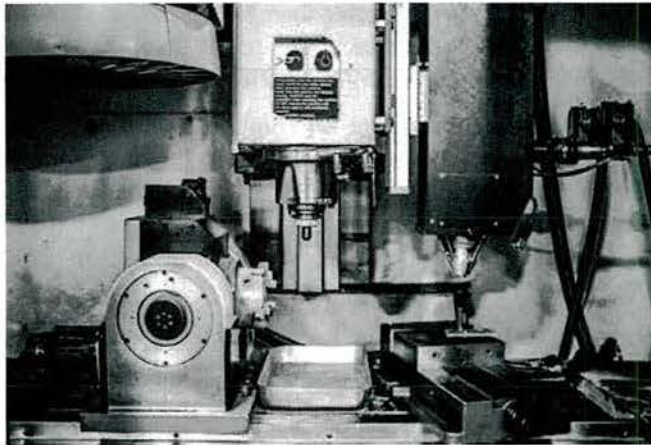
6.3 Process Development

6.3.1 Equipment

The Optomec® Hybrid LENS machine is a 3 axis CNC mill combined with a Laser Engineered Net Shaping system that provides the capability for both additive and subtractive manufacturing within the same enclosure. The LENS machine uses a manufacturing technology where metal powder is fluidized in a stream of argon gas via a spinning perforated disk and blown through a set of nozzles that are concentric with a laser beam. The laser melts a selected region of the metal substrate creating a small melt pool while the powder is blown into the molten metal. The melt pool is protected from oxidation through an argon shield gas which is dispensed through a concentric stream around the laser beam. The LENS machine traverses a path specified by a numerical control language to build layer by layer.

Tool paths were generated by exporting computer aided design models in Stereolithography (.stl) format to a computer aided manufacturing (CAM) software package with a post processor for the LENS that creates machine instructions in the form of G-code control language. The G-code provides the machine with commands that sequential step through the build volume in vertical layers, each containing a planar tool path that the laser or cutter follows. When preparing the toolpath for the Hybrid LENS process, there are various parameters that the operator is required to enter. These parameters include laser power in watts, traverse rate in inches per minute, powder feed rate in revolutions per minute, and vertical offset distance from the substrate.

Once the tool path is imported into the LENS machine operator interface, the part is fixtured inside the enclosure. Then, Argon gas is manually allowed to flow, and powder feed is enabled via the operator interface. The laser system is turned on, and the build is ready to start. The substrate can also be preheated to minimize cracking and decrease the temperature gradient across its length caused by heating from the laser and cooling from convection. A typical Hybrid LENS process for remanufacturing wear components would consist of first machining down the worn surface of the part in question using the CNC mill, then building up the surface using the LENS process, and finally machining down the built surface back to the original dimensions.



Substrates were cut into 2 inch diameter by 0.75 inch thick pucks. These pucks were thicker than those utilized for either thermal spray or cold spray due to the increased localized temperatures caused by the weld pool.

6.3.2 Screening Tests

Screening tests were performed at the beginning of the project to choose suitable setting levels for the design of experiments. Process settings that could be controlled included laser power, powder feed rate, print head traverse rate, offset distance, track distance (or distance between lines of a print), and layer height. Laser power, powder feed rate, and traverse rate were settings that were independent, and easily manipulated through the CAM software. Track distance and layer height, however, were dependent of the print itself. Specifically, track distance was a function of the bead width while layer height was a function of bead height. The thicker the bead that was deposited by the print head, the wider the track distance would have to be to remain consistent with Optomec's recommendation of a 40% bead overlap. Similarly, the taller the bead that was deposited by the print head, the thicker the resulting printed layer would be, and the further up the print head would have to move after finishing a layer to maintain a consistent vertical offset distance. Thus laser power, powder feed rate, and traverse rate were chosen as settings to manipulate in the design of experiments, while track distance and layer height were set individually with each experiment based on other testing to be described later.

Optomec provided a set of baseline settings that they found provided the high quality builds on the LENS machine. These baseline settings were a laser power of 400 Watts, powder feed rate of 4 revolutions per minute, a vertical offset distance of 0.375 inches, and a bead overlap of 40%. Testing showed that these settings do result in high quality prints, however not necessarily for a remanufacturing and repair application for wear surfaces. These settings resulted in prints with uniform microstructure, however, had very thin layers that would result in longer and more costly remanufacturing processes. Thus, in order to understand a wider range of system capability, these settings were selected as either low or nominal levels in the design of experiments.

Screening tests showed that with higher laser power, printed layers become thicker with all other setting remaining constant. This is a result of increased heat into the substrate that forms a larger melt pool that allows for more powder to bind with the pool. A thicker layer is ideal since this would allow for fewer layers to be printed in order to reach a target coating thickness, and therefore a quicker overall processing time. The recommended setting of 400 Watts was already providing thinner layers than desired, and testing showed that a laser power greater than 800 Watts was providing too much heat and was deforming and affecting the material properties of thin parts. Thus, 400 Watts was chosen as the low level and 800 Watts was chosen as the high level, with the midpoint of 600 Watts chosen as the nominal level.

Screening tests also showed that with higher powder feed rates, printed layers also become thicker. Again, since a thicker layer is desired, 4 revolutions per minute was set as the low level. Although the LENS system allowed for much higher powder feed rates, 8 revolutions per minute was set as the high level to get an initial understanding of the system and to keep the prints efficient. 6 revolutions per minute was chosen as the nominal setting.

The vertical offset distance was another factor considered during the LENS process. The vertical offset distance is the distance between the powder nozzles and the surface of the part. The laser beam has a focal distance that is a function of the print head lens and dimensional settings. Optomec recommends that the laser focal point be between 0.050 inches below and above the surface of the substrate depending on the laser power setting, however, testing showed that the ideal distance may vary more depending on process parameters. Thus, to gain a greater understanding of this effect, the recommended offset of 0.375 inches was chosen as the nominal level, while the high and low levels were 0.050 inches above and below the nominal respectively.

Traverse rate was another important factor considered in the screening tests. The faster the print head moved, the less heat that transferred to the part and the faster the layer printed. Thus, it would affect print time and efficiency, as well as layer height. Testing showed that with the 400 Watt laser power setting,

traverse rates faster than 20 inches per minute resulted in layers that were too thin to be viable for remanufacturing, while traverse rates slower than 10 inches per minute with the 800 Watt laser power setting input too much heat into the part and caused deformity even in thicker substrates. Thus 20 inches per minute was chosen as the high level, 10 inches per minute was chosen as the low level, and 15 inches per minute was chosen as the nominal for the design of experiments.

The LENS laser sintering process is similar to that of a welding process. Just like a welding process, a melt pool is first created, then material is fed into the melt pool. It follows that some of the concerns that come with welding should also be considered during the LENS process. Specifically, cracking of the coating was considered as a potential issue. The solution that welders often use is to preheat the part prior to welding [73]. This lessens the temperature differential between the welded area and the rest of the part, thus slowing the cooling rate, and reducing the chance of cracking. Preheating, however, adds difficulty and time to the overall LENS remanufacturing process depending on the size of the part to be remanufactured or repaired, therefore it is relevant research topic studied in this work. To avoid substantial modification of the components microstructure, an upper temperature limit of 300°C (572°F) was selected as the high level, while room temperature was chosen as the low level, and the midpoint of 149°C (300°F) was chosen as the nominal point.

Table 27: Summary of settings and levels for Initial Experiments

Settings	Laser power (W)	Powder Feed Rate (RPM)	Traverse Rate (IPM)	Vertical Offset (in)	Preheat Temp (F)
High	800	8	20	0.425	572
Nominal	600	6	15	0.375	300
Low	400	4	10	0.325	72

A summary of the high and low levels for each relevant setting is shown above in Table 27. Since the screening tests were performed primarily on 80-55-06 ductile iron substrates, these settings were used for the initial design of experiments to gain an initial understanding of the effects that each of the LENS process parameters had on the deposition before further refinement.

6.3.3 Mounting and Polishing Samples

One of the performance metrics that was considered is the quality of the microstructure of the coating. This included the uniformity of the microstructure, as well as percentage of porosity and voids. The microstructure also revealed information on the direction of heat transfer and the rate of cooling. The microstructure specimens were prepared according to the procedure detailed in Section 3.1. Additionally, the polished puck was etched using a 33% HCl in Ethanol solution until grain boundaries were revealed. The microstructure of the sample coating was imaged using an Olympus IX50 Inverted Optical Microscope.

6.3.4 Surface Preparation

As with most coating processes, the surface preparation of the part had an effect on the quality of the coating. Thus, after choosing the settings and levels for the partial factorial experiment, it became necessary to have a standardized procedure for the surface preparation of parts for the experiments. The substrates used for the experiments are saw-cut ductile iron and 9310H steel pucks for circular bars. An experiment to compare various surface preparations was performed to determine if the parts could be kept as saw-cut or if they needed to be milled and/or grit-blasted.

For this surface preparation study, two different surface preparation procedures were compared. The first being a saw-cut surface cleaned with Scotch-Brite to remove oxidation and wiped with isopropyl alcohol and Kim-Wipes. The second procedure for comparison involved milling the saw-cut surface, grit blasting with 36 grit Aluminum Oxide, and wiping with isopropyl alcohol and Kim-Wipes. A sample was printed

on the LENS using each of the surface preparation procedures on a ductile iron puck using machine parameters of 600 Watt laser power, 20 inches per minute traverse speed, 8 revolutions per minute powder feed, 0.375 inches vertical offset, and 72°F substrate temperature. Cross sections of each sample were cut, mounted and polished to be looked at under the Olympus microscope.

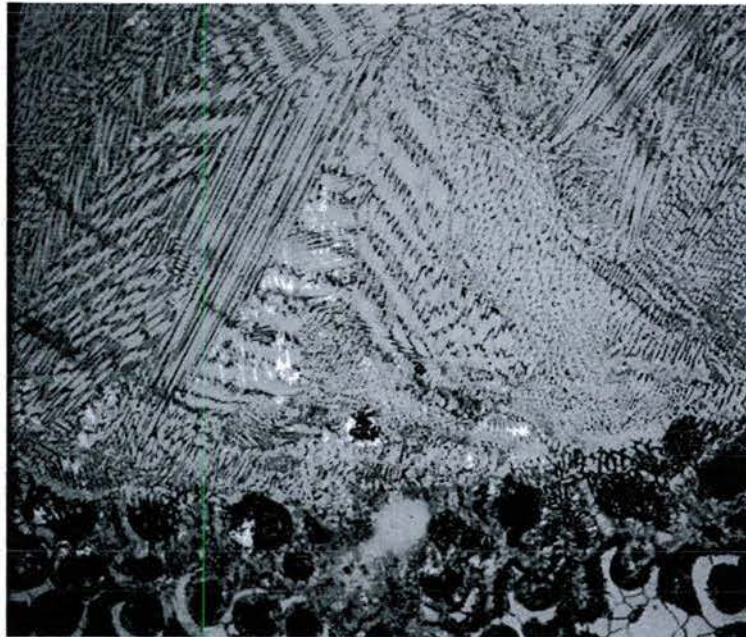


Figure 52: Saw-cut sample, 200x magnification

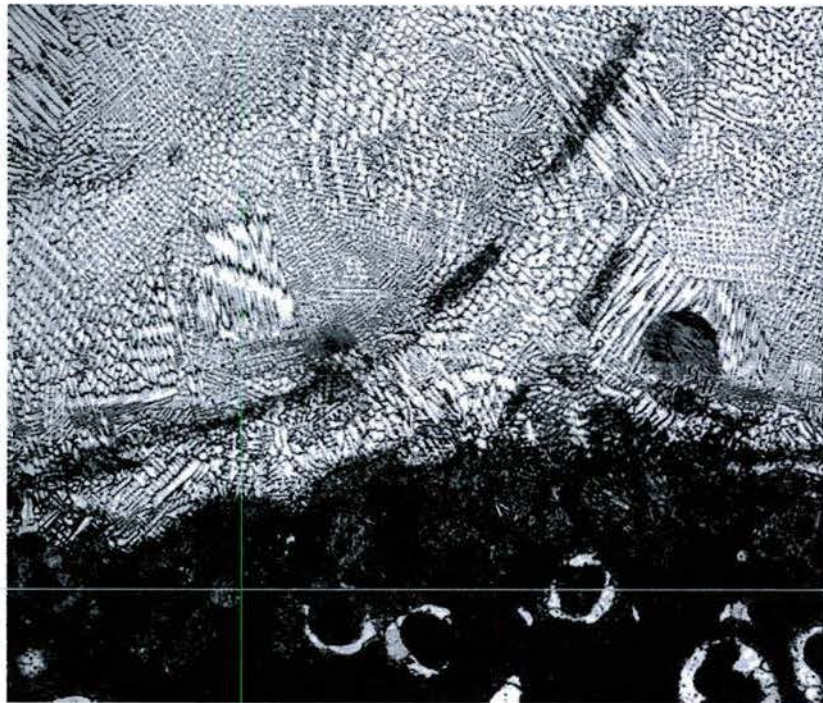


Figure 53: Milled and Grit-blasted sample, 200x magnification

The primary location of interest was the interaction area between the coating and the substrate. As shown in Figure 52 and Figure 53, there was no obvious difference between the two surface preparation procedures. This was expected since the LENS uses a laser to melt the surface of the substrate, so surface roughness should not play a big part in the coating's adherence.

Since it was shown that the different procedures did not have a significant impact on the coating therefore the saw-cut procedure was chosen since it required the least amount of preparation. Although it was ruled the milled/grit-blasted procedure did not have an appreciable effect on surface preparation, grit-blasting by itself was shown to be a very effective method removing oils and oxides on the surface that affect print quality. The final surface preparation procedure employed saw-cut pucks de-greased with isopropyl alcohol and paper towels, grit-blasted with 36 grit Aluminum Oxide, scrubbed with Scotch-Brite pads to remove embedded blasting media, and finally wiped again with isopropyl alcohol and Kim-Wipes

6.3.5 Set-up of the Initial Design of Experiments

An initial design of experiments was developed based on the LENS process parameters that were deemed to have the greatest impact on the remanufacturing process based on the literature review and results of the screening tests. A partial factorial design based on a 2^{5-2} design specification was selected and randomized in order to observe trends in hardness, porosity, and deposition efficiency. The order was randomized in order to demonstrate repeatability of the LENS machine process. Table 28 shows the permutations of settings and levels for each experiment of the partial factorial design. Three replicates of each permutation were performed including the center point. These experiments were performed to obtain initial understanding on the effects of each LENS machine parameter on the quality of the build. These experiments were performed on ductile iron substrates first, followed by the same experiment performed on the 9310H steel substrates.

Table 28: Randomized Partial Factorial Design for Initial Ductile Iron Experiments

2**(5-2) FRACTIONAL FACTORIAL DESIGN						
Group Number	Run #	Substrate Temperature (°F)	Laser Power (W)	Powder Flow (RPM)	Offset Distance (in.)	Traverse Rate (in/min)
Nominal	1	300	600	6	0.375	15
6	2	572	400	8	0.325	20
2	3	572	400	4	0.325	10
3	4	72	800	4	0.325	20
5	5	72	400	8	0.425	10
7	6	72	800	8	0.325	10
1	7	72	400	4	0.425	20
7	8	72	800	8	0.325	10

8	9	572	800	8	0.425	20
7	10	72	800	8	0.325	10
1	11	72	400	4	0.425	20
4	12	572	800	4	0.425	10
2	13	572	400	4	0.325	10
Nominal	14	300	600	6	0.375	15
2	15	572	400	4	0.325	10
4	16	572	800	4	0.425	10
6	17	572	400	8	0.325	20
5	18	72	400	8	0.425	10
8	19	572	800	8	0.425	20
4	20	572	800	4	0.425	10
6	21	572	400	8	0.325	20
3	22	72	800	4	0.325	20
1	23	72	400	4	0.425	20
3	24	72	800	4	0.325	20
5	25	72	400	8	0.425	10
8	26	572	800	8	0.425	20
Nominal	27	300	600	6	0.375	15

Each experiment produced a three layer circular coating on top of a cylindrical substrate. During each experiment, the deposition efficiency was calculated by measuring the change in weight of the specimen and the mass flow rate of powder over the time of the print. After all experiments were completed, each resulting sample was cut, mounted, polished, and etched to reveal its microstructure. From the microstructure image, the porosity was estimated using on ASTM E2109 as a guideline. Hardness measurements were recorded using a Struers DuraScan hardness tester and averaged for each sample. The results of the deposition efficiency, porosity, and hardness were processed using a MATLAB® ANOVA function to generate plots that revealed the effects of each machine parameter on the performance metrics.

Immediately before each of the experiments, the substrate surface was prepared and if the experiment called for a preheat temperature above room temperature, the substrate was then put into the oven for an hour at the target temperature. An hour was chosen to ensure that the entire substrate had enough time to reach the

target temperature, but did not sit in the oven long enough for significant amounts of oxidation to form on the surface. The substrate was then placed in an insulated enclosure for minimal heat loss during transfer from the oven to the LENS machine. The substrate and insulated enclosure was placed within the LENS machine and print started. The LENS machine was then allowed to cool down to room temperature before the next print began to ensure other environmental factors were controlled. The next experiment was prepared similarly such that it was ready by the time the LENS machine was ready to print again. Once all samples were printed, they were then mounted and subject to porosity and hardness measurements.

6.3.6 Bead Width and Bead Height

As witnessed in the Screening Tests, the laser power and traverse rate had an effect on the width and height of the coating bead deposited onto the substrate, therefore, before performing the partial factorial experiment the G-code was uniquely generated for each sample. To generate this code, a separation between laser passes, defined as percent overlap, had to be entered into the CAM software along with bead width. The bead width resulting from each experiment's combination of settings (laser power, traverse rate, standoff, etc.) had to be measured for the software to set the appropriate overlap between coating passes. The recommended overlap percentage was held constant at 40% based on the recommendation from Optomec.

For each sample, three layers were printed onto the substrate. After each layer, the print head moved vertically in the Z direction a distance equal to the thickness of the layer in order to maintain a consistent vertical offset distance between the LENS print head and the coated component. Thus, similarly with bead width, the bead height of each combination of settings had to be measured and entered into the software before design of experiments.

To measure the bead width and bead height of each experiment, a one-inch line was printed using each experiment's settings. The bead width of the line will be measured using calipers, and the bead height was be measured using a dial indicator. Refer to Table 29 for the results of these measurements. Measurements were made on the nominal experiments three times to check for repeatability and found to be consistent. Bead height measurements were taken at three axial locations on each line: start, middle, and end. Some lines varied in height significantly across in length but no trend could be observed between location and bead height. These bead widths and bead heights are used by the software to obtain distance between laser passes and layer height to generate the G-code for each experiment of the partial factorial design.

Table 29: Bead Width and Height Data

Settings								Build Height (in)				
Group #	Run #	Substrate Temperature (°F)	Laser Power (W)	Powder Flow (RPM)	Offset Distance (in.)	Traverse Rate (in/min)	Bead Width (in)	Start	Middle	End	Mean	Avg. Dev.
Nominal	1	300	600	6	0.375	15	0.057	0.0130	0.0140	0.0140	0.0137	0.0004
6	2	572	400	8	0.325	20	0.044	0.0125	0.0120	0.0100	0.0115	0.0010
2	3	572	400	4	0.325	10	0.052	0.0310	0.0310	0.0225	0.0282	0.0038
3	4	72	800	4	0.325	20	0.073	0.0155	0.0160	0.0180	0.0165	0.0010
5	5	72	400	8	0.425	10	0.044	0.0050	0.0045	0.0090	0.0062	0.0019

7	6	72	800	8	0.325	10	0.082	0.0250	0.0230	0.0345	0.0275	0.0047
1	7	72	400	4	0.425	20	0.042	0.0065	0.0065	0.0050	0.0060	0.0007
7	8	72	800	8	0.325	10	0.082	0.0250	0.0230	0.0345	0.0275	0.0047
8	9	572	800	8	0.425	20	0.072	0.0030	0.0035	0.0035	0.0033	0.0002
7	10	72	800	8	0.325	10	0.082	0.0250	0.0230	0.0345	0.0275	0.0047
1	11	72	400	4	0.425	20	0.042	0.0065	0.0065	0.0050	0.0060	0.0007
4	12	572	800	4	0.425	10	0.092	0.0140	0.0090	0.0065	0.0098	0.0028
2	13	572	400	4	0.325	10	0.055	0.0270	0.0350	0.0210	0.0277	0.0049
Nominal	14	300	600	6	0.375	15	0.055	0.0155	0.0150	0.0160	0.0155	0.0003
2	15	572	400	4	0.325	10	0.055	0.0270	0.0350	0.0210	0.0277	0.0049
4	16	572	800	4	0.425	10	0.092	0.0140	0.0090	0.0065	0.0098	0.0028
6	17	572	400	8	0.325	20	0.044	0.0125	0.0120	0.0100	0.0115	0.0010
5	18	72	400	8	0.425	10	0.044	0.0050	0.0045	0.0090	0.0062	0.0019
8	19	572	800	8	0.425	20	0.072	0.0030	0.0035	0.0035	0.0033	0.0002
4	20	572	800	4	0.425	10	0.092	0.0140	0.0090	0.0065	0.0098	0.0028
6	21	572	400	8	0.325	20	0.044	0.0125	0.0120	0.0100	0.0115	0.0010
3	22	72	800	4	0.325	20	0.073	0.0155	0.0160	0.0180	0.0165	0.0010
1	23	72	400	4	0.425	20	0.042	0.0065	0.0065	0.0050	0.0060	0.0007
3	24	72	800	4	0.325	20	0.073	0.0155	0.0160	0.0180	0.0165	0.0010
5	25	72	400	8	0.425	10	0.044	0.0050	0.0045	0.0090	0.0062	0.0019
8	26	572	800	8	0.425	20	0.072	0.0030	0.0035	0.0035	0.0033	0.0002
Nominal	27	300	600	6	0.375	15	0.055	0.0145	0.0155	0.0145	0.0148	0.0004

6.3.7 Layer to Layer Interaction

A three-layer sample was printed to look at the layer to layer interactions on bead height. The sample was printed at 800 Watts, 10 inches per minute, 8 rpm, 0.325 in offset, and 72°F pre-heat. The overall height of the build was taken and compared to the bead height of an individual line. The overall height measured to be about 0.20 inches, nearly four times as tall as the single bead height of 0.053 inches. Looking at a cross-section of the sample under a microscope, the first layer measured thinner than the second and third layers. This result indicates one of two interaction effects: 1) printing stainless steel onto a coating of stainless steel

yielded higher deposition efficiencies than printing on the substrate or 2) the heat generated by the laser into the part over the course of the print increased the overall part temperature therefore making the print more efficient. Using the results of the bead height experiment it was hypothesized that the temperature of the base layer was the dominant factor in bead height, which is directly impacted by one of our experimental factors, substrate temperature. The increase in bead height over the course of the print posed a slight challenge because this variant of the LENS machine did not have feedback to control the step in the Z axis to maintain a constant vertical offset distance. If significantly taller parts were to be created this would pose a larger challenge, however, since only three layers are printed per sample in this work, the resultant changes in offset distance had an insignificant effect on the end result.

Interlayer voids, as illustrated in Figure 54, were detected between layers of the LENS print. These voids are spaced at an even distance across the cross section of the print, with the same pitch as the beads themselves. This suggested the voids were caused by the “peaks and valleys” of the printed layer that resulted from the overlap of adjacent beads, see Figure 55. A difference as large as 0.015 inch between the peak, the highest point of a pass, and the valley, the lowest point located between passes, was measured in the samples. These valleys were not filled in completely by the subsequent layer printed above, creating interlayer voids.



Figure 54: 50x Photo showing interlayer voids

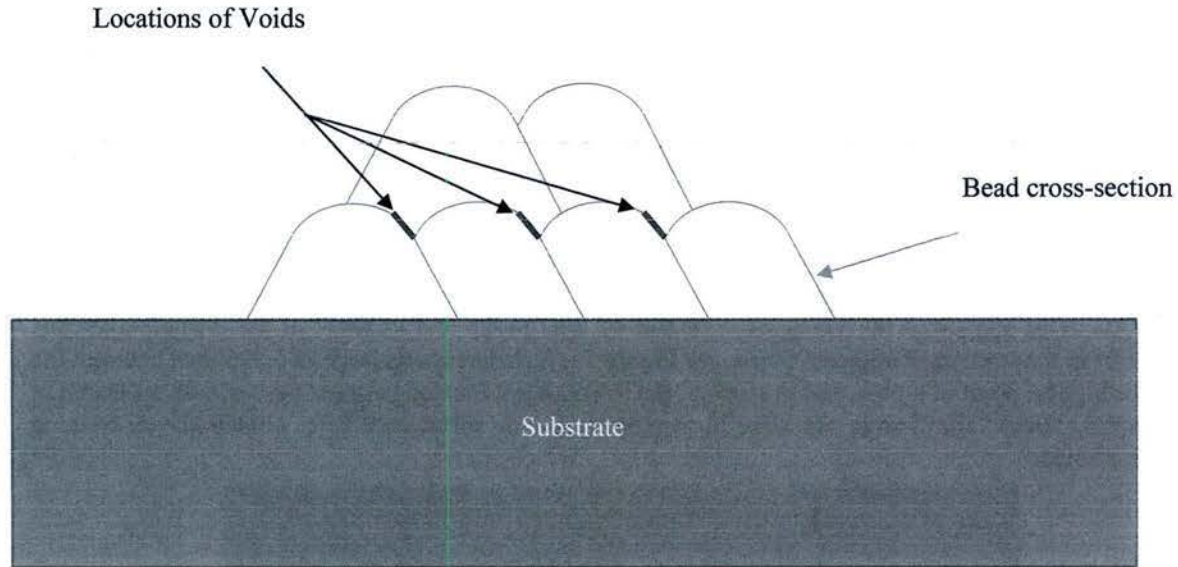


Figure 55: Location of Interlayer Voids

In an attempt to minimize these interlayer voids, the typical 90 degree angular offset between layers was changed to 30 degrees, however no improvement was shown. A 0 degree offset was also tested, but also showed no improvement. The 30 degree offset was kept for future experiments to determine if the combinations of the factors in the design of experiments would have an impact on minimizing the voids.

6.3.8 Definition of DOE Output Measurements

The output of the design of experiments was a set of four measurements: deposition efficiency, build height, porosity, and hardness. Each type of the output measurement was independently processed with the input factors to develop an understanding of response to the factors and their relative impact. Methodology used to collect the four measurements was documented and provided below for reference.

6.3.8.1 Deposition Efficiency Measurements

One of the main objectives of research in remanufacturing processes is cost effectiveness. To evaluate the cost effectiveness of the LENS process, and to find the most cost effective set of parameters, the powder deposition efficiency of each experiment was measured.

To measure powder deposition efficiency, samples are weighed on a scale with resolution to the tenth of a gram prior to printing. The print time was recorded, and the sample with coating was weighed after the print. The deposition efficiency was calculated using Equation 1 below:

$$efficiency = \frac{m_f - m_i}{\dot{m}t} \quad (1)$$

Where:

m_i	Was the initial mass of the sample
m_f	Was the final mass of the sample
\dot{m}	Was the powder mass flow rate of the print head
t	Was the print time

Since the powder flow rate of the print head was controlled by setting the revolutions per minute of the powder feeder, it was necessary to measure and translate feeder RPM to powder mass flow rate. A powder collection mechanism was created with sections of porous wall that allowed the carrier gas to escape but captured the powder. The powder feed was turned on for setting in the DOE for a set amount of time, the collector would capture the powder while releasing the Argon gas, and the difference in mass was used to calculate the mass flow rate of the print head. A linear trend between the powder feed rate and mass flow rate, shown in Figure 56 was obtained, and used in deposition efficiency calculations.

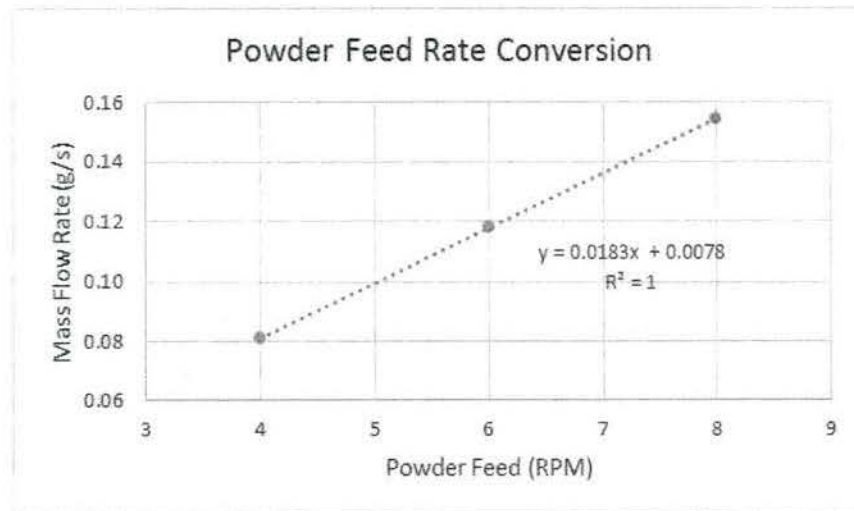


Figure 56: Powder Feed Rate to Mass Flow Rate Measurements

6.3.8.2 Build Height Measurements

An ideal print was one that would build to the target dimensions as quickly as possible, while providing good material properties, to decrease the processing time during remanufacturing production. Thus, it became relevant to track of the build heights of each specimen. As explained previously, although single line bead heights were measured, depending on overlap behavior between beads and layer to layer interaction, the overall build height of a multilayer sample was not equal to the single bead height times the number of passes. The overall build height of each printed sample was the average of measured value collected using a drop gauge. The overall build height was then divided by the number of completed layers to obtain the averaged build height per layer.

6.3.8.3 Porosity Measurements

The porosity of coatings plays a role in the resistance of the remanufactured coating to wear as well as corrosion protection of the underlying material. Porosity of samples was estimated using ASTM E2109 as a guideline for assigning percent porosity to the coatings. Pictures of the sample were taken under 50X magnification using the optical microscope, and then compared with benchmark pictures from the ASTM standard and assigned a percentage. An example of a sample with porosity roughly between 1 and 2% is shown in Figure 57.

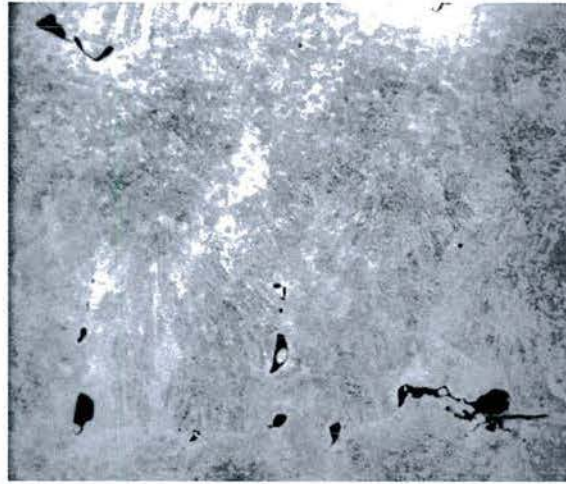


Figure 57: LENS Sample with Porosity

6.3.8.4 Hardness Measurements

As with the porosity, the hardness of the coating plays a role in its wear characteristics especially when paired with softer or harder materials. After polishing and mounting each sample, hardness measurements were taken from the center of beads on the layer closest to the substrate of each sample. Individual beads were not always distinguishable so best judgement was used. The micro-hardness test equipment produced measurements in the Vickers Hardness scale and three measurements were taken on each sample. Hardness values were converted to Rockwell C scale values in the results section.

6.4 DOE Results and Discussions for Ductile Iron Substrate

Nine parameter sets were printed onto ductile iron substrates based on the partial factorial design with 3 replicates for each parameter resulting in a total of twenty seven individual samples. The data provided in Table 30 sorts the samples into groups based on the parameters settings. The “Run #” represented the order in which the experiments were performed in the DOE. The bottom row shows data from the optimal settings down-selected at the end of the experiment. MATLAB® was used to analyze the data using analysis of variance methods, and plot the main effects of each machine parameter, as well as statistical data on their effects.

Table 30: Results from Ductile Iron Experiments

Group	ID	Substrate Temperature (°F)	Laser Power (W)	Powder Flow (RPM)	Offset Distance (in.)	Traverse Rate (in/min)	Efficiency	Build Rate (in3/min)	Build Height (in/layer)	Hardness (HRC)	Total Porosity (%)
1	M7_40020442572	72	400	4	0.425	20	0.0989	0.005	0.015	44.2	0.5
1	M11_40020442572	72	400	4	0.425	20	0.0911	0.004	0.010	42.3	0
1	M23_40020442572	72	400	4	0.425	20	0.0404	0.001	0.004	44.7	0.2
2	M5_40010842572	72	400	8	0.425	10	0.1621	0.012	0.054	55.1	2
2	M18_40010842572	72	400	8	0.425	10	0.1077	0.008	0.034	47.8	1
2	M25_40010842572	72	400	8	0.425	10	0.0497	0.004	0.017	44.6	0.2
3	M3_400104325572	572	400	4	0.325	10	0.1129	0.004	0.014	45.3	0
3	M13_400104325572	572	400	4	0.325	10	0.2084	0.009	0.034	52.7	1
3	M15_400104325572	572	400	4	0.325	10	0.2162	0.008	0.031	55.0	0.5
4	M2_400208325572	572	400	8	0.325	20	0.0967	0.007	0.020	40.7	0.2
4	M17_400208325572	572	400	8	0.325	20	0.1373	0.012	0.033	55.5	0.5
4	M21_400208325572	572	400	8	0.325	20	0.1362	0.011	0.028	54.2	0.5
5	M1_600156375300	300	600	6	0.375	15	0.1250	0.004	0.011	48.6	0.2
5	M14_600156375300	300	600	6	0.375	15	0.2056	0.012	0.032	43.6	1
5	M27_600156375300	300	600	6	0.375	15	0.2423	0.014	0.036	43.2	1
6	M4_80020432572	72	800	4	0.325	20	0.1919	0.008	0.012	46.9	0.2
6	M22_80020432572	72	800	4	0.325	20	-	-	0.009	47.0	0
6	M24_80020432572	72	800	4	0.325	20	0.1385	0.005	0.014	42.0	0.2
7	M6_80010832572	72	800	8	0.325	10	-	-	0.044	41.3	0.2
7	M8_80010832572	72	800	8	0.325	10	0.2718	0.020	0.050	52.3	2
7	M10_80010832572	72	800	8	0.325	10	0.2783	0.019	0.048	46.4	1
8	M12_800104425572	572	800	4	0.425	10	0.2627	0.014	0.021	51.5	0
8	M16_800104425572	572	800	4	0.425	10	0.1031	0.002	0.003	57.9	0.5
8	M20_800104425572	572	800	4	0.425	10	-	-	0.008	55.1	0
9	M9_800208425572	572	800	8	0.425	20	0.2374	0.018	0.030	47.4	0
9	M19_800208425572	572	800	8	0.425	20	0.1519	0.010	0.016	60.8	0
9	M26_800208425572	572	800	8	0.425	20	0.0856	0.017	0.018	52.4	0.2
Optimal	8001012425572	572	800	12	0.425	10	0.2615	0.031	0.080	58.3	3

6.4.1 Deposition Efficiency

An ANOVA analysis was performed with the above data for the ductile iron substrate which generated the main effects plot, refer to Figure 58, showing correlation between each input parameter and the Grade 420 powder deposition efficiency for the coating process. Preheat was labeled “Temp”, laser power labeled “LP”, powder feed rate labeled “RPM”, print heat offset labeled “offset”, and traverse rate in inches per minute labeled “IPM”. From the main effects plot it was apparent that laser power was significantly proportional to deposition efficiency, while vertical offset distance and traverse rate were significantly proportional to the inverse of deposition efficiency. In comparison, preheat temperature and powder flow rate did not play a significant role in this experiment.

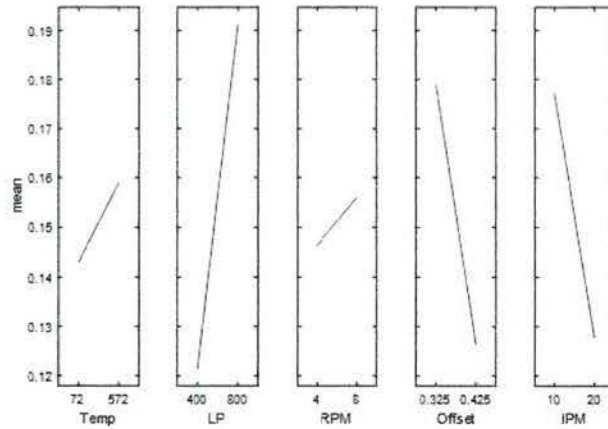


Figure 58: Deposition Efficiency Main Effects Plot

Analysis of Variance					
Source	Sum Sq.	d.f.	Mean Sq.	F	Prob>F
Temp	0.00133	1	0.00133	0.41	0.532
LP	0.02448	1	0.02448	7.62	0.0162
RPM	0.00014	1	0.00014	0.04	0.8383
Offset	0.01609	1	0.01609	5.01	0.0434
IPM	0.01394	1	0.01394	4.34	0.0576
# Temp*LP	0	0	0	0	NaN
# Temp*RPM	0	0	0	0	NaN
# Temp*Offset	0	0	0	0	NaN
# Temp*IPM	0	0	0	0	NaN
LP*RPM	0.00375	1	0.00375	1.17	0.2998
# LP*Offset	0	0	0	0	NaN
LP*IPM	0.00076	1	0.00076	0.24	0.6283
# RPM*Offset	0	0	0	0	NaN
# RPM*IPM	0	0	0	0	NaN
# Offset*IPM	0	0	0	0	NaN
Error	0.04178	19	0.00221		
Total	0.10227	20			

Sequential (Type I) sums of squares. Terms marked with # are not full rank.

Figure 59: ANOVA Statistical Data for Efficiency

The analysis also produced significance levels (P-values) for the effects of the main parameters and some of the parameter interactions on deposition efficiency. Numerical results for the P-values were based on statistical tests to determine the significance of the output response for each input parameter, refer to Figure 59: ANOVA Statistical Data for Efficiency. Laser power had a P-value of 0.016 meaning that it had a relatively high confidence that this input parameter had an effect on powder deposition efficiency. Powder feed rate, on the other hand, had a value of 0.84 meaning that there was low confidence that it imparted a significant effect on powder deposition efficiency.

Based on the observations from the data shown in Figure 58 and the significance levels, it was determined maximum deposition efficiency occurred with increased laser power while decreasing vertical offset and traverse rate. Increasing laser power increased the amount of thermal energy that went into the melt pool. Similarly, moving the laser closer and slowing down the traverse speed increased the heat flux that provided the energy in the melt pool. With more energy, more metal powder was accepted and melted onto the substrate, thus making the print more efficient.

6.4.2 Porosity

The term porosity was used to describe the combined representation of pores and voids that were detected in the micrographs of the coating and the substrate/coating interface. The origin of the pores and voids was a result of interlayer gaps, outgassing of metal or contaminant vapor, and incomplete adherence at the substrate. A plot, refer to Figure 60, representing the effect each of the main machine parameters had on the porosity of the coating was created to determine which parameters had the greatest impact. From Figure 60, it was apparent that powder feed rate (RPM) was significantly proportional to percent porosity, while preheat temperature (Temp) and traverse rate (IPM) were significantly inversely proportional to efficiency. Higher laser power and offset distance also played a role in lowering porosity.

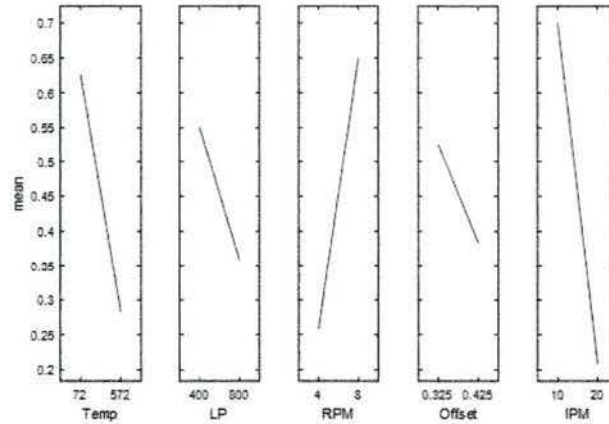


Figure 60: Porosity Main Effects Plot

Source	Sum Sq.	d.f.	Mean Sq.	F	Prob>F
Temp	0.70042	1	0.70042	2.69	0.1202
LP	0.22042	1	0.22042	0.85	0.3709
RPM	0.92042	1	0.92042	3.54	0.0782
Offset	0.12042	1	0.12042	0.46	0.5059
IPM	1.45042	1	1.45042	5.58	0.0312
# Temp*LP	0	0	0	0	NaN
# Temp*RPM	0	0	0	0	NaN
# Temp*Offset	0	0	0	0	NaN
# Temp*IPM	0	0	0	0	NaN
LP*RPM	0.00375	1	0.00375	0.01	0.9059
# LP*Offset	0	0	0	0	NaN
LP*IPM	0.00375	1	0.00375	0.01	0.9059
# RPM*Offset	0	0	0	0	NaN
# RPM*IPM	0	0	0	0	NaN
# Offset*IPM	0	0	0	0	NaN
Error	4.16	16	0.26		
Total	7.57958	23			

Sequential (Type I) sums of squares. Terms marked with # are not full rank.

Figure 61: ANOVA Statistical Data for Porosity

Numerical results for the P-values were calculated to determine the significance of the output response on porosity for each input parameter, refer to Figure 61. Figure 61 also reinforced that traverse rate had the largest effect on porosity, followed by powder feed rate and preheat temperature. Laser power also plays a significant role, and vertical offset plays a minor role. Based on the data shown in Figure 60 and Figure 61, to minimize porosity the traverse rate and preheat temperature should be increased while powder feed rate should be lowered. Porosity was further reduced by increasing laser power and vertical offset distance. An example outgassing porosity was identified by the near circular spots, shown in Figure 62. Another type of porosity resulting from inadequate coating-to-substrate adhesion is provided in Figure 63 for reference. Although the two types were created through different mechanisms, neither are desirable and both can result in origins for fatigue failures.

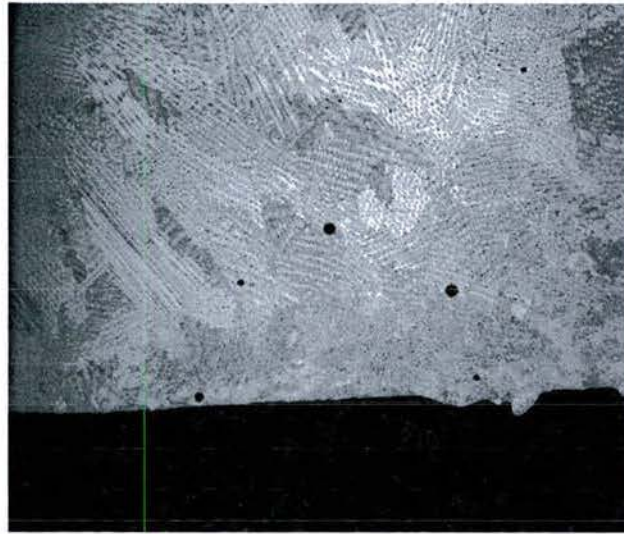


Figure 62: An example of an outgassing porous coating. 100x photo of a Group 4 sample.

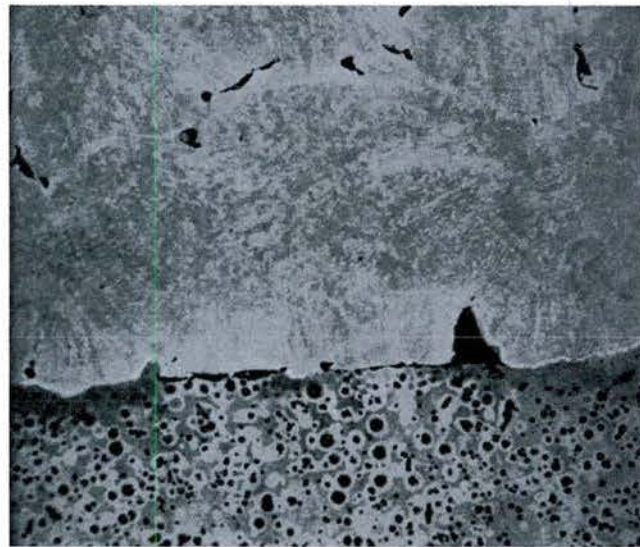


Figure 63: An example of a poor interface porous coating. 50x photo of a Group 5 sample.

Micrographs of all the specimens showed that most samples had minimal porosity due to outgassing. Significantly porous samples were mostly the result of poor interfacial bonding at the substrate and layer-to-layer voids. This suggested that the melt pool needed to be larger at the substrate, to allow for deeper penetration into the surface below the layer to be printed. The results showed that decreased porosity would occur from increased laser power and preheat temperature, while decreasing traverse and powder flow rates. Increasing preheat temperature would decrease the amount of heat transfer away from the active printing zone, while decreasing powder flow rate would decrease the amount of energy from the laser that goes into heating the powder, and let more energy go into creating the melt pool.

6.4.3 Hardness

Microhardness values were recorded and averaged to provide a final value for each specimen. The main effects were plotted, Figure 66, to show the correlation of each machine parameter on the hardness of the Grade 420 coating. From Figure 66, it was apparent that preheat temperature was significantly proportional to hardness, while laser power, powder feed rate, and vertical offset may be proportional to hardness, and traverse rate may be inversely proportional to hardness.

To check that Figure 66 was truly representative of the data set, some outlier data points were removed from the ANOVA analysis, and the results replotted, refer to Figure 67. Outliers may have resulted from voids that were under the surface and hidden from view in the cross section sample. Results from removing outliers reinforced preheat temperature, powder feed, and traverse rate's effect on hardness, but also indicated that laser power and vertical offset had minimal effect on hardness. Plots with removed outliers were also generated for efficiency and porosity, however no change to the initial trends were discovered.

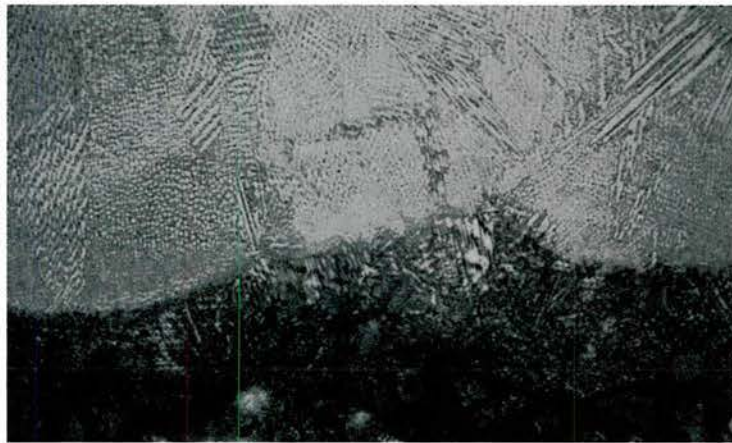


Figure 64 - Run 19 Highest Hardness, 100x



Figure 65 - Run 2, Lowest Hardness, 100x

P-values in Figure 68 reinforced that preheat temperature had the largest effect on hardness, followed by powder feed rate and traverse rate therefore to maximize hardness, preheat temperature and powder flow rate should be high while traverse rate should be low. This is caused by the grain formations that took place during deposition and subsequent cooling of the coating. As seen in Figure 64 and Figure 65, the specimens with columnar grains produce harder specimens.

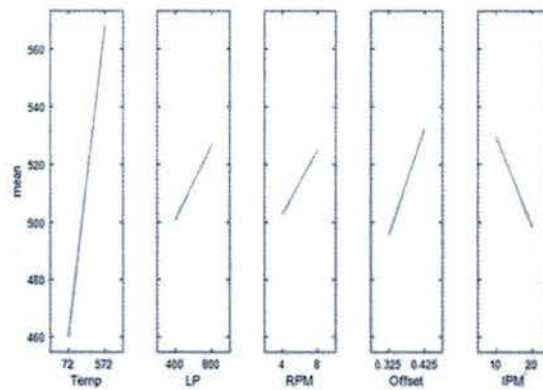


Figure 66: Hardness Main Effects Plot with Outliers

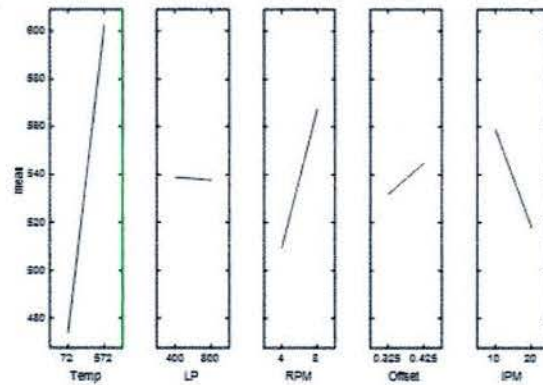


Figure 67: Hardness Main Effects with Removed Outliers

Source	Sum Sq.	d.f.	Mean Sq.	F	Prob>F
Temp	65963.4	1	65963.4	7.27	0.0272
LP	5.4	1	5.4	0	0.9811
RPM	13225	1	13225	1.46	0.2618
Offset	684.7	1	684.7	0.08	0.7905
IPM	6534	1	6534	0.72	0.4208
# Temp*LP	0	0	0	0	NaN
# Temp*RPM	0	0	0	0	NaN
# Temp*Offset	0	0	0	0	NaN
# Temp*IPM	0	0	0	0	NaN
LP*RPM	1444	1	1444	0.16	0.7004
# LP*Offset	0	0	0	0	NaN
LP*IPM	476.7	1	476.7	0.05	0.8245
# RPM*Offset	0	0	0	0	NaN
# RPM*IPM	0	0	0	0	NaN
# Offset*IPM	0	0	0	0	NaN
Error	72587.4	8	9073.4		
Total	160920.7	15			

Sequential (Type I) sums of squares. Terms marked with # are not full rank.

Figure 68: ANOVA Statistical Data for Hardness

6.4.4 Summary of the Ductile Iron Substrate DOE

Results for the DOE were compiled and integrated in to Table 31 to provide a complete picture of all the pros and cons related to increasing each machine parameter. A blue upward arrow represented a positive effect, while a red downward arrow represented an undesirable effect. For example, the blue arrow under Preheat temperature for porosity indicated a decrease in porosity given higher preheat temperature.

Table 31: Comparison of Effects of Machine Parameters on Performance Metrics

	Preheat Temperature	Laser Power	Powder Feed Rate	Vertical Offset	Traverse Rate
Efficiency	—	↑	—	↓	↓
Porosity	↑	↑	↓	↑	↑
Hardness	↑	—	↑	—	↓

From Table 31, it was apparent that most machine parameters had trade-offs in terms of improving or lowering performance metrics. It was clear that a high preheat temperature and laser power are desired since there are no measured downsides, however, modifications to the other machine parameters were not as clear.

6.4.5 Optimization for Wear

The end goal of this research was to understand the effect of the machine input parameters had on coating surfaces that could be employed for remanufacturing of wear surfaces. Based on the aforementioned results, it was decided that the substrate should be preheated to improve porosity and hardness, and laser power should be set at the upper level to improve porosity and deposition efficiency. However, to help select optimal levels for powder feed rate, vertical offset, and traverse rate, another performance metric was considered.

As mentioned before, an ideal coating process would not only result in a strong coating, but also be fast and efficient. Although deposition efficiency is considered, it does not take into account the amount of time a coating process would take in a production environment. An ideal coating process would be able to reach a target thickness with the least amount of layers and time. Thus, ANOVA analysis was also performed on build height data and plotted, refer to Figure 69. Results showed that powder flow rate was proportional to build height, and vertical offset and traverse rate were inversely proportional to build height. This is reinforced by the numerical data in Figure 70 below.

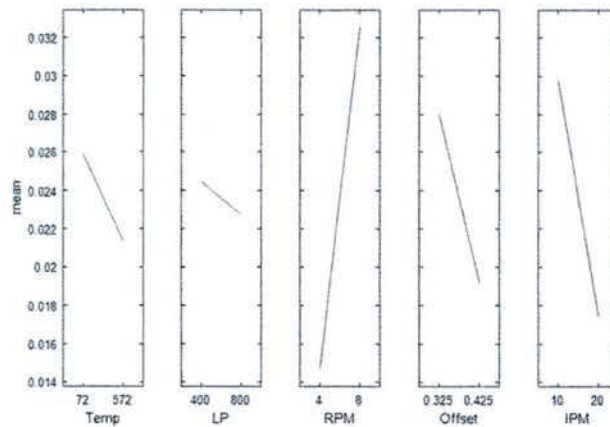


Figure 69: Build Height Main Effects Plot

Source	Sum Sq.	d.f.	Mean Sq.	F	Prob>F
Temp	0.00012	1	0.00012	1.37	0.2586
LP	0.00002	1	0.00002	0.19	0.6668
RPM	0.00192	1	0.00192	21.69	0.0003
Offset	0.00046	1	0.00046	5.24	0.036
IPM	0.00091	1	0.00091	10.25	0.0056
# Temp*LP	0	0	0	0	NaN
# Temp*RPM	0	0	0	0	NaN
# Temp*Offset	0	0	0	0	NaN
# Temp*IPM	0	0	0	0	NaN
LP*RPM	0.00015	1	0.00015	1.64	0.218
# LP*Offset	0	0	0	0	NaN
LP*IPM	0	1	0	0	0.9849
# RPM*Offset	0	0	0	0	NaN
# RPM*IPM	0	0	0	0	NaN
# Offset*IPM	0	0	0	0	NaN
Error	0.00142	16	0.00009		
Total	0.00499	23			

Sequential (Type I) sums of squares. Terms marked with # are not full rank.

Figure 70: ANOVA Statistical Data for Build Height

Thus, to optimize for a quicker coating as well as a hard, efficient, and an impermeable coating; a high powder feed rate, low vertical offset, and low traverse rate was selected as the initial parameter set for future tests, refer to Table 32.

Table 32: Initial Machine Parameter Levels for Ductile Iron Substrate

	Preheat Temperature	Laser Power	Powder Feed Rate	Vertical Offset	Traverse Rate
Level:	High	High	High	Low	Low

There was another factor considered with respect to this model of the Optomec Hybrid LENS machine. Although other models may differ, this specific model had challenges with clogging of its four powder delivery nozzles. During especially high heat processes like those with high laser power, there was a two in three chance that the print would stop due to clogging issues before completion of the three layered samples printed in the partial factorial experiment.

This effect is most likely caused by the copper nozzles heating up during printing, and metal powder sticking and building up inside the nozzles, causing a blockage in the powder flow. This blockage prevented flow of the argon gas and metal powder, both act as a method of cooling for the nozzles, and caused the nozzles to heat up even further which resulted in a buildup on the outside of the nozzle as well.

To minimize the heat buildup on the nozzle, either the heat generation needs to be reduced, or the cooling effects need to be amplified. Although the 400 Watt experiments kept the nozzle temperature lower and never clogged a nozzle, the higher laser power offered too many benefits to be reduced. The powder flow rate was increased, which caused a cooling effect on the nozzle temperature, thus slowing down or preventing nozzle clogging. The surface of the samples measured as high as 1000°F directly after printing, thus moving the nozzles further away by increasing the vertical offset should also decrease nozzle temperature.

To develop a coating process that consistently printed without clogging, the powder feed rate was increased from 8 RPM to 12 RPM, and vertical offset was set as 0.425 inches instead of 0.325 inches. Refer to Table 33 for the final parameters employed.

Table 33: Revised Optimal Settings

	Preheat Temperature	Laser Power	Powder Feed Rate	Vertical Offset	Traverse Rate
Level:	572F	800W	12 RPM	0.425 in	10 IPM

These settings were successful in mitigating clogging, and were selected as the optimal settings for samples to be used in the subsequent wear testing. The settings resulted in an efficiency of 26%, a hardness value of 58 Rockwell C, a porosity of 3%, and a build height of 0.080 inches per layer on average. Refer to **Figure 71** for an image of the microstructure produced using the optimal settings. Although increasing the powder feed rate did increase the porosity, the resulting fatigue strength of the coating was within the requirements discussed later in this report.

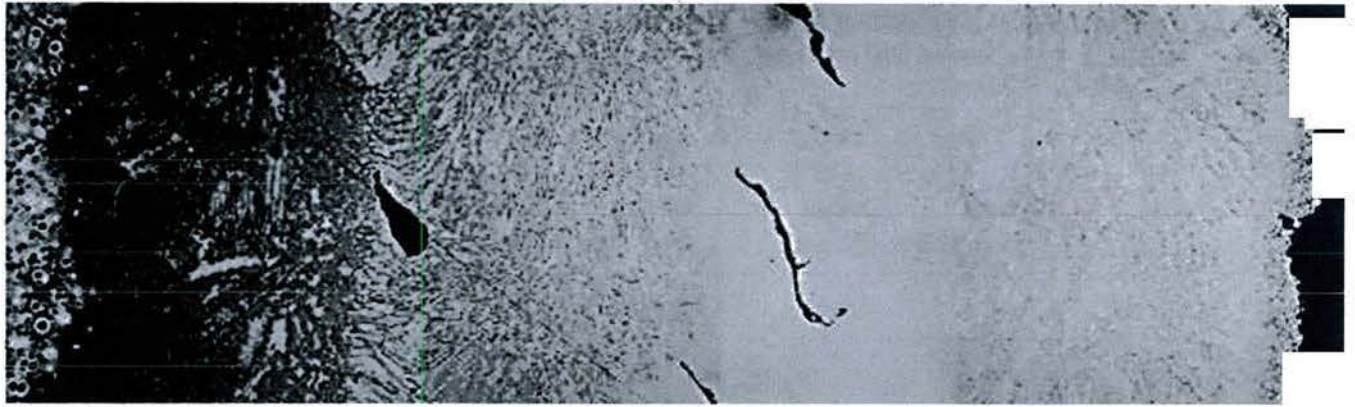


Figure 71: Microstructure of Optimal Coating on Ductile Iron Substrate- Substrate on the Left

6.5 DOE Results and Discussion for 9310H Alloy Steel Substrate

6.5.1 Design of Experiments

An experiment based on a 2^3 full factorial design in randomized order is shown below in Table 35. This experiment takes the knowledge gained from the previous experiment of 420 Stainless Steel coating on 80-55-06 Durabar Ductile Iron substrate, and applies it to a similar experiment on 9310H Alloy Steel substrate.

Table 34: Randomized Partial Factorial Design for 9310H Alloy Steel Experiments

Run #	Laser Power (W)	Offset Distance (in)	Substrate Temperature (°F)	Powder Flow (RPM)	Traverse Rate (in/min)
1	800	0.425	300	14	15
2	800	0.425	72	16	20
3	800	0.425	72	12	10
4	800	0.425	572	12	10
5	800	0.425	572	12	10
6	800	0.425	72	12	20
7	800	0.425	572	16	10
8	800	0.425	72	16	10
9	800	0.425	572	16	20
10	800	0.425	72	16	10
11	800	0.425	72	12	10
12	800	0.425	72	12	20
13	800	0.425	72	12	10
14	800	0.425	300	14	15
15	800	0.425	72	16	20
16	800	0.425	572	16	10
17	800	0.425	572	12	20
18	800	0.425	72	12	20
19	800	0.425	572	12	20
20	800	0.425	572	12	10
21	800	0.425	572	16	10
22	800	0.425	572	16	20
23	800	0.425	72	16	10
24	800	0.425	572	12	20
25	800	0.425	72	16	20
26	800	0.425	572	16	20
27	800	0.425	300	14	15

From the previous experiment, it was revealed that 800 Watt laser power provides the deposition efficiency and porosity that was needed. A higher vertical offset moves the nozzles away from heat from the surface of the sample to lower chances of clogging. Powder flow rate was increased in the previous experiment to increase build height and also prevent clogging. Thus, in this experiment, laser power is fixed at 800 Watts and vertical offset is fixed at 0.425 inches. This allows for a full factorial experiment focusing on a smaller set of machine parameters. Powder flow rate is increased to a range from 12 RPM to 16 RPM, to provide a more focused set of data within bounds that provide the desired thicknesses, while also preventing clogging. Preheat temperature and traverse rate bounds are kept the same from the previous experiment to show how results may differ between substrates.

Similarly, with the previous experiment, three samples will be printed for each experiment, each with three layers of coating. Deposition efficiency, porosity, hardness, and build height will be measured and recorded for ANOVA analysis.

6.5.2 Results

Table 35: Results from 9310H Alloy Steel Experiments

Group	ID	Substrate Temperature (°F)	Laser Power (W)	Powder Flow (RPM)	Offset Distance (in.)	Traverse Rate (in/min)	Efficiency	Build Rate (in3/min)	Build Height (in/layer)	Hardness (HRC)	Total Porosity (%)
1	S3	72	800	12	0.425	10	0.2257	0.026	0.085	56.0	6
1	S11	72	800	12	0.425	10	0.1883	0.021	0.067	55.8	4
1	S13	72	800	12	0.425	10	0.1850	0.022	0.070	54.7	3
2	S6	72	800	12	0.425	20	0.0931	0.010	0.023	56.3	0
2	S12	72	800	12	0.425	20	0.0695	0.007	0.016	55.8	0
2	S18	72	800	12	0.425	20	0.0716	0.009	0.020	55.3	0
3	S8	72	800	16	0.425	10	0.1994	0.030	0.093	54.1	5
3	S10	72	800	16	0.425	10	0.1901	0.029	0.090	55.0	7
3	S23	72	800	16	0.425	10	0.1855	0.030	0.090	53.9	5
4	S2	72	800	16	0.425	20	0.1653	0.025	0.057	55.6	5
4	S15	72	800	16	0.425	20	0.0992	0.015	0.035	55.8	1
4	S25	72	800	16	0.425	20	0.0973	0.014	0.031	56.7	5
5	S1	300	800	14	0.425	15	0.2188	0.030	0.079	55.0	5
5	S14	300	800	14	0.425	15	0.2158	0.030	0.077	54.8	5
5	S27	300	800	14	0.425	15	0.2145	0.029	0.076	55.5	5
6	S4	572	800	12	0.425	10	0.2274	0.027	0.086	54.1	5
6	S5	572	800	12	0.425	10	0.2250	0.027	0.086	53.6	4
6	S20	572	800	12	0.425	10	0.1725	0.021	0.067	56.5	2
7	S17	572	800	12	0.425	20	0.0785	0.009	0.020	54.4	0
7	S19	572	800	12	0.425	20	0.0698	0.008	0.018	55.8	0
7	S24	572	800	12	0.425	20	0.0976	0.011	0.026	57.4	0
8	S7	572	800	16	0.425	10	0.2036	0.031	0.093	55.0	6
8	S16	572	800	16	0.425	10	0.2007	0.032	0.097	55.2	6
8	S21	572	800	16	0.425	10	0.1920	0.031	0.094	54.1	5
9	S9	572	800	16	0.425	20	0.1330	0.020	0.046	55.8	2
9	S22	572	800	16	0.425	20	0.1079	0.015	0.035	54.9	2
9	S26	572	800	16	0.425	20	0.1026	0.014	0.033	56.5	0
Optimal	800201442572	72	800	14	0.425	20	0.0952	0.012	0.025	56.5	0

Results from the full factorial experiment on 9310H Alloy Steel are shown above in Table 35. The final line shows data for the optimal settings chosen at the end of this experiment. Once again, MATLAB's ANOVA analysis was used to plot the main effects of each machine parameter, as well as statistical data on their effects.

6.5.2.1 Deposition Efficiency

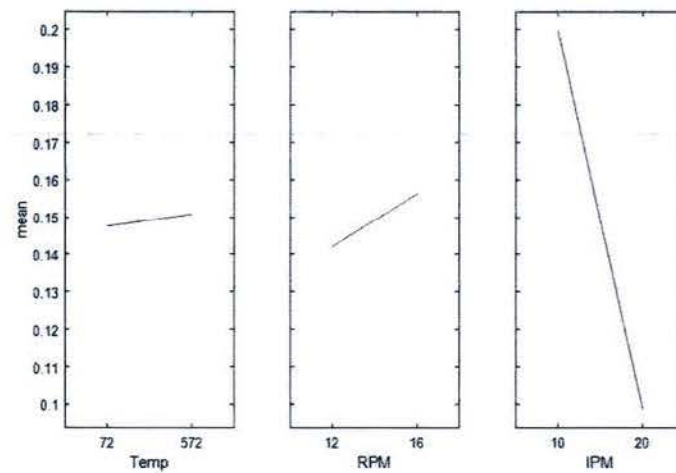


Figure 72: Efficiency Main Effects Plot

Figure 72 above shows a plot representing the effect each machine parameter has on the efficiency of the coating. From Figure 72, it is apparent that powder feed rate is proportional to efficiency, while traverse rate is significantly inversely proportional to efficiency. Preheat temperature does not play as significant a role.

Similarly, the ANOVA analysis in Figure 73 confirms that traverse rate, with a P-value of 0, has a very large effect on efficiency. Powder feed rate also plays a significant effect, with a P-value of 0.11. Preheat temperature is relatively insignificant.

Source	Sum Sq.	d.f.	Mean Sq.	F	Prob>F
Temp	0.00007	1	0.00007	0.16	0.6974
RPM	0.00124	1	0.00124	2.84	0.11
IPM	0.06097	1	0.06097	139.68	0
Temp*RPM	0.00005	1	0.00005	0.12	0.7385
Temp*IPM	0.00012	1	0.00012	0.28	0.6063
RPM*IPM	0.00322	1	0.00322	7.37	0.0147
Error	0.00742	17	0.00044		
Total	0.07309	23			

Sequential (Type I) sums of squares.

Figure 73: ANOVA Statistical Data for Efficiency

6.5.2.2 Porosity

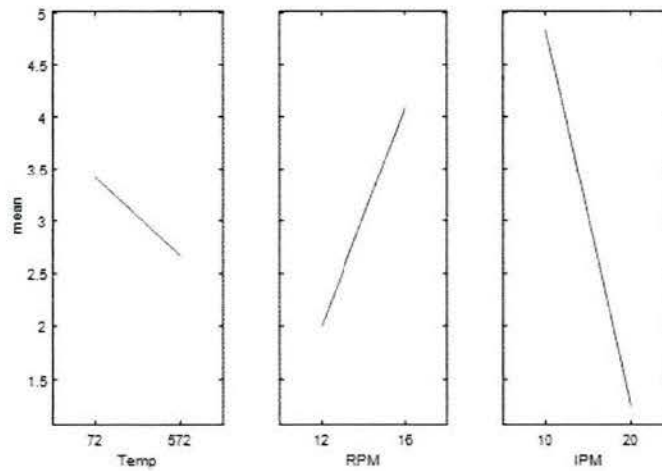


Figure 74: Porosity Main Effects Plot

Figure 74 above shows a plot representing the effect each machine parameter has on porosity of the coating. From Figure 74, it is apparent that traverse rate is significantly inversely proportional to percent porosity, while preheat temperature is also inversely proportional to a lesser degree and powder feed rate is proportional.

Figure 75 reinforces that traverse rate has a very large effect on porosity, once again showing a P-value of 0. Preheat temperature is also significant with a P-value of 0.0012. Powder feed rate, though slightly less significant with a P-value of 0.1802, still has a significant impact on porosity.

Analysis of Variance					
Source	Sum Sq.	d.f.	Mean Sq.	F	Prob>F
Temp	3.375	1	3.375	1.95	0.1802
RPM	26.042	1	26.0417	15.07	0.0012
IPM	77.042	1	77.0417	44.59	0
Temp*RPM	1.042	1	1.0417	0.6	0.4482
Temp*IPM	1.042	1	1.0417	0.6	0.4482
RPM*IPM	1.042	1	1.0417	0.6	0.4482
Error	29.375	17	1.7279		
Total	138.958	23			

Sequential (Type I) sums of squares.

Figure 75: ANOVA Statistical Data for Porosity

6.5.2.3 Hardness

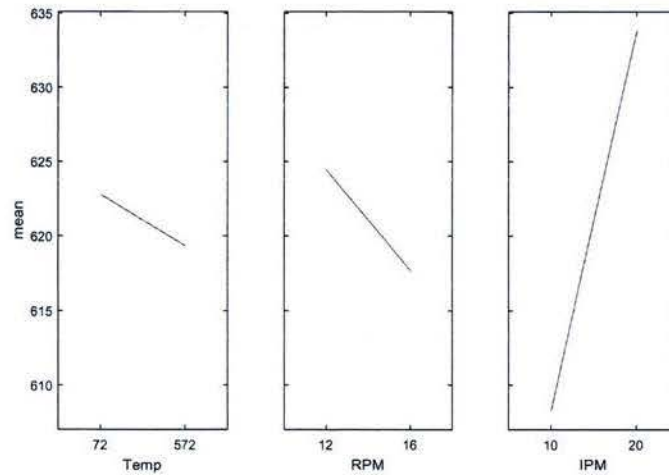


Figure 76: Hardness Main Effects Plot

Figure 76 above shows a plot representing the effect each machine parameter has on the hardness of the coating. Although traverse rate is shown to have the largest effect, note that it only varies hardness by about 20 HV. Preheat temperature and powder feed rate have insignificant effects on hardness.

Similarly, the ANOVA analysis in Figure 77 shows that traverse rate is the only factor with significant impacts on hardness with a P-value of 0.0168.

Analysis of Variance					
Source	Sum Sq.	d.f.	Mean Sq.	F	Prob>F
Temp	71.2	1	71.19	0.13	0.7251
RPM	275.6	1	275.63	0.49	0.4913
IPM	3912.8	1	3912.84	7.02	0.0168
Temp*RPM	156.7	1	156.74	0.28	0.6027
Temp*IPM	4.5	1	4.55	0.01	0.9291
RPM*IPM	368.2	1	368.17	0.66	0.4275
Error	9469.8	17	557.05		
Total	14258.9	23			

Sequential (Type I) sums of squares.

Figure 77: ANOVA Statistical Data for Hardness

6.5.2.4 Build Height

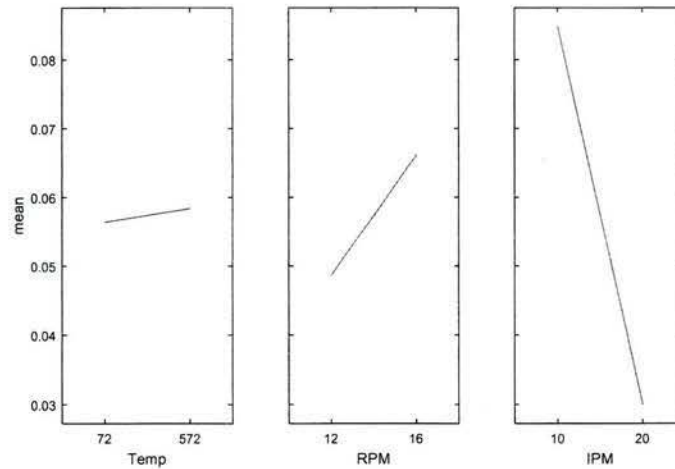


Figure 78: Build Height Main Effects Plot

Figure 78 and Figure 79 show that with slower traverse rates and higher powder feed rates, the coatings get thicker. Substrate temperature had an insignificant impact on build height.

Analysis of Variance					
Source	Sum Sq.	d.f.	Mean Sq.	F	Prob>F
Temp	0.00002	1	0.00002	0.41	0.5315
RPM	0.00184	1	0.00184	31.01	0
IPM	0.01803	1	0.01803	304.04	0
Temp*RPM	0.00001	1	0.00001	0.23	0.6375
Temp*IPM	0.00004	1	0.00004	0.75	0.3973
RPM*IPM	0.00001	1	0.00001	0.21	0.6536
Error	0.00101	17	0.00006		
Total	0.02098	23			

Sequential (Type I) sums of squares.

Figure 79: ANOVA Statistical Data for Build Height

6.5.2.5 Summary of the 9310H Substrate DOE

Table 36: Comparison of Effects of Machine Parameters on Performance Metrics

	Preheat Temperature	Powder Feed Rate	Traverse Rate
Efficiency	—	↑	↓
Porosity	↑	↓	↑
Hardness	—	—	↑
Build Height	—	↑	↓

To summarize the results from the ANOVA studies on the experiments performed on the 9310H Alloy Steel substrates, Table 36 shows how each machine parameter affects each performance metric. Comparing this with the results of the ductile iron study shown in Table 31, it is clear that the type of substrate used has a significant effect on the coating process.

Table 37: Thermal Material Properties of Substrates and Powder

	Density (g/cc)	Thermal Conductivity (W/mK)	Specific Heat Capacity (J/gC)	Melting Point (degC)
Ductile Iron	6.64-7.20	24.2	0.506	1120
9310H Steel	7.85	51.9	0.472	1427
420 SS	7.80	24.9	0.460	1454-1510

Table 37 compares the thermal material properties of the ductile iron and 9310H steel substrates, and the 420 stainless steel powder. Most properties are similar but the thermal conductivity of the steel substrate was more than twice that of the ductile iron substrate. This difference resulted in heat from the laser more quickly conducting through the rest of the substrate resulting in lower temperatures in the localized area of the contact from the laser. Lower localized temperatures result in smaller melt pools, subsequently lowering deposition efficiencies and porosity. This is evident in the results in Table 36.

6.5.2.6 Optimization for Wear

Although preheating the substrates improves porosity, the effect is small and there are no improvements to any other metric. It was determined that the amount of time and preparation it takes to preheat was not worth the benefits it brought.

Even so, from Table 35, it can be seen that the samples from these experiments are much more porous than those from the ductile iron experiments. The higher powder feed rates used in these experiments are cooling

the part such that the laser is not creating an efficient melt pool. Although this allows for the build heights that are desired, it does decrease the deposition efficiency and causes the large voids shown in an example photo in Figure 80. To reduce this effect, traverse rate can be increased, improving both porosity and hardness. This is especially beneficial since traverse rate is the only factor that affects hardness.

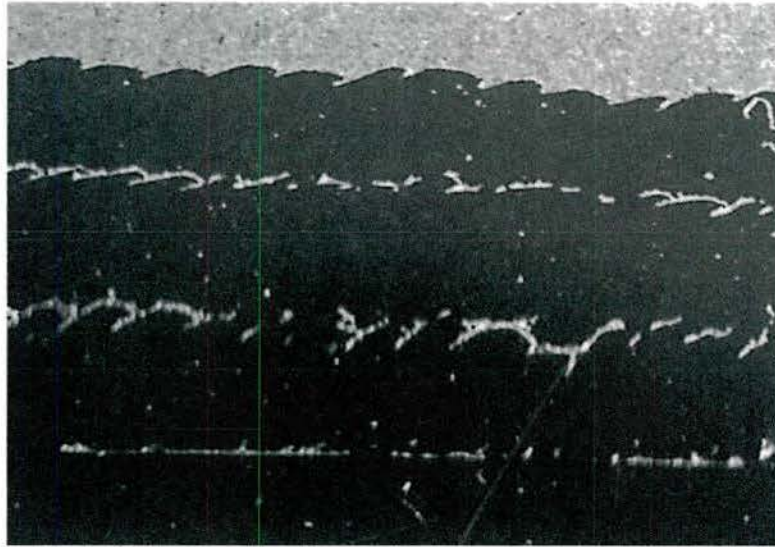


Figure 80: 10x photo of a Group 2 photo showing large voids between layers.

Although high powder feed rate has a negative effect on porosity, it is needed to prevent clogging and provide the build height required to make the process viable for remanufacturing. However, the interlayer and interfacial voids shown in Figure 80 are not acceptable for a strong coating.

Among the samples printed in this full factorial experiment, Group 2 and Group 7 have no porosity. They also have the high traverse rate which had been determined to be optimal. Images of samples from Group 2 and Group 7 are shown in Figure 81 and Figure 82.

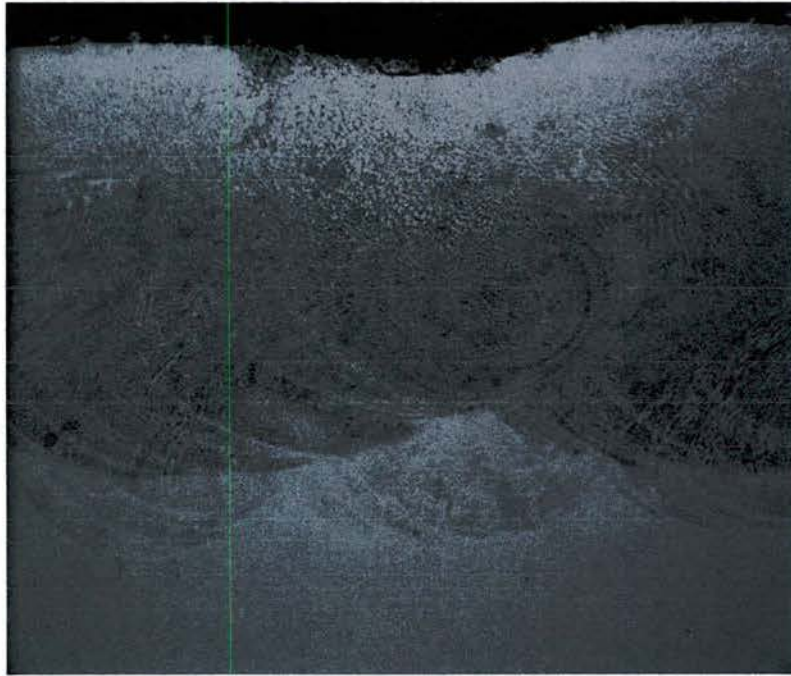


Figure 81: 50x photo of the microstructure of a Group 2 sample.

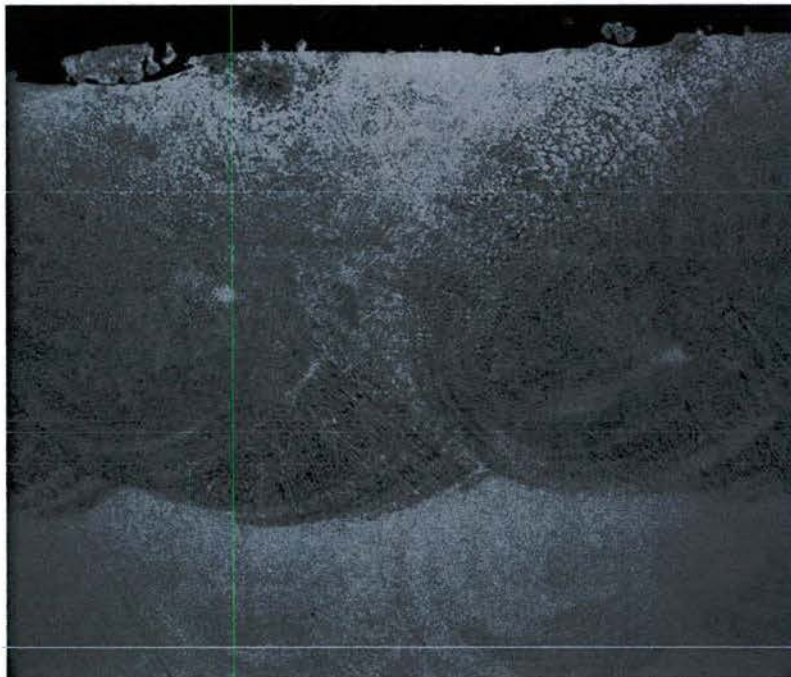


Figure 82: 50x photo of the microstructure of a Group 7 sample.

The microstructure looks uniform and there are no obvious signs of porosity. The only setting that differs between the two groups is powder feed rate and preheat temperature. It was decided that preheat

temperature would be kept as room temperature to save time and preparation work. Powder feed rate was set to the nominal value of 14 RPM.

Table 38: Optimal Settings for 420SS on 9310H Alloy Steel Substrate

	Preheat Temperature	Laser Power	Powder Feed Rate	Vertical Offset	Traverse Rate
Level:	72F	800W	14 RPM	0.425 in	20 IPM

These settings produced a nonporous coating with a hardness of 57 Rockwell C, average layer height of 0.012 inches, at a deposition efficiency of 9.5%. An image of the sample's microstructure is shown in Figure 83.



Figure 83: 50x image of optimal settings for 9310H Alloy Steel

Compared with the optimal settings from the ductile iron experiment, those of the 9310H steel produced thinner coatings much less efficiently. Putting these processes into a remanufacturing setting, the ductile

iron parameters may be able to produce a thick coating with one layer, however subsequent layers would have interlayer porosity. The steel settings would produce nonporous coatings inconsequential of number of layers printed, but would require more layers and time to reach the same thickness.

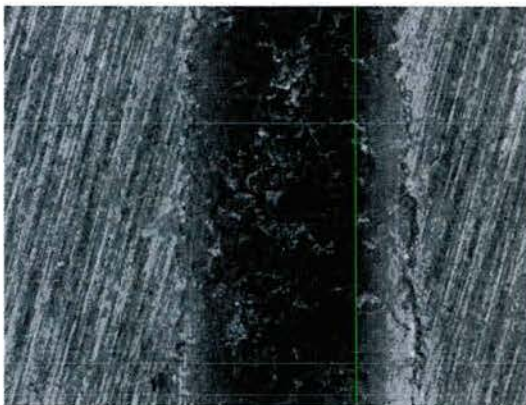
6.6 Further Measurements on optimal Coatings

Upon selection of the optimal parameter sets for steel (Section 6.5.2.6) and ductile iron substrates (Section 6.4.5) to be used in remanufacturing wear surfaces with the LENS machine, additional testing was performed to verify the robustness of the coating. Tests for the wear resistance and tensile strength were performed to expand on the mechanical properties of the coatings and compare them to typical needs in the remanufacturing industry.

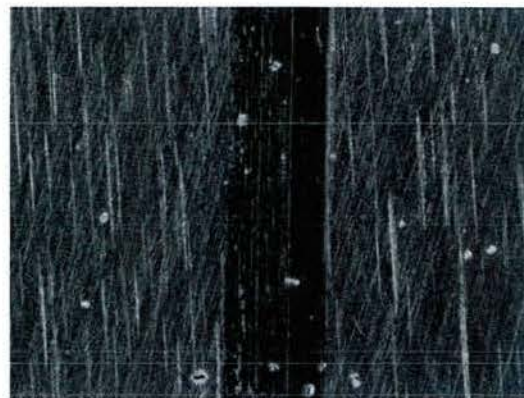
6.6.1 Wear Resistance

Twelve (12) specimens were produced for wear resistance testing. Three specimens were produced for each specimen type: 1) Grade 420 coated on ductile iron substrate 2) Grade 420 coated on 9310H Alloy Steel substrate. Uncoated ductile iron and 9310H steel provided the baseline for this wear testing. The test procedure was based on the ASTM specification and was performed per the process described in Section 3.3 in order to develop comparative wear relationships between material options. Optical photographs were captured along with wear scar measurements to provide a comparison between the substrates and the coating. For this testing, both brass and steel balls were used. The Figure 84 through Figure 87 showed that the wear resistance of the coatings was superior to both of the substrate materials.

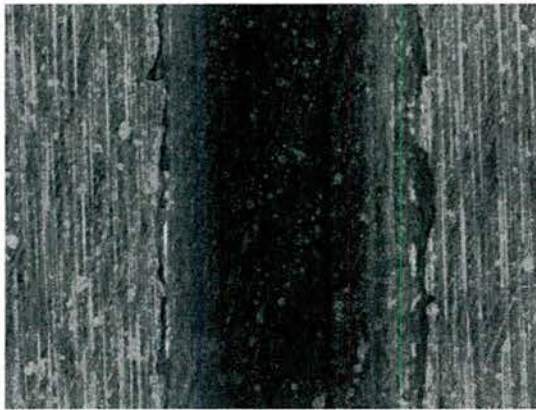
Figure 84 shows that a wider wear scar developed on the uncoated ductile iron and 9310H specimens compared to the Grade 420 coated ductile iron and 9310H specimens.



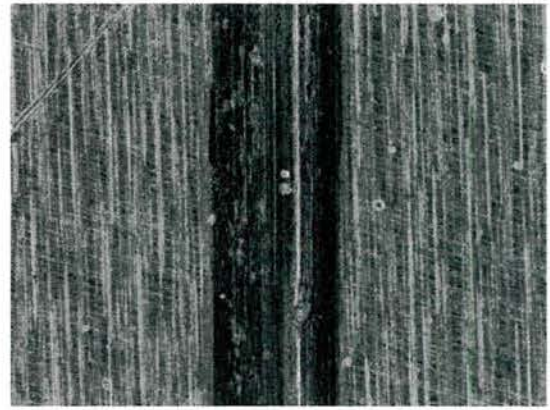
Steel Ball on Ductile Iron



Steel Ball on 420 Coated Ductile Iron



Steel Ball on 9310H



Steel Ball on 420 Coated 9310

Figure 84: Optical Photographs of Wear Scars

The volume of material removed from the balls and pucks was determined to allow for a quantitative comparison between the specimens (refer to Figure 85, Figure 86, and Figure 87). The results showed that there was virtually no wear on the uncoated and 420-coated specimens. However, the softer brass balls exhibited the wear while transferring only enough material to stain the surface of the pucks. Brass balls on 9310H showed the least wear while the greatest wear occurred on the Grade 420 material on 9310H substrates. In Figure 85 the brass ball material wear was also measured to understand the effect that material/process change has on the wear rate and maintenance cycle of mating brass components. The volume removed from the brass balls against Grade 420 on ductile iron was similar in value to bare 9310H. As the hardness values for all the Grade 420 coatings were nearly identical and higher than the bare substrates, the wear differences were attributed to surface finish or microstructure of the specimens.

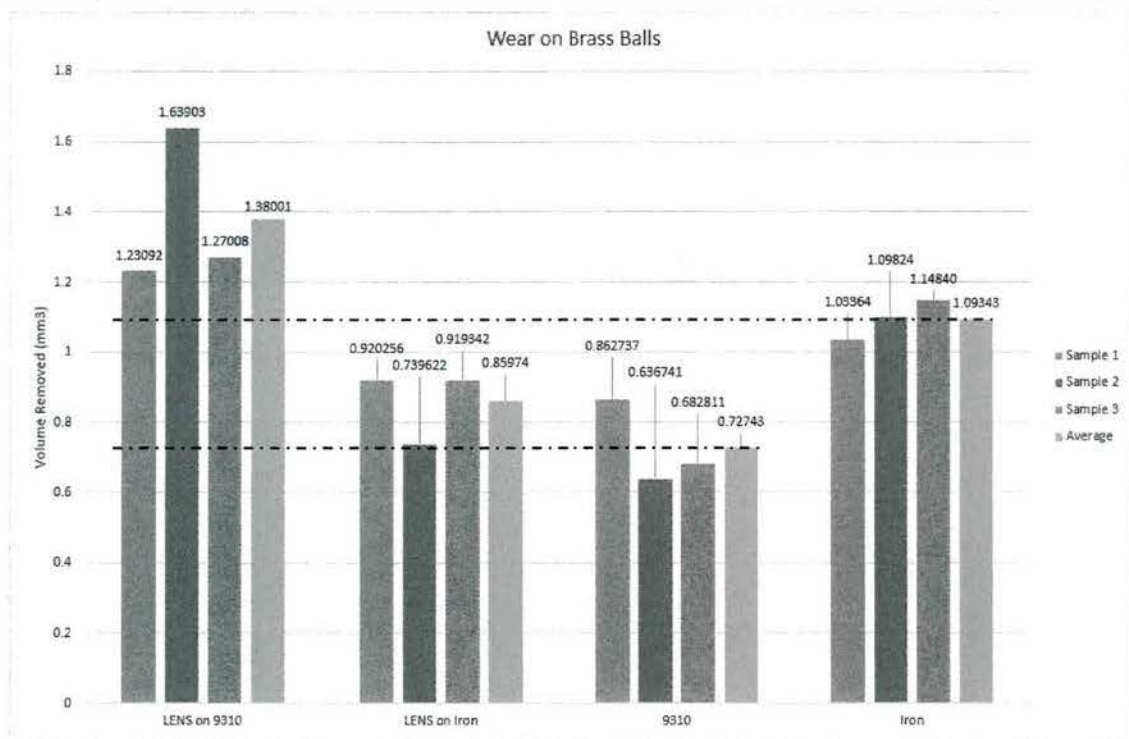


Figure 85: Graph showing volume removed on brass balls through wear testing of samples

Wear of the steel balls showed the opposite to that of the brass balls with the uncoated ductile iron and 9310H specimens exhibiting the greatest amount of wear. The wear of the specimens mirrored the wear results of the steel balls with the bare ductile iron and 9310H materials losing almost four times more material than the Grade 420 on ductile iron and 9310H. The higher wear on the uncoated substrates was due to the difference in hardness between the uncoated specimens and 420 coated specimens. Rockwell C hardness was near 57 HRC for both Grade 420 coatings compared to the 21 HRC for both substrate materials. The greater wear on the balls was probably the result of 3-body wear. Figure 84 shows the wear scars on the uncoated specimens were more jagged and wider than the 420 coated specimens. Thus, during the wear testing debris from the breakdown of the uncoated specimens was brought in the wear interface thereby changing the wear mode from polishing to 3- body wear. 3-body wear is more severe than polishing wear[74].

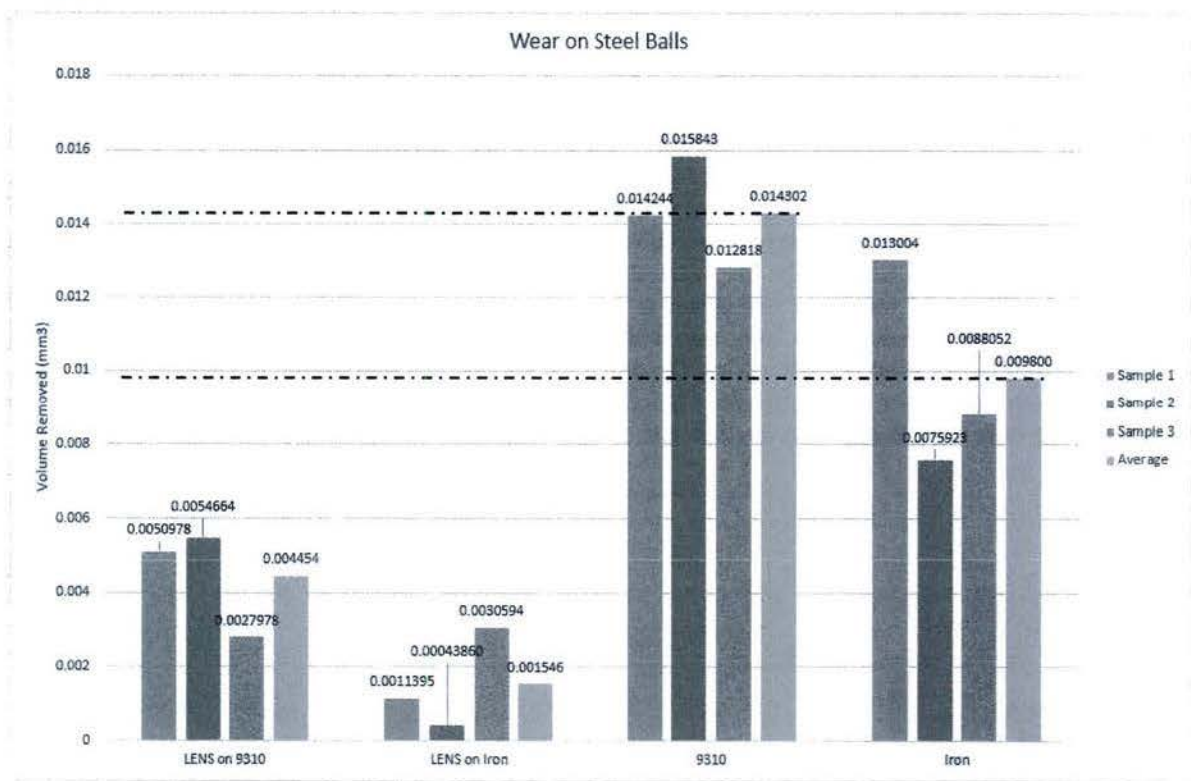


Figure 86: Graph showing volume removed on steel balls through wear testing of samples

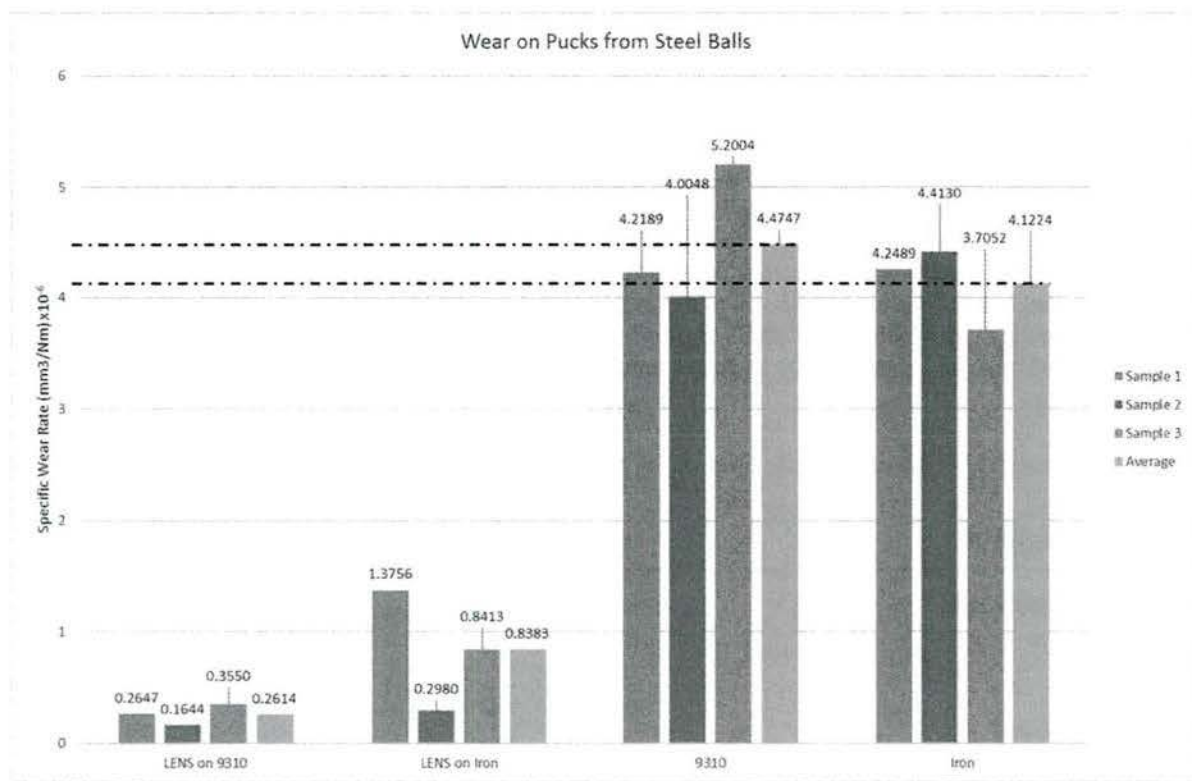


Figure 87: Graph showing wear rate of coatings and substrate benchmarks from wear testing

6.6.2 Tensile Strength

The tensile strength of the coating was a key mechanical property to understand the applicability of the LENS process for remanufacturing wear surfaces. Applications for remanufacturing that have components that witness significant stresses during operation require high intra-coating strength to prevent cracking in the Grade 420 material. To determine the properties of the optimally coated specimens, tensile samples were cut from the 420SS coating material, using wire EDM, that were printed on 5" diameter ductile iron and 9310H steel pucks. The specimens were machined and polished before testing on the Instron test system until failure, and the ultimate tensile strength was recorded, refer to Table 39.

Table 39: Ultimate Tensile Strengths of Optimal Coatings removed from Iron and Steel Substrates

	Sample 1 (ksi)	Sample 2 (ksi)	Sample 3 (ksi)	Average (ksi)
420SS Coating from Iron Substrate	83	97	60	80
420SS Coating from Steel Substrate	149	135	130	138

The steel substrate optimal coatings have significantly higher tensile strengths than that of the iron substrate optimal coatings. This difference in tensile strengths is most likely due to the iron substrate coatings' interlayer porosity, as seen in Figure 88 (particularly on sample IV), and thermal conductivity of the

substrate. The iron substrate coating is meant to be applied in a single pass to prevent interlayer porosity. However, in order to make the tensile specimens, multiple layers were applied. This likely decreased the tensile strength of the coating. It is expected that the 420 SS coating applied to iron in a single pass would perform significantly better in the field.

Comparing the average ultimate tensile strengths of the coatings from Table 39 to the published values for the substrate material in Table 40, the ductile iron and the coating removed from the ductile iron achieved the same strength. However, the 420 SS coating on the 9310H was significantly stronger than the 9310H substrate by 15%. Additionally, the 420 SS coating from the ductile iron substrate was weaker than the published values for annealed 420 SS, once again pointing toward the porosity as slightly weakening the material properties. However, the 420 SS applied to the 9310 alloy steel has a 45% higher strength than the annealed 420 SS, but significantly less than hardened 420 SS.

Table 40: Ultimate Tensile Strength of the Substrate Materials and Stainless Steel

Substrate Material	Published Tensile Strength (ksi)
80-55-06 Ductile Iron	80
9310H	119
420 SS Annealed	95
420 SS Hardened & stress relieved	229



Figure 88: Tensile testing of coatings

6.7 Conclusions

Results were compared to observe the effects substrate properties had on performance. It was found that substrate properties had a significant effect on the properties of the coating. The thermal properties of the substrate combined with the volume and shape of the substrate to impact performance. The ductile iron substrate samples built more efficiently than the 9310H alloy steel substrate samples because a larger weld pool was able to be maintained. Consequently, the two sets of samples also had different resulting optimal settings as well. It was found that the optimal settings for ductile iron were 800W laser power, 10 inches/min traverse rate, 0.2302 grams/second powder feed rate, 0.425 inches vertical offset, and 572°F substrate preheat temperature. The corresponding optimal settings for 9310H alloy steel were 800W, 20ipm, 0.2676 g/s, 0.425 inches, and 72°F. The layer thicknesses processed with the optimized processes for ductile iron and steel were 0.080" and 0.025" respectively.

The strength of the 420 SS coatings was determined to be equal to or slightly greater than the substrate materials. Wear resistance of the coatings, compared to the virgin substrates, showed increased benefit from the coating, however, mating bronze components may wear quicker in machine assemblies based on the data. Overall, the optimized process parameters developed through this research on the LENS machine provide the opportunity to remanufacturing components that have experienced wear using a robust coating process.

7 Overall Research Conclusions

The goal of this research was to identify the optimal coating solutions for the dimensional restoration of 8055-06 ductile iron castings and 9310H gear or shaft seal surfaces. Evaluation of three different additive manufacturing technologies (twin wire arc thermal spray, low pressure cold gas dynamic spray, and laser metal deposition) was performed after conducting an additive material trade study. The trade study identified Grade 420 Stainless Steel as the material that would provide the closest material properties to both the ductile iron and 9310 substrates. 420 SS was also available in both wire and powder forms for testing in all three processes.

The twin-wire arc thermal spray process was optimized on both substrates. For both substrates, twin wire arc provided consistent adhesion values of approximately 8300 psi or more. Coating hardness was measured at 287 or higher on the Vickers scale, which equates to a Rockwell B of 104 or higher. This is slightly higher than the values for both substrate materials. All specimens showed low porosity in the coatings. The 420 SS coatings however showed significantly more wear during tests with a steel ball bearing. The increase in wear is attributed to several factors: 1) porosity and oxides in the material cause the initial fracture of the coatings, 2) the coating cohesion strength is reasonably low, and 3) once the fractures begin to occur, debris particles cause three body wear and increase wear rates. In wear tests with a brass ball, the coating showed no signs of wear, but the wear on the brass balls increased when compared to the substrate materials. Once again, the porosity and oxides in the 420 SS coating impact the wear rates of the brass balls.

The cold spray experiments were designed to evaluate the potential for applying 420 SS to the substrates. Cold spray has typically been used with softer materials. After preliminary testing with Aluminum-Aluminum Oxide and Tungsten Carbide coatings, RIT theorized that application of 420 SSS would require a softer binder material to adhere to the substrates. RIT designed four experiments utilizing high and low mass fractions of Nickel-Aluminum and Copper as separate binder materials. RIT was unsuccessful in applying any combination of Nickel-aluminum and 420 Stainless steel through cold spray. Alternatively, utilizing Copper as a binder, RIT made limited progress in applying 420 Stainless Steel. The Cu-420SS blends adhered with limited success. These coatings showed significant porosity and some oxidation. As additional passes were executed beyond the first pass, the porosity of the coatings worsened. Although RIT

experienced limited success in applying 420 SS, the research identified further areas for evaluation including: Investigation of other novel blends, for example, cermet or ceramic metal blends containing 420 SS, and Determining the effects of annealing or tempering 420 SS powders on coatings.

The Laser Deposition (LENS) process was optimized for both substrates utilizing 420 SS powders. It was found that the substrate thermal properties had a significant impact on the optimal process settings for applying the 420 stainless steel. Therefore application parameters are significantly different between substrates. On 80-55-06 ductile iron, coating hardness was measured at 56.5 Rockwell C, which is significantly higher than the substrate which is measured at 98 Rockwell B scale (approximately 21 Rockwell C) Porosity can be kept to a minimum in single layer applications, which was measured at 0.080" for the optimal settings. The ultimate tensile strength of the 420SS coating on ductile iron was measured at 80 ksi, which matches the strength of the 80-55-06 ductile iron. During wear testing with brass balls, the brass wear was slightly less against the 420SS compared to the ductile iron. Wear testing with a hardened steel ball showed that the coated material and the ball showed significantly less wear when compared to the hardened steel ball against the ductile iron. These results indicate that the LENS process could be utilized for dimensional restoration of 80-55-06 ductile iron components used in sliding wear applications.

For the 9310H substrate, the 420 SS coating hardness was also measures at 56.5 Rockwell C, which is also higher than 9310H at approximately 21 Rockwell C (conversion from 241 HB). Porosity of the coating on 9310H was very low and was not impacted by interlayer porosity. The ultimate tensile strength of the 420SS coating on 9310H was measures at 138 ksi, which is 15% higher than the strength of the 9310H (119 ksi). During wear testing, wear of the brass balls against the 420 SS coating was slightly higher than that of the brass against the 9310H substrate. However, wear testing with steel balls showed significantly lower wear rates for both the steel and coating when compared to the results of testing with a steel ball against 9310H. The lower wear rates can be attributed to an oxide free, dense coating with no porosity. These results indicate that the LENS process could be utilized for dimensional restoration of 9310H alloy components used in wear applications.

When comparing the processes against the components that informed the substrate material selection, the twin-wire arc 420 stainless steel coatings may present a problem for the 8055-06 ductile casting due to the high surface stresses mentioned in Section 2.1. The laser deposition process can apply a durable coating that is resistant to wear and can handle the surface stresses that the component will incur. For the 9310H gear shaft, the wear surface is on a rubber seal. One of the most important characteristic of this surface is the ability to maintain a seal, which is impacted by the porosity of the coating. The 420SS coating applied with the twin-wire arc process to the 9310H substrates exhibited low porosity and is believed to be a simpler, more cost effective repair method for this application.

8 References

- [1] S. Morefield, S. Drozd, V. F. Hock, and W. Abbott, "Measuring Rates and Impact of Corrosion on DOD Equipment," *Advanced Materials Research*, vol. 38, pp. 163-181, 2008.
- [2] G. K. Nikas, "A state-of-the-art review on the effects of particulate contamination and related topics in machine-element contacts," *Proceedings of the Institution of Mechanical Engineers, Part J: Journal of Engineering Tribology*, vol. 224, pp. 453-479, 2010.
- [3] (2017, May 4, 2017). *Aluminum Crack Repair Without Welding*. Available: http://www.locknstitch.com/pdf/aluminum_crack_repair_new.pdf
- [4] (2017, May 4, 2017). *Anyone Can Repair Aluminum and Cast Quickly and Easily with HTS-2000 Brazing Rods*. Available: www.aluminumrepair.com/aluminum_repair.asp
- [5] (2017, May 4, 2017). *Epoxy fill products*. Available: <http://www.alvinproducts.com/Product-Line>
- [6] Moog. (2012, May 4, 2017). *Advanced Surface Repair Capabilities*. Available: http://www.midamericaaviation.com/literature/MidAmerica/Mid_America_Aviation_AG_Cold_Spray_Brochure_Sp_Sep12_S.pdf
- [7] "ASTM E3-11 Standard Guide for Preparation of Metallographic Specimens," ASTM International, West Conshohocken, PA2011.
- [8] "ASTM E1920-03(2014) Standard Guide for Metallographic Preparation of Thermal Sprayed Coatings," ASTM International2014.
- [9] "ASTM E384-16 Standard Test Method for Microindentation Hardness of Materials," ASTM International, West Conshohocken, PA2016.
- [10] "ASTM D4541-09e1 Standard Test Method for Pull-Off Strength of Coatings Using Portable Adhesion Testers," ASTM International, West Conshohocken PA2009.
- [11] "ASTM C633-13 Standard Test Method for Adhesion or Cohesion Strength of Thermal Spray Coatings," ASTM International, West Conshohocken PA2013.
- [12] "ASTM G133-05(2016) Standard Test Method for Linearly Reciprocating Ball-on-Flat Sliding Wear," ASTM International, West Conshohocken PA2016.
- [13] Antelope. (2017, May 4, 2017). *Wearsox*. Available: <http://www.aot-llc.com/Products/WearSox/>
- [14] U. S. I. T. Commission, "Remanufactured Goods: An Overview of the U.S. and Global Industries, Markets, and Trade - USITC Publication 4356," USITC, Ed., ed, 2012.
- [15] K. Cooke, G. Oliver, V. Buchanan, and N. Palmer, "Optimisation of the Electric Wire Arc-Spray Process for Improved Wear Resistance of Sugar Mill Roller Shells," *Surface and Coatings Technology*, vol. 202, pp. 185-188, 2007.
- [16] J. Wilden, J. P. Bergmann, S. Jahn, S. Knapp, F. van Rodijnen, and G. Fischer, "Investigation About the Chrome Steel Wire Arc Spray Process and the Resulting Coating Properties," *ASM International*, vol. 16, pp. 759-767, 2007.
- [17] W. Tillmann, E. Vogli, and M. Abdulgader, "The Correlation Between the Coating Quality and the Moving Direction of the Twin Wire Arc Spraying Gun," *Journal of Thermal Spray Technology*, vol. 19, pp. 409-421, 2010.

- [18] D. J. J. Varacalle, *et al.*, "A Taguchi Experimental Design Study of Twin Wire Electric Arc Sprayed Aluminum Coatings," *ASM International*, vol. 3, pp. 69-74, 1994.
- [19] A. P. Newbery and P. S. Grant, "Oxidation During Electric Arc Spray Forming of Steel," *Journal of Materials Processing Technology*, pp. 259-269, 2006.
- [20] G. Jandin, H. Liao, Z. Q. Feng, and C. Coddet, "Correlations Between Operating Conditions, Microstructure, and Mechanical Properties of Twin Wire Arc Sprayed Steel Coatings," *Materials Science & Engineering*, pp. 298-305, 2003.
- [21] D. J. Varacalle, D. P. Gullen, D. M. Deason, W. Rhodaberger, and E. Sampson, "Effect of Grit-Blasting on Substrate Roughness and Coating Adhesion," *Journal of Thermal Spray Technology*, vol. 15, pp. 348-355, 2006.
- [22] C. Yong-xiong, X. Bin-shi, Y. Liu, L. Xiu-bing, and X. Yi, "Structure and sliding wear behavior of 321 stainless steel/Al Composite Coating Deposited by High Velocity Arc Spraying Technique," *Transactions of Nonferrous Metals Society of China*, vol. 18, pp. 603-609, 2007.
- [23] J. E. Villafuerte, *Modern Cold Spray - Materials, Process, and Applications*: Springer, 2015.
- [24] J. Karthikeyan, "Cold Spray Process," *ASM Handbook, Volume 5A: Thermal Spray Technology*, vol. 5A, pp. 54-59, 2013.
- [25] E. Irissou, J. G. Legoux, A. N. Ryabinin, B. Jodoin, and C. Moreau, "Review on Cold Spray Process and Technology: Part I—Intellectual Property," *Journal of Thermal Spray Technology*, vol. 17, pp. 495-516, 2008.
- [26] G. Bae, Y. Xiong, S. Kumar, K. Kang, and C. Lee, "General aspects of interface bonding in kinetic sprayed coatings," *Acta Materialia*, vol. 56, pp. 4858–4868, 2008.
- [27] E. Irissou, J. G. Legoux, B. Arsenault, and C. Moreau, "Investigation of Al-Al₂O₃ Cold Spray Coating Formation and Properties," *Journal of Thermal Spray Technology*, vol. 16, pp. 661-668, 2007.
- [28] H.-K. Kang and S. B. Kang, "Tungsten/copper composite deposits produced by a cold spray," *Scripta Materialia*, vol. 49, pp. 1169–1174, 2003.
- [29] J. Wang and J. Villafuerte. (2009) Low Pressure Cold Spraying of Tungsten Carbide Composite Coatings. *International Thermal Spray & Surface Engineering*. 1-4. Available: <http://supersonicspray.com/knowledge-docs/en/Low-Pressure-Cold-Spray-of-WC.pdf>
- [30] N. M. Melendez and A. G. McDonald, "Development of WC-based metal matrix composite coatings using low-pressure cold gas dynamic spraying," vol. 214, pp. 101–109, 2013.
- [31] N. M. Melendez, V. V. Narulkar, G. A. Fisher, and A. G. McDonald, "Effect of reinforcing particles on the wear rate of low-pressure cold-sprayed WC-based MMC coatings," vol. 306, pp. 185–195, 2013.
- [32] N. Sacks, "Low pressure cold gas dynamic spraying of tungsten carbide-nickel coatings," *Metal Powder Report*, vol. 71, pp. 356–358, 2016.
- [33] M. Grujicic, C. L. Zhao, W. S. DeRosset, and D. Helfritsch, "Adiabatic shear instability based mechanism for particles/substrate bonding in the cold-gas dynamic-spray process," *Materials and Design*, vol. 25, pp. 681–688, 2004.
- [34] H. C. Rogers, "Adiabatic Plastic Deformation," *Annual Review of Materials Science*, vol. 9, pp. 283-311, 1979.
- [35] U. S. A. R. Laboratory, W. a. M. R. Directorate, M. A. Branch, and S. a. S. Office. (2015, MIL-STD-3021 (W/ CHANGE-2), DEPARTMENT OF DEFENSE MANUFACTURING PROCESS STANDARD: MATERIALS

DEPOSITION, COLD SPRAY (04-MAR-2015). Available: http://everyspec.com/MIL-STD/MIL-STD-3000-9999/MIL-STD-3021_CHG-2_52134/

- [36] H. Assadi, F. Gärtner, T. Stoltenhoff, and H. Kreye, "Bonding mechanism in cold gas spraying," *Acta Materialia*, vol. 51, pp. 4379–4394, 2003.
- [37] T. Stoltenhoff, H. Kreye, and H. J. Richter, "An analysis of the cold spray process and its coatings," *Journal of Thermal Spray Technology*, vol. 11, pp. 542–550, 2002.
- [38] J. Vicek, L. Gimeno, H. Huber, and E. Lugschleider, "A Systematic Approach to Material Eligibility for the Cold Spray Process," in *2003 International Thermal Spray Conference*, Orlando, FL, 2003, pp. 37–45.
- [39] T. Klassen, *et al.*, "Basic principles and application potentials of cold gas spraying," *Materials Science & Engineering Technology*, vol. 41, pp. 575–584, 2010.
- [40] T. Schmidt, F. Gärtner, H. Assadi, and H. Kreye, "Development of a generalized parameter window for cold spray deposition," *Acta materialia*, vol. 54, pp. 729–742, 2005.
- [41] H. Fuknuma, N. Ohno, B. Son, and R. Huang. (2006, *The influence of particle morphology on in-flight particle velocity in cold spray*. Available: <http://plasma.co.jp/about/pdf/2006-4.pdf>
- [42] H. Assadi, *et al.*, "On parameter selection in cold spraying," *Journal of thermal spray technology*, vol. 20, pp. 1161–1176, 2011.
- [43] R. C. Dykhuizen and M. F. Smith, "Gas dynamic principles of cold spray," *Journal of Thermal Spray Technology*, vol. 7, pp. 205–212, 1998.
- [44] F. Raletz, M. Vardelle, and G. Ezo'o, "Critical particle velocity under cold spray conditions," *Surface and Coatings Technology*, vol. 201, pp. 1942–1947, 2006.
- [45] P. S. Phani, D. S. Rao, S. V. Joshi, and G. Sundararajan, "Effect of Process Parameters and Heat Treatments on Properties of Cold Sprayed Copper Coatings," *Journal of Thermal Spray Technology*, vol. 16, pp. 425–434, 2007.
- [46] J. Wu, H. Fan, S. Yoon, H. Kim, and C. Lee, "Measurement of particle velocity and characterization of deposition in aluminum alloy kinetic spraying process," *Applied Surface Science*, vol. 252, pp. 1368–1377, 15 December 2005 2005.
- [47] H. Tabbara, S. Gu, D. G. McCartney, T. S. Price, and P. H. Shipway, "Study on Process Optimization of Cold Gas Spraying," *Journal of Thermal Spray Technology*, vol. 20, pp. 608–620, March 2011 2011.
- [48] A. Moridi, S. Hassani-Gangaraj, M. Guagliano, and M. Dao, "Cold spray coating: review of material systems and future perspectives," *SURFACE ENGINEERING*, vol. 30, pp. 369–395, 2014.
- [49] T. Schmidt. (2006, *The Cold Spray Process and its Optimization*. Available: https://www.hsu-hh.de/download-1.5.1.php?brick_id=JPhURzBBQWhaAW9U
- [50] R. S. T. Inc. (2009, April 18, 2017). *Cold Spray Technology*. Available: <http://www.rusonic.com/tech.htm>
- [51] A. P. Alkhimov, V. F. Kosarev, and S. V. Klinkov, "The features of cold spray nozzle design," *Journal of Thermal Spray Technology*, vol. 10, pp. 375–381, 2001.
- [52] V. Champagne and D. Helfrich, "Critical Assessment 11: Structural repairs by cold spray," *Materials Science and Technology*, vol. 31, pp. 627–634, 2015.

- [53] M. Faccoli, G. Cornacchia, D. Maestrini, G. P. Marconi, and R. Roberti, "Cold Spray Repair of Martensitic Stainless Steel Components," *Journal of Thermal Spray Technology*, vol. 23, pp. 1270-1280, 2014.
- [54] F. Sevilano, P. Poza, C. J. Múnez, S. Vezzù, S. Rech, and A. Trentin, "Cold-Sprayed Ni-Al₂O₃ Coatings for Applications in Power Generation Industry," *Journal of Thermal Spray Technology*, vol. 22, pp. 772-782, 2013.
- [55] D. Wilmot, C. D. Howe, R. Todorovic, and B. Hoiland. (2010) Case Study of Low-Pressure Cold Spray Conductive Coating. *Advanced Materials and Processes*. pp. 63-65. Available: <http://www.asminternational.org/documents/10192/1889953/amp16811p62.pdf/e263837c-3df6-4c3b-8571-d3f61b24656d>
- [56] J. Kim, S. Kim, and J. H. Kim. (2015, April 18, 2017). *Coating Properties of WC-Ni Cold Spray Coating for the Application in Secondary Piping of Nuclear Power Plants*. Available: http://www.kns.org/kns_files/kns/category/34/15A-307%B1%E8%C1%A4%BF%F8.pdf
- [57] P. Nunthavarawong, N. Sacks, and I. Bote, "Effect of powder feed rate on the mechanical properties of WC-5 wt%Ni coatings deposited using low pressure cold spray," *International Journal of Refractory Metals and Hard Materials*, vol. 61, pp. 230–237, 2016.
- [58] K. J. Hodder, J. A. Nychka, and A. G. McDonald, "Comparison of 10 µm and 20 nm Al-Al₂O₃ Metal Matrix Composite Coatings Fabricated by Low-Pressure Cold Gas Dynamic Spraying," *Journal of Thermal Spray Technology*, vol. 23, pp. 839–848, 2014.
- [59] D. Lioma, N. Sacks, and I. Bote, "Cold gas dynamic spraying of WC-Ni cemented carbide coatings," *International Journal of Refractory Metals and Hard Materials*, vol. 49, pp. 365-373, 2015.
- [60] N. B. S. Magagula, N. Sacks, and I. Bote, "Slurry abrasion of WC-4wt%Ni cold-sprayed coatings in synthetic minewater," *Journal of the Southern African Institute of Mining and Metallurgy*, vol. 116, pp. 333-337, 2016.
- [61] P. C. King and M. Jahedi, "Relationship between particle size and deformation in the cold spray process," vol. 256, pp. 1735–1738, 2010.
- [62] K. I. Triantou, D. I. Pantelis, V. Guipont, and M. Jeandin, "Microstructure and tribological behavior of copper and composite copper+alumina cold sprayed coatings for various alumina contents," vol. Volumes 336–337, pp. 96–107, 15 August 2015 2015.
- [63] S. Kumar, G. Bae, and C. Lee, "Deposition characteristics of copper particles on roughened substrates through kinetic spraying," *Applied Surface Science*, vol. 255, pp. 3472–3479, 2009.
- [64] M. Fukumoto, *et al.*, "Effect of Substrate Temperature on Deposition Behavior of Copper Particles on Substrate Surfaces in the Cold Spray Process," *Journal of Thermal Spray Technology*, vol. 16, pp. 643–650, 2007.
- [65] R. Huang, W. Ma, and H. Fukanuma, "Development of ultra-strong adhesive strength coatings using cold spray," *Surface & Coatings Technology*, vol. 258, pp. 832–841, 2014.
- [66] T. Van Steenkiste and J. R. Smith, "Evaluation of coatings produced via kinetic and cold spray processes," *Journal of Thermal Spray Technology*, vol. 13, pp. 274-282, 2003.
- [67] T. Hussain, D. G. McCartney, P. H. Shipway, and D. Zhang, "Bonding Mechanisms in Cold Spraying: The Contributions of Metallurgical and Mechanical Components," *Journal of Thermal Spray Technology*, vol. 18, pp. 364-379, 2009.

- [68] M. M. Sharma, T. J. Eden, and B. T. Golesich, "Effect of Surface Preparation on the Microstructure, Adhesion, and Tensile Properties of Cold-Sprayed Aluminum Coatings on AA2024 Substrates," *Journal of Thermal Spray Technology*, vol. 24, pp. 410-422, 2014.
- [69] T. Marrocco, D. G. McCartney, P. H. Shipway, and A. J. Sturgeon, "Production of titanium deposits by cold-gas dynamic spray: Numerical modeling and experimental characterization," *Journal of Thermal Spray Technology*, vol. 15, pp. 263-272, 2006.
- [70] (2017, September 25, 2017). *Snow Plow Blades*. Available: <http://towmastertruck.com/valley-blades/>
- [71] S. Sampath, X. Y. Jiang, J. Matejicek, L. Prchlik, A. Kulkarni, and A. Vaidya, "Role of thermal spray processing method on the microstructure, residual stress and properties of coatings: an integrated study for Ni-5 wt.%Al bond coats," *Materials Science & Engineering Technology*, vol. 364, pp. 216-231, 2004.
- [72] P. R. Roberge, *Corrosion Engineering*: McGraw-Hill Professional Publishing, 2008.
- [73] E. M. El-Banna, "Effect of preheat on welding of ductile cast iron," *Materials Letters*, vol. 41, pp. 20-26, 1999.
- [74] M. Z. Huq and J. P. Celis, "Expressing wear rate in sliding contacts based on dissipated energy," *Wear*, pp. 375-383, 2002.

9 Appendices

9.1 Appendix A - Ductile Iron Trade Study Data Summary

Material Set: Ductile Iron, Carbon Steel (HSU Cap)	Material type for data - Wrought, Powder, Wire, Welded?	Hardness - Rockwell B (HRB)	Yield Strength (Elastic Limit) (Mpa)	Young's / Elastic modulus (GPa)	Shear modulus / modulus of Rigidity (GPa)	Ultimate Tensile strength (MPa)	Melting Point (°C)	Thermal expansion (CTE @ 20 - 100 C) $\mu\text{m}/\text{m}\cdot^\circ\text{C}$	Corrosion resistance	Machinability
Ductile iron 80-55-06	Wrought	98		159		552		11	Not good	39
...	CS Powder - As sprayed									
...	Wire - As sprayed									
...	Welded	93				581				
1040 carbon steel	Wrought - as rolled	93	415	200	80	620	1520	11.3	Not good	64
...	CS Powder - As sprayed	92								
...	Wire - As sprayed	97								
...	Welded	n/a		n/a		n/a		n/a	n/a	
NiFe Alloy Steels (Invar 36 - 64%Fe 36%Ni) - Annealed	Wrought	80	482.5	141	56	621	1420	1.3	Better than mild steel, not as good as SS	55
...	CS Powder - As sprayed									
...	Wire - As sprayed									
...	Welded	75								
420 SS Annealed	Wrought	100	345	200	77.2	655	1450	10.3	12	50
...	CS Powder - As sprayed	109								
...	Wire - As sprayed	111							Good	
...	Welded								Good	
316L SS	Wrought	79	235	193	77.2	515	1375	16.2	Good	36
...	CS Powder - As sprayed	100								
...	Wire - As sprayed	90							Good	
...	Welded								Good	

Material Set: Steels (SS, Alloy) NiFeCr (Transmission Gear)	Material type for data - Wrought, Powder, Wire, Welded?	Hardness - Rockwell B (HRB)	Yield Strength (Elastic Limit) (Mpa)	Young's / Elastic modulus (GPa)	Shear modulus / modulus of Rigidity (GPa)	Ultimate Tensile strength (MPa)	Melting Point (°C)	Thermal expansion (CTE @ 20 - 100 C) $\mu\text{m/m-}^\circ\text{C}$	Corrosion resistance (PREN for SS)	Galvanic Potential [Corrosion] (volts)
1018 carbon steel	Wrought - as rolled	71	370	200	77	440	1449	11.5	Poor	
...	CS Powder - As sprayed									
...	Wire - As sprayed									
n/a	Welded									
9310 Annealed	Wrought	97	450	190	80	820	1427	11.5	Good	
...	CS Powder - As sprayed	n/a		n/a		n/a		n/a	n/a	
...	Wire - As sprayed	n/a		n/a		n/a		n/a	n/a	
...	Welded									
18-5 SS	Wrought								18	
...	CS Powder - As sprayed									
...	Wire - As sprayed	90								
...	Welded									
420 SS Annealed	Wrought	100	345	200	77.2	655	1450	10.3	12	
420 SS Hardened & Stress Relieved	Wrought	117	1365	200		1580		10.9		
...	CS Powder - As sprayed	109		183.3						
...	Wire - As sprayed	111								
...	Welded									
304L SS	Wrought	82		193		564	1375	16.9	18.1	-0.1 to -0.25
...	CS Powder - As sprayed	n/a		n/a		n/a		n/a	n/a	
...	Wire - As sprayed	95				552				
...	Welded									
316L SS	Wrought - Plate	79	235	193	77.2	515	1375	16.2	24.1	0 to -0.2
...	CS Powder - As sprayed	100		98.43					exhibits a corrosion rate 20 times lower than mild steel substrate but 20-40 times higher than bulk ss 316L	
...	Wire - As sprayed	90								
...	Welded									

Material Set: Steels (SS, Alloy) NiFeCr (Transmission Gear)	Material type for data - Wrought, Powder, Wire, Welded?	Hardness - Rockwell B (HRB)	Yield Strength (Elastic Limit) (Mpa)	Young's / Elastic modulus (GPa)	Shear modulus / modulus of Rigidity (GPa)	Ultimate Tensile strength (MPa)	Melting Point (°C)	Thermal expansion (CTE @ 20 - 100 C) $\mu\text{m}/\text{m}\cdot^\circ\text{C}$	Corrosion resistance (PREN for SS)	Galvanic Potential [Corrosion] (volts)
17-4 PH Steel (H900)	Wrought	114	1170	196		1310	1400	10.8	15	
17-4 PH Steel (Annealed)	Wrought	107	760	196		1030		n/a	Not recommended to use as annealed	
...	Powder - 3D metal printing	101				1050				
...	Wire									
...	Welded									
Inconel 625	Wrought	65		200		724		12.8	Excellent	
...	CS Powder - As sprayed	108								
...	Wire - As sprayed	90				165				
...	Welded									
Inconel 718	Wrought	108		196		1100		13	Excellent	
...	CS Powder - As sprayed	114								
...	Wire - As sprayed	101								
...	Welded	105		25% Elong		1200			Excellent	
Inconel 600	Wrought	80		210		550		13.3	Excellent	
...	CS Powder - As sprayed	n/a		n/a		n/a		n/a	n/a	
...	Wire - As sprayed	n/a		n/a		n/a		n/a	n/a	
...	Welded									
Copper	Wrought	53.5	76	118	45	235	1084	16.8	Excellent	
...	CS Powder - As sprayed									
...	Wire - As sprayed									
...	Welded									
Tungsten-Carbide (WC) - 15% Nickel	Powder - thermal spray		5.8					450		
WC	WC Properties	1733-3600 V (HRC > 78)	432.5	643		450	2870	5.8		
Ni - 200 series annealed (99.6% pure)	Ni Properties	63	148	200		320	1435	13.3		
Ni - 200/201 series cold drawn annealed wire (99.6% pure)		45 - 75	400 - 550	205						
Ni - 200 series cold rolled sheet (99.6% pure)		90	480 - 725			620 - 725				
3CR12	Wrought	97	275	200		450	1430	10.8		